Microanalysis of impactors of the Earth and impact products from the Moon

The origin and evolution of micrometeorites, and tracking bombardment history through chemical and radioisotopic memories of lunar impact spherules.

Simeon Sai Main Hui

March 2011

A thesis submitted for the degree of Doctor of Philosophy of The Australian National University.

DECLARATION

This thesis consists of work carried out at the Research School of Earth Sciences, Australian National University, for the degree of Doctor of Philosophy. I certify that this thesis is my own work, except where otherwise acknowledged, and has not been accepted for the award of any other degree or diploma at any university.

Simeon Sai Main Hui

DEDICATIONS

To my family - for their understanding, support, and dedication to seeing me finish.

To my friends - for I have become a spectre, living up to my nickname. Their company has been limiting the time I spend haunting the hallways and scaring unfortunates linger afterhours.

To Earth Chemistry - the staff and students I spend more time with than my family, in particular those who are always willing to lend a hand during my difficult journey. This department has been my home away from home even though I am, but an honorary member.

To my fellow senior students Seann and Tanya – The last of my cohort, both friends and competitors to the finish line. If this thesis has been good for anything, it is bringing us together during our final leagues.

To the office of the Pink Slippers - With the submission of this thesis will be the changing of the guard. I have found solace in the gifting of the pink slippers. May it serve the next holder as well as it has served me.

And to all other too numerous to mention, you know who you are: colleagues, friends, and fellow students who make up the community. Together, it is this sense of community that has kept me going.

ACKNOWLEDGEMENTS

Firstly, I would like to thank all the members of my supervisory panel (Prof. Trevor Ireland, Dr. Masahiko Honda, Dr. Andrew Christy, and Prof. Richard Arculus) who have all, in some way, contributed to the success of this project. Whether it be proof reading, advice, sharing of technical knowledge or just for a chat (or all of the above), I thank you. A big thank you to Andy for sharing his vast technical knowledge and help perfecting the method employed for the lunar impact spherules. In particular, I would like acknowledge my supervisor, Dr. Marc Norman, for his years of supervision. For the supply of samples for the micrometeorites project and lunar spherules project, I would like to thank Prof. Ralph Harvey of Case Western Reserve University, Cleveland, and the National Aeronautics and Space Agency (NASA) respectively. It is not every day that someone has the chance to handle lunar and other extraterrestrial material. I would also like to thank the Research School of Earth Sciences (RSES) for operating costs (which are significant), and both the RSES and the Australian Federal Government for the scholarship. Being a highly technical project, there are many RSES staff that deserve credit for their contribution to this project. John Maya and Shane Paxton from minerals separation who conducted much of the original work to collect the lunar glasses and who have always been happy to advise on any matters relating to sample separation. A thank you to David Clark and all the members of the RSES workshop for technical advice and readiness to manufacture the equipment I have needed. Then there are all the staff who have helped with calibration, use, treatment of data, and tutelage on the workings of the EMP (Ashley Norris and Dr. Robert Rapp), SEM (Dr. Frank Brink), LA-ICPMS (Dr. Charlotte Allen, Dr. Frances Jenner, and Dr. Guilherme Mallmann), SHRIMP (Dr. Peter Holden and Peter Lanc), and noble gas spectrometers (Dr. Fred Jourdan, and Dr. Marnie Forster). I thank you all. In particular, I would like to thank our host Fred who arranged equipment time (at a subsidised rate!), provided training and expertise during our stay at Curtin University. Lastly, I would like to thank those who have always been available for discussions and advice. Dr. Raquel Salmeron, Prof. Hugh O'Neill, Prof. Malcolm Sambridge and Prof. Ian Jackson have all contributed to the development of many ideas in this thesis. In particular, I want to acknowledge Dr. Charlie Lineweaver for his massive contribution to my knowledge of the statistical arts which were employed in this thesis.

ABSTRACT

This thesis consists of two topics, the study of terrestrially-collected micrometeorites and lunar impact spherules. The purpose of the first project was primarily method development, although a study of micrometeorite petrography, chemistry, atmospheric alteration, and potential origin ensued. A classification system was developed with a focus on transitional internal textures to highlight the sequence of alteration occurring during atmospheric heating. Micrometeorite composition was used to identify potential parent bodies which are likely to be chondritic. More importantly, it was found that iron metal micrometeorites are likely to form due to separation from a stony micrometeorite body due to immiscibility and, following separation, oxidise to form a FeO glassy cap. Failing that they fully oxidise to form iron oxide micrometeorites.

The main topic is the lunar impact spherules which are impact-melts that record their original target composition (major and trace elements), formation age, and integrated exposure age. This is the first study to integrate all these data for individual impact spherules. A method was developed to cater for the requirements of this project and several analytical techniques were tested. The major and trace elements were employed to understand the petrographic characteristics of the impact spherules including the formation of volatile and siderophile crusts and their composition, and how composition affects colour. The compositional data were also used to determine the provenance of the impact spherules and whether they are likely to be produced during impacts into soils or rocks. The first impact spherule age distribution for low potassium, locally-derived impact spherules has also been developed in this study consists of 26 impact spherules. The main features of the formation age distribution are a peak in spherules with ages <400Ma and a minima between 2Ga and 3.2Ga. However, the integrated exposure ages do not exceed 500Ma regardless of the formation age. The greatest achievement of this project is the use of these integrated compositional and age data to constrain selection effects that act on impact spherule records. The contribution of exotic spherules and production of duplicate impact spherules in single impact events was found to contribute minimally to the first order interpretations. Exotic spherules were few in number and duplicate impact spherules more commonly have ages >1Ga indicating that the <400Ma peak in spherule production is not due to overrepresentation.

In essence, the results indicate that the impact spherule record in its current state is not representative of the lunar impact history, but is the product of various selection effects, some of which can be constrained using the techniques developed in this study.

TABLE OF CONTENTS

ELECTRONIC ANNEX

LIST OF FIGURES

LIST OF TABLES

LIST OF EQUATIONS

PREFACE

Bombardment of the Earth-Moon System

Collisions between planetary bodies are an important process in their formation, modification, and evolution. Bombardment of the inner solar system is of particular interest because it has shaped the Earth and evolution of terrestrial life (Hartmann et al., 2000; Lineweaver and Norman, 2009; Ryder, 2002). Reconstruction of the bombardment history of the Earth-Moon system, however, is only possible using records that have been preserved in the terrestrial and lunar environments. Naturally, the preservation of bombardment records is more favourable on the Moon due to the relative lack of geologic and anthropogenic disturbance when compared to the Earth. Currently, there are several types of lunar bombardment records including craters, impact-melt breccias, and terrestrially-collected lunar meteorites. These records are proxies that contain chemical and isotopic memories of discrete impact events from which information such as impact flux and origin can be determined. Lunar impact spherules, the main subject of this thesis, have been recently recognised as a potential lunar bombardment record. Lunar impact spherules are sub-millimetre-sized glasses formed by quenching of impact-melts generated during impact events. Each impact spherule contains the isotopic memory of the time of formation and geochemical memory of the place of impact. Most importantly, lunar impact spherules are the most abundant impact record contained within the lunar regolith.

The Cosmic Spherules Project

The cosmic spherules project is the first step to achieving the goals set out by the lunar impact spherules project. The original motivation for this pilot study was to become familiar with sample handling and analytical methods, and eventually develop a tailored method for the lunar impact spherules project. The cosmic spherules were collected from the Lewis Cliff Ice Tongue, Antarctica and supplied by Professor Ralph Harvey of Case Western University, Cleveland. The similarity in shape and size of the cosmic spherules, as well as the relative ease of obtaining them, makes them an ideal substitute to study before working on the more precious and irreplaceable impact spherules. Unfortunately, the cosmic spherules were found to be unsuitable as a substitute for

methods testing due to an outer coating of glacial flour and heterogeneous internal structure. However, the project was continued since much time and effort had been spent for data collection. The resulting study has been restructured to make use of the petrography and major and trace element data that were collected. Using these data, it has been possible to relate the petrographic and compositional changes experienced by cosmic spherules to their origins and thermal alteration during passage through the Earth's atmosphere.

Lunar Impact Spherules Project

Prior to this project, there were two previous studies of lunar impact spherule that established the formation age distributions of impact spherules from Apollo 12 and 14. Both records, however, show distinct differences in bombardment history. The motivation for this thesis was to establish a third record from an independent site, Apollo 16. Additionally, the aim was to develop a method which would allow integration of major and trace element abundances and radioisotopic ages for individual impact spherules that were hundreds of microns in size. The integration of these data is lacking in previous studies, but provides additional resolution to constrain contributions to the impact flux from exotic events and identify groups of impact spherules related to a single impact event. Effectively, this allows the contributions to particular peaks in the impact record to be assigned to potential causes, thus allowing elimination of selection effects and providing additional information on the geological evolution of the Moon, horizontal transport of particles, and geochemical nature of the impact spherules.

This project requires the development of a method to minimise sample consumption as impact spherules from Apollo 16 were expected to be more difficult to date due to their low potassium content. Although a method was developed, it could not be tested with cosmic spherules as analogues. Attempts to produce spherical particles from known glass standards were unsuccessful. Consequently, theoretical constraints followed by testing conducted on shards of known glass standards was used to determine the actual effects on a variety of analytical apparatuses. A further test of the methods was conducted by recovering lunar impact spherules that were deemed unsuitable for dating

(i.e. small samples with low potassium content). These impact spherules were mounted, polished, re-analysed using more conventional methods, and compared to the results achieved from the previous method.

Thesis Structure

Since there are two topics that are presented in this thesis, the thesis chapters are arranged accordingly:

Presented in Chapter 1 is the study on cosmic spherules, a type of terrestrially-recovered micrometeorite. This chapter provides a brief review of the current micrometeorite and cosmic spherule literature including previous attempts to classify them, their origins, and their compositional characteristics. The remainder of the chapter presents new sets of major and trace element data for cosmic spherules recovered from the Lewis Cliff Ice Tongue deposit in Antarctica and discusses the effects of atmospheric entry on their chemistry and petrography. New insights into the origin of the stony and iron cosmic spherules will be presented.

Chapter 2 describes the development and testing of the method used to prepare and mount the lunar impact spherules presented in chapter 3. The lunar samples are mounted using this method which employs conductive carbon putty, Leit-C-Plast (LCP). The LCP mount is designed to minimise sample loss during preparation and handling during and between analyses. However, analysis of unpolished samples conserves the sample at the expense of lower analytical quality. In this chapter, the effect of unpolished surfaces on the analytical quality were quantified using known glass standards for data acquired using the electron microprobe (EMP), sensitive high-resolution ion microprobe (SHRIMP), and laser ablation – inductively coupled plasma mass spectrometer (LA-ICPMS).

Chapter 3 presents the background for the lunar impact spherules project followed by justification of the lunar impact spherules project. The background includes a summary of the physical processes that occur during impacts that lead to the formation of lunar

impact spherules. Factors that contribute to the petrographic and chemical characteristics of impact spherules are presented including a review of the current impact spherule literature. This is followed by an introduction to the Apollo 16 study site summarising the geological characteristics of the site and region.

Chapter 4 reports the petrographic and chemical characteristics of the impact spherules. Since it has not been possible to evaluate the methods using a less valuable substitute, a number of lunar impact spherules were reanalysed both as unpolished and polished samples. The first portion of this chapter details the results and subsequent identification of a volatile- and siderophile-rich crust. This is followed by an introduction of a visual classification system based on impact spherule shapes, features, and cleanliness. Generic relationships between petrographic features are compared to impact spherule colour, which is a rough indicator of sample chemistry. The database of compositional data acquired from 272 impact spherules is then utilised to determine the overall provenance of impact spherules at the Apollo 16 site based on sample statistics.

Chapter 5 is a short chapter that reports the results from radioisotopic dating of a selection of 30 lunar impact spherules. Formation and exposure ages are described, and the impact spherule record as a whole is discussed.

Chapter 6 aims to identify the potential selection effects that affect the impact spherule record. A review and comparison with previous studies are made, highlighting the potential differences between the results and their significance. This chapter also integrates the compositional data from previous chapters to constrain the contribution of exotic impact spherules and potentially duplicate impact spherules from the overall record. Implications for the bombardment flux as "seen" by impact spherules, and bombardment flux as a whole, are discussed with an emphasis on possible biases in the records. Conclusions about this project are drawn and recommendations for future work are proposed.

CHAPTER 1:

COSMIC SPHERULES PROJECT

1.1 Chapter Outline

This chapter begins with an introduction into the project and collection site, the Lewis Cliff Ice Tongue, Antarctica. Prior to this study, only 32 micrometeorites from the Lewis Cliff deposit were described. This is followed by a brief review of the cosmic spherule literature, including descriptions of environments from which micrometeorites and cosmic spherules have been collected, current classification schemes and main textural groups, and the compositional characteristics of the cosmic spherules. In the results section, major element, trace element, and petrographic data are presented for an additional 127 cosmic spherules from the Lewis Cliff deposit. Based on the results, an alternative classification scheme, which focuses more on transitional features, is proposed. The presence of transitional textures makes petrographic classification difficult to apply without a greater understanding of the effects of thermal alteration, which obscures the nature of the precursor material. Using optical microscope petrography, supported by scanning electron micrographs and major element and trace element compositions, this alternative classification builds on the earlier work of Taylor et al. (2000). The discussion revolves around the origin of the cosmic spherules and evolution of textures and compositions that preserve information about the conditions experienced by cosmic spherules during passage through the Earth's atmosphere.

1.2 Introduction

1.2.1 Objectives

The original aims of the cosmic spherules project were to gain familiarity with handling and analysing small particles, and to develop a technique for the lunar impact spherules project using the cosmic spherules as a test case. Petrography and major and trace elements were collected for this purpose. Cosmic spherules, however, are an unsuitable proxy for lunar glasses because of their glacial coatings and heterogeneous internal mineralogy. The data collected for this purpose was substantial and consequently used

to study the effects of atmospheric entry and determine the likely origins of the cosmic spherules. To address some ambiguities on the origin, formation and cross-collection relationships of cosmic spherules, this project will bolster the amount of described cosmic spherules from the Antarctic Surface collection.

In summary, the aims of the project are to:

1) Gain experience and expertise in working with small extraterrestrial particles.
2) Increase the amount of described cosmic spherules in the Antarctic Surface collection by providing new major element compositions.
3) Develop a classification system for use under the petrographic microscope.
4) Provide trace element analyses in an attempt to determine the origin and formation of spherules from this collection.
5) Draw links between the major and trace element compositions and petrography relating them to alteration processes.

1.2.2 Location

Micrometeorites for this project were collected from the Lewis Cliff Meteorite Grounds in the Walcott Névé region of the Trans-Antarctic Mountains, Antarctica (see Figure 1), more specifically, from moraine at Station D on the tip of the Lewis Cliff Ice Tongue. The following section is a brief summary of the Lewis Cliff Deposit given in Cassidy et al. (1992) and Harvey (2003).

The Lewis Cliff meteorite deposits consist of three sections: the Lewis Cliff Ice Tongue, the nearby Meteorite Moraine and the South Lewis Cliff Icefields. The Lewis Cliff Ice Tongue and South Lewis Cliff Icefield were first discovered in 1985. The Ice Tongue runs along the bottom of the Lewis Cliff, slopes down to the north and ends with a large terminal moraine. It has a relief of 75m and is separated into an upper and lower section by an escarpment about halfway down. Strong winds blow from south to north down the length of the glacier, which has redistributed material in the area. To the east of the Ice Tongue lies the Meteorite Moraine. The Meteorite Moraine serves as a barrier to aeolian transport, creating a natural trap for aeolian material. This area is rich in meteorite

material, but it is mixed with terrestrial rocks. Located 3km to the south is the South Lewis Icefield, which is an example of a blue ice meteorite trap.

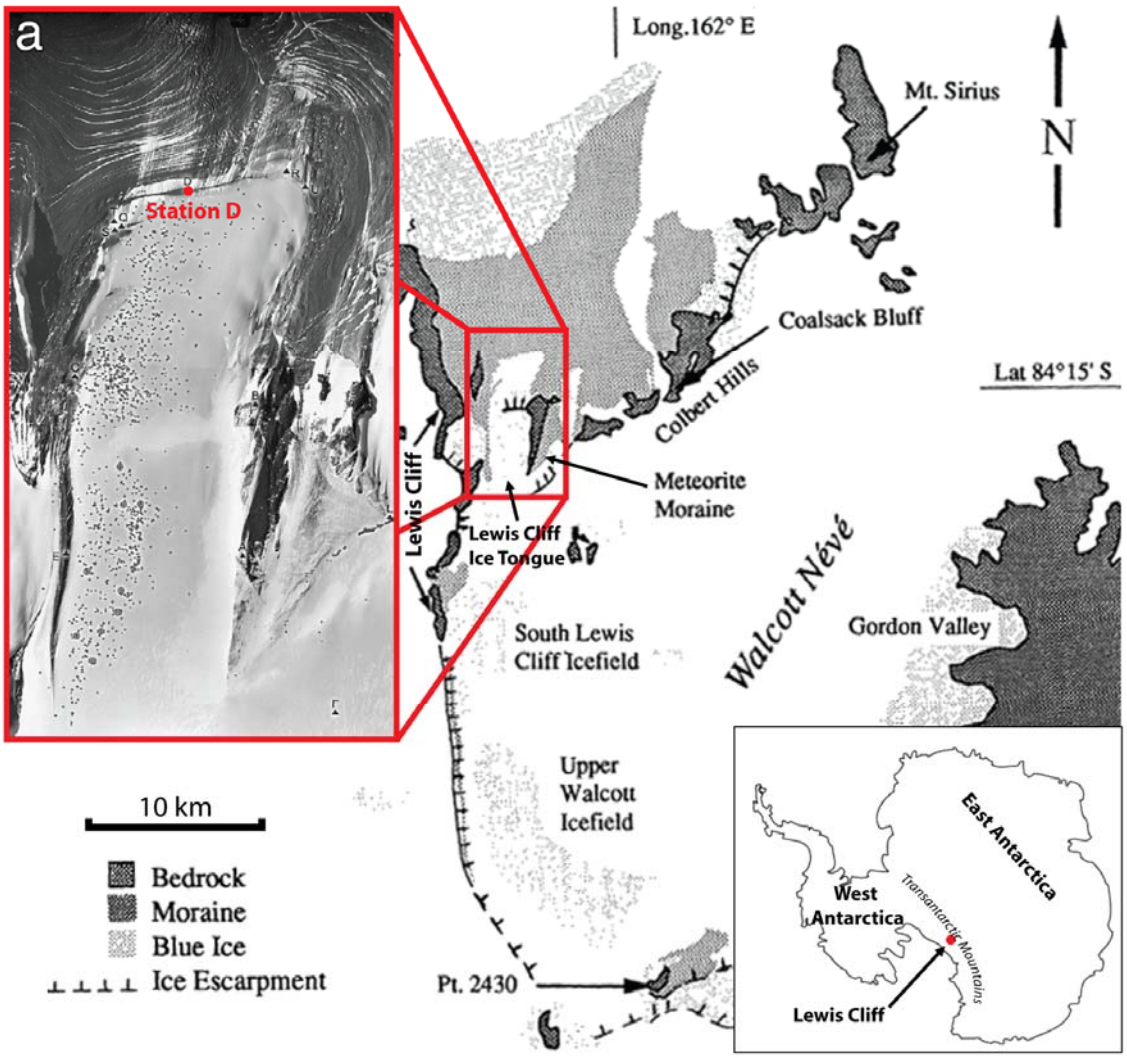

Figure 1. Map of the Walcott Névé region of the Transantarctic Mountains, Antarctica. Inset a) shows a mosaic of vertical aerial photographs of the Lewis Cliff Ice Tongue (LCIT) overlain with points where meteorites have been found. Samples for this project were collected from Station D on the tip of the ice tongue.

Modified from Cassidy et al. (1992) and Harvey (2003)

1.3 Background

Micrometeorites are extraterrestrial particles less than 1mm in size, collected from the Earth's surface. They have been accumulating on the Earth's surface over long periods of time, and are therefore a valuable window into the past and present composition of materials accreted to the Earth. Micrometeorites contribute an estimated 30,000 tons of extraterrestrial material per year to Earth (Love and Brownlee, 1993) and they sample a variety of different extraterrestrial materials. However, the passage of these particles through the Earth's atmosphere can thermally alter the particles in a number of ways. Micrometeorites that have experienced melting during passage through the Earth's atmosphere are recrystallised into particles known as cosmic spherules. As such, it is important that the alteration processes are studied, to better understand the nature of micrometeorite precursors and the accretion history of the Earth.

1.3.1 Micrometeorite Collections

Micrometeorites were first described and identified as extraterrestrial particles as early as 1891 by Murray and Renard (1891). After Murray and Renard (1891), micrometeorites found in deep sea sediments (Brownlee et al., 1979), and terrestrial sediments (Czajkowski et al., 1983) including swamps (Krinov, 1959), desert sands (Fredriksson and Gowdy, 1963), and even Archaean terrains (Deutsch et al., 1998), were recognised. Recent recovery efforts are centred on deposits of micrometeorites from Greenland and Antarctica since Maurette et al. (1986) and Yiou and Raisbeck (1987) respectively, discovered locations where natural processes concentrate micrometeorites (known as "stranding surfaces" or traps). Antarctica in particular, has been identified as a suitable location for micrometeorite collection because it has colder summers, which prevent the formation of melted ice water at most micrometeorite collection sites (Maurette, 2006). Antarctica is also relatively isolated from continental wind-borne dust which must travel over 2,500km over the oceans to reach it. According to Maurette (2006), wind-borne dust and grains greater than about 20 microns in size tend to settle into the oceans before reaching Antarctica. Consequently, terrestrial matter is less abundant in the stranding surfaces and results in less dilution, therefore easier recovery, of micrometeorites.

The largest micrometeorite collections are found at a number of locations in Antarctica (Harvey and Maurette, 1991; Iwata and Imae, 2002; Maurette et al., 1991; Rochette et al., 2008; Taylor et al., 2000; Yada and Kojima, 2000), Greenland (Maurette et al., 1986; Robin et al., 1990), and from the deep sea sediments of the Pacific Ocean (Blanchard et al., 1980; Brownlee et al., 1997), just to name a few. Of these collections, cosmic spherules can be grouped into four types of deposits: the Deep Sea Spherules (DSS) (Blanchard et al., 1980; Brownlee et al., 1997), Greenland Spherules (GS) (Robin et al., 1990), the Antarctic Surface (AS) (Harvey and Maurette, 1991), and South Pole Well Water (SPWW) (Taylor et al., 1998). A short description of these deposits is given below.

Deep Sea Spherule deposit (DSS)

One of the earliest studies of micrometeorites from deep sea sediments was conducted by Blanchard et al. (1980) who extracted over 700 cosmic spherules from box cores of mid-Pacific abyssal clays ~5000m deep. One hundred of these were sectioned, described and analysed leading to an early classification of the cosmic spherules. A later collection of over 400 cosmic spherules were recovered in 1976 using a giant tow magnet dragged along the Pacific Ocean floor at 5300m depth 1000km east of Hawaii (Brownlee et al., 1979). The results for this study are published in Brownlee et al. (1997) and supplemented by cosmic spherules from other collections due to the collection mechanism only sampling particles >100μm in size and biasing toward magnetic particles (Brownlee et al., 1997). Weathering, more specifically seawater etching, affects spherules from this deposit as it removes interstitial glass from the exposed edges of the spherule (Brownlee et al., 1997).

Greenland Spherules deposit (GS)

In 1984 and 1987 attempts were made to collect micrometeorites from the melt zones of the Greenland ice sheets and the Jakobson ice field both near Søndre Strømfiord (Maurette, 2006). Dark sediment, dubbed “cryoconites”, was recovered from the bottom of blue lakes formed from the melting of ice. A total of ~2000 cosmic spherules were collected from these deposits (Maurette et al., 1987), but few appear to have been

studied. This was probably due to the environment from which the samples were collected. According to Maurette (2006), secretions from biogenic activity, etching of the periphery of the sample (also see Maurette et al., 1986), destruction of friable particles due to the harsh purification methods employed, and constant aqueous alteration destroy metals and sulfides and leach carbonates and sulfates. All these activities limited the usefulness of the samples. These problems triggered the move to collect samples from Antarctica, where weathering is expected to be less pronounced since the ice is less likely to melt (Maurette, 2006).

Antarctic Surface Deposits (AS)

There are a number of localities on the Antarctic surface from which micrometeorites have been recovered. These localities are typically in regions that naturally concentrate micrometeorites, such as blue ice stranding surfaces and moraine deposits. Micrometeorites are typically collected by artificially melting ice collected from these deposits to liberate micrometeorite-rich glacial sands.

Blue ice stranding surfaces are a typical target for macro and micro meteorite collections. The Cap-Prudhomme (Kurat et al., 1994; Maurette et al., 1991), Yamato Mountains (Yada et al., 2004; Yada and Kojima, 2000), and the Sôya Coast (Iwata and Imae, 2002) are examples of locations that contain such deposits. Blue ice is formed in front of mountain barriers where the buttressing effect (two opposing forces uplifting ice at the contact) forces the deeper, highly compressed ice to the surface (Corti et al., 2003). The uplifted section of ice experiences increased wind ablation and weathering. This process exposes old material that once landed on the surface and was incorporated into the ice. Maurette (2006) also notes that it is possible for material on the surface, especially micrometeorites, to be incorporated into the ice. This is because the micrometeorites are dark and are easily heated by solar radiation, allowing them to melt their way into the ice until they freeze again. Although this process increases micrometeorite yield, Maurette (2006) argues it can also be responsible for the leaching of elements such as Ca, S and Ni.

Moraine deposits have also been targets of meteorite collection expeditions because they are a rich source of meteorites (Harvey and Maurette, 1991; Koeberl and Hagen, 1989). Moraines are deposition sites of weathered (and transported) glacial material. In Antarctica, sub-surface obstructions can also force weathered material onto the ice surface to form a moraine. The Elephant Moraine and moraines at the Lewis Cliff are examples of moraine deposits (Figure 2). There is no bedrock exposure and only bare ice is present in the $50km^2$ collection grounds (Cassidy et al., 1992). Moraines are effective wind barriers and can accumulate micrometeorites that have undergone aeolian transport (Harvey, 2003). However, according to Cassidy et al. (1992), the work needed to collect meteorites from these deposits is demanding since there are literally thousands of rocks to search, most of which are terrestrial.

South Pole Well Water deposit (SPWW)

More recently, a source of micrometeorites known as the South Pole Well Water deposit has been discovered in Antarctica (Figure 2). Taylor et al. (1998) recovered the first micrometeorites from this collection at the Amundsen-Scott South Pole station drinking water well. Micrometeorites are easily included into the Antarctic ices and are likely to be quite numerous compared to the larger meteorites. This makes the ice a natural source of micrometeorites, although there is no natural concentration mechanism. However, as the ice is melted to recover drinking water, micrometeorites (and other particles) are liberated and sink to the bottom of the well, naturally increasing the yield of micrometeorites. The potential for a micrometeorite collection was realised and exploited by researchers pumping warm water into the well to enhance the liberation of the extraterrestrial particles. Recovery of the liberated particles is done by using specialised suction equipment (large underwater vacuum cleaner). Over 3,000 micrometeorites have been recovered from this deposit already (Taylor et al., 2005a).

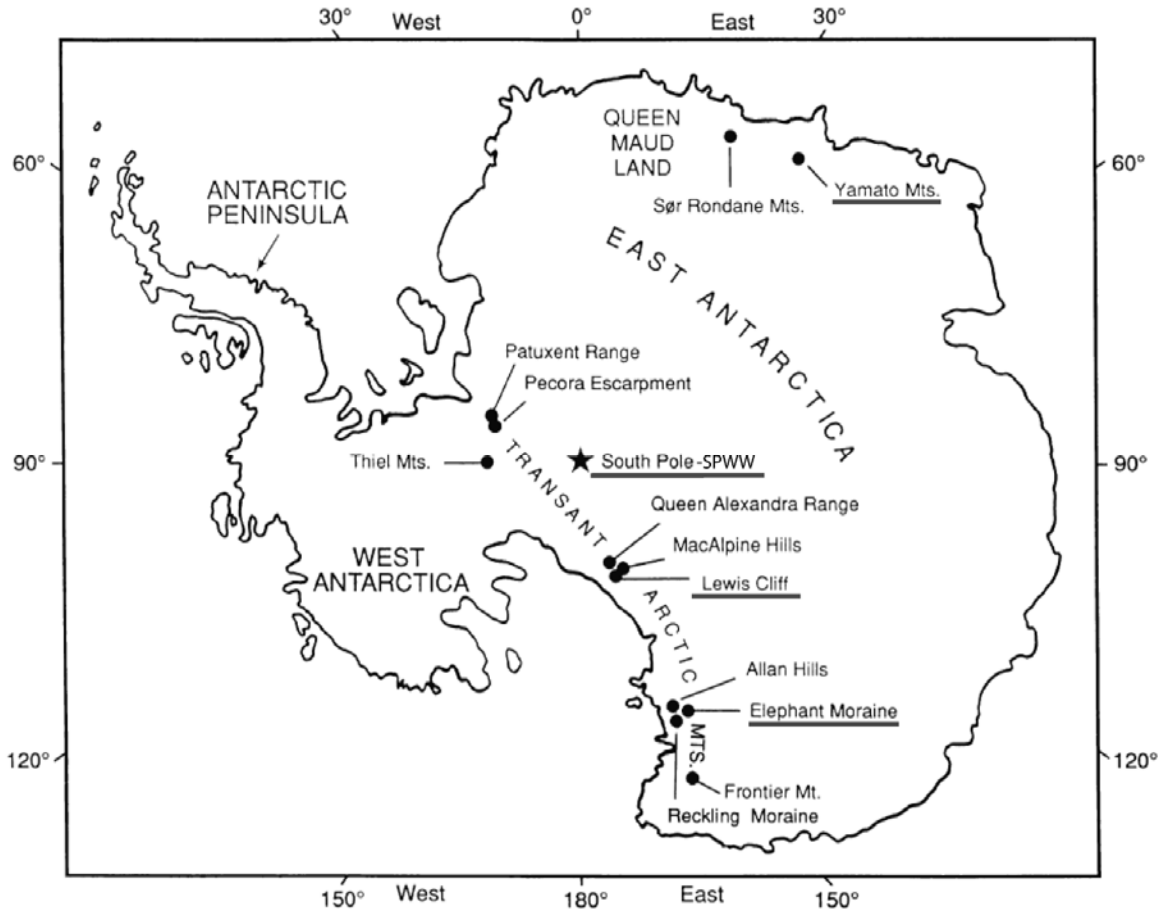

Figure 2. Map of Antarctica showing the locations of stranding surfaces (traps) where major concentrations of meteorites have been found. Underlined are the several meteorite collections from Antarctica: the South Pole Well Water deposit at the South Pole, Yamato Mountains, Elephant moraine, and the Lewis Cliff deposits.

Modified from Cassidy et al. (1992)

1.3.2 Types of Micrometeorites

Micrometeorites are frequently compared and contrasted to their macro-meteorite counterparts, in particular, to aggregates of silicate, sulfide, and metal known as chondrites. Chondites have chemical compositions that closely approach that of the sun, and are divided into three supergroups: carbonaceous, ordinary, and enstatite chondrites (Hutchison, 2004). Micrometeorites are typically associated with the carbonaceous and ordinary supergroups. Carbonaceous chondrites are further subdivided into twelve subgroups (CI, CM, CO, CV, CK, CR, CH, and four ungrouped) named after prominent type examples (e.g. CI-Carbonaceous Ivuna) that exhibit different proportions of refractory to moderately volatile elements (Wasson and Kallemeyn, 1988). Ordinary chondrites, the most common group, are further subdivided into three subgroups (H, L, and LL) based on the decreasing ratio of metal to silicate from H to LL subgroups (Wasson and Kallemeyn, 1988).

Currently there are no standard classification systems for micrometeorites, although recently Genge et al. (2008) proposed a unified micrometeorite classification scheme. In general, most of the literature refers to three groups of micrometeorites listed below.

Unmelted Micrometeorites

The first group is the unmelted micrometeorites, which escaped significant frictional melting from atmospheric entry. Taylor et al. (2005b) found that the abundance of unmelted particles increases with decreasing sizes, which was predicted by Love and Brownlee (1991) who modelled the effect of entry conditions on extraterrestrial particles. The unmelted micrometeorites are further separated into two subgroups, fine-grained and coarse-grained varieties, both of which are irregular in shape (Figure 3).

The fine-grained variety has been least heated and are composed of a matrix of tiny, and highly unequilibrated, mineral assemblages which may contain larger inclusions. Within this assemblage there are refractory nebular condensates (Calcium Aluminium Inclusions: CAIs) similar in oxygen isotope composition to those found in the CI, CM

and CR groups of carbonaceous chondrites (Maurette, 2006). Also present in some fine-grained unmelted micrometeorites are magnetite framboids which relates them directly to the CI chondrites (Maurette, 2006).

The coarse-grained variety is much rarer than the fine-grained unmelted micrometeorites and contains a "few single crystals of anhydrous silicate (pyroxene and olivine in about the same abundance)" (Maurette, 2006). According to Brownlee et al. (1980), coarse-grained unmelted micrometeorites from the Deep Sea Spherule collection contain Fe and Ni metal spheres within the silicate portions, as well as troilite as an interstitial mineral. These characteristics, as well as the occasional fusion crust associated with this type of micrometeorite, prove that these particles are of extraterrestrial origin. Based on chemical composition, Kurat et al. (1994) suggested that unmelted micrometeorites are most similar to CM chondrites, although they show signs of terrestrial alteration.

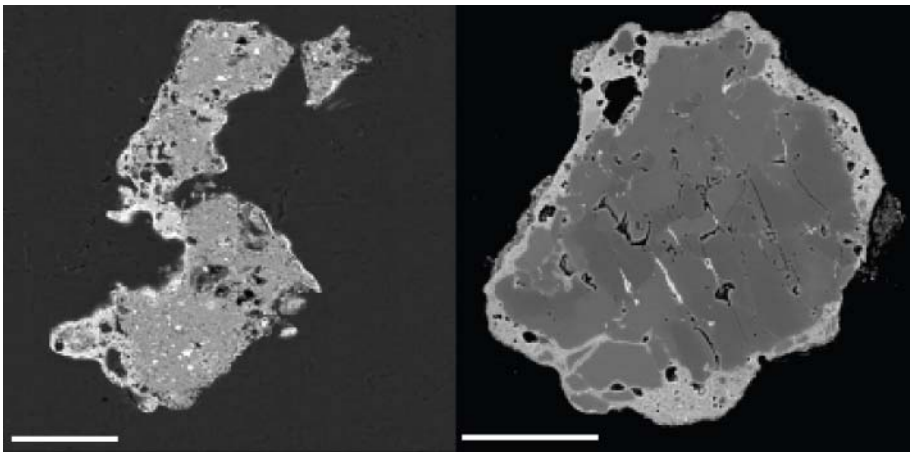

Figure 3. Scanning electron micrographs of unmelted micrometeorites. The fine-grained (left) and coarse-grained (right) micrometeorites are both irregular in shape. Scale bars are 50μm in length.

Micrographs from Taylor et al. (2005b)

Scoriaceous Micrometeorites

The second group is the scoriaceous micrometeorites (Figure 4), which are unique because they are highly vesicular. This type of micrometeorite is thought to represent a partially molten transition between the unmelted micrometeorites and the melted cosmic spherules discussed below. These were originally fine grained micrometeorites that have experienced atmospheric heating causing the loss or partial loss of volatiles such as water, organics, and hydrous minerals (Kurat et al., 1994). Mineralogically, these spherules are heterogeneous and contain relic olivine of varying composition, magnetite, chromite, and iron/iron nickel sulfides (Taylor et al., 2000).

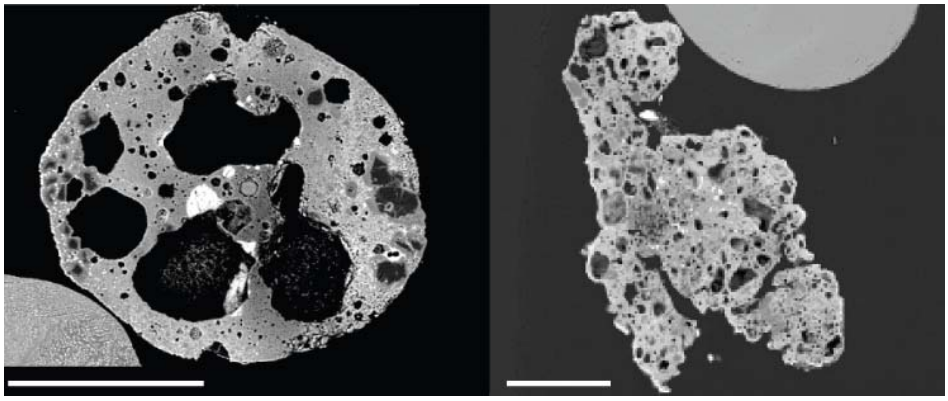

Figure 4. Scanning electron micrographs of scoriaceous (right) micrometeorites. Scale bars are 100μm in length.

Micrographs from Taylor et al. (2005b)

Cosmic Spherules

The third group are the cosmic spherules, which have experienced the greatest amount of heating from entering the Earth's atmosphere (Figure 5). The description adopted by Maurette (2006) indicates that "cosmic spherules are micrometeorites that were fully melted upon atmospheric entry" although relic grains are found in particles that could be classified as cosmic spherules. However, Taylor et al. (2000) chose to define cosmic spherules as partially to wholly melted micrometeorites to accommodate cosmic spherule-like particles that contain relic grains. A large portion of most micrometeorite

collections consists of cosmic spherules, which are found in greater abundances in small size fractions (Maurette, 2006).

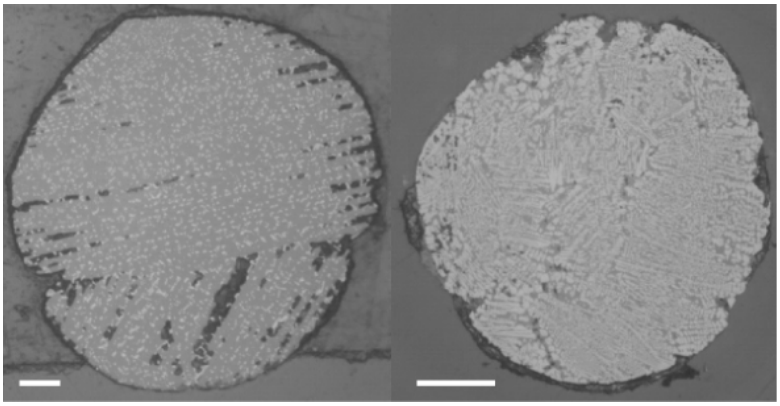

Figure 5. Polished sections of cosmic spherules from the Lewis Cliff Ice Tongue, Antarctica viewed under a petrographic microscope. Scale bars are 100μm in length.

1.3.3 Cosmic Spherule Textures and Composition

Several papers have described the textures of cosmic spherules, but no standard classification has yet to be adopted. One of the most recent and comprehensive classifications was developed by Taylor et al. (2000) which was later incorporated into the recent classification by Genge et al. (2008). In the Taylor et al. (2000) classification, there are two broad groups: the iron spherules, which consist of petrographically bright phases such as iron metals or iron oxides (i.e. magnetite), and the stony spherules which contain predominately silicate glass or olivine.

Stony Spherules

The stony spherules are subdivided into a number of classes based on their petrographic textures. Each texture appears to represent different degrees of heating experienced by the micrometeorite prior to quenching into a cosmic spherule (Taylor et al., 2005a). The following sequence of cosmic spherule textures from least to most heated was established in Taylor et al. (2005a), based on the change in composition of refractory versus volatile major elements.

1. "Relic grain-bearing" cosmic spherules are the least heated as they contain relic grains of olivine, metal, or sulfides that were not completely melted.
2. Porphyritic spherules contain equidimensional olivine and magnetite crystals in interstitial glass.
3. Barred olivine textures contain "parallel band(s) of euhedral crystals with magnetite and glass occupying the interstitial regions" (Blanchard et al., 1980).
4. Cosmic spherules that have cryptocrystalline textures appear glassy or featureless, but show structure under cross-polarisation; they have also been referred to as "glassy spherules" (Taylor et al., 2000).
5. Glass, or vitreous, spherules are highly rounded and consist of mafic glass. Oddly, the glass spherules also fit the description of cryptocrystalline textures as they show internal structure in a scanning electron micrograph presented in Maurette et al. (1986). However, Maurette et al. (1986) also noted that their absence in the DSS deposits may indicate that they are more fragile than cryptocrystalline textures. Additionally, the composition is more siliceous than cosmic spherules with cryptocrystalline textures (Taylor et al., 2005a).
6. Spherules enriched in refractory major elements Ca, Al, and Ti are coined Calcium Aluminium Titanium-rich (CAT) spherules (Taylor et al., 2005a; Taylor et al., 2000) and are thought to have experienced the most heating. Petrographically, CAT textures resemble barred olivine textures, but lack magnetite.

Overall, the original composition of stony cosmic spherules appears to be chondritic, based on a combination of major element and minor element compositions, mineralogy, and various isotopic studies (e.g. see Blanchard et al., 1980; Brownlee et al., 1997; Clayton et al., 1986; Koeberl and Hagen, 1989; Taylor et al., 2005a). However, Brownlee et al. (1997) and Taylor et al. (2000) both indicate that most stony spherules are depleted in siderophile (i.e. Fe, Ni, Co) and volatile (i.e. Na, S) elements relative to chondritic compositions for the DSS and SPWW collections, respectively. The volatile depletion can be attributed to the vaporisation during atmospheric entry (Greshake et al., 1998). The depletion of siderophile elements, however, is still a controversial topic.

Iron Spherules

Iron spherules are subdivided into 2 types, the I-type and the G-Type. These terms are based on descriptions by Blanchard et al. (1980) who define I-type (Iron type) spherules as cosmic spherules that consist mostly of iron (magnetite, wustite, or hematite) and nickel oxides with or without Fe/Ni metal (see also Brownlee, 1985). The Fe oxide I-types tend to have >60wt.% Fe and <10wt.% Ni content, whereas the metallic Fe/Ni I-types can have equal amounts of Fe and Ni (Robin et al., 1987). A trace element study conducted by Nozaki et al. (1998) found that these spherules are enriched in Ni and Co and depleted in Cr, Ga, and Ge.

G-type (Glassy type) spherules are distinguished from I-types by the intergrowth of magnetite in a matrix of interstitial glass, which produces a dendritic texture. Like the I-type spherules, they consist mostly of Fe and Ni; however, the G-type also contains a significant silicate component (Si, Mg, Al, Ca: Blanchard et al., 1980). Compositionally, G-type spherules have <60wt.% Fe and >8wt.% silicate components (Robin et al., 1987). Despite being coined a "glassy" spherule, particles with such textures can have a high percentage of Fe and Ni oxides, like the I-types. G-type spherules are not to be confused with glassy spherules, which can also refer to a type of stony cryptocrystalline cosmic spherule.

Cross-Collection Compositional Characteristics

In general, most of the large cosmic spherule collections have spherules that are texturally and chemically similar to each other. To demonstrate this point, Taylor et al. (2000) has plotted the major components (Mg, Fe, Si) of all cosmic spherules on a ternary diagram (Figure 9). In general, this figure shows a cluster of stony cosmic spherules around the middle of each ternary diagram. Although unlabelled, cosmic spherule textures are also tied into this diagram. Glassy textures tend to plot closer to the Fe poor side of the diagram. On the iron rich side are iron cosmic spherules, I-types are closest to the Fe corner, while G-types create the apparent line that joins the stony and iron cosmic spherule groups on the DSS collection (Brownlee et al., 1997). The marked difference in abundance of Fe-rich spherules grading to more

silicate spherules in the DSS compared to the other collections is attributed to their collection method which has preferentially collected more magnetic spherules creating a sampling bias. However, major element data for the Antarctic surface collection is sparse compared to the other collections because fewer spherules were studied. Hence, it is hard to draw definitive similarities between the AS and other collections. This project has helped fill this gap, as discussed in the remainder of this chapter.

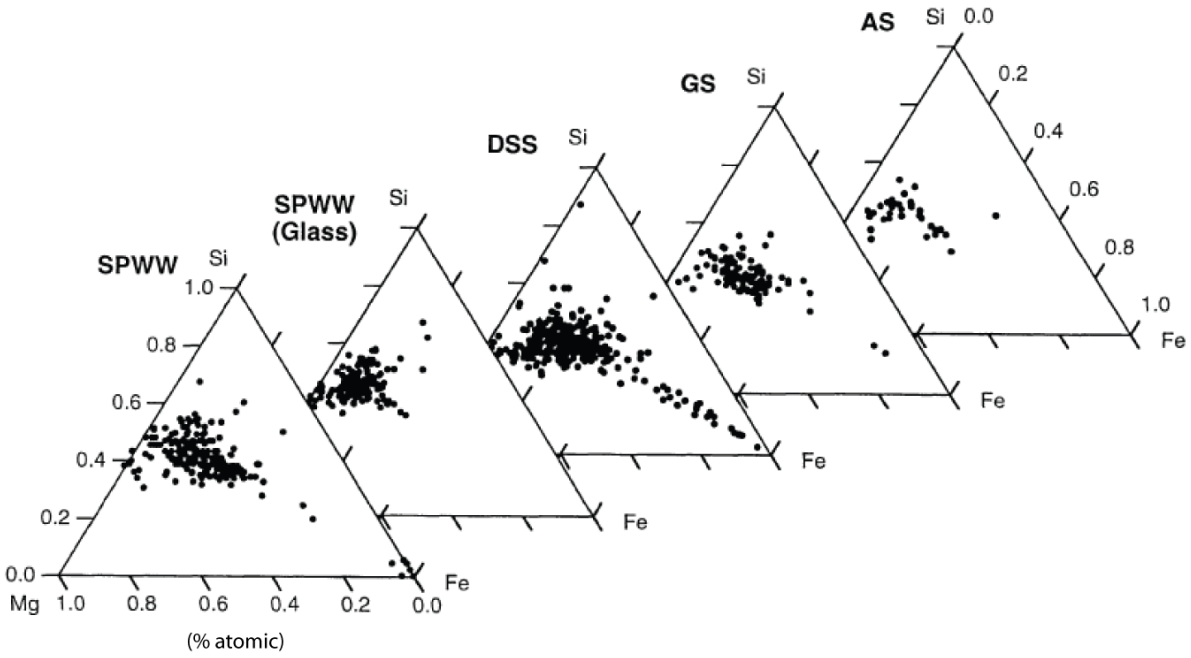

Figure 6. Magnesium, Si, Fe (atom) ternary diagrams illustrating where SPWW spherules plot relative to other large spherule collections. (a) Energy-dispersive x-ray analyses of 240 SPWW spherules. (b) Microprobe analyses of 169 SPWW glass spherules (different particles from those shown in (a). (c) 500 deep-sea spherules plotted using data from Brownlee et al. (1997). (d) Greenland spherules (72 stony, 46 glass) from Robin (1988). (e) Antarctic surface spherule data (12 barred olivine, 20 glass) from Harvey and Maurette (1991).

Diagram and caption from Taylor et al. (2000)

1.4 Method

Sediment from the moraine of the Lewis Cliff Ice Tongue was collected by Professor Ralph Harvey of Case Western Reserve University, Cleveland and collaborators using large stainless steel spoons and stored in Nalgene containers. The sediment was then warmed slowly in flow hoods to remove snow and ice, and the dried material was provided for this project.

Further separation of the dried material was conducted at the Research School of Earth Sciences (RSES), Australian National University (ANU). The sediment was cleaned of adhering material using a combination of ultrasonication in ethanol, soapy water, and rinsing with ultrapure water. A stainless steel sieve was used to remove the coarse pebbles (>1.4mm). The remaining material was split into two size fractions using a 420µm stainless steel sieve (1.44mm-420µm and <420µm). Nylon sieves were then used to further separate the <420µm material into finer fractions (100µm-420µm and 50µm-100µm). The remaining material was retained as a <50µm fraction. Each fraction (except for the <50µm) was further processed into heavy and light fractions by Shane Paxton from mineral separations RSES using 2.96g/cm^3 and 3.3g/cm^3 heavy liquids. Using a hand magnet, highly magnetic material from each fraction was separated and stored separately.

Using fine-point tweezers, single-hair brushes and a binocular microscope, spherular objects (inferred to be extraterrestrial) were hand-picked from all size and density fractions of the moraine material. A calibrated camera unit attached to the microscope was used to measure the long and short axes of all cosmic spherules. A total of 132 spherules were mounted in epoxy resin, cut, and polished to expose the interior of the samples. ImageJ image processing software (Rasband, 1997-2008) was used to determine the percent coverage of mineral phases on photographs of the exposed surface.

Major element compositions were determined using the JEOL 6400 scanning electron microscope (SEM) at the Electron Microscopy Unit (EMU) of the Australian National University. The instrument was set up and calibrated by Dr. Frank Brink prior to use. A suite of standard elements was analysed including: Na, Mg, Al, Si, S, K, Ca, Ti, Cr, Mn, Fe, Ni and Co. Most elements had been calibrated between March to May of 2007 (analyses conducted on May 2007). Mn and Co were calibrated in July and August in 2005 respectively. Using energy-dispersive x-ray analysis (EDXA), major elements were measured on individual phases using fixed spot beam analyses (~5μm) where possible, while bulk element analyses were conducted by beam rastering adjusted to encompass the sample surface. Quantitative compositions were calculated using the ZAF method (3 iterations). Beam currents were set to 15kV. Data from samples with raw totals lower than 85% were discarded; the remaining analyses were normalised to 100% totals. Metallic Fe and Ni in some cosmic spherules were distinguished from oxide equivalents using total sums based on calculations with and without oxygen.

Half of the sample population (70 spherules, >120μm diameter) were analysed for trace element abundances using a Laser Ablation-Inductively Couple Mass Spectrometry (LA-ICP-MS) system at RSES. The system consists of an ArF^+ Excimer (193nm) laser and an Agilent 7500 quadrupole ICP-MS. Ablation was conducted under a He + H atmosphere, and ablation products mixed with an Ar carrier gas for transport to the ICP-MS. A description of the instrumentation is provided by Eggins et al. (1998). The instrument was tuned for optimum sensitivity by Dr. Charlotte Allen prior to analysis. Multiple analyses on single spherules were undertaken where possible, with spot diameters of 70μm and 54μm for smaller spherules at a laser repetition rate of 5Hz. For stony spherules, data were standardised using NIST612 glass calibrated to BHVO-2G, BIR-1G and BCR-2G USGS glasses (See Norman et al., 2004 for preferred values). Each analysis was normalised to CaO wt.% for stony cosmic spherules. For iron-rich (I-type) spherules, data were normalised to Fe wt% using NIST612 glass, the Lombard iron meteorite and synthetic sulfide standards (GXR-1, STDGL, RTS-3, RTS-4 each from Norman et al., 2003a) for calibration of element sensitivities. The total analysis time for each sample was 80 seconds, preceded by a 30 second background on the

carrier gas prior to each analysis. LAB-RAT software developed by Kallio (2007) was employed for data reduction.

1.5 Results

1.5.1 Petrography and Classification

An important consideration for classification of cosmic spherules is the wide variety of textures, including numerous examples of transitional types, which result from the continuum of conditions experienced during atmospheric entry. Spherule textures result from an interplay of heating intensity and duration, followed by rapid cooling, which are in turn controlled by factors such as angle of entry, velocity of the particle, and the size of the particle (Love and Brownlee, 1991). In combination, these inputs (and perhaps others) generate a range of cosmic spherule textures from least to most thermally altered. Current classification schemes focus on well-defined examples of cosmic spherule textures, but in fact most spherules have textures that could be considered as 'transitional' between the type examples. The following classification builds on previous efforts (Genge et al., 2008; Taylor et al., 2000) by emphasising transitional textures and their relation to thermal alteration. In this project, a cosmic spherule is defined as an approximately spherular micrometeorite that has experienced partial to significant thermal alteration during passage through the Earth's atmosphere. Thermal alteration has created textures that indicate partial melting (i.e. containing relic materials) through to those that have experienced complete melting. The descriptions of cosmic spherules are presented in Table 2 and Table 1 with corresponding images, as viewed under a reflected light petrographic microscope and scanning electron microscope, in Figure 8 and Figure 7 respectively. A preliminary version of this classification and geochemical data was presented in Hui et al. (2007).

Table 1. Petrographic description of Stony/Silicate Cosmic Spherules as seen under a petrographic microscope and in scanning electron micrographs. Please see Figure 7 for the actual images.

	Description
Relic Grain Bearing (RGB-Type) Fig. 12-1	These cosmic spherules consist mostly of minerals from precursors that have not been melted. According to Taylor et al. (2000), the relic grains can be olivine, metal or sulfide grains. Although the relic grains are not readily recognisable under the petrographic microscope they contrast with the surrounding material in scanning electron micrographs. Olivine crystals with inclusions of metallic Fe/Ni and sulfides suggest they are relic materials typical of RGB-Type spherules. Newly crystallised olivine will often envelop relic material. The presence of relic material indicates that these types of spherules have experienced the least amount of heating.
Micro-Porphyritic (MP-Type) Fig. 12-2	The microporphyritic cosmic spherule contains a matrix of very fine-grained zoned olivines with a forsterite (Mg_2SiO_4) rich core grading to a more fayalitic (Fe_2SiO_4) rich rim. This is observable as a lighter colour at the rims of the crystals under the SEM and the petrographic microscope, but is very subtle in the latter case. Larger grains may be present within the spherule and can contain relic grains (see Fig. 12-2c). Vesicles can make up about half the spherule. In our collection, MP-type spherules are the rarest type and tend appear in the smaller size fractions (<150μm diameter).
Porphyritic (P-Type) Fig. 12-3	Porphyritic spherules contain large equant olivine crystals which are visibly zoned even under a petrographic microscope. Spinel can make up from 1-49% of the surface area of a section. Although relic grains can be found in these types of spherules they are rare.
Transitional 1 (T1-Type) Fig 12-4	This cosmic spherule is transitional between the porphyritic textures and feather olivine textures (see below) containing both textures in a single spherule. This type of spherule texture is rare for our collection. Most only contain small areas which have porphyritic textures.

Table 1. *Continued.*

Feather (FO-Type) Fig. 12-5	Present in all sizes, this type of cosmic spherule exhibits one of the most common textures. Under the petrographic microscope the brightest minerals (spinel) appear dotted throughout the spherule with little to no linearity. Although these types of spherule appear similar to P-type or MP-type, they are distinguished by a variety of olivine morphologies that can either be chaotic in orientation or display some linearity with thin bars of olivine forming lattice structures. Spinels are smaller than those in P-type spherules. In some FO-type spherules the larger spinel crystals appear to be broken into smaller crystals, as though they were partially melted (Fig. 12-5c).
Transitional 2 (T2-Type) Fig 12-6	This texture is transitional between the feather olivine types and barred olivine types (see below) in that it shows both textures in a single spherule. This type of texture is quite common.
Barred Olivine (BO-Type) Fig. 12-7	As described in the Taylor et al. (2000) classification, the defining characteristic of the barred olivine textures are long, chain olivine structures that can extend over the length of the spherule. Bar widths of these structures are larger than those exhibited in FO-type spherules. Spinel occurs in the glassy interstitial spaces between the olivine crystals making them appear to form linear arrangements across the sample surface.
Crypto-Crystalline (CC-Type) Fig. 12-8	These cosmic spherules appear glass-like and featureless at low magnifications under a petrographic microscope. They can sometimes contain what appear to be fine wispy textures or spots of spinel only seen under higher magnifications. Under the SEM these spherules show much more structure, with some spherules displaying textures like BO-type spherules except with finer, more densely packed bars. Other CC-Type textures look analogous to myrmekitic textures from quenched melt or domains with globular outlines (Fig. 12-7c). Crypto-crystalline samples are most abundant in the larger size fractions and tend have more irregular or elongate (cigar) shapes.

Table 1. *Continued.*

Glass	Glass cosmic spherules are absent from our collection. Perhaps this is because the environment of our collection site is too abrasive to preserve this kind of spherule compared to more pristine environments such as the SPWW. Glass spherules are described in Genge et al. (2008) and Taylor et al. (2000).
CAT	CAT spherules are also absent from our collection. Again it may be a preservation issue or perhaps, as they are quite rare, a sampling bias. Although we have cosmic spherules with slightly elevated Ca, Al, and Ti, the textures described by Taylor et al. (2000) were not found.
Exotic Spherules	
	A small number of cosmic spherules have very different textures compared to other cosmic spherules in our collection. It is possible that these cosmic spherules may be extraterrestrial particles that originate from a different parent body, or experienced a different set of conditions on atmospheric entry. Some cosmic spherules are thought to have originated from bodies such as the asteroid 4Vesta (Taylor et al., 2007).

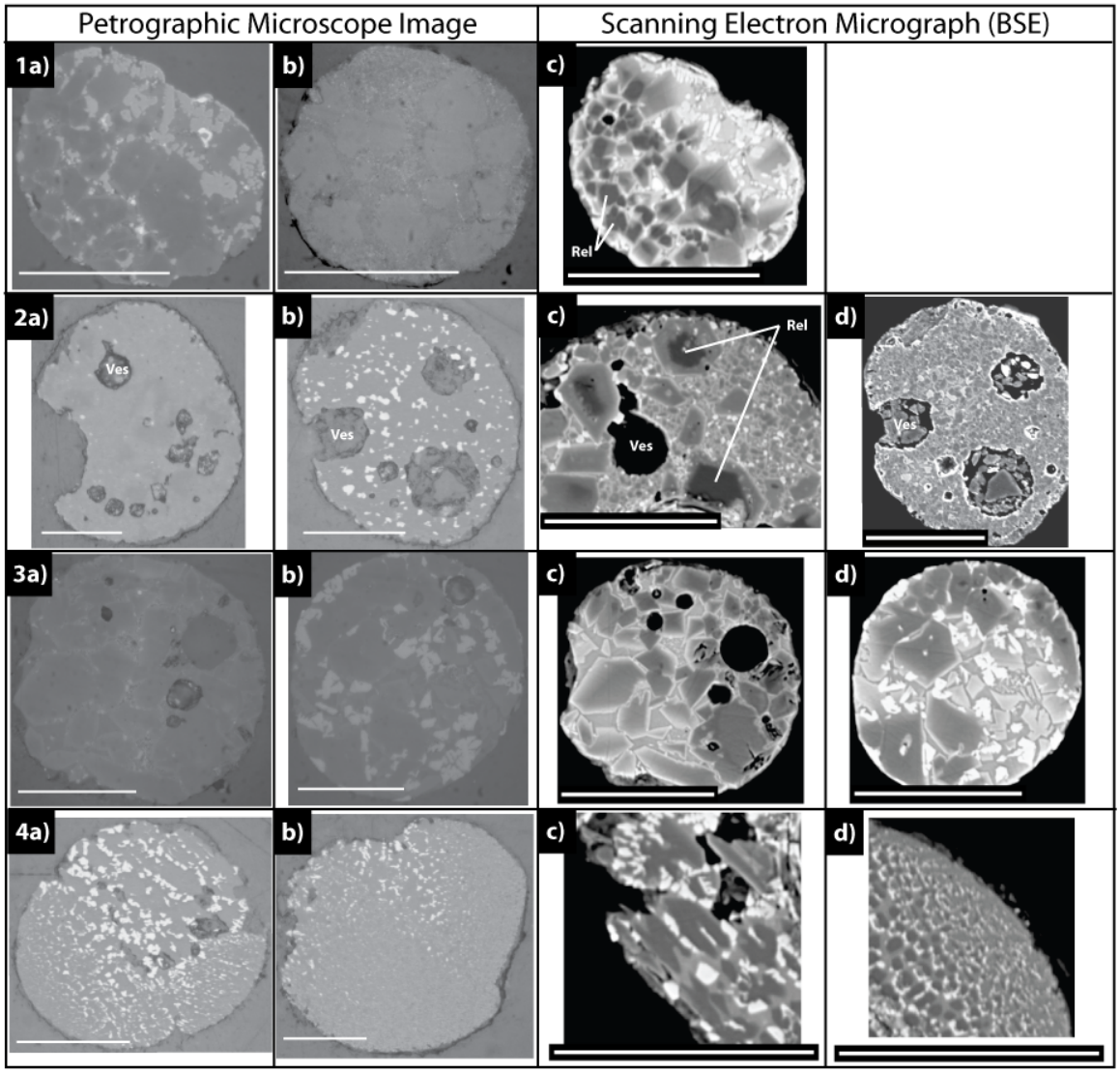

Figure 7. Stony/Silicate Cosmic Spherules as seen under a petrographic microscope and scanning electron microscope (BSE). All scale bars are 50μm. See Table 1 for descriptions. Rel = relic grains. Ves = vesicles.

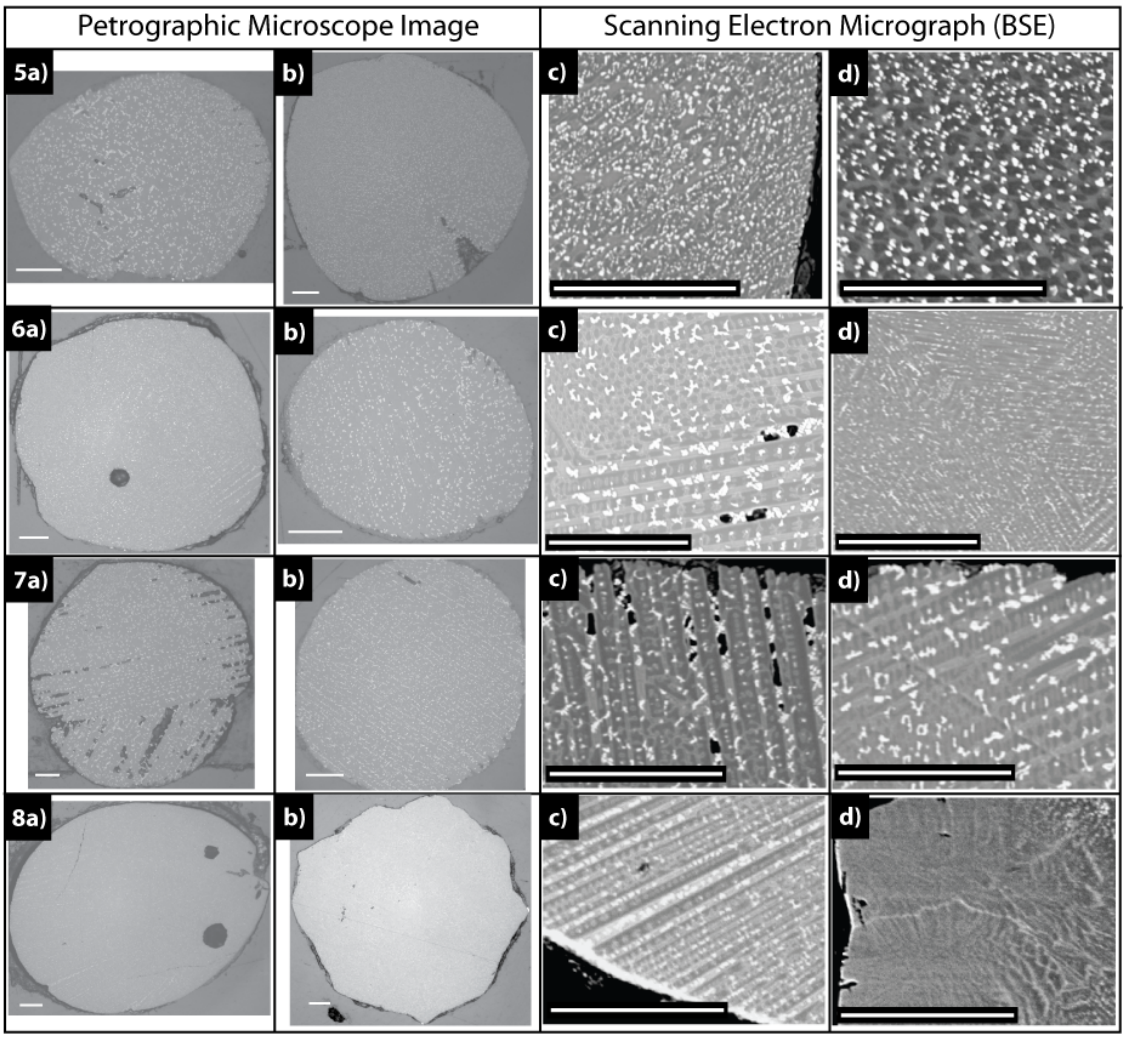

Figure 7. *Continued*

Table 2. Petrographic description of iron/nickel-iron and dendritic cosmic spherules as seen under a petrographic microscope and scanning electron micrographs. See Figure 8 for the actual images.

	Description
Iron/nickel-iron Spherules (I-Types) Fig. 11-1	These micrometeorites appear bright under reflected light. SEM-EDXA analyses of these spherules show that they are composed of Fe oxide or Fe/Ni oxide mix. When viewed under the SEM, two bright phases can be identified that form subtle intertwined dendritic patterns clearly seen in backscatter micrographs in Figure 11-1c and 1d. They are present in all size ranges. In smaller size fractions (<70μm diameter), glassy (fragile) FeO rich caps may be present (See Fig. 11-1b). These rarer kinds of I-type spherules with caps tend to have metallic cores. Occasionally beads similar in appearance to I-type spherules can be seen within or attached to the perimeter of stony spherules. These are referred to here as a metallic beads/cores, which are possible precursors to the I-type spherule according to Brownlee et al. (1984) (see Figure 20).
Dendritic Spherules (D-Types) Fig. 11-2	Dendritic spherules have distinct dendritic textures, which contrast strongly to those seen in I-types which can be quite subtle. The brighter phase is a mix of iron oxides while the darker phase is composed of a silicate material (See Fig. 11-2a and 2b). There are also finer patterned varieties which are made up of cross-hatches of iron oxides (See Fig. 11-2c and 2d). In the literature these spherules are often referred to as G-types. This term originates from Blanchard et al. (1980) who described this type of spherule and coined them as "glassy spherules". This name was changed in this thesis to avoid confusion with the glass cosmic spherules described in Taylor et al. (2000)

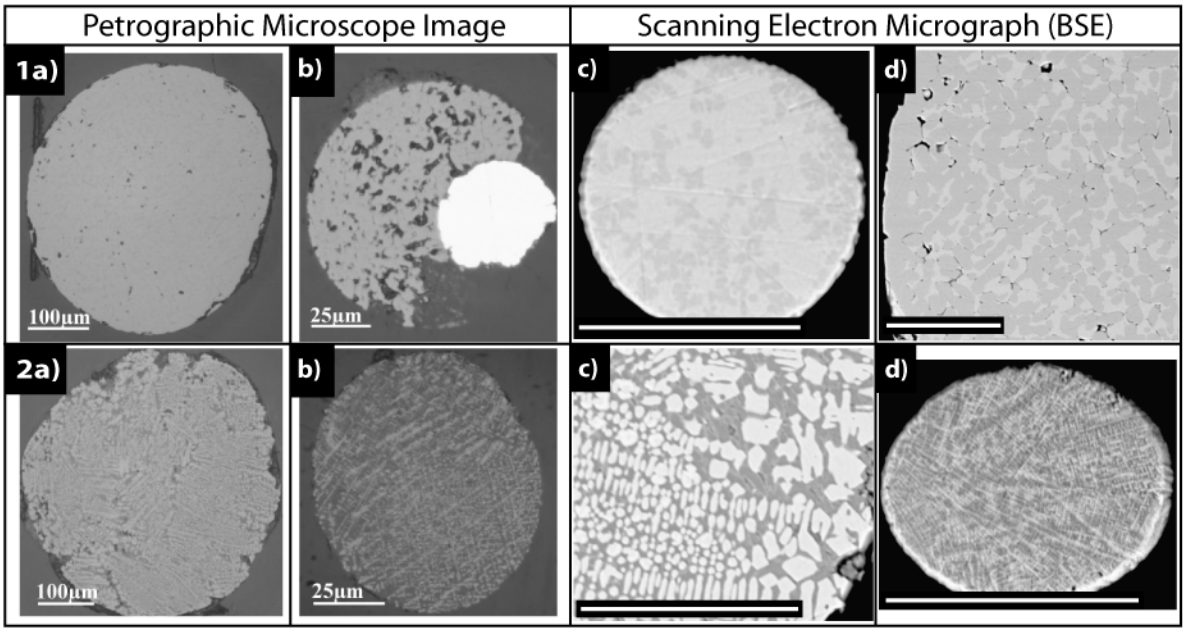

Figure 8. Iron/nickel-iron and Dendritic Cosmic Spherules as seen under a reflected light microscope and scanning electron microscope (BSE). Scale bars for the micrographs are 50µm. For descriptions please see Table 2.

The majority (72%) of cosmic spherules from the Lewis Cliff Ice Tongue occur in the size range of 50-200µm (Figure 9). These spherules tend to be slightly elongate, even cigar shaped in rare instances, as shown by the mismatch between the histograms for the measured long and short axes (Figure 9a). Based on a simple count of texture types, certain cosmic spherule textures appear to predominate (refer to Figure 9b). I-types, characterised by iron-rich mineralogy in oxide or metallic states, are most common (21%), followed closely by stony spherules with feather olivine (FO-type) textures (19%), and those with textures transitional from feather olivine to barred olivine (T2-types; 19%). Porphyritic (P-type) textures are intermediate in abundance (13%). Dendritic (D-type), barred olivine (BO-type) or cryptocrystalline (CC-type) textures range in abundance from 5-8%, whereas those with microporphyritic (MP-types), textures transitional from porphyritic to feather olivine (T1-types) and those consisting largely of relic grains (RGB-types) are rare (1-3%).

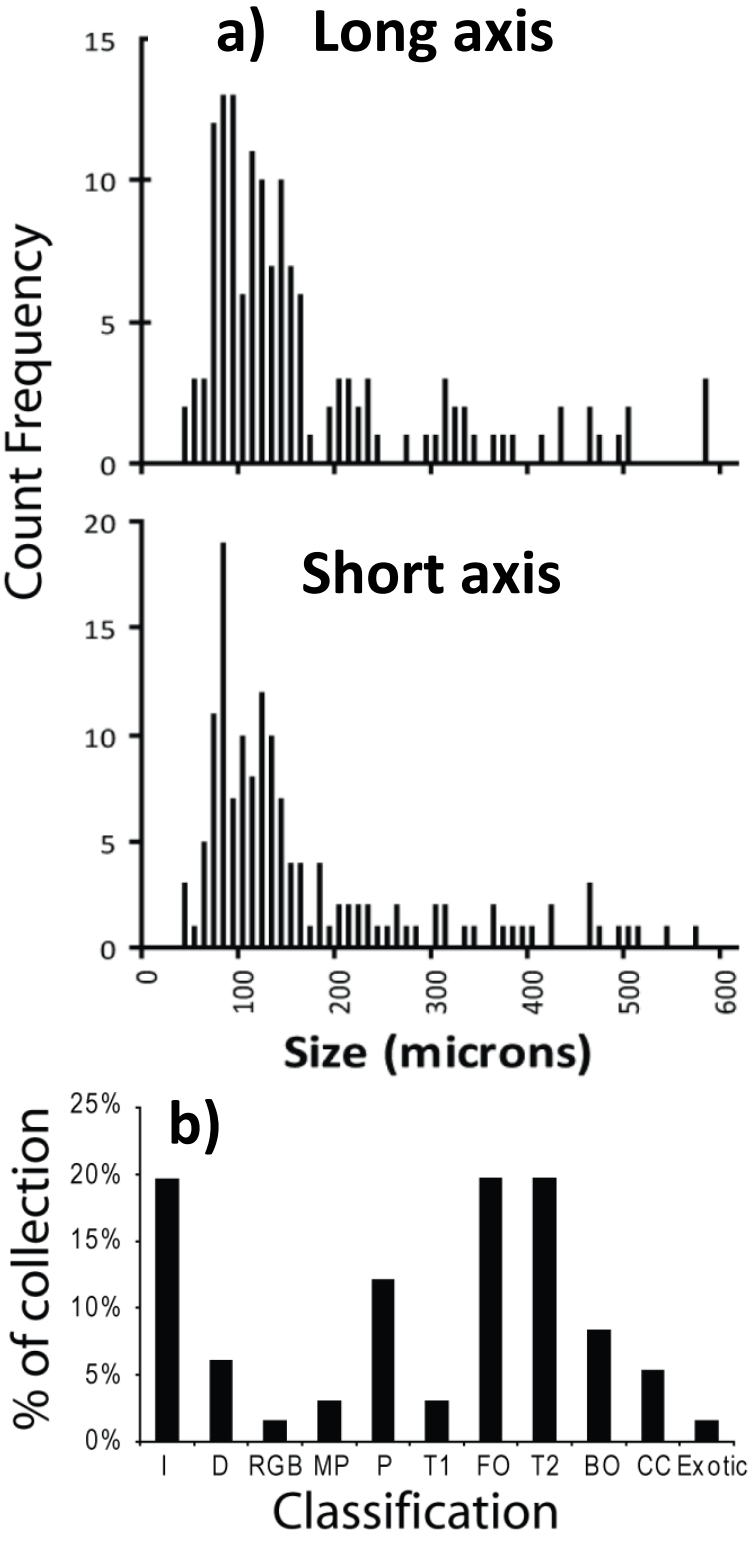

Figure 9. Histogram of lengths of **a)** long axes and short axes of cosmic spherules. **b)** relative abundance of cosmic spherule textures as a percentile of the total collection. See Table 2 and Table 1 for descriptions.

1.5.2 Major and Trace Element Composition

Stony/silicate Group Spherules

Table 3 presents the bulk major element chemistry of each textural class in the stony/silicate group cosmic spherules. These compositions appear consistent with those presented in Taylor et al. (2005a). Two dominant minerals have been identified in all stony textures: olivine, which may exhibit zoning, and spinel group minerals, usually magnetite with variable substitution of the magnesioferroite component. The bulk composition of individual stony spherules reflects the proportions of silicate to spinel with increased abundances of MgO and SiO_2 in spinel-poor spherules, and higher FeO in spinel-rich spherules. The proportions of olivine to spinel are highly variable, with spinel occupying anywhere from 1-49% of the total exposed surface area of the polished spherule. In combination with the melt textures, major element compositions provide strong evidence for an extraterrestrial origin of these spherules. Major element compositions of the bulk stony spherules are distinguished from terrestrial compositions by their high MgO (22.98-30.84 wt.%) and low Al_2O_3 (1.04-2.68 wt.%) contents.

Figure 10 presents the bulk trace element chemistry of the stony cosmic spherules. Common to all stony comic spherules is the strong depletion of moderately volatile lithophile and chalcophile trace elements (e.g. Rb, Cu, Zn, Ga, Ge) to levels near the detection limits. The loss of Ge suggests temperatures in excess of 1200°C (Klöck et al., 1994). Siderophile elements Co and Ni are also depleted in stony cosmic spherules to varying degrees, with chondrite normalised values of 0.4-0.7 and 0.2-0.4 respectively, depending on the type of chondrite normalisation used. Platinum is generally below detection with a few exceptions. Refractory lithophile trace elements are present in generally chondritic relative abundances and lack features indicating differentiated, igneous precursors.

Table 3. Scanning Electron Microscope Energy Dispersive X-ray Analyses of 91 Stony Cosmic Spherules. Data are presented in the form mean ± one standard deviation. Na_2O, K_2O, TiO_2, MnO, CoO and NiO were also analysed, but were typically below detection.

Oxide	RGB-Type n=2	MP-Type n=3	P-Type n=16	T1-Type n=4
MgO	23.41 ± 5.57	22.98 ± 5.49	23.55 ± 7.15	22.94 ± 3.47
Al_2O_3	1.77 ± 0.42	2.22 ± 1.74	2.66 ± 1.24	3.12 ± 0.99
SiO_2	35.72 ± 15.38	34.93 ± 2.89	35.39 ± 4.66	35.94 ± 1.04
CaO	1.62 ± 0.37	0.82 ± 0.22	2.22 ± 1.18	2.49 ± 1.49
Cr_2O_3	0.51 ± 0.10	0.52 ± 0.19	0.49 ± 0.17	0.49 ± 0.11
FeO	35.80 ± 20.66	38.26 ± 5.08	34.60 ± 8.64	34.11 ± 2.27
NiO			0.97 ± 0.46	1.08 ± 0.51
Analytical Total	94.44 ± 9.57	98.05 ± 6.70	101.16 ± 5.09	99.17 ± 7.93
	FO-Type n=25	T2-Type n=26	BO-Type n=11	CC-Type n=7
MgO	22.94 ± 3.09	23.53 ± 3.86	25.22 ± 2.59	30.84 ± 6.36
Al_2O_3	3.12 ± 1.28	2.92 ± 0.69	2.39 ± 0.86	2.23 ± 0.94
SiO_2	35.94 ± 2.35	35.23 ± 2.63	35.42 ± 2.41	42.27 ± 2.83
CaO	2.49 ± 1.38	2.71 ± 1.37	1.70 ± 0.74	1.30 ± 0.59
Cr_2O_3	0.49 ± 0.13	0.48 ± 0.15	0.39 ± 0.09	0.45 ± 0.19
FeO	34.11 ± 4.06	34.38 ± 5.23	34.54 ± 3.69	22.63 ± 8.74
NiO	1.08 ± 0.36	1.07 ± 0.59	0.99 ± 0.42	
Analytical Total	99.17 ± 4.19	99.34 ± 3.68	98.96 ± 5.69	98.63 ± 7.06

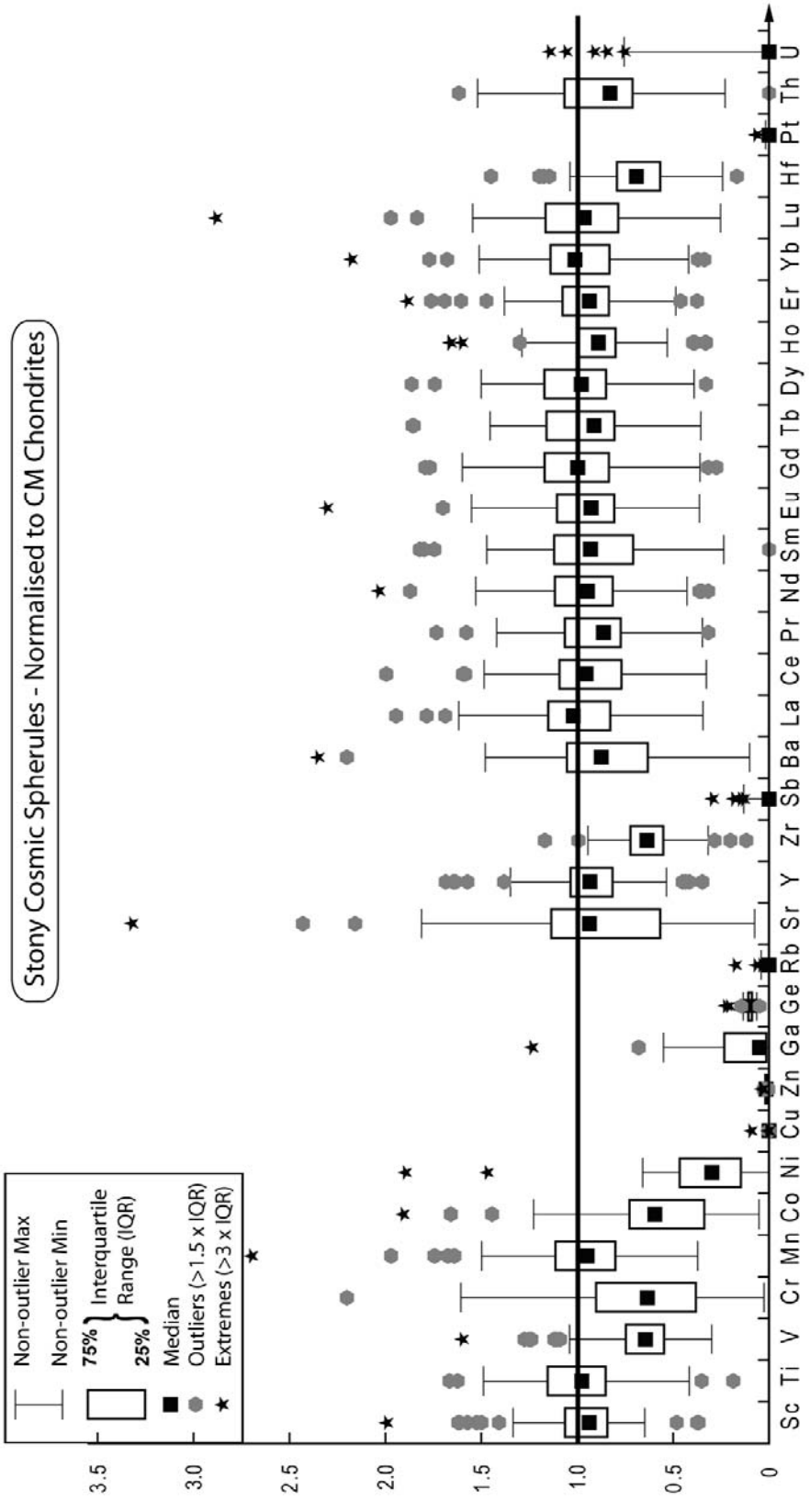

Figure 10. Trace element abundances of 60 stony cosmic spherules normalised to CM-chondrite composition of Wasson and Kallemeyn (1988). Note the general depletion of moderately volatile siderophile and chalcophile elements (e.g. Rb, Cu, Zn, Ga, Ge), and siderophiles Ni, Co, and Pt.

Iron-Rich Group Spherules

Compared to the stony/silicate group spherules, I-types have a small range of major element abundances and are composed predominately of iron and nickel (Table 4). Fe and Ni are present as either oxides or metals, with oxides being more common. The oxide and metallic I-types both have a strong negative relationship between the Fe and Ni contents. Figure 11 highlights the difference between oxide and metallic I-types with oxide I-types showing more scatter reflected by the lower R^2 value (0.986) compared to the metallic equivalents which have an R^2 value of 0.993. The oxide I-types also show a more restricted range with the FeO contents of most spherules exceeding 90 wt.%. Metallic I-types have a larger variation with Fe^0 contents ranging from 13.89 wt.% to 93.95 wt.%.

Trace element patterns for all iron/nickel-iron spherules are complementary to those of stony spherules (Figure 12a). Compared to chondrite compositions, the I-type spherules are depleted in refractory lithophile and chalcophile elements and the siderophile element, Pd. Non-volatile, highly siderophile elements are also highly enriched with the median value at 2.5x for Fe to 20x for Pt. Platinum nuggets also appear to be present and are inferred from ablation profiles due to changes in Pt abundance over a few points. The nuggets manifest as large interquartile ranges (>30) in Figure 12.

The dendritic spherules (D-types) have a range of compositions, with end-members which are similar in composition to stony spherules and others that are more like I-type spherules. The trace elements of D-types are a hybrid of both stony and iron-rich spherule signatures (Figure 12b). Like the I-types spherules, the dendritic spherules are enriched in siderophile elements compared to the stony cosmic spherules. However, they also contain refractory lithophile and chalcophile elements above detection which is more atypical of I-type cosmic spherules.

Table 4. Scanning Electron Microscope Energy Dispersive X-ray Analyses of 26 iron/nickel-iron cosmic spherules and 8 dendritic cosmic spherules. Data are presented in the form mean ± one standard deviation. Na_2O, K_2O, TiO_2, MnO, CoO and NiO were also analysed, but were typically below detection.

Oxide	D-Type n=8	I-Type n=19	Metallic	I-Type n=7
MgO	14.24 ± 8.15	0.38 ± 0.02	Fe^0	70.37 ± 21.07
Al_2O_3	1.71 ± 0.83	0.39 ± 0.18	Ni^0	22.56 ± 16.71
SiO_2	22.47 ± 10.98	0.89 ± 1.07		
CaO	1.74 ± 1.70	0.53 ± 0.26		
Cr_2O_3	0.44 ± 0.19	0.42 ± 0.14		
FeO	57.14 ± 21.13	91.85 ± 12.18		
NiO	3.82 ± 3.11	6.94 ± 5.41		
Analytical Total	98.84 ± 2.60	98.67 ± 4.61		102.62 ± 2.23

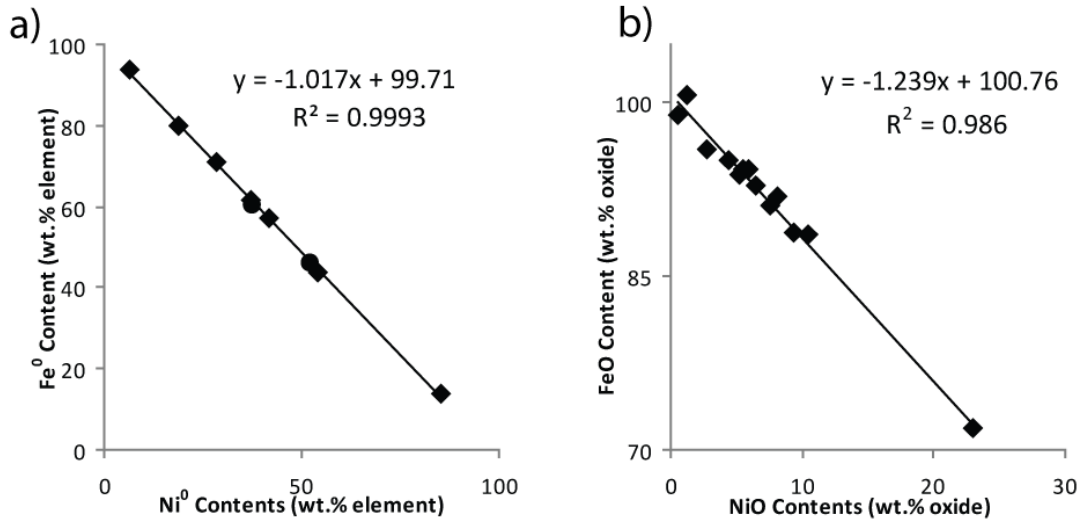

Figure 11. Strong linear relationships between a) iron and nickel metal in I-type spherules (diamonds) and metallic beads located within stony cosmic spherules (circles) and, b) iron and nickel oxides in I-type spherules

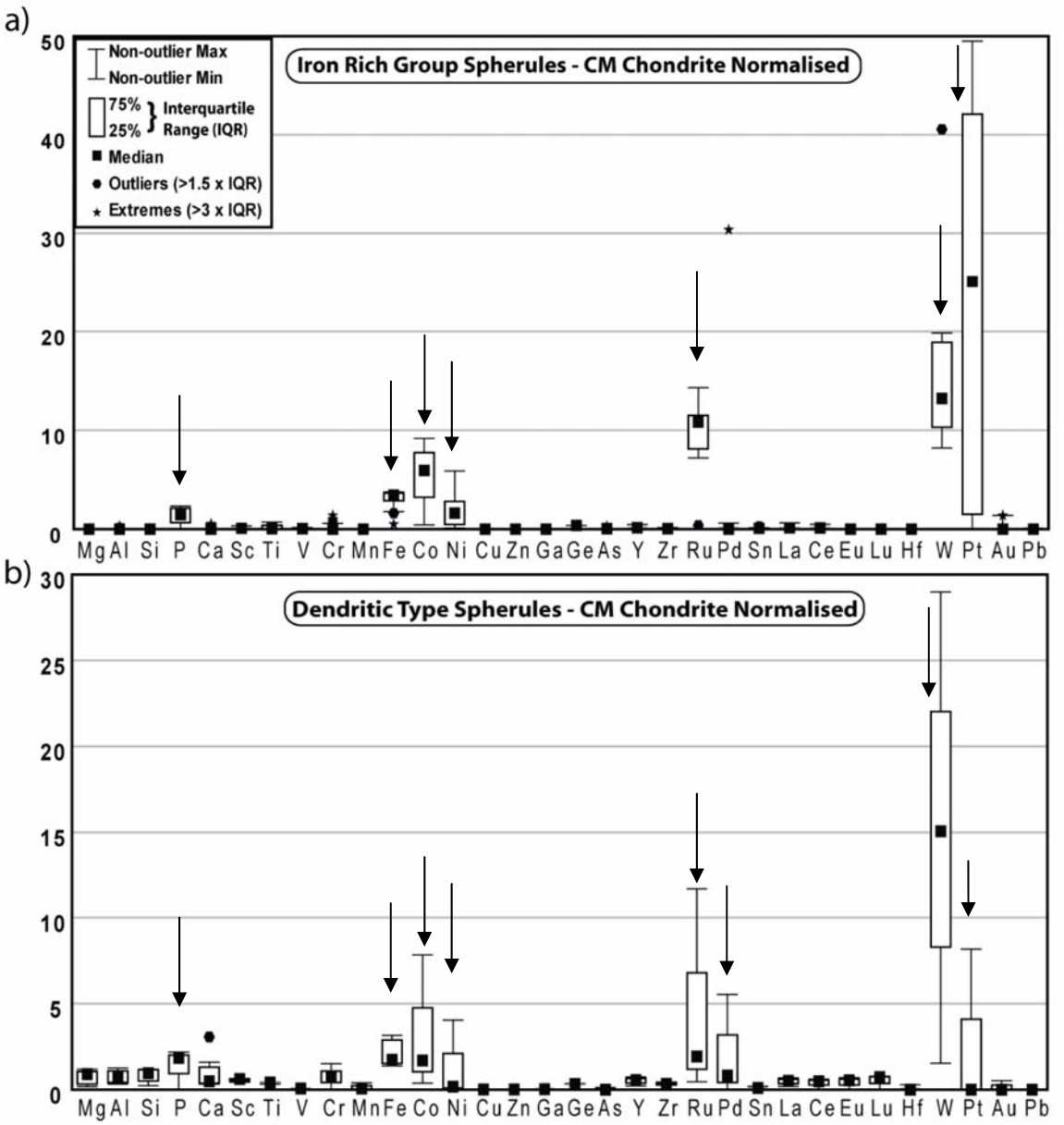

Figure 12. Major and trace element abundances of a) 7 iron/iron-nickel cosmic spherules and b) 3 dendritic cosmic spherules normalised to CM-chondrite composition of Wasson and Kallemeyn (1988). Enrichment of siderophile elements are marked by the arrows. Note that I-type spherules are typically depleted in silicate elements (e.g. Mg, Al, and Si). Dendritic spherules have modest levels of lithophile elements in addition to more siderophilic elements which reflect the coexisting metal and silicate melt.

Cross-Collection Comparisons

In Taylor et al. (2000), data from other large cosmic spherule collections were compared on a ternary diagram of Mg, Si and Fe. Data from this study have been added to this diagram (Figure 13). In general, most of the large cosmic spherule collections have spherules that are texturally and chemically similar to one another. The majority of silicate/stony spherules plot near the centre, while I-type spherules plot near the Fe corner of the diagram. A line consisting dominantly of D-type spherules appears to join the two distinct groups. A similar observation was also made by Brownlee et al. (1997) for cosmic spherules in the DSS collection. Brownlee et al. (1997) also noted that preferential collection of more magnetic spherules in the DSS collection lead to a biased representation of Fe-rich compositions. It should be noted that the same textural relationships described in other collections also exist in cosmic spherules from this project.

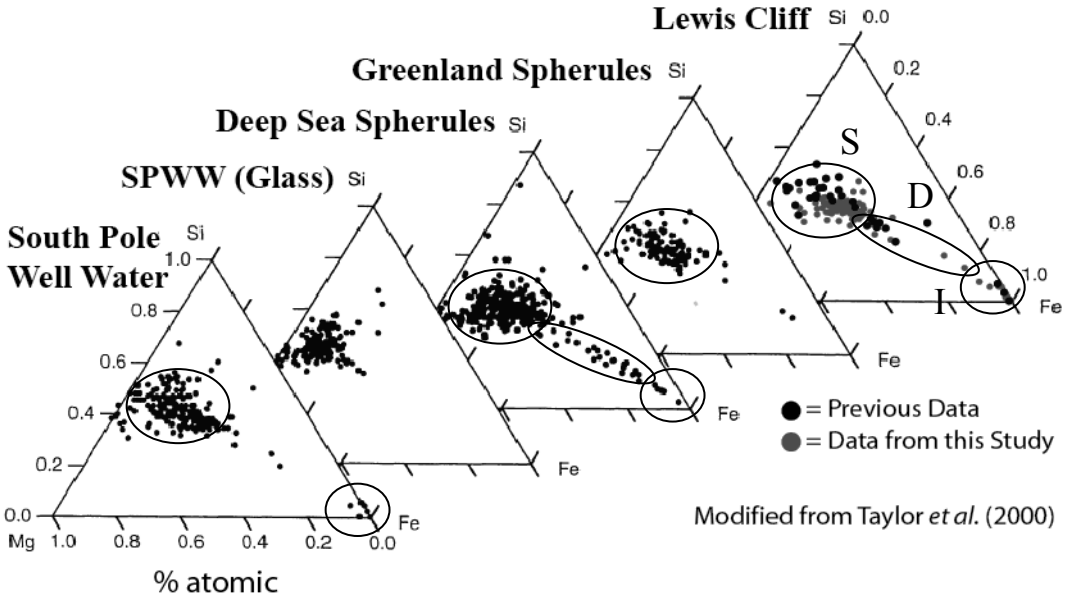

Figure 13. Ternary diagram (Mg, Si, Fe) modified from Taylor et al. (2000) with the addition of data from this study. Stony (S), dendritic (D), and iron-type (I) cosmic spherules plot in distinct regions in this figure for the Deep Sea Spherules and Lewis Cliff collections.

1.6 Discussion

1.6.1 Textural and Compositional Evolution of Stony Cosmic Spherules

Cosmic Spherule Analogues

Previous work and this study have shown that the stony cosmic spherules are chondritic in major and trace element composition (See Brownlee et al., 1997; Kurat et al., 1994; Taylor et al., 2000). The chondritic composition of stony cosmic spherules allows comparison of melt textures with synthetic analogues. Cosmic spherule textures can be related to the number of nuclei remaining during melting, which will be dependent on variables such as heating intensity (peak temperatures) and heating duration. One of the earliest experimental studies was conducted by Hashimoto (1983), who melted and quenched synthetic chondrite compositions and recorded the textures and major element changes that occurred. Samples were heated in a furnace at 10^{-5} Torr at temperatures ranging from 1700-2000°C with durations from 1.29-129 minutes. It was possible to recreate the textures of the barred olivine structure and cryptocrystalline structures by vaporising 0-25% and 35-52.5% of the sample followed by quenching, respectively. Wang et al. (2001) conducted the same experiments as Hashimoto (1983), but used a wider range of temperatures (1400-2000°C) and longer durations (0-300 minutes at the peak temperatures). Heating below the liquidus (estimated at 1580°C) created porphyritic textures due to the presence of relic nuclei in the melt (heterogeneous nucleation). Increased heating duration at sub-liquidus temperatures produced larger porphyritic crystals due to progressive destruction of relic nuclei. Melting above the liquidus produced barred olivine textures due to a lack of relic nuclei (homogeneous nucleation). The combined experiments of Hashimoto (1983) and Wang et al. (2001) reproduced most textures seen in cosmic spherules. The compositional changes determined by Hashimoto (1983) are illustrated in Figure 14 which shows an increasing MgO (and minor amounts of SiO_2) and decreasing FeO concentrations in the early stages of heating, followed by depletion of MgO and SiO_2 and enrichment of CaO and Al_2O_3 with increasing degrees of vaporisation. These observations agree with the compositions of the textural groups presented in Taylor et al. (2005a), again reinforcing

the compatibility of experimentally-produced textures and those that are produced from atmospheric heating.

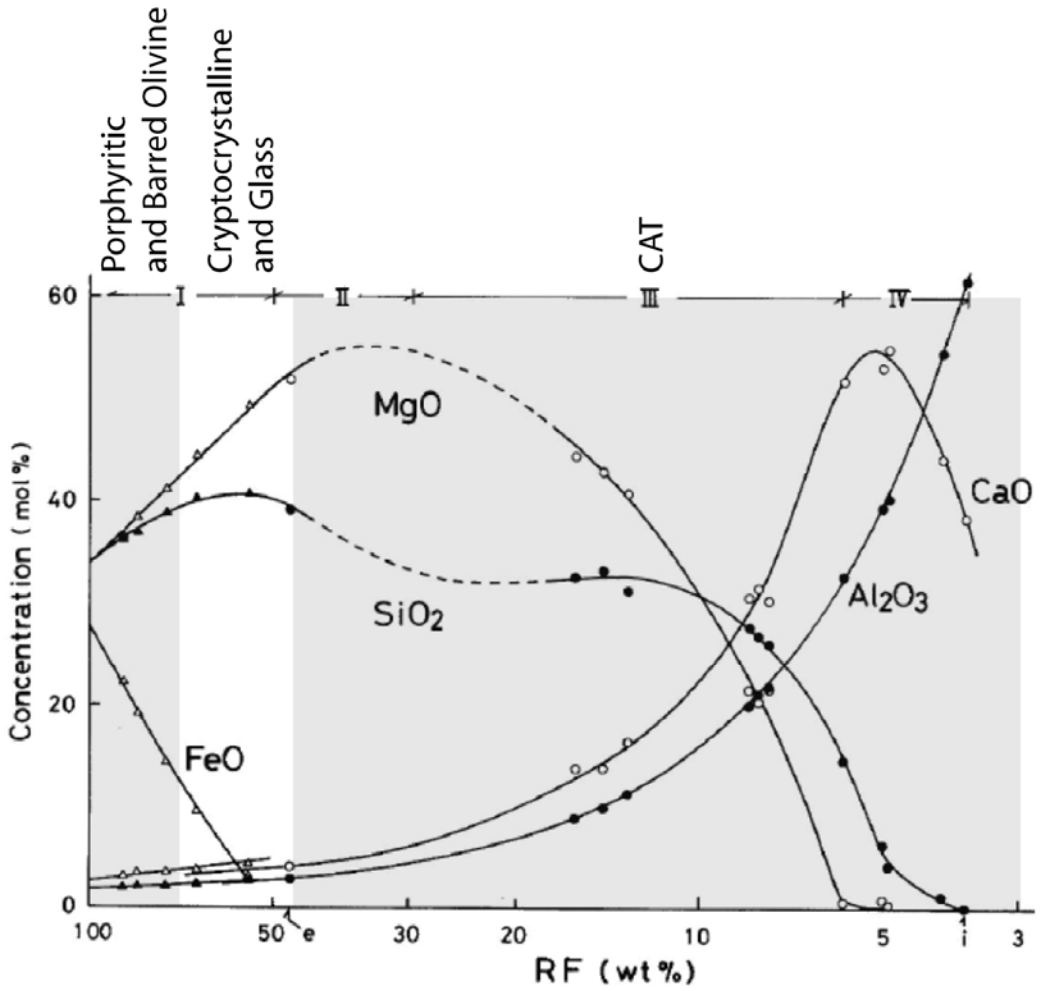

Figure 14. Sequential change in chemical composition of evaporation residues. RF (residual fraction) = 100 – VF (vaporized fraction). Triangles: the experimental data of Hashimoto (1983) at 1,800°C. Circles: the data of Hashimoto and Kumazawa (1979) at 1,800°C except e (1,700°c) and i (1,900°C). Data between RF=40 and 20 are lacking, so that the lines of MgO and SiO_2 are interpolated by taking account of their relative volatilities in this compositional range. The shaded zones indicate how cosmic spherule textures and compositions described in Taylor et al. (2005a) may relate to their experimental equivalents produced by Hashimoto (1983).

Modified from Hashimoto (1983)

Crystallisation experiments for chondrule textures are also good analogues for understanding cosmic spherules. The most notable difference between cosmic spherules and chondrules is the absence of spinel, a result of lower Fe contents (5-10 wt.%) in the chondrule analogues, however, olivine morphology is comparable. To summarise the results of Lofgren and Russell (1986) and Lofgren (1989), porphyritic textures form as a result of heterogeneous nuclei when cooling begins. The size of the porphyritic crystals increases and abundance decreases as temperature increases. Barred olivine textures are produced above liquidus temperatures when few nucleation sites exist. The bar width is also a function of nucleation; fewer nucleation sites result in wider chain olivine (bar) structures. Glassy textures can be produced by complete destruction of all nuclei followed by quenching. The conditions needed to generate olivine morphologies and textures in experimentally produced chondritic melts are similar to those in chondrules. Hence, nucleation theory can also be applied to cosmic spherule textures. However, experimental analogues are geared to produce well-defined textures under certain conditions which are invaluable in the interpretation of transitional forms seen in cosmic spherules.

In summary, melt texture experiments using synthetic CI (minus volatiles) materials and crystallisation experiments of chondrule textures produce textures similar to those seen in cosmic spherules. Heating to sub-liquidus temperatures (calculated at <1580°C by Wang et al., 2001) allows for the growth of porphyritic textures due to presence of relic nuclei in the melt (heterogeneous nucleation). Heating above the liquidus temperatures allows for barred olivine structures to form by homogeneous nucleation from the melt. Extended duration experiments above liquidus temperatures results in formation of cryptocrystalline textures (Hashimoto, 1983).

Stony Cosmic Spherules Texture Development

For all cosmic spherule there exists a boundary in peak temperature-heating duration space that determines whether a particle is partially or fully melted. The following section is a description of cosmic spherule textures and their relationship to peak temperature and heating duration as interpreted from data collected in this project. See Figure 15 for a graphical representation of this concept.

RGB-Type spherules are mostly made up of relic material. This means that the precursor particles have not been exposed to peak temperatures and durations that were sufficient to remove relic materials. However, these conditions were sufficient to partially melt and produce a round particle shape. This makes them the least thermally altered of the cosmic spherules.

The MP-Types and P-Types can (rarely) contain relic materials in a small number of grains. If present in these textures, relic materials (observable as irregular and particularly dark regions in backscatter micrographs) are typically within recrystallised olivine grains. Spherules with relic grains are more thermally altered than RGB-types, but less thermally altered than those without. P-Type spherules may have experienced an extended duration of heating at sub-liquidus temperatures, which produced small numbers of relatively coarser olivine crystals on cooling. MP-Type spherules experienced shorter heating durations. However, the grain size of the precursor also influences the spherule texture. Hewins and Fox (2004) determined that single rapid heating events applied to chondrule analogues with starting grain sizes of 0-20μm generate textures equivalent to those seen in microprophyritic cosmic spherules. In order for the textures to coarsen into a porphyritic cosmic spherule equivalent, either a coarser starting material or an extended heating duration (by up to 30 minutes) depending on the peak temperature is needed. Traversal of the atmosphere by most particles takes mere seconds although there are certain conditions (10μm diameter particle at grazing incidences) that will allow a particle to experience extended heating durations through multiple low heat (<100°C), aerobraking manoeuvres before being captured (Love and Brownlee, 1991). This, however, requires fine-tuning of entry

conditions (i.e. entry angles tuned to three significant figures) in the Love and Brownlee model (1991) which implies that the initial comic spherule texture may be controlled more by the size of grains in the immediate precursor, in this case fine-grained or coarse-grained micrometeorites.

At super-liquidus temperatures the cosmic spherule precursor is fully molten, though nucleation points can still exist in the melt. As with the analogues, a barred olivine texture is developed. However, the results of this study indicate that a feather olivine stage is developed under slightly less intense heating, based on the co-existence of these textures with porphyritic textures in T1-type and with barred olivine textures in T2-type spherules. There are no zoned olivines in the feather olivine texture. The fayalitic components of the zoned olivines are the first to melt forming an Fe-rich melt and leaving behind a more Mg-rich olivine. Upon quenching of the particle the Fe-rich melt forms a glassy mesostatsis which also hosts spinel (magnetite) and surrounds the relic Mg-rich crystals/lathes resulting in a texture controlled by the arrangement of the relic grains. As temperature increases, the melt evolves to more Mg-rich compositions as more of the relic material is melted, which will result in the formation of progressively smaller and more Mg-rich laths. A point is reached where the remaining relic grains are removed allowing crystals to grow uninhibited by relic material in small sections of the particle; this defines the next texture group (T2). Mg# in this case may in principle, be used to determine the temperature of formation assuming equilibrium conditions, but because of the small size of the lathes an accurate analysis is difficult.

On cooling from near-liquidus temperatures “barred” textures form due to chain olivine crystallising in a semi-aligned/lattice form with thin and short bars. These textures are present in the T2-type spherules and, if the particle is exposed for longer durations above liquidus temperatures, will develop BO-type textures through destruction of nuclei, resulting in wider and longer bars (Wang et al., 2001). Continued destruction of nuclei leads to a reduction in spinel size, followed by a change in spinel arrangement that is characteristic of the CC-type textures. Like the chondrule analogues, complete destruction of nuclei will probably result in glass textures while the development of

CAT textures may be a mineralogical artefact of Ca, Al and Ti concentration as seen, to a lesser extent, in the Wang et al. (2001) experiments.

The new transitional forms T1 and T2 proposed in this study have textures that suggest some type of thermal gradient existed at the time these particles were quenched, leading to heterogeneous distribution of relic nuclei. This is possible if heat was applied to only a portion of the spherule's surface, with heat needing to diffuse through the particle from the heat input direction. The thermal conductivity of cosmic spherules was examined in Love and Brownlee (1991), who concluded that cosmic spherules were essentially isothermal, and hence thermal gradients could be ignored given the parameters in their model (dense and solid particles). In order to produce transitional textures, it is necessary to prevent complete melting of the incoming particle before it is quenched, to preserve the thermal gradient. Reduction of thermal conduction through porous materials, such as those of scoriaceous micrometeorites, can only be achieved below the melting temperatures because melt will infill the vesicles. Transitional spherules studied in this thesis are fully melted and lack any vesicles, so a porosity buffer seems unlikely. Also, the incoming particles cannot tumble (rotate) during heating since the tumbling process will evenly disperse heat through the particle, eliminating the thermal gradient, as opposed to the situation of a static particle which is only heated from one side. Perhaps the most efficient method of producing transitional textures is by shortening the heating duration by entry into the atmosphere at high angles and high speeds, although this method will increase the peak temperature. A non-rotating particle exposed to only short durations of high temperature may be the best method for preserving the thermal gradient needed to produce transitional textures.

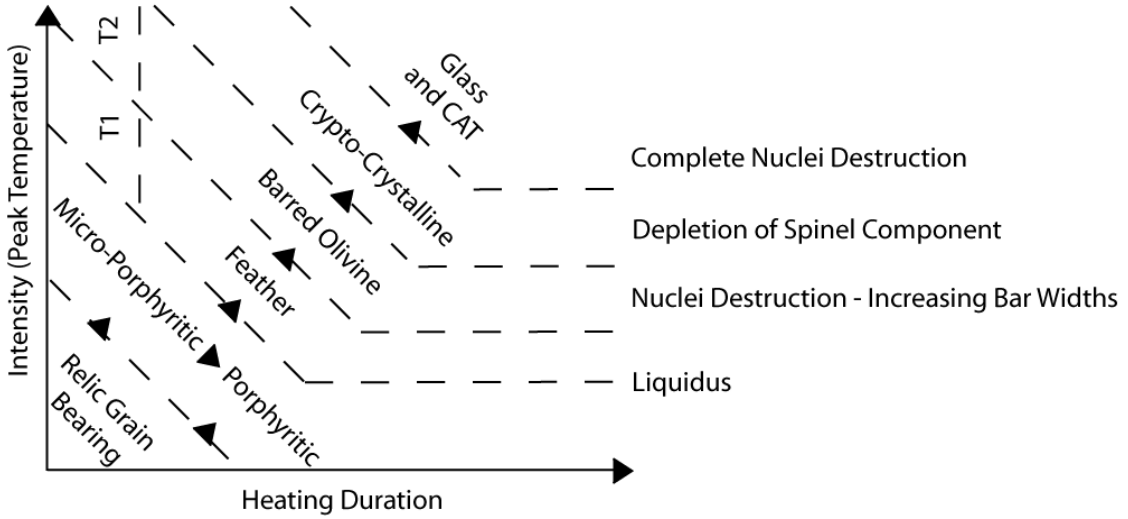

Figure 15. Conceptual model for the evolution of cosmic spherule textures through peak temperature-heating duration space. The least heated cosmic spherules, the relic grain bearing spherules, evolve through a sequence of textures that are controlled by nuclei destruction.

Particle Size and Relationship to Stony Spherule Texture

According to the modelling by Love and Brownlee (1991), incoming particles experience mass loss such that their final size is about 1.5-2 times less than the original size for particles greater than 50μm. Also stated in this model is the relationship between size and peak temperature experienced by the incoming particle, with large sizes experiencing higher peak temperature. Assuming this is true, textures indicative of lower temperatures should be associated with small particles. Figure 16 indeed shows this relationship, with the median size (and size variability) increasing for textures indicative of high temperatures. Therefore, the relation between particle size and thermal alteration intensity (inferred through melt textures) can be used to constrain the particle size component of the entry conditions identified by Love and Brownlee (1991).

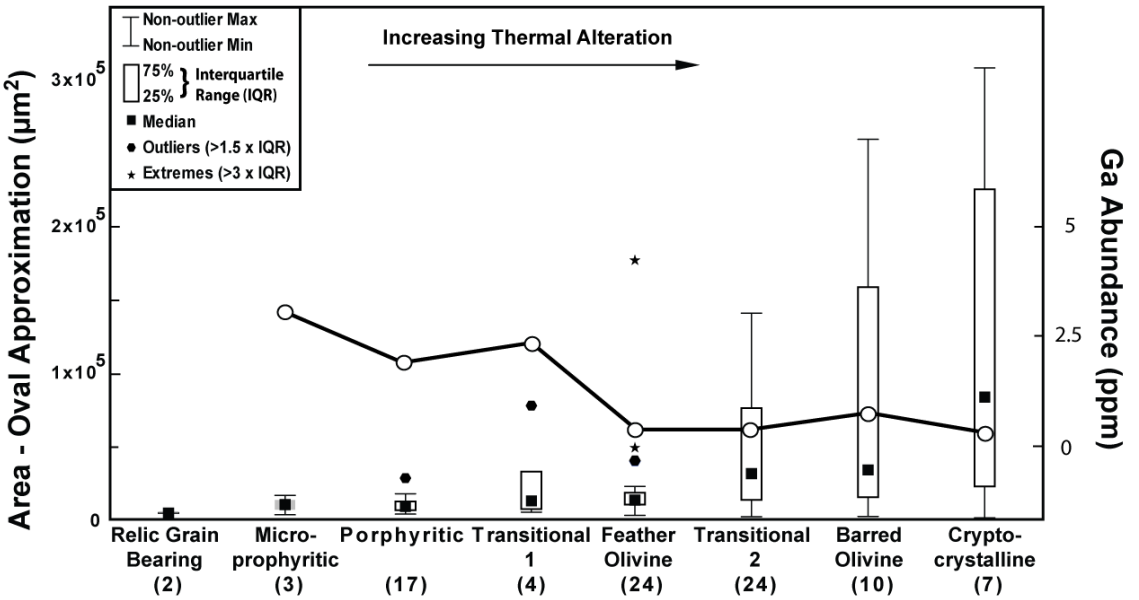

Figure 16. Textural groups of stony cosmic spherules and their relationship to size of the particle. With increasing thermal alteration the average size and variability of size in the cosmic spherules increases. Median gallium abundance (open circles joined with solid line) is also plotted and decreases with increasing thermal alteration because it is a volatile element.

Compositional Evolution

During atmospheric entry, cosmic spherules may experience significant thermal alteration which can lead to a depletion of volatile elements. In a study of optical emissions left by micro-meteor trails, Janches et al. (2009) was able to determine that volatile elements such as Na and K are lost early during atmospheric heating, followed later by Fe, Mg and Si, and the refractory element Ca. Pulse heating experiments aimed at simulating the effect of atmospheric entry on the composition of chondrites by Greshake et al. (1995) and Greshake et al. (1998), indicate that moderately volatile trace elements like Zn, Ga, Ge, and Cu are likely to be volatilised during atmospheric entry. The same depletion in the moderately volatile trace element is present in the stony cosmic spherule chemistry. Higher/detectable concentrations of moderately volatile elements such as Cu, Ga, and Rb are found in the less heated MP-type and PO-type cosmic spherules, which suggests volatilisation is responsible for the depletion of these elements observed in spherules with more strongly heated textures.

In addition to the volatile element depletion, common to all stony cosmic spherules, the composition of cosmic spherules varies according to texture. The major element compositions of P-type, FO-type and T2-type are compositionally similar, with all oxides falling within ±1% relative. Refractory elements like Al_2O_3 and CaO, however, have a larger range of ±16% relative (~0.5 wt.%), but are expected to increase in relative concentration as more volatile elements are lost. Minor changes in composition suggest that the texture change is largely related to the presence of remaining nuclei, rather than being compositionally controlled. The major element composition of BO-type and CC-type spherules differs from previous groups. CC-type spherules are depleted in CaO, Al_2O_3, and in particular, FeO, but enriched in MgO and SiO_2 compared to other spherule groups. BO-type spherules are compositionally transitional, with only minor depletion (<1wt.%) in CaO and Al_2O_3 and enrichment of MgO by ~1wt.%. It is unclear what would lead to the apparent depletion of the two most refractory major elements (CaO and Al_2O_3) in CC-type and BO-type spherules. Janches et al. (2009) suggest that depletion of refractory elements only occurs after the depletion of Mg, Si, and Fe, so it is unlikely that Ca and Al have been volatilised. The apparent depletion in Ca and Al is more likely due to variable sampling of the heterogeneous mineralogy in cosmic spherules. However, Fe is clearly depleted in a number of CC-type spherules, resulting in the apparent bulk increase of other elements. This may be related to the scarcity of spinels in such spherules. In addition to the depletion of the dominant Fe component, depletion of siderophile trace elements, Co and Ni in particular, is seen to be highest in CC-type spherules (ratios of CC-type spherule/CM chondrite of 0.23 and 0.08 respectively). The cause of depletion of the siderophile elements will be discussed later, along with I-type origins.

1.6.2 Origins of Stony Cosmic Spherules

Stony Cosmic Spherule Precursors

Mineralogical and chemical studies of the less thermally altered counterparts to cosmic spherules (i.e. unmelted and scoriaceous micrometeorites and interplanetary dust particles: IDPs), suggest that many of them are broadly similar to carbonaceous chondrites. Mineralogical evidence such as the presence of a "combination of phyllosilicates with coarse grained minerals (olivine and pyroxene) point towards a source similar to that of CM carbonaceous chondrites" (Kurat et al., 1994). However, micrometeorites show some mineralogical and chemical differences to the CM chondrites (c.f. Engrand and Maurette, 1998; Genge et al., 1997; Kurat et al., 1994) though differences such as the lack of carbonates, sulfates, depletion of volatiles, and siderophiles can be attributed to terrestrial alteration and thermal alteration during atmospheric entry. There are also some micrometeorites with features that are comparable to CR and CI chondrites such as high pyroxene abundance (Kurat et al., 1994), but again there are also some important differences (c.f. Engrand and Maurette, 1998). Oxygen isotopes, originally conceived to differentiate and classify meteorites, also place carbonaceous chondrites as the likely precursor to the majority of micrometeorite population (Clayton et al., 1986; Engrand et al., 1999; Suavet et al., 2010; Taylor et al., 2005a; Yada et al., 2005). Maurette (2006) makes the bold claim that "About 99% of them [Antarctic micrometeorites] are only related to the CI- and CM-type subgroups of the primitive volatile-rich chondrites" based on mineralogical, chemical and isotopic compositions. In summary, the literature suggests that micrometeorites appear to be carbonaceous in origin with some distinct differences that may, or may not, result from terrestrial and atmospheric alteration.

If cosmic spherules are simply more thermally altered versions of IDPs and other micrometeorites, they should also exhibit carbonaceous compositions, albeit with stronger volatile element depletions and a lack of original mineralogy. According to Brownlee et al. (1997), ~80% of cosmic spherules in the DSS collection are most similar to CM chondrites based on the distribution peaks of Mg/Si, Al/Si, Ca/Si, Ti/Si,

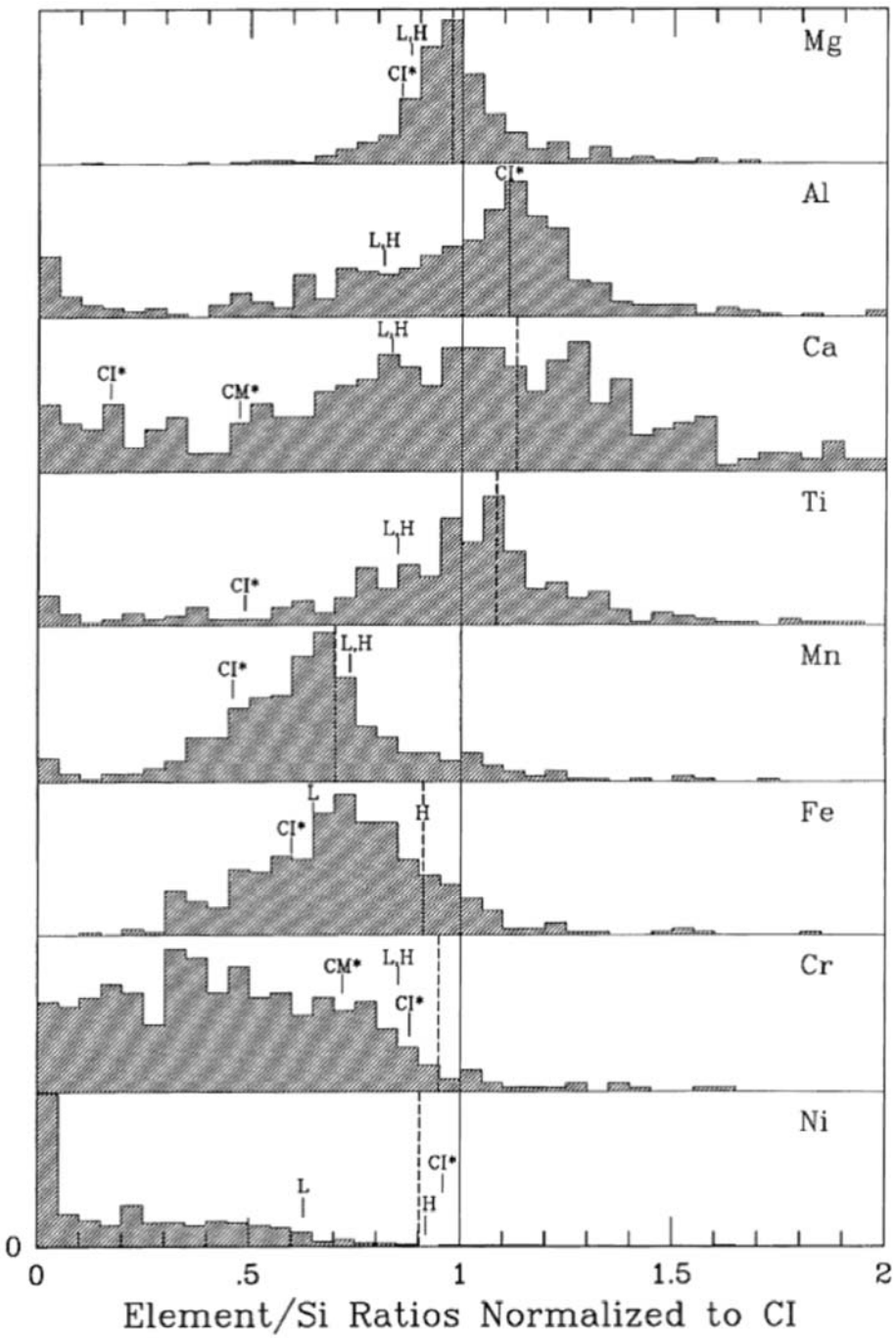

Figure 17. Element to Si ratios normalized to CI (Anders and Grevesse, 1989) for all stony cosmic spherules 100 μm and greater in size. Dashed line indicates mean CM chondrite composition (Wasson and Kallemeyn, 1988), CI and CM indicate mean CI and CM matrix compositions (McSween and Richardson, 1977), and H and L indicate mean H chondrite and L chondrite compositions (Wasson and Kallemeyn, 1988).

Diagram from Brownlee et al. (1997)

Mn/Si, and Fe/Si ratios (Figure 17). Taylor et al. (2005a) also notes that, based on Mg/Al and Si/Al ratios, 70% of cosmic spherules from the SPWW were similar to CI, CM or less likely CO and CV chondrites. Overall, it seems like there is overwhelming evidence that cosmic spherules and their less thermally altered counterparts have carbonaceous chondrite-like precursors.

Other Possible Origins

Although the majority of cosmic spherules have appeared to be related mineralogically and chemically to carbonaceous chondrites, the results of the DSS and SPWW studies indicate that the minority of stony cosmic spherules, in this case about 20-30%, may have originated from other bodies. Walter et al. (1995) found that 1% of the Antarctic micrometeorites are mineralogically related to ordinary chondrites. Furthermore, a recent discovery by Rochette et al. (2008) indicated that a small percentage of ordinary chondrites, and even chondrules, were found in their samples from the Transantarctic Mountains, Antarctica. More recently, Suavet et al. (2010) studied 33 micrometeorites from the Transantarctic Mountains using oxygen isotopes and found that 9 of the 33 are likely to have ordinary chondrite precursors.

Brownlee et al. (1997) have also suggested that at least 5% of DSS spherules may be sourced from a non-chondritic Fe-rich source. They suggest that "it could be that they are samples from a distinct enstatite-metal-rich asteroid type or they could be nebular products that exist as millimetre sized components in finer-grained matrix material" because of minor element similarities, but maintain there is not an "exact match". Taylor et al. (2007) discovered a small number of cosmic spherules in the SPWW collection (<1%) that have non-chondritic Fe/Mn versus Fe/Mg ratios, but instead suggest they may be related to igneous eucrites, many of which may have originated from the asteroid 4Vesta (see also Cordier et al., 2011). A single achondrite has also been identified by Gounelle et al. (2006) based on exsolution lamellae and differentiated REE pattern.

Comets are also a potential parent body of cosmic spherules. Models of atmospheric entry of micrometeoritic material by Love and Brownlee (1991) suggests that primary particles of <30μm size entering the atmosphere may be cometary as their entry velocities typically exceed 15km/sec (the minimum velocity of dust generated by comets with perihelia <l AU). Raisbeck and Yiou (1989) also argued that a significant portion of micrometeorites were cometary in origin based on the ^{10}Be exposure age of 21 cosmic spherules with broadly spread exposure ages <4Ma peaking at 0.25Ma. Raisbeck and Yiou (1989) indicated that spherules produced from chondritic meteorites should exhibit a narrow range of older exposure ages since chondritic meteorites had orbits that were less varied compared to comets. However, the search for cometary micrometeorites from an identifiable parent body is still underway; success will represent a major breakthrough in this field of research (Duprat et al., 2007).

Lastly, it has been suggested that cosmic spherules represent a reservoir or source that has not been sampled as macro-meteorites. Based on the distribution of D/H ratios, Maurette (2000) suggests that cosmic spherules and micrometeorites in general, sample a type of material that is not represented in current meteorite collections. The D/H ratios are very similar to the Standard Mean Ocean Water (SMOW) value of terrestrial oceans and Maurette (2006) argues that this is not because of terrestrial contamination, since the D/H ratios of the Antarctic ice is 1.5 times less than that of SMOW. Furthermore, Maurette (2000) suggested that micrometeorites may have been a significant contributor of water to the Earth's oceans accounting for ~15% of the water in the oceans today.

Precursor Identification

Cosmic spherules are a collection of various particles that can originate from a number of sources, but chondrite-like chemistries seem to predominate, as observed in this and many other studies. The CM chondrite-like precursors appear to make up the majority of many cosmic spherule collections (Brownlee et al., 1997; Clayton et al., 1986; Kurat et al., 1994; Taylor et al., 2005a).

Typically, a graph utilising Si/Al vs. Mg/Al ratios is used to illustrate the difference between carbonaceous and non-carbonaceous chondrites (see Figure 18). This graph shows that cosmic spherules have more in common with carbonaceous chondrites, as they scatter around the trend line defined by carbonaceous chondrites. There may also be some cosmic spherules that are not carbonaceous in nature, but this cannot be determined using this figure. However, it is possible to statistically quantify the dissimilarity between individual cosmic spherules and potential precursors, based on the major and trace element chemistries. Using a simple statistical method, mean absolute percentage error (MAPE: Equation 1), the composition of an individual cosmic spherule can be compared to a variety of chondrite subgroups.

$$MAPE = \frac{1}{n}\sum_{i=1}^{n}\left|\frac{f_i - y_i}{f_i}\right| \quad \textbf{[1]}$$

Where n = number of variables, in this case, the number of elements being evaluated (i.e. for 5 major elements: Fe, Mg, Ca, Al, and Si)

f_i = abundance of *i* in an individual spherule where *i* is equal to a single variable (i.e. for major elements: Fe, Mg, Ca, Al, or Si)

y_i = abundance of *i* in a chondritic precursor where *i* is equal to a single variable (i.e. for major elements: Fe, Mg, Ca, Al, or Si)

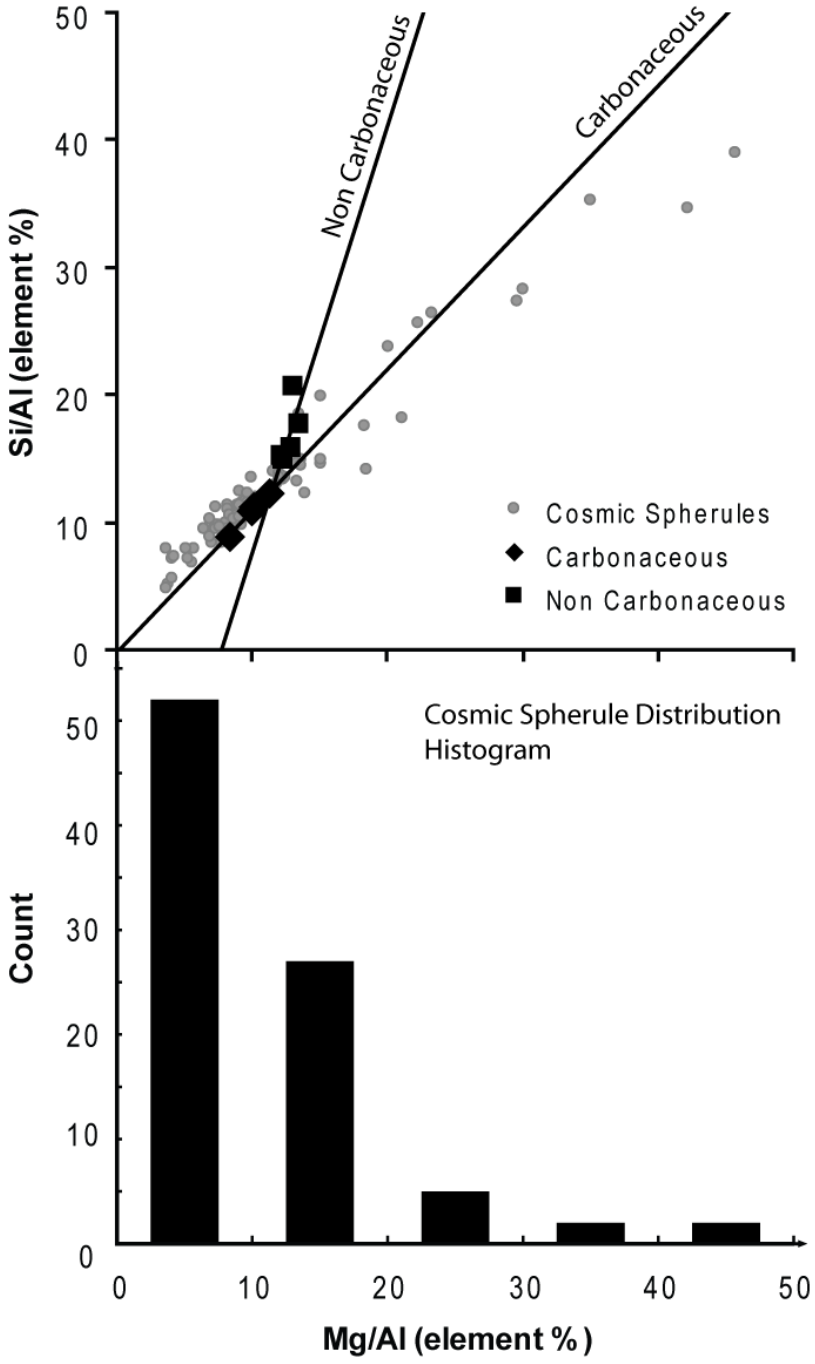

Figure 18. Si/Al and Mg/Al ratios of cosmic spherule and chondrite groups. Cosmic spherules have more in common with carbonaceous chondrites as they plot closer to the carbonaceous trendline. Outlying cosmic spherules are low in Al due to variable sampling of each cosmic spherule. The histogram shows the number of spherules in the cluster near the carbonaceous trendline in the plot above.

The MAPE value of each chondrite subgroup compared to an individual cosmic spherule is calculated. The smallest MAPE value for an individual cosmic spherule corresponds to the closest compositional match. For this analysis, the volatile-free mean composition of chondrite groups presented in Wasson and Kallemeyn (1988) has been used. This analysis assumes that all volatiles have been lost due to heating during atmospheric entry. CR (Kallemeyn et al., 1994) and CK (Kallemeyn et al., 1991) chondrite compositions were also considered, but for major elements only, since there are only limited constraints on the trace element abundance. Note that cosmic spherule precursors are not only limited to chondrites, as previously discussed, and that this analysis only matches to the chondritic precursors considered here. A total of 60 stony cosmic spherules that have been analysed for both major and trace element composition are used in this calculation.

Table 5. The median Mean Absolute Percentage Error (MAPE) value for the stony cosmic spherule population when compared to various chondrite subgroups. Higher numbers reflect increasing dissimilarity between the stony cosmic spherules and the chondrite subgroup.

	Major Elements	Trace Elements	Trace Elements (minus volatile and siderophile elements)
CI	0.18	13.3	0.46
CM	0.16	8.5	0.43
CO	0.16	5.6	0.41
CV	0.21	5.4	0.41
CR	0.18		
CK	0.18		
H	0.19	4.1	0.48
L	0.20	4.1	0.47
LL	0.24	3.9	0.47
EH	0.28	12.1	0.55
EL	0.23	8.0	0.53

A summary of the MAPE comparison is presented in Table 5.Based on major elements only, the cosmic spherule population as a whole is most similar to CM or CO carbonaceous chondrite groups, which both have a MAPE of 0.16. For trace elements, however, the ordinary chondrites stand out as the most similar to the cosmic spherule population. LL, H, and L chondrites have MAPE values of 3.7, 4.1, and 4.1 respectively. Yet, all these MAPE values are extraordinarily high and manifest due to the depleted volatile and siderophile abundances in the cosmic spherules compared to typical chondrite compositions. The volatile and siderophile elements can be justifiably removed from this analysis to improve the MAPE values assuming that these elements may be depleted during atmospheric entry and metal bead loss, respectively. Additionally, trace elements are normalised to Ca such that more robust ratios are compared instead of variable abundances. The resulting change favours carbonaceous chondrites CV and CO with MAPE values of 0.41. This is followed by ordinary chondrites with MAPE values ranging from 0.47-0.48. The poorest matches are enstatite chondrites with MAPE values of 0.53 to 0.55. This result is more comparable with the major element analysis. It suggests that the cosmic spherule population as a whole is dominantly carbonaceous in composition. However, examination of MAPE on an individual spherules basis may be a more robust approach given that cosmic spherules can originate from a large variety of parent bodies. The major elements suggest that 40/60 of the cosmic spherules best fit to carbonaceous chondrites, 12/60 to ordinary chondrites, and 8/60 to enstatite chondrites. The trace elements suggest 4/60 cosmic spherules are best fitted to ordinary chondrites, 12/60 to enstatite chondrites, and 44/60 to carbonaceous chondrites, in particular, the CV and CO subgroup.

A few conclusions can be drawn from the results of this statistical analysis. First, major elements appear to lack the resolution needed to subdivide cosmic spherules into chondrite subgroups. In this case, the trace element fits suggest that most cosmic spherules are similar to carbonaceous chondrites, a conclusion supported by the literature. However, CV and CO subgroups appear to best fit most cosmic spherules in this analysis compared to other carbonaceous groups. This conclusion is not shared by Taylor et al. (2005a), who suggest that CV and CO chondrites are the least similar to the

SPWW cosmic spherules, but also note that natural variability in composition preclude directly relating any stony cosmic spherule with a C-chondrite. A similar conclusion can be drawn from this study. Although it is possible to identify a best fit, it does not exclude other chondrite subgroups, as these can be difficult to resolve. Compounding this difficulty is the heterogeneous mineralogy of the analytical surfaces which may not be representative of the true bulk chemistry.

1.6.3 Siderophile Depletion in Stony Spherules and I-Type Origins

Iron Meteorites Precursors

According to Nozaki et al. (1998), the origin of the I-type spherules has been controversial for over three decades. Initially, I-types were thought to be ablation products of iron meteorites because "they possessed identical mineralogy with the fusion crusts of iron meteorites" (Blanchard et al., 1980). Based on the consistent abundance of the cosmogenic isotope ^{10}Be in both I-type spherules and iron meteorites, Yiou et al. (1985) also suggested that I-type spherules could be ablation products of iron meteorites. A subsequent study by Nozaki et al. (1998) explores this possibility using trace element compositions of I-type spherules from the DSS collection.

Nozaki et al. (1998) divided I-types spherules into two groups: those with <25ppm Mn and those with >25ppm Mn. They assumed that spherules in the Mn-poor group are most similar to iron meteorites, in particular the IIIAB group because iron meteorites are generally Mn-poor, and the IIIAB is the largest group of iron meteorites. There is little reasoning for this assumption and they proceed to compare low-Mn I-types to the Cape York IIIAB meteorite (Figure 19). However, Figure 19 shows that I-types have an excess of Cr and depletion of Ni, Ga, and Ge compared to the Cape York IIIAB meteorite. Nozaki et al. (1998) hypothesise that at oxygen fugacity where liquid magnetite is stable (i.e. where Co, Ni, Mn, Ga, and Ge are in the form Cr_2O_3, MnO, Co, Ni, Ga_2O_3, and GeO_2, respectively), Cr is refractory and enriched relative to the other elements, Ga and Ge are volatile and vaporised, and Ni could be lost in a Ni-rich bead. They compare I-type spherule composition to those of chondrites concluding that I-types can only be produced from ablation of metallic chondrite melts under restricted ranges of oxygen fugacity. Hence by inference, they suggest that the precursor is more likely to be an iron meteorite, but do not rule out chondritic precursors. Nozaki et al. (1998) consider the Mn-rich group to be neither derived from iron meteorites nor chondrites.

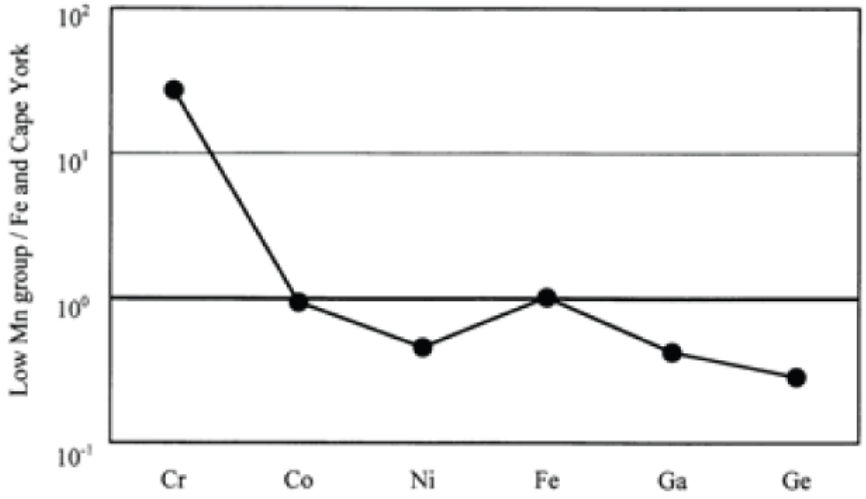

Figure 19. The mean elemental abundances of low Mn I-type spherules normalized to Fe and the IIIAB Cape York iron meteorite, showing that relative abundance decreases from left to right in the diagram.

Diagram from Nozaki et al. (1998)

Chondritic Precursors

Both Yiou et al. (1985) and Nozaki et al. (1998) also highlight the possibility that I-type spherules could also have been products of metallic chondrite melts. Herzog et al. (1999) calculated the Fe, Ni, and Cr abundance of I-type spherules prior to evaporative loss during atmospheric entry and found that the I-type composition was more comparable with metals found within chondrites than with iron meteorites. They suggest that most I-type spherules were discrete metal particles prior to entry into the Earth's atmosphere that were released during collisions, or formed in reducing processes, on a meteoroid or parent body. Xue et al. (1995) also share this point of view since ^{10}Be and ^{26}Al contents of two I-type spherules in their study indicate that they were probably originally irradiated as meteoritic metal in an object less than a few centimetres in size. However, Herzog et al. (1999) have also noted that a few rarer I-types may have formed during atmospheric entry.

I-type formation during atmospheric entry was first proposed by Brownlee et al. (1984) (see Figure 20) who suggested that it is possible to produce an I-type spherule during melting of a chondritic particle. This is due to the formation of an immiscible metallic Fe-Ni liquid within the silicate melt which then physically separates due to density differences. Once separated, the metallic bead would then shrink in size and become more Ni-rich as Fe oxidises to form a FeO shell. Continued oxidation would cause the loss of Ni, which would leave a residue of only the most refractory Platinum Group Elements (PGEs).

Evidence for this process includes the depletion of Fe, Ni, Cr, and Co (i.e. the I-type forming elements) in the stony cosmic spherules of the Deep Sea Spherule collection (Brownlee et al., 1997). Brownlee et al. (1997) noted that "Although there is no compelling evidence from this study for the origin for siderophile depletion (of stony cosmic spherules), we favour a model where metal is formed and lost during atmospheric entry". Taylor et al. (2000) and Genge and Grady (1998) noted that Fe-Ni or FeS beads could be found on the edges of stony spherules, and that some stony spherules showed signs of having lost a metal bead (i.e. beads on the edge of spherules close to separations and indentations where beads may have been lost). Further support for the Brownlee et al. (1984) model is given in Taylor et al. (2005a) who quantify the amount of δ^{57}Fe isotope fractionation in stony cosmic spherules experienced. The fractionation of these isotopes occurs as a result of evaporation and mass loss during atmospheric entry and can be used to constrain such processes. Assuming that the stony cosmic spherule was originally compositionally similar to a CM chondrite, Taylor et al. (2005a) showed that the heavier δ^{57}Fe abundance in stony spherules does not increase as the fraction of total Fe decreases, which is expected if evaporation alone were responsible for iron loss. Most spherules, save for the CAT and glass spherules, do not show enrichment of δ^{57}Fe. Therefore, Taylor et al. (2005a) interpreted that Fe loss occurred through removal of a siderophile rich bead concluding that "as a rule most of the Fe present in sCS [stony Cosmic Spherules] is lost by ejection before it has a chance to evaporate". Engrand et al. (2005) suggests that "good anti-correlation between the Fe

and Ni contents of all [I-Type] spherules suggests a common precursor that underwent successive stages of melting and fragmentation".

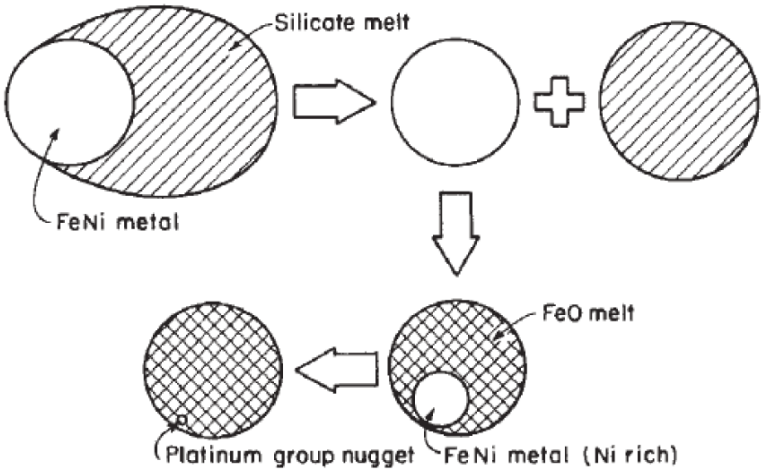

Figure 20. The Brownlee et al. (1984) model for the most common sequence of events that produces iron cosmic spheres containing PGE-rich residues (referred to as the platinum group nugget). Upon melting triggered during atmospheric entry, a micrometeorite forms a composite particle of molten silicate and metal as shown in the upper left of the diagram. The separation of the molten silicate and metal components stems from inertial forces which act to separate the two components due to their large density difference, thus forming a molten silicate sphere and metal sphere. Continued oxidation of the metal sphere causes the iron to rapidly develop an iron oxide shell which allows more siderophilic elements, such as PGEs, to concentrate in the shrinking metal core. Continued heating may vaporise the oxide shell, leaving only the nugget which could be PGE-rich if most of the iron and nickel leave the core when oxidation is complete.

Diagram from Brownlee et al. (1984)

Support for the Brownlee Model

In this thesis, it was found that siderophile elements are depleted in stony cosmic spherules relative to chondritic values. In addition, FeO, Co, and Ni are most depleted in CC-type spherules. In contrast to moderately volatile lithophile elements like Rb, the depletion of Ni, Co, and Pt in stony spherules cannot be caused by volatilisation during atmospheric heating as these are relatively refractory elements. The results of this study consistent with the literature, however, the chemistry and petrographic relationships of cosmic spherules in this study provide further evidence for I-type formation through mechanisms proposed in the Brownlee et al. (1984) model.

If I-type spherules are formed through metal/silicate immiscibility there should be physical evidence for the co-existence, and perhaps separation, of the two phases. Though rare, there are a few spherules in this study that are believed to illustrate the physical separation of an iron-rich bead from the stony spherule. A sequence has been constructed using these examples to show iron-rich bead separation from a silicate cosmic spherule in Figure 21. Here three stages of iron-rich core separation are shown: cosmic spherules show a core near the edge of a silicate spherule, exposed on the outer rim, and finally one that seems on the verge of separating by forming a nipple on the perimeter of the stony spherule. No spherules were found to have a metallic core in the middle of the spherule in this study. Since these rare spherules were probably flash cooled in mid-air, most spherules would not have the chance to form cores or would have already lost their cores at this stage. Similar observations have been made by other authors. For example, Taylor et al. (2005a) noted that many spherules from the South Pole Well Water collection contain Fe-Ni or FeS beads that are "located near spherule edges that appear close to separation; indentations in the spherule edges showing where beads may have been lost.". Although the state of the beads (metallic or oxide) was not mentioned in Taylor et al. (2005a), the beads of that were studied in this thesis are metallic with finger-like intergrowths of Fe and Ni metal.

In addition to the petrography, the iron-rich spherules (I-type and D-type) have major and trace element compositions that are complementary to those of the stony spherules

(regardless of different chondritic normalisation values). In the case of D-type spherules, outliers and extremes that are not siderophile elements represent the mixed composition of the dendritic spherules. The I-type spherules are enriched in siderophile elements (P, Fe, Co, Ni, Ru, Rh, Pd, W, and Pt) and depleted in all the other elements analysed relative to D-types (Fig 7a). However, a number of lithophile elements are present in select I-type spherules in minor concentrations, (up to 2 wt.%). This may be the result of silicate material trapped within the I-type spherule during segregation of these particular I-types from the silicate spherule. D-type spherules may be formed in a similar process. Entrapment of varying amounts of silicate material in a segregating iron-rich melt would have chemical characteristics similar to D-types, although the texture of a particle formed in this fashion is debatable.

The observation that all I-type spherules show a strong linear relationship between Fe and Ni (Figure 11) suggests that all I-type spherules have probably evolved from similar precursors. Metallic I-types and metallic beads in stony/silicate spherules in particular, share a strong one-to-one (Fe:Ni) relationship. However, the oxidised I-types have a slightly different relationship (1.25:1, NiO:FeO), which suggests either a difference in precursor chemistry or a difference created by atmospheric processing. One interesting difference between the oxide and metallic I-types is the presence of a wüstite (FeO) shell. Spherules with a shell have metallic interiors and those without are oxidised throughout. According to Herzog et al. (1999), evaporation of I-type spherules begins from the molten metal phase (initial separation from the spherule) and is only protected from evaporation when oxides form as a result of reaction with atmospheric oxygen. Additionally, the formation of a FeO shell appears to be dependent on particle size such that oxidised I-types are dominant in the large size fractions, whereas metallic I-types are dominant in the smaller sizes (<70μm). This suggests that peak temperature may affect either the formation or the retention of a FeO shell. One could conclude that formation and retention of such a shell allows metallic Fe in the I-type spherule to be consumed in the formation of the shell. This minimises evaporation and concentrates Ni in the still-metallic core, leading to a one-to-one relationship between Fe and Ni in the core. Spherules that do not form or retain their shells, possibly as a result of higher peak

temperatures, experience preferential evaporation of the Fe metal in the core, leading to a higher Fe/Ni mass ratio. This is eventually followed by complete oxidisation thus slowing the concentration of NiO relative to FeO in the now oxidised core. This process may explain why Ni contents do not exceed ~20 wt.%. However, if NiO-rich cores existed, it would indicate that oxidation may have occurred as a result of post-depositional terrestrial weathering in the absence of a protective shell. Major and trace element analyses of the metallic beads within spherules also offer clues to the separation process. Although only two such examples were analysed in this project, both are highly evolved with >40wt.% Ni. This suggests that metallic beads unable to separate from the host silicate spherule also evolve in the same fashion as those that separate and form oxide shells.

In summary, this study supports previous suggestions that I-type spherules were formed through metal/silicate immiscibility triggered by melting of the stony cosmic spherule, with subsequent oxidation of the melt during atmospheric entry. A petrographic sequence of metallic bead loss has been proposed and is supported by complementary chemical patterns between the I-type and stony cosmic spherules. Metallic beads within stony spherules and metallic I-types (with FeO shells) share a constant Fe/Ni ratio suggesting a common precursor. The chemistry and petrography can be interpreted as follows: Melting of the chondritic precursor followed by subsequent oxidation of the melt causes metal/silicate immiscibility, allowing the formation of a metallic bead within a stony/silicate spherule if quenched. The metallic bead becomes smaller and richer in Ni and PGEs as Fe is removed to consume oxygen. If the metallic bead separates from the stony/silicate cosmic spherule, the metallic bead is reclassified as an I-type spherule. I-type spherules that are able to redirect oxidation by siphoning Fe into a glassy FeO cap allow more noble elements to retreat into the shrinking core, keeping it metallic, much like those unable to separate from the stony/silicate spherules. This process removes Fe from the core, increasing the relative bulk concentration of other siderophile elements such as Ni and platinum-group elements. This model satisfies the condition of a common compositionally evolving precursor as suggested in Figure 11.

Many I-type spherules, however, are completely oxidised perhaps because of an inability to form or sustain a glassy FeO shell.

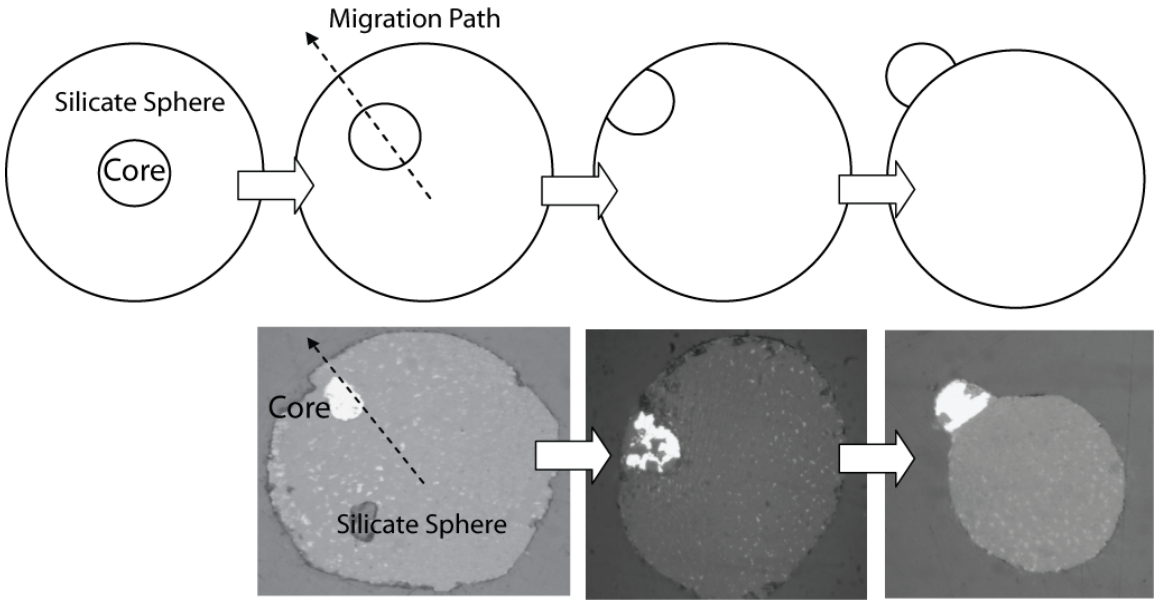

Figure 21. Petrographic evidence suggesting immiscibility and eventual separation of a metallic bead from a spherule, based on processes described by Brownlee et al. (1984). Once separated, the metallic bead is reclassified as an I-type spherule.

1.7 Chapter Conclusion

Cosmic spherules from the Lewis Cliff site in Antarctica have been analysed for major and trace element abundances and have been described and classified according to petrographic features. A refined classification system for use under petrographic microscopes has been developed. This study has also increased the number of spherules described in this region by about four fold. The larger number of described cosmic spherules from this region allows examination of the global characteristics of other cosmic spherule collections. All the major cosmic spherules collections (South Pole Well Water, Deep Sea, Greenland, and Antarctic Surface Spherules) have similar major element compositions. Textures described in the SPWW, DSS and GS collections, in general are compatible with those seen in the AS collections. Hence, the majority of cosmic spherules, regardless of the collection location, have probably originated from similar materials and undergone similar thermal alteration processes during passage through the Earth's atmosphere. Loss of volatile and moderately volatile lithophile elements along with siderophile element depletion in stony cosmic spherules and enrichment of siderophile elements in the iron/nickel-iron group spherules are probably common in the other cosmic spherule collections as observed in the Antarctic Surface spherules. These may well be general features that result from the atmospheric oxidation and heating of the precursors.

Using both major and trace element data has also provided insight into the origin of the stony/silicate and iron/nickel-iron cosmic spherules. Analysis of the major and trace element data highlights the predominance of chondritic precursors, dominated by carbonaceous chondrites, although a single subgroup cannot be identified definitively. Further evaluation of the major and trace element data using statistical methods may allow the determination of the proportion of carbonaceous to non-carbonaceous chondrite precursors. Better constraints on the effects of atmospheric, terrestrial and perhaps extraterrestrial processing are needed for confident and precise identification of precursors and factors affecting their contribution to cosmic spherule characteristics. In particular, identification of selection effects that may contribute to a dominance of

carbonaceous chondrites is necessary. Convincing evidence has been found for the Brownlee et al. (1984) model for the formation of the iron/nickel-iron group spherules. Petrographic relationships between a stony/silicate sphere and iron-rich bead and the complementary depletion of siderophile elements in cosmic spherules and enrichment in iron/nickel-iron spherules are evidence that metal/silicate immiscibility in stony cosmic spherules is responsible for the creation of iron/nickel-iron spherules.

1.8 Chapter References

ANDERS E. and GREVESSE N. (1989) Abundances of the elements: Meteoritic and solar. *Geochimica et Cosmochimica Acta* **53**(1), 197-214.

BLANCHARD M. B., BROWNLEE D. E., BUNCH T. E., HODGE P. W. and KYTE F. T. (1980) Meteoroid ablation spheres from deep-sea sediments. *Earth and Planetary Science Letters* **46**(2), 178-190.

BOGARD D. (1995) Impact ages of meteorites: A synthesis. *Meteoritics* **30**, 244-268.

BROWNLEE D. E. (1985) Cosmic Dust: Collection and Research. *Annual Review of Earth and Planetary Sciences* **13**(1), 147-173.

BROWNLEE D. E., BATES B. and SCHRAMM L. (1997) The elemental composition of stony cosmic spherules. *Meteoritics and Planetary Science* **32**, 157-175.

BROWNLEE D. E., BATES B. A., PILACHOWSKI L. B., OLSZEWSKI E. and SIEGMUND W. A. (1980) Unmelted Cosmic Material in Deep Sea Sediments (Abstract). *Lunar and Planetary Science XI*, 109-111.

BROWNLEE D. E., BATES B. A. and WHEELOCK M. M. (1984) Extraterrestrial platinum group nuggets in deep-sea sediments. *Nature* **309**(5970), 693-695.

BROWNLEE D. E., PILACHOWSKI L. B. and HODGE P. W. (1979) Meteorite Mining on the Ocean Floor (abstract). In *10th Lunar and Planetary Science Conference*, pp. 157-158, Houston, Texas.

CASSIDY W., HARVEY R., SCHUTT J., DELISLE G. and YANAI K. (1992) The meteorite collection sites of Antarctica. *Meteoritics and Planetary Science* **27**(5), 490-525.

CLAYTON R. N., MAYEDA T. K. and BROWNLEE D. E. (1986) Oxygen isotopes in deep-sea spherules. *Earth and Planetary Science Letters* **79**(3-4), 235-240.

CORDIER C., FOLCO L. and TAYLOR S. (2011) Vestoid cosmic spherules from the South Pole Water Well and Transantarctic Mountains (Antarctica): A major and trace element study. *Geochimica et Cosmochimica Acta* **75**(5), 1199-1215.

CORTI G., ZEOLI A. and BONINI M. (2003) Ice-flow dynamics and meteorite collection in Antarctica. *Earth and Planetary Science Letters* **215**(3-4), 371-378.

CZAJKOWSKI J., ENGLERT P., BOSELLINI A. and OGG J. G. (1983) Cobalt enriched hardgrounds-New sources of ancient extraterrestrial materials. *Meteoritics and Planetary Science* **18**, 286-287.

DEUTSCH A., GRESHAKE A., PESONEN L. J. and PIHLAJA P. (1998) Unaltered cosmic spherules in a 1.4-Gyr-old sandstone from Finland. *Nature* **395**(6698), 146-148.

DUPRAT J., ENGRAND C., MAURETTE M., KURAT G., GOUNELLE M. and HAMMER C. (2007) Micrometeorites from Central Antarctic snow: The CONCORDIA collection. *Advances in Space Research* **39**(4), 605-611.

EGGINS S. M., KINSLEY L. P. J. and SHELLEY J. M. G. (1998) Deposition and element fractionation processes during atmospheric pressure laser sampling for analysis by ICP-MS. *Applied Surface Science* **127-129**, 278-286.

ENGRAND C. and MAURETTE M. (1998) Carbonaceous micrometeorites from Antarctica. *Meteoritics & Planetary Science* **33**(4), 565-580.

ENGRAND C., MCKEEGAN K. D. and LESHIN L. A. (1999) Oxygen isotopic compositions of individual minerals in Antarctic micrometeorites: further links to carbonaceous chondrites. *Geochimica et Cosmochimica Acta* **63**(17), 2623-2636.

ENGRAND C., MCKEEGAN K. D., LESHIN L. A., HERZOG G. F., SCHNABEL C., NYQUIST L. E. and BROWNLEE D. E. (2005) Isotopic compositions of oxygen, iron, chromium, and nickel in cosmic spherules: Toward a better comprehension of atmospheric entry heating effects. *Geochimica et Cosmochimica Acta* **69**(22), 5365-5385.

FREDRIKSSON K. and GOWDY R. (1963) Meteoritic debris from the Southern California desert. *Geochimica et Cosmochimica Acta* **27**(3), 241-242.

GENGE M. J., ENGRAND C., GOUNELLE M. and TAYLOR S. (2008) The Classification of Micrometeorites. *Meteoritics and Planetary Science* **43**(3), 497-515.

GENGE M. J. and GRADY M. M. (1998) Melted micrometeorites from Antarctic ice with evidence for the separation of immiscible Fe-Ni-S liquids during entry heating. *Meteoritics and Planetary Science* **33**(3), 425-434.

GENGE M. J., GRADY M. M. and HUTCHISON R. (1997) The textures and compositions of fine-grained Antarctic micrometeorites: Implications for comparisons with meteorites. *Geochimica et Cosmochimica Acta* **61**(23), 5149-5162.

GOUNELLE M., SPURNÝ P. and BLAND P. A. (2006) The orbit and atmospheric trajectory of the Orgueil meteorite from historical records. *Meteoritics & Planetary Science* **41**(1), 135-150.

GRESHAKE A., KLOCK W., ARND P., MAETZ M., FLYNN G. J., BAJT S. and BSICHOFF A. (1998) Heating experiments simulating atmospheric entry heating of micrometeorites: Clues to their parent body sources. *Meteoritics and Planetary Science* **33**, 267-290.

GRESHAKE A., KLOECK W., ARNDT P., MAETZ M. and BISCHOFF A. (1995) Volatile Element Abundances in Micrometeorites: Evidence for the Loss of Copper, Germanium, and Zinc During Atmospheric Entry Heating (abstract). *Lunar and Planetary Science Conference* **26**, 509.

HARTMANN W. K., RYDER G., DONES L. and GRINSPOON D. (2000) The Time-Dependent Intense Bombardment of the Primordial Earth/Moon System. In *Origin of the Earth and Moon* (eds. R. M. Canup and K. Righter), pp. 493-512. The University of Arizona Press.

HARVEY R. (2003) The Origin and Significance of Antarctic Meteorites. *Chemie der Erde - Geochemistry* **63**(2), 93-147.

HARVEY R. P. and MAURETTE M. (1991) The Origin and Significance of Cosmic Dust from the Walcott Névé, Antarctica. In *Proceedings of Lunar and Planetary Science*, pp. 569-578. Luna and Planetary Institute, Houston.

HASHIMOTO A. (1983) Evaporation metamorphism in the early solar nebula-evaporation experiments on the melt FeO-MgO-SiO_2-CaO-Al_2O_3 and chemical fractionations of primitive material. *Journal of Geochimica* **17**, 111-145.

HASHIMOTO A. and KUMAZAWA M. (1979) Evaporation Metamorphism of Primitive Material in the Early Solar Nebula. *Earth and Planetary Science Letters* **43**, 13-21.

HERZOG G. F., XUE S., HALL G. S., NYQUIST L. E., SHIH C. Y., WIESMANN H. and BROWNLEE D. E. (1999) Isotopic and elemental composition of iron, nickel, and chromium in type I deep-sea spherules: implications for origin and composition of the parent micrometeoroids. *Geochimica et Cosmochimica Acta* **63**(9), 1443-1457.

HEWINS R. H. and FOX G. E. (2004) Chondrule textures and precursor grain size: an experimental study. *Geochimica et Cosmochimica Acta* **68**(4), 917-926.

HUI S. S. M., NORMAN M. D. and HARVEY R. P. (2007) The petrography and chemistry of cosmic spherules from Lewis Cliff, Antarctica. In *Australian Space Science Conference* (ed. W. Short), pp. 84-97. National Space Society of Australia Ltd, Sydney, Australia.

HUTCHISON R. (2004) *Meteorites: a petrologic, chemical and isotopic synthesis*. Cambridge University Press.

IWATA N. and IMAE N. (2002) Antarctic micrometeorite collection at a bare ice region near Syowa Station by JARE-41 in 2000. *Antarctic meteorite research* **15**, 25-37.

JANCHES D., DYRUD L. P., BROADLEY S. L. and PLANE J. M. C. (2009) First observation of micrometeoroid differential ablation in the atmosphere. *Geophysical Research Letters* **36**.

KALLEMEYN G. W., RUBIN A. E. and WASSON J. T. (1991) The compositional classification of chondrites: V. The Karoonda (CK) group of carbonaceous chondrites. *Geochimica et Cosmochimica Acta* **55**(3), 881-892.

- (1994) The compositional classification of chondrites: VI. The CR carbonaceous chondrite group. *Geochimica et Cosmochimica Acta* **58**(13), 2873-2888.

KALLIO A. (2007) LAB-RAT. In *On the Geochemistry and Cosmochemistry of Rubidium and Cesium*. Ph.D Thesis. Research School of Earth Sciences, Australian National University.

KLÖCK W., FLYNN G. J., SUTTON S. R., BAJT S. and NEUKING K. (1994) Heating Experiments Simulating Atmospheric Entry of Micrometeorites (abstract). In *25th Lunar and Planetary Science Conference*, pp. 713, Houston, Texas.

KOEBERL C. and HAGEN E. H. (1989) Extraterrestrial spherules in glacial sediment from the Transantarctic Mountains, Antarctica: Structure, mineralogy, and chemical composition. *Geochimica et Cosmochimica Acta* **53**(4), 937-944.

KRINOV E. L. (1959) Über die Natur der Mikrometeoriten. *Chemie der Erde - Geochemistry* **20**, 28-35.

KURAT G., KOEBERL C., PRESPER T., BRANDSTATTER F. and MAURETTE M. (1994) Petrology and geochemistry of Antarctic micrometeorites. *Geochimica et Cosmochimica Acta* **58**(18), 3879-3904.

LINEWEAVER C. H. and NORMAN M. D. (2009) The Bombardment History of the Moon and the Origin of Life on Earth. In *8th Australian Space Science Conference* (eds. W. Short and I. Cairns). National Space Society of Australia Ltd, Canberra.

LOFGREN G. (1989) Dynamic cyrstallization of chondrule melts of porphyritic olivine composition: Textures experimental and natural. *Geochimica et Cosmochimica Acta* **53**(2), 461-470.

LOFGREN G. and RUSSELL W. J. (1986) Dynamic crystallization of chondrule melts of porphyritic and radial pyroxene composition. *Geochimica et Cosmochimica Acta* **50**(8), 1715-1726.

LOVE S. G. and BROWNLEE D. E. (1991) Heating and thermal transformation of micrometeoroids entering the Earth's atmosphere. *Icarus* **89**(1), 26-43.

- (1993) A Direct Measurement of the Terrestrial Mass Accretion Rate of Cosmic Dust. *Science* **262**(5133), 550-553.

MAURETTE M. (2006) *Micrometeorites and the Mysteries of Our Origins*. Springer. pp. 330.

MAURETTE M., DUPRAT J., ENGRAND C., GOUNELLE M., KURAT G., MATRAJT G. and TOPPANI A. (2000) Accretion of neon, organics, CO2, nitrogen and water from large interplanetary dust particles on the early Earth. *Planetary and Space Science* **48**(11), 1117-1137.

MAURETTE M., HAMMER C., REEH N., BROWNLEE D. E. and THOMSEN H. H. (1986) Placers of Cosmic Dust in the Blue Ice Lakes of Greenland. *Science* **233**(4766), 869-872.

MAURETTE M., JEHANNO C., ROBIN E. and HAMMER C. (1987) Characteristics and mass distribution of extraterrestrial dust from the Greenland ice cap. *Nature* **328**(6132), 699-702.

MAURETTE M., OLINGER C., MICHEL-LEVY M. C., KURAT G., POURCHET M., BRANDSTATTER F. and BOUROT-DENISE M. (1991) A collection of diverse

micrometeorites recovered from 100 tonnes of Antarctic blue ice. *Nature* **351**(6321), 44-47.

MCSWEEN H. Y. and RICHARDSON S. M. (1977) The composition of carbonaceous chondrite matrix. *Geochimica et Cosmochimica Acta* **41**(8), 1145-1161.

MURRAY J. and RENARD A. F. (1891) Report on the Deep-Sea deposits Based on the Specimens Collected During the Voyage. In *Report on the scientific results of the H.M.S. "Challenger" during the years 1873-76, Deep-Sea Deposits*.

NORMAN M., ROBINSON P. and CLARK D. (2003) Major and Trace Element Analysis of Sulfide Ores by Laser-Ablation ICP–MS, Solution ICP–MS, and XRF: New Data on International Reference Materials. *The Canadian Mineralogist* **41**, 293-305.

NORMAN M. D., GARCIA M. O. and BENNETT V. C. (2004) Rhenium and chalcophile elements in basaltic glasses from Ko'olau and Moloka'i volcanoes: Magmatic outgassing and composition of the Hawaiian plume. *Geochimica et Cosmochimica Acta* **68**(18), 3761-3777.

NOZAKI W., NAKAMURA T., IIDA A., MATSUOKA K. and TAKAOKA N. (1998) Trace element concentrations in iron type cosmic spherules determined by the SR-XRF method. In *Twenty-third Symposium on Antarctic Meteorites, NIPR Symposium* (ed. T. Hirasawa), pp. 199. National Institute of Polar Research, National Institute of Polar Research, Tokyo.

RAISBECK G. M. and YIOU F. (1989) Cosmic ray exposure ages of cosmic spherules. *Meteoritics and Planetary Science* **24**, 318.

RASBAND W. S. (1997-2008) ImageJ, http://rsb.info.nih.gov/ij/. National Institutes of Health, Bethesda, Maryland, USA.

ROBIN E. (1988) Des poussieres cosmique dans les cryoconites du Groenland: Nature, origine et applications. Ph.D. thesis. Universite de Paris-Sud.

ROBIN E., CHRISTOPHE MICHEL-LEVY N., BOUROT-DENISE M. and JEHANNO C. (1990) Crystalline micrometeorites from Greenland blue lakes: their chemical composition, mineralogy and possible origin. *Earth and Planetary Science Letters* **97**(1-2), 162-176.

ROBIN E., JEHANNO C. and MAURETTE M. (1987) Characteristics and origin of Greenland Fe/Ni cosmic grains. In *18th Lunar and Planetary Science Conference*, pp. 593-598, Houston, Texas.

ROCHETTE P., FOLCO L., SUAVET C., VAN GINNEKEN M., GATTACCECA J., PERCHIAZZI N., BRAUCHER R. and HARVEY R. P. (2008) Micrometeorites from the Transantarctic Mountains. *Proceedings of the National Academy of Sciences* **105**(47), 18206-18211.

RYDER G. (2002) Mass flux in the ancient Earth-Moon system and benign implications for the origin of life on Earth. *Journal of Geophysical Research (Planets)* **107**(E4), 13.

SUAVET C., ALEXANDRE A., FRANCHI I. A., GATTACCECA J., SONZOGNI C., GREENWOOD R. C., FOLCO L. and ROCHETTE P. (2010) Identification of the parent bodies of micrometeorites with high-precision oxygen isotope ratios. *Earth and Planetary Science Letters* **293**(3-4), 313-320.

TAYLOR S., ALEXANDER C. M. O. D., DELANEY J., MA P., HERZOG G. F. and ENGRAND C. (2005a) Isotopic fractionation of iron, potassium, and oxygen in stony cosmic spherules: Implications for heating histories and sources. *Geochimica et Cosmochimica Acta* **69**(10), 2647-2662.

TAYLOR S., HERZOG G. F. and DELANEY J. S. (2007) Crumbs from the crust of Vesta: Achondritic cosmic spherules from the South Pole water well. *Meteoritics & Planetary Science* **42**(2), 223-233.

TAYLOR S., LEVER J. H. and HARVEY R. P. (1998) Accretion rate of cosmic spherules measured at the South Pole. *Nature* **392**(6679), 899.

- (2000) Numbers, types, and compositions of an unbiased collection of cosmic spherules. *Meteoritics & Planetary Science* **35**(4), 651-666.

TAYLOR S., MATRAJT G., LEVER J. H., JOSWIAK D. J. and BROWNLEE D. E. (2005b) Size Distribution of Antarctic Micrometeorites. In *Dust in Planetary Systems*, pp. 145-148. European Space Agency Publications, Kauai, Hawaii.

WALTER J., KURAT G., BRANDSTATTER F., KOEBERL C. and MAURETTE M. (1995) The Abundance of Ordinary Chondrite Debris Among Antarctic Micrometeorites (abstract). *Meteoritics* **30**(5), 592-593.

WANG J., DAVIS A. M., CLAYTON R. N., MAYEDA T. K. and HASHIMOTO A. (2001) Chemical and isotopic fractionation during the evaporation of the FeO-MgO-SiO2-CaO-Al2O3-TiO2 rare earth element melt system. *Geochimica et Cosmochimica Acta* **65**(3), 479-494.

WASSON J. T. and KALLEMEYN G. W. (1988) Compositions of Chondrites. *Philosophical Transactions of the Royal Society of London. Series A, Mathematical and Physical Sciences* **325**(1587), 535-544.

XUE S., HERZOG G. F., SOUZIS A., ERVIN M. H., LAREAU R. T., MIDDLETON R. and KLEIN J. (1995) Stable magnesium isotopes, ^{26}Al, ^{10}Be, and ^{26}Mg/^{26}Al exposure ages of iron meteorites. *Earth and Planetary Science Letters* **136**(3-4), 397-406.

YADA, TORU, NAKAMURA, TOMOKI, TAKAOKA, NOBUO, NOGUCHI, TAKAAKI, TERADA, KENTARO, YANO, HAJIME, NAKAZAWA, TAKAKIYO, KOJIMA and HIDEYASU (2004) *The global accretion rate of extraterrestrial materials in the last glacial period estimated from the abundance of micrometeorites in Antarctic glacier ice*. Terra, Tokyo, JAPAN. pp. 13.

YADA T. and KOJIMA H. (2000) The collection of micrometeorites in the Yamato Meteorite Ice Field of Antarctica in 1998. *Antarctic meteorite research* **13**, 9-18.

YADA T., NAKAMURA T., NOGUCHI T., MATSUMOTO N., KUSAKABE M., HIYAGON H., USHIKUBO T., SUGIURA N., KOJIMA H. and TAKAOKA N. (2005) Oxygen isotopic and chemical compositions of cosmic spherules collected from the Antarctic ice sheet: Implications for their precursor materials. *Geochimica et Cosmochimica Acta* **69**(24), 5789-5804.

YIOU F. and RAISBECK G. M. (1987) Cosmic Spherules from an Antarctic Ice Core. *Meteoritics* **22**, 539.

YIOU F., RAISBECK G. M. and BROWNLEE D. (1985) ^{10}Be in Iron Type Cosmic Spherules: Evidence for a Differentiated Parent Body. *Meteoritics* **20**, 791-792.

CHAPTER 2:

TECHNICAL DEVELOPMENTS

2.1 Introduction

The lunar impact spherules project required careful planning from the beginning since the impact spherules are precious samples in limited supply. A lunar impact spherule is similar to a cosmic spherule in both shape and size, but more fragile and delicate as it is composed mostly of glass. Experience handling cosmic spherules from the previous chapter directly feeds into the technical developments that accommodate the unique nature of the lunar impact spherules and project goals. This chapter outlines the development of an approach to handling and analysing the lunar impact spherules involving both theoretical and practical tests to quantify the suitability of the methods.

The key development was an analytical plan that minimised micron-sized sample consumption. To maximise the amount of information obtainable on micron-sized particles, it was imperative to preserve as much sample volume as possible. Ideally, methods such as those suggested in Zolensky et al. (2000) for Interplanetary Dust Particles (IDPs) should be employed. The Zolensky et al. (2000) method involves conversion of micron-sized samples into ultra-thin sections using microtoming techniques which are then distributed for various types of analyses. However, conversion of samples into delicate wafer-thin sections using such techniques is very time consuming, and may not be applicable for some types of materials or analyses (e.g. LA-ICP-MS). A more common approach to sample conservation is to design an analytical plan whereby a sample is exposed to progressively more destructive analyses, thus minimising damage, sample consumption, and element fractionation. However, much of the sample can be lost during preparation, before analysis even begins. For example, conventional epoxy button mounts require that the sample be polished to expose a flat analytical surface for maximising analytical precision. Polishing abrades away portions of precious samples and can lead to complete loss through "plucking" from the mount. The approach in the current study was to develop a new mounting technique and analytical plan to minimise loss and alteration at each stage.

CHAPTER 2 Technical developments

The technical aim for the lunar impact spherules project was to collect petrography and major and trace element composition and date individual impact spherules, while retaining their identity at each stage. Using glasses of known composition, a number of methods were evaluated using the following criteria:

1. Ease of sample preparation and minimal handling
2. Potential disturbance of samples from external sources of heat during mounting or recovery
3. Transferability between analytical equipment
4. Ease and success of sample recovery

The Leit-C-Plast (LCP) method developed in the current study was deemed to be the most suitable and involves compressing unpolished samples into the LCP putty. The remainder of this chapter describes the LCP method and outlines the development and testing of this technique that is designed minimise sample preparation, preparation time, and handling. While this method minimises the amount of sample consumed without too much preparation, it comes at the cost of analytical quality as samples are analysed unpolished. Consequently, the theoretical effects of an unpolished lunar impact spherule on analytical quality for each instrument are discussed in this chapter and calculations are made to quantify the effect. Shards of glass standards were also measured (as extremes in geometry) and compared to conventional polished sections to quantitatively estimate the effect of unpolished analytical surfaces.

2.2 Method Development

The Leit-C-Plast Mount - Schematic and Description

A number of mounting methods were considered for this project, with the advantages and disadvantages of each weighed against the analytical plan. As stated earlier, the focus was to minimise handling and the conservation of sample for $^{40}Ar/^{39}Ar$ radioisotopic dating. Conventional epoxy mounts were considered too wasteful of material needed for $^{40}Ar/^{39}Ar$ dating, despite providing the best analytical surface. The crystalbond mounts as described in Delano et al. (2007), whereby individual spherules are mounted in 6mm aluminium tubing using Crystalbond (509) adhesive (See Structure Probe Inc., 2009), were considered too time consuming in preparation and analysis for the purposes of this study. Additionally, this technique required undesirable heat treatment of the adhesive to 121ºC and polishing (albeit conservative amounts of polishing) of the sample. However, this method does provide a good analytical surface with minimal sample loss. Other methods, including carbon paint/tape, adhesives, and pressed samples in pliable substrates (e.g. Au, In, S), were considered to be too insecure, requiring excessive handling, not conductive and/or were difficult to recover samples for $^{40}Ar/^{39}Ar$ dating. This lead to the development of a new mounting method focused specifically on sample conservation, but also integrating the best aspects of other mounting methods.

The Leit-C-Plast mount (LCP mount) was designed as a standard 2.5cm diameter button mount for compatibility between different analytical devices (Figure 22). Compatibility between different analytical apparatuses ensures that the samples did not need to be handled further or remounted. The mount consists of forty-nine 0.8mm diameter holes, arranged in an asymmetric grid for orientation, drilled into the middle $1cm^2$ of an aluminium button. The small, centred grid was needed for compatibility with the SHRIMP which has a limited area of analysis. Leit-C-Plast, conductive carbon putty (graphite in polyisobutylene) can then be compressed into the holes of the mount. Samples were then placed on the putty on the mounting surface, pushed into the putty and carbon coated.

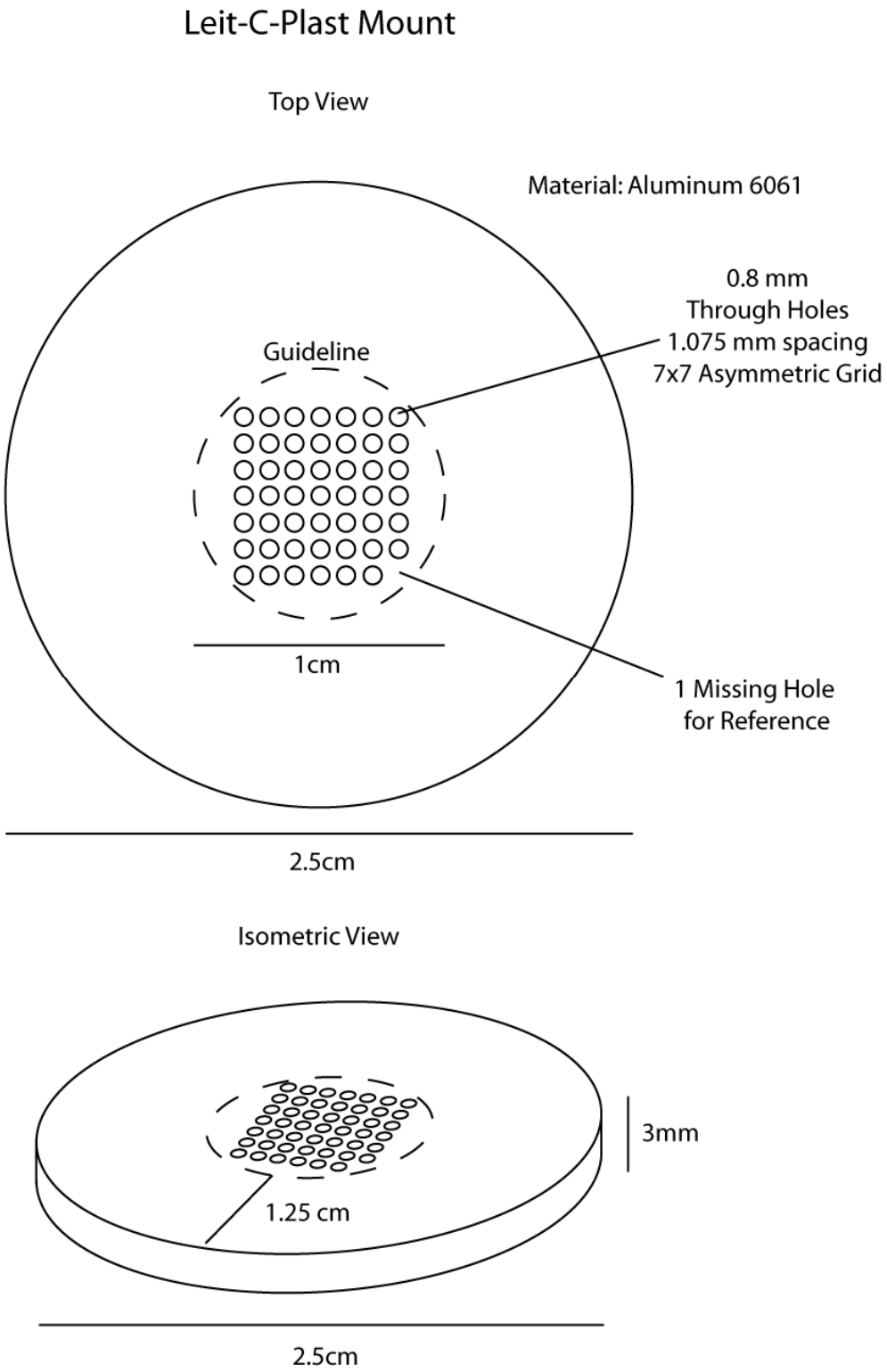

Figure 22. Schematic of the Leit-C-Plast mount.

The mounting method is as follows:

1. Two glass plates are covered with a layer of Parafilm.
2. Place the mounting surface of a LCP mount on one of the Parafilm covered plates.
3. Place a rubber O-ring around the holes on the cushion surface and smear a suitable amount of Leit-C-Plast in the O-ring. There should be enough Leit-C-Plast to fill the holes while forming a 1-2mm cushion.
4. Place the second Parafilm covered disc on top of the O-ring and Leit-C-Plast
5. Apply a moderate amount of pressure (by hand or vice) to the top glass plate where the O-ring and Leit-C-Plast reside. The Leit-C-Plast will fill the holes, and the O-ring will keep the cushion consolidated. Excess pressure will cause the putty to overflow the mount holes; moderate pressure over the span of 3-4 minutes is best.
6. Remove the LCP mount by quickly peeling off the Parafilm on both surfaces. Do not slowly peel off the Parafilm, it will stretch and deform.
7. Remove the O-ring; the Leit-C-Plast should not stick to it. The end result should look something like the picture in Figure 23. Excess putty that may have smeared onto other parts of the mount may be cleaned off using ethanol.
8. Place the LCP mounts on an aluminium foil boat, mounting surface face up. Place the boat in an oven at 175°C for 12 hours.
9. The putty will have lost volume and will have retreated into the LCP mount holes. The cushion can then be compressed again using the Parafilm covered glass plates until the surface of the putty is again flush with the mounting surface, this can be done by hand. Step 8 is repeated; this time the putty should not have lost volume. Proceed to step 10.
10. LCP mounts are then evacuated in a vacuum and noted for any bulging of the putty (see Figure 24). Mounts that remain undeformed are suitable for mounting samples.
11. Individual spherules can be pressed into the putty using a glass slide to ensure that the top of the spherule is level with the mount and other spherules.

Recovery and cleaning of the sample is straightforward, using the following method:

1. Prod the corresponding hole at the back of the LCP mount in which the impact spherule to be removed is located. Use a blunted pin or aluminium rod with a diameter that snugly fits within a hole. This will cause the impact spherule to come out of the mount along with a tube of LCP putty.
2. Using tweezers, pick up the impact spherule and transfer it into a 1mL centrifuge vial with snap-top lid. Take a small amount of putty along with the spherule and do not try to pluck the impact spherule free from the LCP putty.
3. Add 0.1mL of ethanol, and wash the impact spherule to the bottom of the vial if it is stuck on the side of the tube and close the lid.
4. Place vial in an ultrasonic bath for 20 seconds.
5. Open the lid and decant the ethanol into a Petri dish making sure the impact spherule stays within the vial. Note that the surface tension should keep it stuck to the vial wall, but the Petri dish is there in case the impact spherule falls out.
6. Repeat steps 4-6 until the impact spherule appears clean and decanted ethanol is not coloured black.
7. Transfer impact spherule to a boat made from a sheet of A4 paper and examine under the binocular microscope. If any LCP putty is still adhering to the impact spherule transfer it back to the vial and repeat from step 3. If the impact spherule appears clean then transfer impact spherule to a clean vial.
8. Add 0.1mL of ultrapure water and place vial in ultrasonic bath for 20 seconds.
9. Decant the ultrapure water into a Petri dish.
10. Repeat steps 8 to 10 twice.
11. Place the vial with lid open in a vial holder and leave in a secure fume cupboard. The ultrapure water should evaporate within a few minutes.

There are some disadvantages to this method including increased uncertainties in analysing unpolished non-flat surfaces, the effects of which will be discussed in the following section. Additionally, unpolished samples yield no petrographic information and make rim-core traverses difficult.

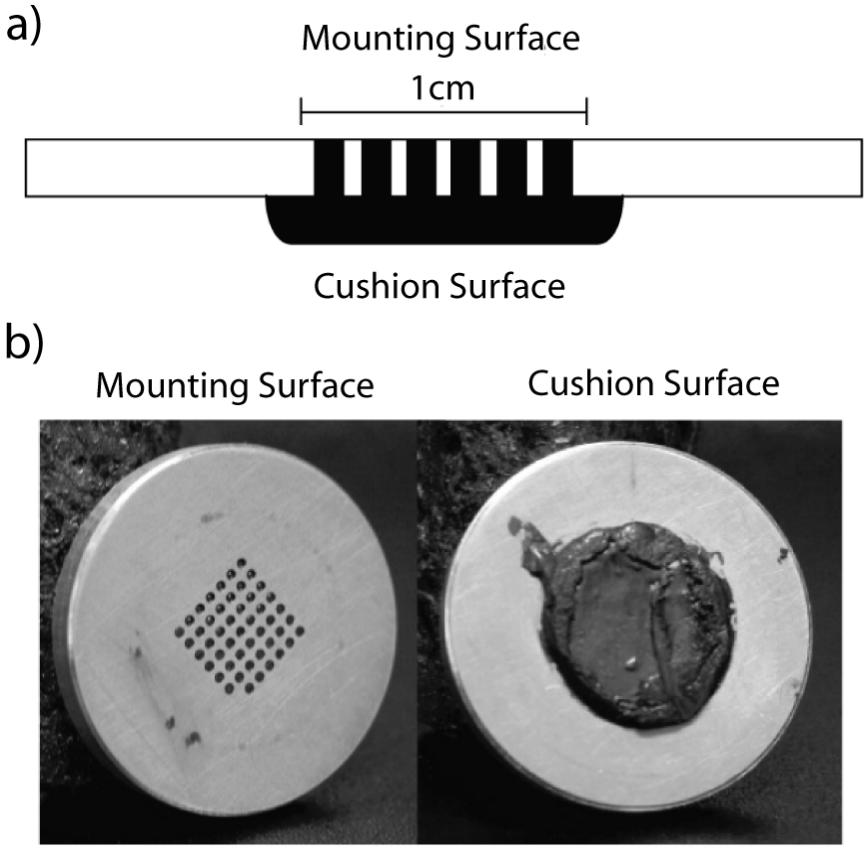

Figure 23. a) Diagrammatic side view of a Leit-C-Plast mount **b)** Photograph of a Leit-C-Plast mount

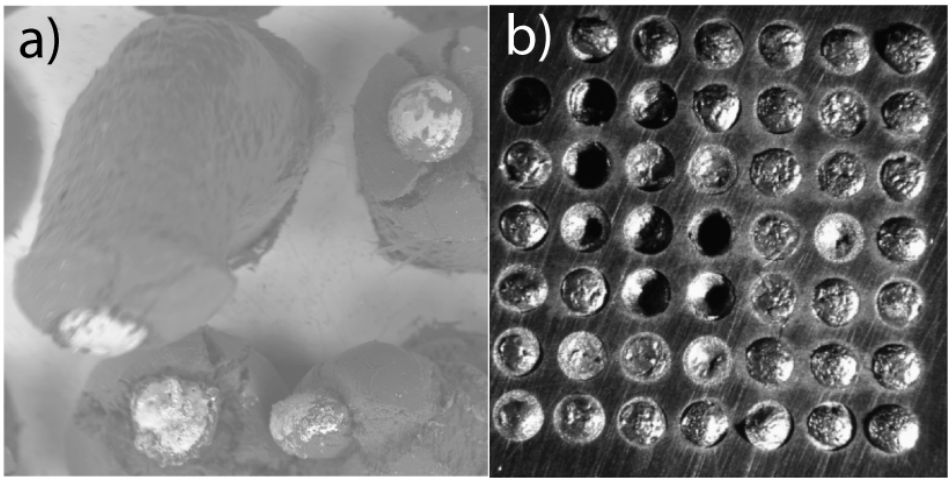

Figure 24. a) Scanning electron micrograph (BSE) depicting extreme deformation of the Leit-C-Plast **b)** Photograph of bulging deformation of the Leit-C-Plast

2.2.1 Brief Review of the Instrumentation

Electron Microprobes

Electron Microprobe (EMP) analyses are a non-destructive method for measuring major element abundances. Summarising Reed (1993), the basic principle behind electron microprobe analysis (EMPA) is the excitation of selected volumes of interest in a solid sample with an electron beam. The amount of material that is excited is controlled by variables such as beam current, spot size, sample properties (density and composition), and tilt of the sample. It is also possible to raster the beam across the sample surface to reduce beam damage to the sample and/or excite a larger area of the sample. The excitation of the sample material produces X-rays which are counted and compared to pure element standards or known composition compounds (usually minerals and glasses).

There are two systems for counting the X-rays: Energy-Dispersive Spectrometers (EDS) and Wavelength-Dispersive Spectrometers (WDS). The EDS system is essentially a semiconductor with an energy gap that stops most electrons from conducting at room temperature. Upon contact with an X-ray photon the energy is absorbed by the semiconductor and dissipated by producing a current that can be measured. X-rays from different elements produce different energies and these are measured over a period of time, averaged and used to produce a histogram (or spectrum) of counts for different energies (keV). Peaks from the spectrum of the sample are then compared to the peaks from standards of known composition (primary standard) to calculate the apparent composition of the sample using 'Castaing approximation' (Equation 2). Each element can have a different primary standard; for the best results the primary standard should be a similar type of material to the unknown.

Essentially, 'Castaing approximation' takes the ratio of the measured intensities of the peaks (for each element) and multiplies the known abundance in the standard by this ratio to scale the apparent composition of the unknown. A number of corrections are then applied to the apparent composition, which in turn is reported as the "true

composition". These corrections will be discussed in more detail in the following section on quantitative corrections.

$$C'_A(sp) = \left[\frac{I_A(sp)}{I_A(st)}\right] C_A(st) \quad \textbf{[2]}$$

where $C'_A(sp)$ = Apparent Element Abundance of Unknown

$I_A(sp)$ = Measured Intensity of Unknown

$C_A(st)$ = Element Abundance of Standard

$I_A(st)$ = Measured Intensity of Standard

Source: Reed (1993)

In a WDS system, X-rays first strike a crystal that focuses select X-ray wavelengths into a proportional counter (Figure 25), where each X-ray is converted to an electrical signal and counted (Reed, 1995). The purpose of the crystal is to enhance the peaks by sharpening them, such that peaks that may have overlapped are clearly separated at the cost of signal intensity. Unlike the EDS system, which collects the whole spectrum at once, this method requires that the spectrum be analysed in segments (background-, peak, background+). The crystal is manoeuvred each time to another segment of the spectrum, thus leading to increased analysis time. To offset this problem multiple spectrometers are used, each working simultaneously and configured to measure different peaks, usually with different crystals. The advantages of the WDS are gains in resolution needed to separate overlapping peaks and better detection limits as backgrounds of peaks are also measured and corrected during the analysis. The conversion to quantitative data is, like the EDS system, obtained by comparing the sample to primary standards.

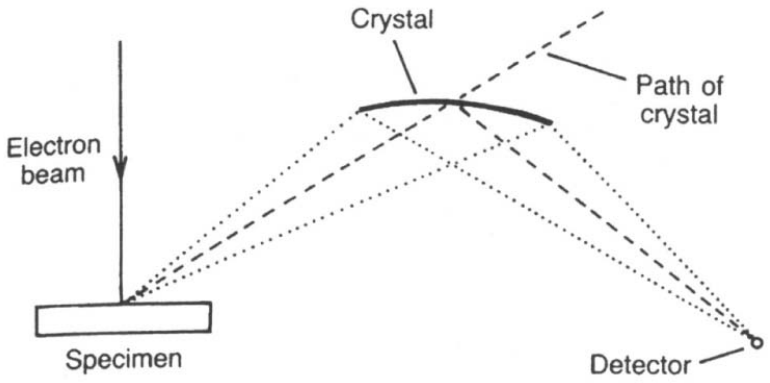

Figure 25. Geometry of a Wavelength-Dispersive Spectrometer (WDS) used in quantification of element abundances.

Diagram from Reed (1995)

Sensitive High Resolution Ion MicroProbe (SHRIMP)

Ion microprobe methods are the most effective technique for precisely determining trace element abundances while conserving material. The Sensitive High Resolution Ion Microprobe (SHRIMP) at the Research School of Earth Sciences uses an O^- primary beam that strikes the sample surface, creating and sputtering secondary ions (see Ireland, 1995 for details). Most of the sample matrix is ejected as neutral particles, but those ejected as ions are accelerated through an electrostatic field. A magnet is then used to select the masses to be analysed and allows these ions through the exit slit into an ion counter at the end of the machine. Only a small amount of the sample is destroyed, the equivalent of a 30µm diameter spot, 1µm deep in a 30 minute session. Prior to analysis, the characteristic masses of the elements to be analysed must be located with mass scans of standard glasses of known composition. Once all the masses are located and adjusted, the peak locations are locked into the software. An energy filter can be inserted at this stage to remove interference species, typically molecules with lower energy, but also hydrides and oxides. The energy filter will reduce the overall signal (number of ions reaching the counter) so it is necessary to increase the voltage to increase the amount of ions sputtered to offset for that loss. In situations where interferences cannot be eliminated by analysis of a different isotope of the element of interest or by energy filtering, a standard containing only the interfering

isotope is needed. The contribution of the interference can then be manually removed from the signal of the unknown.

The SHRIMP does not determine absolute trace element abundances, but relies on comparison with a calibration standard, similar in concept to the EMP. The SHRIMP software reports all abundances as the ratio of the element in question to a minor isotope of Ca or SiO, typically Ca^{44} or SiO^{44} for most silicate minerals such as the lunar glasses. The 'Castaing approximation' (Equation 2) is then used to scale the concentration of the primary standard to the ratio of intensities (in this case also ratios) to obtain the unknown concentration. The equation is as follows:

$$\left(\frac{\left(\frac{x}{y} \right)_{\text{unknown}}}{\left(\frac{x}{y} \right)_{\text{standard}}} \right)_{\text{counts/second}} = \left(\frac{\text{unknown}}{\text{standard}} \right)_{\text{concentration}}$$

$$\text{Unknown}_{\text{concentration}} = \left(\frac{\left(\frac{x}{y} \right)_{\text{unknown}}}{\left(\frac{x}{y} \right)_{\text{standard}}} \right)_{\text{counts/second}} \times \text{Standard}_{\text{concentration}}$$

where : x = *Trace element in question*

y = *Minor isotope of major element* (Ca^{44} *or* SiO^{44})

Laser Ablation – Inductively Coupled Plasma Mass Spectrometry (LA-ICPMS)

The basis for ICPMS is the introduction of solid or liquid samples into an inductively coupled plasma generating ions, which are then focused using cones and lenses, separated by mass, and counted. Laser ablation introduces samples into the ICPMS by using a pulsed laser beam to ablate small amounts of sample, thus creating a plume of plasma and fine particulates that are transported into the ICPMS via a carrier gas. After ionisation in the plasma and focusing through the cone and lenses, ions of the sample will undergo mass selection typically with a quadrupole or time of flight (ToF) techniques. In this project, a quadrupole mass spectrometer was used. Quadrupole mass spectrometers rapidly peak hop through multiple elements which selects the masses that are to pass through to a detector (electron multiplier or photomultiplier tube) where they are counted. Care must be taken to avoid ablation deposits that form around previously ablated regions as these can be enriched in more volatile elements (Eggins et al., 1998).

Quantitative elemental abundances are obtained by measurement of the signal intensity at selected interference-free mass peaks for predetermined durations (peak hopping). The intensity of each peak measured in the sample is then compared to a primary standard using the 'Castaing approximation' (Equation 2). Ratios of the unknown element to a minor isotope of a major element of the samples are scaled to the primary standard in the same approach used in SHRIMP analyses. However, additional corrections need to be applied if the sample is introduced using the laser ablation technique; these will be detailed in the following section. A disadvantage of the LA-ICP-MS method is greater consumption of sample compared to the SHRIMP, offset by greater analytical precision. Ablation pits formed from spot sizes that are 62μm in diameter are typically 40-80μm deep tapering slightly towards the bottom of the pit (See Eggins et al. (1998) for details). This is estimated to consume ≤3-6% of the volume of a 200μm diameter spherule during 100 second of ablation.

2.2.2 Quantitative Corrections

Major Element Composition from Electron Microprobe Analysis

A number of different types of corrections are applied to quantitative data from electron microprobes. The factors involved with these corrections are collectively known as the ZAF corrections and include the atomic number correction (Z), absorption correction (A) and fluorescence correction (F). The atomic number and absorption corrections account for variable electron penetration and backscattering, and absorption potentials of X-rays given off by elements of different atomic numbers. The fluorescence correction accounts for the extra energy given off by a sample, which manifests as a fluorescence surface. All these corrections are automatically applied in most microprobe software. These corrections are applied for ideal flat surfaces (i.e. polished), but can be extended to the treatment of ideal curved surfaces. Although lunar impact spherules are rarely ideal curved surfaces, evaluating the quantitative differences between the ideal flat and curved surfaces can be used to determine the best balance between analytical quality and sample conservation. The following paragraphs are summarised from Goldstein et al. (2003) and Reed (1993):

In essence, the "Z" coefficient can be expressed as the mean atomic number and consists of two variables: penetration and backscatter. The "Z" correction acts to correct the difference between the sample and standard should they differ in mean atomic number. Penetration into the sample is effected by the "stopping power" of the sample and thus penetration decreases as "Z" increases. However, with increasing "Z" the mass of sample that is penetrated increases. These two effects counterbalance each other (less material is penetrated, but is denser), so the backscatter variable becomes dominant. Backscatter rapidly increases with "Z" and results in reduced X-ray intensity. Hence, if the sample has a higher mean atomic number than the standard, the sample will have a lower X-ray intensity relative to the standard, manifesting as a lower concentration without the "Z" correction. Therefore, the concentration of the sample is scaled upwards if the mean atomic number of the sample is higher than the standard, and vice versa.

The "A" coefficient is a correction for the integrated absorption of X-rays passing through a sample as a function of the generation of X-rays through electron interaction with depth. Electron beams excite a volume of sample from which X-rays are produced at various depths. The excitation volume varies as a function of the beam conditions (spot size and accelerating voltage) and sample characteristics (mean atomic number and if present any layering). X-rays that are generated from the excitation volume must pass through varying amounts of material, dependent on depth of generation, in order to reach the detector. X-ray production as a function of depth can be seen in Figure 26. Production of X-rays initially increases with depth due to deflection of incident electrons from the electron beam, which increases the amount of material they interact with, thus generating more X-rays. Once the trajectories of the electrons are randomised (φ (pz) maximum), scattering and deceleration of electrons through the sample prevents the generation of X-rays deeper in the sample. This function is collectively known as phi-rho-z (φ(ρz)) and a variety of different methods have been developed to accurately model its behaviour. The distribution of the φ(ρz) function is used to calculate the absorption correction factor.

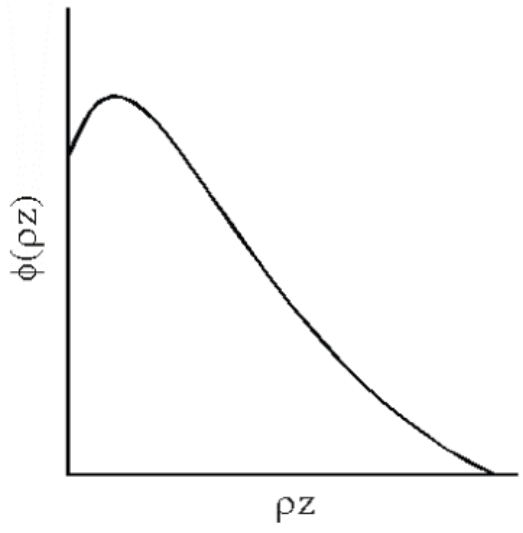

Figure 26. Example of a phi-rho-z (φ(ρz)) curve.

The last type of correction that is applied is the fluorescence ("F") correction. Fluorescence occurs when X-rays of an element are further excited by more energetic X-rays beyond the critical excitation energy. Typically the fluorescence correction is small and is not always necessary. Fluorescence can be derived from the φ(ρz) distribution used for the calculation of the absorption correction. The φ(ρz) function can be rearranged to determine the φ(ρz) of secondary X-rays generated by primary X-rays (electron-generated). Primary X-rays will be absorbed as they pass through the sample and generate secondary X-rays which will in turn also be absorbed as they exit the sample and reach the detector. The additional counts generated by the secondary X-rays determine the fluorescence correction.

Of these corrections the absorption correction is the most significant and is even more important when examining irregular geometries. This will be evident in the following discussion.

Curved Surface Attenuation in Electron Microprobe Corrections

As previously mentioned, corrections are applied to data from electron microprobe analyses assuming a flat surface. However, for unpolished samples, the surface of a lunar impact spherule is usually roughly spherical or cigar-shaped, and occasionally irregular/splash-like. A good approximation for the effect on the corrections can be determined using a series of simple calculations comparing the attenuation distance of an ideal flat sample and a spherical surface (Figure 27). On a flat surface, the attenuation distance can be calculated using trigonometry. For example, an arbitrary penetration depth (depth at which an electron generates an X-ray) of 2400nm and detector incidence angle of 50° will yield an interaction distance (amount of material said X-ray must penetrate to reach the surface) of ~3133nm using the formula below:

$$Sin\,50 = \frac{Penetration\ Depth\,(d)}{x} \qquad \textbf{[3]}$$

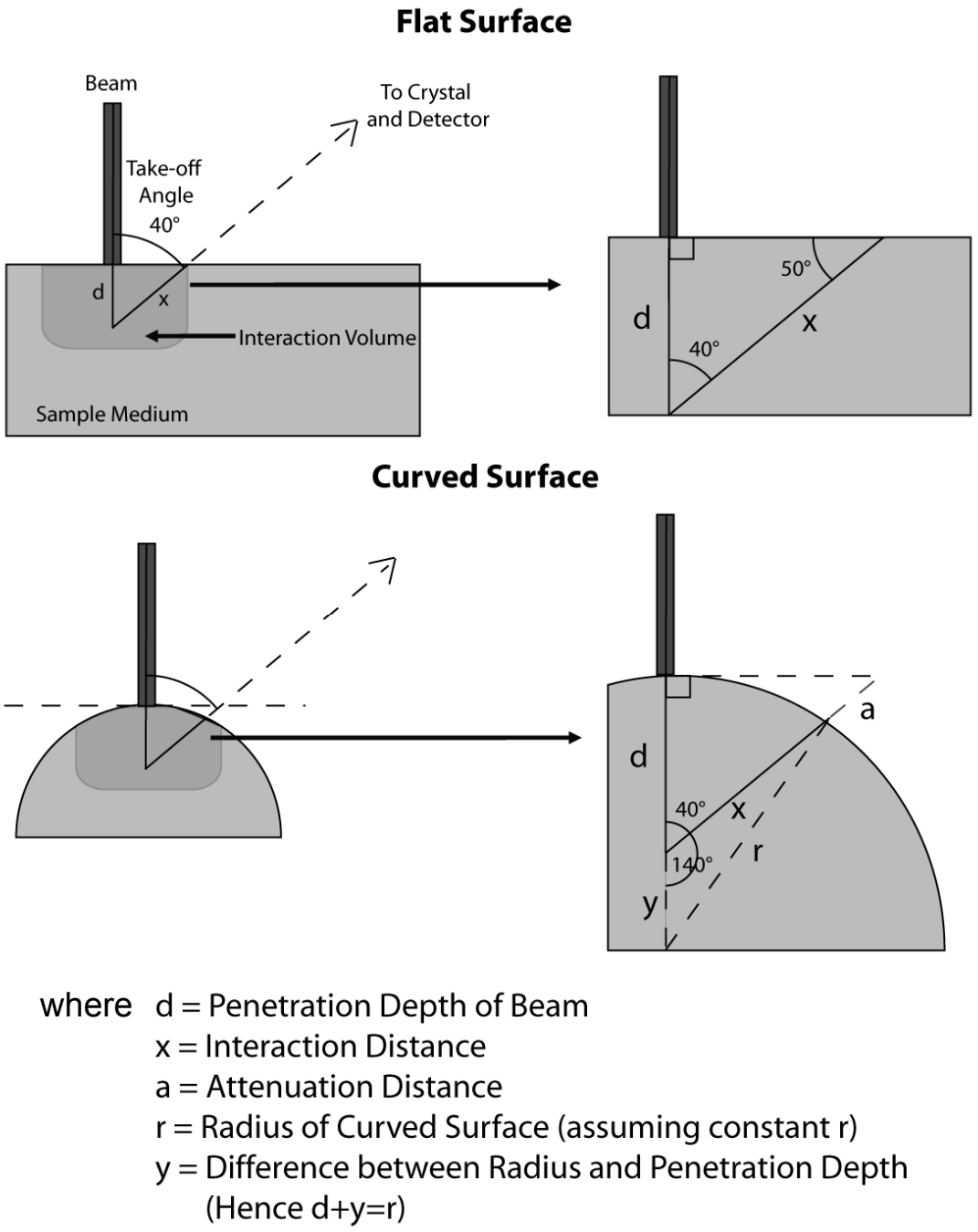

Figure 27. Geometric difference between analysing a flat surface compared to a curved surface. The curved surface has an attenuation distance which is the difference between the interaction distance on a flat surface compared to a curved surface. Constant radius is assumed for the curved surface.

$$x_{Flat\ Surface} = \frac{Penetration\ Depth\ (d)}{Sin\ 50} = \frac{2400nm}{Sin\ 50} = 3132.98nm$$

For curved surfaces, assuming a constant radius, it is also possible to calculate the interaction distance. However, it should be noted that this distance is shorter as penetration depth increases, due to the nature of the curved surface. The difference is known as the attenuation distance, which is simply the interaction distance of a flat surface minus the interaction distance of a curved surface. Transformation of the Cosine Law in the following manner allows the attenuation distance to be determined:

$$r^2 = x^2 + y^2 - 2xyCos(180 - Detector\ Angle)$$

$$\text{where}\quad y = r - d$$

$$\therefore r^2 = x^2 + (r-d)^2 - 2x(r-d)Cos140$$

$$x^2 + (r-d)^2 - 2x(r-d)Cos140 - r^2 = 0$$

Rearrangement into a quadratic equation $(ax^2 + bx + c = 0)$ is necessary to solve the interaction distance of the curved surface relative to radius (spherule size).

Expanding:

$$x^2 + r^2 + 2rd + d^2 - 2(r-d)Cos140\ x - r^2 = 0$$

Now solving this equation:

$$x^2 - 2(r-d)Cos140\ x - d(2r-d) = 0$$

Now the variables for a quadratic equation are available

$$(ax^2 + bx + c = 0)$$

where $a = 1$

$$b = -2(r-d)Cos(140)$$

$$c = -d(2r-d)$$

These variables can be inserted into the quadratic equation to solve for x:

$$x = \frac{-b + \sqrt{b^2 - 4ac}}{2a}$$

$$x_{Curved\ Surface} = \frac{2(r-d)Cos140 + \sqrt{((-2(r-d)Cos140)^2 + 4d(2r-d)}}{2} \quad \textbf{[4]}$$

Therefore, knowing the radius of the spherule and penetration depth, it is possible to determine the interaction distance on a curved surface. Figure 28a shows the change in interaction distance between a flat surface, 50μm diameter curved surface, and 200μm diameter curved surface. The difference in interaction distance between curved and flat surfaces increases as penetration depths increases and spherule diameter decreases. Figure 28b is replotted to show attenuation difference (curved surface distance/flat surface distance) as a function of curved surface radius and penetration depth. In order to determine the effect of this curved surface on the absorption coefficient for lunar spherules, modelling of the behaviour of electrons is required.

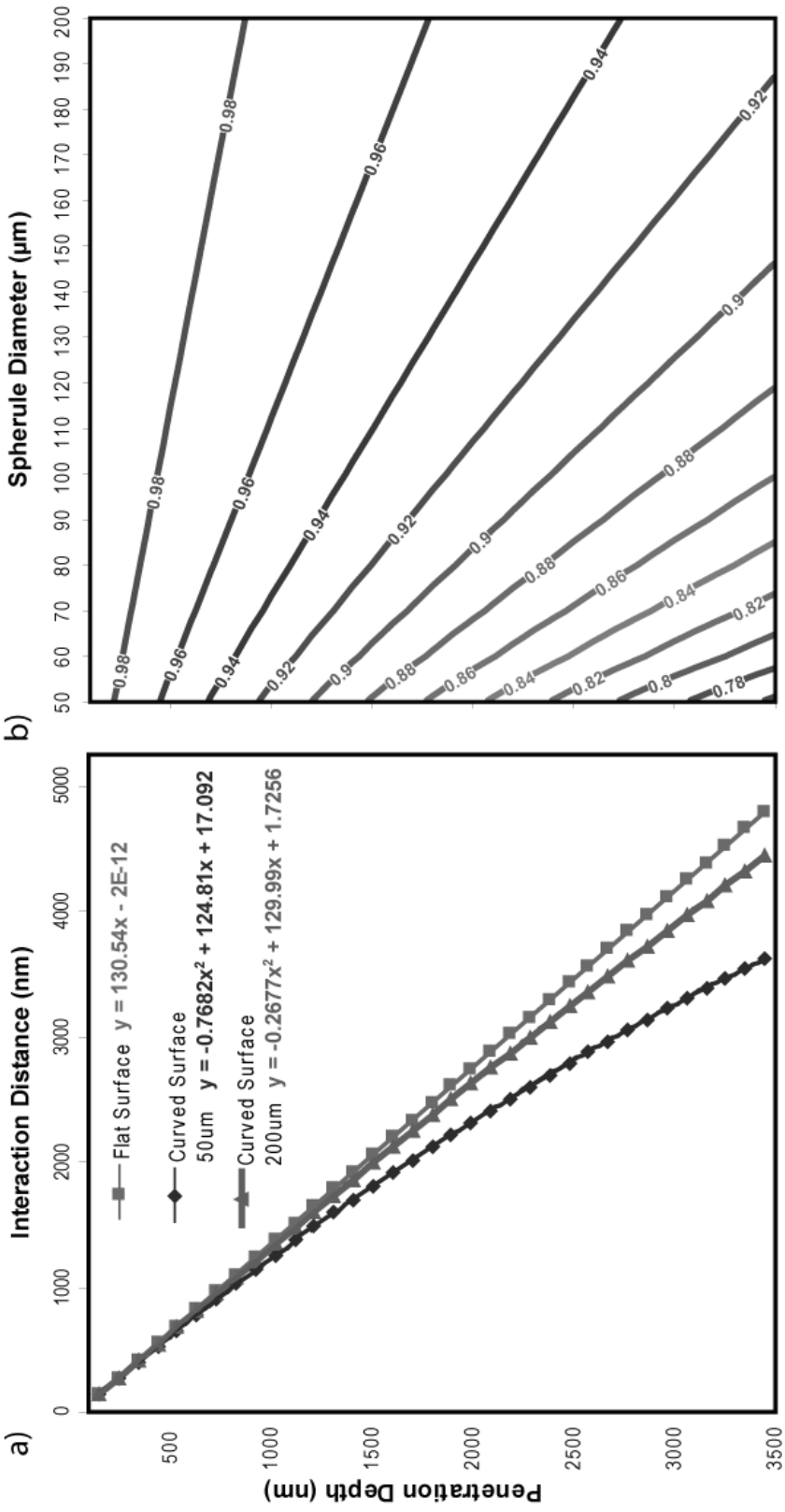

Figure 28. a) Comparison of the interaction distance as a function of depth in flat and curved surfaces **b)** percentage difference in interaction distance (contours) between a flat surface and a curved surface as a function of penetration depth and spherule diameter

Using CASINO (Drouin et al., 2007), a Monte Carlo simulation tool for electron trajectories in solids, it is possible to model the X-ray depth distributions. Beam conditions used in the CASINO simulation match those to be used for EMP analyses of the lunar impact spherules (15keV accelerating voltage, 20μm spot size). Preliminary analyses of the lunar impact spherules indicate that the majority of spherules have chemistry consistent with lunar highlands soils, hence a typical mature highlands soil will be used (compositions compiled by Lucey et al., (2006); density assumed to be that of anorthite: 2.76g/cm^{-3}) as the model substrate. A simulation of 5000 electrons was run to determine the φ(ρz) profiles for the elements modelled in the simulation. Using these φ(ρz) profiles it is possible to determine the absorption correction of a curved surface on the apparent chemistry using the following formula (see Figure 29):

$$\text{Absorption Correction} = f(x) = \int_0^\infty \phi(pz)\exp(-xpz)d(pz) / \int_0^\infty \phi(pz)(pz) \qquad \textbf{[5]}$$

Source: Reed (1993)

where x = Z-correction x Interaction Distance.

The CASINO model generates theoretical φ(ρz) profiles providing the absorbed/attenuated and absolute intensities needed to determine the absorption correction. From these profiles it is possible to determine the absorption correction for the modelled substrate for each element by determining the area beneath f(x). The absorption correction can also be changed such that the interaction distance is not a linear function with depth, but determined using the interaction distance as calculated from equation 4. The results are presented in Figure 30 and show that as the diameter of the curved surface decreases, the absorption correction becomes increasingly overestimated. The area beneath f(x) was calculated using the trapezoidal rule. Lighter elements and LIII lines are most affected by absorption, a result of the Z-correction and lower energies respectively. Hence, when an analysis is conducted on a curved surface: $f(x)_{Curved} > f(x)_{Flat}$

Ultimately, these corrections will have an effect on the results (mass concentrations) of the analysis. The apparent concentration given in equation 2 is converted to a true concentration by the product of the different components of the ZAF correction. Hence:

$$"True" \ Concentration = Apparent \ Concentration \times \left(\frac{ZAF_{Sample}}{ZAF_{\text{Standard}}}\right) \qquad \textbf{[6]}$$

The absorption correction, f(x), in equation 5 is inverted to obtain the absorption correction factor used in the conversion of apparent to "true" concentration (i.e. ZAF = Z x 1/f(x) x F). Thus when an analysis is conducted on a curved surface, the "true" concentration is underestimated due to an over zealous f(x) correction such that:

$$\frac{1}{f(x)_{Curved}} < \frac{1}{f(x)_{Flat}}$$

$$\therefore ZAF(Sample)_{Curved} < ZAF(Sample)_{Flat}$$

The result is an underestimation of the corrected mass concentration in curved surface samples. The microprobe software assumes flat surface geometry when displaying corrected data; however, as shown above, it overestimates the absorption correction manifesting in the results as particularly low totals (89-98%; <2% lower totals can result from instrumental variability on ideal flat surfaces) especially for lighter elements. This is exacerbated should the electron beam strikes off-centre such that there is little absorption, leading to X-rays flooding the detector. Since real samples are unlikely to have ideal surfaces (and perfect beam placement), as these models have assumed, the modelled errors are only a minimum. As such, analytical totals ranging between 89-98% could be expected from more rugged surfaces of small samples (<200µm diameter). These data can be normalised to 100% and used, but will introduce scatter and bias towards heavier elements as a function of spherule diameter. Analytical totals lower than 89% should be discarded as this likely indicates a severe offset of the beam,

or something sample-related that is interfering with the analysis (i.e. vesicular sample, topography or adhering mineral grains). Impact spherules with diameters of <75µm should be avoided to minimise the effect of over-correction to <5%.

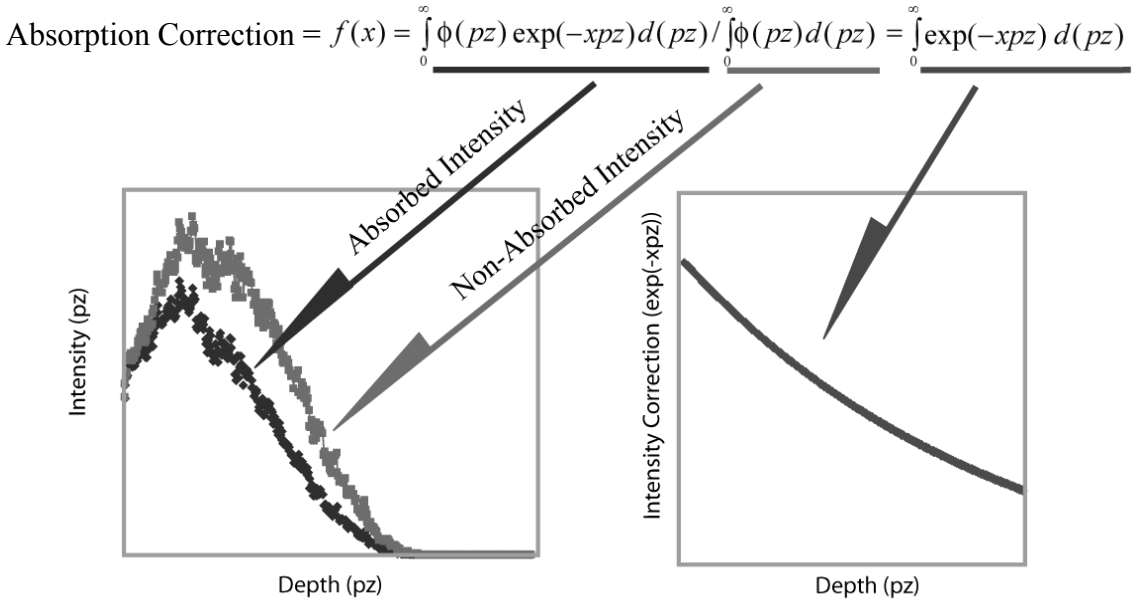

where x = Z-correction x Interaction Distance

Figure 29. An example of a phi-rho-Z (φ(ρz)) profile and its relationship to the absorption correction. The absorbed intensity is measured in a microprobe and is scaled to a non-absorbed intensity by applying the absorption correction. On a flat surface the absorption correction is a constant varying with depth. The integrated area beneath the intensity correction curve determines the absorption correction.

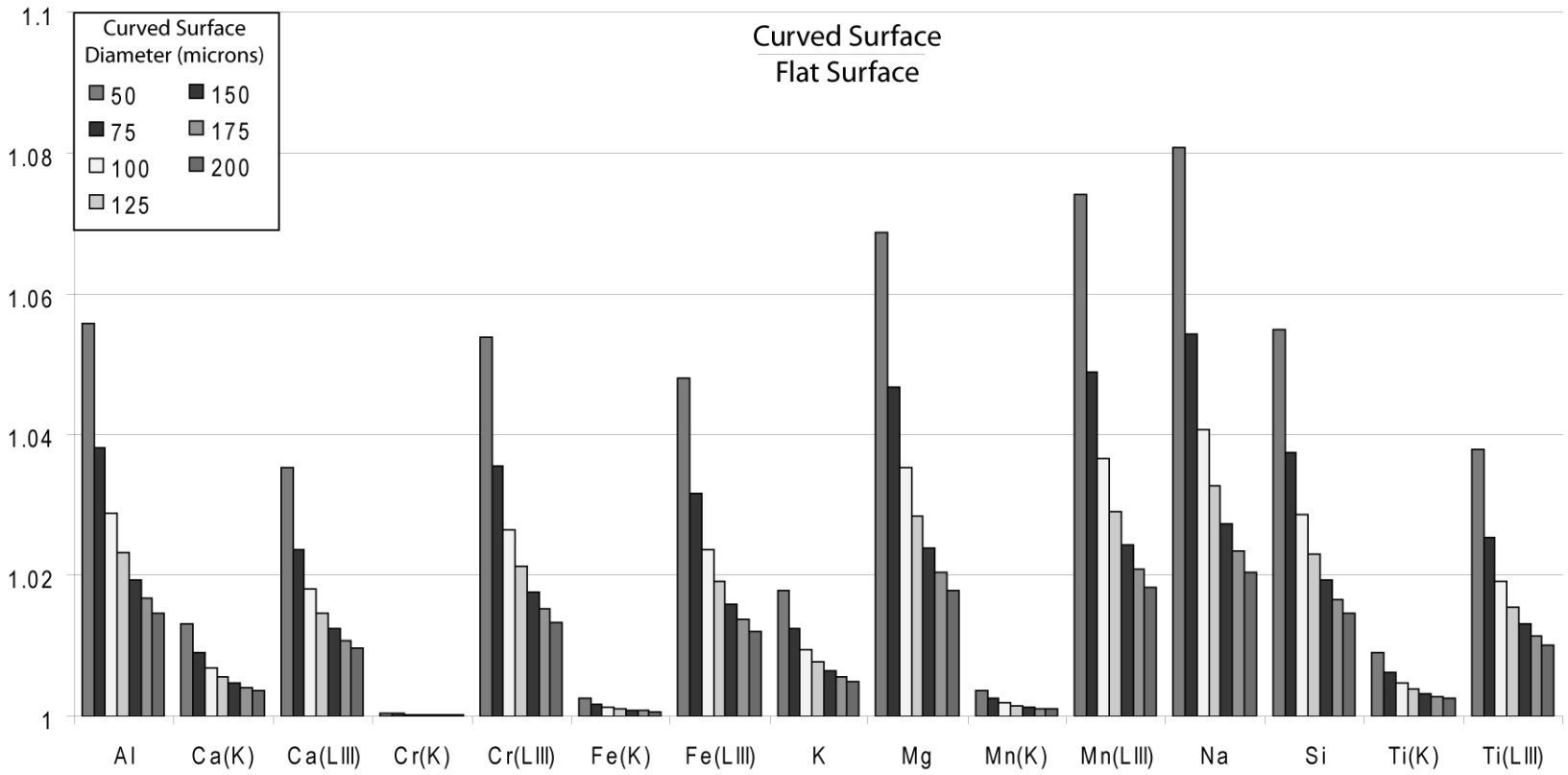

Figure 30. The effect of the absorption coefficient, f(x), for each element as a function of curved surfaces of variable diameters. Results are normalised to that of a flat surface such that elements with values closer to one are least affected by the surface geometry. Results are modelled from the CASINO program (Drouin et al., 2007) using a substrate similar to that of average mature lunar highlands soil. This graph shows that lighter elements and small diameters in the curved surfaces increase the difference between curved and flat attenuation corrections most.

Trace Elements from SHRIMP

There are two main problems with obtaining trace element abundances from SHRIMP. The first is the production of complex isobaric interferences in the REE region, which can be removed either with increased mass resolution, or energy filtering. According to Ireland (1995), the use of high mass resolution restricts measurement precision, requires extremely good magnet control, and affects the matrix sensitivity of ionic ratios; therefore use of energy filtering is preferable, though a well-documented standard is imperative. The well-documented standard is needed to determine the differences in ionisation efficiency of the standard and sample. Ionisation efficiency is affected by the composition and atomic structure of the material (Ireland, 1995; Shimizu and Hart, 1982) and affects how efficiently the sample and standard ionise. Materials with higher ionisation potentials give higher counts relative to materials with lower ionisation potentials. Derivation of concentrations from a sample with different ionisation efficiency compared to the standard will require a scaling coefficient that accounts for differences in apparent counts. Corrections for trace element abundance are not necessary when analysing samples with the same ionisation efficiency as the standard. In the absence of such a standard, one must be manufactured using synthetic materials. When analysing samples with a variety of compositions, a number of synthetic standards must be manufactured with compositions that bracket the natural variety of compositions in the sample. Hence, when the synthetic standards are analysed, the scaling factor for difference in ionisation efficiency can be obtained and propagated into the calculation for converting counts into concentrations.

Since lunar impact spherules are mostly glassy particles, there are a number of glass standards (USGS, MPI-DING) that can be used. Manufacture of a standard is also relatively easy as glass shards can be produced by quenching synthetic melts. Another method is to take suitable homogenous impact spherules and determine the trace element abundances independently with an alternate method (such as laser ablation-ICPMS). These impact spherules can then be used as working standards from which to derive ionisation efficiency. A combination of glass standards and the impact spherule

working standards is a method employed by other authors studying impact spherules (i.e. Delano et al., 2007; Zellner et al., 2002).

Analytical results from the SHRIMP, however, may also be affected by surface topography though there is no literature examining this effect on trace element measurements. For high precision oxygen isotope ratios, however, Ickert et al. (2008) demonstrated that the flange of the sample holder 5mm away from the sample can cause instrumental mass fractionation of up to ~4‰. Kita et al. (2009) have also determined that, for oxygen isotopes, topography of 10μm on a poorly polished analytical surface degrades the analytical precision by about 5‰. Trace element abundances, however, are more variable so are less sensitive to surface topography. There does not appear to be any literature that quantifies the effect of surface irregularity for trace element quantification. Therefore, a comparison of polished versus unpolished standards was deemed necessary.

Trace Elements from LA-ICPMS

Laser ablation ICPMS techniques are less sensitive to geometry and typical sample preparations range from polished sections to rough sawn blocks and even mineral grains mounted with a binder or adhesive (Perkins and Pearce, 1995). Although geometry is not an issue for the quantification of trace element abundances, other issues can arise from the interaction of the laser and sample. These issues include variable ablation yield between the sample and standard, element fractionation during profile analysis, and assumption of an invariant internal standard (e.g. Ca) during profile analysis.

Variable ablation yields result from differences in the ablation potential between the sample and the standard. However, even with a matrix-matched sample and standard, large differences can result from fluctuations in laser output resulting in a semi-quantitative analysis (Günther et al., 1999). Additionally, depth profiling can cause significant element fractionation as the pit deepens due to the reduction in laser ablation efficiency and condensation of the plasma plume onto the sides of the pit (Eggins et al., 1998). Internal standardisation can correct for the issues mentioned previously, but

requires the assumption that the internal standard is invariant through a profile or track. This may be problematic as the abundance of the internal standard determined using an independent method (i.e. EMP) is not be representative of the volume or location sampled by the LA-ICPMS. Therefore, it is important that the internal standard be fairly homogeneous in both the sample and standard.

2.3 Method Evaluation

2.3.1 Leit-C-Plast Behaviour Under Vacuum

The first test that was conducted evaluated the compatibility of the Leit-C-Plast with the high vacuum conditions of the SHRIMP. A sample-free mount (post-heat treatment) was placed in the exchange chamber of the SHRIMP-RG at the Research School of Earth Sciences. The chamber was evacuated and pressure was recorded during the turbo pump evacuation process (Figure 31). Achievement of optimal operational pressures (<$6.0x10^{-7}$ mbars) within an hour indicates that there was minimal degassing in the Leit-C-Plast compared to epoxy mounts which can take hours to achieve optimal pressures. No deformation of the putty was observed.

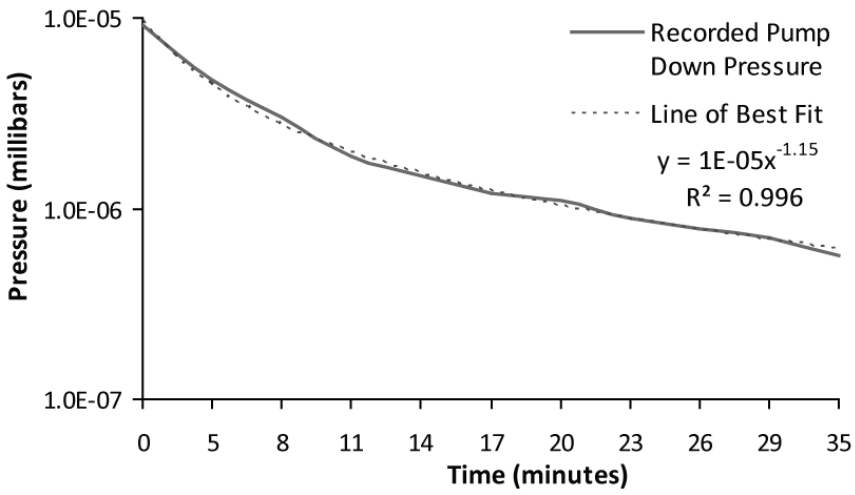

Figure 31. Pressure vs. time after activation of the turbo pump on the SHRIMP-RG with a sample-free Leit-C-Plast mount in the vacuum chamber.

Although Leit-C-Plast appears to be suitable for the SHRIMP's high vacuum environment, the putty deforms in the vacuum environment of the carbon coater and electron microprobe without heat treatment. Mounted samples extrude above the mount surface carried by a tube of Leit-C-Plast in extreme cases (Figure 24). Although the sample is not lost in this process, it cannot be analysed as it exceeds the focus range of the EMP and SHRIMP. There are two possible explanations for this behaviour:

1. The relatively slow pumping rate of the carbon coater compared to the SHRIMP leading to low strain rates and the putty behaving plastically. This causes the Leit-C-Plast to bulge up above the mount surface.
2. The orientation of the mount with respect to the vacuum pump/evacuation valve. It is possible that suction acting perpendicularly to exposed putty surfaces causes greater deformation than the suction acting from the side of the LCP mount, as is the case with the orientation of samples in the SHRIMP.

Regardless, the resulting heat treatment and pre-mounting evacuation test of the LCP mounts eliminated these problems. The heat treatment removes the thinner xylene which hardens the Leit-C-Plast, hence making it more resilient to deformation. The pre-mounting evacuation is an added quality control check.

2.3.2 Major Element Abundances – Polished vs. Unpolished

In the previous section, the effects of a curved surface on the analytical results were calculated. In addition to the modelling, a number of standards were also analysed on the LCP mount to confirm the model results. Although models provide an understanding of the effects of a curved surface, they are based on a number of ideal situations. As such, it is important to test this understanding using real standards under conditions similar to those for real samples and evaluate the results. Attempts were made to convert shards of USGS and MPI-DING glass standards into rounded particles to approximate the shape of lunar impact spherules (See Nitkiewicz and Sterner, 1988 for the mill design). Although the production of spherular standards was possible, milled standards typically took on an elongate shape. In addition, milled standards <5mm could not be produced as they either shattered or escaped the mill. As a result, shards of the standard glass were mounted and carbon coated to approximate an irregular surface, which as an extreme end-member, but could be compared to polished section equivalents to determine the effects that the irregular surfaces may have on the quantitative result.

The Cameca SX100 Electron Microprobe at the Research School of Earth Sciences was selected for this purpose. Primary mineral standards were calibrated by Dr. Robert Rapp prior to each session with secondary standards (VG-2: mid-ocean ridge basalt and K412: standard glass) analysed during each session. Beam conditions were set to 15keV and 10nA current. A focused beam was used and multiple analyses were conducted on each standard on the most irregular surfaces. A series of standards was prepared in a LCP mount which will be referred to as the calibration mount. Analytical totals vary between 46-104wt.% with an average of 98.4 ± 4.7% (1σ). Two standard deviations indicate that 95% of the analytical totals should range from 89-108wt.%, similar to that determined by theoretical modelling. Totals within this range were normalised to 100% and further outliers were discarded. The results of this study are tabulated in Table 6 and show that, even for irregular geometries, most analyses are accurate within ~10% of the reference values. Elements in low abundances (<1 wt.%) tend to have higher errors associated with them due to counting statistics, which can be improved with increases in the allocated counting times for these elements. Some variability is expected from standard to standard as calibration standards are not always suitable for all types of materials. For example, Bo Ploi 2 is a clinopyroxene and not an international standard glass; thus the chemistry is not as well inter-calibrated. Overall, this preliminary study shows that the EMP can indeed be used to collect reliable major element abundances on irregular surfaces.

Table 6. Electron microprobe analyses of glass and irregular shards of mineral standards prepared in a Leit-C-Plast mount. A minimum of two points is used to determine the composition of each shard. Where multiple shards were analysed, the combined average composition is used for comparison with the reference value. Values within 5% of the reference value are highlighted in green; values within 10% are highlighted in blue.

	Cr_2O_3	MnO	K_2O	Na_2O	CaO	TiO_2	MgO	Al_2O_3	SiO_2	FeO
USGS BCR-2G #1 (n=2)		0.22	1.89	3.19	7.12	2.28	3.7	13.92	55.19	12.48
#2 (n=3)		0.24	1.94	3.2	7.1	2.33	3.67	14.18	54.99	12.34
Reference										
(Wilson, 1997)			1.79	3.16	7.12	2.26	3.59	13.5	54.1	12.42
Measured/Preferred			1.07	1.01	1	1.02	1.03	1.04	1.02	1
MPI-DING ATHO (n=3)		0.13	2.91	2.46	1.77	0.27	0.09	12.62	76.34	3.41
Reference										
(Jochum et al., 2006)		0.11	2.64	3.57	1.7	0.26	0.1	12.2	75.6	3.27
Measured/Preferred		1.18	1.1	0.69	1.04	1.04	0.85	1.03	1.01	1.04
MPI-DING T1G (n=3)		0.15	2.15	2.98	7.86	0.78	3.93	17.79	57.1	7.25
Reference										
(Jochum et al., 2006)		0.13	1.96	3.13	7.1	0.76	3.75	17.1	58.6	6.44
Measured/Preferred		1.21	1.1	0.95	1.11	1.04	1.05	1.04	0.97	1.13
MPI-DING GOR132G (n=3)	0.4	0.22	0.04	0.81	8.88	0.3	22.37	11.4	45.01	10.56
Reference										
(Jochum et al., 2006)		0.15	0.03	0.83	8.45	0.31	22.4	11	45.5	10.1
Measured/Preferred		1.46	1.31	0.97	1.05	0.99	1	1.04	0.99	1.05
MPI-DING GOR128G (n=3)	0.29	0.18	0.04	0.57	6.02	0.27	26.63	10.19	46.19	9.61
Reference										
(Jochum et al., 2006)		0.18	0.04	0.57	6.24	0.29	26	9.91	46.3	9.81
Measured/Preferred		0.99	1.16	1	0.97	0.95	1.02	1.03	1	0.98
MPI-DING ML3BG (n=3)	0.01	0.21	0.45	2.24	11.19	2.27	6.58	14.22	51.29	11.53
Reference										
(Jochum et al., 2006)		0.17	0.39	2.4	10.5	2.13	6.59	13.6	51.4	10.9
Measured/Preferred		1.26	1.16	0.93	1.07	1.07	1	1.05	1	1.06
MPI-DING KL2G (n=3)	0.05	0.18	0.55	2.26	11.81	2.79	7.25	13.57	50.24	11.3
Reference										
(Jochum et al., 2006)		0.17	0.48	2.24	10.9	2.56	7.34	13.2	50.3	10.7
Measured/Preferred		1.09	1.15	1.01	1.08	1.09	0.99	1.03	1	1.06
MPI-DING StHs6/80G (n=5)		0.08	1.38	3.14	5.52	0.75	1.94	18.61	63.97	4.6
Reference										
(Jochum et al., 2006)		0.08	1.29	4.44	5.28	0.7	1.97	17.8	63.7	4.37
Measured/Preferred		1.02	1.07	0.71	1.05	1.06	0.98	1.05	1	1.05
Synthetic lunar glass 1 #1										
(n=3)	0.17	0.24	0.03	0.19	12.26	6.88	7.81	13.57	44.69	14.16
#2 (n=3)	0.24	0.2	0.02	0.15	11.1	6.27	7.62	13.32	48.53	12.55
Reference										
(Carlton et al., 1992)	0.16	0.18	0.01	0.16	11.85	5.98	7.17	13.05	47.1	13.08
Measured/Preferred	1.28	1.22	2.38	1.06	0.99	1.1	1.08	1.03	0.99	1.02
Bo Ploi 2 CPX #1 (n=3)	0.02	0.12	0	1.84	18.65	1.81	11.98	10.95	47.1	7.54
#2 (n=3)		0.16	0.02	1.67	20.25	2.01	11.33	10.35	46.34	7.86
#3 (n=3)	0.01	0.17	0.01	1.7	20.28	2.02	11.18	10.82	45.91	7.9
Reference										
(Norman et al., 1996)	0.01	0.13		1.3	20.6	1.79	12.37	9.2	47	6.65
Measured/Preferred	0.76	1.17		1.34	0.96	1.09	0.93	1.16	0.99	1.17

2.3.3 Trace Element Abundances – Polished vs. Unpolished

SHRIMP

Using the same carbon coated calibration mount utilised in the major element trial, trace elements for each standard were obtained using the SHRIMP-RG. The SHRIMP-RG was operated using a mass resolution of ~5000 (at the 1% level) with an O_2^- primary beam running at 3nA. Source and collector slits were set at 350µm and 450µm, respectively. The energy filter was also set to 15eV. During this session there were problems with the calibration of certain peak locations and machine breakdowns that limited the number of samples that were analysed.

The BSE images in Figure 32 show the locations of SHRIMP spots on shards of a well-characterised mineral, Bo Ploi clinopyroxene (Norman et al., 1996). It shows that all the analyses were made on irregular surfaces. A total of four analyses were made on irregular shards surfaces and two on polished sections. The results are presented in Figure 33 which show that scatter in the shards is about twofold more than the scatter in polished sections. The average composition of the shards is within 10% of the average composition of the polished sections. All are, however, systematically offset from the reference values (Figure 33). This is not a result of different ionisation potentials between the shards and polished section as both are the same sample. The systematic offset may be due to the more random sputtering trajectories due to surface irregularities, which will result in more ions being filtered out by the source slit (Ireland, 1995). This results in fewer ions reaching the ion counter and subsequently a lower apparent concentration.

Following the SHRIMP session on the SHRIMP-RG, an attempt to improve the routine was conducted on SHRIMP 1; however, another breakdown halted progress. Further sessions were planned, but cancelled due to the discovery that some, possibly all, impact spherules have an outer crust with a composition that may not be representative of the bulk spherule (mentioned in the previous section). Since the SHRIMP only penetrates ~ 1 µm in 30 minutes, the analysis will be heavily biased towards a crust composition and copious amounts of SHRIMP time would be necessary to drill beyond

the crust. In this case, the laser ablation ICPMS proved to be a more suitable instrument as it has the capacity to ablate faster than the SHRIMP, provides a real time depth profile, and is less susceptible to geometry effects (Perkins and Pearce, 1995). Additionally, the trace element profiles can be used to determine the compositional difference between the crust and interior and estimate the thickness of the crust.

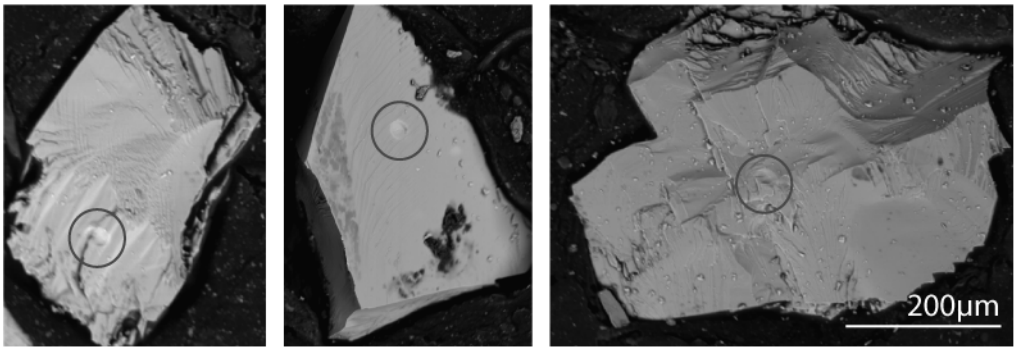

Figure 32. Backscatter electron (BSE) images of three of four analysed shards of the Bo Ploi clinopyroxene. The circles mark the location of the SHRIMP spots, all of which are located on irregular surfaces.

LA- ICPMS

A total of five shards of USGS standard glass TB-1G embedded in the LCP calibration mount was also analysed with polished equivalents of the standard for comparison. The LA-ICP-MS system consists of an Excimer (193nm) laser and a quadrupole Agilent 7500 ICP-MS. Prior to use, the equipment was tuned and calibrated by Dr. Charlotte Allen and Dr. Frances Jenner. The ablations were conducted under a He + H atmosphere and mixed with an Ar carrier gas for transport to the ICPMS. A description of the instrumentation is provided by Eggins et al., (1998). Spot diameters were set to 62µm and at a laser repetition rate of 5Hz. Data were standardised using NIST612 glass calibrated to BHVO-2G, BIR-1G and BCR-2G USGS glasses (See Norman et al., (2004) for preferred values). Each analysis was normalised to CaO wt.% to correct for variable ablation yield. Data reduction was conducted using a MS Excel spreadsheet provided by Dr. Charollete Allen. The total analysis time for each sample was 50 seconds including a 20 second background on the carrier gas prior to each analysis. The

results are shown in Figure 34 and indicate that the average and 2σ errors of most trace elements fall within 10% of the preferred values for the TB-1G shards (See Norman et al., 2004 for preferred values). Only chromium exhibits more variability than most other trace elements. The shards and polished section are comparable with only notable difference in the Rb abundances which appears to be underestimated in the shards, possibly due to small number statistics. Overall, the geometry did not appear to have a large effect on the trace element composition of the TB-1G shards during LA-ICPMS analyses.

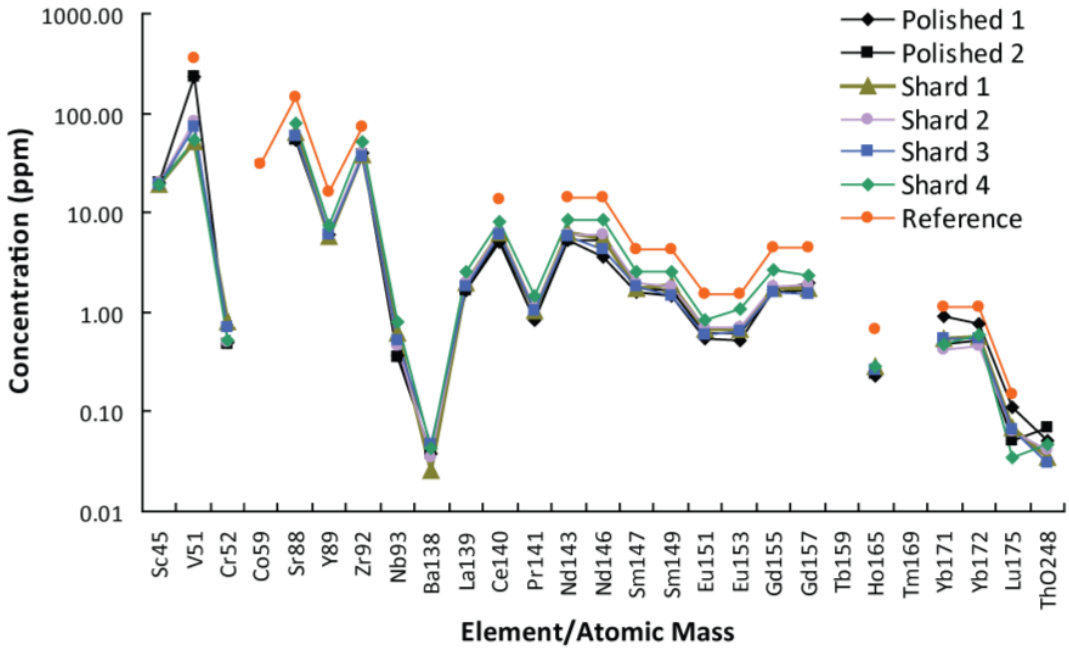

Figure 33. Graph displaying the results of the first calibration routine for analysis of trace elements on the SHRIMP. Two polished sections and four shards of Bo Ploi, a well quantified clinopyroxene megacryst (Norman et al., 1996), were analysed. Trace element abundances of the polished sections and shards match closely, but differ from the reference value and may be due ionisation efficiency or sample topography.

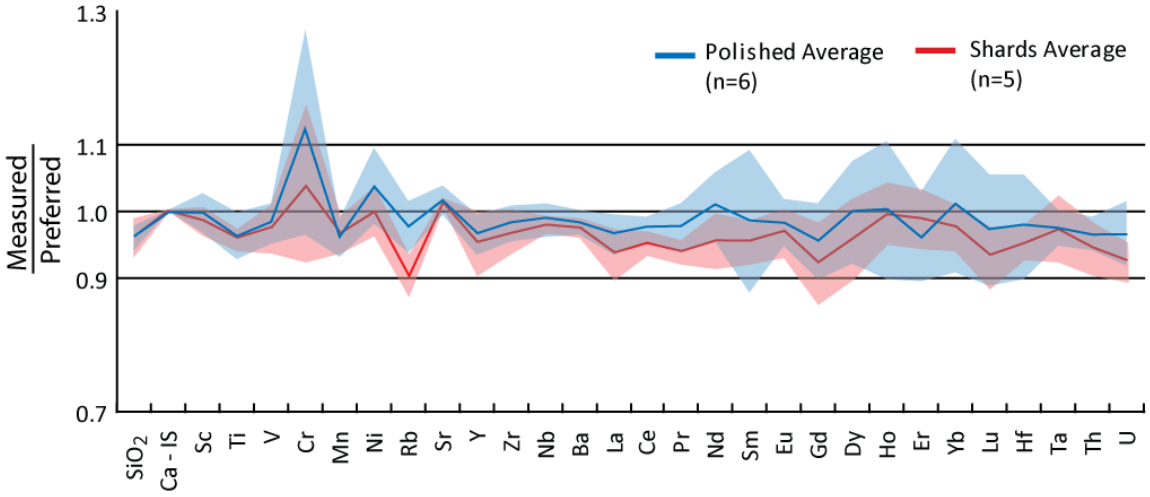

Figure 34. Measured/preferred abundance (See Norman et al., 2004 for preferred values) of trace elements in shards of USGS standard glass TB-1G as shards and as polished sections analysed by laser ablation ICPMS. The shaded areas show 2σ variations.

2.4 Summary

In summary, a new mounting method was developed with a specific focus on conservation of sample, minimal handling during analysis, and relatively short preparation time. These advantages, however, come at the expense of analytical quality. The results presented in this chapter have allowed quantification of that expense through theoretical and quantitative analysis of major and trace element compositions conducted on unpolished sample standards. The theoretical models run to determine the effect of a curved surface on major element analyses indicate that lower totals are to be expected of curved surfaces, but an appropriate balance between analytical precision and sample size can be reached. The effect of the absorption correction on each element analysed can also be adjusted if necessary. Although the ideal sample analogue (spherical known glass standard) could not be produced, quantitative tests conducted on shards of glass standards show that the results of electron microprobe, SHRIMP, and LA-ICPMS analysis of the irregular shards are comparable within 10% of the polished equivalents. These results give confidence to the implementation of this method in the lunar impact spherules project.

2.5 Chapter References

ALLEN C. C., MCKAY D. S. and MORRIS R. V. (1992) Lunar oxygen - The reduction of glass by hydrogen. In *Engineering, construction, and operations in space III* (eds. W. Z. Sadeh, S. Sture and R. J. Miller), pp. 629-640 Denver, Colorado.

DELANO J. W., ZELLNER N. E. B., BARRA F., OLSON E., SWINDLE T. D., TIBBETTS N. J. and WHITTET D. C. B. (2007) An integrated approach to understanding Apollo 16 impact glasses: Chemistry, isotopes, and shape. *Meteoritics & Planetary Science* **42**, 993-1004.

DROUIN D., COUTURE A. R., JOLY D., TASTET X., AIMEZ V. and GAUVIN R. (2007) CASINO Monte Carlo Simulation Program v2.42. http://www.gel.usherbrooke.ca/casino/.

EGGINS S. M., KINSLEY L. P. J. and SHELLEY J. M. G. (1998) Deposition and element fractionation processes during atmospheric pressure laser sampling for analysis by ICP-MS. *Applied Surface Science* **127-129**, 278-286.

GOLDSTEIN J., LYMAN C., NEWBURY D., LIFSHIN E., ECHLIN P., SAWYER L., JOY D. and MICHAEL J. (2003) *Scanning Electron Microscopy and X-Ray Microanalysis*. Springer.

GÜNTHER D., JACKSON S. E. and LONGERICH H. P. (1999) Laser ablation and arc/spark solid sample introduction into inductively coupled plasma mass spectrometers. *Spectrochimica Acta Part B: Atomic Spectroscopy* **54**(3-4), 381-409.

ICKERT R. B., HIESS J., WILLIAMS I. S., HOLDEN P., IRELAND T. R., LANC P., SCHRAM N., FOSTER J. J. and CLEMENT S. W. (2008) Determining high precision, in situ, oxygen isotope ratios with a SHRIMP II: Analyses of MPI-DING silicate-glass reference materials and zircon from contrasting granites. *Chemical Geology* **257**(1-2), 114-128.

IRELAND T. R. (1995) Ion Microprobe Mass Spectrometry. *Advances in Analytical Geochemistry* **2**, 1-118.

JOCHUM K. P., STOLL B., HERWIG K., WILLBOLD M., HOFMANN A. W., AMINI M., AARBURG S., ABOUCHAMI W., HELLEBRAND E., MOCEK B., RACZEK I., STRACKE A., ALARD O., BOUMAN C., BECKER S., DÜCKING M., BRÄTZ H., KLEMD R., DE

BRUIN D., CANIL D., CORNELL D., DE HOOG C.-J., DALPÉ C., DANYUSHEVSKY L., EISENHAUER A., GAO Y., SNOW J. E., GROSCHOPF N., GÜNTHER D., LATKOCZY C., GUILLONG M., HAURI E. H., HÖFER H. E., LAHAYE Y., HORZ K., JACOB D. E., KASEMANN S. A., KENT A. J. R., LUDWIG T., ZACK T., MASON P. R. D., MEIXNER A., ROSNER M., MISAWA K., NASH B. P., PFÄNDER J., PREMO W. R., SUN W. D., TIEPOLO M., VANNUCCI R., VENNEMANN T., WAYNE D. and WOODHEAD J. D. (2006) MPI-DING reference glasses for in situ microanalysis: New reference values for element concentrations and isotope ratios. *Geochemistry Geophysics Geosystems* **7**.

KITA N. T., USHIKUBO T., FU B. and VALLEY J. W. (2009) High precision SIMS oxygen isotope analysis and the effect of sample topography. *Chemical Geology* **264**(1-4), 43-57.

LUCEY P., KOROTEV R. L., GILLIS J. J., TAYLOR L. A., LAWRENCE D., CAMPBELL B. A., ELPHIC R., FELDMAN B., HOOD L. L., HUNTEN D., MENDILLO M., NOBLE S., PAPIKE J. J., REEDY R. C., LAWSON S., PRETTYMAN T., GASNAULT O. and MAURICE S. (2006) New Views of Lunar Geoscience: Understanding the Lunar Surface and Space-Moon Interactions. In *New Views of the Moon* (eds. B. L. Jolliff, M. Wieczorek, C. K. Shearer and C. Neal), pp. 83-219.

NITKIEWICZ A. and STERNER S. M. (1988) An improved Bond air mill for the preparation of spherical single crystals. *American Mineralogist* **73**(5-6), 662-666.

NORMAN M. D., GARCIA M. O. and BENNETT V. C. (2004) Rhenium and chalcophile elements in basaltic glasses from Ko'olau and Moloka'i volcanoes: Magmatic outgassing and composition of the Hawaiian plume. *Geochimica et Cosmochimica Acta* **68**(18), 3761-3777.

NORMAN M. D., PEARSON N. J., SHARMA A. and GRIFFIN W. L. (1996) Quantitative Analysis of Trace Elements in Geological Materials by Laser Ablation ICPMS: Instrumental Operating Conditions and Calibration Values of NIST Glasses. *Geostandards and Geoanalytical Research* **20**(2), 247-261.

PERKINS W. and PEARCE N. (1995) Chapter 7: Mineral Microanalysis by laserprobe inductively coupled plasma mass spectrometry. In *Microprobe Techniques in the*

Earth Sciences (eds. P. Potts, J. Bowles, S. Reed and M. Cave), pp. 291-325. Chapman & Hall.

REED S. (1995) Electron Probe Microanalysis. In *Microprobe Techniques in the Earth Sciences* (eds. P. Potts, J. Bowles, S. Reed and M. Cave), pp. 49-139. Chapman & Hall.

REED S. J. B. (1993) *Electron microprobe analysis*. Cambridge University Press.

SHIMIZU N. and HART S. R. (1982) Applications of the Ion Microprobe to Geochemistry and Cosmochemistry. *Annual Review of Earth and Planetary Sciences* **10**(1), 483.

STRUCTURE PROBE INC. (2009) Crystalbond™ and Wafer-mount™ Mounting Adhesives, pp. http://www.2spi.com/catalog/mounts/crystalbond-wafer-mount.shtml.

WILSON S. A. (1997) The collection, preparation, and testing of USGS reference material BCR-2, Columbia River, Basalt. U.S. Geological Survey Open-File Report 98-xxx.

ZOLENSKY M. E., PIETERS C., CLARK B. and PAPIKE J. J. (2000) Small is Beautiful: The analysis of nanogram-sized astromaterials. *Meteoritics and Planetary Science* **35**, 9-29.

CHAPTER 3:

INTRODUCTION AND BACKGROUND

3.1 Introduction

This chapter marks the beginning of the lunar impact spherules project, the main topic of this thesis. Lunar impact spherules are micron to centimetre-sized particles formed during impact events where shock-induced melting of the lunar regolith and impactor produce quenched melt splashes that can be deposited locally or ejected far beyond the point of impact (Chao et al., 1970; Delano et al., 1982; Glass, 1971). Impact spherules and other impact glasses make up a significant portion of all lunar soils (3-5%) (McKay et al., 1991). As such, they are an abundant medium from which it is possible to date individual impacts and can be used to reconstruct the bombardment history of the Moon, and by proxy, that of the Earth. Additionally, the provenance of lunar impact spherule can be determined as they acquire the composition of the material from which they were formed.

The aim of this project was to provide additional constraints on the lunar impact spherule record by studying spherules from the Apollo 16 site. In addition to impact spherules, a number of other impact products may be formed during impact events (e.g. craters, breccias, and impact-melts), some of which can be dated radioisotopically (absolute ages) or relatively (relative age). There are inconsistencies, however, when each of these lunar bombardment records are compared since each record has a different view of lunar bombardment history. This has lead to some controversial interpretations which will be briefly reviewed in this chapter. The remainder of the chapter will review the petrographic and geochemical characteristics of the lunar impact spherules. These characteristics are indicators of what was impacted, the likely locations of impact, and how impact spherules may have been altered during their residence in the regolith. Understanding these processes is an essential part of understanding the impact history as recorded by impact spherules.

3.2 The Lunar Impact Spherules Project

3.2.1 Project Aims

The lunar impact spherules project aims to add to the understanding of a newly emerging record of lunar bombardment. However, there are processes such as lunar 'gardening' (churning of the lunar surface by impacts) that can over-print the impact record. These processes are not fully understood and only add to the current multitude of controversial interpretations of lunar bombardment. In many of these cases, the inability to obtain major and trace element chemistry, radioisotopic ages, and cosmogenic exposure ages on single spherules limit the usefulness of the impact spherule data. The primary aim of this study, and purpose of the extensive method development discussed in the previous chapter, is to eliminate this shortcoming. This allows for the exploration of some outstanding issues such as:

- Trade-offs between trace element data needed to further resolve impact spherule provenance and the acquisition of formation and exposure ages
- Contribution of local versus exotic impact spherules to impact age distributions
- Production of multiple spherules in single impact events

The samples for this study come from a soils sampled at Apollo 16 Station 6 (66031,65). The primary reason for the selection of this site is the absence of an impact spherule age distribution for this region. The Apollo 16 site is the oldest surface sampled by the Apollo missions, hence should have an older and more continuous record (Culler et al., 2000). Additionally, Apollo 16 also has the advantage of being in different terrain that is geographically distant from the previous studies (Culler et al., 2000; Levine et al., 2005) allowing for a more global view of impact history to be constructed. Unwanted volcanic materials are rarer in the Apollo 16 regolith and based on mass balance models, only 6% of <1mm material in the regolith is expected to be volcanic (Zeigler et al., 2006). A drawback with Apollo 16 impact spherules is the generally low-K abundance that will make radioisotopic dating using K-Ar and related $^{40}Ar/^{39}Ar$ methods more challenging.

3.3 Background

3.3.1 Lunar Bombardment Records

The lunar bombardment history is recorded in a variety of geologic features, some of which can be observed or collected terrestrially. The simplest of these is crater counting, a photo-geologic technique whereby craters in a given area are tallied by size and relation to other craters (Neukum et al., 1975). Crater counting studies have produced size-frequency-distributions (SFD) for lunar impacts, two of which are prominent in the literature. The "Hartmann SFD" and "Neukum SFD" are derived using different mathematical descriptors (see Neukum et al., 2001) and calibrated to obtain crater production functions. The Hartmann Production Function used crater counts on the Canadian shield to predict the lunar mare age (3.6Ga) and determined that an "early intense bombardment" was needed to account for the higher crater densities on the lunar highlands (Hartmann, 1965, 1966). The Neukum Production Function was calibrated using crater retention ages (Neukum, 1983). The most recent incarnation of the Neukum production function is calibrated using absolute ages of returned lunar samples given in Stöffler and Ryder (2001) (see Neukum et al., 2001). The crater production functions derived from the "Hartmann SFD" and "Neukum SFD" share some similarities, but both assume that the general size-frequency distribution of lunar impactors remained the same during the entire history of the Moon (Stöffler et al., 2006). This assumption is challenged by Strom and Neukum (1988) and Strom et al. (1992), who argued that the post-mare production function is different to that during the "early heavy bombardment" (>4.1Gya).

One of the keys to understanding the lunar bombardment history is the crystalline impact-melt breccias. These products result from the impact-melting of the lunar crust and are incorporated into various lunar rocks. Turner et al. (1973) and Tera et al. (1974) noted that widespread isotopic disturbance occurred at ~3.9Ga in melt breccias and anorthosites from Apollo 15, 16, and 17. The disturbance was attributed to an impact event or a series of impact events that occurred within a short time period (<200Ma), termed the lunar cataclysm or Late Heavy Bombardment (LHB). Subsequent studies on

the impact-melt breccias have confirmed the clustering of ages (e.g. Dalrymple and Ryder, 1993; Dalrymple and Ryder, 1996; Norman et al., 2006; Turner and Cadogan, 1975); see Papike et al. (1998) and Stöffler et al. (2006) for compilations of impact-melt ages. The nature of the LHB is a controversial topic. The sharp decline in impact rates post-LHB is not strongly disputed, but whether a sharp increase in impact flux triggered the LHB is (Chapman et al., 2007). One argument is that the lack of rocks older than ~4.0Ga rules out extensive early basin formation and is evidence that such impacts are rare (Ryder, 1990; Ryder, 2002); therefore the spike in impact activity can only be explained by a LHB. However, it is also argued that older impact-melts may have been pulverised by subsequent impacts, thus biasing the record. This is termed the "stonewall" effect (Hartmann, 1975, 2003). Haskin et al. (1998) also advocated that the narrow band of impact-melt breccias reflect a single impact event, the one that formed the Imbrium basin, which covered all the Apollo highland sites with ejecta deposits hundreds of metres thick. Consequently, Chapman et al. (2007) argued the Apollo landing sites were all on the near-side and from regions prominently affected by the Imbrium basin-forming impact event; therefore the impact-melt ages are biased toward that single event. More recently, Norman (2009) also notes that the LHB hypothesis hinges on accurately defined lunar basin ages that are not well constrained.

Terrestrially-collected lunar meteorites were only recognised after the advent of the Apollo missions and are another type of lunar bombardment record. Lunar meteorites are less geographically constrained than other lunar materials sampled during the Apollo missions and contain crystallised impact-melt clasts which can be radioisotopically dated to construct age distributions. The collective data from these studies (Cohen, 2008a, b; Cohen et al., 2000, 2005; Cohen et al., 2002; Fernandes et al., 2004; Fernandes et al., 2000) show a broad distribution of ages from 1.0Ga-4.3Ga with a possible peak at 3.4Ga (see Figure 35). However, only 9 of 74 impact-melt clasts have ages consistent with the LHB period. Chapman et al. (2007) suggest that "there is a strong sampling bias favouring recent impact-melts and against older ones" based on their interpretation of the lunar meteorite data.

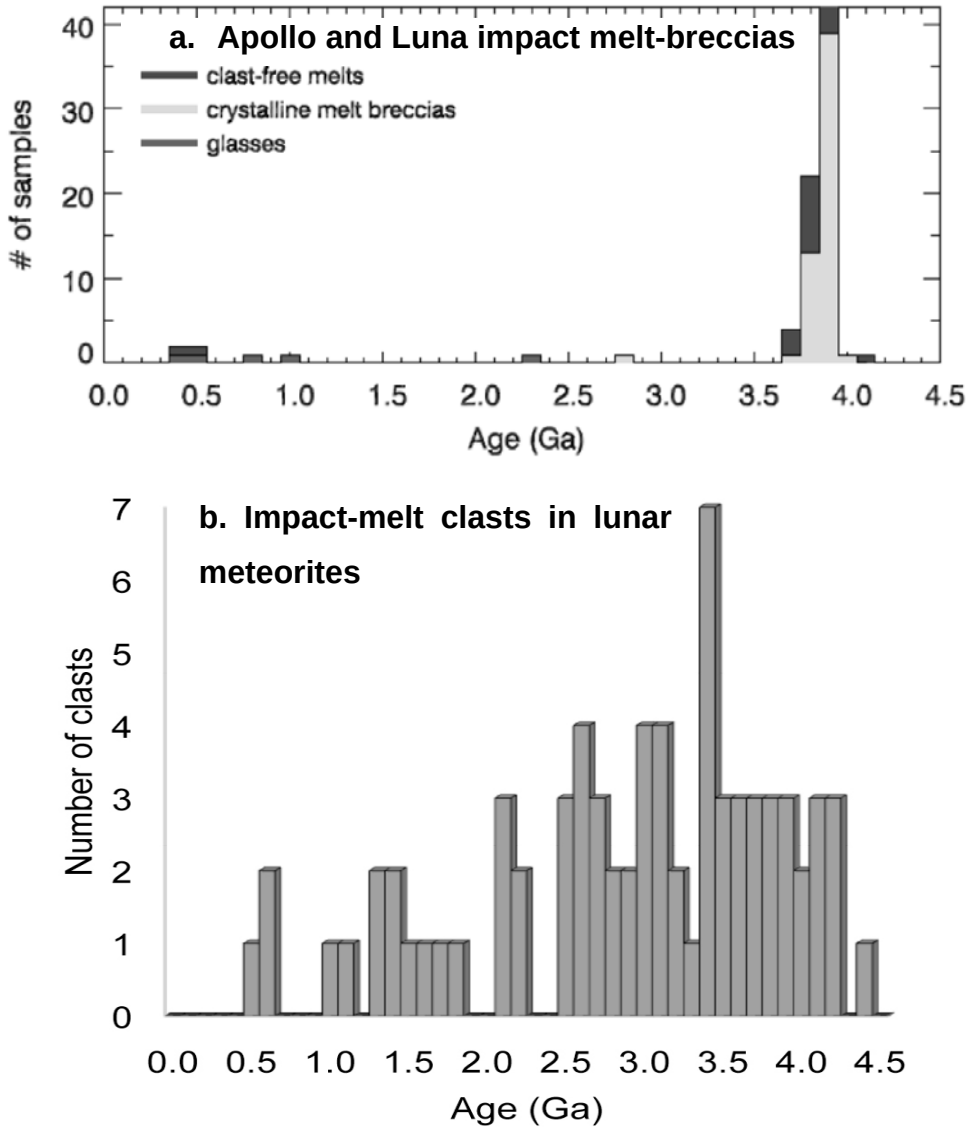

Figure 35. Impact-reset age distribution for lunar impact-melts collected from **a)** the Apollo and Lunar missions and **b)** lunar meteorites

Diagrams from Cohen (2002) and Cohen (2008b)

Recent investigation of lunar impact spherules has shown that they can also be used to understand the lunar bombardment history. One of the first impact spherule age distributions to emerge from this work was presented in Culler et al. (2000) who used the $^{40}Ar/^{39}Ar$ method to obtain the formation age of impact spherules from Apollo 14 soils. Culler et al. (2000) dated enough impact spherules to produce an age distribution and suggested that they were a representative medium from which to study impact history. Following this study, Levine et al. (2005) also produced an age distribution for Apollo 12. Although there were a number of marked differences between both records they also share a number of similarities. Impact spherules from both locations showed a wide distribution of ages making them a more suitable record of post-LHB impact events. This characteristic is probably because the impact spherules sample younger impact craters than the other lunar bombardment records (Culler et al., 2000; Hartmann et al., 2007). Impact age distributions established by both Culler et al. (2000) and Levine et al. (2005) did not show any increase in spherule production during the LHB period as well as a lack of spherules >4.0Ga, contrary to the data from impact-melt breccias. The most striking feature shared by both records is the spike in the number of spherules with an age of <400Ma. The <400Ma ages suggest an increase in recent impact activity; however, could also indicate over-representation of young spherules contributed from young craters (Culler et al., 2000; Levine et al., 2005).

The lack of comprehensive chemical data from previously dated impact spherules studies limits the ability to determine the contribution of these spherules from young craters and spherule provenance. Major element chemistry was acquired by Levine et al. (2005), but only for discrimination of volcanic versus impact spherules. Culler et al. (2000) stated that earlier work indicated that the majority of spherules from typical landing sites are dominantly of impact origin, although it is unclear whether this refers to the spherules dated in Culler et al. (2000). More recent studies have made more use of the major elements in addition to radioisotopic dating. Delano et al. (2007) used this integrated approach to date high-K impact spherules found in the Apollo 16 soils and suggested that these spherules were exotic to the site and transported vast distances because of their unique chemistry. Delano et al. (2007) also noted that five of these

exotic spherules have ages of ~3.8Ga suggesting a possible large impact event towards the end of the LHB. Following this study, Zellner et al. (2009b) constrained the impact history using the same methods as Delano et al. (2007) for spherules from Apollo 14, 16, and 17 sites. Zellner et al. (2009b) found a specific event at ~800Ma which was evident in 9 mostly mafic impact spherules. The integrated geochemical and geochronological approach allowed Zellner et al. (2009b) to determine the provenance of each dated spherule and hence conclude that there may have been a episode of lunar-wide bombardment at ~800Ma given multiple spherules from different landing sites were formed around this time. Prior to the this project, however, there have not been any studies that have integrated both major and trace element chemistry with radioisotopic dates for single impact spherules.

3.3.2 Lunar Impact Spherule Formation

Lunar impact spherules are formed by the quenching of melt that is produced in an impact event. Existing impact spherules are also modified and redistributed by subsequent impacts. The following paragraphs describe the processes that occur during impact events and how they affect the impact spherules. Most of the detail on the impact process has been summarised from Melosh (1989).

During each impact a complex series of thermal and mechanical processes occurs to form the crater and impact ejecta products such as the lunar impact spherules. In brief, an impact event can be broken into three stages: contact and compression, excavation, and modification (see Figure 36). The contact and compression stage involves transferral of energy between the projectile and target. Upon initial impact with the surface, high-velocity jets of melted regolith will be ejected from the impact site. Hydrodynamic flow impact modelling by Vickery (1993) indicate that jets contain 5% of melted material from the impactor for 0° (perpendicular) impact angles, and up to 30% for 75° (oblique) impact angles. The jet itself could be melt or vapour that is squirted into the environment usually at velocities faster than the incoming projectile and at low angles. Vickery (1993) suggests that jetting is a feasible method to produce

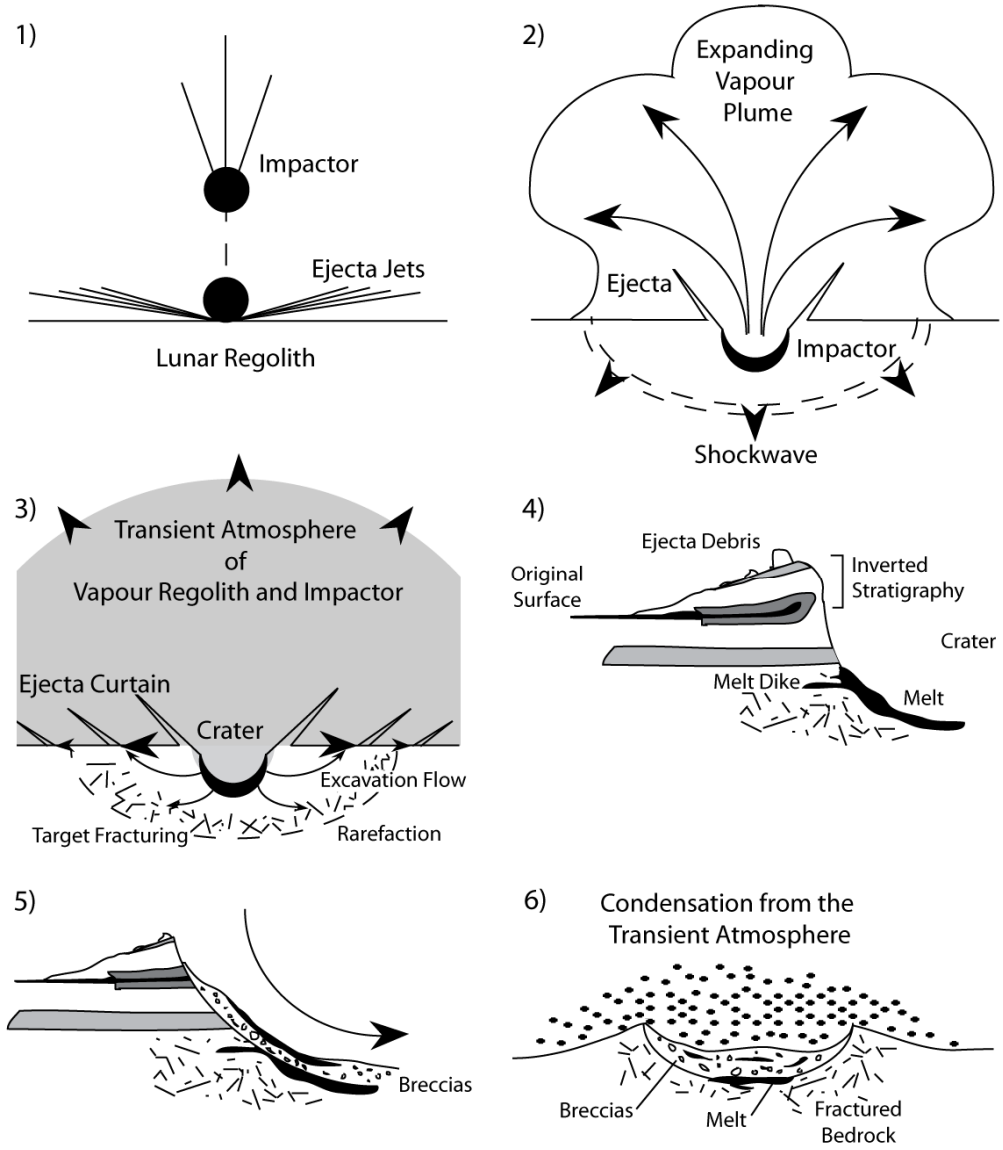

Figure 36. Diagrammatic representation of impact process for a simple (>10km) crater on the Moon **1)** Initial impact and the formation of high-velocity ejecta jets **2)** Unloading of the projectile, expansion of the vapour plume, propagation of the shockwave and initial ejecta **3)** Ejecta curtain propagation through the regolith produced by the evacuation flow, fracturing of the bedrock by rarefaction, and vapour plume expansion creating a transient atmosphere **4)** Close up of a crater rim to show the inverted stratigraphy **5)** Slumping of unstable slope during the modification stage **6)** Cooling of the transient atmosphere causing the condensation from the centre of the plume outward

Diagrams inspired by Melosh (1989)

tektites which are beads of quenched impact melt ejected from the site. The lunar equivalent of the tektite is the lunar impact spherule, which may also be produced in jets during the early stages of impacts into the lunar surface. Eventual vibration and decay of the fluid jets will allow the melt to quench in a variety of shapes such as those seen in tektites and lunar impact spherules (Chernyak and Nussinov, 1975; Chernyak and Nussinov, 1976). However, morphologically, impact spherules lack flanges (rims formed due to air resistance) without an Earth-like atmosphere on the Moon and are also more colourful than their terrestrial equivalents (see Figure 37).

Figure 37. Photo mosaic of a selection of impact glasses from this study (66031,65) observed under a binocular microscope. A range of photos were chosen to show the variety of shapes colours and other features such as adhering crusts, hollow spherules and broken elongate features.

The excavation stage begins almost immediately after the contact and compression stage. There are two major processes that occur simultaneously: mechanical and thermal alteration, followed by displacement of the target, and vapour plume formation. The energy of the projectile contacting the target material is such that the target material yields and deforms, slowing the projectile. The strong compressive energy is mediated

by a shockwave in the target material that compresses the target followed closely by a rarefaction wave that causes an equal amount of tensional stress to the target. Before the target's tensile strength is exceeded, cracks form, propagate, and fragment the target. The shock of the impacting bodies can cause the target to flow plastically, melt or vaporise as a function of the peak pressure and depth below the surface. Figure 38 demonstrates this behaviour for an iron meteorite striking an anorthosite target. In this situation, a vapour plume may form if the projectile speed exceeds ~6km/sec. If the impactor were of a less dense material the peak pressures would be reduced. For example, if the impactor were also an anorthosite, the peak pressures would be reduced by ~25% for a velocity of 5km/sec up to a reduction of 40% for faster velocities (Ahrens and Okeefe, 1977).

Occurring synchronously is the initial displacement of material (ejecta), triggered by the shockwave, and the formation of a vapour plume. The vapour plume will overtake the initial ejecta producing a "transient atmosphere of regolith and impactor" (Melosh, 1989), some of which would be lost to space. As the shockwave passes through the target, it displaces the target producing an evacuation flow where material moves away from the impact site. This process creates the crater, and material that rises above the pre-impact surface forms a curtain of ejecta, which is ballistically thrown from the impact site. The ejecta curtain provides an environment where impact-melt may also be ballistically ejected to form lunar impact spherules or transport existing impact spherules to distant locations. Molten ejecta in the ejecta curtain quench to more elongate forms through sufficient particle rotation to overcome viscosity before quenching to glass during free-flight above the lunar surface (Bastin and French, 1970; Fulchignoni et al., 1971). The ejecta curtain can also overturn stratigraphy at the crater rims excavating buried material and burying material previously on the surface. Fragments of the target may be launched into space to eventually fall to Earth as lunar meteorites, another important record of lunar impact history.

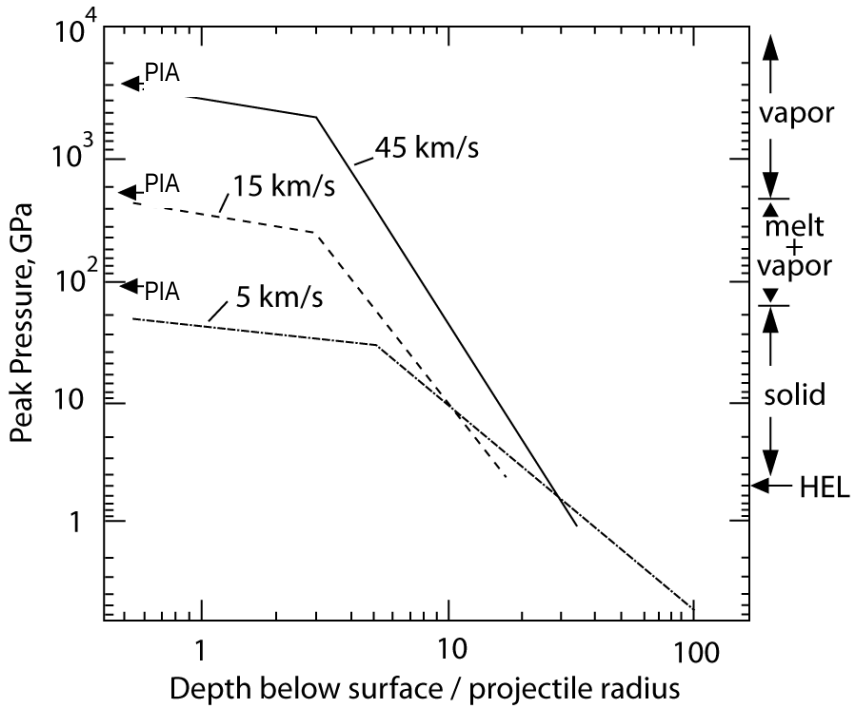

Figure 38. The decline in peak shock pressure as a function of depth below the surface for an iron meteorite striking an anorthosite target at 5, 15, and 45 km/second. At first, the pressure falls slowly from the maximum given by the planar impact approximation (arrows marked "PIA"). However, at depths greater than a few projectile radii, it falls more rapidly. The rate of fall is faster for the higher velocity impacts. The scale on the right-hand side of the plot shows the Hugoniot Elastic Limit (point at which elastic deformation of the target rock begins) of the target and the pressure ranges over which melt and vapour form.

Diagram from Ahrens and Okeefe (1977)

The modification stage is the final phase of crater formation. During this stage, the crater is subject to gravitational collapse and elastic rebound. The crater shape is determined by the characteristics of the target (cohesion, viscosity, density, and surface gravity), impactor (composition), and impact conditions (speed, angle) that govern the resulting crater dimensions (crater depth, diameter). These factors can be combined into a strength and flow parameter in a phenomenological model to determine the morphology of the crater (see Figure 39). Outside the stable regime, mixing of breccias, impact-melt, and shocked debris occurs by slumping of material down the steep interior

walls of the crater. In this environment, the mixing of these materials can produce melt-rocks and impact-melt breccias, but also redistribute existing material within the crater. More elastic regimes result in the isostatic rebound of the target material producing central peaks and formation of rings from shear stresses. Finally, cooling of the transient atmosphere results in condensation of volatile-rich products from the centre of the plume outwards towards the extremities. This volatile condensate can form discrete spherules or condense onto the surfaces of exposed materials such as soils, rocks, and impact spherules.

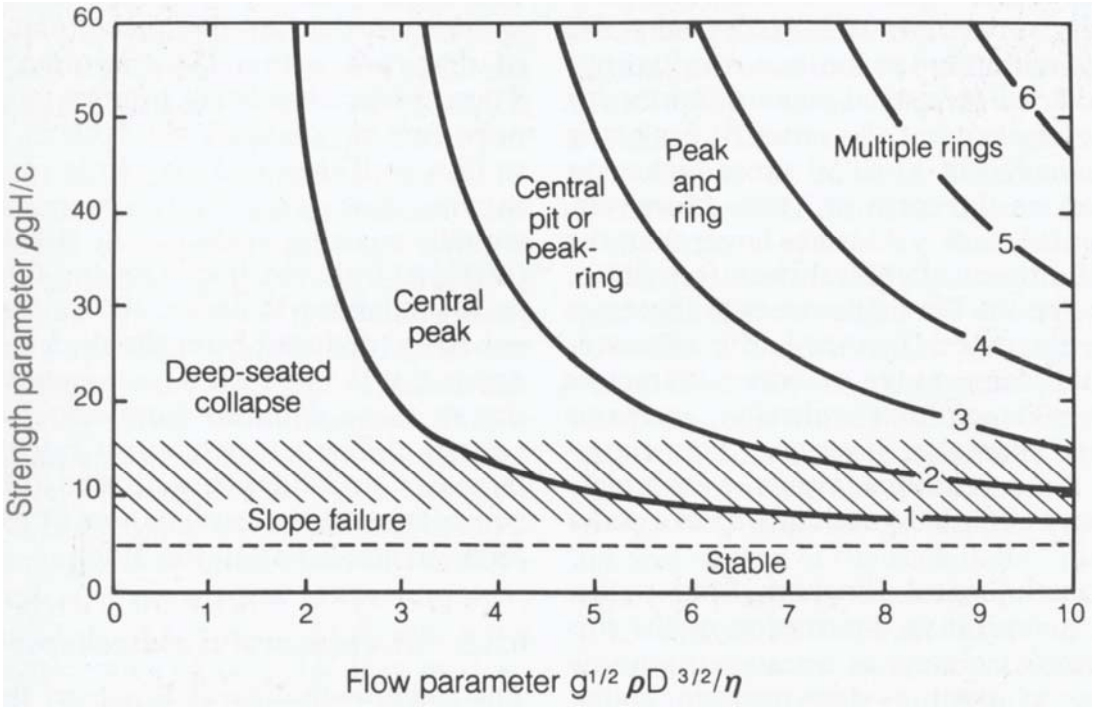

Figure 39. The phenomenological model of crater collapse predicts that the crater's final form depends upon two dimensionless combinations of the Bingham parameters cohesion *c* and viscosity *v* with the target density ρ, surface gravity *g*, crater depth *H* and diameter *D*. For large values of the flow parameter, the impacted substrate acts in a purely plastic manner allowing the energy of the impact to be transmitted, similar to ripples transmitting the energy from a pebble dropped into water. This allows central peaks and rings to form, provided the strength parameter is sufficiently large.

Diagram from Melosh (1982)

The number, size, shape, and distribution of impact spherules formed in any single impact has not been studied previously. It is also unclear what kinds of situation do not produce impact spherule. Although it is likely that the number of impact spherules produced is likely proportional to the amount of melt generated and perhaps the angle of impact, no definitive relationship has been established.

3.3.3 Field Setting

Global Overview

Impact spherules are composed of three main components derived from the three types of lunar terrains: the highlands, maria and KREEP. Generally, the materials derived from the highlands are feldspathic (Ca and Al-rich) and appear light in colour, while materials from the maria are basaltic (Fe and Ti-rich) and appear darker. KREEP or KREEPy are terms used to describe material rich in incompatible elements (potassium, rare earth elements, phosphorous) formed by concentration of residual liquid left over from the solidification of the lunar magma ocean, as these elements do not fit into many rock-forming minerals (Vaniman et al., 1991). KREEP does not imply a specific major element composition, but KREEPy materials are typically noritic. The source of the KREEP appears to correspond to the Oceanus Procellarum and Imbrium terrain (referred to as the Procellarum KREEP terrain or PKT) based on K, Th and U concentrations obtained from the gamma ray spectrometer on the Lunar Prospector spacecraft (Jolliff et al., 2000). Later work by Prettyman et al. (2006) employed 2º (~150km^2) pixel resolution to calibrate the major element and radioactive element abundances collected by gamma ray spectrometry on Apollo samples and lunar meteorites. Data from lower altitude passes are also available and provide better resolution to pixel sizes of 0.5 º (~45km^2), but at the expense of counting time (Lawrence et al., 2003; Lawrence et al., 2002). Gamma ray spectrometry is also limited to the near-surface as it only penetrates the top ~20cm of regolith (Prettyman et al., 2006). Figure 40 shows the distribution of KREEP and mare relative to the location of Apollo 16 based on approximate Th and FeO contents, respectively.

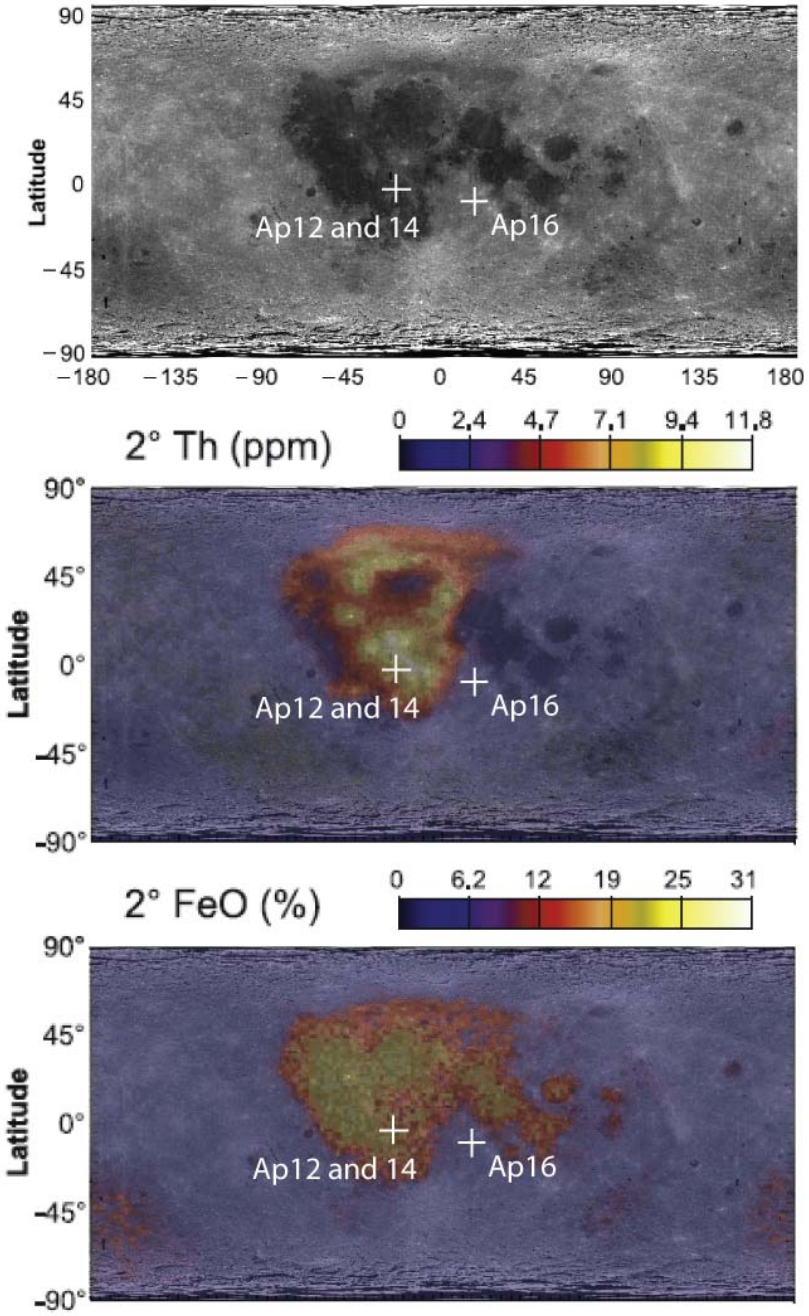

Figure 40. Mosaic of images from the Clementine spacecraft of the lunar surface overlain with Th and FeO distribution on the lunar surface determined using the gamma ray spectrometer on the Lunar Prospector. KREEP distribution is highlighted by high Th abundance whereas FeO is used to distinguish between the Fe-poor feldspathic highlands and basaltic mare. Pixel resolution of 2º (~150km^2), Mercator projection.

Modified from images and results of Prettyman et al. (2006)

The Apollo 16 landing site is located on the near-side central highlands. According to Zeigler et al. (2006) Apollo 16 landing site is ~350km from the nearest source of KREEP, and about 220km from the nearest source of mare material. Orbital X-ray Fluorescence (XRF) spectrometers aboard the Apollo 16 module are able to resolve broad features down to 30km^2 and will be discussed in the following section.

The Apollo 16 Site and Surrounding Region

The following sections are a very brief summary of the geology at the Apollo 16 site. The information is largely summarised from Ulrich et al. (1981) and the Apollo Field Geology Investigation (1973).

The Apollo 16 mission was designed to sample material from the heavily cratered central lunar highlands. More specifically, the Apollo 16 mission was to sample the morphologically distinct Cayley Plains and Descartes Mountains. Together, these units cover 11% of the lunar near-side with the Cayley Plains being the most widespread and possibly representing a Moon-wide geologic unit originally thought to be volcanic formations (Muehlberger et al., 1980). Post-Apollo 16, the dominance of cataclastic, fragmental, melt-bearing and polymict breccias in returned samples suggested that both the Cayley Plains and Descartes Mountains are dominantly impact deposits. The Descartes Mountains are a more localised unit and virtually unique to the Moon (Muehlberger et al., 1980). Figure 41 is a metric image, taken by the shuttle camera, of the Apollo 16 area and shows the three physiographic units: the relatively flat Cayley Plains, the more furrowed Descartes Mountains and to the far east the Kant Plateau. Figure 42 shows an enlarged metric image of the Apollo 16 landing site and surrounds overlain with the geological features observed and traverses conducted during the mission. The sampling traverses were designed to sample the Cayley Formation regolith near where the lunar module touched down and the areas to the north and south thus providing information on lateral variation in the stratigraphy. North Ray and South Ray craters were chosen as the upper and lower bounds to the profile, but also because they were young craters that allowed sampling of deeper regolith. Although South Ray crater

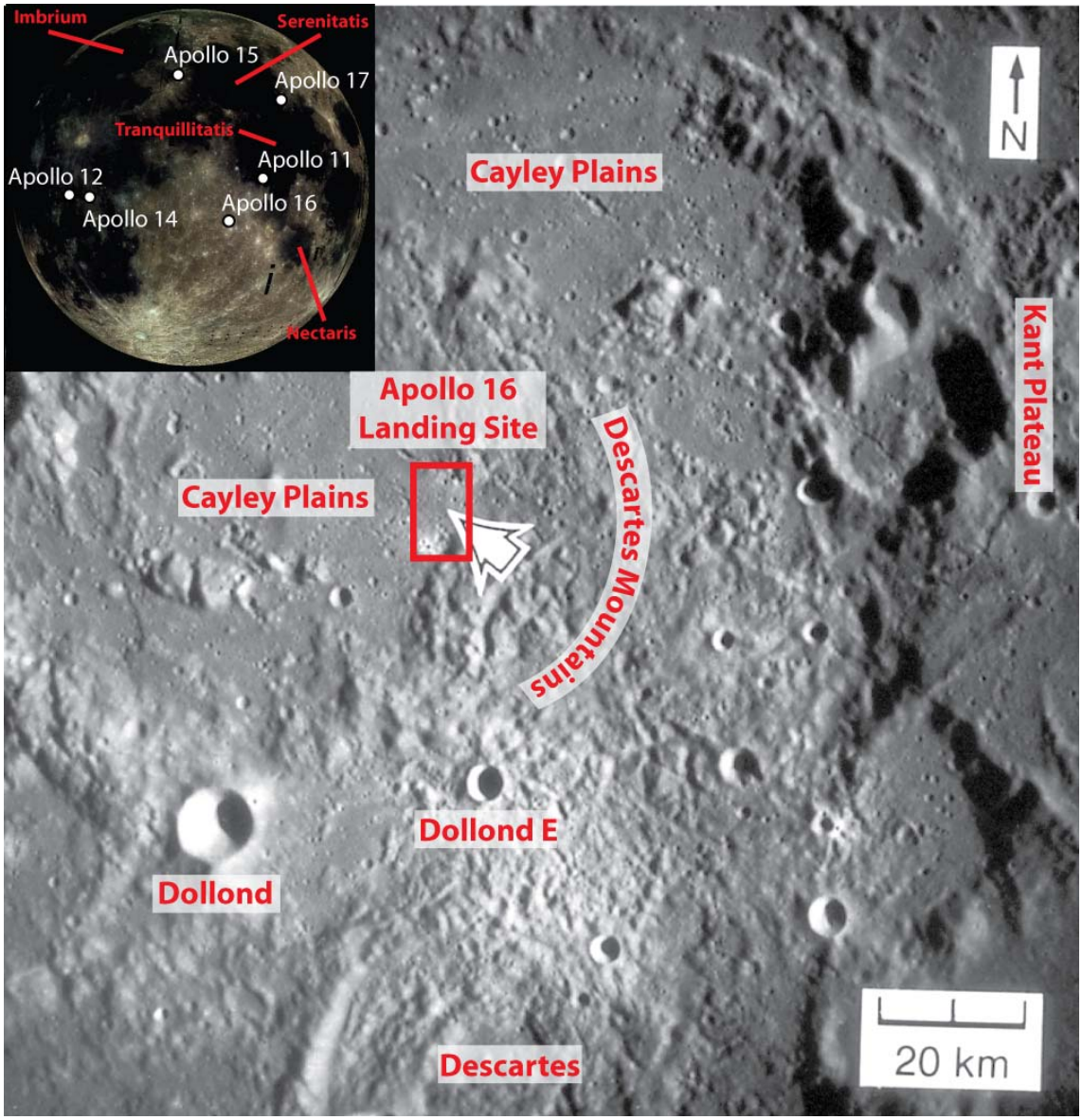

Figure 41. Clementine Mosaic of the near-side of the Moon overlain with location of the Apollo missions and surrounding major basins. Enlarged is an Apollo metric image (Frame ID AS16-0161 [M]) of the Apollo 16 landing area. The dark and relatively flat regions are known as the Cayley Plains. The rugged terrain is known as the Descartes Mountains and the elevated region to the east is known as the Kant Plateau. The arrow points to the location where the landing module touched down.

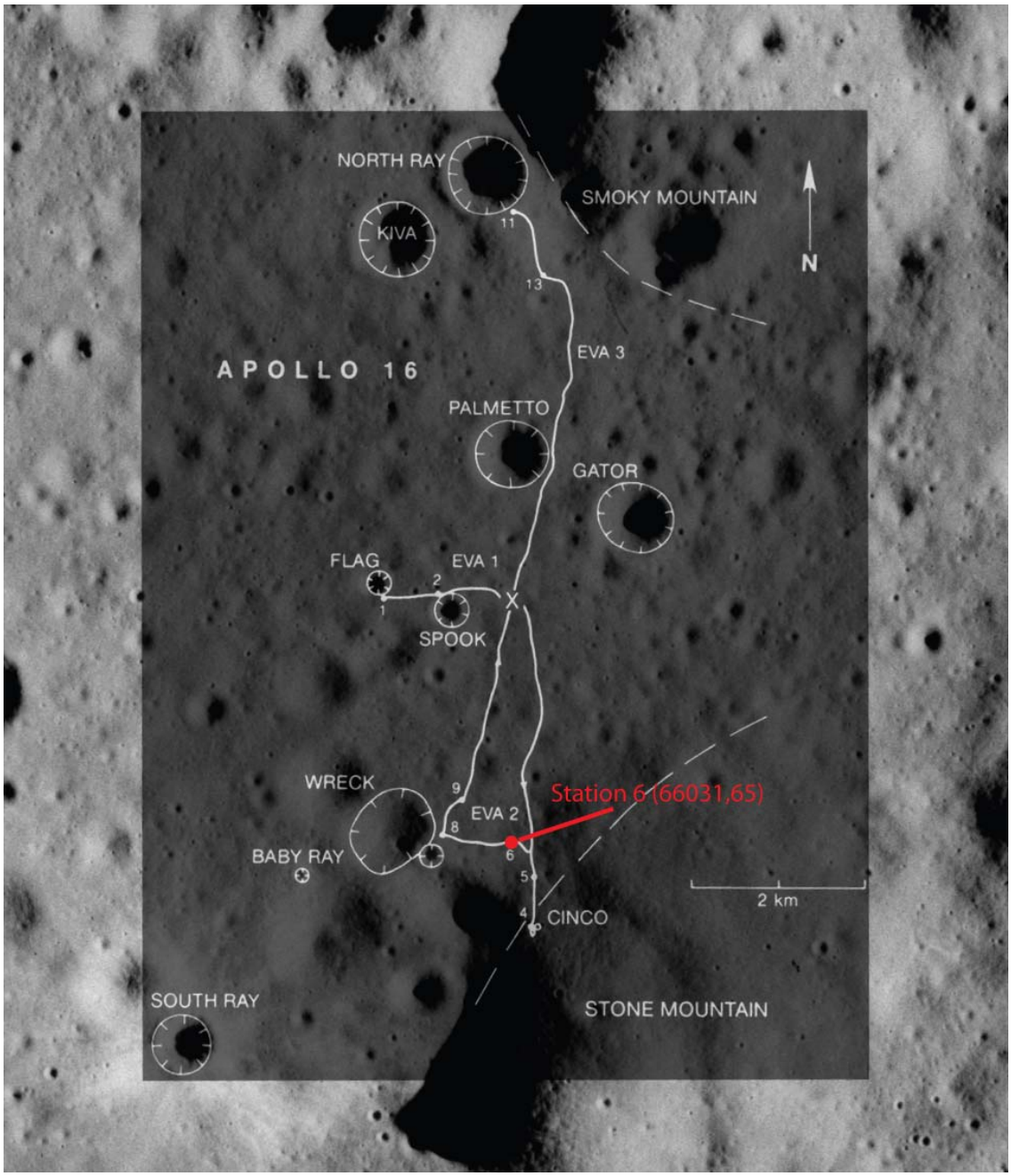

Figure 42. A zoomed-in portion of Apollo metric image (frame ID AS16-M-0162) of the Apollo 16 landing site and surrounds overlain with information on the geologic features and traverses completed at Apollo 16.

Modified from NASA/JSC/Arizona State University (2008)

was not visited, rays and other ejecta are prominent in the orbital photography and likely affect a large portion of the southern half of the landing site and were intended to be sampled at Stations 8 and 9 (Ulrich et al., 1981). ^{81}Kr-Kr exposure dating of ejecta, mostly breccias thought to be delivered by rays from South Ray crater, suggest the formation of the crater occurred at 2Ma (see summary in Drozd et al., 1974; Eugster, 1999). North Ray crater was originally thought to be a good location to sample the Cayley Plains (Muehlberger et al., 1980), but analyses on the North Ray crater rocks have shown that they are more representative of Descartes material (Lindstrom and Salpas, 1981; Norman, 1981; Ulrich, 1973). ^{81}Kr-Kr exposure age dating of soils and boulders collected from the rim of North Ray crater suggest crater formation at 50Ma (see summary in Drozd et al., 1974). Stone Mountain to the south of the Lunar module was the original target for recovery of Descartes material (Muehlberger et al., 1980). Three sites (Stations 4, 5, and 6) samples across the supposed Cayley-Descartes boundary. Station 6 was located at the base of Stone Mountain, Station 4 on a higher location at Cinco a., and Station 5 in an intermediate location between Stations 4 and 6.

Station 6, the location where the lunar impact spherules in this study were recovered, is located close to, but on the Cayley side of the geological contact between the Cayley and Descartes Formations. It was originally selected so the amount and/or rates of downhill transport due to slumping could be determined (Muehlberger et al., 1980). Samples for Station 6 were taken along the rim and western wall of an unnamed 10m diameter crater. There are numerous shallow craters as well as half-metre angular blocks and 10-20cm fragments covering ~1% of the surface. The source of the fragments and several perched rocks may have been transported by a ray from South Ray crater, although there are no large block fields visible. It has also been suggested that Descartes material may have "mass wasted" (slumped) into Station 6 thus explaining the chemical similarity of materials from both sides of the inferred Cayley-Descartes contact; however, this hypothesis has yet to be confirmed.

Soil Compositions and Variation

Although the Apollo 16 mission had been planned to sample a number of geographically and morphologically distinct settings, early results indicated that the "samples recovered appear grossly similar in lithologic type(s) and relative abundance, even within individual sampling stations where statistically significant samples could be collected" (Muehlberger et al., 1980: also see Apollo Field Geology Investigation, 1973; Ulrich et al., 1981; Wilshire et al., 1973). At the time, only North Ray crater soils stood out because they are significantly enriched in Al and depleted in Fe, Ti and Ni compared to the other soils (Ulrich et al., 1981). More recent literature suggest that the Cayley and Descartes formations are lithologically, compositionally, and physically different (Wilhelms, 1987). The soils from the Cayley Formation are typically more mafic and KREEPy than those from the Descartes Formation, due mainly to the contribution of two groups of impact-melted rocks and material common in the Cayley soils (James, 1981). One group has a "low-K Fra Mauro Basalt" (LKFM) composition (17-21wt.% Al_2O_3, mafic, and KREEP-rich), whereas the other has a noritic-anorthosite composition (29-31wt.% Al_2O_3). Intermediate compositions also exist, referred to as Very-High-Alumina (VHA) Basalts (21-26wt.% Al_2O_3), which is thought to characterise typical Cayley material (James, 1981). Collectively, Korotev (1994) refer to the VHA basalt components as the mafic impact melt breccias (MIMBs), which are the source of KREEP at Apollo 16. These are divided into groups based on their KREEP content with group 1 being the most mafic and KREEPy, followed by group 2 representing the VHA basalts (Korotev, 1994). Feldspathic KREEP-poor impact-melt breccias are classified as group 3 and 4. Group 4 are nearly exclusive to North Ray Crater (Korotev, 1994). As previously noted, the Descartes Formation may have been sampled from Stations 11 and 13 around North Ray crater and is represented by fragmental feldspathic breccias with melt-poor matrices, but can also contain clasts of KREEP (Lindstrom and Salpas, 1981; Lindstrom and Salpas, 1983; Norman, 1981; Norman et al., 2010). The Descartes Formation soils are typically more aluminous than the Cayley soils with orbital X-ray data indicating Al_2O_3 abundance as high as 29wt.% and are most similar to materials from the Kant Plateau (Andre and El-Baz, 1981).

A number of mixing trends have been proposed by Korotev (1997; 1981, 1982; 1994) to account for the compositional diversity of the regolith. Based on Sm/Sc ratios of material from the Apollo 16 site, Korotev (1997) argues that most of the compositional variation of Apollo 16 material can be explained in a simple three component system consisting of pre-basin material (mostly anorthosites and feldspathic breccias), MIMBs, and mare material. Based on this model, the typical mature Cayley soil consists of ~65% pre-basin materials, 29% MIMBs, and 6% mare materials. The MIMBs that makes up a large portion of the typical mature Cayley soil, was thought to be introduced into the Apollo 16 region as primary ejecta from the Imbrium impact (Korotev, 1997).

Origin of the Cayley and Descartes Formations

There are two schools of thought for the origin of the Apollo 16 impact deposits. One view suggests that the samples are predominantly of local origin whereas the other view suggests that samples were sourced from basin-related areas. Arguments for a predominantly "local" origin are based on "mass wasting" and debris surges from local topographic highs though contribution of primary Imbrium was suggested to make up not more than ~15% of the soils (Oberbeck, 1975). This hypothesis suggests that all features at Apollo 16 were created by impacts that churned and reworked dominantly "local" regolith. A different argument for a "local" origin was presented by Head (1974) who suggested that the flatness of the Cayley morphology reflects the original flatness of large crater floors created by ejecta fallback and coherent melt sheets. Head (1974) does, however, suggest that the Descartes material is of a different origin, namely pure Necatris ejecta.

Arguments for a mostly basin-related origin for the Apollo 16 site are based on proximity to major impact basins (Imbrium, Serenitatis, and Nectaris), which may have contributed varying amounts of material to the Apollo 16 region (Haskin et al., 2002; Spudis, 1984; Ulrich et al., 1981; Wilhelms, 1987) dominated by impact products (impact melts and breccias). Based on crater counting of the Cayley Plains, Neukum (1977) suggests that there may be genetic relationships between the formation of the Cayley Plains and Imbrium or Orientale. The main argument for Imbrium being the

dominant event contributing material to Apollo 16 was the transitional contacts between the Cayley and Descartes units, based on photogeological interpretations (Hodges et al., 1973; Ulrich, 1973; Ulrich et al., 1981). Recent impact ejecta modelling by Petro and Pieters (2006) attempted to model the contribution of major impact basins to the Apollo 16 region. Depending on the mixing model used, Apollo 16 regolith could be 50-60% ancient crustal material with 10% contribution each from Imbrium, Serenitatis and Nectaris, with the remaining portion being from other impact basins for a homogeneous mixing model. In a 'no-mixing' scenario, the Apollo 16 surface regolith would be dominated by ejecta from Imbrium. Based on regolith compositions from Apollo 16 soils, Korotev (1997) argues that significant mixing must have occurred on the Cayley mega-regolith prior to development of the present surface, as the present regolith is similar to the ancient regolith breccias. This argument suggests that the input of material from Imbrium into the Apollo 16 regolith lies between the extreme scenarios suggested by Petro and Pieters (2006), but closer to the homogeneous mixing scenario. A recent study of the ages and compositions of clasts in the Descartes breccias by Norman et al. (2010) also proposed that these breccias, collected from North Ray crater, are consistent with derivation from the Imbrium basin-forming impact event. These breccias have petrographic and geochemical signatures of KREEPy and Mg-Suite components indicative of origin from the PKT. The emplacement age of the youngest clasts is consistent with that of Apollo 15 melt rocks that define the age of the Imbrium event. In the interpretation of Norman et al. (2010), both the Cayley and Descartes Formation resulted from the Imbrium event and compositional differences between these formations "may reflect pre-impact stratigraphy or lateral heterogeneity in the lunar crust".

3.3.4 Lunar Impact Spherules- Petrographic Features

Lunar impact spherules exhibit a large variety of petrographic features, some of which are created during formation while others are created during residence in the lunar regolith. Impact spherule shapes are fashioned through processes briefly mentioned in the previous section. Additionally, impact spherules may be damaged or shattered into irregular shards from ballistic transport at suborbital speeds or during residence in the

lunar regolith (Delano et al., 2007). A point of contention, however, is the formation of oblate and dumbbell-shaped impact spherules. Mueller and Hinsch (1970) proposed that rotation of a particle allows for elongation, but at some point surface tension prevents further elongation of the melt allowing it to quench as a dumbbell. More irregular forms were probably insufficiently melted or did not reach a temperature where surface tension could overcome viscosity (Pugh, 1972). Based on this argument, it would be expected that impact spherules produced from more aluminous compositions (i.e. highlands targets) will not produce as many dumbbell shapes compared to more mafic compositions as they are more viscous. Chernyak and Nussinov (1975), however, argue that if rotation were the primary mechanism for elongation, then S-shaped glasses should also be formed due to Coriolis accelerations; however these are not observed in reality. The most recent articles on this topic, Bastin (1979, 1980), provide several arguments for the rotational mode of formation. These include measured differences between the curvature of dumbbells and those produced by jets. Bastin (1979, 1980) also hypothesise that migration of heavier particles towards the extremities and vesicles towards the core of dumbbells and dampening of Coriolis forces through viscosity should occur. It is not certain whether there is any closure on this topic as articles become scarce after Bastin (1979, 1980).

Colours can also be used to discriminate between materials derived from the highlands (feldspathic composition) and those derived from the mare (basaltic composition). A study by Naney et al., (1976) on impact spherule colours in a thin section from the Apollo 16 drill core showed that colour is a good first-order discriminant for impact spherule provenance. The clear, gray and brown colours were often associated with chemistry typical of Apollo 16 (highlands) while more colourful reds, oranges, yellows and greens were exotic to the site and more likely to be originated from the mare. However, colours are prone to interpretative errors and can vary depending on factors such as specimen thickness and viewing angle.

Reconstruction of a good impact record requires dates exclusively from impact spherules. However, volcanic spherules may be interspersed amongst the impact glasses in the regolith and, if mistaken as an impact spherule, will pollute the impact record. For example, non-spherical volcanic glasses could be mistaken for impact glasses as some have a similar variety of shapes as seen in impact spherules (Delano, 1993; Weber et al., 2010). Discrimination between volcanic and homogenous impact glasses is difficult without geochemical analyses. However, some petrographic features (e.g. clasts, schlerin, Fe-metal blebs, vesicles) are a good first-hand indicator of impact or volcanic origin and are discussed below.

Lunar impact spherules can be sub-divided into two broad petrographic groups, those that are homogeneous and those that are heterogeneous. There are few homogeneous impact spherules that are free of mineral fragments and contain few vesicles. More commonly, impact spherules can contain crystallisation textures indicative of rapid cooling, undigested mineral inclusions, flow structures (schlieren), vesicles, surface coatings and Fe-Ni spheres (Chao et al., 1970). Some of these features, such as the schlieren and undigested mineral inclusions are usually absent in volcanic glasses, but are not diagnostic features (Delano, 1986). Schlieren result from the flow of molten materials and are highlighted in impact spherules by entrapped particles in the glass (i.e. minerals, Fe-Ni spheres) or from incompletely mixed melts (See et al., 1986). Vesicles are likely to have formed from the release of trapped gas during impact melting (Mueller and Hinsch, 1970) and are probably derived from implanted gases already present on the lunar surface (Scarlett et al., 1977). Surface coatings can consist of rock powders adhering to the surface of the impact spherules as well as mineral inclusions acquired while the impact spherule was still partially molten. It is also possible for other nearby impacts to generate melts that coat impact spherules residing in the regolith. These coats may subsequently erode through sputtering caused by the interaction of high energy particles or ablation from micro-impactors. Such micro-impacts cause localised vaporisation of the target which can condense and deposit nanophase Fe (Sasaki et al., 2001). Larger Fe-Ni spheres could result from contamination from the impactor or may be formed as a result of separation and crystallisation of an immiscible

Fe-Ni-P liquid from a KREEPy melt in highly reducing environments (McKay et al., 1973). However, many of these features cannot be observed without mounting and polishing the impact spherules.

The unequivocal identification of impact versus volcanic spherules is thus difficult and unreliable. There are limits to identification of provenance and discriminating between impact and volcanic derived spherules using petrography. Impact spherule chemistry, however, is an additional constraint that can be obtained with little damage to the original spherule.

3.3.5 Lunar Impact Spherules - Chemistry

The presence of lunar impact spherules has been recognised since studies of lunar soils in the early 70's. One of the earliest papers examined glassy spherules found in the Apollo 11 regolith (Winchell and Skinner, 1970). This paper concluded that the glassy spherules were impact products due to their inhomogeneity, both within individual spherules and between spherule groups, and their large range of compositions. In contrast, volcanic spherules display both intra-sample (within single spherules) and inter-sample (clustering of volcanic spherules from a common source) chemical homogeneity (Delano, 1986). Additionally, volcanic spherules have higher Mg/Al ratios (>1.5) than mare regoliths and impact glasses, with Mg strongly correlated with Ni, indicating little meteoritic contamination (Delano, 1986). These criteria make it possible to discriminate between volcanic and impact spherules and were employed by Levine et al. (2005) and possibly Culler et al. (2000) prior to radioisotopic dating.

Silica-rich micron-sized spherules with volatile enrichments (Na, K, S, P) and Al-poor compositions have also been found in the lunar regolith and coined VRAP (Volatile-Rich, Al_2O_3 Poor) by Keller and McKay (1991; 1992). These are not impact spherules since VRAP glasses are condensation products from impact-generated vapour. More recently, Warren (2008) has also documented the presence of other likely condensation products referring to them as GASP (Gas-Associated Spheroidal Precipitates). GASP spherules condense from impact-vapour before the VRAP spherules as their

composition is less volatile (SiO_2, MgO, FeO as opposed to K_2O and Na_2O) (Warren, 2008).These products can be found in the regolith as discrete particles or adherents on the surfaces of other particles. A complementary highly refractory phase, HASP (High Al_2O_3, SiO_2 Poor), is also present in the regolith is "similar [in bulk composition] to the Ca- and Al- rich inclusions of the Allende meteorite" (Naney et al., 1976). Keller and McKay (1993) concluded that HASP spherules were derived from aluminous source rocks that were stripped of volatiles through impact processes leaving a refractory residue. These materials are highly fractionated products of the regolith of which impact spherules are only a small component. Such products cannot be considered to be a representative component of the impact spherule chemistry even though they can adhere to spherule surfaces as they cumulate over several impacts in different targets.

Impact spherules were collectively studied as lunar glasses in the earlier literature (pre-1990's). The rationale behind these studies was the use of lunar glasses as remote samplers of a wider variety of lunar materials not sampled directly during the Apollo missions (Reid et al., 1972c). Subsequent studies have focused on the identification of parental rock types (known as the "rock type hypothesis") for the impact glasses (e.g. Chao et al., 1972; Glass, 1976; Naney et al., 1976; Ridley et al., 1973; Warner et al., 1979). Since then, it has been demonstrated that the bulk major and trace element compositions of the impact glasses are more representative of the regolith compositions (e.g. Delano, 1991; Glass, 1976; Meyer, 1978; Vaniman, 1990; Zellner et al., 2002). The regolith compositions are mixtures of at least a few percent of the three lunar "terrains" (highlands, maria, and KREEP) defined earlier by Jolliff et al. (2000) with their spatial distribution shown in Figure 40 (Lucey et al., 2006). These "terrains" are distinct in their major and trace element compositions typically distinguished using Fe and Th (as a signature of KREEP) in plots like Figure 43. These "terrains" can be thought of as end-members though there is not a specific end-member composition, thus the end-members occupy a range or field in Figure 43. The spread of soil compositions from the Apollo sites in Figure 43 also suggests that mixing of the end-member components may occur. In particular, there are some mixing trends between bulk soil and discernable impact glass groups within Apollo sites which highlight some of the

more dominant groups (Delano, 1975; Delano et al., 1982; Kempa et al., 1980). For example, the "low-K Fra Mauro Basalt" (LKFM) (Reid et al., 1972c) is one group that shares similar compositions to breccias and melt rocks and, is present in all Apollo and Luna landing sites (Delano, 1991).

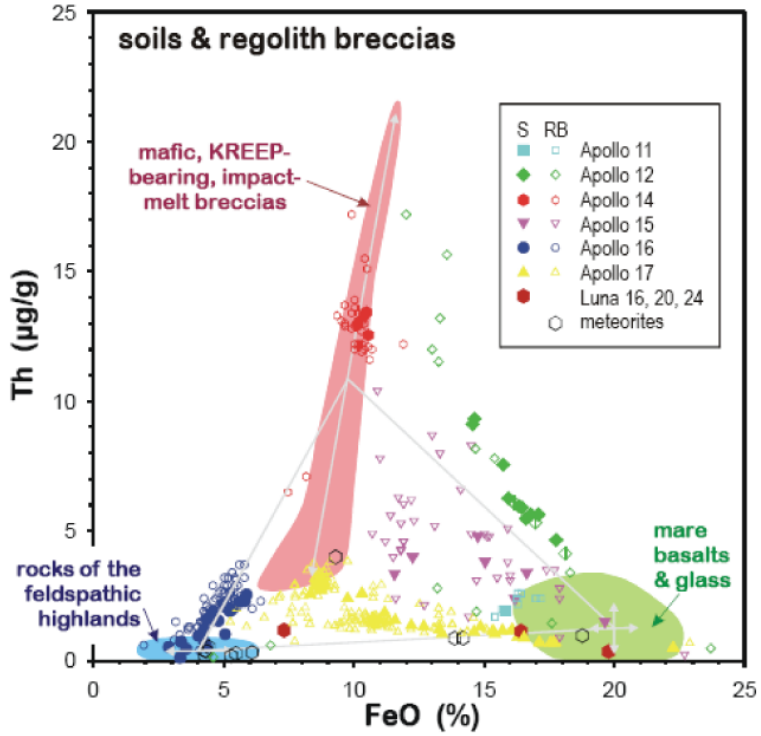

Figure 43. Plot of the major element iron and trace element thorium content of Apollo soils (S: filled symbols) and regolith breccias (RB: open symbols), Luna soils and lunar meteorites. Thorium is used to identify KREEPy material (red field) and iron is used to distinguish between highlands (blue field) and mare (green field).

Diagram from Korotev (2001)

3.3.6 Lunar Impact spherule Provenance

As previously mentioned, the melt that quenches to form impact spherules is dominantly derived from the ejected impact melted regolith with minor inputs from the impactors. As a result, the impact spherule chemistry retains a compositional memory of the target from which each spherule was created (Delano, 1991; Glass, 1976). However, some controversy exists over exactly what an impact spherule samples, whether it is the top few centimetres of soil, or a deeper portion of the regolith. Given that it is still unclear if impact spherules are only produced from certain-sized impacts (i.e. micro-impacts into soil or basin-forming impacts), both soil and regolith will be used interchangeably to describe the target. Impact spherules are not constrained to their location of origin and can be transported ballistically during impact events or from other regolith processes (e.g. slumping). As such, impact spherules collected from each Apollo site have a mix of locally-derived and exotic impact spherules. Reid et al (1972a) proposed a system of classification that conveniently expressed glass compositions in terms of the equivalent rock name. This was adopted by early researchers studying lunar glasses and is prevalent in the early literature. In this system, high-Ca and high-Al glasses were called anorthosite and have 0-10% normative mafic minerals; gabbroic anorthosites have 10-22.5%; anorthositic gabbro 22.5-35%; and gabbro have 35-65%. In addition to this nomenclature, discrete compositional groups may also be named after the formation in which they were found and their compositional characteristics (e.g. HKFM: High K Fra Mauro). The following paragraphs will briefly summarise the literature available concerning characteristics of impact spherules at each Apollo landing site (see Figure 44 for spatial distribution). However, since some early studies did not make the distinction between impact glass and spherules, a broader summary of impact glasses will be given instead. Note that the following descriptions only cover impact glasses and spherules.

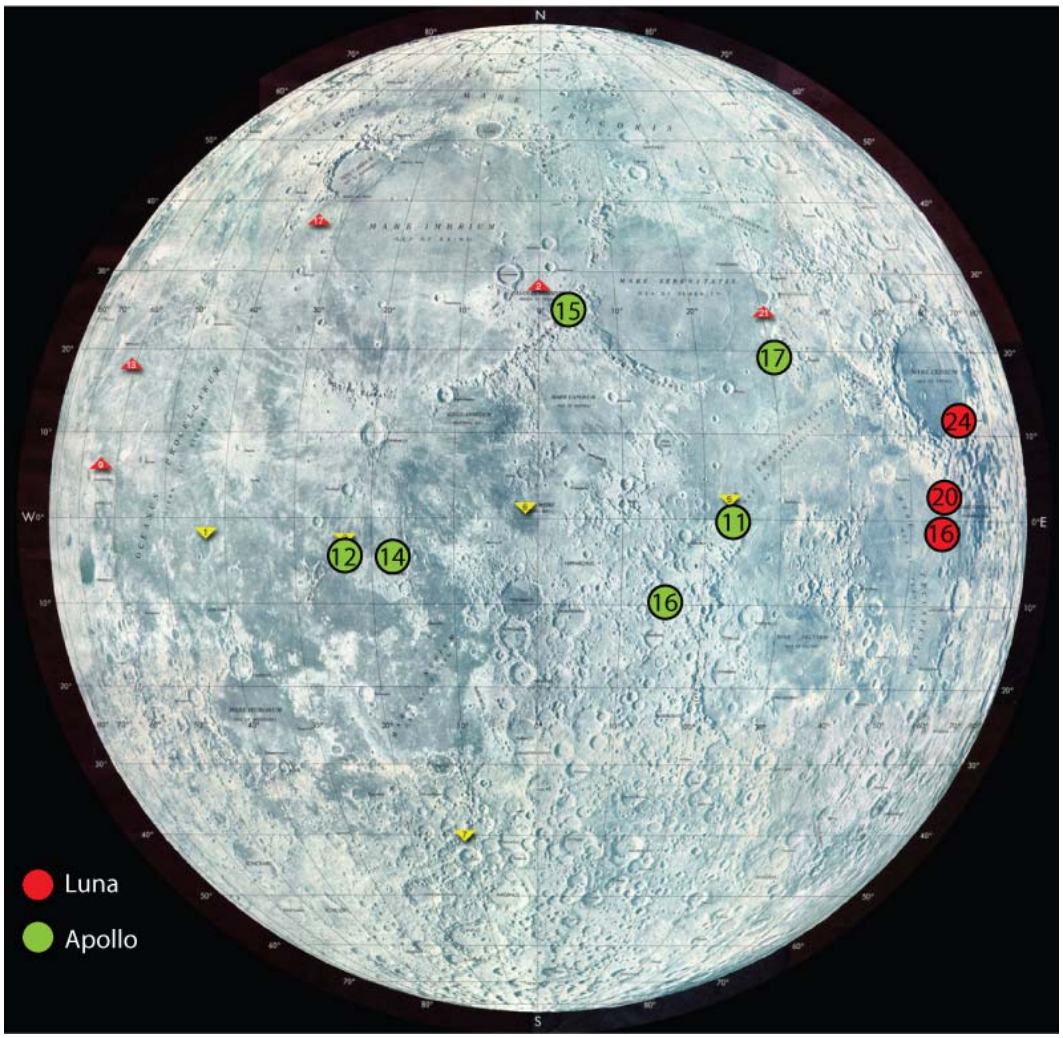

Figure 44. Map showing the spatial distribution of the Apollo and Luna sites from which the candidate soils were collected.

Modified from Williams (2003)

Apollo 11

The Apollo 11 landing site was located within Mare Tranquillitatis about 40-50km from the nearest mare/highland boundary. The samples returned from this mission consisted mostly of soils, basaltic rocks (high-Ti basalts), similar to those on Earth, and impact-produced breccias. Plagioclase-rich anorthosite (rock) fragments were found within the breccias and soils and are thought to have originated from the nearby highlands and mixed into the Apollo 11 regolith by impact-gardening (Wood, 1970). The impact glasses from this site have a wide range of compositions and colours, although most are

brown or pale green (Chao et al., 1970). Chao et al. (1970) found that homogeneous glasses in particular fall into well defined chemical groups. Of the mare-composition glasses, there are three broad groups: Tranquillitatis Basalt A, B and C. Tranquillitatis A glasses form a larger group and represent the variation in soil compositions found at Apollo 11 with the addition of an aluminous component, but lacks impact glasses with the composition of the larger igneous rocks in the region (Reid et al., 1972c). Tranquillitatis B glasses show little spread in composition with very high Fe and Ti and are a distinct red-brown in colour. Similar glasses have been found at the Apollo 12 and 14 sites; however, no crystalline rock equivalents have been found (Reid et al., 1972c). Tranquillitatis C is a small group that is compositionally similar to low-K Fra Mauro basalt (LKFM), a term coined by Reid et al. (1972a) to describe material with basaltic compositions at the Apollo 14 site. The non-mare glasses are dominantly anorthositic gabbro in composition and are likely to have originated from the lunar highlands. The term "highland basalt" and Very-High-Al (VHA) basalts (Taylor et al., 1991) was, and is still, used to describe this component even though the term may be inappropriate as this component does not represent extrusive volcanic rocks (Korotev, 1997; Wilhelms, 1987). Korotev (1997) advocates that both LKFM and "highlands basalt" belong to the broader category of mafic impact-melt breccias (MIMBs) each forming two main compositional groups. Rarer, more anorthositic glasses are also present and are likely to be derived from feldspar grains. The distribution of glass compositions is bimodal, with most impact glasses clustering near the pyroxene (mare) composition (Winchell and Skinner, 1970). Delano et al. (1982) argue that the impact glasses at this site show clear evidence for highlands/mare mixing and an additional volcanic component. They suggest that no other additional component, other than the assortment of regolith at the Apollo 11 site, is necessary to explain the compositional variation in impact glasses, soils, and breccias.

Apollo 12

The Apollo 12 landing site was located within Oceanus Procellarum, a flat mare site that is part of the Fra Mauro formation and close to exposures of non-mare material. Although the landing site is dominated by ejecta from several >100m craters, the

surface regolith is quite thin, ranging from 1-2m in the vicinity of Surveyor Crater to 10m at the rim (Rhodes et al., 1977). Apollo 12 impact glasses have variable compositions suggesting that the regolith has "a considerable range in mare/highlands proportions" (Delano et al., 1982). Like the Apollo 11 site, there is a group of glasses with an anorthositic composition and, on the other extreme, a group of glasses with basaltic composition (Glass, 1971). In general, the impact glasses from this site reflect that of the local materials and are lower in TiO_2 than the Apollo 11 glasses (Chao et al., 1970). The anorthositic glasses are typically yellow-green in colour, whereas basaltic glasses are dark brown, red, or green (Glass, 1971). Glass (1971) also notes that the impact glasses with basaltic compositions have a similar compositional range and average composition of basaltic fragments of Apollo 12 breccia 12013. Based on mixing curves, Delano (1982) suggests that all Apollo 12 glasses can be produced by mixing any Apollo 12 soil (12008 in particular) with Apollo 14 soil (14240) as a highlands end-member. Much of the non-mare material at the site is the same as that which predominates at the Fra Mauro site (Reid et al., 1972c). Results from Glass (1971) indicate that high alkali glasses make up about 20% of the population of glasses studied and have a KREEPy signature. Some anorthositic gabbro is present (16% of population studied) though more anorthositic composition glasses are rare (Reid et al., 1972c).

Apollo 14

The Apollo 14 landing site was located on hilly terrain north of the Fra Mauro crater and was the first attempt to sample what was thought to be lunar "highlands". Post-Apollo, however, it became apparent that most samples that were collected at the Apollo 14 site were somehow related to the Imbrium basin. One interpretation is that materials from the Fra Mauro formation is part of the primary Imbrium ejecta blanket (Wilhelms, 1987). The impact glasses at this site are basaltic in composition, but differ from mare basalts as they relatively depleted in Fe and Ti and enriched in Al, K and Ba (i.e. KREEPy in nature; Apollo Soil, 1971). The terms Low-K Fra Mauro (LKFM) and High-K Fra Mauro (HKFM) were adopted in Reid et al. (1972b) to describe materials with basaltic compositions characteristically similar to Apollo 14 samples. The

designations low-K and high-K were used to indicate the presence of KREEP, which were associated with high-K samples. The large majority of impact spherules at the Apollo 14 site have HKFM compositions. A minority have compositions that reflect that of the anorthositic gabbros (i.e. "highlands basalt") and LKFM compositions (Zellner et al., 2002). Other compositional groups are generally rare (Wentworth and McKay, 1991). The impact glasses with an anorthositic gabbro composition are typically colourless to pale green (Chao et al., 1972). The remaining impact glasses are typically yellowish-green to green in colour (Chao et al., 1972). Based on the surface composition determined using the Clementine gamma-ray spectrometer, Zellner et al., (2002) was able to identify potential source locations for the "highlands basalt" by comparing maps of Fe and Ti abundance extracted from the Clementine ultraviolet-visible images (Lucey et al., 2000) and impact glass chemistry. Zellner et al. (2002) concluded that the impact glasses could be ballistically transported or excavated locally from underlying units below the Fra Mauro Formation by impact events, but are unable to distinguish the origin.

Apollo 15

The Apollo 15 landing site was located near the boundary between the highlands and massifs and the mare on the rim of the Imbrium basin. According to Best and Minkin (1972), the impact glasses at this site are highly variable in colour and composition (HKFM, LKFM, highlands basalt and various mare compositions were recognised). About 35% of these glasses were derived from mare materials while the remaining 65% were likely to be of highlands affinity (Best and Minkin, 1972). Apollo 15 yellow glasses studied in Delano et al. (1982) show restricted compositional ranges (~5wt.% TiO_2, 20wt.% FeO, 1700ppm K and 5ppm Th) and are not derived from local materials, but may have developed on the eastward lobe of Eratosthenian lavas and been transported into the site by the Aristillus event. However, based on the ages of the Apollo 15 yellow glasses (~3.35Ga), Spangler and Delano (1984) noted that the this hypothesis is not feasible. Other studies of Apollo 15 impact glasses are lacking in the literature.

Apollo 16

The Apollo 16 landing site was located on the central lunar highlands away from the dominantly mare locations of previous missions. The Apollo 16 site is probably the most comprehensively studied site when it comes to impact glasses and spherules. There are a variety of compositional groups ranging from highly anorthositic glass through to exotically-derived mare basalt glasses. The most prominent group have anorthositic gabbros compositions (MIMBs) and are clear, brown, gray or pale green in colour (Naney et al., 1976). About 78% of the population studied in Delano (1992) are "locally-derived" (i.e. CaO/Al_2O_3 <0.75: Zeigler et al. (2006)) while the remaining 22% are "mare-derived" (i.e. CaO/Al_2O_3 >0.75). Given this criteria it would have been better to refer to these as felsic and mafic groups. A similar study of impact glass by Korotev et al. (2010) found that 65% of the impact glass had compositions that were consistent with the local regolith. However, Korotev et al. (2010) also noted that as much as 75% of the impact glass in the 64-210μm size range are exotic to Apollo 16 based on Mg#. Delano et al. (2007) also made an interesting discovery by finding that 90% of intact glasses were "locally-derived", but only 60% of the shattered glass fragments were "locally-derived". They suggested that exotic spherules may tend to be damaged or shattered on contact from their high-velocity impact. In summary, it appears that spherules with exotic compositions tend to be biased toward small sizes and damaged spherules/shards.

Apollo 16 mafic glasses tends to be orange, yellow and green in colour (Naney et al., 1976), and can be divided into three subgroups: basaltic, incompatible trace element (ITE i.e. KREEPy) rich and mare-highlands mixed. The high-Ti basaltic impact glasses have broadly similar compositions to high-Ti basalts at the Apollo 11 and 17 sites while low-Ti basalts are similar to pigeonite basalts at the Apollo 12 site (Delano et al., 1982; Zeigler et al., 2006). Basaltic glasses and KREEPy glasses make up a large portion of the mafic glasses. The KREEPy glasses are most similar to the Fra Mauro Formation of the Apollo 14 site and basaltic-andesite glasses of Zeigler (Delano et al., 2007; Zeigler et al., 2004). Zeigler et al. (2006) notes that >95% of these basaltic and KREEPy glasses are impact glasses with ~5% being pyroclastic in origin. The remaining glasses are

made up of mare-highlands mixed impact glasses and are typically high-Al basaltic glasses, probably formed from impact mixing of a basalt and feldspathic highlands material. The Naney et al. (1976) study of impact glasses from core sections showed that highlands-derived groups have compositions most similar to the <1mm fine soil fraction which tends to be most abundant at depth. These glasses were typically clear/colourless, but also pale green. Green-coloured glasses were more abundant near the surface of the core, but typically representative of a volcanic origin. A smaller portion of green-coloured spherules have compositions similar to HASP glasses. According to Korotev et al. (2010), these HASP glasses make up about 3% of the particles in their study.

Apollo 17

The Apollo 17 landing site was situated in the Taurus-Littrow Valley on the highland/mare boundary near the south-eastern rim of the Serenitatis basin. The valley floor underlying the landing site consists of high-Ti mare basalts formed at ~3700 Ma (Heiken et al., 1974). Remote and Earth-based observations note that further to the west of the landing site are low-Ti mare basalts (i.e. Jolliff et al., 2000). The massifs surrounding the site are consistent with a mixture of noritic impact melt, feldspathic granulitic material, and variable amounts of high-Ti mare basalt along flanks at the lower elevations based on corrected Clementine data (Robinson and Jolliff, 2002). The local regolith thus reflects mechanical mixtures (i.e. from impact mixing) of these components. Glasses are typically bright orange in colour or opaque. Most glasses with mare compositions are remarkably homogeneous both within each glass and as a group suggesting that they may have been volcanically-derived (Warner et al., 1979). Some glasses with mare compositions have been identified and studied in Zellner et al. (2009a). Impact glasses, on the other hand, are more compositionally variable and reflect the range of local soil compositions (Adena et al., 2009; Warner et al., 1979). Other, rarer impact glasses with compositions that suggest formation and subsequent transport from the anorthositic highlands, PKT, and low-Ti mare terrains have also been found (Adena et al., 2009; Delano et al., 1991; Warner et al., 1979; Zellner et al., 2009a).

3.3.7 Regolith Gardening on the Moon – Effects on Lunar Impact Spherule Record

The lunar regolith can be considered an end-product that has been heavily influenced by the lunar impact history and other geological interactions. Materials that make up the lunar regolith include mineral fragments, rock and breccia fragments, glasses and agglutinates. The lunar regolith is reworked as a result of space weathering due to a combination of macro and micro meteorite impacts, solar wind and cosmic ray interactions. Impacts in the regolith cause large particles to break-up into smaller fragments (comminution). Fragments can also be bound together from melt generated in an impact (agglutination). Finally, impacts overturn the regolith.

The lunar impact spherule record can be altered by the effects of lunar 'gardening'. Impact spherules can be buried, re-exposed and destroyed through lunar evolution which will skew the record of bombardment. Quantification of these effects is difficult as the bombardment flux will directly affect the intensity and depth of regolith 'gardening'. Gault et al. (1974) modelled turnover of the regolith and concluded that the upper millimetres of the regolith are often turned over producing a mixed layer. Deeper layers are turned over at sparser intervals; for example it requires 10^7 years to assure that regolith at the 1cm depth is turned over once (Gault et al., 1974). This study indicates that the depth at which impact spherules are collected can be a potential bias in their record of lunar bombardment. Given this behaviour it might be expected that spherules on the near-surface are more biased toward young impacts while deeper spherules are biased towards older impacts. In addition to the problem of burial and exposure, subsequent destruction of older materials by younger impacts (i.e. the "stonewall" effect: Hartmann, 1975; Hartmann, 2003) may also act to bias the record towards younger spherules. Chapman et al. (2007), however, note that it is unclear what biases may be acting on samples which have escaped destruction as a result of regolith gardening as these are the ones that have been collected and studied.

3.4 Summary

- Lunar bombardment history can be reconstructed using some of the products that are formed during impact events. Each record created from these impact products has a unique interpretation of impact history and has lead to some controversial hypotheses, such as the LHB.
- Of these impact products, lunar impact spherules have been used to create one of the newest bombardment records.
- Impact spherules are abundant in the regolith making them ideal for reconstructing impact history and as remote samplers because they record both time of formation and composition of the target regolith.
- Two previous studies have produced impact spherule age distributions at Apollo 12 (Levine et al., 2005) and Apollo 14 (Culler et al., 2000). An impact spherule age distribution for Apollo 17 spherules is also emerging (Zellner et al., 2009a). There are many similar features in these distributions such as a lack of >4.0Ga ages and a spike in <400Ma ages. However, there are also some distinct differences that will be discussed in later chapters. It is unclear what factors or biases are contributing to the record.
- Prior to this study, there have not been any studies that have integrated both major and trace element chemistry with radioisotopic dates on single impact spherules

3.5 Chapter References

ADENA K., CHRISTY A. and NORMAN M. (2009) Geochemistry of volcanic and impact glasses from the Taurus-Littrow Region on the Moon. In *9th Australian Space Science Conference* (eds. W. Short and I. Cairns). National Space Society of Australia Ltd, Sydney, Australia.

AHRENS T. J. and OKEEFE J. D. (1977) Equations of state and impact-induced shock-wave attenuation on the moon. In *Impact and explosion cratering: Planetary and terrestrial implications - Proceedings of the Symposium on Planetary Cratering Mechanics* (eds. D. J. Roddy, R. O. Pepin and R. B. Merrill), pp. 639-656. Pergamon Press, Inc.

ANDRE C. G. and EL-BAZ F. (1981) Regional Chemical Setting of the Apollo 16 Landing Site and the Importance of the Kant Plateau (abstract). In *12th Lunar and Planetary Science Conference*, pp. 22-24.

APOLLO FIELD GEOLOGY INVESTIGATION T. (1973) Apollo 16 Exploration of Descartes: A Geologic Summary. *Science* **179**(4068), 62-69.

APOLLO SOIL S. (1971) Apollo 14: Nature and origin of rock types in soil from the Fra Mauro formation. *Earth and Planetary Science Letters* **12**(1), 49-54.

BASTIN J. A. (1979) The origin of the shapes of lunar globules. *Moon and the Planets* **21**, 283-288.

- (1980) Rotating lunar globules. *Nature* **283**(5742), 108-108.

BASTIN J. A. and FRENCH W. J. (1970) The formation of lunar globules. *Proceedings of the Geological Society, London* **1664**, 238-246.

BEST J. B. and MINKIN J. A. (1972) Apollo 15 glasses of impact origin. *The Apollo 15 lunar samples*, 34 - 39.

BOGARD D. (1995) Impact ages of meteorites: A synthesis. *Meteoritics* **30**, 244-268.

CHAO E. C. T., BEST J. B. and MINKIN J. A. (1972) Apollo 14 glasses of impact origin and their parent rock types. In *The 3rd Lunar Science Conference*, pp. 907-925.

CHAO E. C. T., BOREMAN J. A., MINKIN J. A., JAMES O. B. and DESBOROUGH G. A. (1970) Lunar Glasses of Impact Origin: Physical and Chemical Characteristics

and Geologic Implications. *Journal of Geophysical Research* **75**(35), 7445-7479.

CHAPMAN C. R., COHEN B. A. and GRINSPOON D. H. (2007) What are the real constraints on the existence and magnitude of the late heavy bombardment? *Icarus* **189**(1), 233-245.

CHERNYAK Y. and NUSSINOV M. (1975) Some problems of dynamics of lunar regolith glass particle formation. *Earth, Moon, and Planets* **13**(4), 363-376.

CHERNYAK Y. B. and NUSSINOV M. D. (1976) On the mechanisms of lunar regolith glass particle formation. *Nature* **261**(5562), 664-666.

COHEN B. A. (2002) Geochemical and Geochronological Constraints on Early Lunar Bombardment History (Abstract No. 1984). In *33rd Annual Lunar and Planetary Science Conference*, Houston, Texas.

COHEN B. A., SWINDLE T. D. and KRING D. A. (2000) Support for the Lunar Cataclysm Hypothesis from Lunar Meteorite Impact Melt Ages. *Science* **290**(5497), 1754-1756.

COHEN B. A., SWINDLE T. D. and KRING D. A. (2005) Geochemistry and 40Ar-39Ar geochronology of impact-melt clasts in feldspathic lunar meteorites: Implications for lunar bombardment history. *Meteoritics & Planetary Science* **40**, 775.

COHEN B. A., SWINDLE T. D., TAYLOR L. A. and NAZAROV M. A. (2002) ^{40}Ar-^{39}Ar Ages from Impact Melt Clasts in Lunar Meteorites Dhofar 025 and Dhofar 026 (abstract. 1252). In *33rd Annual Lunar and Planetary Science Conference*, Houston, Texas.

CULLER T. S., BECKER T. A., MULLER R. A. and RENNE P. R. (2000) Lunar Impact History from ^{40}Ar/^{39}Ar Dating of Glass Spherules. *Science* **287**(5459), 1785-1788.

DALRYMPLE G. B. and RYDER G. (1993) ^{40}Ar/^{39}Ar Age Spectra of Apollo 15 Impact Melt Rocks by Laser Step-Heating and Their Bearing on the History of Lunar Basin Formation. *J. Geophys. Res.* **98**(E7), 13085-13095.

- (1996) Argon-40/argon-39 age spectra of Apollo 17 highlands breccia samples by laser step heating and the age of the Serenitatis basin. *J. Geophys. Res.* **101**(E11), 26069-26084.

DELANO J. (1986) Pristine Lunar Glasses: Criteria, Data and Implications. *Proceedings of the 16th Lunar and Planetary Science Conference, Part 2* **91**(B4), D201-D213.

DELANO J. W. (1975) Petrology of the Apollo 16 mare component - Mare Nectaris. In *6th Lunar Science Conference*, pp. 15-47. Pergamon Press, Inc, Houston, Texas.

- (1991) Geochemical comparison of impact glasses from lunar meteorites ALHA81005 and MAC88105 and Apollo 16 regolith 64001. *Geochimica et Cosmochimica Acta* **55**(11), 3019-3029.

- (1992) Major-Element Compositions of Glasses in Apollo 16 Cores 60014 (Station 10) and 64001 (Station 4) (abstract). In *23rd Lunar and Planetary Science Conference*, pp. 303.

- (1993) Compositional heterogeneity within a dumbbell-shaped Apollo 15 green glass: Evidence for simultaneous eruption of different magmas. In *24th Lunar and Planetary Science Conference*, pp. 393-394, Houston, Texas.

DELANO J. W., LINDSLEY D. H. and RUDOWSKI R. (1982) Glasses of impact origin from Apollo 11, 12, 15, and 16 - Evidence for fractional vaporization and mare/highland mixing. In *Lunar and Planetary Science Conference XII*, pp. 339-370. Pergamon Press, Huston.

DELANO J. W., LIU Y.-G. and SCHMITT R. A. (1991) Geochemistry of Apollo 17 Impact Glasses: Regolith Compositions (abstract). *22nd Lunar and Planetary Science Conference*, 309-310.

DELANO J. W., ZELLNER N. E. B., BARRA F., OLSON E., SWINDLE T. D., TIBBETTS N. J. and WHITTET D. C. B. (2007) An integrated approach to understanding Apollo 16 impact glasses: Chemistry, isotopes, and shape. *Meteoritics & Planetary Science* **42**, 993-1004.

DROZD R. J., HOHENBERG C. M., MORGAN C. J. and RALSTON C. E. (1974) Cosmic-ray exposure history at the Apollo 16 and other lunar sites: lunar surface dynamics. *Geochimica et Cosmochimica Acta* **38**(10), 1625-1642.

EUGSTER O. (1999) Chronology of dimict breccias and the age of South Ray crater at the Apollo 16 site. *Meteoritics & Planetary Science* **34**(3), 385-391.

FERNANDES V. A., BURGESS R. and TURNER G. (2000) Laser argon-40-argon-39 age studies of Dar al Gani 262 lunar meteorite. *Meteoritics & Planetary Science* **35**(6), 1355-1364.

FULCHIGNONI M., FUNICIELLO R., TADDEUCCI A. and TRIGILA R. (1971) Glassy spheroids in lunar fines from Apollo 12 samples 12070,37; 12001,73; and 12057,60. In *Lunar Science Conference*, pp. 937-948. The MIT Press.

GAULT D. E., HOERZ F., BROWNLEE D. E. and HARTUNG J. B. (1974) Mixing of the lunar regolith. In *5th Lunar Science Conference*, pp. 2365-2386. Pergamon Press, Inc., Houston, Texas.

GLASS B. P. (1971) Investigation of Glass Recovered from Apollo 12 Sample 12057. *Journal of Geophysical Research* **76**(23), 5649-5657.

- (1976) Major element composition of glasses from Apollo 11, 16, and 17 soil samples. In *7th Lunar Science Conference*, pp. 679-693. Pergamon Press, Inc., Houston, Texas.

HARTMANN W. K. (1965) Secular changes in meteoritic flux through the history of the solar system. *Icarus* **4**(2), 207-213.

- (1966) Early lunar cratering. *Icarus* **5**(1-6), 406-418.

- (1975) Lunar "cataclysm": A misconception? *Icarus* **24**(2), 181-187.

- (2003) Megaregolith evolution and cratering cataclysm models: Lunar cataclysm as a misconception (28 years later). *Meteoritics & Planetary Science* **38**(4), 579-593.

HARTMANN W. K., QUANTIN C. and MANGOLD N. (2007) Possible long-term decline in impact rates: 2. Lunar impact-melt data regarding impact history. *Icarus* **186**(1), 11-23.

HASKIN L. A., KOROTEV R. L., ROCKOW K. M. and JOLLIFF B. L. (1998) The case for an Imbrium origin of the Apollo thorium-rich impact-melt breccias. *Meteoritics & Planetary Science* **33**(5), 959-975.

HASKIN L. A., KOROTEV R. L., GILLIS J. J. and JOLLIFF B. L. (2002) Stratigraphies of Apollo and Luna Highland Landing Sites and Provenances of Materials from the

Perspective of Basin Impact Ejecta Modeling (abstract). In *33rd Annual Lunar and Planetary Science Conference*, Houston, Texas.

HEAD J. W. (1974) Stratigraphy of the descartes region (Apollo 16): implications for the origin of samples. *Earth, Moon, and Planets* **11**(1), 77-99.

HEIKEN G. H., MCKAY D. S. and BROWN R. W. (1974) Lunar deposits of possible pyroclastic origin. *Geochimica et Cosmochimica Acta* **38**(11), 1703-1704.

HODGES C. A., MUEHLBERGER W. R. and ULRICH G. E. (1973) Geologic setting of Apollo 16. In *4th Lunar Science Conference*, pp. 1-25.

JAMES O. B. (1981) Petrologic and age relations of the Apollo 16 rocks - Implications for subsurface geology and the age of the Nectaris basin. In *12th Lunar and Planetary Science Conference*, pp. 209-233. Pergamon Press, Houston, Texas.

JOLLIFF B. L., GILLIS J. J., HASKIN L. A., KOROTEV R. L. and WIECZOREK M. A. (2000) Major lunar crustal terranes: Surface expressions and crust-mantle origins. *J. Geophys. Res.* **105**.

KELLER L. P. and MCKAY D. S. (1991) Analytical Electron Microscopy of Fine-Grained Glass Spheres in Apollo 16 Soil 61181 (abstact). *Abstracts of the Lunar and Planetary Science Conference* **22**, 703.

- (1992) Micrometer-sized glass spheres in Apollo 16 soil 61181 - Implications for impact volatilization and condensation. In *Lunar and Planetary Science Conference*, pp. 137-141. Lunar and Planetary Institute, Houston, Texas.

- (1993) Discovery of Vapor Deposits in the Lunar Regolith. *Science* **261**(5126), 1305-1307.

KEMPA M. J., PAPIKE J. J. and WHITE C. (1980) The Apollo 16 regolith - A petrographically-constrained chemical mixing model. In *11th Lunar and Planetary Science Conference*, pp. 1341-1355. Pergamon Press, Houston, Texas.

KOROTEV R. (1997) Some things we can infer about the Moon from the composition of the Apollo 16 regolith. *Meteorit. Planet. Sci.* **32**, 447-478.

KOROTEV R. L. (1981) Compositional trends in Apollo 16 soils. In *12th Lunar and Planetary Science Conference*, pp. 577-605. Pergamon Press, Houston, Texas.

- (1982) Comparative geochemistry of Apollo 16 surface soils and samples from cores 64002 and 60002 through 60007. In *13th Lunar and Planetary Science Conference*, pp. A269-A278, Houston, Texas.

- (1994) Compositional variation in Apollo 16 impact-melt breccias and inferences for the geology and bombardment history of the Central Highlands of the Moon. *Geochimica et Cosmochimica Acta* **58**(18), 3931-3969.

- (2001) On the Systematics of Lunar Regolith Compositions (abstract). In *32nd Annual Lunar and Planetary Science* Houston, Texas.

KOROTEV R. L., ZEIGLER R. A. and FLOSS C. (2010) On the origin of impact glass in the Apollo 16 regolith. *Geochimica et Cosmochimica Acta* **74**(24), 7362-7388

LAWRENCE D. J., ELPHIC R. C., FELDMAN W. C., PRETTYMAN T. H., GASNAULT O. and MAURICE S. (2003) Small-area thorium features on the lunar surface. *J. Geophys. Res.* **108**(E9), 5102.

LAWRENCE D. J., FELDMAN W. C., ELPHIC R. C., LITTLE R. C., PRETTYMAN T. H., MAURICE S., LUCEY P. G. and BINDER A. B. (2002) Iron abundances on the lunar surface as measured by the Lunar Prospector gamma-ray and neutron spectrometers. *J. Geophys. Res.* **107**(E12), 5130.

LEVINE J., BECKER T. A., MULLER R. A. and RENNE P. R. (2005) $^{40}Ar/^{39}Ar$ dating of Apollo 12 impact spherules *Geophysical Research Letters* **32**(15), L15201.

LINDSTROM M. M. and SALPAS P. A. (1981) Geochemical studies of rocks from North Ray Crater, Apollo 16. In *12th Lunar and Planetary Science Conference*, pp. 305-322. Pergamon Press, Houston Texas.

- (1983) Geochemical studies of feldspathic fragmental breccias and the nature of North Ray Crater ejecta. *J. Geophys. Res.* **88**(S2), A671-A683.

LUCEY P., KOROTEV R. L., GILLIS J. J., TAYLOR L. A., LAWRENCE D., CAMPBELL B. A., ELPHIC R., FELDMAN B., HOOD L. L., HUNTEN D., MENDILLO M., NOBLE S., PAPIKE J. J., REEDY R. C., LAWSON S., PRETTYMAN T., GASNAULT O. and MAURICE S. (2006) New Views of Lunar Geoscience: Understanding the Lunar Surface and Space-Moon Interactions. In *New Views of the Moon* (eds. B. L. Jolliff, M. Wieczorek, C. K. Shearer and C. Neal), pp. 83-219.

LUCEY P. G., BLEWETT D. T. and JOLLIFF B. L. (2000) Lunar iron and titanium abundance algorithms based on final processing of Clementine ultraviolet-visible images. *J. Geophys. Res.* **105**(E8), 20297-20305.

MCKAY D. S., HEIKEN G., BASU A., BLANFORD G., SIMON S., REEDY R., FRENCH B. M. and PAPIKE J. (1991) The Lunar Regolith. In *Lunar Sourcebook: A User's Guide to the Moon* (eds. G. Heiken, D. T. Vaniman and B. M. French), pp. 285-356. Cambridge University Press.

MCKAY G. A., KRIDELBAUGH S. J. and WEILL D. F. (1973) The occurrence and origin of schreibersite-kamacite intergrowths in microbreccia 66055. *Proceedings of the Lunar Science Conference* **4**, 811.

MELOSH H. J. (1982) A schematic model of crater modification by gravity. *Journal of Geophysical Research (Solid Earth)* **87**(B1), 371–380.

- (1989) *Impact Cratering - A Geologic Process*. Oxford University Press.

MEYER C., JR. (1978) Ion microprobe analyses of aluminous lunar glasses: A test of the "rock type" hypothesis. *Proceedings of the 9th Lunar and Planetary Science Conference*, 1551-1570.

MUEHLBERGER W. R., HÖRZ F., SEVIER J. R. and ULRICH G. E. (1980) Mission objectives for geological exploration of the Apollo 16 landing site. In *Conference on the Lunar Highlands Crust* (eds. R. B. Merrill and J. J. Papike), pp. 1-49. Pergamon Press, Houston, Texas.

MUELLER G. and HINSCH G. W. (1970) Glassy Particles in Lunar Fines. *Nature* **228**(5268), 254-258.

NANEY M. T., CROWL D. M. and PAPIKE J. J. (1976) The Apollo 16 drill core - Statistical analysis of glass chemistry and the characterization of a high alumina-silica poor (HASP) glass. In *7th Lunar Science Conference*, pp. 155-184. Pergamon Press, Inc., Houston, Texas.

NASA, JSC and ARIZONA STATE UNIVERSITY (2008) Image of the Week - 12/30/2008: Exploring the Lunar Highlands pp. http://apollo.sese.asu.edu/LIW/20081230.html.

NEUKUM G. (1977) Different ages of lunar light plains. *Earth, Moon, and Planets* **17**(4), 383-393.

- (1983) Meteoritenbombardement and Datierung Planetarer Oberflächen. University of Munich.

NEUKUM G., IVANOV B. A. and HARTMANN W. K. (2001) Cratering Records in the Inner Solar System in Relation to the Lunar Reference System. *Space Science Reviews* **96**(1), 55-86.

NEUKUM G., KÖNIG B. and ARKANI-HAMED J. (1975) A study of lunar impact crater size-distributions. *Earth, Moon, and Planets* **12**(2), 201-229.

NORMAN M. D. (1981) Petrology of suevitic lunar breccia 67016. In *Proceedings of the 12th Lunar and Planetary Science Conference*, pp. 235-252. Pergamon Press, Houston, Texas.

- (2009) The Lunar Cataclysm: Reality or "Mythconception"? *ELEMENTS* **5**(1), 23-28.

NORMAN M. D., DUNCAN R. A. and HUARD J. J. (2006) Identifying impact events within the lunar cataclysm from 40Ar-39Ar ages and compositions of Apollo 16 impact melt rocks. *Geochimica et Cosmochimica Acta* **70**(24), 6032-6049.

- (2010) Imbrium provenance for the Apollo 16 Descartes terrain: Argon ages and geochemistry of lunar breccias 67016 and 67455. *Geochimica et Cosmochimica Acta* **74**(2), 763-783.

OBERBECK V. R. (1975) The Role of Ballistic Erosion and Sedimentation in Lunar Stratigraphy. *Rev. Geophys.* **13**(2), 337-362.

PAPIKE J. J., RYDER G. and SHEARER C. K. (1998) Lunar samples. *Reviews in Mineralogy and Geochemistry* **36**(1), 5.1-5234.

PETRO N. E. and PIETERS C. M. (2006) Modeling the provenance of the Apollo 16 regolith. *Journal of Geophysical Research* **111**, E09005.

PRETTYMAN T. H., HAGERTY J. J., ELPHIC R. C., FELDMAN W. C., LAWRENCE D. J., MCKINNEY G. W. and VANIMAN D. T. (2006) Elemental composition of the lunar surface: Analysis of gamma ray spectroscopy data from Lunar Prospector. *J. Geophys. Res.* **111**.

PUGH M. J. (1972) Rotation of Lunar Dumbbell-shaped Globules during Formation. *Nature* **237**(5351), 158-159.

REID A. M., RIDLEY W. I., HARMON R. S., WARNER J., BRETT R., JAKES P. and BROWN R. W. (1972a) Highly aluminous glasses in lunar soils and the nature of the lunar highlands. *Geochimica et Cosmochimica Acta* **36**(8), 903-912.

REID A. M., WARNER J., RIDLEY W. I. and BROWN R. W. (1972b) Major Element Composition of Glasses in Three Apollo 15 Soils. *Meteoritics and Planetary Science* **7**(3), 395-415.

REID A. M., WARNER J., RIDLEY W. I., JOHNSTON D. A., HARMON R. S., JAKEŠ P. and BROWN R. W. (1972c) The major element compositions of lunar rocks as inferred from glass compositions in the lunar soils. In *Proceedings of the Lunar Science Conference*, pp. 363-378.

RHODES J. M., BRANNON J. C., RODGERS K. V., BLANCHARD D. P. and DUNGAN M. A. (1977) Chemistry of Apollo 12 mare basalts - Magma types and fractionation processes. In *8th Lunar Science Conference*, pp. 1305-1338. Pergamon Press, Inc., Houston, Texas.

RIDLEY W. I., REID A. M., WARNER J. L., BROWN R. W., GOOLEY R. and DONALDSON C. (1973) Glass compositions in Apollo 16 soils 60501 and 61221. In *4th Lunar Science Conference*, pp. 309-321.

ROBINSON M. S. and JOLLIFF B. L. (2002) Apollo 17 landing site: Topography, photometric corrections, and heterogeneity of the surrounding highland massifs. *J. Geophys. Res.* **107**(E11), 5110.

RYDER G. (1990) Lunar samples, lunar accretion and the early bombardment of the moon. *EOS Transactions* **71**, 313.

- (2002) Mass flux in the ancient Earth-Moon system and benign implications for the origin of life on Earth. *Journal of Geophysical Research (Planets)* **107**(E4), 13.

SASAKI S., NAKAMURA K., HAMABE Y., KURAHASHI E. and HIROI T. (2001) Production of iron nanoparticles by laser irradiation in a simulation of lunar-like space weathering. *Nature* **410**(6828), 555-557.

SCARLETT B., BUXTON R. E. and FAULKNER R. G. (1977) Formation of Glass Spheres on the Lunar Surface. *Philosophical Transactions of the Royal Society of London. Series A, Mathematical and Physical Sciences* **285**(1327), 279-284.

SEE T. H., H\RZ F. and MORRIS R. V. (1986) Apollo 16 Impact-Melt Splashes: Petrography and Major-Element Composition. *J. Geophys. Res.* **91**.

SPANGLER R. R. and DELANO J. W. (1984) History of the Apollo 15 yellow impact glass and sample 15426 and 15427 *Journal of Geophysical Research, Supplement* **89**, B478-B486.

SPUDIS P. D. (1984) Apollo 16 site geology and impact melts - Implications for the geologic history of the lunar highlands. In *15th Lunar and Planetary Science Conference*, pp. C95-C107, Houston, Texas.

STÖFFLER D. and RYDER G. (2001) Stratigraphy and Isotope Ages of Lunar Geologic Units: Chronological Standard for the Inner Solar System. *Space Science Reviews* **96**(1), 9-54.

STÖFFLER D., RYDER G., IVANOV B. A., ARTEMIEVA N., CINTALA M. and GRIEVE R. (2006) Cratering History and Lunar Chronology. In *New Views of the Moon* (eds. B. L. Jolliff, M. A. Wieczorek, C. K. Shearer and C. R. Neal), pp. 519-596.

STROM R. G., CROFT S. K. and BARLOW N. G. (1992) The Martian impact cratering record. In *Mars*, pp. 383-423.

STROM R. G. and NEUKUM G. (1988) The cratering record on Mercury and the origin of impacting objects. In *Mercury*, pp. 336-373.

SWINDLE T. D., ISACHSEN C. E., WEIRICH J. R. and KRING D. A. (2009) 40Ar-39Ar ages of H-chondrite impact melt breccias. *Meteoritics & Planetary Science* **44**(5), 747-762.

TERA F., PAPANASTASSIOU D. A. and WASSERBURG G. J. (1974) Isotopic evidence for a terminal lunar cataclysm. *Earth and Planetary Science Letters* **22**(1), 1-21.

TURNER G. and CADOGAN P. H. (1975) The history of lunar bombardment inferred from Ar-40-Ar-39 dating of highland rocks. In *6th Lunar Science Conference*, pp. 1509-1538. Pergamon Press, Inc., Houston, Texas.

TURNER G., CADOGAN P. H. and YONGE C. J. (1973) Argon selenochronology. In *Proceedings of the Lunar Science Conference*, pp. 1889-1914.

ULRICH G. E. (1973) A geologic model for North Ray Crater and stratigraphic implications for the Descartes region. In *4th Lunar Science Conference*, pp. 27-39.

ULRICH G. E., HODGES C. A. and MUEHLBERGER W. R. (1981) Geology of the Apollo 16 Area, Central Lunar Highlands. In *Geological Survey Professional Paper 1048*, pp. 539. National Aeronautics and Space Administration.

VANIMAN D., DIETRICH J., TAYLOR G. J. and HEIKEN G. (1991) Exploration, Samples, and Recent Concepts of the Moon. In *Lunar Sourcebook: A User's Guide to the Moon* (eds. G. Heiken, D. T. Vaniman and B. M. French), pp. 4-26. Cambridge University Press.

VANIMAN D. T. (1990) Glass variants and multiple HASP trends in Apollo 14 regolith breccias. In *20th Lunar and Planetary Science Conference*, pp. 209-217, Houston, Texas.

VICKERY A. M. (1993) The Theory of Jetting: Application to the Origin of Tektites. *Icarus* **105**(2), 441-453.

WARNER R. D., TAYLOR G. J. and KEIL K. (1979) Composition of glasses in Apollo 17 samples and their relation to known lunar rock types. *Proceedings of the 10th Lunar and Planetary Science Conference* **2**, 1437-1456.

WARREN P. H. (2008) Lunar rock-rain: Diverse silicate impact-vapor condensates in an Apollo-14 regolith breccia. *Geochimica et Cosmochimica Acta* **72**(14), 3562-3585.

WEBER A. K., HEAD J. W., SAAL A. E., WEINREICH T. and WILSON L. (2010) Volatiles in Lunar Fire Fountaining Eruptions and the Effect of Rotation on Droplets in Free Flight. In *41st Lunar and Planetary Science Conference (abstract No. 1533)*, pp. 1208, Houston, Texas.

WENTWORTH S. J. and MCKAY D. S. (1991) Apollo 14 glasses and the origin of lunar soils. In *21st Lunar and Planetary Science Conference*, pp. 185-192, Houston, Texas.

WILHELMS D. (1987) The Geologic History of the Moon. In *US Geological Survey Professional Paper 1348*, pp. 302.

WILSHIRE H. G., STUART-ALEXANDER D. E. and JACKSON E. D. (1973) Apollo 16 Rocks: Petrology and Classification. *J. Geophys. Res.* **78**(14), 2379-2392.

WINCHELL H. and SKINNER B. J. (1970) Glassy spherules from the lunar regolith returned by Apollo 11 expedition. In *Proceedings of the Apollo 11 Lunar*

Science Conference (ed. A. A. Levinson), pp. 957-964. Pergammon Press, Houston, Texas.

WOOD J. A. (1970) Petrology of the Lunar Soil and Geophysical Implications. *J. Geophys. Res.* **75**(32), 6497-6513.

ZEIGLER R. A., KOROTEV R. L., JOLLIFF B. L., HASKIN L. A. and FLOSS C. (2004) Apollo 16 Mafic Glass: Geochemistry, Provenance, and Implications. In *Lunar and Planetary Science Conference XXXV*, Houston, Texas.

- (2006) The geochemistry and provenance of Apollo 16 mafic glasses. *Geochimica et Cosmochimica Acta* **70**(24), 6050-6067.

ZELLNER N. E. B., DELANO J. W., SWINDLE T. D., BARRA F., OLSEN E. and WHITTET D. C. B. (2009a) Apollo 17 regolith, 71501,262: A record of impact events and mare volcanism in lunar glasses. *Meteoritics & Planetary Science* **44**(6), 839-851.

- (2009b) Evidence from 40Ar/39Ar ages of lunar impact glasses for an increase in the impact rate ~800 Ma ago. *Geochimica et Cosmochimica Acta* **73**(15), 4590-4597.

ZELLNER N. E. B., SPUDIS P. D., DELANO J. W. and WHITTET D. C. B. (2002) Impact glasses from the Apollo 14 landing site and implications for regional geology. *Journal of Geophysical Research* **107**(E11), **12**-1 - **12**-13.

CHAPTER 4:

PETROGRAPHY AND CHEMISTRY

4.1 Introduction

Presented in the chapter are results stemming from the study of lunar impact spherules petrography and chemistry. The impact spherules were collected from Apollo 16 soil (66031) which consisted of a <1mm fine split from Apollo 16 soil (66030) that was collected at station 6, along with a sizeable breccia (66035). A total of 272 impact spherules were studied all of which are >75μm in diameter (see Chapter 2 for discussion on limiting analytical error of curved surfaces). Basic petrographic characteristics were documented including sizes, magnetic susceptibility, shape, and colour prior to any geochemical analyses. After the geochemical analyses, impact spherules suitable for dating were then identified, analysed, and separated. These spherules will be discussed in more detail in the follow chapters 5 and 6.

This chapter begins by establishing a petrographic classification for unpolished and polished impact spherules. Geochemical characteristics of the impact spherule population are then presented and discussed including the accuracy of unpolished versus polished analyses, their relation to the petrographic features in the classification, and how they relate to lunar targets and provenance. The presence of siderophile and volatile crusts were also recognised from the comparison of unpolished versus polished analyses. The nature of these crusts and the effect on impact spherule chemistry were examined as they affect the analysis of unpolished spherules more than the geometry.

The discussion first focuses the controversial topic concerning whether locally-derived impact spherules were produced from impacts into rocks or soils. Diagnostic trace element ratios and statistical methods were used to determine if this issue could be resolved using impact spherules from this study. Following this topic, impact spherule petrography and chemistry were then used to establish relational clusters and groups. Possible constraints on how conditions during formation and subsequent alteration may have affected impact spherule petrography were identified.

4.2 Methods

Separations of Apollo 16 soil (66031,65) were conducted at the Research School of Earth Sciences (RSES), Australian National University, by John Mya and Shane Paxton. A total of 1.02g of material was sieved using disposable nylon meshes into >250µm, 150-250µm, 75-150µm, 25-75µm and <25µm fractions. A number of methods were trialled including use of heavy liquids (3.3g/cm^3) and rolling separation using the Frantz magnetic separator at different stages of the separation methods. The finalised method is as follows: the 150-250µm, 75-150µm, and 25-75µm fractions were further separated using a burette filled with ethanol, affixed perpendicular to the tracks of a Frantz magnetic separator. Using this method, impact spherules could be divided into groups based on the ampere (A) setting of the magnetic separator. A 0.1A split was created followed by 0.5A magnetic and non-magnetic splits. The >250µm and <25µm fractions were not processed in this fashion. Spherular objects were then handpicked from all fractions using a binocular microscope and single-hair brush.

A total of ~700 spherular objects were separated from the lunar soil and manipulated into mounts using a single-hair brush. A lower size limit of 75µm was imposed to limit analytical errors from analysis of curved surfaces to ≤5% based on calculations presented in Chapter 2: Quantitative Corrections for Electron Microprobe Analyses. Additionally, given the low-K content of Apollo 16 impact spherules, spherules <75µm in diameter are probably too small for radioisotopic dating and were not studied further. This limits the number of suitable impact spherules to 272 in the >75µm size fractions, which were mounted unpolished into a Leit-C-Plast (LCP) Mount as per the methods developed Chapter 2. Prior to mounting each spherule, additional petrographic characteristics were documented including shape, colour, special characteristics (e.g. vesicles, damage), and the dimensions of each impact spherule measured using a calibrated Nikon OPTIPHOT-2 binocular microscope. Figure 45 summarises how petrographic characteristics was determined in a flow diagram.

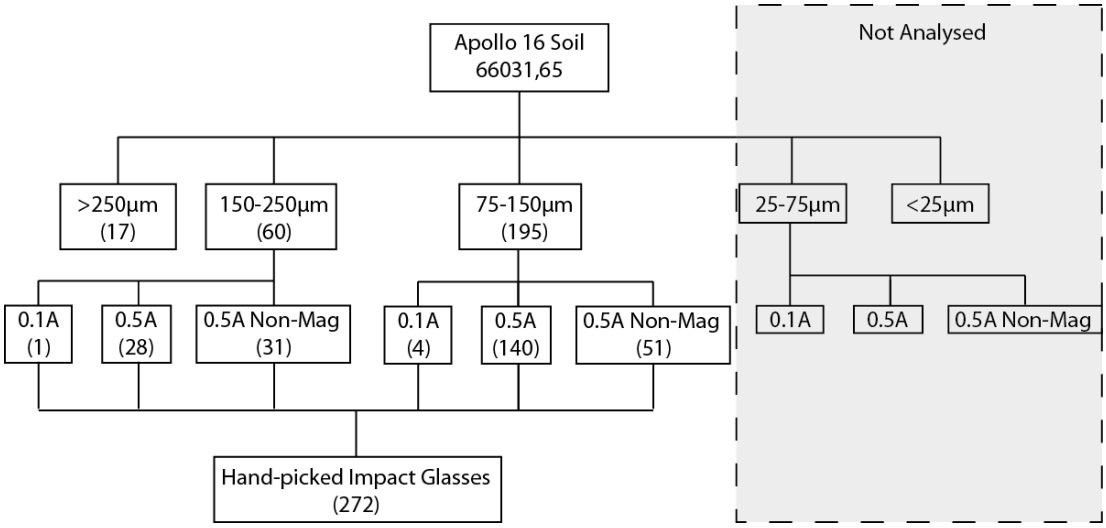

Figure 45. Flow diagram showing the sequence of methods used to document impact spherule petrography

Major element compositions were determined for the 272 spherules prepared in the LCP mounts using the Cameca SX100 Electron Microprobe at RSES. Primary mineral standards were calibrated by Dr. Robert Rapp prior to each session with secondary standards (VG-2, K412, and USGS glass TB-1G) analysed during each session. Beam conditions were set to 15kV and 20nA current with a 20µm defocused beam to minimise alkali element migration. Multiple analyses were conducted on unpolished sample surfaces. Analytical totals outside the range of 89% to 111% were discarded. Acceptable analytical totals were normalised to 100% and, combining at least three separate analyses of a single impact spherule, used to determine the average composition and compositional variability of the surface. Sixty seconds were allocated to each analysis with one spectrometer dedicated to counting the potassium peak. An accurate measurement of potassium was necessary to evaluate the suitability of each impact spherule for $^{40}Ar/^{39}Ar$ dating. Since the impact spherules were typically low in potassium, dedication of one spectrometer to potassium to increases the counting statistics was necessary. At this stage thirty of the most suitable impact spherules for $^{40}Ar/^{39}Ar$ dating were identified using methods that will be presented in the following chapter.

Trace element abundances were acquired from individual impact spherules using a laser ablation-ICPMS system at RSES. The system consists of an Excimer (193nm) laser and a quadrupole Agilent 7500 ICMPS. Prior to use, the equipment was tuned by Dr. Charlotte Allen and Dr. Frances Jenner. The ablations was conducted under a He + H atmosphere and mixed with an Ar carrier gas for transport to the ICP-MS. A description of the instrumentation is provided by Eggins et al. (1998). Data were collected in time-resolved mode consisting of one sweep of the mass range per 0.4 seconds. Data were standardised using NIST612 glass calibrated to BHVO-2G, BIR-1G and BCR-2G USGS glasses (see Norman et al. (2004) for preferred values). Each analysis was normalised to CaO wt.% to correct for variable ablation yield. A few analyses were normalised to SiO_2 wt.% where CaO abundance was found to vary down-profile. Data were reduced using an MS Excel spreadsheet developed by Dr. Charlotte Allen. Several analytical sessions were conducted with slight differences in the analysis time and laser repetition rate, but a fixed spot diameter of 62μm. Twenty-eight impact spherules were analysed at a laser repetition rate of 5Hz for 50 seconds consisting of a 20 second background on the carrier gas prior to each analysis. These were the initial set of impact spherules selected for their $^{40}Ar/^{39}Ar$ dating suitability, assuming that two spherules could be dated per day during a two week analytical session. Later, another two spherules were selected to make up the thirty that were dated. Thirty-nine impact spherules were analysed using the same conditions, but with an extended 120 seconds including a 20 second background. This provided an extended the ablation profile so that trace element variations in the crust could be better resolved. The remaining 95 spherules were analysed at 10Hz for 60 seconds including a 20 second background for bulk compositions. A total of 162 impact spherules were analysed for trace element abundances. The amount of material ablated from each impact spherule was estimated. At this stage, the thirty most suitable impact spherules for radioisotopic dating were retrieved, cleaned, and sent for irradiation.

Following major and trace element analyses, those spherules not selected for radioisotopic dating were recovered from the LCP mount, cleaned, and embedded into epoxy mounts for polishing. Where possible, these spherules were reanalysed for major and trace element composition using the exact same routine specified earlier so that the unpolished and polished analyses could be compared. Only a limited number (83) of glasses could be reanalysed for major element compositions and even fewer (48) for trace element compositions, as material was limited after the initial geochemical analysis. For trace element analyses, however, a smaller spot diameter of 28µm was adopted for 15 samples where sample material was limited. For these smaller samples the repetition rate was increased from 5Hz to 7Hz to offset the reduction in ablated material from the smaller spot diameter. Select samples were imaged using a petrographic microscope and SX100 Electron Microprobe to produce backscatter electron micrographs. A summary of the analytical methods is presented in Figure 46. All data are available in the electronic annexes.

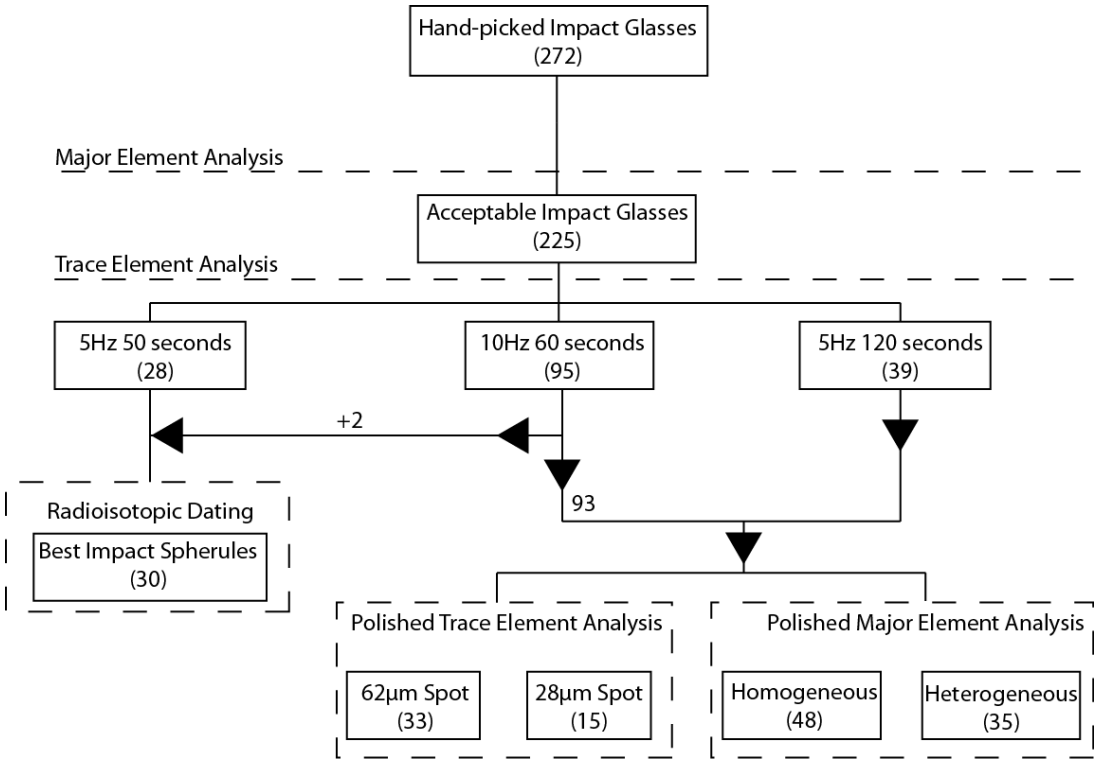

Figure 46. Flow diagram showing the sequence of methods employed for geochemical analyses

4.3 Results

4.3.1 Petrography

The size distribution of the ~700 spherular objects separated from Apollo 16 soil (66031,65) is skewed towards the smaller particles, with 94% of spherules being less than 200μm in size (Figure 47). Over 60% of these particles are smaller than the limit (75μm) that was imposed to reduce analytical errors stemming from curved surfaces. Consequently, these particles were not further studied. This may have introduced a size-dependent selection effect, although there is no data to demonstrate how this may have affected the results of this study. There is little information in the literature about the petrographic and chemical characteristics of <75μm particles, but several authors have noted that these spherule populations have a higher portion of HASP, VRAP, or GASP glasses (Keller and McKay, 1991; Keller and McKay, 1992; Norris et al., 1992; Norris et al., 1993; Warren, 2008). If so, the lower size limit may have worked to the advantage of this project by excluding many refractory and volatile glasses. Of the 272 impact spherules selected for further study, 82 (30%) are non-magnetic.

Figure 48 presents a visual classification system was developed to group spherules with similar shapes and features. Overall, the lunar impact glasses are highly spherical (refer to Figure 48 for the axial dimensions and nomenclature used): 46% of the glasses studied are spherular, 34% are ellipsoidal, 15 % are elongate and 5% are irregularly shaped. The irregularly shaped particles often have “splash”-like shapes with one particular particle showing welding of three separate spherules. More commonly, smaller grains are welded to the spherule surfaces producing impact spherule crusts. Although this is observable in all spherules, some have accumulated a thicker crust than others. “Clean” glasses make up 29% of this collection, “dusted” glasses make up 39% and “crusty” glasses make up 32%. Other features that were noted include signs of damage/breakage (6%), dumbbell shapes (1%), and clearly vesicular or hollow spherules (2%). Colours were also recorded and placed in five broad groups: green, clear, black/opaque, yellow/orange, and hybrid (multiple colours, usually a combination of black and clear).

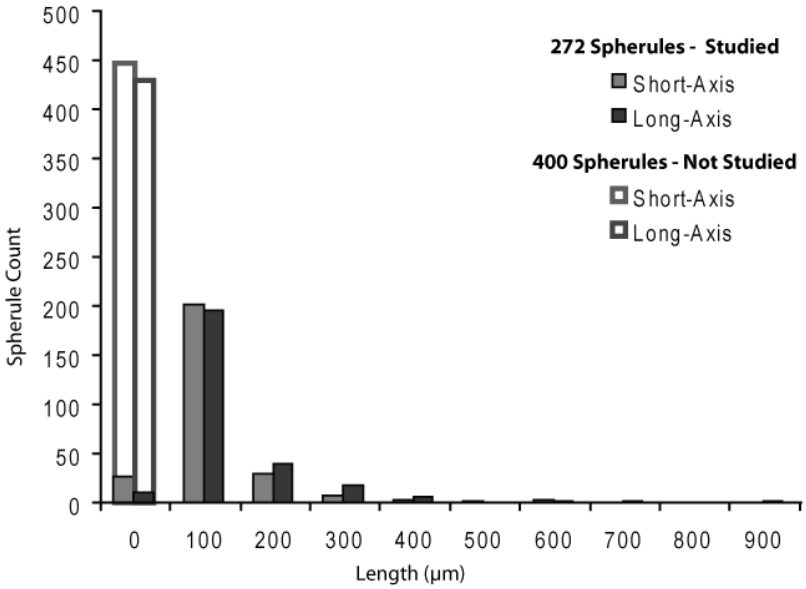

Figure 47. Size distribution of the ~700 spherular objects separated from lunar soil (66031). Measurements are made using a calibrated binocular microscope. The 272 spherules selected for further study (>75µm) are represented by the filled bars. The remaining unused ~420 spherules (<75µm) are represented by the unfilled bars.

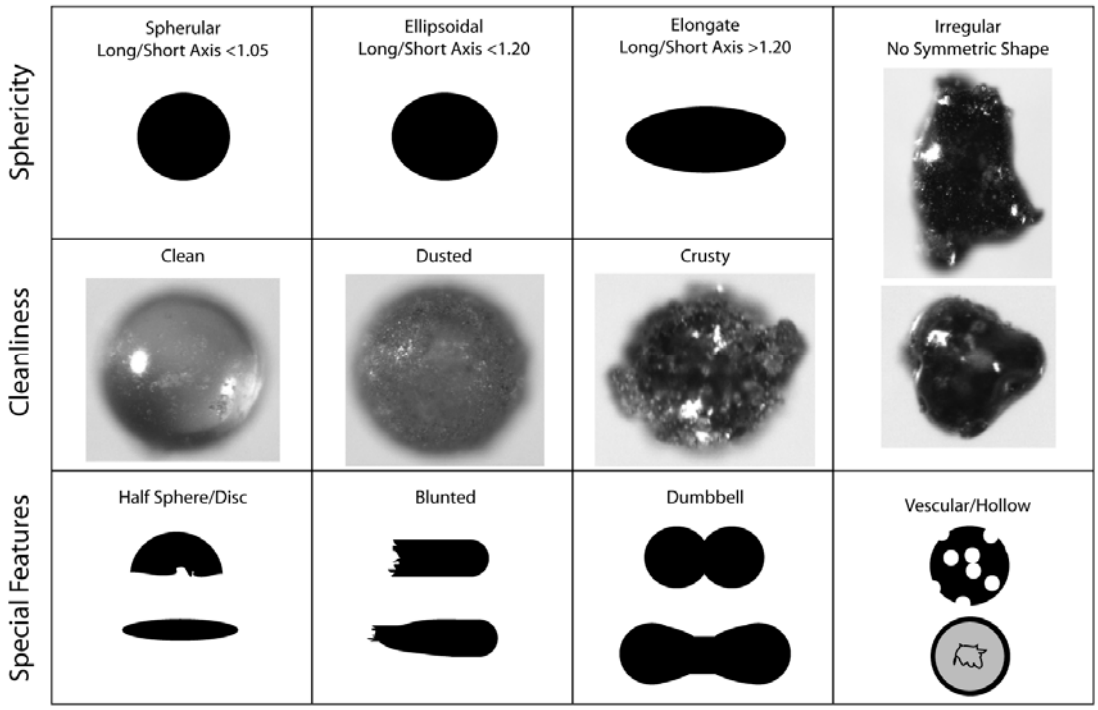

Figure 48. Classification system developed for shapes and features of lunar impact glasses as seen under a binocular microscope.

Figure 49 plots the relationship among the petrographic features and sizes (arranged into 50μm bins). There are a number of important trends to note. First, black/opaque spherules tend to be more magnetic than other colours, appear to become less abundant in the smaller size ranges, and have fewer spherular impact spherules than the other colour groups. Clear, green, and yellow/orange groups tend to be more spherular and non-magnetic. Clear and yellow/orange groups tend to become more abundant in the smaller size bins, 75-100μm in particular. Figure 49 c) and d) indicates that the cleanliness of the impact spherules is not related to the magnetic susceptibility or size, although crusty spherules are rarer in the 75-100μm.

Based on internal structures, after some impact spherules were polished, spherules can be sorted into two broad textural groups: homogenous and heterogeneous impact spherules (Figure 50). The homogenous impact spherules are glassy and have few features observable with petrographic microscopes and electron backscatter imaging (Figure 50a) although cracks, fractures, and occasional flow banding (schlieren) can be seen. The heterogeneous impact spherules can be further subdivided into three groups based on internal features. Figure 50b shows a backscatter electron micrograph of a heterogeneous impact spherule with a partially digested grain. Melts that formed this impact spherule were either not sufficiently hot and/or did not have enough time to digest foreign grains that were encapsulated. Particles showing crystal growth (Figure 50c) have crystals typically set in a matrix of quenched melt so the general sphericity is maintained even though the crystals are elongate in shape. The last type of heterogeneous impact spherule is vesicular and contains few too many undigested grains (Figure 50d), some of which are still angular, suggesting that the melt was not of a sufficiently elevated temperature to digest the grain(s). Impact spherules may contain metal beads scattered throughout the spherule and outer crusts are often visible. The outer crust consists of fine adhering particulates or more rarely a large adhering mineral grain.

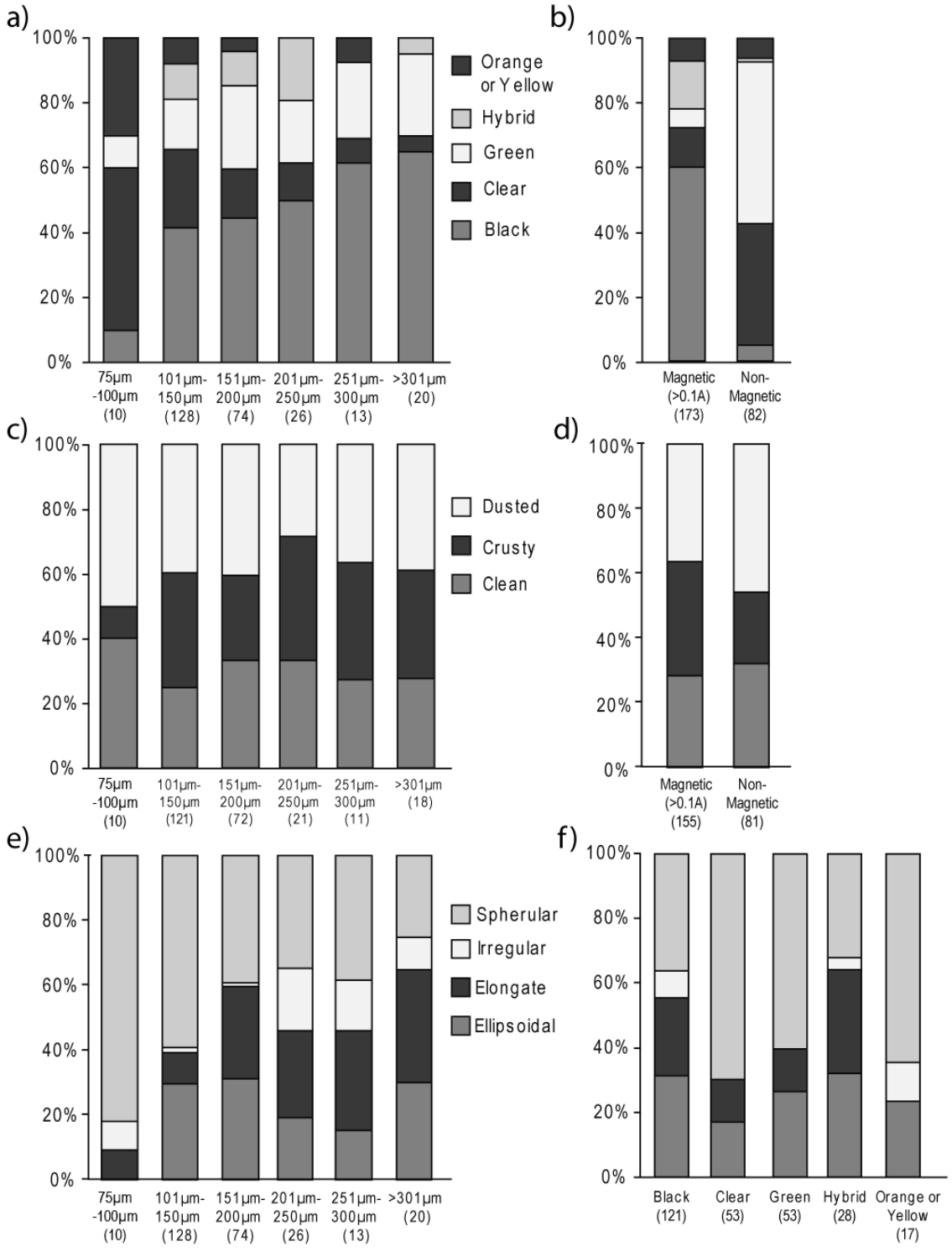

Figure 49. Plots illustrating the relationships among various petrographic features including size, magnetic susceptibility, cleanliness and colour. Bracketed numbers on the x-axis indicate the number of spherules in each bin.

Of the 117 impact spherules polished and imaged using the petrographic microscope, 62 (52%) are homogeneous while 55 (47%) are heterogeneous. Of the heterogeneous spherules, 12 (10%) clearly showed signs of crystallisation. It is unclear how many heterogeneous spherules contain partially digested minerals as they are difficult to identify without the use of backscatter electron micrographs. Figure 51 shows the relationships between spherule colour, shape, and internal textures observed on a polished section of the spherule. Spherules with homogeneous textures tend to have lighter colours (i.e. clear and green) whereas spherules with heterogeneous textures tend to be black in colour. Heterogeneous spherules tend to be less spherical than homogeneous spherules with the exception of crystallised heterogeneous spherules.

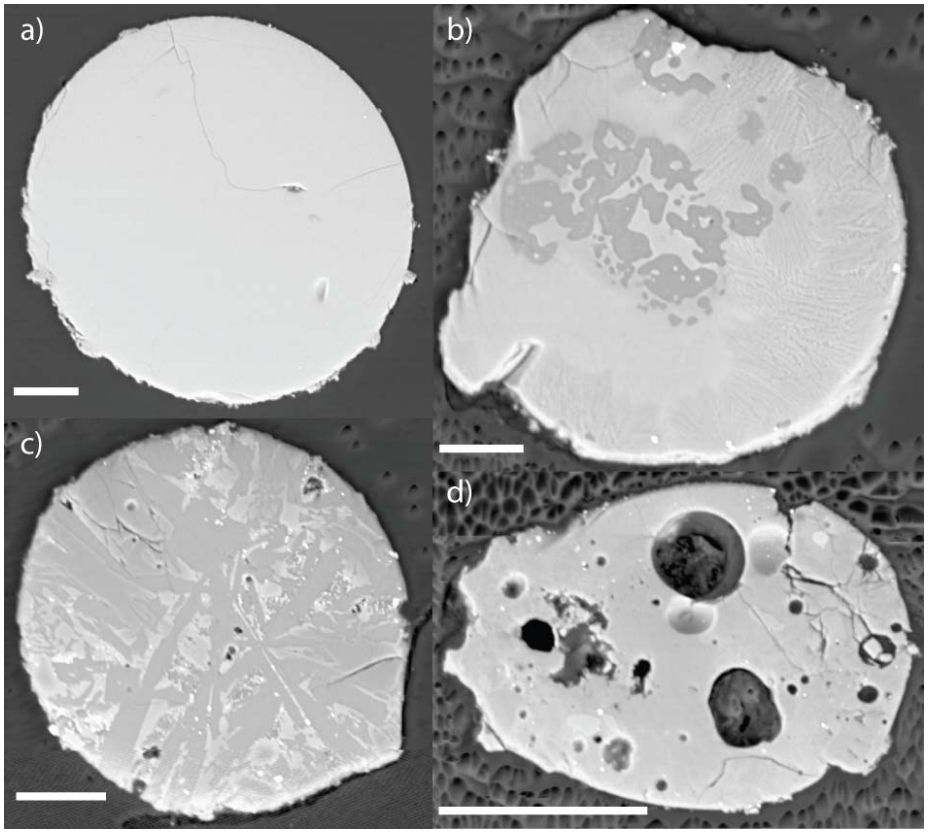

Figure 50. Backscatter electron micrographs of **a)** homogeneous impact spherule with a thin adhering crust **b)** heterogeneous impact spherule with partially digested mineral and crystallisation at the rims **c)** heterogeneous impact spherule containing elongate crystals **d)** vesicular heterogeneous impact spherule containing relic grains. Scale bars are 50μm in length.

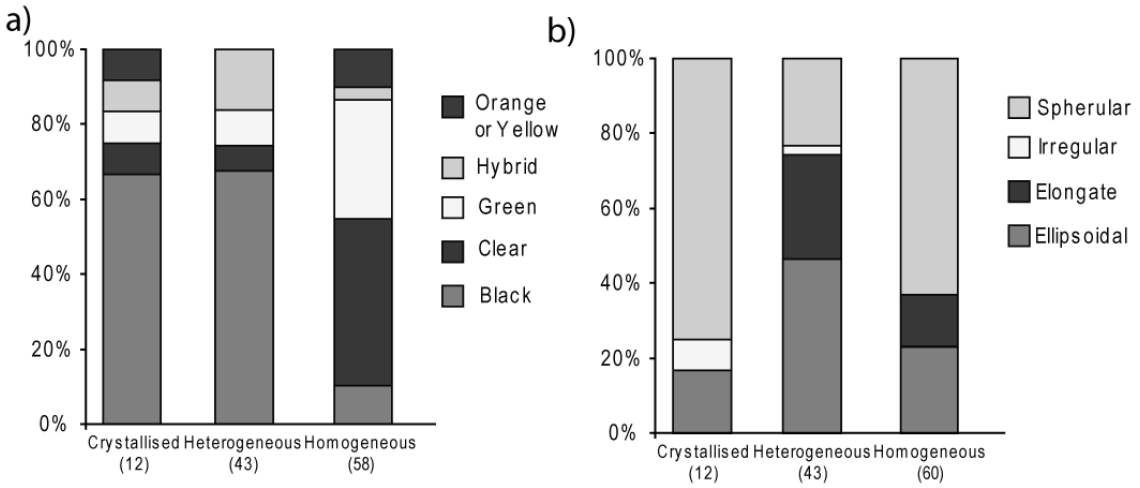

Figure 51. Plots illustrating relationships between the type of internal texture and the spherule colour and shape. Bracketed numbers on the x-axis indicate the number of spherules in each bin.

4.3.2 Analytical Accuracy – Unpolished versus Polished Section Analyses

Major Elements

Prior to discussing the results, it is important that the possible biases and implications of the novel mounting technique used in this study be discussed. In the methods it was noted that lunar impact spherules were analysed as both unpolished and polished sections in order to determine the bias of using unpolished impact spherule data. Theoretical modelling was also conducted to determine the possible quantitative correction biases earlier in Chapter 2. This modelling suggested that the unpolished geometry would underestimate lighter elements such as Na, Mg, Al, and Si compared to heavier elements such as Fe on an ideal convex surface. Given the lower size limit of 75μm, the quantitative correction bias should be less than 5%.

A total of 48 homogeneous impact spherules out of 83 were analysed as both unpolished and polished sections to determine the effect of analysing a curved surface (see Figure 52). Relative to the polished section analyses, Al_2O_3, FeO, and MgO abundances tend to be more compositionally variable on unpolished surfaces, but tend

to still fall within error of the polished section compositions. This suggests that analyses on unpolished sections generally reflect that of the impact spherule interior, but are prone to larger errors. However, the unpolished analyses also show systematic enrichment of SiO_2 and enrichment of Na_2O and K_2O abundances in 41 out of 48 (85%) of the spherules, by more than 10% (relative), compared to the polished section equivalents. A complementary, systematic depletion of CaO and TiO_2 is also observed. This does not relate to undigested minerals since only homogenous glasses were selected for this analysis. The enrichment of Si, Na, and K, and the depletion of Ca in the unpolished analyses contradict the prediction of light element underestimation due to surface curvature modelled in Chapter 2. The enrichment of volatile elements on spherule surface might suggest fractionation of elements based on volatility or subsequent deposition of volatile material. This may explain why impact spherules have relatively more potassic rims and calsic cores as observed by Levine et al. (2006) and in the current study. Additionally, unpolished analyses show larger variations in surface composition, illustrated by the larger vertical error bars in Figure 52. Since major element compositions are normalised to 100%, the effect of adhering grains will be to increase the variability and alter the average composition of the surface (e.g. increased variability and average composition of Fe may result from inclusion of a surface grain of Fe^0 during analysis). In combination, the volatile element enrichment (Na, K, and Si) and adhering grains of regolith appear to have produced a compositionally distinct outer layers. Although there may still be geometric effects, the differences between the unpolished and polished sections seem to be dominated by the presence of an outer crust.

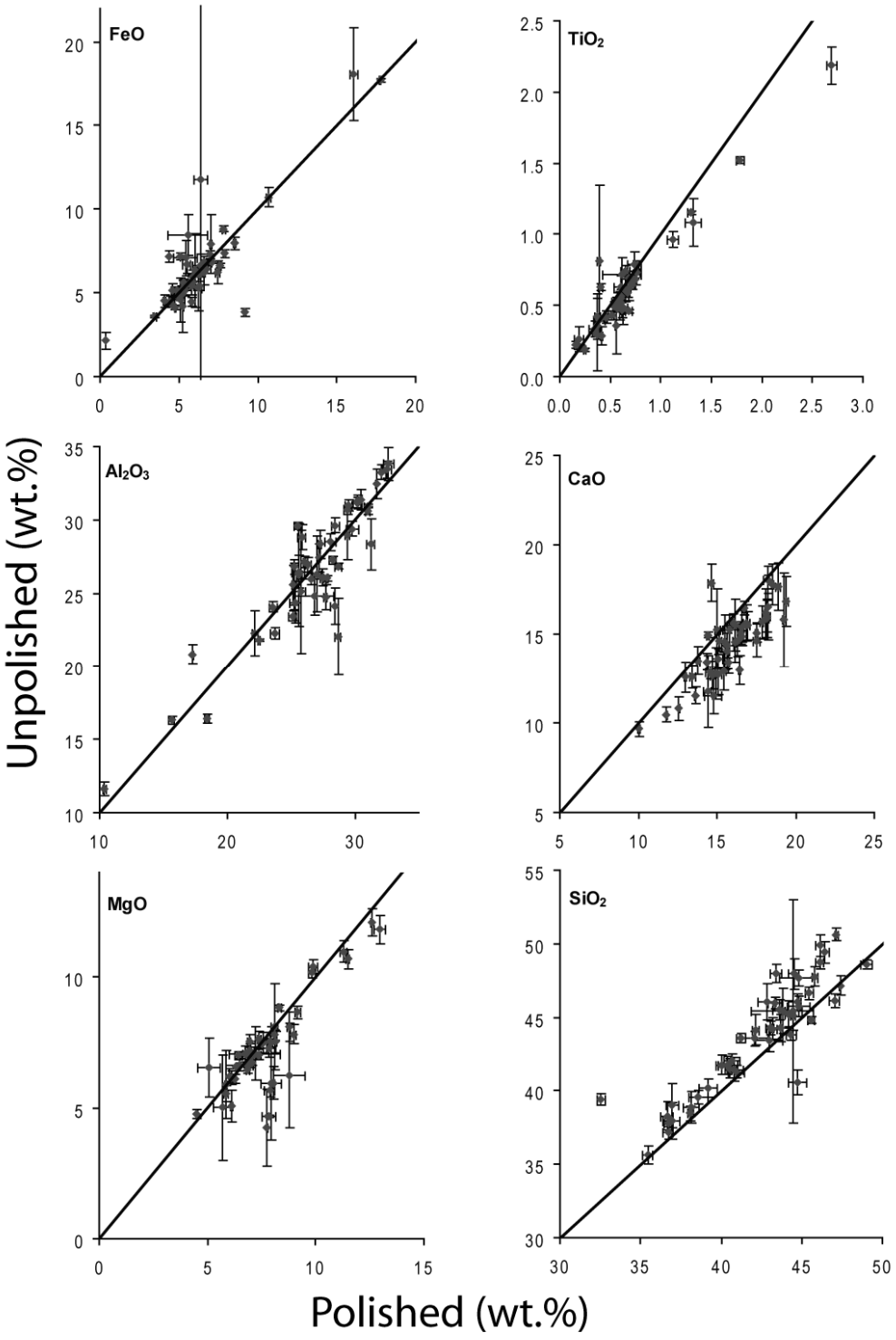

Figure 52. Major element abundances of 48 selected homogenous lunar impact spherules as an unpolished vs. polished sample. Error bars represent the variability in each point (average of at least three good analyses of a single sample) and are at one standard deviation. The 1:1 line is also shown.

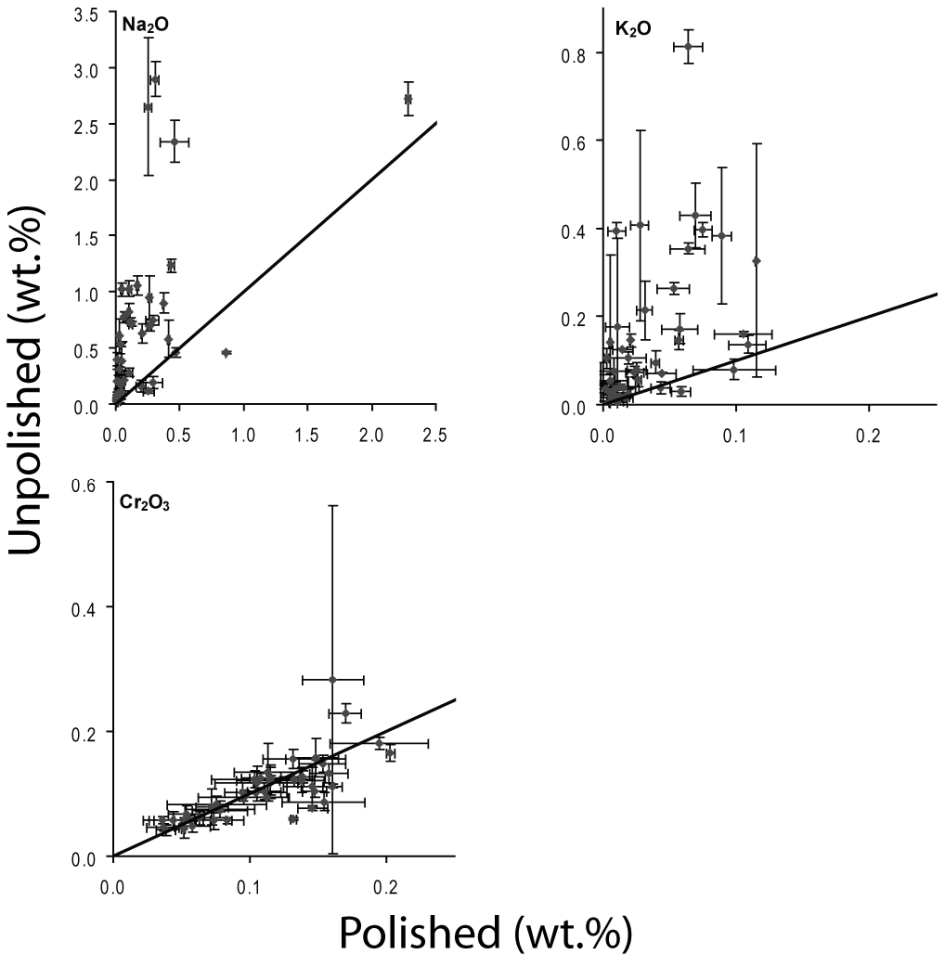

Figure 52. (cont.)

Trace Elements

Analysis of unpolished lunar impact spherules using the LA-ICPMS yield trace element profiles from the rims of the spherules into the cores. Ablation pits from the unpolished analyses are, on average, 62µm in diameter and taper slightly towards the bottom of the pit. Based on the depth to pulse relationship of NIST glass established in Eggins et al. (1998) (Equation 7), the depth of the ablation pits would be ~56µm (~500 pulses) assuming that NIST glass and impact spherules ablate at the same rate.

$$Depth\ (\mu m) = 0.0993 \times x + (2.56 \times 10^{-5} \times x^2) \qquad \textbf{[7]}$$

Where x = Number of pulses during an analysis

Formula from Eggins et al. (1998)

Assuming a perfect cylindrical pit and a spherical sample, one analysis would consume ~2% of a 200μm diameter spherule. The ablation profiles are useful in determining possible core-rim effects as suggested by the major element analyses. Homogenous glasses, such as the NIST and USGS standard glasses used for calibration, are expected to yield relatively flat trace element profiles that decrease in raw counts as ablation yields decrease with ablation pit depth (see Eggins et al., 1998). However, relatively few lunar impact spherules have homogenous profiles. Trace element profiles for impact spherules can generally be divided into three regions: gas background, "crust" and "core" signals (see Figure 53). The "crust" signal occurs in the first few ablations and is typically characterised by a peak in abundances of the siderophile trace elements Ni and Co and occasionally the volatile trace element Rb. The enrichment spike equates to an average thickness of 4.2 ± 3.2μm (1σ), using Equation 7 to convert pulses to thickness. The count rates eventually stabilise to a "core" signal after a few microns (e.g. see Figure 53). The abundances of Rb and Ni in the "crust" signal are on average enriched by almost 2x compared to the "core" concentrations. Figure 54 illustrates the change in Ni/Co ratios as a function of ablation time. In the first 10 seconds of ablation the Ni/Co ratio is typically higher and corresponds with higher Ni concentrations near the spherule surface. Trace element profiles showing this effect have been identified in 50 of 162 impact spherules. The siderophile elements (e.g. Ni; Figure 53) on occasion, show slightly depleted signals after the initial enrichment, before returning to the "core" composition.

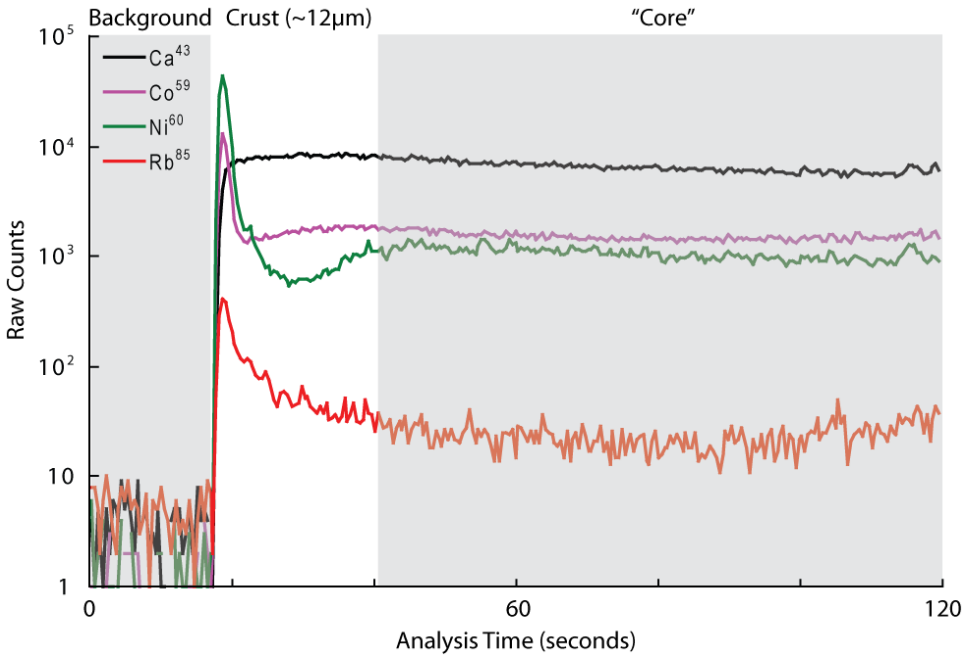

Figure 53. Raw counts of the normalising element Ca, siderophile trace elements Ni and Co, and volatile trace element Rb in a lunar impact spherule (LS6-56) during LA-ICPMS analysis. This profile illustrates the enrichment of Ni, Co and Rb in the upper ~2µm of the rim of an impact spherule. Following this, Ni and Co are slightly depleted before returning to a more consistent "core" value.

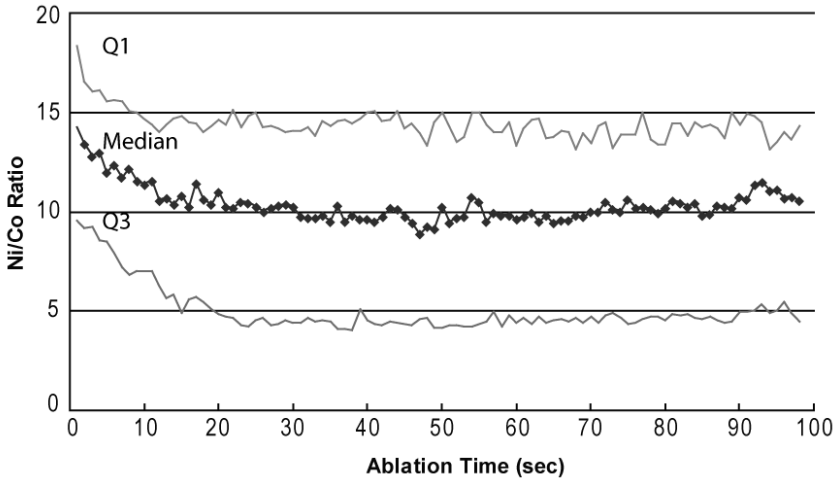

Figure 54. Ni/Co ratios (wt.% abundance) as a function of ablation time in 40 lunar impact spherules analysed using laser ablation ICP-MS. The first 10 seconds (~5µm depth) shows an increase in the median Ni/Co ratio resulting from preferential enrichment of Ni on the near-surface "crust" relative to Co.

The "core" section, taken as the flattest or most consistent part of the profile, is used to calculate the trace element composition of the impact spherules. The "crust" is kept separate from the "core" compositions as the crust is added by subsequently during residence in the regolith and does not represent the composition of the terrain from which the spherule was produced (see discussion in previous chapter). Nuggets or mineral grains, inferred from ablation profiles by changes in certain elements over a few points, are often present in "core" sections. The nuggets are dominantly Ni or Ni + Co in composition, but nuggets of Zr + Hf (+ Ti), Ti + REE, and Zr + REE composition also appear, suggesting the presence of mineral grains (undigested to partially digested) or other inclusions (i.e. melt or refractory phases). These need to be removed before the trace element composition is calculated.

A total of 33 impact spherules were analysed both as unpolished and polished sections so that the "core" compositions could be compared. Note that the "core" composition is an average of time slices through the parts of the spherule considered to best represent the bulk composition. Fifteen spherules analysed using a 62μm spot and, due to small sample sizes, another eighteen were analysed using a 28μm spot. However, eight of the impact spherules have yielded heterogeneous core compositions, consistent with large deviations in major element analyses. This heterogeneity is attributed to the presence of clasts and therefore these spherules are not included in this comparison. Note that the reduction in spot size also leads to a ~5 fold reduction in ablation volume. Although the ablation speed was increased from 5Hz to 7Hz there is still a ~3.5 fold reduction in ablation volume. Consequently, sensitivity and lower limits of detection (see electronic annex for data) are poorer as there is less material passing through the ICPMS, decreasing counting statistics.

Figure 55 compares a selection of trace element abundances in the "core" sections of impact spherules analysed as polished and unpolished sections. In general, the "core" compositions of unpolished sections are comparable to the compositions of the polished sections (i.e. within 1σ error), with the some exceptions. For example, the abundance of Ni and Rb is still enriched and highly variable on some unpolished "core" sections,

which may indicate a deeper residual "crust" signature extending into the "core". Other trace elements, especially the refractory rare earth elements, are remarkably consistent in polished and unpolished sections. A small (~5%) systematic enrichment of some trace element abundances in the polished section analyses is observable resulting from the use of the Ca as the internal standard, which is depleted in the volatile rims relative to the core. However, the differences between the trace element abundance of "core" sections in unpolished impact spherules versus the polished equivalent are sufficiently small to justify the use of the "core" section abundances.

In summary, major and trace element compositions of individual spherules, analysed as unpolished and polished sections, have been compared. Figure 52 and Figure 55 clearly show that difference between unpolished and polished analyses are minimal and compositions are generally within 1σ. However, analysis of the spherule surfaces (unpolished major elements and the "crust" signal of trace elements) indicate that there is a concentration of volatile (Na, K, Si, and Rb) and siderophile (Ni and Co) elements. The dominance of the "crust" on the geochemistry indicates that while surface geometry of unpolished spherules may affect the analysis, it is of a second order effect compared to the "crust". One additional, but minor, drawback to the unpolished analysis is the small (~5%) systematic enrichment of Si and depletion of Ca for unpolished analyses. Since these are used as internal standards to calculate trace element abundances, the trace element abundance will also be systematically enriched or depleted, depending on the internal standard used. However, the uncertainties in the internal standard do not affect the trace element pattern or the use of ratios (see description of equipment and corrections for quantitative data in Chapter 2: Technical developments). Additionally the variability of absolute abundance appears to be relatively small (~5%). Therefore the trace element data are still sound, but less weight should be placed on the volatile and siderophile elements that are characteristic of the "crust". In hindsight, an invariant element should have been collected and used as the internal standard during trace element analysis. Titanium may have proved to be a good internal standard; however, it was not given sufficient counting time on the EMP to accurately constrain the composition.

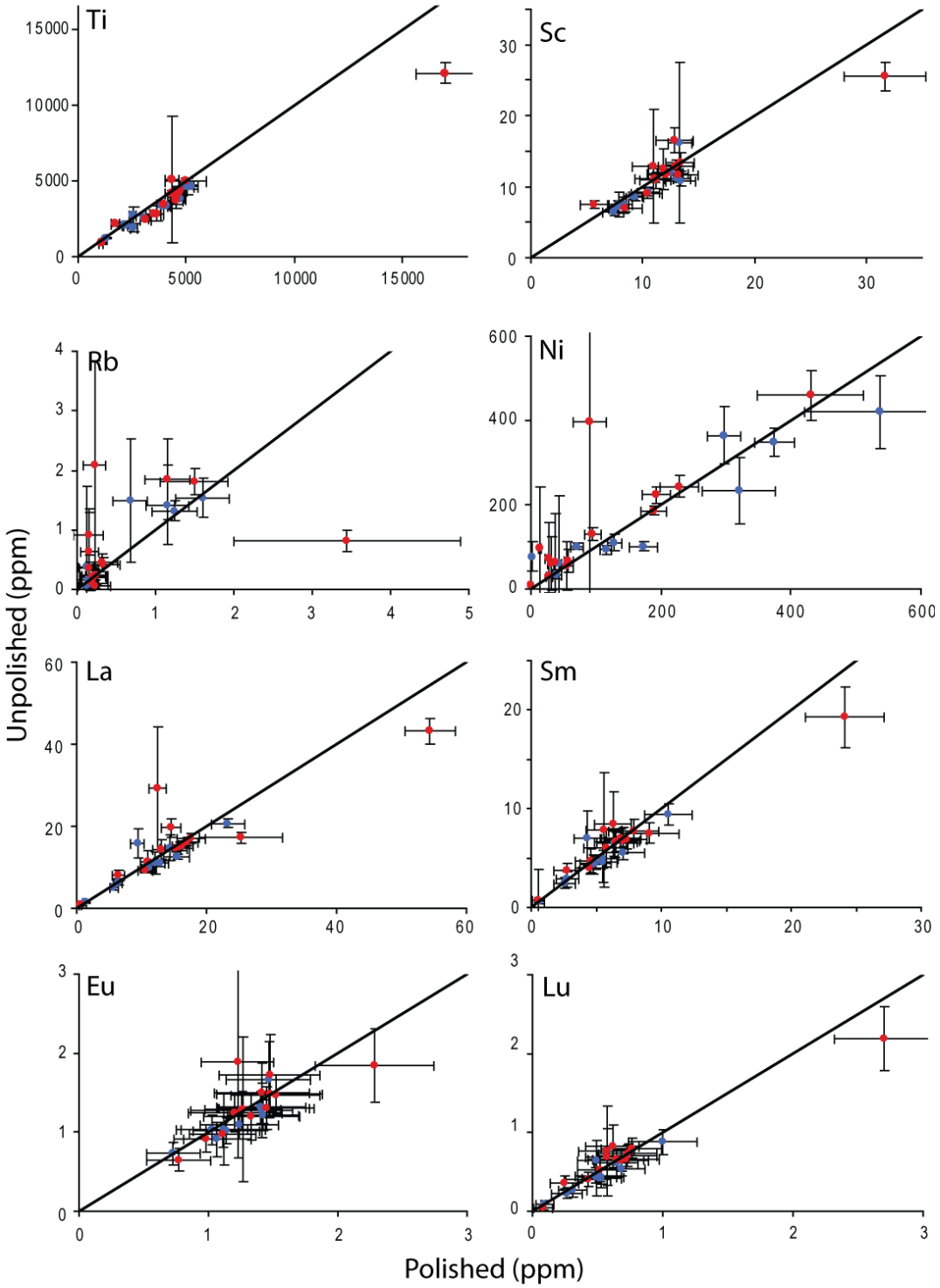

Figure 55. Selection of trace element abundances of 25 selected homogenous lunar impact spherules as an unpolished vs. polished sample. Red points were analysed with a 62µm spot at 5Hz. Blue points were analysed with a 28µm spot at 7Hz. Error bars are at one standard deviation. The 1:1 line is also shown.

4.3.3 Provenance of Impact Spherules from 66031,65

Major Element Chemistry

A total of 272 unpolished impact spherules were analysed in this study, 225 particles of which had acceptable analytical totals that were consistent with typical lunar impact spherule compositions (data available in electronic annex). It was noted in the previous chapter that impact spherules retain a compositional memory of the target lithology, in particular the bulk regolith, from which each spherule was created. Generally, the composition of each spherule will relate to one of the major lunar lithologies: the feldspathic highlands, basaltic mare, or KREEP. Consequently, there will be positive correlations between elements associated with the feldspathic highlands, Ca and Al contained mostly in plagioclase, which correlate negatively with elements associated with the basaltic mare, Fe + Mg (+ TiO_2) contained in pyroxene and olivine (and ilmenite).The Al_2O_3 abundance of impact spherules in the current study ranges from 11.6wt.% to 34.3wt.% reflecting the presence of basaltic mare-derived spherules through to feldspathic highlands-derived spherules. Correspondingly, the FeO + MgO correlate negatively with Al_2O_3 ranging from 29.8wt.% for the least feldspathic spherule to 12.0wt.% for the most feldspathic spherule. This compositional feature is also seen in many other lunar materials and is typically plotted as a mixing line between the plagioclase (Al_2O_3) and pyroxene (FeO+MgO) components (Korotev et al., 2010; Lucey et al., 2006). Lucey et al. (2006) calculated that the plagioclase-pyroxene mixing line, based on typical Apollo soils, intercept Al_2O_3 at 36.4wt.%. However, Korotev (2010) indicate that the mixing line for impact glasses intercept Al_2O_3 at 38.6wt.% which suggests depletion of SiO_2 in impact glasses compared to the typical Apollo soils (2010). Figure 56 show the impact spherules of the current study, a selection of Apollo soils compositions from Lucey et al. (2006), and the Korotev (2010) impact glass plagioclase-pyroxene mixing line in a plagioclase versus pyroxene plot. The impact spherules of the current study plot close to the Korotev (2010) mixing line which too suggests that they are depleted in SiO_2 compared to the typical Apollo soils. This feature is not altogether unexpected since SiO_2 appear to concentrate on spherules surfaces along with other volatile elements such as Na_2O and K_2O (see Figure 52).

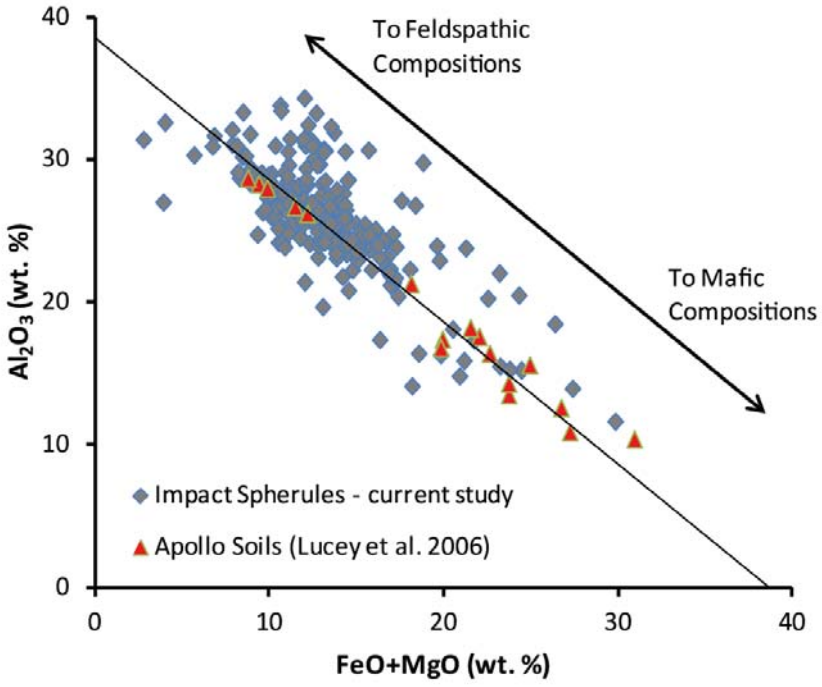

Figure 56. Plot of Al_2O_3 versus FeO+MgO showing 225 impact spherules from this study fall on a mixing line defined by Korotev (2010). Most impact spherules cluster toward feldspathic compositions typical of the Apollo 16 soils. There are fewer mafic spherules which are compositionally similar to mare basalts. Typical errors are about the size of the symbols.

Another dominant feature of impact spherules in the current study shown in Figure 56 is the tendency towards more feldspathic compositions. Figure 57 employs Ca/Al ratios to distinguish between mineralogical differences between the plagioclase-rich highlands (low Ca/Al ratios) and clinopyroxene-rich mare (high Ca/Al ratios) to segregate impact spherules into highlands, mixed highlands-mare, and mare groups. Table 7 presents the average composition of the impact spherules from each of these compositional groups. A total of 164 (73%) impact spherules fall within the highlands compositional group and are likely to be locally-derived. Korotev (2010) noted that a similar percentage (65%) of the clean impact glasses (<210µm diameter) in their study are of local origin, although slightly differ in composition to the feldspathic highland materials with higher MgO and TiO_2, and lower Na_2O, K_2O, and P_2O_5 content. A further 25% have mixed highland-mare compositions which Zeigler et al. (2006) suggest are possibly a mixture

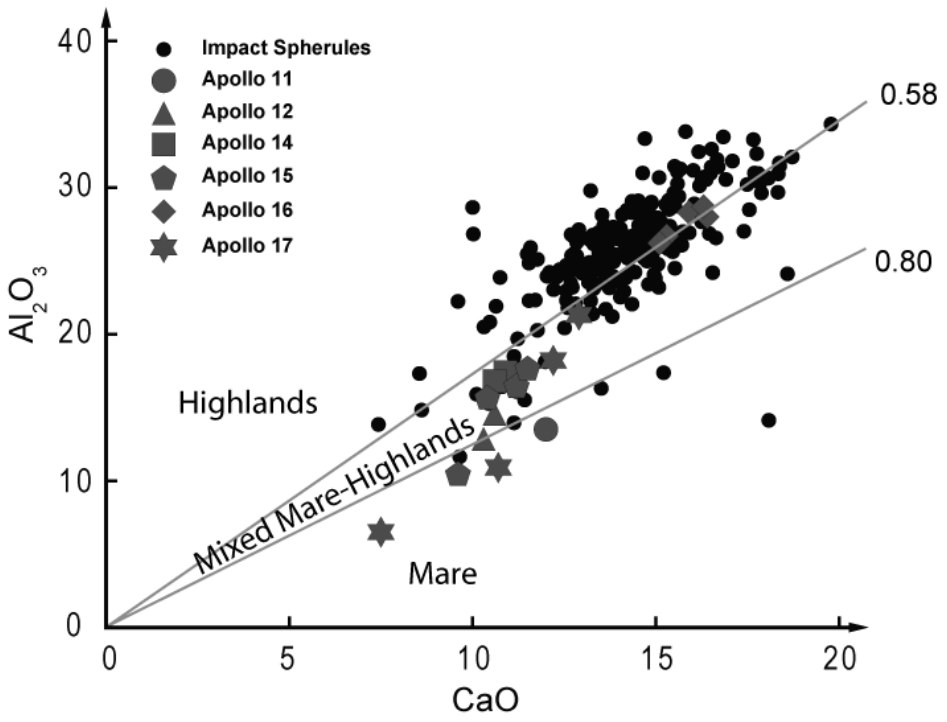

Figure 57. Plots of major element oxides CaO and Al_2O_3 used to distinguish between highlands, mixed mare-highlands, and mare impact glasses. The boundary between "pure" highlands and mixed mare-highlands, and mixed mare-highlands and mare is given by CaO/Al_2O_3 ratios of 0.58 and ~0.80 respectively (Naney et al., 1976). Also plotted are the compositions of regolith samples collected during the Apollo missions, as compiled by Lucey et al. (2006). Typical errors are about the size of the symbols.

of multiple lithologic precursors formed by large impacts, such as the Theophilus basin-forming event, that punch through and incorporate the highlands veneer and underlying mare. A more unlikely scenario is mixing of local and exotic material during impact 'gardening' (Zeigler et al., 2006). The remaining 2% have more mare-like compositions, but do not correspond to any of mare groups established in Zeigler et al. (2006). These rarer spherules are placed in an ungrouped category as they are not similar to any lunar lithology, or mixture of lunar lithology and could be mixed highlands-mare or KREEPy spherules (Zeigler et al., 2006). In the latter case, these spherules would have clearly originated, and been subsequently transported, from locations hundreds of kilometres from the collection site.

Table 7. Major element composition of 225 lunar impact spherules determined using electron microprobe. Although 272 were analysed, 47 were rejected based on poor totals and chemistry that is inconsistent with impact spherules. Impact spherules are divided into groups based on the Ca/Al ratios of the major lunar lithologies. Data are presented as weight percent oxides in the form mean ± one standard deviation.

	Highlands (164)	Mixed Highlands-Mare (57)	Mare (4)
FeO	6.08 ± 2.17	8.11 ± 3.63	10.3 ± 5.23
Na_2O	0.53 ± 0.54	0.67 ± 0.87	0.79 ± 0.24
TiO_2	0.54 ± 0.23	0.79 ± 0.63	0.96 ± 0.30
CaO	14.0 ± 1.84	14.6 ± 2.37	14.1 ± 3.51
Al_2O_3	26.7 ± 3.16	23.8 ± 4.39	14.8 ± 2.53
SiO_2	44.9 ± 3.45	44.5 ± 3.20	47.6 ± 1.08
MgO	6.73 ± 2.10	6.92 ± 2.19	10.6 ± 1.49
K_2O	0.14 ± 0.14	0.25 ± 0.53	0.24 ± 0.14
Cr_2O_3	0.12 ± 0.08	0.15 ± 0.06	0.29 ± 0.14

The KREEP component of the impact spherules may be distinguished using the K content. Figure 58 plots K_2O abundance of impact spherules of the current study against Al_2O_3 as a discriminant of highlands versus mare. The K_2O abundance in impact spherules range from 0.01wt.% up to 3.63wt.%. The two spherules with K_2O abundance >1.5wt.% are more noritic in major element composition which suggest that they may have originated from the Procellarum KREEP terrain. Korotev (2010) chose to define spherules with >0.2wt.% K_2O as being atypical of the feldspathic highlands and likely to be of non-local origin. By this definition, a total 43 (19%) impact spherules will be likely be of non-local origin. Although elevated K abundance is characteristic of KREEP, K does not correlate perfectly with the other characteristic elements of KREEP, such as the incompatible trace elements, because K can also partition into K-feldspar (Lucey et al., 2006). Additionally, the use of K as a proxy for KREEP for impact spherules in the current study may not be as sound since the unpolished analyses are affected by a volatile crust. Consequently, the discussion of KREEP and identification of KREEPy spherules will be reserved for the following section where trace element data are presented.

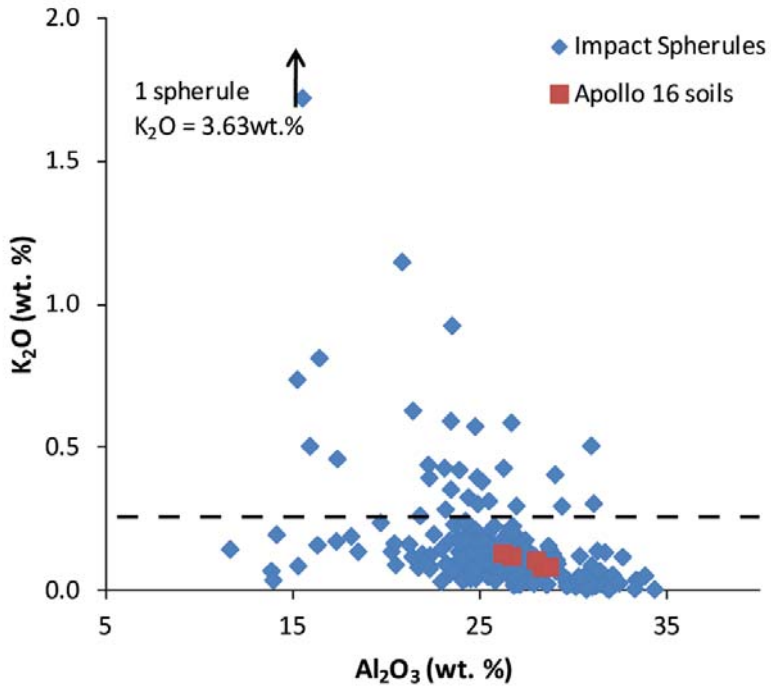

Figure 58. Plot of K_2O (discriminant of KREEP) and Al_2O_3 (discriminant of feldspathic highlands versus basaltic mare) in impact spherules of this project and Apollo 16 soils (Lucey et al., 2006). The dashed line marks the 0.2wt.% K_2O boundary used by Korotev (2010) to define spherules likely to be of non-local origin and atypical of the feldspathic highlands. Typical errors are about the size of the symbols.

The major element analyses of impact spherules from Apollo 11, 12, 14, 16, and 17 are collated in Figure 59. The major element data for the Apollo 16 impact spherules are from this project. The apices of the triangle in this figure are rough indicators of the three different lunar terrains, but do not strictly define these compositions (see Korotev, 2001). In general Figure 59 shows impact spherule clusters in the vicinity of the soils from which they were collected indicating that many are probably of 'local' origin. However, these clusters are not tight and often extend into other compositional regions which may indicate mixing of components from different lunar terrains. Impact spherules with exotic compositions are also present at each collection site, suggesting subsequent transport from the original place of formation.

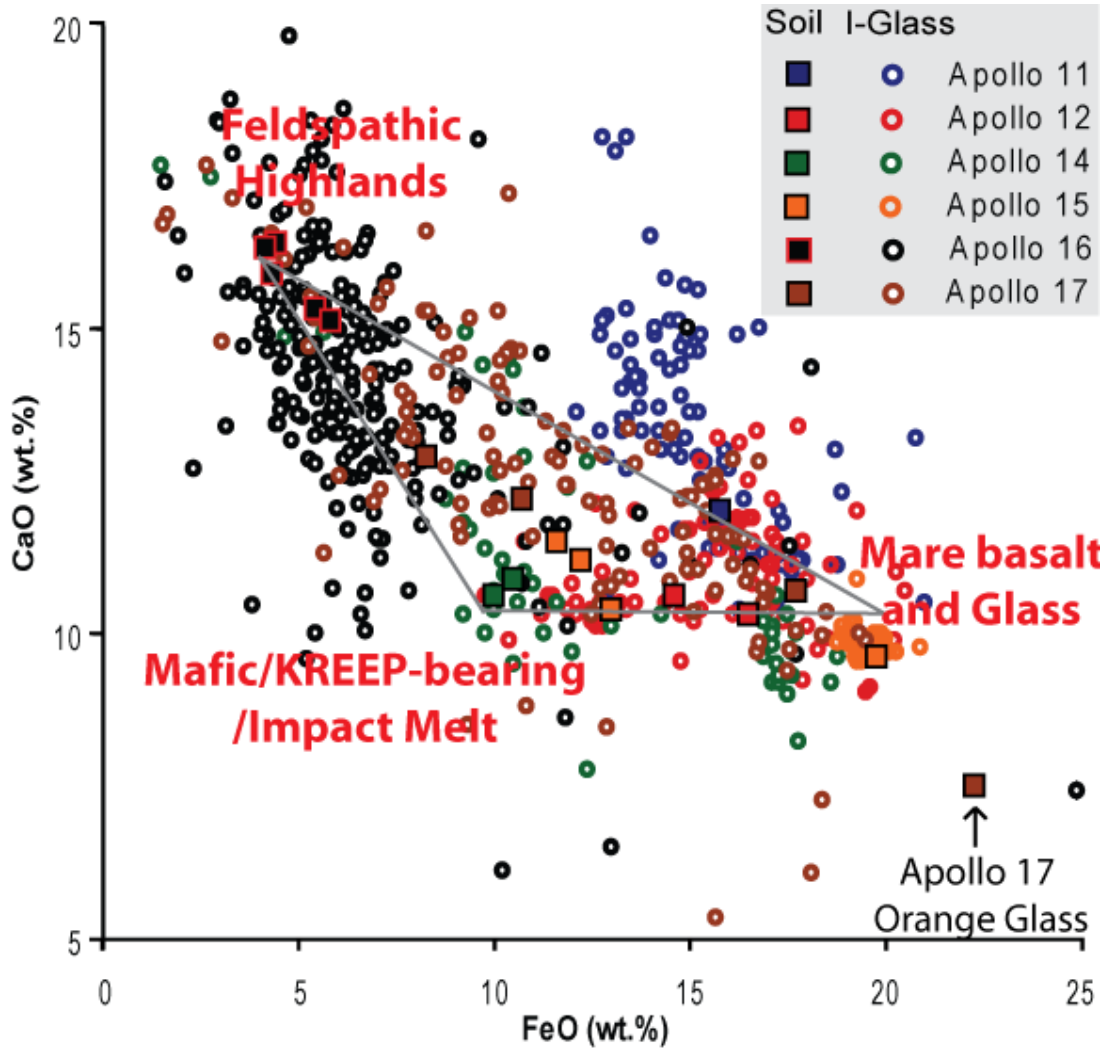

Figure 59. Variation of CaO and FeO (total Fe expressed as FeO) for the lunar regolith (see Lucey et al., 2006 for compositions) and impact glasses (I-Glass). Compositions of impact glasses from Apollo 11, 12, 14, and 15 are sourced from Delano et al. (1982), Chao et al. (1972) and Zellner (2002). All Apollo 16 data points are impact spherules from this study. Compositions of Apollo 17 impact glasses are from Adena et al. (2009). Impact glasses from each site are generally more variable in composition than in the host soils, with the exception of the Apollo 15 impact glasses (See Delano et al., 1982). This characteristic prompted their early use as representative samplers of soils not collected during the Apollo missions. The Apollo 17 orange glass soil is dominated by pyroclastic glass spherules and distinct from other soil compositions.

In addition to the impact spherules, a total of three VRAP spherules, (SiO_2 abundances exceeding 65wt.%) and one HASP spherule (48wt.% Al_2O_3) was found. Spherules of pyroclastic origin were not identified amongst these impact spherules using MgO/Al_2O_3 ratios. The impact spherules of this study have MgO/Al_2O_3 ratios between 0.04 and 1.17 (1.25 marks the transition into pyroclastic glasses: Delano, 1986). However, pyroclastic glasses have been recognised previously in the regolith of the Apollo 16 landing site (Delano, 1986; Delano and Rudowski, 1980; Shearer and Papike, 1993; Zeigler et al., 2006).

To summarise, a variety of glassy particles were found in this study most of which were lunar impact spherules. The spherules of this study exhibit a range of compositions which could reflect a complex combination of the availability of compositionally different targets, lateral transport, and subsequent alteration during residence in the regolith. The majority (73%) of spherules were locally derived with the remaining spherules being mixed highlands-mare and mare, both of which could be exotic to the collection site. Using major elements alone, it is difficult to determine more about their origin and subsequent alteration during residence in the lunar regolith, especially given that K cannot be used as an indicator of KREEP. However, the ability to collect both major and trace elements prior to radioisotopic dating in this project will allow for a more detailed study of impact spherule geochemistry.

Trace Element Chemistry

A total of 159 out of 225 impact spherules that were analysed for major element compositions were also analysed for trace element compositions. “Core” compositions could be calculated from a total of 159 impact spherules and were used as additional constraints to impact spherule provenance. Trace element abundances can be used to discriminate between the mare, highlands, and KREEP components on the basis of incompatible trace element fractionation into plagioclase (+ve Eu and low REE), clinopyroxene (LREE depleted and relatively HREE enriched), or residual melt (high REE and -ve Eu), respectively (refer to discussion in Chapter 3: Background). The abundance of CI-normalised Rare Earth Elements and Eu anomaly are diagnostic for

determining spherule origin. Figure 60 shows the REE patterns for impact spherules in this study. Nine (6%) impact spherules are consistent with more KREEPy compositions, which are being derived from incompatible element-rich melts and are characterised by high REE concentrations relative to other lunar materials, with a strong negative Eu anomaly. Figure 61 shows the distribution of impact spherules in this project in a FeO versus Th plot. The KREEP component in the Apollo soils is typically carried in mafic impact-melt breccias (MIMBs) with Th concentrations between 4-8ppm at Apollo 16 and 17 (Lucey et al., 2006). However, there are up to nine impact spherules that may exceed 8ppm Th abundance and could be exotic to the collection site. Two impact spherules exceed this limit outside 2σ uncertainties.

A total of 137 (87%) impact spherules have REE patterns that cluster within the red zone designated "Apollo 16"; to avoid clutter, these are not plotted individually. The "Apollo 16" band roughly represents the variability of REE patterns in the local Apollo 16 soils, but also extends into more KREEPy compositions. This band is constrained using the average soil compositions presented in Lucey et al. (2006) which includes more atypical soils found at the Apollo 16 site (i.e. soils from North Ray Crater). Impact spherules within this zone are characterised by light REE enrichments, variable REE abundance, and small negative Eu anomalies.

One (0.6%) impact spherule has light REE depletion consistent with materials from a low REE abundance mare, such as 78256 which is a very low titanium (VLT) basalt from the Apollo 17 site. Typically, mare samples also exhibit small negative Eu anomalies which is absent from this sample. As this is one of the impact spherules selected for radioisotopic dating, further discussion of this sample will be reserved for the following chapter.

Of the remaining 12 impact spherules, six (3.2%) are consistent a model composition of the feldspathic highlands estimated from feldspathic lunar meteorites (Korotev et al., 2003). Unlike most of the regolith at the Apollo 16 site, these samples are characteristically REE-poor with strong positive Eu anomalies. The remaining six

(3.2%) impact spherules with REE abundances between the feldspathic highlands and Apollo 16 soils may be mixtures of a dominantly feldspathic component with more KREEPy materials such as the Apollo 16 soils.

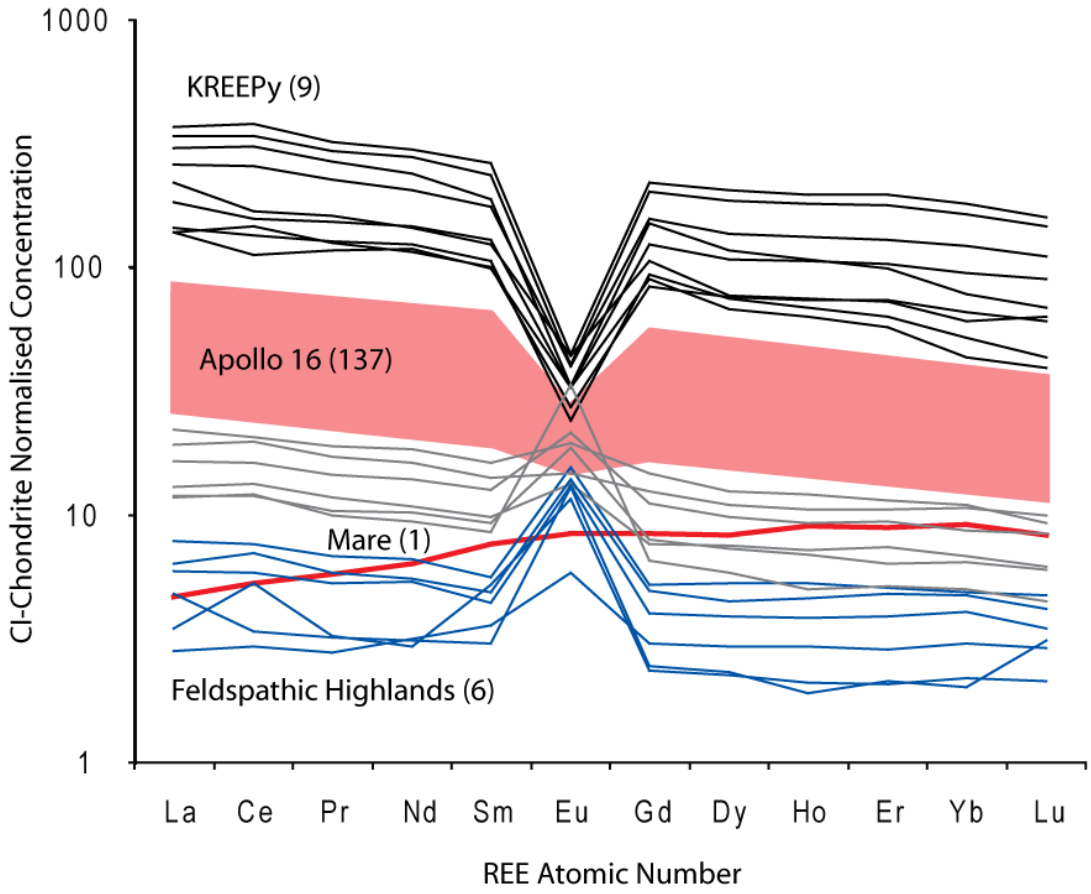

Figure 60. Chondrite normalised rare earth element (REE) abundances for 159 impact spherules. The majority of the impact spherules are clustered within the light red band which roughly corresponds to the composition of the materials from Apollo 16 (see Lucey et al., 2006). KREEP-rich samples (black lines) exhibit high REE abundances with strong negative Eu anomalies. Those of the feldspathic highlands (blue lines) exhibit low REE abundances and strong positive Eu anomalies. Only one impact spherule (red line) analysed for trace elements has the light REE depletion consistent with the mare.

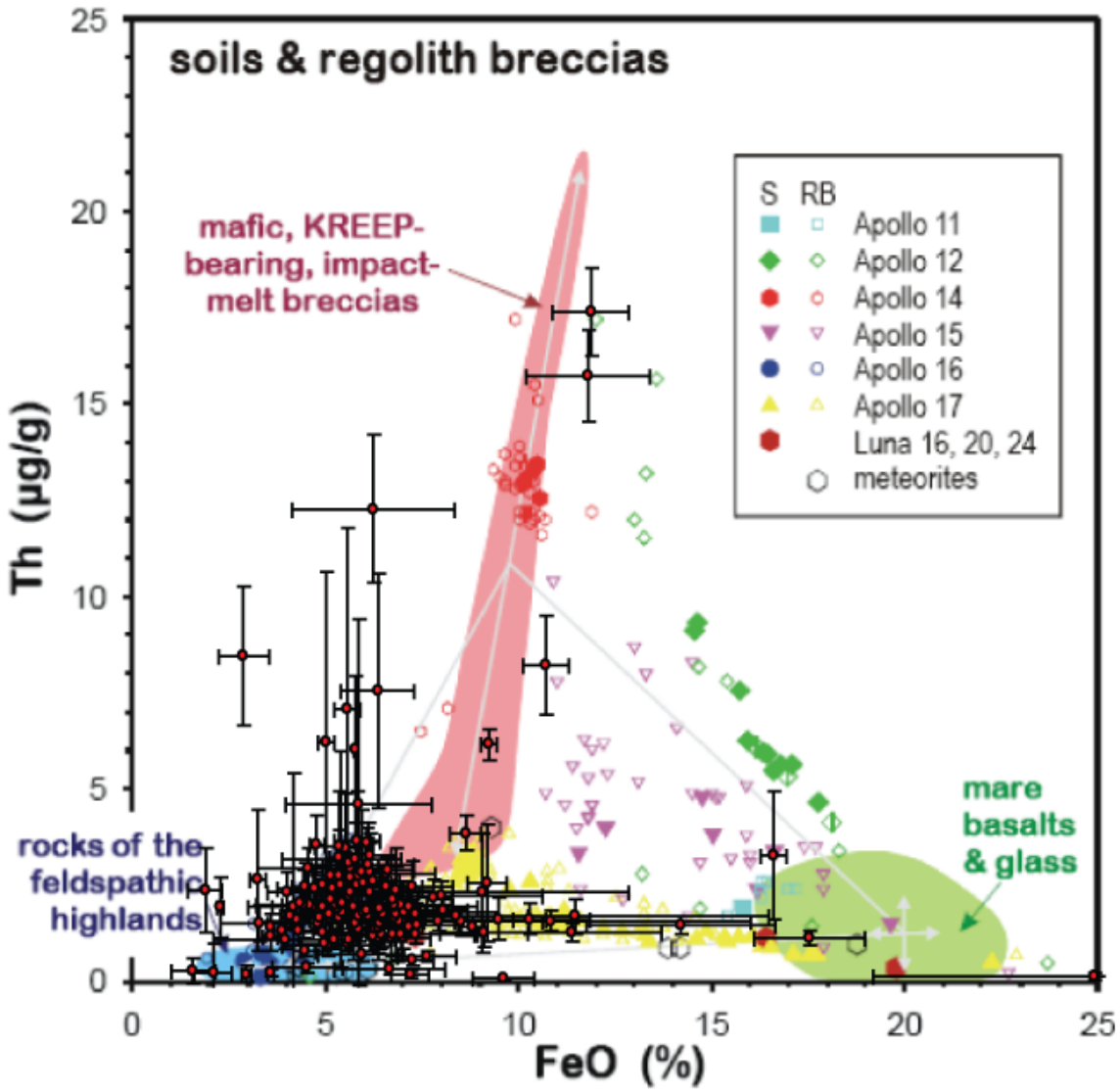

Figure 61. A plot of FeO versus Th content of impact spherules in this project superimposed onto a compilation of soil and regolith breccias by Korotev (2001). FeO is used to distinguish between highlands and mare compositional groups while Th is an indicator of the KREEP component. The majority of impact spherules in this project cluster around the soil compositions at Apollo 16, but extend toward the mare and KREEPy components. Error bars at 1σ.

4.4 Discussion

4.4.1 Impact Spherule Production from Soils or Rocks?

In the previous chapter, it was noted that impact glass was originally used as a remote sampler of parental rocks, but studies since then have indicated that impact glasses are more representative of the bulk regolith. That is not to say that impact glass is exclusively formed from bulk regolith as it is also possible that many are produced from rocks and mineral fragments within the regolith or from outcrops. In the following discussion, two methods will be utilised to attempt to constrain impact spherule origin. The first method will employ diagnostic trace element ratios which can distinguish compositionally distinct lithological components at the Apollo 16 site using a plot of Sc (partitions into pyroxene – proxy for mafic components) versus Sm (proxy for KREEPy components) (see Norman and Ryder, 1980). This will test the hypothesis that impact glasses may be compositional mixtures of the lithologies available at the Apollo 16 site (Korotev, 1997) and the Hörz and Cintala (1997) view that because impact glass compositions clustering around those of lithologies, they must be derived from crystalline rock surfaces. The second method will challenge this view by employing a chi-squared statistical analysis to gauge the amount of composition variability required in local soils to produce impact spherules exclusively from the regolith.

Mixing models by Korotev (1997; 1994) indicate that the regolith is composed of a variety of compositionally distinct lithological components. Figure 62 is presented in Korotev (1997) and shows the Sc versus Sm distribution of model Apollo 16 rocks identified in Korotev (1994), mature Cayley soils (<1mm fines collected from the Cayley surface that have experienced high degrees of bombardment, impact mixing, and irradiation), and regolith particles (from surface soils and cores). Non-KREEPy lunar impact spherules from this project are superimposed onto Figure 62. A spread of impact spherule and regolith particle compositions straddles the mafic impact-melt breccias (MIMBs) and noritic anorthosites (NAn) which represent KREEPy and feldspathic rock compositions, respectively. However, the current Apollo 16 spherule compositions tend

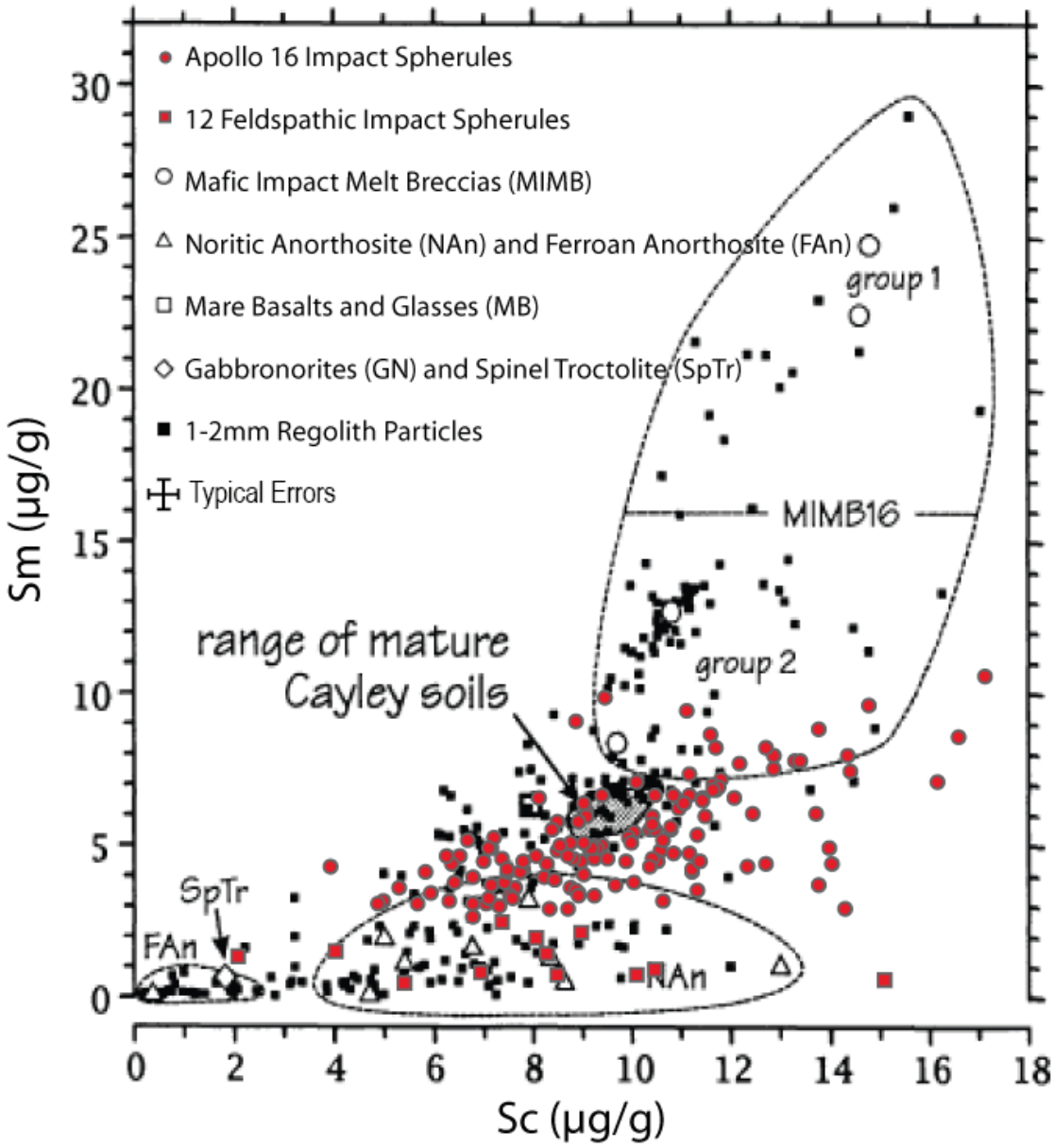

Figure 62. Plot of Sc and Sm concentration for model Apollo 16 rocks (open symbols and fields) and 1-2mm regolith particles from Korotev (1997) (black symbols). Superimposed onto this diagram are the lunar impact spherules of this project (red symbols). The distribution of impact spherules falling within the Apollo 16 band in Figure 60 (red circles) is similar to the distribution of the 1-2mm regolith particles. More feldspathic impact spherules of this project (red squares) typically fall within the field corresponding to the noritic anorthosites.

Modified from Korotev (1997)

to cluster between these fields, although more towards the feldspathic NAn field the upper bounds of which appear to be defined by the composition of crystalline feldspathic impact-melt breccias (Group 3 in Korotev, 1994). According to Korotev (1997), the regolith particles in and near the mature Cayley soils field are composed of regolith breccias and agglutinates. The rest of the regolith particle distribution between the MIMB and Nan field have compositions consistent with glassy melts (Korotev, 1997), mostly glassy rock coatings, but also a few impact-melt splashes and spherules thought to have been produced during the South Ray Crater event and other events that produce feldspathic impact-melt breccias (Korotev, 1994; Morris et al., 1986). Morris et al. (1986) argue that these glassy melts, referred to as Group A Impact Melt Splashes, represent bedrock or megaregolith based on the absence of a high-Ti mare component and were excavated by South Ray Crater since many of the glassy coats have ~2Ma exposure ages.

Few impact spherules in this project plot within the mature Cayley soil field in Figure 62. The mature Cayley soil field is based on 36 soil samples collected from the central and southern Apollo 16 sites including 78% of the soils sampled from the top 10cm sampled in drive cores (Korotev, 1997). This suggests that most impact spherules were not produced from impacts into wide-spread mature soil, but rather from impacts into feldspathic impact-melt breccias, bedrock, or feldspathic rock fragments. If South Ray Crater ejecta reached the collection site (Station 6), as suggested by Ulrich et al. (1981), and sampled bedrock, as suggested by Morris et al. (1986), the surface soil may be saturated in impact-melts and spherules produced from that event, thus supporting the hypothesis of a rock-dominated origin. Impact spherules of a more KREEPy composition could be produced from MIMBs or mixtures of MIMBs and more feldspathic components. This argument suggest that most impact spherules were produced from rocks and regolith fragments; however, note that the remaining surface soils in the region consist of more compositionally diverse submature (19%) and immature soils (3%) (Korotev, 1997) which could also produce impact spherules of a more feldspathic nature than the mature soils. More importantly, a source of more immature soils can be found at depth since soil maturity decreases, though irregularly,

with depth (Korotev and Morris, 1993; Korotev et al., 1997; Korotev et al., 1984). This source of soils could be accessed by a sufficiently large impact that penetrates the surface soils and incorporates deeper, less mature soil. Note also that finer soil fractions, especially the <10μm fraction, are more compositionally extreme (feldspathic highlands and KREEP) than the coarser fractions that make up the bulk soil (Papike et al., 1982). In this case, smaller impacts may favour the production of impact spherules from finer fractions of the soils as they would be easier to melt.

Impact spherules of this project with compositions more feldspathic than the typical Apollo 16 soils are shown in Figure 62. The low Sm content of these spherules (<2.5ppm) is consistent with formation from KREEP-poor lithologies. The spread in Sc abundances for these feldspathic impact spherules indicate that they may originate from a number of compositionally distinct materials. Using diagnostic trace element ratios such as Sr/Ba, Ti/Sm, and Sc/Sm, it is possible to distinguish between igneous suites of rocks on the basis of elemental fractionation into various lunar rock-forming minerals (Norman et al., 2010; Norman and Ryder, 1980). Figure 63 compares the Sr/Ba ratios of feldspathic impact spherules with selected rock and regolith components and reveals two distinct impact spherule populations. Impact spherules with Sr/Ba <4 correspond to the moderately feldspathic impact spherules that plot between "feldspathic highlands" and Apollo 16 soils in Figure 60 and distribute towards rocks with increasing amounts of KREEP (i.e. Group 3 feldspathic impact-melt breccias of Korotev, 1994). Impact spherules with Sr/Ba ratios >6 correspond with impact spherules with the lowest incompatible trace element abundances in Figure 60 and are intermediate between the estimated feldspathic lunar highlands (Korotev et al., 2003) and more feldspathic compositions (e.g. ferroan anorthosites). Within the Apollo 16 site, the feldspathic impact spherules have compositions that are similar to those of regolith fragments and rocks collected from North Ray Crater (Korotev, 1996; Norman et al., 2003b; Norman et al., 2010; Stöffler et al., 1985), and within the Cayley regolith (~18% of the 1-2mm particles plotted in Figure 62 are anorthositic). More mafic varieties (i.e. those with higher Sc content) are rarer (Jolliff and Haskin, 1995). However, these impact spherules

could have been produced in soils exotic to the Apollo 16 site, since material from Mountains (Lindstrom and Salpas, 1981; Norman, 1981; Ulrich, 1973).

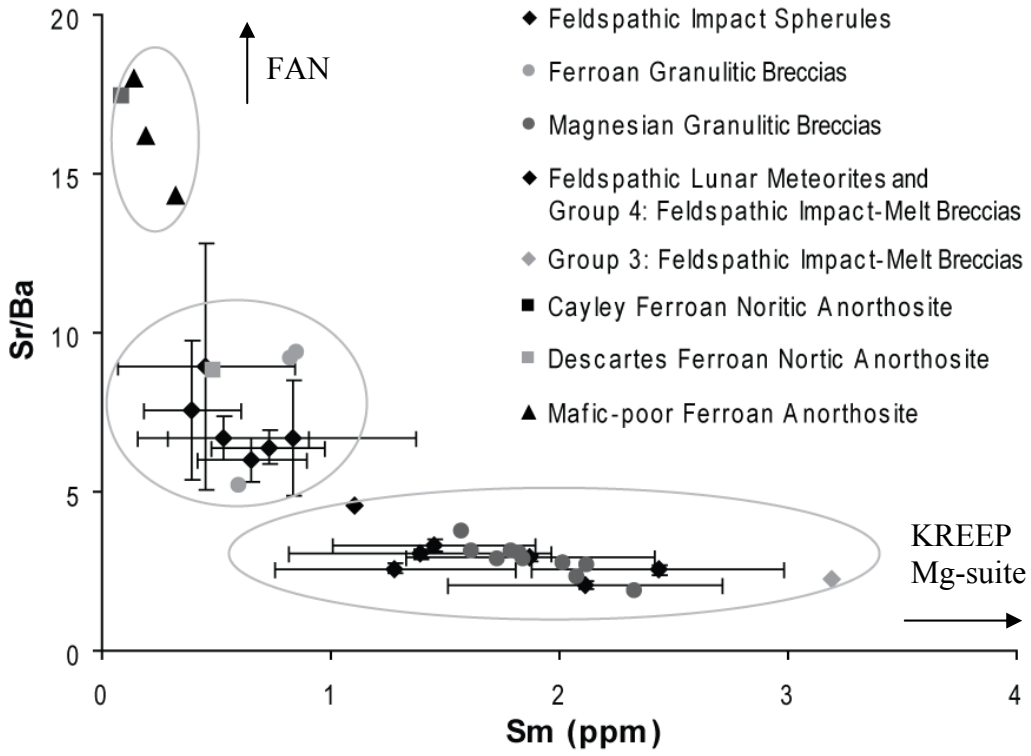

Figure 63. Sr/Ba ratios versus Sm abundance in the feldspathic impact spherules of this project (1σ errors). Also plotted are the feldspathic model rocks from Korotev (1997) including ferroan and magnesian granulitic breccias compiled by Lindstrom and Lindstrom (1986), averages of Group 3 and 4 feldspathic impact-melt breccias (Korotev, 1994), feldspathic highlands estimated from lunar meteorites (Korotev et al., 2003), ferroan noritic anorthosite fragments from the Cayley and Descartes regolith (Jolliff et al., 2000), and clasts of mafic-poor ferroan anorthosite from a fragmental breccia 67016 (Norman et al., 2010).

The KREEPy impact spherules identified in Figure 60 are not shown in Figure 62 since many plot outside the boundaries of this figure. Four impact spherules fall within the field that corresponds to the composition of the Korotev (1994) mafic impact melt breccias (MIMBs). These crystallised rocks are the most common lithology at the Apollo 16 site and are divided into groups based on their incompatible trace element

(ITE) content (Korotev, 1994). The "Group 1" MIMBs the most ITE-rich, poikilitic melt breccias. The "Group 2" MIMBs are more aluminous and have lower ITE abundances than the "Group 1" breccias. The "Group 2" mafic impact melt breccias have also been referred to as very-high aluminium (VHA) basalts in the early literature. According to Korotev (1994), ~35% of the Apollo 16 regolith consists of "Group 1" and "Group 2" mafic impact melt breccias. In Figure 62, one impact spherule plots within the "Group 2" MIMB16 field and three spherules fall within 1σ error of the "Group 1" MIMB16 field. If these spherules were produced locally, are likely to be a product of impacts into mafic impact melt breccias and rocks. The remaining five KREEPy spherules, however, cannot have been produced from the materials available at the Apollo 16 site and are likely to be derived from KREEP-rich material exotic to the Apollo 16 site.

To summarise, based on Figure 62 alone, the overwhelming majority of the 225 impact spherule population analysed during this project were probably not produced from bulk mature Cayley soils or regolith breccias, but could have been produced from locally available rocks and fragments within the regolith. This analysis also suggests that if impact spherules were produced from soils, an immature soil lacking KREEP and mare components would be required. Only six impact spherules can confidently be identified as exotic to the Apollo 16 site, although an additional twelve feldspathic impact spherules may have been produced from soils in the adjoining Descartes Mountains. However, it was also noted that the bulk mature Cayley soils, while wide-spread, may not be the only soil that is sampled by impact spherules. Other types of soils at the Apollo 16 site or surrounding region, sub-mature and immature soils at depth (>10cm), and the fine <10μm fractions of soils can also be preferentially sampled by impacts, hence may still produce the compositional variability seen in impact spherules. In the following section, a statistical method will be used to determine whether it is possible to produce impact spherules using only Apollo 16 soils.

4.4.2 Comparison of Impact Spherule and Soil Compositions

In the previous section, it was shown that trace element ratios suggest that the majority of impact spherules do not have compositions that suggest formation from mature Cayley soils which make up a large portion of the surface soils at the Apollo 16 site. However, it was noted that these impact spherules may have formed from more immature local soils relatively uncontaminated by mare and KREEP components (e.g. immature soil at depth, fine soil fractions, and other soils from Apollo 16 and surrounds). Since impact spherules could be produced from impact events that sample both small and large volumes of the target, bulk mature Cayley soils is probably too limited in composition to represent other soil targets, even though it is wide-spread. Here, the hypothesis that impact spherules can be produced using only soils will be tested by comparing the probability of overlap between individual impact spherule compositions and those of a selection of both local and exotic soils.

Statistical Method

In Chapter 1: The Cosmic Spherules Project, mean absolute percentage error was used to determine the similarity between cosmic spherules and chondritic parent bodies. In this section, a different approach will be used, known as the chi-squared goodness of fit method, since more comprehensive data were collected in this project. This method can be used to assign a probability to the compositional overlap between individual lunar impact spherules and a selection of soils (candidates) from which they may have originated. The selection of soils can then be ranked to determine which soil is most similar to the impact spherule. The chi-squared goodness of fit can be used to evaluate major and trace element data individually or combined into a single variable (chi-squared) with the following formula:

$$x^2 = \sum_{i=1}^{n} \left(\frac{f_i - y_i}{\sqrt{\sigma_f^2 + \sigma_y^2 + \sigma_z^2}} \right) \quad \textbf{[8]}$$

Where n = number of inputs (degrees of freedom)

f_i = Sample element/Al ratio

y_i = Soil element/Al ratio

σ_f = Analytical Errors on the Sample (1σ)

σ_y = Analytical Errors on the Soil (1σ)

σ_z = Other Errors (e.g. systematic)

The probability of the match can then be calculated using the cumulative chi-squared distribution conveniently available as the CHIDIST function in Microsoft Excel. The advantage of chi-squared over the mean absolute error used in Chapter 1 is that the variation in the sample and candidate soil can also be considered in the fit. However, this method assumes that all variables are independent, which should preclude most major and trace elements because they are highly correlated. Yet, some highly-correlated major and trace elements contain diagnostic data for determining provenance (i.e. La-Lu), which means that these data should not be combined into a weighted variable that effectively removes that information. The drawback of having correlated elements in the chi-squared equation is an artificially over-estimated probability of fit, although the actual ranking of one candidate to another will not be affected. However, a probability of match can be determined if the effective degrees of freedom (i.e. number of independent variables) are determined.

The effective degrees of freedom can be determined by the number of degrees of freedom needed to fit the lowest chi-squared values of the impact spherule distribution to the chi-squared probability density function. In other words, what is the smallest number independent variables (i.e. elements) needed to characterise the most compositionally similar spherules. This can be done by comparing each spherule to all the others studied, thus producing a population of chi-squared values that describe the

compositional variability of the impact spherule population. This distribution for the combined major and trace element data are shown in Figure 64 where chi-squared values are binned to 0.5 intervals. The chi-squared values at this stage are only indicators of relative similarity (the lower the number, the more similar the composition) since the number of independent variables has not yet been established. The shape of this distribution indicates that there are few spherules that are "very similar" in composition, but quickly peak at chi-squared values where they are "similar". Think of these spherules as having originated from the Apollo 16 soils which are variable from site to site, but still relatively similar across the region. The distribution slopes more gently down to higher chi-squared values which indicate a progression from one distinct composition to another. This can be thought of as a progression of spherules with compositions becoming more mafic due to mixing of two end-member compositions. The lowest number of variables needed to fit a chi-squared probability density function to the chi-squared distribution (see Figure 64) then dictates the effective of degrees of freedom (see Figure 65 for a graphical representation).

For the major elements the effective degrees of freedom were determined to be 9; however, close examination of the chi-squared calculations indicated that Na_2O and K_2O introduce the greatest amount of variability, probably because they are typically associated with volatile crusts (see Figure 52). There are two methods for accommodating Na_2O and K_2O enrichment associated with the impact spherules. The first involves increasing the variability of these elements by an average enrichment factor. However, since the enrichment factor varies widely in concentration in each impact spherule, application of an average enrichment factor to all impact spherules is not appropriate. The second, and most preferable method, is to remove Na_2O and K_2O from the chi-squared fits, although this reduces the effective degrees of freedom to seven. However, since these volatiles are two of the three main discriminants between the feldspathic lunar meteorite and the North Ray Crater candidate soils, TiO_2 content will be the only means to differentiate between the two soils. As a precaution, Rb, Ni, and Co were also removed from the calculation of effective degrees of freedom as they too are typically associated with crusts (see Figure 53). The effective degrees of

freedom for trace elements were calculated at 11. If major and trace elements are combined into a single chi-squared variable, there are 18 effective degrees of freedom.

The effective degrees of freedom for the major elements appear to be overestimated since seven major elements were considered and seven effective degrees of freedom were returned. This indicates that there are no correlations between any of the major elements even though strong correlations occur amongst other lunar materials (see Haskin and Warren, 1991). However, compositional variability can be introduced from selective volatilisation or condensation, reduction of Fe into Fe^0, and adhering of regolith or other materials during impact processing. Given that analytical precision was sacrificed for sample conservation, through analysis of unpolished impact spherules, surficial inconsistencies would contribute to degrading the inter-element correlations. The result may be overestimated major element match probabilities.

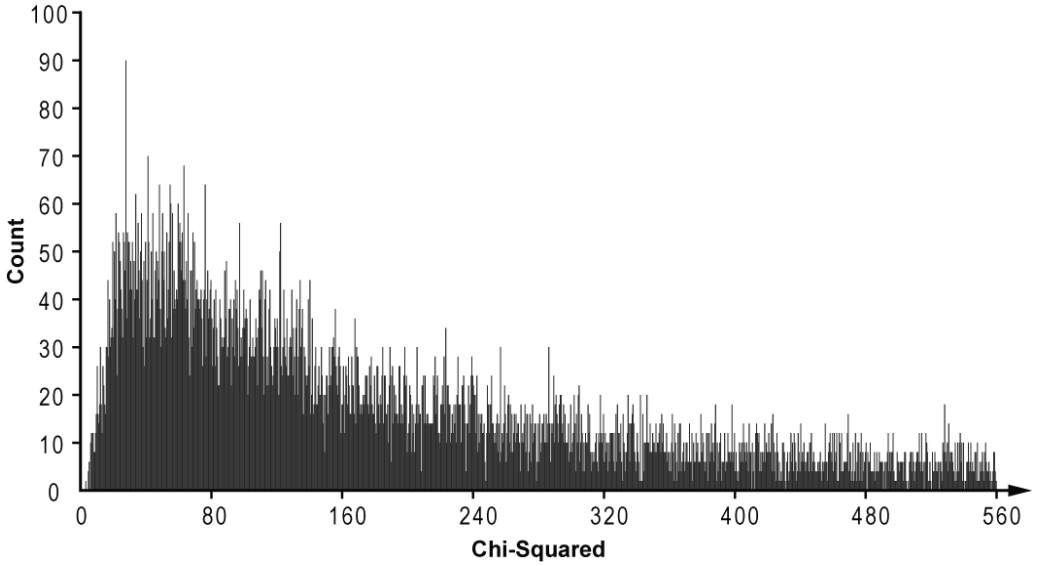

Figure 64. Distribution of impact spherule pairs as a function of chi-squared if major and trace elements are combined into one chi-squared value. Chi-squared values are a qualitative measure of degree of similarity of compositions. The shape of this histogram reflects the compositional dispersion in the impact spherule population. There are few spherules with low chi-squared values ("very similar"), but there are a range of spherules with increasingly dissimilar compositions. See text for a more detailed description of this histogram.

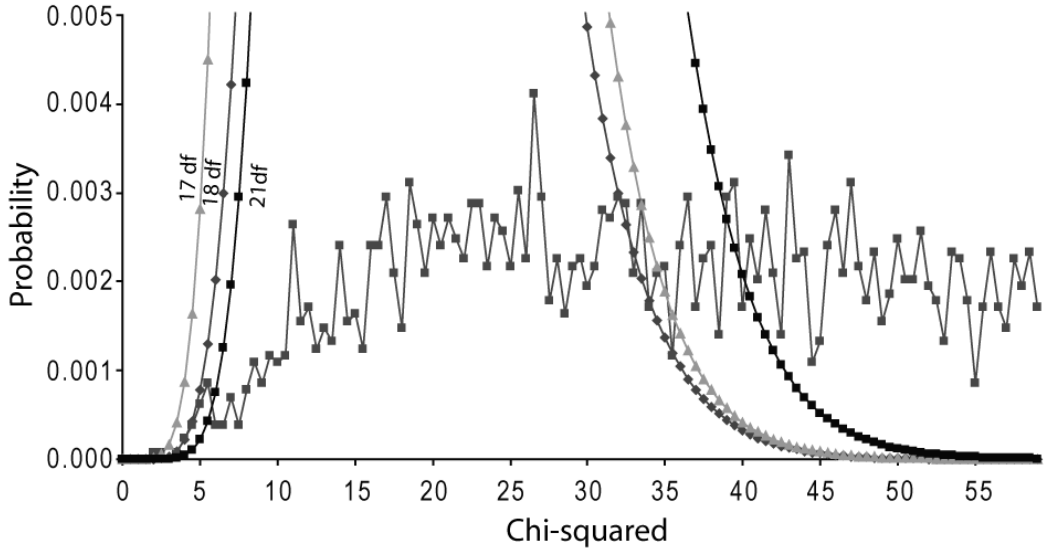

Figure 65. Distribution of impact spherule pairs observed in Figure 64 compared with the chi-squared probability density functions using 17, 18, and 21 degrees of freedom. The effective degrees of freedom are taken as 18, since values >18 overshoot the beginning of the impact spherule distribution and values <18 begin too early.

Candidate Soils

The candidate soils are the selection of soil compositions that will be compared with impact spherule compositions using the chi-squared statistical analysis. Ideally, a wide variety of lunar soils should be considered in this numerical model. However, only a small percentage of the lunar surface has been directly sampled. Wider coverage of lunar surface soil composition is available with remotely sensed data from the Lunar Prospector which provide some constraints on the spatial variation in bulk regolith compositions to ~ 20cm depth (Prettyman et al., 2006). However, the spatial resolution is limited to a minimum raster size (i.e. resolution) of ~150km (Prettyman et al., 2006). Thus, smaller scale variations, such as those within the scale of a landing site, are unresolvable. Therefore, only returned samples can be used to determine whether it is possible to produce the current diversity of impact spherule compositions from the local soils. The mean soil compositions used in this analysis are summarised in Lucey et al. (2006) and include a selection of soils typical and more atypical (e.g.

immature soil from North Ray Crater) of the Apollo 16 regolith. In addition, the mean soil compositions from other Apollo and Luna missions (see Figure 44 for geographical distribution) from Lucey et al. (2006) and a feldspathic highlands candidate (see Korotev et al., 2003 for composition) were also be included in the analysis. However, the variability of all these candidate soil compositions has not been constrained (see Lucey et al., 2006 for discussion). The Lunar Sourcebook (Haskin and Warren, 1991) presents a more comprehensive and more statistically oriented compositional dataset of lunar materials. However, selective removal of key data or missing values renders this dataset largely unusable for this purpose. Note that the variability (expressed as 1σ standard deviation) of each element is an essential value in Equation 8, and it was necessary to specify an uncertainty, either zero or a percentage of the mean abundance. Only impact spherules with compositions within 2σ analytical uncertainties of a candidate will register with statistically significant matching probabilities (i.e. >5%) if the candidate has zero variability. The effect of increasing variability in the candidate composition is a reduction of the chi-squared value and an increase of matching probability as increasingly dissimilar impact spherule compositions are included. The amount of variability needed to account for >95% of impact spherule compositions can be used to evaluate whether the current suite of candidates is representative of the types of targets that have been sampled by impact spherules. The following sections will consider the major and trace element fits separately as these have been acquired by different methods. Trace element/Al ratios have also been used, for reasons previously discussed in 4.3.2 Analytical Accuracy – Unpolished versus Polished Section Analyses. The results are summarised in Figure 66 and described in the following subsections.

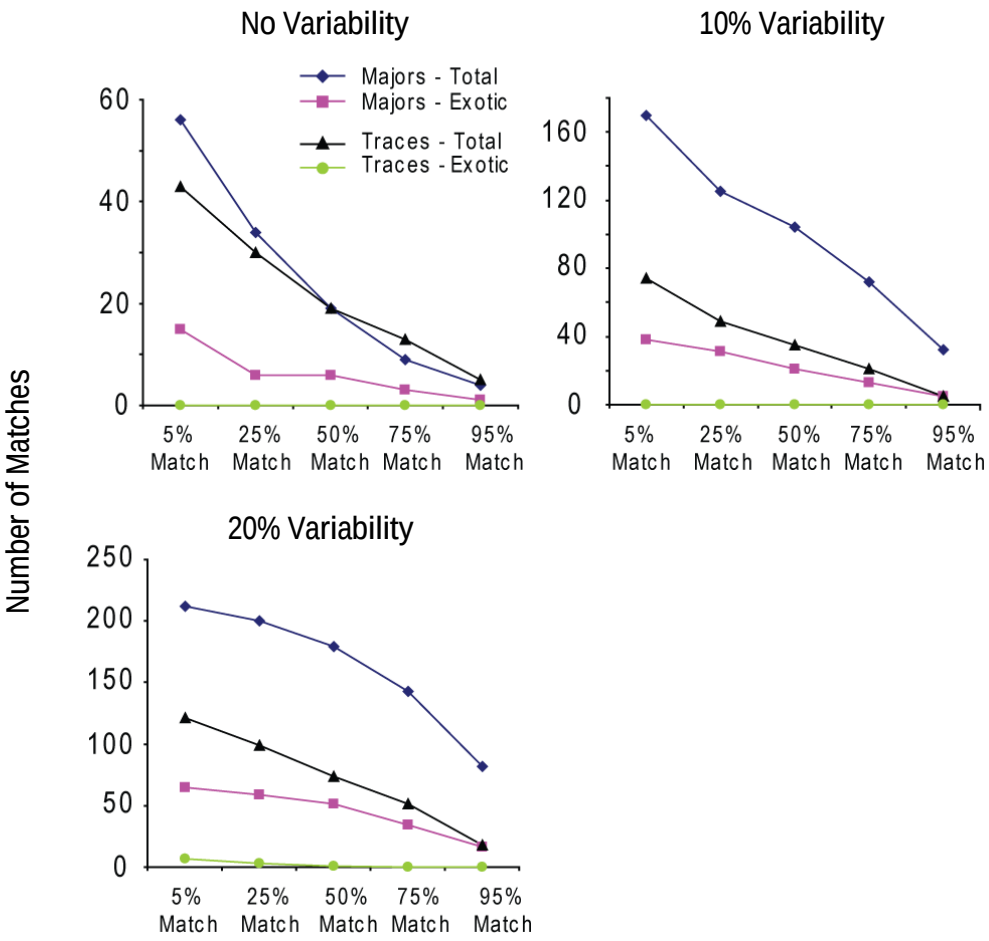

Figure 66. Results of chi-squared goodness of fit tests between lunar impact spherules of this study and candidate soil compositions from Lucey et al. (2006). These plots show the number of impact spherules which overlap in composition with candidate soils as a function of probability. Few impact spherules have a statistically significant probability (P>5%) of overlapping candidate soil compositions. If 10% variability is introduced into the soils (1σ standard deviation set as a percentage of the mean abundance), the number of statistically significant spherule-soil composition overlaps increases. A total of 20% variability in the soils is required for be statistically significant overlap of spherule-soil composition in 212/225 (94%) spherules for major element compositions. For trace element compositions at 20% variability in soils, only 121/159 (76%) statistically significant overlaps are possible. This exercise indicates that the majority of the current impact spherule population could be produced from the limited selection of candidate soils if their compositional variability exceeded 20%.

Major Element Matches

There are 4 impact spherules with major element fits at >95% probability and with zero variability in the candidate composition (leftmost plot in Figure 66). Three of these impact spherules match local soils, with two matching Apollo 16 Station 5 and 6 and one matching the mature Cayley soil. Only one impact spherule is not consistent with the Apollo 16 candidates and matches Luna 20 soils. As the probability of a match decreases, the number of local spherule matches increases in a broadly linear fashion. However, the ratio of local to exotic spherules for major element fits remains consistent at 3-6 local spherules per exotic spherule at all match probabilities. Only three exotic impact spherules are identified with confidence >75%, with two matching Luna 20 soils and the last matching feldspathic lunar meteorites. Spherules that match Luna 20 soils often closely match to Apollo 16 soils, indicating that the spherules often have major element compositions that are similar to those of the Luna 20 and Apollo 16 soils (i.e. are richer in FeO and MgO, and more depleted in Al_2O_3 than the Apollo 16 soils). However, both the Luna 20 and feldspathic lunar meteorite compositions are not necessarily exotic to the Apollo 16 site. Only 56 out of 225 (25%) impact spherules match to any candidate at P>5% (probability of match), indicating that the variability of the candidate compositions is too restrictive.

If the variability of the candidate soils is increased, the number of matches also increases. Thirty-two spherules have >95% probability of matching a soil candidate with a 1σ variability equal to 10% of the mean abundance. Note that these 32 impact spherules include the 4 impact spherules that match the candidate soils with no soil variability, so an additional 28 impact spherules have a composition similar to soil candidates. Of these 28 impact spherules, 24 are derived from local soils with 7 matching mature Cayley soils, 10 matching Stations 5 and 6 soils, 5 matching soil from Station 1, and 5 matching the more immature feldspathic soils present at North Ray Crater. Of the four exotic spherules, two match Luna 20 soils, one match the feldspathic lunar meteorite candidate, and the last match Apollo 15 Station 6 soils which comprise mafic KREEP lithologies. A total of 170 out of 225 (76%) impact spherules now match to any candidate at P>5%.

If the candidate soil variability is increased to 20% of the mean abundance, a total of 82 impact spherules (i.e. an additional 50 impact spherules) can be considered to be the same (i.e. P>95%) as the soil candidates within 20% variability. The additional 11 exotic spherules mostly match Luna 20 (6), however, the remaining exotic spherules match to a diverse number of candidates. Two match mare-poor soils from the South Massif of the Apollo 17 site (~6% mare Korotev and Kremser, 1992) and one matches each of Apollo 12 soil, typical Apollo 14 soil, and feldspathic lunar meteorites. Given that 225 impact spherules were analysed for major element composition, these 82 impact spherules make up ~36% of the total population. Reducing the match probability to P>50% increases the number of matches to 179 out of 225 (~80%), and reduction of the match probability to >5% increases the number of matches to 212 out of 225 (94%). This result suggests that soil variability of ~20% of the mean abundance is required to produce close to all the impact spherules using only the current suite of candidate soils. The 13 remaining impact spherules with probability <5% are significantly different to be considered as poorly represented by the selection of candidates. At these conditions (P>5% and 20% variability) a significant majority (147 out of 212: 70%) of the impact spherules in this project are of local origin, with most matching the mature Cayley soils (40) and Station 5 and 6 soils (63), with a roughly equal distribution among the other Apollo 16 soils. The remaining 30% (65) impact spherules match exotic soil candidates, in particular Luna 20 (37), Apollo 17 South Massif mare-poor soils (12), and feldspathic lunar meteorite (8) candidates.

Trace Element Matches

Five impact spherules have trace element compositions that match a candidate soil at >95% probability with no soil variability. All are consistent with Apollo 16 soils. As the probability of match decreases, the number of impact spherules with trace element compositions most similar to Apollo 16 candidates increases. At 5% match probability there are 43 matches, again all locally-derived. The matches are fairly evenly distributed with 10-11 matches each to mature Cayley soil, Station 1, and immature North Ray Crater soils. Interestingly, soils from Stations 4, and 5 and 6 at the southern end of the landing site only have 6 matches each despite being in close proximity or within the

collection site. The lack of matches to the Station 5 & 6 candidate soil could indicate that either the candidate is a poor representative of the soils or that many impact spherules have not originated from soils near the site of collection. However, it is also possible that the lack of variability in the candidates has limited the number of matches. If candidate soil variability at the 1σ level is set at 10% of the mean abundance, there are no additional matches at P>95%. However, at >5% probability the number of matches almost doubles to 74. This can be improved further by increasing the variability in candidate compositions to 20% of the mean abundance. At P>95% there are 18 out of 159 (11%) potential matches, and with a lower match probability of >5%, a total of 121 out of 159 (76%) potential matches. The consistently low number of matches at P>95% indicates that very few impact spherules have a trace element composition that is the same as one of the candidate soils, but as probability decreases the number of matches increases in a linear fashion.

Of the 121 matches at variability at 20% and P>5%, 114 match best to Apollo 16 soil candidates, with the remaining best 7 matching to candidates with compositions exotic to the Apollo 16 site. There are 29 impact spherules that match best with the typical mature Cayley soil candidate, 27 that match the Stone Mountain (Station 4) soil candidate, 24 that match Station 1 soils, and 16 that match immature North Ray Crater soils. Only 18 out of 123 (15%) locally-matched impact spherules have compositions similar to soils at the collection site (Station 5 & 6 candidate). This result indicates that the lack of impact spherules that match to the Station 5 & 6 candidate is not a result of a lack of variability in the candidate compositions. According to Ulrich (1981), the Station 6 region may have accumulated a thick layer of Descartes material from mass wasting (slumping) of Stone Mountain. Additionally, Station 6 is located on the edge of a ray from South Ray Crater that has contributed material to the site. Both these possibilities appear to be reflected in the chi-squared fits as numerous matches to the typical mature Cayley soil (i.e. ejecta from South Ray Crater) and Stone Mountain soil candidates. However, given that the samples in this project were collected from the rim of an unnamed 10m wide crater, it is possible that the sample is heavily biased toward the local crater ejecta. Of the 7 exotic matches, four match best to the Luna 20 soil

candidate and the mare-poor Apollo 17 South Massif soil candidate, Apollo 15 Apennine Front, and Apollo 11 soil candidate all have one match each. Impact spherules that match the Luna 20 candidate have lower REE abundances, whereas the Apollo 11 and 15 matches are KREEPy. The scarcity of impact spherules with chemistry exotic to the Apollo 16 site indicates that, although transport of spherules within hundred kilometre scales (within Apollo 16-like soils) occurs routinely, transport of spherules from distances of hundreds of kilometres is more uncommon. The remaining 38 (25%) impact spherules have poor matches to any candidate soil may be impact spherules formed from materials other than soil (e.g. rocks) or of a soil composition not represented by the candidates.

Integrated Major and Trace Element Matches

In this section impact spherules analysed with both major and trace element data will be compared to determine the consistency of the separate chi-squared fits. The major and trace element chi-squared fits could have been combined to form a new chi-squared value, although this approach is biased, as there are more trace element variables than major element variables. Instead, the consistency between best major and trace element matches of each impact spherule will be compared. Three types of results will be considered: the first is an exact agreement where both the major and trace element fits agree on a specific soil candidate. The second is a site agreement and occurs when the major and trace element fits disagree on a candidate, but agree on a broader region (e.g. within an Apollo site). The last is a mismatch when the major and trace element fits disagree on a candidate and can occur if impact spherules are derived from materials such as rocks (e.g. anorthosites), breccias or soils different in composition to the candidate soils. Impact events that form these impact spherules are likely to be small as larger impact events are increasingly more likely to sample “bulk” regolith. Note that there are only 145 possible matches since the trace element fits determined that 16 impact spherules are sufficiently dissimilar to the candidate soils.

At >95% probability and with no soil variability, there are no exact agreements and only one site agreement. The site agreement is consistent with the Apollo 16 soil candidates. At lower matching probabilities, the number of impact spherules with site agreements increases (15 at P>5%) and two of these are exact agreements. At this match probability, there is also one mismatch between the major and trace element fits. This mismatch occurs when the major element suggests the Luna 20 candidate whereas the trace element suggests an Apollo 16 candidate. However, as previously stated, materials with Luna 20-like (highland basalt) compositions are also present at Apollo 16. At >95% probability and with 1σ variability of the candidate composition increased to 10% of the mean abundance there are no additional impact spherules that can be compared. However, at lower probability limits (>5%) there are 13 exact agreements, 48 site agreements, and 5 mismatches. In total, there are 66 out of 159 (41.5%) agreements possible and as previous sections have already indicated, this level of variability is too restrictive. If the 1σ variability of the candidate compositions is increased to 20% of the mean abundance and impact spherules with probability >5% are considered, there are 115 out of 159 (72%) agreements.

Under these conditions there are 28 exact agreements, 68 site agreements, and 19 mismatches. The exact agreements include 11 impact spherules with compositions similar to the collection site (Station 5& 6) soils, and six impact spherules each with compositions similar to the typical mature Cayley soil and five matches to the immature North Ray Crater soil candidates. There are only three impact spherules with compositions similar to the Stone Mountain candidate and two from Station 1 soils. There is also one impact spherule with an exact match to the Luna 20 candidate. The site agreements consist entirely of matches to the Apollo 16 soil candidates. The significant number of impact spherules with Apollo 16 site agreements is disconcerting and indicates that resolving impacts in different locations within the Apollo 16 site (~12km^2) is difficult. However, the variability in major element compositions of impact spherule is often more than the differences between compositions of the Apollo 16 candidates. Thus, the major element fits may not identify the correct candidate. Part of

the problem also lies with the poorly-constrained spatial and compositional variation of the candidate soils.

There are 19 mismatches between major and trace element fits. Thirteen of these occur between a major element fit to Luna 20 and a trace element fit to an Apollo 16 soil or vice versa. As previously stated, many impact spherules have compositions that straddle between that of the Apollo 16 and Luna 20 candidates. Thus, it is feasible that mismatches between these candidates are actually not significant. Two mismatches involve the Apollo 16 soil candidates and the feldspathic lunar meteorite candidate which, without the Na and K variables in the major element fits, are difficult to discern from the Apollo 16 soils. That leaves four impact spherules that have mismatches that indicate that either they may be a composition that is either a result of mixing of different soil components, is a soil not represented by the candidates, or derived from a target that is not a soil. It is also possible that the impact spherules have an outer layer different in composition to the inner "bulk" spherule. Given the analytical technique employed in this study, the signal from the outer layers would have been removed for the trace elements, but not for major element analyses therefore resulting in a mismatch between the major and trace element fits.

Summary

The chi-squared fits in the previous sections have provided information about the impact spherules and the potential source materials from which they were created. One of the greatest problems with approach is the lack of wider spatial and compositional constraints on the candidate soils. However, this problem can be approached in a different way by asking this question: How much variability in the candidate compositions is necessary to account for >95% of all impact spherule compositions at statistically significant probabilities (>5%) assuming they can only be produced from the current selection of soils? If the percentage of variability were low (a few percent), the impact spherules would be well represented by the suite of candidates. Higher variability indicates increasing dissimilarity between the selection of soils and that other

soils with different compositions may have contributed to forming the current population of impact spherules.

The results of this analysis are tabulated in Table 8. For the major element, about 20% variability (expressed as 1σ standard deviation of the mean) is needed to account for 95% of the impact spherule population. Trace elements, however, require at least 40% variability. Such high variability is required because a number (~20%) of the impact spherule population is not well represented by the candidate soils, although ~75% of the impact spherules in this study can be produced from the suite of candidate soils if variability is on the order of 20%. At these percentages it becomes difficult to discern between different sampling points within a landing site which would explain the number of Apollo 16 site agreements. However, it is still possible to discriminate among soils from the different Apollo landing sites. This suggests that the impact spherules are sampling regional targets with compositions broader than that of the Apollo 16 landing site if the landing site is well represented by the suite of candidates. However, it is difficult to ascertain how representative the current suite of candidates is without more constraints.

Table 8. Tabulated results of the chi-squared statistical analysis showing the percentage of the spherule population that match to a soil composition at select soil variability and probability of overlap in spherule and soil compositions.

Major Elements

Soil Variability	Probability of Overlap 5%	25%	50%	75%	95%
0%	25%	15%	8%	4%	2%
10%	76%	56%	46%	32%	14%
20%	94%	89%	80%	64%	36%
30%	99%	97%	93%	88%	63%
40%	100%	99%	95%	55%	84%
50%	100%	100%	99%	97%	92%

Trace Elements

Soil Variability	Probability of Overlap 5%	25%	50%	75%	95%
0%	27%	19%	12%	8%	3%
10%	47%	31%	22%	13%	3%
20%	76%	62%	47%	32%	11%
30%	91%	85%	75%	59%	32%
40%	94%	93%	88%	81%	58%
50%	96%	94%	93%	91%	75%

Both Na and K introduce the most variability in this numerical model. Removing these elements from the major element fit improves the probabilities of match significantly for many impact spherules. However, doing so reduces the effectiveness of the major element fits thus leading to several possible mismatches between impact spherules and the Apollo 16 soils, and feldspathic lunar meteorite candidates. In this case, the trace elements are probably a more reliable discriminant between the Apollo 16 local soils and feldspathic lunar meteorite. If so, the trace element fits suggest that the majority of impact spherules were not derived from surficial soils collected at the same site where the impact spherules were collected (Station 6). The typical Cayley soil and those of Station 4 closer to Stone Mountain, rank most highly in the trace element fits indicating that these local spherules may have formed during the South Ray Crater event or from mass wasting from Stone Mountain, respectively given these rankings. However, the collection site is located near a 10m crater and possibly samples an impact spherule population that is an unearthed mixture of various populations from different sources that have been added to the site from different time periods. In the following chapter, another piece of vital information that has been collected during this project will be introduced and can shed light on the uncertainties mentioned in this chapter.

The controversial question of whether impact spherules originate from rocks or soils remains unanswered. The chi-squared modelling of this project indicate that the selection of Apollo and Luna soils, and the feldspathic meteorite composition cannot produce the current impact spherule population without increased soil variability. This variability may be introduced in large impacts that sample a mixture of soils/lithologies, or perhaps the selection of soils simply does not fully represent the variability of soils that produced the impact spherules. The diagnostic trace element ratios, however, indicate that some impact spherules could be rocks. If anything, it is likely that spherules are produced from both rocks and soils, although it is unclear if one source is more dominant than the other. As arguments in Hörz et al. (2000) emphasise, the proportion of impact spherules produced from rocks versus soils may have changed over the history of the Moon.

4.4.3 Impact Spherule Chemistry and Relations to Petrography

Impact Spherule Chemistry and Colour

A number of previous studies have indicated that it is possible that impact spherule composition has an effect on the spherule colour and thus, may be used as a preliminary indicator of impact spherule provenance (See Chao et al., 1972; Chao et al., 1970; Naney et al., 1976). Colour can be affected by a number of factors including ambient light levels, sample thickness, vesicles, and crystal structure. The impact spherule population can be split into two predominant groups: The light-coloured spherules consisting mostly of clear and green spherules and the dark spherules consisting of black-coloured and hybrid spherules. The orange/yellow-coloured spherules can be considered a third, but minor group.

Table 9 presents the average major element composition of unpolished impact spherules subdivided into colour groups. All colour groups do not differ dramatically from each other for major element compositions with the possible exception of the yellow/orange group. This group has relatively higher average FeO, TiO_2, MgO and K_2O abundances, and lower CaO and Al_2O_3 abundances. However, there is only one impact spherule (LS7-65) in this group that is consistent with a mare provenance. Using principal component analysis (PCA) and cluster analysis, it may be possible to determine if there is a relationship between major element composition and colour variation. The following PCA and cluster analysis was conducted using StatistiXL (Roberts and Withers, 2007), a statistical add-on for Microsoft Excel. Figure 67 is a PCA plot of spherule major element chemistry and colour using a correlation matrix. There are broadly three vectors representing a refractory component (Al_2O_3, CaO), mafic component (MgO, FeO) and volatile component (Na_2O, K_2O). Of less statistical significance are the TiO_2, Cr_2O_3 and SiO_2 contents. The chemical variance is described using two principal components in Figure 67. Factor 1 (x-axis) is most strongly controlled by Al_2O_3 versus FeO and MgO abundance, which are diagnostic elements for determining the ratio of plagioclase (highlands) to pyroxene and olivine (mare). A smaller contribution to the x-axis variance is produced by CaO versus TiO_2 and Cr_2O_3.

Table 9. Average major element composition of colour groups of 225 unpolished lunar impact spherules analysed by electron microprobe. Data are presented as weight percent oxides in the form mean ± one standard deviation. Colours were determined during sample preparation prior to analysis.

	Black (102)	Clear (45)	Green (44)	Hybrid (20)	Yellow/Orange (14)
FeO	7.21 ± 3.01	5.32 ± 1.77	6.26 ± 1.92	6.09 ± 3.16	9.30 ± 3.80
Na_2O	0.59 ± 0.67	0.57 ± 0.64	0.49 ± 0.52	0.54 ± 0.68	0.76 ± 0.76
TiO_2	0.64 ± 0.42	0.54 ± 0.21	0.57 ± 0.33	0.49 ± 0.18	0.99 ± 0.70
CaO	13.58 ± 1.70	15.39 ± 1.88	15.08 ± 1.71	14.31 ± 2.26	12.62 ± 2.46
Al_2O_3	24.68 ± 3.33	27.80 ± 4.10	27.46 ± 3.62	26.26 ± 2.84	22.19 ± 5.70
SiO_2	46.07 ± 2.30	43.32 ± 4.33	42.96 ± 3.05	46.03 ± 2.76	45.16 ± 4.11
MgO	6.85 ± 2.38	6.76 ± 1.88	6.93 ± 1.86	5.96 ± 1.97	8.28 ± 2.18
K_2O	0.18 ± 0.19	0.16 ± 0.24	0.10 ± 0.11	0.14 ± 0.11	0.45 ± 0.94
Cr_2O_3	0.15 ± 0.09	0.11 ± 0.07	0.12 ± 0.07	0.13 ± 0.07	0.18 ± 0.10

Factor 2 (y-axis) is most strongly controlled by Na_2O, K_2O and SiO_2 versus CaO and Al_2O_3 contents, which could represent either volatile versus refractory components or sodic versus calcic plagioclase. However, given that a volatile-rich crust was identified on the unpolished surfaces of the impact spherules, it is likely that the y-axis represents a volatile versus refractory component. Only a total of 58.9% of the variance can be explained using two principal components indicating that such an approach is oversimplified. At least six components are needed to describe 93.8% of all variance; TiO_2, Cr_2O_3 and SiO_2 contents being the least important. Naney et al. (1976) who undertook a similar exercise, were able to account for 90-95% of all variance using Al, K, and Ti. The likely explanation of the discrepancy between the results of Naney et al. (1976) and those of the current study relate to the use of unpolished impact spherule data in this project, which are susceptible to crustal and geometric interferences.

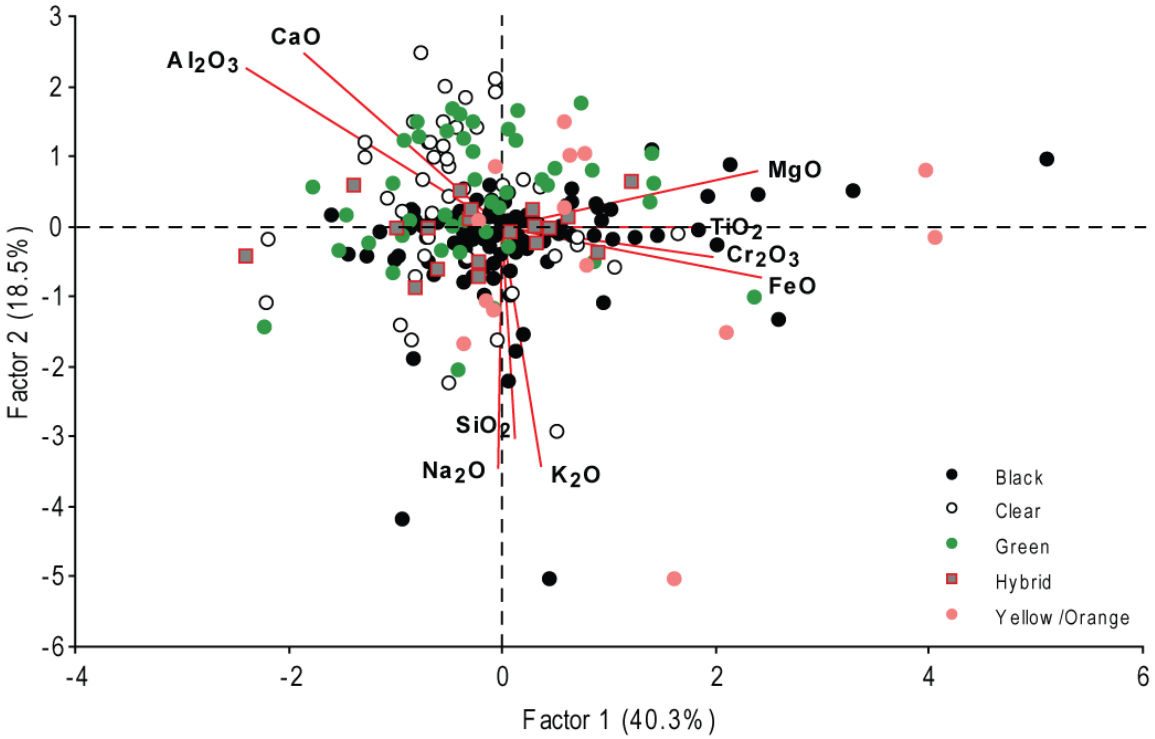

Figure 67. Principal component analysis of major element composition and colour of 225 unpolished lunar impact spherules. This analysis simplifies the data into two components (brackets show the % variance that can be described by each factor) in an attempt to identify the key factors that affect colour. A refractory component (Al_2O_3, CaO), mafic component (MgO,TiO_2,Cr_2O_3, FeO) and volatile component (Na_2O, SiO_2, K_2O) form three compositional vectors. However, only a total of 58.9% of the variance in spherule compositions can be explained using two components. See text for a detail description of the principal components.

Another approach is to establish compositional groups by dissimilarity in major element chemistry using cluster analysis. Figure 68 shows the results of the cluster analysis using Euclidean distance as a measure of difference and with the furthest neighbour method. This method effectively highlights the outlying groups which are most dissimilar to the spherule population as a whole and identifies them as a group. Overlaying these groups onto the PCA plot illustrates the colour and chemical tendencies of the major groups (Figure 69). The major element compositions of each group are presented in Table 10.

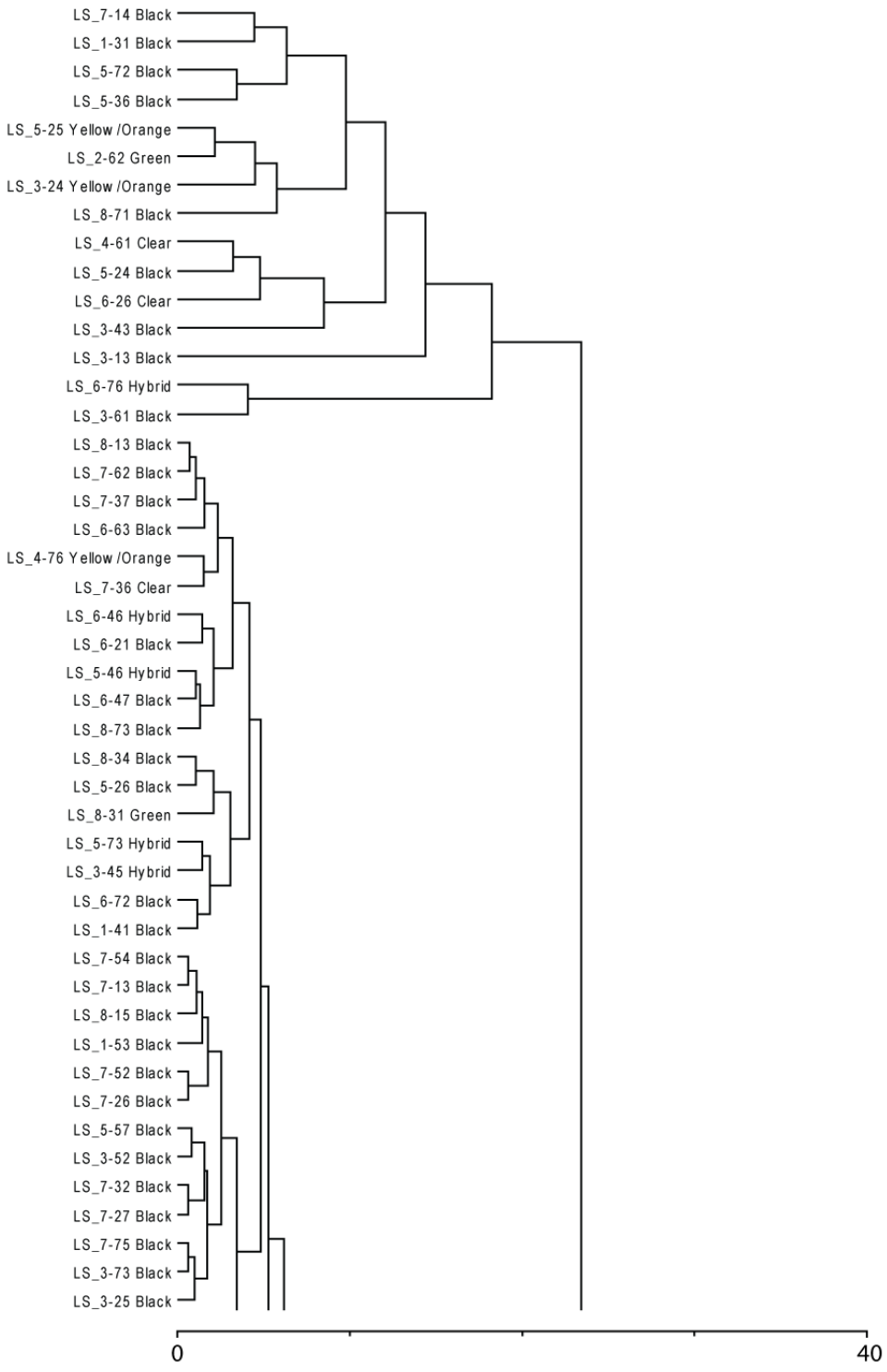

Figure 68. Results of cluster analysis (Euclidean distance is employed as a measure of difference with the furthest neighbour method) using major element compositions of 225 impact spherules. The composition of the five broadest groupings are presented in Table 10 and discussed in the following text.

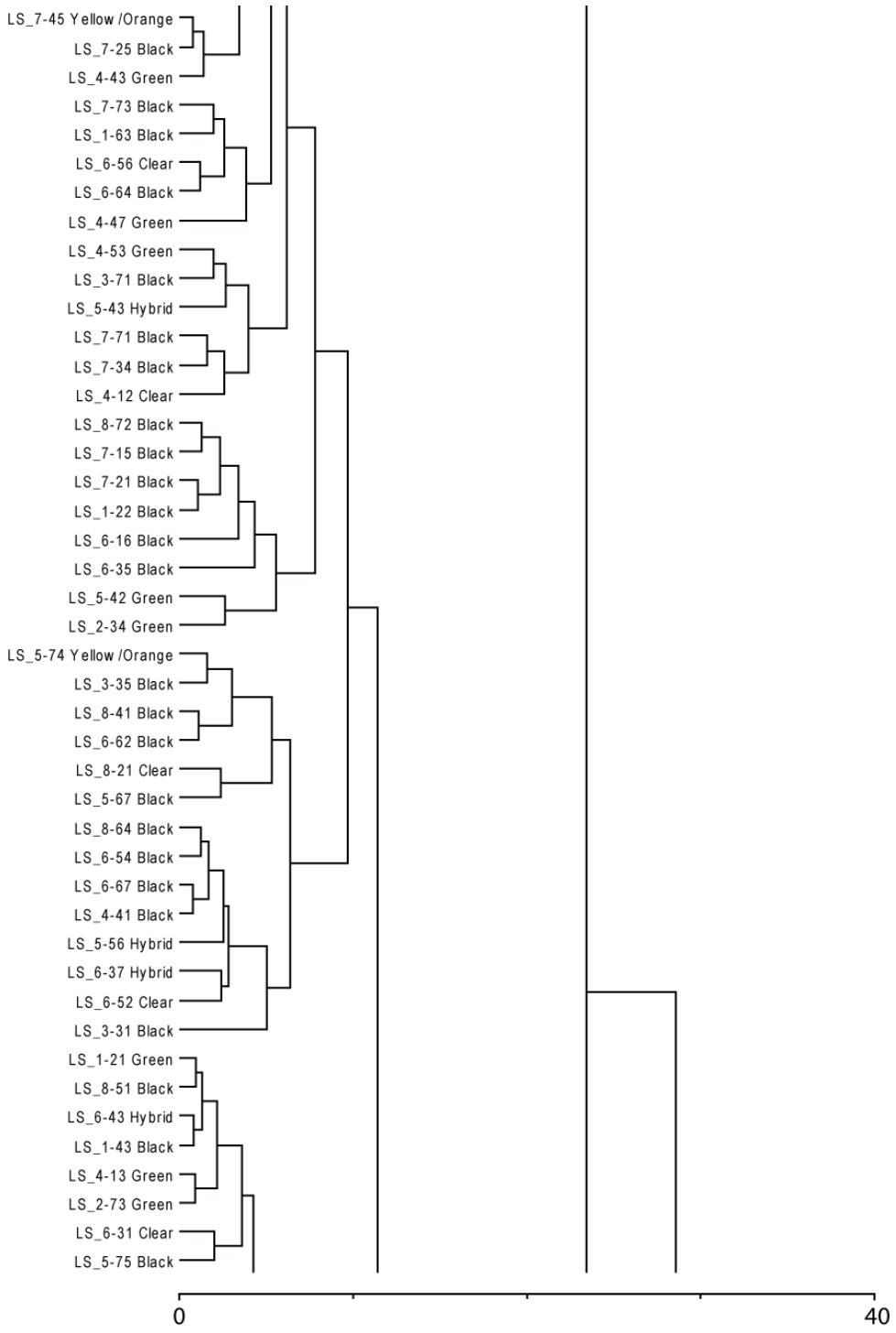

Figure 68. Continued

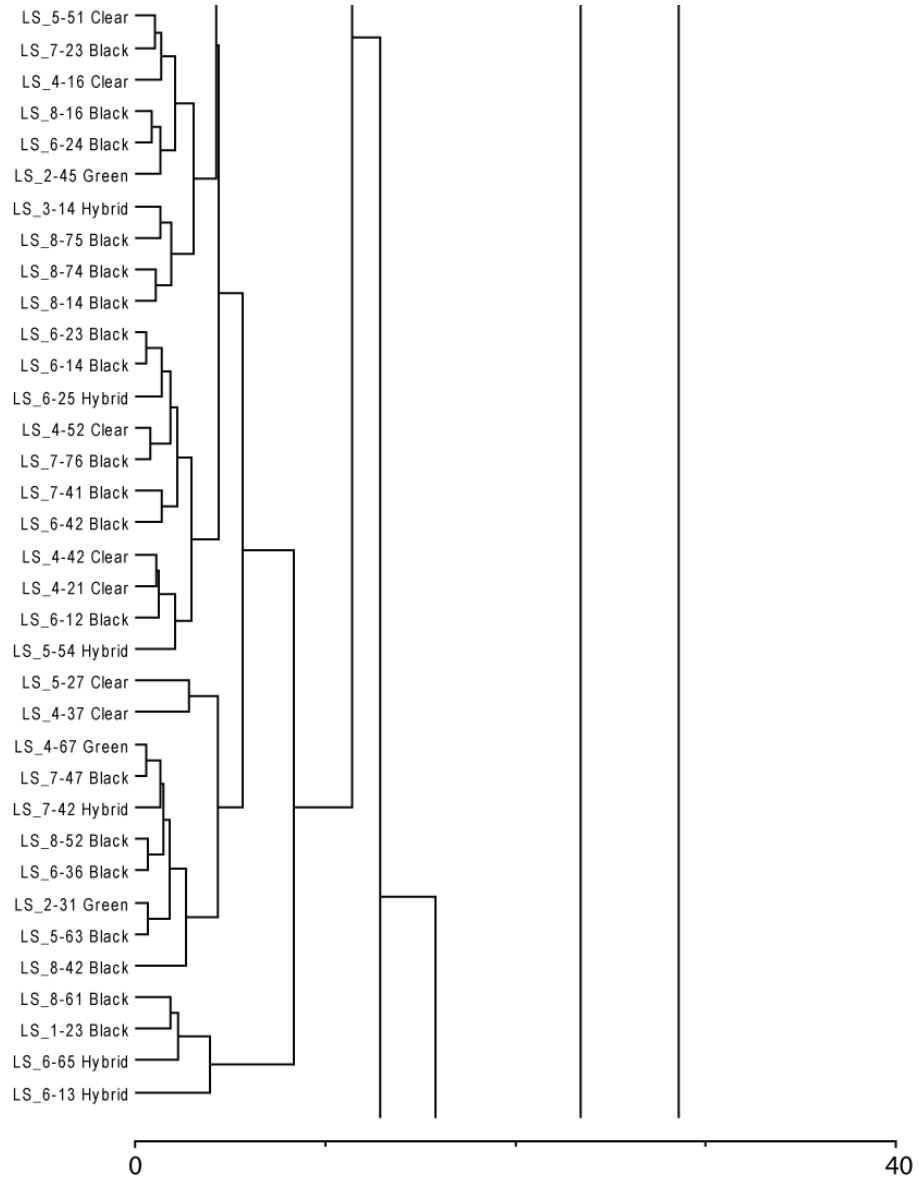

Figure 68. Continued

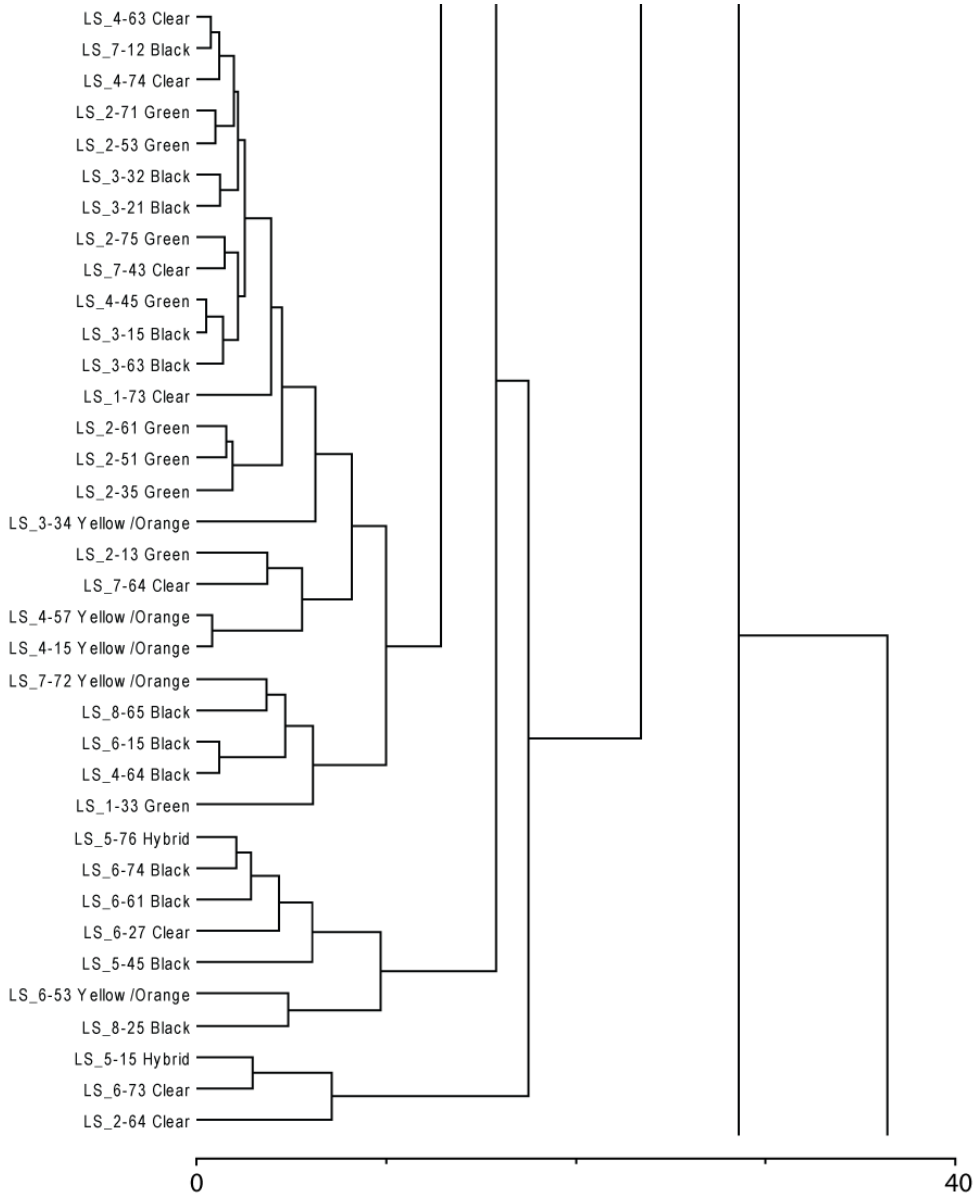

Figure 68. Continued

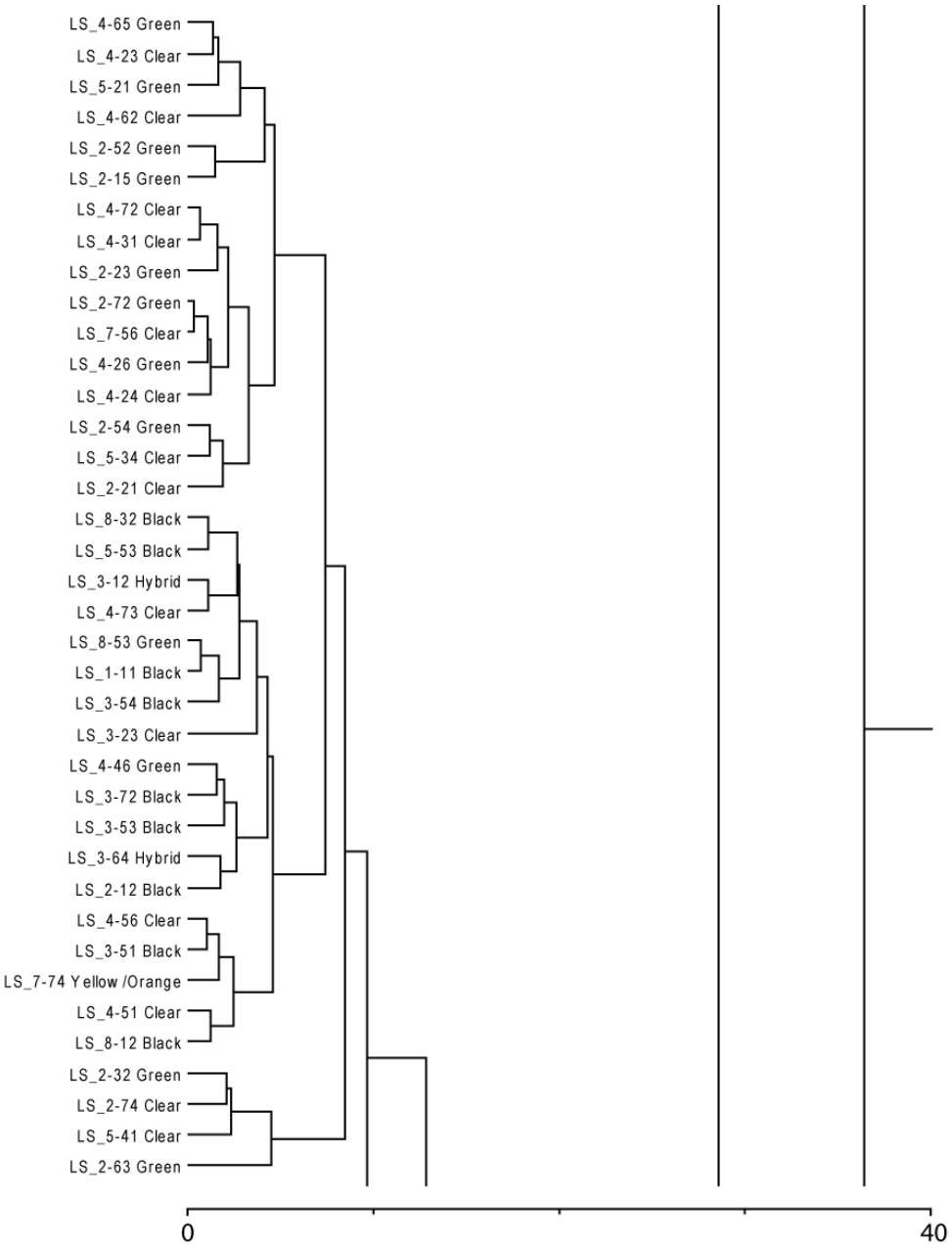

Figure 68. Continued

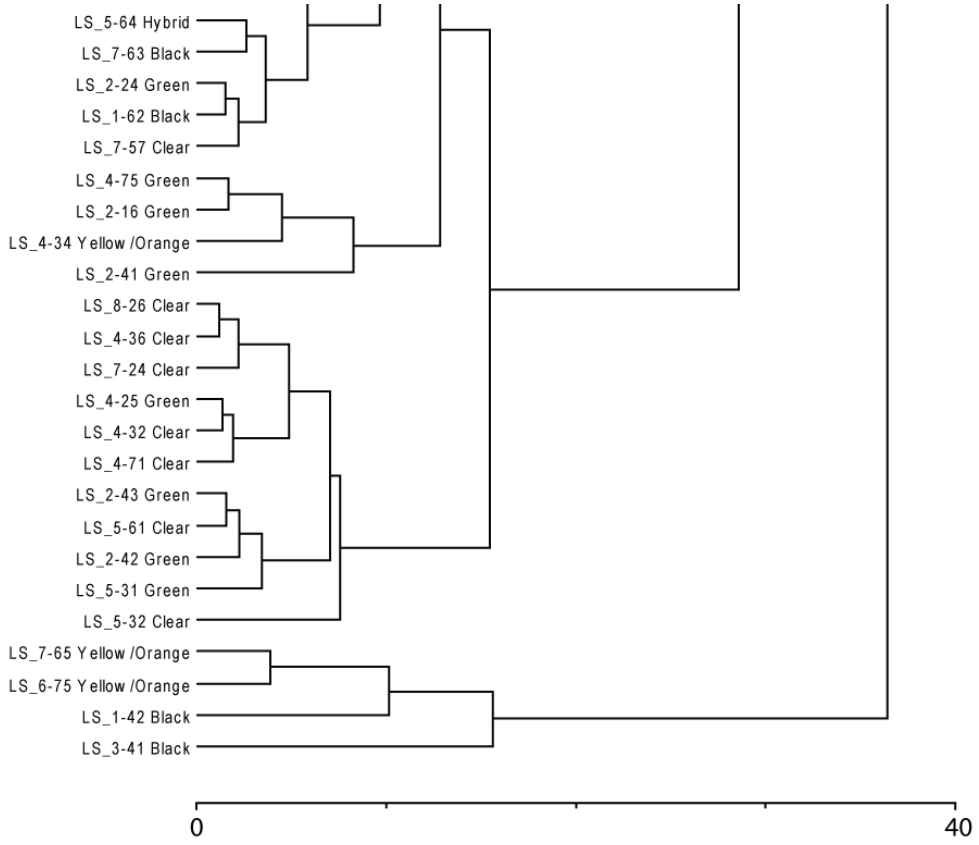

Figure 68. Continued

Table 10. Major element compositions of 225 lunar impact spherules arranged into groups of dissimilarity using cluster analysis. See text for description and comparison of each group to other impact glasses from the literature. Data are presented as weight percent oxides in the form mean ± one standard deviation.

	Group 1 (4)	Group 2 (59)	Group 3 (15)	Group 4 (3)	Group 5 (144)
FeO	19.18 ± 3.84	5.39 ± 1.41	11.37 ± 3.38	1.69 ± 0.21	6.46 ± 1.65
Na_2O	1.88 ± 2.48	0.35 ± 0.49	0.67 ± 0.45	0.66 ± 0.50	0.63 ± 0.57
TiO_2	1.01 ± 0.99	0.52 ± 0.17	1.30 ± 0.94	0.11 ± 0.03	0.57 ± 0.22
CaO	9.91 ± 1.82	16.28 ± 1.47	12.29 ± 2.48	16.87 ± 0.47	13.66 ± 1.40
Al_2O_3	13.73 ± 1.59	29.98 ± 1.84	17.94 ± 2.75	30.34 ± 2.95	25.24 ± 2.12
SiO_2	42.12 ± 4.52	41.16 ± 2.83	45.87 ± 3.68	48.35 ± 2.09	46.31 ± 2.18
MgO	11.19 ± 4.35	6.12 ± 1.57	9.80 ± 3.05	1.86 ± 0.55	6.76 ± 1.67
K_2O	0.49 ± 0.82	0.08 ± 0.10	0.51 ± 0.90	0.08 ± 0.04	0.19 ± 0.24
Cr_2O_3	0.35 ± 0.14	0.09 ± 0.06	0.21 ± 0.08	0.04 ± 0.01	0.14 ± 0.08

Group I spherules are most dissimilar to the other spherules and trend heavily toward most mafic compositions. There are 2 black and yellow/orange spherules in this group only one of which has a mare provenance (see Figure 60). The remaining three, however, are locally-derived according to CaO/Al_2O_3 ratios and REE patterns, but exhibit Fe-rich compositions suggesting that Fe may have been overestimated due to metallic beads on the surface. Group II, on the other hand, exhibit more refractory compositions that plot along the Al and Ca vectors. Spherules in this group are dominantly clear or green (35% each) with a small proportion of black spherules (10%). Group III plot along the mafic vectors and, according to major element provenance, contain three impact spherules of mare provenance with most of the rest being of mixed highlands-mare provenance. From REE patterns, three of these impact spherules are also KREEPy. About 60% of Group III consists of black spherules with the remaining colours making up approximately equal proportions of the remaining 40%. Group IV spherules plot away from the other groups and are found between the volatile and refractory vectors. These spherules tend to be quite felsic in composition and consists of 2 clear spherules and 1 hybrid. Group V makes up the largest portion of impact spherules that tend to cluster in the middle and extend toward the other components. Although it is possible to break up Group V into smaller subdivisions, little additional information can be gained. Colour-wise, 50% of the spherules are black with the remaining colours making up equal proportions of the remaining 50%. Groups I and III broadly consist of mare, KREEP, and mixed mare-highlands whereas Groups II and IV consist of more feldspathic components typical of the local soils, in particular North Ray Crater soils, or more broadly, the Descartes Mountains (see Norman, 1981).

Figure 67 and Figure 68 indicate that green and clear spherules (Groups II and IV) trend towards the feldspathic highlands component. Impact spherules of both colours are not distinct in major element composition making the distinction between these colours unclear. Figure 49 indicates that the green colours tend to be more abundant in larger spherules, the opposite being true for clear/transparent spherules. The presence of large clear spherules and small green spherules, however, argues that optical thickness is not a major contributor to the colour difference. A clue to explain the difference between

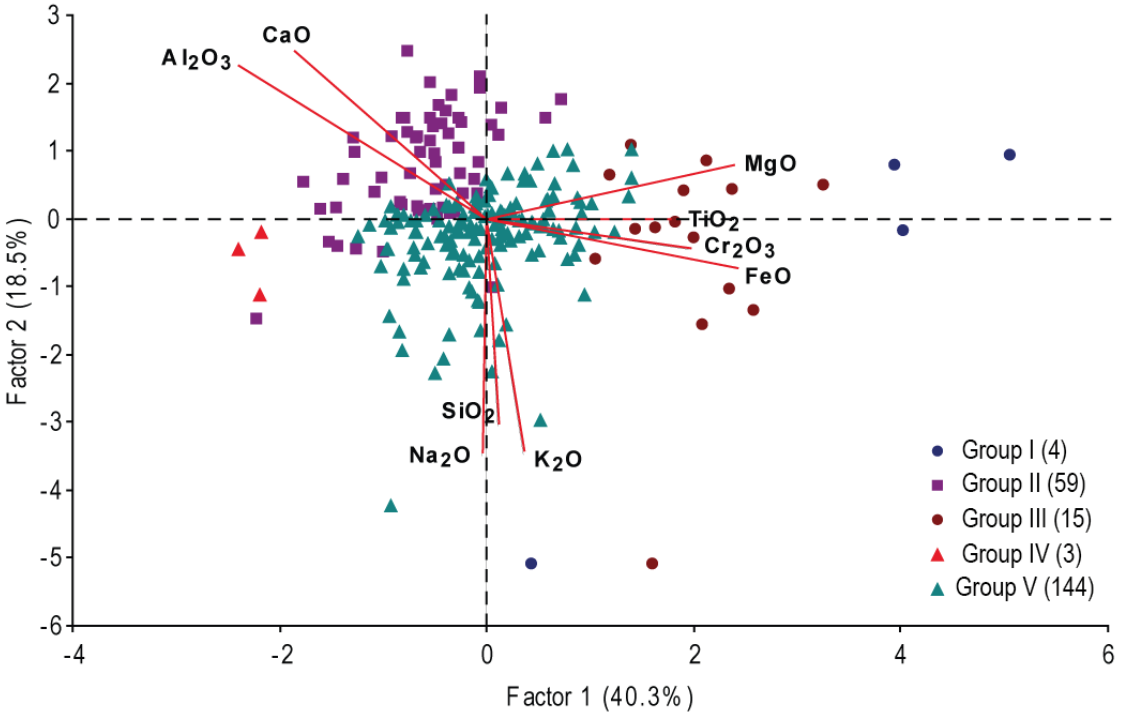

Figure 69. Principal component plot using two components derived from major element composition of lunar impact spherules and groups established using cluster analysis (using Euclidean distance as a measure of difference and with the furthest neighbour method). The higher the group number, the more dissimilar it is to the spherule population as a whole.

clear and green spherules may lie in the work of Naney et al. (1976) who studied the chemistry of glass particles in the Apollo 16 drill core. The Apollo 16 drill core is located near the lunar module and sampled the regolith to a depth of ~2.2m. Naney et al. (1976) noted that, despite a lack of systematic variations in chemistry with depth in the core, green-coloured spherules are more abundant in the upper 1.8m of the Apollo 16 drill core and were typically associated with mare or highly aluminous HASP compositions. Neither mare nor HASP spherules are present in green impact spherules from the current study, which suggests that the difference between the clear and green colours might be a result of exposure, as suggested in Naney et al. (1976). Interestingly, production of glass of "highlands basalt" composition from synthetic materials also fails to produce green glasses (Handwerker et al., 1977). The petrographic features of group

II and IV indicate that they have homogeneous textures, are generally more spherical, smaller in size and are non-magnetic. The aluminous composition of these glasses makes them better glass formers and would likely contribute to the generally homogenous textures. Both the smaller size and generally viscous aluminous compositions will increase the surface tension allowing the formation of highly spherular shapes.

The yellow/orange spherules of Groups I and III tend to have more mafic (Fe, Mg, Ti and Cr) or volatile (Si, Na, and K) compositions (Figure 67). Naney et al. (1976) noted that these colours typically signify impact spherules with exotic compositions (mare and KREEP), in particular the orange colours which have originated from impacts into mare basalts. Meyer and Tsai (1975) have also noted that LKFM glasses with higher Ti contents can be pale yellow. However, CaO/Al_2O_3 ratios indicate that none of the yellow/orange impact spherules are of mare origin. The trace element abundances of three yellow/orange impact spherules, however, are consistent with KREEP compositions in Figure 60. One particle shows some physical damage and vesicles that may change the optical properties of the spherule. Additionally, yellow/orange coloured impact spherules are most common in the <100μm size fraction. It is unclear whether composition, petrographic features, or both contribute to these colours.

The black (opaque) and hybrid spherule colours, typically associated with Group V, do not appear to particularly favour any vector, indicating that their colour may result from something other than chemical composition (e.g. degree of crystallisation or presence of a crust). These impact spherules tend to have heterogeneous textures, are generally more elongate, large in size and magnetic (Figure 51). The generally heterogeneous nature suggests that the impact-melts that formed these spherules contained or acquired unmelted clasts and quenched prior to complete digestion of the particles. This could occur if impact-melt contacted the lunar surface prior to quenching into an impact spherule. Assimilation of the soil may also release implanted solar-wind gases such as H and He. Hydrogen can react with FeO in the glass and convert it to metallic Fe (McKay et al., 1991) and nanophase-Fe^0, which would increase the magnetic properties

of the spherule and darken the colour (Loeffler et al., 2008; Sasaki et al., 2003; Sasaki et al., 2001). The degree of crystallisation may also relate to colour, as is the case for the chemically uniform Apollo 17 black glasses (Arndt and von Engelhardt, 1987; Glass, 1976). This suggestion is supported by the relation between crystallisation textures and opaque/black colours in Figure 51.

Conclusions drawn from both the PCA and cluster analysis are similar: impact spherule colours provide some indication of composition (e.g. green and clear colours are typically feldspathic), but they do not form exclusive groups. It is unclear what produces yellow/orange colours, but it may be a combination of composition and petrography. However, colour is related to a number of other petrographic characteristics which provide some understanding of the conditions in which these impact spherules may have formed. Symes et al. (1998) calculated (based on the Stefan-Boltzmann equation (Equation 9)) that a 200µm sphere of melt with a composition of An_{90} at 1800°K would cool at a rate of ~3300°K/sec by radiation in space, which is sufficient to cause the melt to instantly quench to a glass bead.

$$\frac{dT}{dt} = \frac{6\varepsilon\sigma}{D_p C_p}(T^4 - T_s^4) \quad \textbf{[9]}$$

Where T = Initial temperature

T_s = Ambient temperature (200°K)

D = Spherule diameter (cm)

ρ = Density (g/cm^3)

Cρ = Specific heat of composition at 1800°K (calories/g/K)

σ = Stefan-Boltzmann constant (1.355 x 10^{-12} calories/cm^2/K^4)

ε = Total emissivity (0.7)

For derivation of this formula see Arndt et al. (1979).

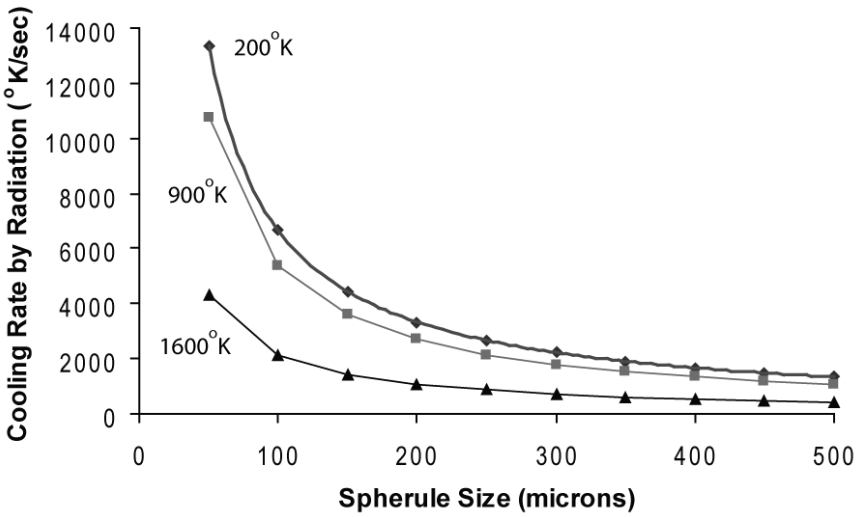

Figure 70. Effect of melt sphere size and ambient temperature on the cooling rate by radiation according to the Stefan-Boltzmann equation (Equation 9). Composition of the melt is An_{90} and melt temperature is 1800ºK.

Based on this equation, there are three key variables that could alter the outcome: impact spherule diameter, ambient temperature, and target composition. As the volume of the melt increases, the cooling by radiation rate decreases. For example, a 500µm sphere of melt would cool by radiation at a rate of 1335°K/sec. A higher ambient temperature brought about by the conversion of energy to heat within the vapour cloud (Melosh, 1989) would reduce the cooling rate as the temperature differential between the melt sphere and the environment would be smaller. The relationship between these two factors is shown in Figure 70 which suggests that melts of <100µm diameters are likely to instantly quench to homogeneous glass. The composition of the target will also affect the cooling rate and tendency for crystallisation. According to Arndt et al. (1979), synthetic melts with the composition of mare basalts crystallise between critical cooling rates of 47-24ºC (i.e. minimum rate of cooling to avoid crystallisation: Uhlmann, 1972) while anorthositic melts did not crystallise at all.

The conditions that would favour the production of the clear and green impact spherules are small melt volumes, anorthositic targets, and large differences between the melt temperature and ambient temperature. Instantaneous quenching in these conditions would prevent crystallisation and the inclusion of clasts. The shapes may be kept

spherical due to the more viscous nature of anorthositic melts. The petrography and chemistry of the clear and green impact spherules supports these observations as they are more abundant in small sizes, are more anorthositic in composition, generally homogeneous, and highly spherical (Figure 51). The splash-like forms and even crystallisation (which requires even lower critical cooling rates) in the black and hybrid impact spherules, on the other hand, would be produced if the melt volume was large, compositions were more mafic, and the difference between ambient and melt temperatures were small. These conditions keep the melt in a liquid state so that they have time to envelop regolith clasts thrown up in the ejecta cloud, partially digest the clasts, distort in shape to elongate and "splash" on targets, and in some cases, crystallise. Crystallised impact spherules would be produced if the melt volume was large and ambient temperature high, thus slowing the rate of cooling by radiation. However, note that quenching may be enhanced if melt envelopes cold clasts which prevents crystallisation. Again the petrography and chemistry of the black and hybrid impact spherules support these observations as they tend to be slightly more mafic, are typically large and non spherical in size and shape, and heterogeneous in internal texture (Figure 51).

Impact Spherule Crusts

Trace element profiles may also provide insight into the other processes affect impact spherule colour. Over 70% of lunar impact spherules observed under the petrographic microscope in this study appear to have an outer layer made up of adhering rock powder and mineral grains. The near-surface of the impact spherules is characterised by enrichment of the volatile major elements Na and K (Figure 52), and volatile trace element Rb (Figure 53). The surface-correlated volatiles suggest that there may be condensation of impact-produced vapours onto impact spherule surfaces. For this to occur, an impactor with a minimum speed of ~10 km/sec is needed to causing melting, regolith mixing and, most importantly, the formation of a vapour cloud (see Figure 38). The resulting hot transient atmosphere will eventually cool enough for condensation of VRAP (Keller and McKay, 1991; Keller and McKay, 1992), GASP (Warren, 2008) and other vapour condensate deposits. The refractory elements that are not volatilised can be

concentrated in the residual liquids that will eventually form HASP spherules. The surfaces of other lunar mineral grains would have also been affected by this process and can be used as a comparison to impact spherules. Inclusion-rich rims on the surfaces of lunar mineral grains are formed largely by deposition of impact-generated vapours (Keller and McKay, 1997). The inclusion-rich rims contain abundant Fe-metals (kamacite: FeNi alloy) and Fe sulfides in an amorphous silicate matrix, with some displaying inclusion stratigraphy built up from episodic processes (Keller and McKay, 1997). The impact spherule cross-sectioned in Figure 50a is an example of a highly spherical impact spherule that has small irregularities that form a discontinuous outer condensate deposit. Kurat and Keil (1972) suggest that the thickness of the crust as a whole may be related to the size of the event, and perhaps only form in large events because vapours from small impacts are likely to condense as finely dispersed and discrete particles rather than continuous rims. However, multiple generations of impacts, even small ones, should accumulate to produce a thicker layered crust. Experimental vapour condensate analogies indicate that the major element composition of these rim deposits are rich in the alkalis (Na and K), Si and Fe (Hapke et al., 1975). An alternative process that may result in surface-correlated volatile enrichment is adsorption from the lunar atmosphere (Madey et al., 1998; Sprague et al., 1992). Adsorption from the lunar "atmosphere" onto glass surfaces would involve physical bonding of a free volatile atom (Na or K) at non-bridging oxygen sites (Madey et al., 1998). However, given that impact events are much more likely to occur and result in comparatively thicker rims of vapour deposits, adsorption probably has a small effect.

The crusts of impact spherules in this study have many similar compositional characteristics to those produced by vapour deposition. Particularly telltale signatures of impact vapour deposits are enrichment in volatile major elements (Na and K) and Si on the near-surface rim(s) of the impact spherules. Although there is a detectable Si enrichment on the near-surface, most spherules do not show any change in Fe abundance between the crust (unpolished analyses) and "core". Surface-correlated Fe results from the condensation of impact vapours and results in the production of iron nanoparticles (np-Fe^0) depending on the composition of the target (Loeffler et al., 2008;

Sasaki et al., 2003; Sasaki et al., 2001). It is difficult to explain this discrepancy as the bulk analyses in this study were not designed to determine the nature of rim deposits on lunar impact spherules, but rather to test the consistency of analysis on non-flat surfaces. If the crust is thin (i.e. sub-micron) and np-Fe^0 is sparse, the contribution of Fe from the crust may be insignificant compared to the total interaction volume in an EMP analysis. Such thin volatile layers (~0.1μm) have been observed in GASP spherules (Warren, 2008). Given that the cleanest, most homogeneous spherules were chosen for this comparison, there may already have been a selection bias toward spherules without inclusion-rich rims and hence, no surface-correlated Fe. There are, however, other siderophiles that are surface-correlated.

Trace element profiles of impact spherules with crusts typically show surface-correlated enrichment of Ni and Co (Figure 53). Impact-vapour deposition, as previously discussed, would create surface-correlated deposits of volatile elements and Fe-Ni-Co phases (e.g. kamacite, np-Fe^0, troilite). The siderophile signal is removed when calculating the "core" compositions, although a relationship still exists between Ni, Co, and Rb determined from "core" signals and colour of the impact spherules. Figure 71 shows the "core" Ni versus Rb abundance and is colour coded such that information on magnetic susceptibility and spherule colour is also shown. Non-magnetic impact spherules are typically Ni and Rb-poor and clear or green in colour. Magnetic impact spherules, however, contain higher abundances of Ni and Rb, and are typically black or of a hybrid colour. The relationship between colour, magnetic susceptibility, and siderophile element present in crusts suggests that the development of a crust may be the primary cause of dark/opaque colours.

Enrichment of the siderophile elements Ni and Co in the near-surface crusts strongly suggests some type of meteoritic input, but can also result from a combination of more complex processes. Accretion of lunar materials such as metallic grains in the soil by impact-melt splashes or other accretion processes would be an obvious candidate since the average Apollo 16 soil contains ~2% meteoritic siderophile elements from chondritic meteoroids (Hörz et al., 1991). The correlation between crustal volatiles and

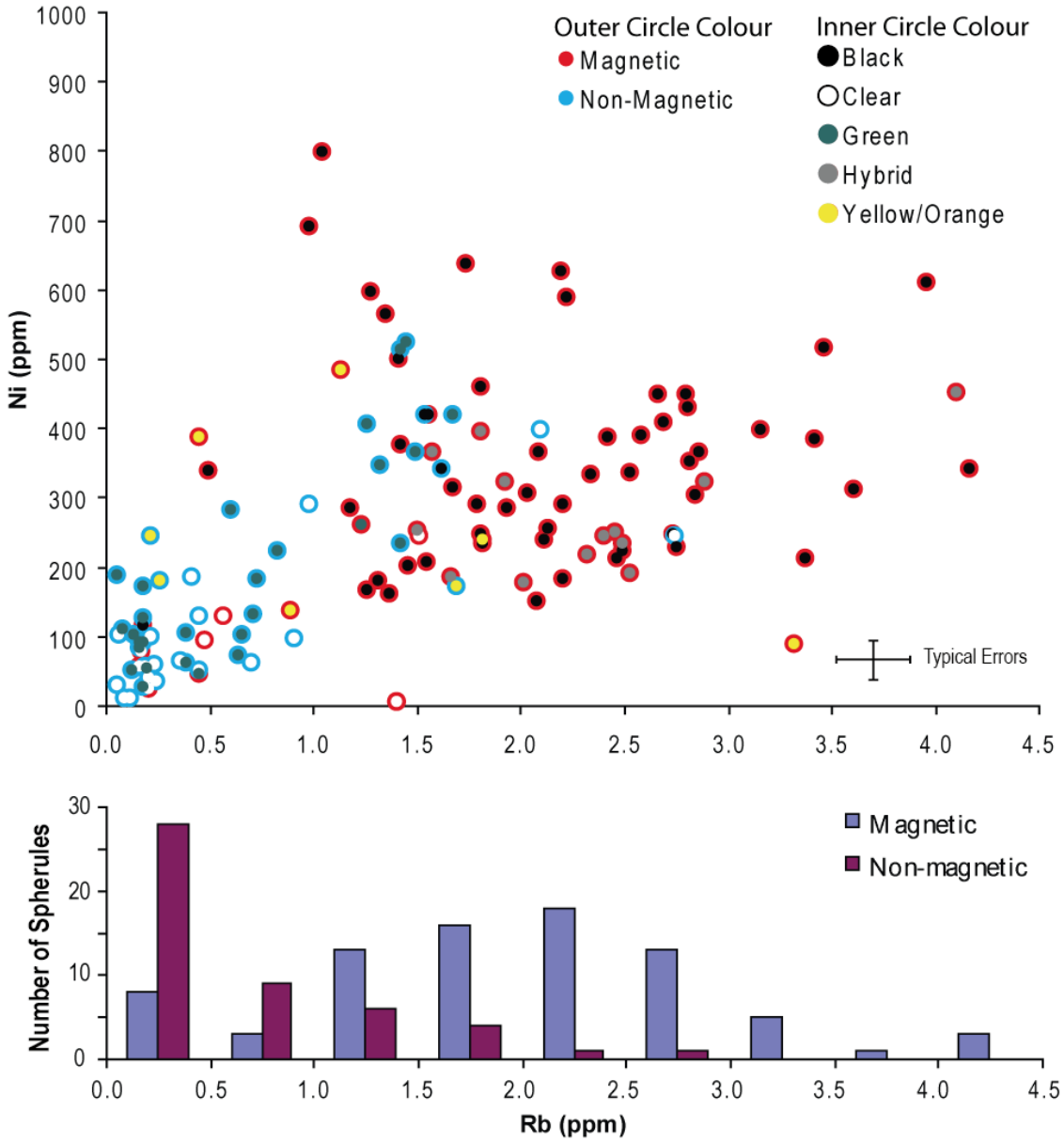

Figure 71. "Core" trace element abundance of Ni versus Rb in the 130 unpolished lunar impact spherules. Plotted are spherule colours and the magnetic susceptibility. As the abundance of Ni and Rb increase, the number of magnetic spherules increases and the non-magnetic spherules decreases. Rubidium in particular has a strong selection effect. Shown below the plot is a histogram of magnetic versus non-magnetic spherules as a function of Rb abundance.

siderophiles in Figure 71 suggests that impact-deposition would act to increase the magnetic susceptibility of the spherule and darken the surface (Keller and McKay, 1997; Liu et al., 2007; Pieters et al., 1993; Sasaki et al., 2001). Reduction of siderophile elements on the near-surface of impact spherules, triggered by the release of solar-wind implanted H and C in the regolith, is another method for bringing siderophile elements to the surface. This can occur during impacts events and results in the release of solar-wind implanted H and C as H_2O and CO causing Fe^{++} reduction to metal and aggregation in silicates (Housley et al., 1973a; Housley et al., 1973b). Although this process best describes the formation of agglutinates, it is also applicable to lunar impact spherules. Hydrogen is released from lunar soils between 300-700°C (Gibson and Moore, 1972; Gibson and Johnson, 1971) and can interact with the surfaces of impact spherules causing partial reduction of siderophile element oxides on the surface. Alternatively, redistribution of Ni-Co metal beads formed by metal/silicate immiscibility in the near-surface crust of an impact-melt may also achieve the same effect. The spatial distribution of metal beads in a molten spherule that has quenched rapidly would probably be random and their size small. Longer quenching times may result in agglomeration of the siderophilic melts, but concentration on the near-surface could occur if rotational forces are involved. Rotation of impact-melt prior to quenching would result in elongate to dumbbell shaped spherules (spheroids), but may also cause heavy particles such as metals beads to migrate to the outer perimeter, and vesicles (if any) towards the middle (Bastin, 1979; Bastin and Volborth, 1974). The dumbbell in Figure 72 may be an example of such processes.

The contribution of each of the above processes can be evaluated as each would produce distinct features. Impact-vapour deposition might produce discrete metal beads in an amorphous matrix as a continuous deposit. Impact-splashes and accreted materials, on the other hand, might produce discontinuous overlapping layers. Both these processes could occur over an exposed spherule surface, although may not be continuous over the whole spherule. Impact spherules subject to rotation during formation are likely to display a gradation of particle sizes with the heaviest particles located furthest from the core. In addition, elongated impact spherules are more likely to be black/opaque in

colour from the accumulation of metal (and other) particles. If reduction of the near-surface, coupled with surficial impact melting, were to cause migration and aggregation of siderophiles, they would be depleted from the region adjacent to the region affected. This would manifest as an apparent depletion after the surface-correlated enrichment (e.g. see Figure 53). However, very few impact spherules have trace element profiles such as that of sample LS6-56, (Figure 53) making it hard to distinguish "crust" from the bulk spherule. The methods in this study were not designed to resolve the contributions of processes that may lead to surface-correlated siderophile enrichment. Given that impact-vapour deposition does occur, as clearly indicated by the surface-correlated volatiles, surface-correlated siderophiles formed from a mixture of regolith and impactor condensates are likely to dominate.

Figure 72. A dumbbell-shaped impact glass (LS5-43) possibly formed by the rotation of impact-melts prior to quenching to an impact spherule. This spherule shows dark extremities and a clearer central region which may be the result of migration of heavy particles to the outer perimeters during rotation.

4.5 Chapter Conclusions

The lunar impact spherule population has been characterised in this study both petrographically and chemically. Prior to chemical analysis, impact spherules were classified according to their size, shape, colour and features using a classification system developed during this study. Relationships were then found among the size, colour and sphericity with smaller impact spherules tending to be colourless or clear and highly spherical. Larger impact spherules tended to be darker and more irregular. The shape probably becomes more spherical with smaller size as surface tension is stronger in smaller particles, but may also result from the composition of the melt; anorthositic melts are more viscous, hence better glass formers. Colour, however, was found to be affected by several factors including the composition of the target, crusts formed due to exposure and gardening, and optical thickness which may be altered on damaged spherules. Other petrographic features likely resulted from the condition of formation; these include homogeneous and heterogeneous textures, crystallisation and inclusion of lithic fragments, some of which are partially digested. Modelling the quenching rate of melt droplets in space suggests that melt droplets <100 microns in size should quench to homogeneous glasses. Given the conditions of the model, crystallised internal structures are most likely to form in large volume melts and where ambient temperature are high, such as those generated by external sources of heat from the impact or proximity to hot impact-melt.

The addition of both major and trace element data allows for quantification of many of these petrographic features, but also allows the provenance of individual impact spherules to be determined. However, the first step was to quantify whether there were significant differences between analyses on unpolished (non-flat) versus polished surfaces. It was found that the major element characteristics of unpolished impact spherules are not affected by the geometry, in contrast to the modelling in Chapter 2. This leads to the observation that the presence of crusts may affect the analyses which was later confirmed by trace element profiles. Many impact spherules have a surface that contains impact-condensed volatiles Na, K, and Rb. Trace element profiles through

the surface of many impact spherules also show a layer a few microns thick with elevated concentrations of the siderophile elements Ni and Co. These impact spherules were also typically black and magnetic, indicating that the siderophile-rich crusts contribute to the darkening of impact spherule surfaces. These crusts could be produced by impact-deposition, inclusion of siderophiles in the regolith, impact-triggered reduction of Fe, and rotation of an impact melt. The major element chemistry was quantitatively compared to impact spherule colour using principal component analysis as well as cluster analysis. However, neither could establish clear colour-composition groups, although clear and green-coloured impact spherules tended to have aluminous and calcic compositions. However, it was noted that the nature of the unpolished analyses and crusts affected the inter-element correlations resulting in an inability to distinguish compositional groups.

To determine the provenance of each impact spherule, diagnostic major and trace elements ratios, rare earth element plots, and chi-squared fitting were used. Diagnostic trace elements ratios indicate that the impact spherules were not derived from mature Cayley soils, but instead were produced by impacts into rock components that the regolith is derived from. Another method was used to challenge this interpretation by determining how much variability in the Apollo soils was needed to produce the whole impact spherule population of this project. The chi-squared fits allowed individual spherules to be quantitatively compared to a suite of candidates using a probability of match derived from the chi-squared values. However, unlike the diagnostic trace element ratios, the chi-squared analysis suggests that the majority (~75%) of impact spherule population were formed using local Apollo 16 soils, if a 1σ variability of 20% is assumed for the mean composition of the candidate soils. The major element composition of >95% of the impact spherule population can be produced from the candidate suite of soils at statistically significant probabilities (>5%), but for trace element compositions, only ~75% of the impact spherule population can be produced from the candidate suite of soils. This indicates that either the suite of candidates is unsuitable as it lacks spatial and compositional variety to be representative of soils at the Apollo 16 site or not all candidates are produced by soils (i.e. a minority were

produced from rocks as suggested by the diagnostic trace elements ratios). There was no closure on the controversial question of whether impact spherules were produced from soils or rocks. However, this analysis does place some constraints on how much variability is needed to produce most of the impact spherule population.

The next chapter will present formation and exposure ages for selected impact spherules from this study. These data are needed to constrain geologic and impact processes that may be selectively affecting the impact spherule population.

4.6 Chapter References

ADENA K., CHRISTY A. and NORMAN M. (2009) Geochemistry of volcanic and impact glasses from the Taurus-Littrow Region on the Moon. In *9th Australian Space Science Conference* (eds. W. Short and I. Cairns). National Space Society of Australia Ltd, Sydney, Australia.

ARNDT J., FLAD K. and FETH M. (1979) Radiative cooling experiments on lunar glass analogues. In *10th Lunar and Planetary Science Conference*, pp. 355-373. Pergamon Press, Houston, Texas.

ARNDT J. and VON ENGELHARDT W. (1987) Formation of Apollo 17 Orange and Black Glass Beads. *J. Geophys. Res.* **92**(B4), E372-E376.

BASTIN J. A. (1979) The origin of the shapes of lunar globules. *Moon and the Planets* **21**, 283-288.

BASTIN J. A. and VOLBORTH A. (1974) The ellipsoidal and dumbbell-shaped inclusions within particulate lunar globules. *Icarus* **21**(1), 112-120.

CHAO E. C. T., BEST J. B. and MINKIN J. A. (1972) Apollo 14 glasses of impact origin and their parent rock types. In *The 3rd Lunar Science Conference*, pp. 907-925.

CHAO E. C. T., BOREMAN J. A., MINKIN J. A., JAMES O. B. and DESBOROUGH G. A. (1970) Lunar Glasses of Impact Origin: Physical and Chemical Characteristics and Geologic Implications. *Journal of Geophysical Research* **75**(35), 7445-7479.

DELANO J. (1986) Pristine Lunar Glasses: Criteria, Data and Implications. *Proceedings of the 16th Lunar and Planetary Science Conference, Part 2* **91**(B4), D201-D213.

DELANO J. W., LINDSLEY D. H. and RUDOWSKI R. (1982) Glasses of impact origin from Apollo 11, 12, 15, and 16 - Evidence for fractional vaporization and mare/highland mixing. In *Lunar and Planetary Science Conference XII*, pp. 339-370. Pergamon Press, Huston.

DELANO J. W. and RUDOWSKI R. (1980) Apollo 16 green glass (abstract). In *11th Lunar and Planetary Science Conference*, pp. 222–224.

EGGINS S. M., KINSLEY L. P. J. and SHELLEY J. M. G. (1998) Deposition and element fractionation processes during atmospheric pressure laser sampling for analysis by ICP-MS. *Applied Surface Science* **127-129**, 278-286.

GIBSON E. K., JR. and MOORE G. W. (1972) Inorganic gas release and thermal analysis study of Apollo 14 and 15 soils. In *Proceedings of the 3rd Lunar Science Conference*, pp. 2092-2040. MIT Press.

GIBSON E. K., JR. and JOHNSON S. M. (1971) Thermal analysis-inorganic gas release studies of lunar samples. In *Proceedings of the 2nd Lunar Science Conference*, pp. 1351-1366. MIT Press.

GLASS B. P. (1976) Major element composition of glasses from Apollo 11, 16, and 17 soil samples. In *7th Lunar Science Conference*, pp. 679-693. Pergamon Press, Inc., Houston, Texas.

HANDWERKER C. A., ONORATO P. I. K. and UHLMANN D. R. (1977) Viscous flow, crystal growth, and glass formation of highland and mare basalts from Luna 24 pp. 483-493. Pergamon Press, Inc., Houston, Texas.

HAPKE B., CASSIDY W. and WELLS E. (1975) Effects of vapor-phase deposition processes on the optical, chemical, and magnetic properties OE the lunar regolith. *Earth, Moon, and Planets* **13**(1), 339-353.

HASKIN L. and WARREN P. H. (1991) Lunar Chemistry. In *Lunar Sourcebook: A User's Guide to the Moon* (eds. G. Heiken, D. T. Vaniman and B. M. French), pp. 357-476. Cambridge University Press.

HÖRZ F. and CINTALA M. (1997) The Barringer Award Address Presented 1996 July 25, Berlin, Germany: Impact experiments related to the evolution of planetary regoliths. *Meteoritics & Planetary Science* **32**(2), 179-209.

HÖRZ F., GRIEVE R., HEIKEN G., SPUDIS P. and BINDER A. (1991) Lunar Surface Processes. In *Lunar Sourcebook: A User's Guide to the Moon* (eds. G. Heiken, D. T. Vaniman and B. M. French), pp. 61-120. Cambridge University Press.

HORZ F., MULLER R. A., BECKER T. A., CULLER T. S., KARNER D. B. and RENNE P. R. (2000) Time-Variable Cratering Rates? *Science* **288**(5474), 2095a-.

HOUSLEY R. M., CIRLIN E. H. and GRANT R. W. (1973a) Characterization of Fines from the Apollo 16 Site. In *4th Lunar Science Conference*, pp. 2729-2735.

HOUSLEY R. M., GRANT R. W. and PATON N. E. Origin and characteristics of excess Fe metal in lunar glass welded aggregates. In *4th Lunar Science Conference*, pp. 2737-2749.

- (1973b) Origin and characteristics of excess Fe metal in lunar glass welded aggregates. In *Proceedings of the 4th Lunar Science Conference*, pp. 2737-2749.

JOLLIFF B. L., GILLIS J. J., HASKIN L. A., KOROTEV R. L. and WIECZOREK M. A. (2000) Major lunar crustal terranes: Surface expressions and crust-mantle origins. *J. Geophys. Res.* **105**.

JOLLIFF B. L. and HASKIN L. A. (1995) Cogenetic rock fragments from a lunar soil: Evidence of a ferroan noritic-anorthosite pluton on the Moon. *Geochimica et Cosmochimica Acta* **59**(11), 2345-2374.

KELLER L. P. and MCKAY D. S. (1991) Analytical Electron Microscopy of Fine-Grained Glass Spheres in Apollo 16 Soil 61181 (abstact). *Abstracts of the Lunar and Planetary Science Conference* **22**, 703.

- (1992) Micrometer-sized glass spheres in Apollo 16 soil 61181 - Implications for impact volatilization and condensation. In *Lunar and Planetary Science Conference*, pp. 137-141. Lunar and Planetary Institute, Houston, Texas.

- (1997) The nature and origin of rims on lunar soil grains. *Geochimica et Cosmochimica Acta* **61**(11), 2331-2341.

KOROTEV R. (1997) Some things we can infer about the Moon from the composition of the Apollo 16 regolith. *Meteorit. Planet. Sci.* **32**, 447-478.

KOROTEV R. L. (1994) Compositional variation in Apollo 16 impact-melt breccias and inferences for the geology and bombardment history of the Central Highlands of the Moon. *Geochimica et Cosmochimica Acta* **58**(18), 3931-3969.

- (1996) On the Relationship between the Apollo 16 Ancient Regolith Breccias and Feldspathic Fragmental Breccias, and the Composition of the Prebasin Crust in the Central Highlands of the Moon. *Meteoritics and Planetary Science Supplement* **31**, 403-412.

- (2001) On the Systematics of Lunar Regolith Compositions (abstract). In *32nd Annual Lunar and Planetary Science* Houston, Texas.

KOROTEV R. L., JOLLIFF B. L., ZEIGLER R. A., GILLIS J. J. and HASKIN L. A. (2003) Feldspathic lunar meteorites and their implications for compositional remote sensing of the lunar surface and the composition of the lunar crust. *Geochimica et Cosmochimica Acta* **67**(24), 4895-4923.

KOROTEV R. L. and KREMSER D. T. (1992) Compositional variations in Apollo 17 soils and their relationship to the geology of the Taurus-Littrow site. In *Proceedings of Lunar and Planetary Science*, pp. 275-301. Lunar and Planetary Institute, Houston, Texas.

KOROTEV R. L. and MORRIS R. V. (1993) Composition and maturity of Apollo 16 regolith core 60013/14. *Geochimica et Cosmochimica Acta* **57**(19), 4813-4826.

KOROTEV R. L., MORRIS R. V., JOLLIFF B. L. and SCHWARZ C. (1997) Lithological variation with depth and decoupling of maturity parameters in Apollo 16 regolith core 68001/2. *Geochimica et Cosmochimica Acta* **61**(14), 2989-3002.

KOROTEV R. L., MORRIS R. V. and LAUER H. V., JR. (1984) Stratigraphy and Geochemistry of the Stone Mountain Core (64001/2). *J. Geophys. Res.* **89**(S1), C143-C160.

KURAT G. and KEIL K. (1972) Effects of vaporization and condensation on Apollo 11 glass spherules: implications for cooling rates. *Earth and Planetary Science Letters* **14**(1), 7-13.

LINDSTROM M. M. and LINDSTROM D. J. (1986) Lunar Granulites and Their Precursor Anorthositic Norites of the Early Lunar Crust. *J. Geophys. Res.* **91**(B4), D263-D276.

LIU Y., TAYLOR L. A., THOMPSON J. R., SCHNARE D. W. and PARK J.-S. (2007) Unique properties of lunar impact glass: Nanophase metallic Fe synthesis. *American Mineralogist* **92**(8-9), 1420-1427.

LOEFFLER M. J., BARAGIOLA R. A. and MURAYAMA M. (2008) Laboratory simulations of redeposition of impact ejecta on mineral surfaces. *Icarus* **196**(1), 285-292.

LUCEY P., KOROTEV R. L., GILLIS J. J., TAYLOR L. A., LAWRENCE D., CAMPBELL B. A., ELPHIC R., FELDMAN B., HOOD L. L., HUNTEN D., MENDILLO M., NOBLE S., PAPIKE J. J., REEDY R. C., LAWSON S., PRETTYMAN T., GASNAULT O. and MAURICE S. (2006) New Views of Lunar Geoscience: Understanding the Lunar

Surface and Space-Moon Interactions. In *New Views of the Moon* (eds. B. L. Jolliff, M. Wieczorek, C. K. Shearer and C. Neal), pp. 83-219.

MADEY T. E., YAKSHINSKIY B. V., AGEEV V. N. and JOHNSON R. E. (1998) Desorption of alkali atoms and ions from oxide surfaces: Relevance to origins of Na and K in atmospheres of Mercury and the Moon. *J. Geophys. Res.* **103**.

MCKAY D. S., HEIKEN G., BASU A., BLANFORD G., SIMON S., REEDY R., FRENCH B. M. and PAPIKE J. (1991) The Lunar Regolith. In *Lunar Sourcebook: A User's Guide to the Moon* (eds. G. Heiken, D. T. Vaniman and B. M. French), pp. 285-356. Cambridge University Press.

MELOSH H. J. (1989) *Impact Cratering - A Geologic Process*. Oxford University Press.

MEYER H. O. A. and TSAI H.-M. (1975) Lunar glass compositions: Apollo 16 core sections 60002 and 60004. *Earth and Planetary Science Letters* **28**(2), 234.

MORRIS R. V., SEE T. H. and HÖRZ F. (1986) Composition of the Cayley formation at Apollo 16 as inferred from Impact Melt Splashes. *Journal of Geophysical Research* **91**(B13), E21-E42.

NANEY M. T., CROWL D. M. and PAPIKE J. J. (1976) The Apollo 16 drill core - Statistical analysis of glass chemistry and the characterization of a high alumina-silica poor (HASP) glass. In *7th Lunar Science Conference*, pp. 155-184. Pergamon Press, Inc., Houston, Texas.

NORMAN M. D. (1981) Petrology of suevitic lunar breccia 67016. In *Proceedings of the 12th Lunar and Planetary Science Conference*, pp. 235-252. Pergamon Press, Houston, Texas.

NORMAN M. D., BORG L. E., NYQUIST L. E. and BOGARD D. D. (2003) Chronology, geochemistry, and petrology of a ferroan noritic anorthosite clast from Descartes breccia 67215: Clues to the age, origin, structure, and impact history of the lunar crust. *Meteoritics & Planetary Science* **38**, 645-661.

NORMAN M. D., DUNCAN R. A. and HUARD J. J. (2010) Imbrium provenance for the Apollo 16 Descartes terrain: Argon ages and geochemistry of lunar breccias 67016 and 67455. *Geochimica et Cosmochimica Acta* **74**(2), 763-783.

NORMAN M. D., GARCIA M. O. and BENNETT V. C. (2004) Rhenium and chalcophile elements in basaltic glasses from Ko'olau and Moloka'i volcanoes: Magmatic

outgassing and composition of the Hawaiian plume. *Geochimica et Cosmochimica Acta* **68**(18), 3761-3777.

NORMAN M. D. and RYDER G. (1980) Geochemical constraints on the igneous evolution of the lunar crust. In *11th Lunar and Planetary Science Conference*, pp. 317-331. Pergamon Press, Houston, Texas.

NORRIS J. A., KELLER L. P. and MCKAY D. S. (1992) Impact glasses from the less than 20-micrometer fraction of Apollo 17 soils 72501 and 78221 In *LPI Technical Report*, pp. 44-45 Lunar and Planetary Institute

- (1993) Impact glasses from the ultrafine fraction of lunar soils. *Twenty-Fourth Lunar and Planetary Science Conference. Part 3: N-Z*, 1093-1094.

PIETERS C. M., FISCHER E. M., RODE O. and BASU A. (1993) Optical Effects of Space Weathering: The Role of the Finest Fraction. *J. Geophys. Res.* **98**(E11), 20817-20824.

PRETTYMAN T. H., HAGERTY J. J., ELPHIC R. C., FELDMAN W. C., LAWRENCE D. J., MCKINNEY G. W. and VANIMAN D. T. (2006) Elemental composition of the lunar surface: Analysis of gamma ray spectroscopy data from Lunar Prospector. *J. Geophys. Res.* **111**.

ROBERTS A. and WITHERS P. (2007) StatistiXL. http://www.statistixl.com/default.aspx.

SASAKI S., KURAHASHI E., YAMANAKA C. and NAKAMURA K. (2003) Laboratory simulation of space weathering: Changes of optical properties and TEM/ESR confirmation of nanophase metallic iron. *Advances in Space Research* **31**(12), 2537-2542.

SASAKI S., NAKAMURA K., HAMABE Y., KURAHASHI E. and HIROI T. (2001) Production of iron nanoparticles by laser irradiation in a simulation of lunar-like space weathering. *Nature* **410**(6828), 555-557.

SHEARER C. K. and PAPIKE J. J. (1993) Basaltic magmatism on the Moon: A perspective from volcanic picritic glass beads. *Geochimica et Cosmochimica Acta* **57**(19), 4785.

SPRAGUE A. L., KOZLOWSKI R. W. H., HUNTEN D. M., WELLS W. K. and GROSSE F. A. (1992) The sodium and potassium atmosphere of the moon and its interaction with the surface. *Icarus* **96**(1), 27-42.

STÖFFLER D., BISCHOFF A., BORCHARDT R., BURGHELE A., DEUTSCH A., JESSBERGER E. K., OSTERTAG R., PALME H., SPETTEL B., REIMOLD W. U., WACKER K. and WANKE H. (1985) Composition and evolution of the lunar crust in the Descartes highlands, Apollo 16. In *15th Lunar and Planetary Science Conference*, pp. C449-C506, Houston, Texas.

SYMES S. J. K., SEARS D. W. G., TAUNTON A., AKRIDGE D. G., HUANG S. and BENOIT P. H. (1998) The crystalline lunar spherules: Their formation and implications for the origin of meteoritic chondrules. *Meteoritics and Planetary Science* **33**(1), 13-29.

UHLMANN D. R. (1972) A kinetic treatment of glass formation. *Journal of Non-Crystalline Solids* **7**(4), 337-348.

ULRICH G. E., HODGES C. A. and MUEHLBERGER W. R. (1981) Geology of the Apollo 16 Area, Central Lunar Highlands. In *Geological Survey Professional Paper 1048*, pp. 539. National Aeronautics and Space Administration.

WARREN P. H. (2008) Lunar rock-rain: Diverse silicate impact-vapor condensates in an Apollo-14 regolith breccia. *Geochimica et Cosmochimica Acta* **72**(14), 3562-3585.

WILLIAMS D. R. (2003) Lunar Landing Site Map National Aeronautics and Space Administration, http://nssdc.gsfc.nasa.gov/planetary/lunar/moon_landing_map.jpg.

WINCHELL H. and SKINNER B. J. (1970) Glassy spherules from the lunar regolith returned by Apollo 11 expedition. In *Proceedings of the Apollo 11 Lunar Science Conference* (ed. A. A. Levinson), pp. 957-964. Pergammon Press, Houston, Texas.

ZEIGLER R. A., KOROTEV R. L., JOLLIFF B. L., HASKIN L. A. and FLOSS C. (2006) The geochemistry and provenance of Apollo 16 mafic glasses. *Geochimica et Cosmochimica Acta* **70**(24), 6050-6067.

ZELLNER N. E. B., SPUDIS P. D., DELANO J. W. and WHITTET D. C. B. (2002) Impact glasses from the Apollo 14 landing site and implications for regional geology. *Journal of Geophysical Research* **107**(E11), **12**-1 - **12**-13.

CHAPTER 5:

GEOCHRONOLOGY - RADIOISOTOPIC DATING AND EXPOSURE AGES

5.1 Introduction

This chapter presents results of $^{40}Ar/^{39}Ar$ radioisotopic dating of thirty impact spherules in this study. The chapter starts with a brief background section on the $^{40}Ar/^{39}Ar$ technique including formulae for the calculation of formation and exposure ages. Following this, the approached used to select the thirty impact spherules most suitable for radioisotopic dating is outlined. This is followed by a discussion of the analytical methods. A total of twenty-one out of the thirty impact spherules yielded a statistically acceptable age and ages could be inferred from five other spherules. These were used to establish the first impact spherule age distribution which consists mostly of low-K locally-derived Apollo 16 spherules. The age distributions shows that about a third of the impact spherules have <400Ma ages, consistent with previous age distributions established for the Apollo 12 and 14 sites. Exposure ages for fifteen impact spherules could also be established and suggest that impact spherules, both young and old, have not spent >500Ma on the surface.

This new record allows comparison of impact spherule records across four different collection sites, Apollo 12, 14, 16, and 17. These independent records are combined in the discussion and were used to develop a more diverse impact spherule record which shows a "U"-shaped distribution of abundant young (<500Ma) and old (>2.5Ga) impact spherules. The controversial idea of a late heavy bombardment is tested with this record, but the record does not provide further constraints. However, the impact spherule record appears to better represent the more recent bombardment history, which appears to reflect ages of impact resetting in the meteorite population indicating that they may be related.

5.2 Background

5.2.1 Basis for Dating using the K-Ar and $^{40}Ar/^{39}Ar$ Method

The potassium-argon (K-Ar) and related ^{40}Ar-^{39}Ar techniques are powerful tools for determining the formation ages of lunar impact spherules. The basis for both these methods is the radioactive potassium isotope ^{40}K which has a half-life of 1250 million years and decays to ^{40}Ca and ^{40}Ar. Radiogenic argon is formed in about 10.5% of ^{40}K decays via electron capture or more rarely by positron emission (McDougall and Harrison, 1999). The designation $^{40}Ar^*$ is used to refer to the radiogenic argon produced by in situ decay of a mineral, rock or glass. In K-Ar dating, it is necessary to know the abundance of ^{40}K which is usually derived by measuring total K and then calculating ^{40}K abundance based on the known $^{40}K/K$ ratio. It is assumed that the only source of ^{40}Ar is from in-situ decay of ^{40}K. If there are other sources of argon isotopes (e.g. atmospheric), corrections must be made to remove these sources or the "true" age can be overestimated.

The $^{40}Ar/^{39}Ar$ dating technique is an advanced K-Ar dating technique which removes the need to obtain the abundance of ^{40}K by other means. Instead, ^{40}K is determined using reactor-produced ^{39}Ar, which is not a naturally occurring isotope. ^{39}Ar is a proxy for the abundance of ^{39}K which can be converted to ^{40}K, thus bypassing the need to determine ^{40}K directly. The $^{40}Ar/^{39}Ar$ dating technique can overcome problems with sample inhomogeneity and is in general more precise (as separate analyses are not needed for K abundance) than the K-Ar dating techniques allowing smaller samples to be analysed (McDougall and Harrison, 1999). Additionally, the K-Ar technique requires total fusion (complete release of gasses) of the sample. The major advantage of the $^{40}Ar/^{39}Ar$ technique over K-Ar dating is the ability to conduct step-wise heating. Step-wise heating (also known as incremental heating) involves a series of heating steps starting from below the fusion point resulting in release of deeper or more strongly-bonded argon in the mineral lattices with increasing temperature (Kelley, 1995). At each step the argon is analysed and collated into an age spectrum that can be interrogated for information such as the sources of argon, internal distribution of argon (i.e. surface-

correlated solar wind or crystalline), and subsequent disturbances that have changed the argon composition of the sample (Dickin, 2005).

The $^{40}Ar/^{39}Ar$ technique requires preparation of samples for irradiation in a nuclear reactor so that ^{39}Ar can be produced from ^{39}K (denoted as $^{39}Ar_K$) through the $^{39}K(n,p)$ ^{39}Ar reaction. This reaction involves the interaction of neutrons emitted from the nuclear reactor interacting with ^{39}K nuclei which produces ^{39}Ar through the emission of a proton (McDougall and Harrison, 1999). Some of these reactor-produced isotopes affect those that are essential for calculating the age of a sample (i.e. ^{40}Ar can also be produced by Ca in a reactor); therefore these contributions need to be corrected prior to calculation of an age. The following sections will summarise the reactor-produced and naturally occurring argon isotopes and corrections or assumptions that need to be adopted.

5.2.2 Sources of Argon Isotopes and Age Corrections

Reactor-produced Argon Isotopes

Irradiation of samples for $^{40}Ar/^{39}Ar$ dating can produce unwanted reactor-produced isotopes of argon created mainly from calcium, potassium, and chlorine in the sample in addition to those needed for $^{40}Ar/^{39}Ar$ dating. The duration of irradiation is typically selected such that there is sufficient production of ^{39}Ar while minimising the production of other interfering reactor-produced isotopes (see McDougall and Harrison, 1999). A simplified table of reactor-produced argon isotopes (Table 11) indicates that the main interferences on ^{40}Ar, ^{39}Ar, and ^{36}Ar isotopes used for formation age dating result from of reactor-produced ^{39}Ar from ^{42}Ca and ^{36}Ar from ^{40}Ca, which can significantly affect the age, especially in young samples where the Ca/K ratio is >10 (Kelley, 1995). Most of the impact spherules selected for this study have Ca/K ratios well above 10 (median: 121). However, ^{37}Ar is also produced during irradiation, mostly from ^{40}Ca, and can be used to correct for reactor-produced ^{36}Ar and ^{39}Ar (see Brereton, 1970). The samples must be analysed within a year of irradiation because of the need to accurately measure reactor-produced ^{37}Ar for the corrections (Kelley, 1995).

Table 11. Simplified table of reactions that produce argon isotopes during neutron irradiation (modified from McDougall and Harrison, 1999). The key reactions that contribute the most reactor-produced argon are highlighted.

	Calcium	Potassium	Argon	Chlorine
^{36}Ar	$^{40}Ca \rightarrow {}^{36}Ar$			$^{35}Cl \rightarrow {}^{36}Cl \rightarrow {}^{36}Ar$
^{37}Ar	$^{40}Ca \rightarrow {}^{37}Ar$	$^{39}K \rightarrow {}^{37}Ar$	$^{36}Ar \rightarrow {}^{37}Ar$	
^{38}Ar	$^{42}Ca \rightarrow {}^{38}Ar$	$^{39}K \rightarrow {}^{38}Ar$ $^{41}K \rightarrow {}^{38}Cl \rightarrow {}^{38}Ar$	$^{40}Ar \rightarrow {}^{38}Cl \rightarrow {}^{38}Ar$	$^{37}Cl \rightarrow {}^{38}Cl \rightarrow {}^{38}Ar$
^{39}Ar	$^{42}Ca \rightarrow {}^{39}Ar$ $^{43}Ca \rightarrow {}^{39}Ar$	$^{39}K \rightarrow {}^{39}Ar$ $^{40}K \rightarrow {}^{39}Ar$	$^{38}Ar \rightarrow {}^{39}Ar$ $^{40}Ar \rightarrow {}^{39}Cl \rightarrow {}^{39}Ar$	
^{40}Ar	$^{43}Ca \rightarrow {}^{40}Ar$ $^{44}Ca \rightarrow {}^{40}Ar$	$^{40}K \rightarrow {}^{40}Ar$ $^{41}K \rightarrow {}^{40}Ar$		

Another source of reactor-produced argon isotopes result from chlorine isotopes ^{35}Cl and ^{37}Cl which form ^{36}Cl and ^{38}Cl during neutron irradiation, and produce ^{36}Ar and ^{38}Ar after subsequent beta decay. The chlorine-derived ^{36}Ar can introduce errors into the calculation of formation ages, but due to the relatively slow decay of ^{36}Cl to ^{36}Ar (half-life of $3x10^5$ years), the generation of sufficient ^{36}Ar to interfere with age calculations is minimal (McDougall and Harrison, 1999). Additionally, since chlorine isotopes are converted to argon isotopes by thermal neutrons, the production of chlorine-derived argon can be further reduced using cadmium shielding (McDougall and Harrison, 1999; Roddick, 1983). Furthermore, it is possible to correct for chlorine-derived ^{36}Ar by measuring chlorine-derived ^{38}Ar and also estimate the chlorine content of a sample (Roddick, 1983). The contribution of chlorine-derived ^{38}Ar, however, can be much more significant even when cadmium shielding is employed due to the short half-life of ^{38}Cl (37.2 minutes) (McDougall and Harrison, 1999). Calculation of the formation age is proportional to the Cl/^{40}Ar* ratio, irradiation conditions, and time elapsed since irradiation (Roddick, 1983). For example, the Hb3gr (hornblende) standard has a Cl abundance of ~2400ppm which introduces 1-3% error to the age; >5% errors are possible if the time elapsed since irradiation is significant (Roddick, 1983). Excess ^{38}Ar

produced from ^{37}Cl does not significantly affect the formation age calculation as it is not used, but will significantly affect the exposure age. The soils and regolith breccias at the Apollo 16 site typically contain <100ppm Cl; ~500ppm is about the maximum Cl concentration in lunar materials collected during the Apollo and Luna missions (Haskin and Warren, 1991) therefore the interference from reactor-produced Ar isotopes produced from Cl should be minimal.

Sources of Argon Isotopes in Lunar Impact Spherules

As extraterrestrial samples from a body lacking an atmosphere, lunar impact spherules are subject to the effect of various factors such as solar wind and cosmic ray interactions that can produce argon isotopes. These isotopes can, in some cases, be corrected using the other argon isotopes, but assumptions may need to be made about the others since it is not always possible to discriminate between different sources of argon. The natural sources of argon in lunar impact spherules can be grouped into two categories: the trapped component and the cosmogenic component. The trapped component ($Ar_{trapped}$) includes argon that may have been incorporated into the impact spherule during formation or during residence in the regolith. For lunar samples, the trapped component consists of solar wind argon and parentless $^{40}Ar^*$ from decay elsewhere on the Moon.

The solar wind component of the lunar regolith incorporated during impact spherule formation has a $(^{38}Ar/^{36}Ar)_{solar}$ ratio estimated at 0.1869 (Hohenberg et al., 1978). In addition to the solar wind, there may also be parentless $^{40}Ar^*$ produced from in situ decay of ^{40}K in other materials on the lunar surface (Ar^*_{lunar}). This parentless $^{40}Ar^*$ may subsequently be incorporated onto impact spherule surfaces from adsorption and condensation of impact vapour. Manka and Michel (1970) indicate that between 5-8.5% of the Ar^*_{lunar} can be released into the lunar "atmosphere" by degassing of lunar materials which are subsequently reimplanted back into surface materials by solar winds. Hoffman et al., (1973) and Hodges (1977) note that the mass spectrometer left at the Apollo 17 site shows diurnal fluctuations of ^{40}Ar in the lunar atmosphere resulting from adsorption of the gas during the night onto the lunar surface and desorption during the day. In this case, the surface-correlated Ar_{lunar} is loosely bound to particle surfaces

and is probably released at low temperatures during stepwise heating (Levine et al., 2007; Manka and Michel, 1970).

The cosmogenic component (Ar_{cosmo}) consists of argon produced by spallation and neutron capture in Fe, Ca, K, and Ti, triggered by cosmic ray bombardment. These reactions produce ^{36}Ar, ^{37}Ar, and ^{38}Ar in the top meter of the surface as a function of depth due to shielding of deeper materials from cosmic ray bombardment by shallower materials in the lunar regolith (Hohenberg et al., 1978; Reedy et al., 1983). The spallation of Ca to ^{38}Ar forms the basis for cosmic ray exposure dating (Turner et al., 1971) and can be used to determine the integrated exposure history of impact spherules (Levine et al., 2007). However, this requires that the contribution of excess ^{38}Ar from ^{37}Cl and spallation of Fe, K and Ti is negligible or can be corrected. Theoretical calculations of $^{38}Ar_{cosmo}$ production as a function of regolith shielding from cosmic ray bombardment are given in Hohenberg et al. (1978) and indicate that spallation from Ca:K:Ti:Fe occurs at ratios of approximately 1:1:0.1:0.05 with the production from Fe and Ti decreases as the amount of shielding increases. Production of $^{38}Ar_{cosmo}$ from spallation of Ca and K has often been deduced by adopting a $(^{38}Ar/^{36}Ar)_{cosmo}$ production ratio of ~1.5 (Hohenberg et al., 1978; Korochantseva et al., 2007; Turner et al., 1971). The contribution of Ar_{cosmo} from spallation of K is removed using the equations that will be detailed in the following section.

The last potential source of argon isotopes, referred to as excess argon (Ar_{excess}), comes from the degassing of mineral clasts that may be present within the impact spherule. Heterogeneous impact spherules may contain incompletely degassed mineral clasts that can potentially release excess argon (e.g. see Dickin, 2005). Changes in the Ca/K ratio derived through argon isotopes may be used to determine when this occurs.

5.2.3 Calculation of Formation and Exposure Ages

The $^{40}Ar/^{39}Ar$ technique requires a homogenous standard with known release patterns and age as a flux monitor. This monitor is needed to measure the efficiency and amount of ^{39}K transformed into ^{39}Ar, which is a function of the neutron flux and is represented by a constant known as the *J* factor (McDougall and Harrison, 1999). Note that the *J* Factor may vary as a function of the position of the sample in the reactor, and within the capsule, as the neutron flux may be different. After corrections are made for the reactor-produced argon isotopes, radioactive decay, and atmospheric contamination, the relevant *J* factor can be calculated using the following equation:

$$J = \frac{(\exp \lambda t) - 1}{^{40}Ar*/^{39}Ar_K} \qquad \textbf{[10]}$$

where t = age of the flux monitor

$^{40}Ar*/^{39}Ar_K$ = measured ratio of the flux monitor

For total fusion analyses, the measured argon isotopic composition of the sample can be used to calculate the age of the sample with the following equation:

$$t = \frac{1}{\lambda} \ln\left(1 + J \frac{^{40}Ar*}{^{39}Ar_K}\right) \qquad \textbf{[11]}$$

where Combined decay constant $\lambda = \lambda_{\beta}^{-} + \lambda_e + \lambda_e^{'}$ (Steiger and Jäger, 1977)

J = irradiation constant (see Equation 10)

$^{40}Ar*$ = radiogenic ^{40}Ar

$^{39}Ar_K$ = ^{39}Ar derived from the conversion of ^{39}K

However, total fusion analyses using the $^{40}Ar/^{39}Ar$ technique are essentially equivalent to K-Ar analyses. The strength of the $^{40}Ar/^{39}Ar$ technique is in stepwise heating, allowing the different sources of argon isotopes to be resolved. The following sections describe in detail the calculations involved in determining formation and exposure ages

from the $^{40}Ar/^{39}Ar$ analyses. Note that corrections must be made prior to any calculations, although atmospheric contamination is not necessary for lunar material (McDougall and Harrison, 1999). Refer to previous sections for details.

The $^{40}Ar/^{39}Ar$ technique: Age Plateaus and Isochrons

Stepwise heating of samples allows for the age from the $^{40}Ar^*/^{39}Ar$ ratio to be calculated at each step starting from below the fusion point of the sample. This is plotted against the cumulative fraction of ^{39}Ar released so that the age at each step is proportional to the total amount of ^{39}Ar released in that step. This approach is able to distinguish between various sources of argon, some of which may be lightly adsorbed and released at low temperatures (i.e. Ar_{lunar}), and others which may be bound more strongly in mineral phases (Kelley, 1995). Additionally, it is possible to identify events that may have lead to loss of argon, such as subsequent heating post-formation, and to identify sources of excess argon such as mineral clasts. Once identified, additional sources of excess argon can be excluded from the age calculations. Figure 73 illustrates examples of an ideal and a disturbed $^{40}Ar/^{39}Ar$ age spectrum. In the ideal $^{40}Ar/^{39}Ar$ age spectrum example, it is possible to define a series of consecutive steps agreeing at the 95% confidence level and satisfying a probability of fit (P) $\geq$ 0.05. If these steps are distributed over a minimum of 3 steps and include a significant percentage of total ^{39}Ar released (>50%), a plateau age can be defined and is equal to the weighted mean of all the steps involved. However, the formation age obtained from the plateau has not been corrected for $Ar_{trapped}$, which can affect the formation age as discussed earlier. To determine the $Ar_{trapped}$ component for extraterrestrial samples, $^{40}Ar/^{39}Ar/^{36}Ar$ isotope correlation diagrams are employed (McDougall and Harrison, 1999). Both ^{40}Ar and ^{39}Ar are normalised to a primordial isotope, typically $^{36}Ar_{solar}$ (i.e. interference-corrected), and each step of an analysis is plotted as ellipses encompassing 1σ or 2σ errors in $^{40}Ar/^{36}Ar$ versus $^{39}Ar/^{36}Ar$ space. A regression through these points represents a mixture of trapped and radiogenic ^{40}Ar (relative to ^{36}Ar) with the $^{40}Ar/^{36}Ar$ intercept equal to the $^{40}Ar/^{36}Ar$ ratio of the trapped end-member (see Figure 74). The regression must include at least three steps agreeing at the 95% confidence level and satisfying a probability of fit (P) $\geq$ 0.05. The drawback of this plot, however, is due to the fact that the ^{36}Ar isotope

is measured with the poorest precision leading to large errors and seemingly linear correlations (McDougall and Harrison, 1999). This problem can be circumvented by using an inverse isochron diagram that plots $^{36}Ar/^{40}Ar$ versus $^{39}Ar/^{40}Ar$ (see Figure 74). For more discussion on the properties of isochron plots see Turner (1971) and Kelley et al. (1986). In this project, the inverse isochron plot is used exclusively to graphically determine the trapped and radiogenic argon abundances for each heating step in each analysis, and thus assess if the mixing line falls within the definitions of an isochron. Once the trapped component is determined using the inverse isochron plot, the new ^{40}Ar value for the trapped component can then be inserted into the age calculations to produce more representative formation ages.

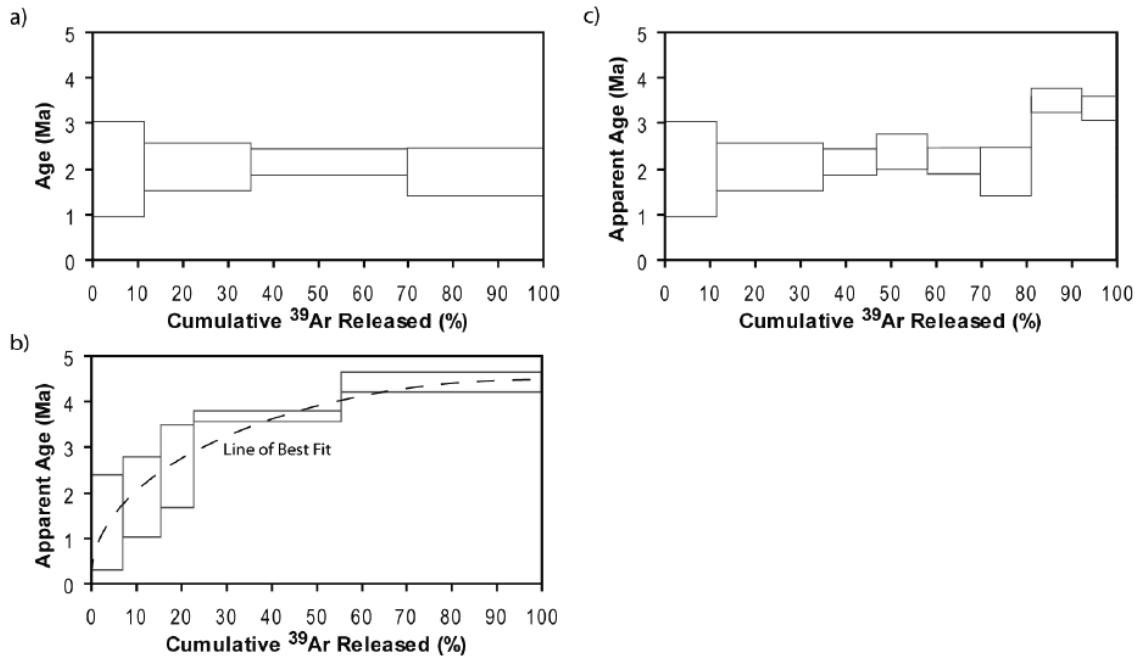

Figure 73. Simple examples of **a)** an ideal $^{40}Ar/^{39}Ar$ age spectrum from which to derive a plateau age, **b)** a $^{40}Ar/^{39}Ar$ age spectrum showing diffusive loss of radiogenic argon after formation from which the fraction of argon lost can be calculated from the line of best fit, and **c)** a $^{40}Ar/^{39}Ar$ age spectrum showing release of excess argon in the last heating steps possibly release from incompletely degassed clasts in the highest temperature steps.

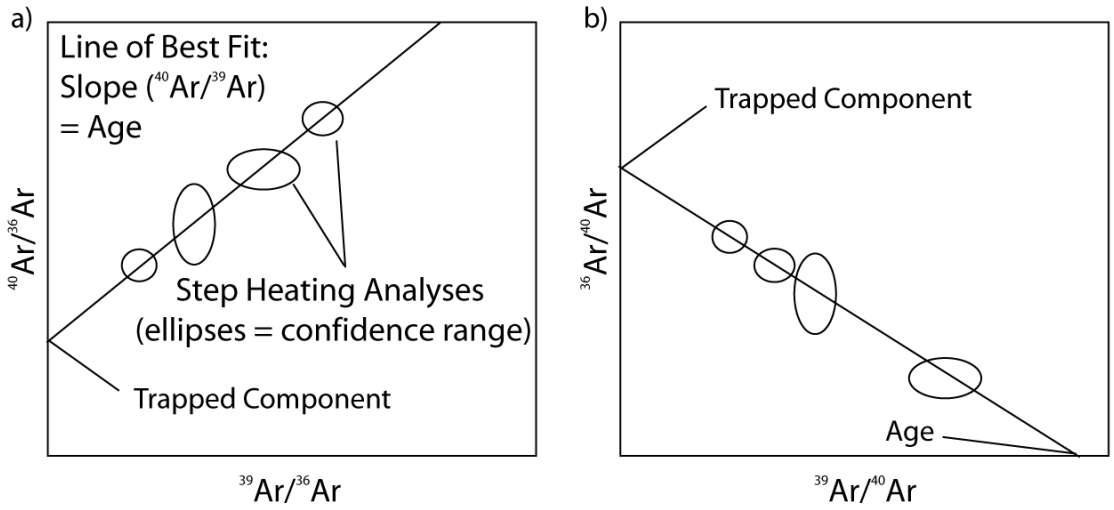

Figure 74. Simple example of **a)** a normal isochron and **b)** a reverse isochron. Each step-heating analysis is represented as points with error bars as ellipses. The sample age is calculated using the line of best fit in **a)** whereas the age can be calculated from the x-axis intercept in **b)**.

Exposure Age Calculations

Cosmic ray exposure (CRE) ages are calculated based on the spallation of Ca to ^{38}Ar by interaction of cosmic rays with the sample. As previously discussed, samples residing in the top metre of the lunar regolith are exposed to cosmic rays which produce spallation products (Reedy et al., 1983). However, overlying regolith acts as a shield, therefore reducing the production of spallation products (Hohenberg et al., 1978). Since the basis of CRE age calculation is the production of spallation of Ca to ^{38}Ar, corrections must be applied for other spallation products. The resulting CRE age will be integrated over the lifetime of an impact spherule through multiple exposure/burial cycles as there is no known mechanism that resets the Ca-spallation-produced ^{38}Ar abundance in the impact spherule. The following equation is used to determine the amount of ^{38}Ar in the sample per gram of Ca (see Hennessy and Turner, 1980 for derivation):

$$\frac{^{38}Ar}{Ca} = 1.13 \times \frac{^{38}Ar}{^{37}Ar} \times \alpha \times J \times 7.012 \times 10^{-3} \quad \textbf{[12]}$$

where

1.13 relates to the $^{38}Ar/^{37}Ar$ ratio to the cosmogenic-only component (Hennessy and Turner, 1980).

α = proportionality factor to convert $^{38}Ar/^{37}Ar$ into $^{38}Ar/Ca$ (Equation 13)

J = J factor (Equation 11)

7.012×10^{-3} = constants of K-decay and unit conversion to make $^{38}Ar/Ca$ into cc STP/g

$$\alpha = \left(\frac{K}{Ca}\right) \div \left(\frac{^{39}Ar*}{^{37}Ar}\right) \quad \textbf{[13]}$$

The $^{38}Ar/^{37}Ar$ ratio of the sample is determined using isotope correlation diagrams with $^{38}Ar/^{36}Ar$ versus $^{37}Ar/^{36}Ar$ ratios with uncertainties propagated at the 1σ level (see "cosmochron method" in Levine et al., 2007). Identification of sources unrelated to the CRE ages can then be identified and removed and the $^{38}Ar/^{37}Ar$ ratio can be determined using a regression through the remaining steps satisfying the same statistical conditions for the calculation of formation age from normal and inverse isochrons. Once the $^{38}Ar/Ca$ content of the sample is ascertained, it is then possible to determine the exposure age assuming a nominal production rate of ^{38}Ar from spallation of Ca (Equation 14). The rate of $1.4 \times 10^{-8} cm^3$ STP ^{38}Ar /gram of Ca/Ma is typically adopted for this calculation following Turner et al. (1971) and is based on spallation rates from lunar rocks (Huneke et al., 1972).

$$t_{exposure} = \left(\frac{^{38}Ar}{Ca}\right)_{Sample} \div \left(\frac{^{38}Ar}{Ca}\right)_{Production} \quad \textbf{[14]}$$

5.3 Method

Suitability of Lunar Impact Spherules for $^{40}Ar/^{39}Ar$ dating

To evaluate the suitability of individual impact spherules for $^{40}Ar/^{39}Ar$ dating, a sensitivity test was conducted by estimating the potential $^{40}Ar^*$ yield using a series of calculations based on Equation 11. Equation 11 is rearranged such that it is expressed in terms of the $^{40}Ar^*$ yield from individual samples:

$$^{40}Ar^*(mol/g) = {}^{40}K(mol) \times \frac{\lambda_e + \lambda_e^{'}}{\lambda} \times \left[(\exp \lambda t) - 1\right] \times W \qquad \textbf{[15]}$$

Where $\frac{\lambda_e + \lambda_e^{'}}{\lambda}$ = inverse decay constant of ^{40}K to ^{40}Ca via beta capture = $\frac{1}{9.54}$

Combined decay constant $\lambda = \lambda_\beta^- + \lambda_e + \lambda_e^{'}$ = 5.543 x 10^{-10} per annum

t = time in years

W = sample weight in grams

^{40}K (mol) was determined using K_{total} expressed as K_2O (wt.%) determined by EMP on LCP-mounted impact spherules (see previous chapter), assuming that the major element analyses for K_{total} are representative of the "bulk" K abundance using the following equation:

$$^{40}K(mol) = \left(K_2O_{(wt\%)} \times C(K_2O \rightarrow K) \div 100 \right) \times \frac{^{40}K}{K} \qquad \textbf{[16]}$$

where $C(K_2O \rightarrow K)$ = conversion factor to convert K_2O to K wt.% = 0.83013

$^{40}K/K$ = mol fraction of ^{40}K with respect to total K

The sample weight (W) was estimated by using the dimensions obtained during the initial petrographic study. The mass of each impact spherule is estimated using the general volume formula of a spheroid (Equation 17) multiplied by the density which is assumed to be 3 g/cm^3. Although masses of a small number of impact spherules were measured using a microbalance available at the Research School of Earth Sciences, ANU, the calculated densities of most spherules were <1 g/cm^3. This value is inconsistent with glass densities that ranges from 1.0 - >3.32 g/cm^3 in Carrier et al. (1991), and the assumption of a 3 g/cm^3 density. Although low densities can result from vesicles within the impact spherules, the problem appears to lie with measurements obtained with the microbalance. The formation age of the sample is not known so a range of ages was assumed in order for ^{40}Ar* to be calculated.

$$V = \frac{4}{3}\pi a^2 b \qquad \textbf{[17]}$$

Where V = volume of a sphere

a and b = the measured short and long axes, respectively

The argon isotopic analyses were conducted in collaboration with Dr. Fred Jourdan, Curtin University, using a MAP 215-50 at the John de Laeter Centre of Mass Spectrometry. Instrument performance (sensitivity and background level) of this spectrometer is given in Table 12. The yield of ^{40}Ar* in each impact spherule as a function of age was converted to a signal (mV) using Equation 15. An optimal signal of 400mV above background was set as the minimum required from an impact spherule for a single heating step with each subsequent heating step requiring an additional 400mV of signal. The results are presented in Table 12 which shows the number of impact spherules that could be dated at variable spherule ages and number of heating steps by the MAP 215-50 at Curtin University.

Having estimated the ^{40}Ar* abundance of each impact spherule over a range of possible formation ages, thirty impact spherules with the highest ^{40}Ar* abundance, consisting

mostly of spherules with local origin, were selected for $^{40}Ar/^{39}Ar$ dating. The number of impact spherules chosen was based on the availability of lab time and funding. These impact spherules were recovered from the LCP mounts using the recovery method outlined in Chapter 2 (The Leit-C-Plast Mount - Schematic and Description) and subsequently sent to Dr. Fred Jourdan at Curtin University to be prepared and sent for irradiation.

Table 12. Sensitivity analysis for $^{40}Ar/^{39}Ar$ of lunar impact spherules using the MAP 215-50 noble gas spectrometer at Curtin University. Sensitivity and blank level of the machine was obtained from Dr. Fred Jourdan (pers. Comm.). A total of 225 impact spherules (>75μm diameter, measured K abundance) were tested. Each step is calculated for an optimal signal of 400mV for $^{40}Ar^*$ and a range of potential spherule ages were used.

Apparent Sensitivity (ccSTP/mV)	4.48E-13
High Temperature Blank (ccSTP)	2.24E-12
Number of Spherules suitable for dating	
No. Heating Steps	1 -Fusion
100Ma	16
250Ma	35
4000Ma	221
No. Heating Steps	3
100Ma	9
250Ma	14
4000Ma	200
No. Heating Steps	10
100Ma	5
250Ma	8
4000Ma	126

5.3.1 Radioisotopic Dating using the $^{40}Ar/^{39}Ar$ Method

Dr. Fred Jourdan prepared the thirty lunar impact spherules selected for $^{40}Ar/^{39}Ar$ dating by loading into 5 large wells of a 1.9 cm diameter and 0.3 cm deep aluminium disc. These wells were bracketed by three small wells that included Hb3gr hornblende used as a neutron fluence monitor for which an age of 1074 ± 5 Ma was adopted and a good

inter-grain reproducibility has been demonstrated (Jourdan and Renne, 2007; Jourdan et al., 2006; Turner et al., 1971). The discs were Cd-shielded (to minimize undesirable nuclear interference reactions) and sent for 30 hours of irradiation in the Hamilton McMaster University nuclear reactor (Canada) in position 5C.

The $^{40}Ar/^{39}Ar$ analyses were performed at the Western Australian Argon Isotope Facility at Curtin University, operated by a consortium consisting of Curtin University and the University of Western Australia. Analyses were supervised by Dr. Fred Jourdan and conducted by the author and Dr. Marc Norman during a two week visit to Curtin University between the 28th April to the 11th May 2009. The samples were step-heated using a 110 W Spectron Laser System, with a continuous Nd-YAG (IR; 1064 nm) laser rastered over the sample for a minute to ensure a homogenously distributed temperature. The gas was purified in a stainless steel extraction line using two SAES AP10 getters to minimise the volume and blank of the line, and enhance the volume of Ar transmitted to the mass spectrometer. During the initial analyses, the first few impact spherules were found to be quite clean (i.e. the gas did not have to be further purified from contaminants). Consequently, it was decided that one getter was unnecessary and was bypassed to improve the background levels. Ar isotopes were measured in static mode using the MAP 215-50 mass spectrometer (resolution of ~600; sensitivity of $2x10^{-14}$ mol/V) with a Balzers SEV 217 electron multiplier mostly using 9 to 10 cycles of peak-hopping. Preparation and calibration of the equipment was performed by Dr. Fred Jourdan. The data acquisition was performed with the Argus program written by M.O. McWilliams and run under a LabView environment. The raw data were processed using the ArArCALC software (Koppers, 2002) and statistics (MSWD and Probability) are calculated using the Isoplot/Ex plugin for Microsoft Excel (Ludwig, 2006). Ages have been calculated using the decay constants recommended by Steiger and Jäger (1977). All errors are propagated into the final result.

Prior to sample analysis, the Hb3gr hornblende standards were analysed. The mean J-values computed from standard grains within the small pits are all consistent with a value of 0.0103800 ± 0.0000311 (0.29%) determined as the average and standard

deviation of J-values for the small wells within each irradiation disc. Mass discrimination was monitored using an automatic air pipette and provided a mean value of 1.00148 ± 0.00046 per dalton (atomic mass unit). The correction factors for interfering isotopes were $(^{39}Ar/^{37}Ar)_{Ca} = 7.30x10^{-4}$ (± 11%), $(^{36}Ar/^{37}Ar)_{Ca} = 2.82x10^{-4}$ (± 1%) and $(^{40}Ar/^{39}Ar)_{K} = 6.76x10^{-4}$ (± 32%). Blanks were monitored every 3 to 4 steps and typical ^{40}Ar blanks range from 1 x 10^{-16} to 2 x 10^{-16} mol.

Criteria for the determination of plateaus were adopted from Jourdan et al. (2009):

- Plateaus must include at least 70% of ^{39}Ar and should be distributed over a minimum of 3 consecutive steps agreeing at 95% confidence level and satisfying a probability of fit (P) ≥ 0.05.
- Plateau ages are given at the 2σ level and are calculated using the mean of all the plateau steps, each weighted by the inverse variance of their individual analytical error.
- Mini-plateaus are defined similarly except that they include between 50% and 70% of ^{39}Ar.
- Integrated ages (2σ) are calculated using the total gas released for each Ar isotope.
- Inverse isochrons include the maximum number of steps with P ≥ 0.05.
- The uncertainties on the $^{40}Ar^*/^{39}Ar$ ratios of the monitors are included in the calculation of the integrated and plateau age uncertainties, but not the errors on the age of the monitor and on the decay constant (internal errors only, see discussion in Min et al., 2000).

Exposure ages were calculated using the methods outlined in 5.2.3. Calculation of Formation and Exposure Ages. Initial treatment and interpretation of individual analyses were conducted in collaboration with, and approved by, Dr. Fred Jourdan.

5.4 Results

A total of twenty-six formation ages were obtained from the thirty dated lunar impact spherules which range from zero age through to ~4.4Ga. Cosmogenic exposure ages could be calculated from fifteen of the impact spherules. The results are summarised in Table 13 and are described in the following text.

In terms of $^{40}Ar/^{39}Ar$ formation ages, seventeen out of the thirty impact spherules selected for dating were found to have concordant plateau and isochron ages derived using at least a mini-plateau supported by a minimum three-point isochron with probability ≥5% (e.g. **Figure 1**Figure 75a). Four impact spherules have ages derived using either a mini-plateau or minimum three-point isochron with probability ≥5% (e.g. Figure 75b). Together these 21 out of 30 (70%) impact spherules are considered to have statistically acceptable ages. Compared to previous studies (Culler et al., 2000; Levine et al., 2005) of impact spherules from Apollo 12 and 14, the yield of acceptable isochrons is slightly higher despite the K-poor highlands provenance of most of the spherules in this project. A further five impact spherules from this study have ages, but are not statistically acceptable as defined in the methods (e.g. Figure 75b); one has no measurable radiogenic argon and is inferred to have a zero age. These "useable", but not statistically acceptable, impact spherules are all very young (<400Ma) as they all contain very little or no in-situ radiogenic argon from K-decay. The remaining four impact spherules did not yield useful data and results were discarded (e.g. Figure 75c). These samples typically exhibit a high amount of scatter, argon loss, or formation ages that span the age of the Moon (e.g. see LS3-25 in Table 13). For details of individual sample chemistry and interpretation of $^{40}Ar/^{39}Ar$ data refer to the Appendix 1 and 2 respectively. For the individual argon release patterns see electronic annex 4.

The formation ages generally cluster in the 0-600Ma and 3500-4500Ma ranges, with few spherules having intermediate ages (see Figure 76). Three features can be inferred from the Figure 76 histogram: a peak in impact spherule production early in lunar history between 4.4-3.2Ga, a minimum in spherule production between 3.2Ga and

2.0Ga, and an increase in spherule production <2.0Ga leading a spike in from 400Ma to present. Spikes in the Figure 76 ideogram do not necessarily represent periods of intense spherule production, but are ages of very well-constrained impact spherules. Note that impact spherules without statistically acceptable ages are still "useable" and have not been excluded from the current study. Four of these useable spherules have ages that were calculated from the final step(s) due to a lack of measurable $^{40}Ar^{*}$, but all have formation ages of <400Ma. Assuming that these spherules should indeed be older, the only way to apparently decrease the age would be to increase the abundance of ^{39}Ar, which is simply not possible as ^{39}Ar is a reactor product, or decrease the $^{40}Ar^{*}$ abundance. The latter can be done by heat generated by another impact, in which case the spherule still records an impact event albeit not the one that formed it, or heat generated by volcanic activity, evidence of which is lacking at the Apollo 16 site (Muehlberger et al., 1980). The K-rich crusts on impact spherules could serve to increase the yield of ^{39}Ar during irradiation, but these surface-correlated gases should (and were for the spherules without statistically acceptable ages) be degassed during early low-temperature steps of the analysis (Levine et al., 2007; Manka and Michel, 1970). Therefore, these impact spherules without statistically acceptable ages still record the most recent impact event and can be inferred to be young.

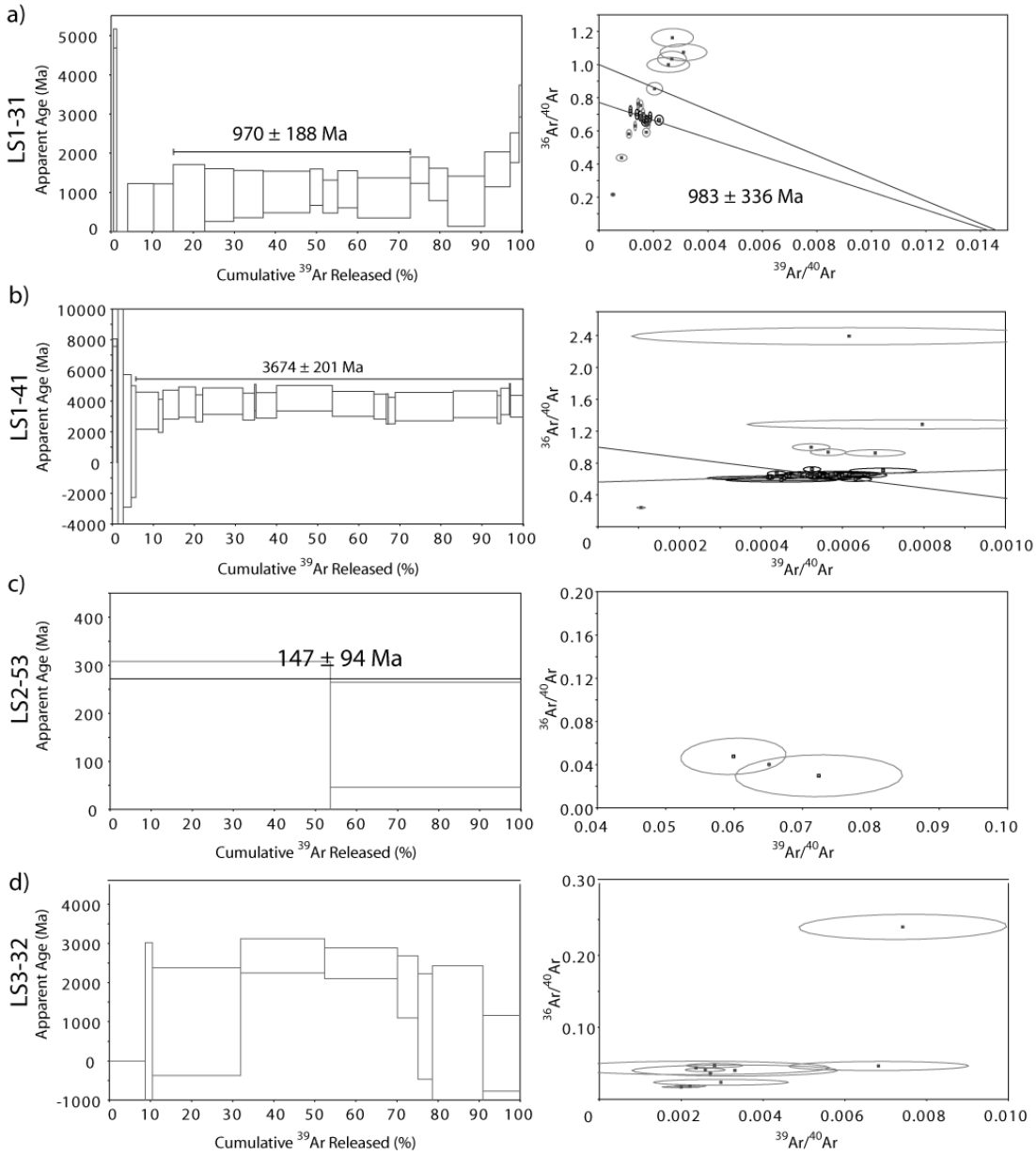

Figure 75. Examples of plateau and isochron diagrams from **a)** a well-constrained sample with both concordant plateau and reverse isochron ages **b)** a well-constrained sample with only a statistically-acceptable plateau age **c)** a sample inferred to be young, but not statistically acceptable as defined in the methods and **d)** a discarded sample showing significant argon loss.

Table 13. $^{40}Ar/^{39}Ar$ radiometric age determinations of thirty lunar impact spherules. Compositions presented with errors at the 1σ level while ages are all quoted at the 2σ level. All ages are in Ma.

Sample ID	Quality	Al_2O_3 abundance (wt.%)	K_2O abundance (wt.%)	Age Plateau	No. Isochron Steps (Total Non-Blank Steps)	Plateau Coverage (^{39}Ar Released %)	MSWD (Probability)	Reverse Isochron age	MSWD (Probability)	Exposure Age	MSWD (Probability)
LS1-21	Useable	26.74 ± 0.10	0.22 ± 0.01	152 ± 8	1 (3)	100	13 (0%)	147 ± 36	75 (0%)	2 ± 0.2	0.029 (86%)
LS1-22	Statistically Acceptable	23.67 ± 0.08	0.09 ± 0.00	360 ± 95	5 (13)	87	0.41 (80%)	361 ± 157	2 (11%)	36 ± 12	0.39 (76%)
LS1-31	Statistically Acceptable	20.26 ± 1.09	0.13 ± 0.01	970 ± 188	8 (22)	58	0.21 (98%)	983 ± 336	0.83 (55%)	83 ± 38	1.06 (38%)
LS1-33	Statistically Acceptable	21.38 ± 3.56	0.11 ± 0.03	3717 ± 482	7 (9)	82	0.16 (99%)	3693 ± 1565	0.85 (51%)	407 ± 68	0.28 (89%)
LS1-41	Statistically Acceptable	23.59 ± 0.42	0.23 ± 0.05	3674 ± 201	20 (26)	94	0.41 (99%)			111 ± 86	1.6 (10%)
LS1-42	Statistically Acceptable	15.50 ± 0.96	1.72 ± 0.03	1242 ± 39	7 (16)	64	1.9 (8%)	1294 ± 64	2.2 (5%)	2 ± 1	0.57 (72%)
LS1-43	Statistically Acceptable	27.30 ± 0.30	0.15 ± 0.01	371 ± 79	7 (8)	97	0.16 (99%)	367 ± 83	0.26 (93%)	220 ± 6	0.9 (48%)
LS1-53	Discarded	24.86 ± 1.98	0.30 ± 0.08		0 (10)						
LS1-73	Statistically Acceptable	25.42 ± 0.25	0.15 ± 0.01	1738 ± 380	5 (6)	86	0.31 (87%)	1878 ± 626	0.43 (73%)	461 ± 14	0.32 (57%)
LS2-31	Statistically Acceptable	28.71 ± 1.70	0.14 ± 0.09	1629 ± 729	3 (3)	100	0.86 (42%)	1926 ± 1338	35.83 (0%)		
LS2-43	Useable	29.66 ± 0.94	0.03 ± 0.01	0 ± 26	3 (3)	100	0.86 (42%)	200 ± 700	0 (100%)		
LS2-45	Statistically Acceptable	27.30 ± 0.29	0.11 ± 0.01	1505 ± 104	5 (6)	94	0.63 (64%)	1530 ± 121	1.14 (33%)		
LS2-53	Useable	26.54 ± 0.56	0.19 ± 0.06	147 ± 94	2 (2)	100	0.097 (76%)				
LS2-62	Statistically Acceptable	15.90 ± 0.63	0.50 ± 0.04	498 ± 14	3 (6)	63	1.7 (19%)	497 ± 102	3.2 (7%)	311 ± 1591	2.7 (10%)
LS2-63	Statistically Acceptable	30.93 ± 1.15	0.50 ± 0.02		4 (7)			154 ± 134	0.89 (41%)	105 ± 21	2.9 (5%)

Table 13. Continued

Sample ID	Quality	Al_2O_3 abundance (wt.%)	K_2O abundance (wt.%)	Age Plateau	No. Isochron Steps (Total Non-Blank Steps)	Plateau Coverage (^{39}Ar Released %)	MSWD (Probability)	Reverse Isochron age	MSWD (Probability)	Exposure Age	MSWD (Probability)
LS2-71	Useable	26.62 ± 0.36	0.22 ± 0.06	294 ± 31	1 (Fusion age)	100	0 (100%)				
LS3-15	Statistically Acceptable	26.08 ± 0.46	0.10 ± 0.00	4372 ± 270	6 (10)	88	0.21 (96%)	4277 ± 1691	0.51 (73%)	240 ± 222	0.55 (70%)
LS3-21	Statistically Acceptable	26.03 ± 0.41	0.08 ± 0.01	3436 ± 171	9 (11)	99	0.67 (72%)	3521 ± 196	0.90 (51%)	243 ± 73	0.16 (96%)
LS3-24	Statistically Acceptable	14.82 ± 0.51	3.62 ± 0.40	276 ± 63	4 (7)	89	0.49 (69%)	286 ± 134	24 (0%)	306 ± 101	0.25 (62%)
LS3-25	Discarded	26.74 ± 2.07	0.14 ± 0.03	2813 ± 2699	4 (7)						
LS3-32	Discarded	25.39 ± 1.23	0.20 ± 0.07		0 (9)						
LS3-43	Useable	14.11 ± 0.91	0.19 ± 0.01		1 (1)						
LS3-52	Statistically Acceptable	25.75 ± 2.03	0.22 ± 0.02	4255 ± 384	7 (10)	67	0.57 (75%)	4507 ± 1046	2 (8%)	437 ± 124	0.94 (39%)
LS3-53	Discarded	29.36 ± 1.71	0.29 ± 0.24		0 (8)						
LS3-71	Statistically Acceptable	23.18 ± 2.61	0.09 ± 0.03	2565 ± 299	9 (11)	91	0.31 (96%)	2619 ± 576	0.77 (59%)	172 ± 86	0.72 (61%)
LS4-12	Statistically Acceptable	23.49 ± 0.14	0.92 ± 0.01	3862 ± 52	7 (7)	100	0.68 (67%)	3867 ± 53	0.93 (46%)		
LS4-21	Statistically Acceptable	25.60 ± 0.17	0.15 ± 0.02	339 ± 145	3 (4)	80	1.07 (34%)	337 ± 305	13.15 (0%)		
LS5-67	Statistically Acceptable	28.62 ± 1.35	0.12 ± 0.00	1913 ± 728	3 (6)	69	0.015 (99%)	1962 ± 1059	0.06 (81%)		
LS5-72	Statistically Acceptable	16.07 ± 0.49	0.78 ± 0.07	938 ± 151	3 (4)	100	1.14 (32%)	996 ± 324	3.7 (6%)		
LS6-31	Statistically Acceptable	26.66 ± 3.59	0.58 ± 0.31	560 ± 70	3 (3)	100	0.7 (50%)	565 ± 124	3.9 (5%)		

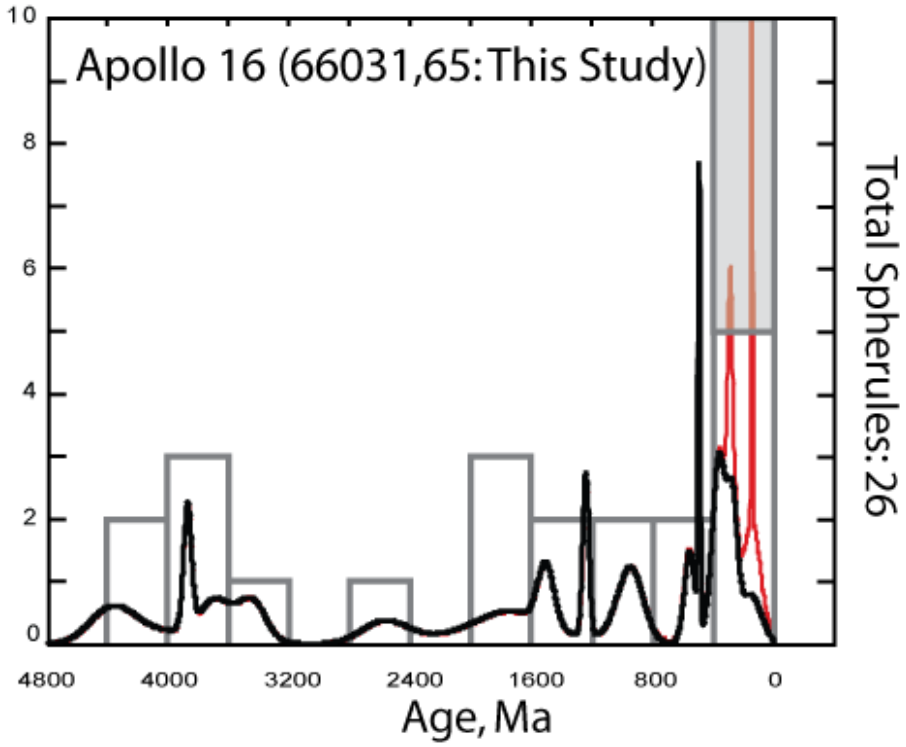

Figure 76. Impact spherule production as recorded by impact spherules from Apollo 16 Station 6 (66031,65). The histograms show the number of impact spherules at each time period (400Ma bins). The solid black ideogram is the sum of the age Gaussian distributions from impact spherules with statistically acceptable ages only. Note that well-constrained ages of individual impact spherules (typically high-K) will produce spikes in the ideogram that may not be representative of the global rate of production. The shaded parts of the histogram represent impact spherules without statistically-acceptable ages that fall within that bin. The red peaks in the 0-400Ma age bin indicate the change to the ideogram if the impact spherules without statistically-acceptable ages are included.

In addition to formation ages, it was also possible to calculate the cosmic ray exposure ages for fifteen of the thirty particles, fourteen of which have statistically acceptable formation ages (Figure 77). The exposure ages indicate that the impact spherules collected from this site have not been exposed for longer than ~600Ma over their lifetimes. Most young impact spherules (<500Ma) have exposure ages that are roughly within a factor of two of their formation ages, indicating that they have spent at least half their lifetimes in the top metre of regolith where they were exposed to cosmic rays

(Reedy et al., 1983). Older spherules, however, appear to have spent a relatively small fraction of their lifetime exposed within the top metre of the regolith as suggested by low ratios of exposure to formation age. However, recall that the efficiency of Ca spallation to ^{38}Ar varies as a function of depth up to a metre. If the top metre is considered "exposed", the exposure age of some impact spherules may be underestimated due to regolith shielding compared to unshielded impact spherules. Using the $^{38}Ar_{Ca}$ production rates from Hohenberg et al. (1978) and assuming uniform shielding from pure anorthosite (density: 2.69g/cm^3), the production of $^{38}Ar_{Ca}$ at ~85cm depth is underestimated compared to particle shielded by ~2cm of pure anorthosite by ~11%. However, even with an 11% underestimation of the exposure age, the >3Ga impact spherules have still spent a smaller fraction of their lifetime exposed on the lunar surface compared to the younger impact spherules.

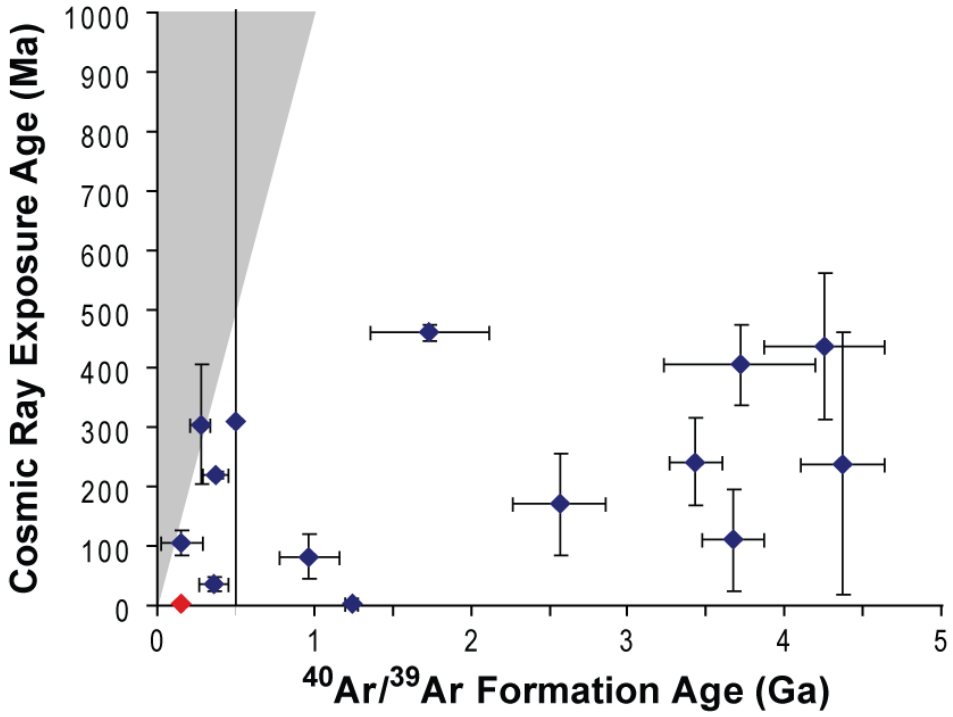

Figure 77. Plot of exposure age versus formation age of fifteen lunar impact spherules in this study. The shaded grey area is the zone where exposure age > formation age. The red point is LS1-21 which does not have a statistically acceptable formation age, but has a very young exposure age. Error bars are ± 2σ.

5.5 Discussion

5.5.1 Impact Spherule Record of Lunar Bombardment

Lunar impact spherules are a relatively recent entry as a recognised tools used to assess the timing of lunar impact. Prior to the current study, the lunar bombardment record as inferred through lunar impact spherule production was mostly based on the records from Apollo 12 (Levine et al., 2005) and 14 (Culler et al., 2000; Levine, 2004). These studies established impact spherule production histograms similar to Figure 76, but better populated with 109 and 81 spherules respectively. Both these sites consist mostly of impact spherules with mare, mixed highlands/mare, and Fra Mauro compositions (refer to Chapter 4: Background) which made them ideal, high-K specimens for $^{40}Ar/^{39}Ar$ dating. More recently, Zellner et al. (2009a) published seven impact spherules formation ages that are the beginnings of an age distribution at the Apollo 17 site. Impact spherules of mare, highlands, and Fra Mauro compositions were dated in the latter study. The Apollo 16 spherule record established in this study complements previous studies because the current impact spherules dated are typically feldspathic, but there are also spherules with KREEPy and mare compositions (refer to Table 13 and following chapter). Together, the Apollo 12, 14, and 16 spherules make up the majority of the data available for the impact spherule record. Note, however, that the shape of the distribution is heavily influenced by the Apollo 12 and 14 records since they are the most populated.

The combination of all impact spherule records is shown in Figure 78a, but note there are two prominent selection effects (statistical bias due to selection of individuals or groups over others) that influence this figure. The most pronounced selection effect occurs with the inclusion of glasses studied by Delano et al. (2007) and Zellner et al. (2009b), as these specifically studied K-rich glass shards (with a shared 3.8Ga age) and 800Ma glasses, respectively. Glasses of these ages are over-represented when compared to populations dated in the earlier Apollo 12 (Levine et al., 2005) and 14 (Culler et al., 2000; Levine, 2004) studies. This produces two spikes in the record, the more obvious spike at 800Ma and the smaller spike at 3.8Ga. The second selection effect stems from

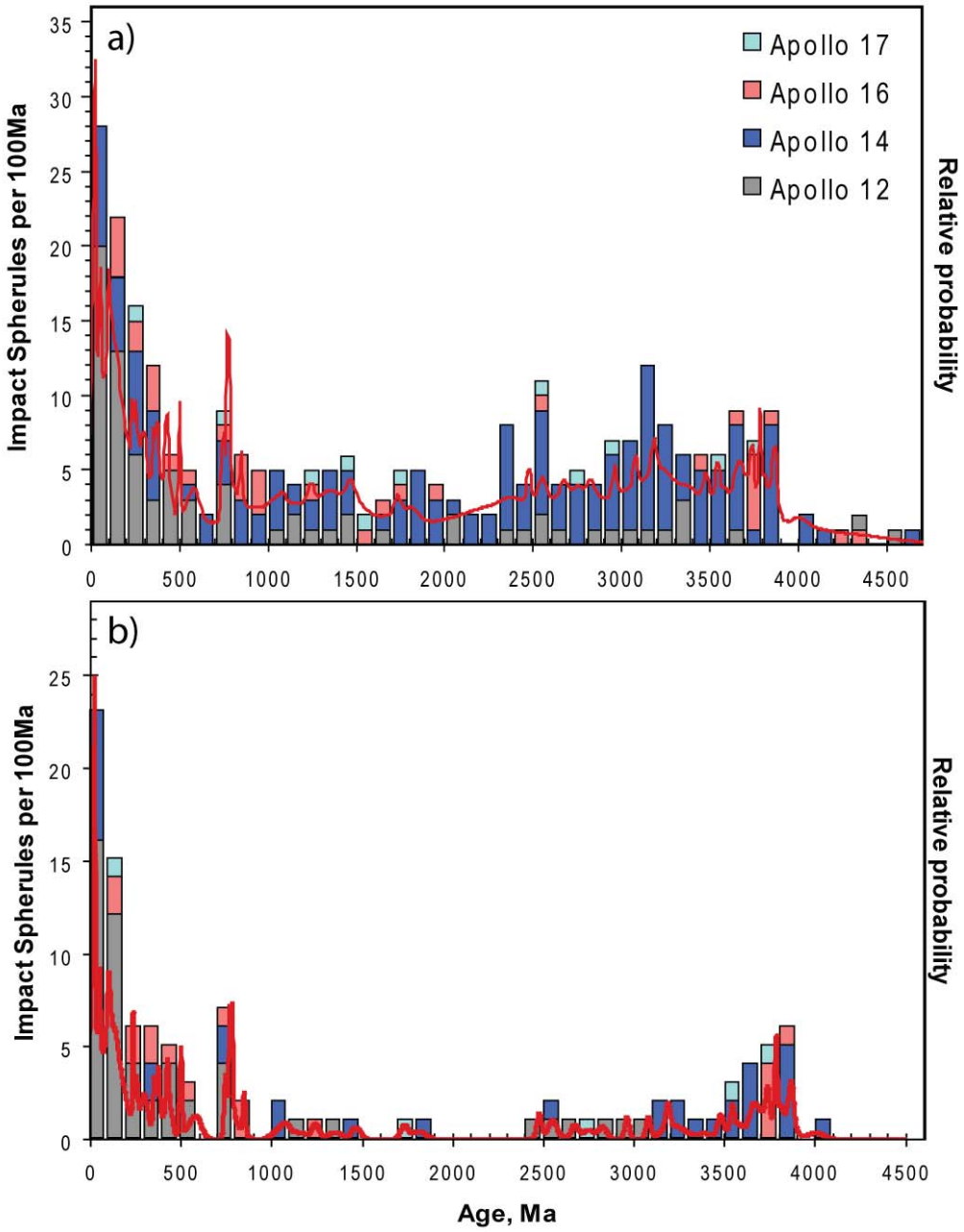

Figure 78. Lunar bombardment history as shown by the histogram (100Ma bins) and ideogram of **a)** all impact spherules **b)** impact spherules with uncertainties ≤100Ma. Sources of data include: Apollo 12 (Levine et al., 2005), Apollo 14 (Culler et al., 2000; Levine, 2004; Zellner et al., 2009b), Apollo 16 (This study; Delano et al., 2007; Zellner et al., 2009b), and Apollo 17 record (Zellner et al., 2009a). This diagram is influenced by a number of selection effects that will be discussed in the following chapter. For now, they are assumed to have a second order effect.

the inclusion of multiple glasses that may have formed a limited number of impact events (Delano et al., 2007; Zellner et al., 2009b) and/or inclusion of glasses potentially volcanic in origin (Culler et al., 2000; Levine, 2004). Delano et al. (2007) noted that the impact glasses dated in their study were specifically selected for having a HKFM composition, are likely to be exotic to the Apollo 16 site, and all have ages ~3.8Ga with small 2σ errors (<60Ma). They concluded, based on major element chemistry and ages, that these glasses may have been formed by a single impact event. Similarly, Zellner et al. (2009b) concluded that only seven represent distinct were recorded in the nine particles that were dated. If each of these glasses is treated as a separate impact event, as they are in Figure 78, the impact glass record will be skewed towards events that produce multiple glasses (large impact events?). The ability to identify duplicate impact spherules from the same event using major elements can negate this selection effect. However, compositional information was not available (or not used in this manner) in the earlier records from Apollo 12 (Levine et al., 2005) and 14 (Culler et al., 2000; Levine, 2004). The following discussion will focus on the broader trends shown by the combined impact record (Figure 78), for the moment, assuming that selection effects are a second order addition to the primary impact record. A more detailed discussion on selection effects, their influence on the impact record, and methods employed in the current study for negating their influence will be presented in the following chapter.

The combination of all impact spherule records in Figure 78a reveals some interesting features. The first is a paucity of impact spherules older than ~3.9Ga which appears as an abrupt decline in both the ideogram and histogram. The second is a gradual decline in impact activity from 3.9Ga to about 2.5Ga reaching a minimum between 2.5Ga and 1.5Ga in Figure 78a, or between 2.4Ga and 1.9Ga according to Figure 78b. The third feature is a rapid increase in impact spherule production from ~500Ma to the present, ignoring the 800Ma spike as it is a selection bias. The same features exist even when impact spherules with age uncertainties of >100Ma are removed (Figure 78b) suggesting that these observations are not due to scatter of poorly-constrained impact spherule ages. If these are faithful records of the lunar bombardment history, they suggest that impact spherule production was most prominent starting from 3.8-3.9Ga.

Coincidentally, this period coincides with a spike in impact activity recorded by lunar melt breccias and has lead to the controversial idea of a late influx of impactors known as the Late Heavy Bombardment (LHB). Following this influx is a more gradual decline in impact spherule production. If a LHB is invoked, this would represent the tailing end of an earlier increase in impactors. Impact modelling by Gomes et al. (2005) (Nice model: also see Bottke et al., 2010; Strom et al., 2005) have been able to provide a trigger for the LHB hypothesis and reproduce the sudden increase in impact activity followed by more gradual decline. In this model, the migration of the giant planets (Jupiter and Saturn) destabilises a disk of planetismals (the remains of which, is now known as the Kuiper Belt) causing them to scatter into the inner solar system and thus trigger a LHB. The classic Neukum (1983) crater production rate, derived from crater counting, also indicates that a decline in >1km diameter craters between 4Ga-3Ga, a trend broadly reflected in Figure 78b. A LHB would also be consistent with a lack of >4.0Ga impact spherules as these are likely to have been destroyed or buried from resurfacing (see Wilhelms, 1987) and, therefore not sampled by the Apollo missions. However, based on models for crater production functions that suggest an even greater cratering rate prior to 4.1Ga (Hartmann, 1975, 2003; Neukum et al., 2001), Hartmann (2003) argues "that impact melts on average spend more time near the surface than crustal and plutonic rocks hence are destroyed more efficiently by cratering after their formation" concluding that "most of the impact melt material that came to reside in the upper 100m of the lunar megaregolith before 4.1 Gyr ago was physically pulverized to sizes smaller than have been dated by available techniques". This counter-argument would also explain the lack of >4.0Ga ages. However, impact spherules with >4.1Ga formation ages do exist as do other lunar materials (e.g. see Nyquist and Shih, 1992; Pidgeon et al., 2007). In this case, the focus should shift from why there is an apparent increase in activity at 4.0Ga declining to 1.5Ga rather than why there is a lack of >4.0Ga ages.

The characteristic decline of impact activity from 4.0-1.5Ga period in impact spherule record is also shared by impact-reset age distributions of lunar meteorites (Cohen et al., 2000) and other types of meteorites (Bogard, 1995). This suggests that the 4.0-1.5Ga

decline is not unique to the impact spherules and that they may be a primary record of decline from a period of large-scale bombardment. However, in its current state, the lunar impact spherule record does not provide further constraints on the LHB. Conversely, lunar impact spherules appear to better record more recent impact activity, unlike other lunar impact records currently available.

Two outstanding features of the more recent impact history are the 800Ma spike in impact activity and gradual increase in activity from ~500Ma to present. As discussed previously, the 800Ma spike is produced by the inclusion of data from Zellner et al. (2009b), which introduces a selection bias towards those ages. That is not to say that impact activity was insignificant during that time, but instead indicates that, compared to the rest of the record, the spike may be an artefact of over-represented. However, the presence of four 800Ma impact spherules, with 2σ errors < 34Ma, in the Apollo 12 record (Levine et al., 2005), suggests that the 800Ma may be real rather than a selection effect from using these data. Additionally, the 800Ma spike also coincides with the age of the Copernicus event (800 ± 15Ma: Bogard et al., 1994) and non-mare rocks at Apollo 12 also thought to have been influenced by this event (Barra et al., 2006). Regardless, impact spherules show a gradual increase in impact activity over the past ~500Ma contrary to the conclusions of Hartmann (2007) who recently adjusted the crater production function to reflect an impact rate in a state of decline during this period. This apparent increase in impact rate is of interest as it suggests that the Moon, and by proximity the Earth, is in a period of enhanced bombardment. The possible triggers for enhanced bombardment may result from relatively recent collisions within the asteroid belt. This period of may be related to the L-chondrite breakup event, which is most accurately defined by fossil meteorites found in Sweden with ages of ~470Ma (Korochantseva et al., 2007). Impact reset ages of terrestrially-recovered L-chondrite (c.f. Bogard, 1995) and LL-chondrite (Jourdan et al., 2010) meteorites have a tendency to cluster around the same time, between 300-600Ma. Additionally, the H-chondrite record compiled from various sources by Swindle et al. (2009) also shows an increase in impact reset ages over a similar period (see Figure 79). It is also interesting to note that, in the L, LL, and H chondrite records, there is an early peak in impact reset ages >3.4Ga

indicating an intense early bombardment. This "U" shaped distribution of impact ages is also similar to the impact spherule record, suggesting that they may represent an actual increase in impact activity triggered by the event or events that produced the impact-reset age distribution of meteorites. According to Bogard (1995), the early intense bombardment recorded by HED meteorites, chondrites, and lunar samples suggests that this early peak in activity may have involved disruption of planetismals and affected the entire inner Solar System, a conclusion echoed in the results of the more recent Nice model (Gomes et al., 2005). However, conclusions about the impact history should not be drawn using only the impact spherule age distributions without some understanding of the potential selection biases. These selection biases are considered in the following chapter.

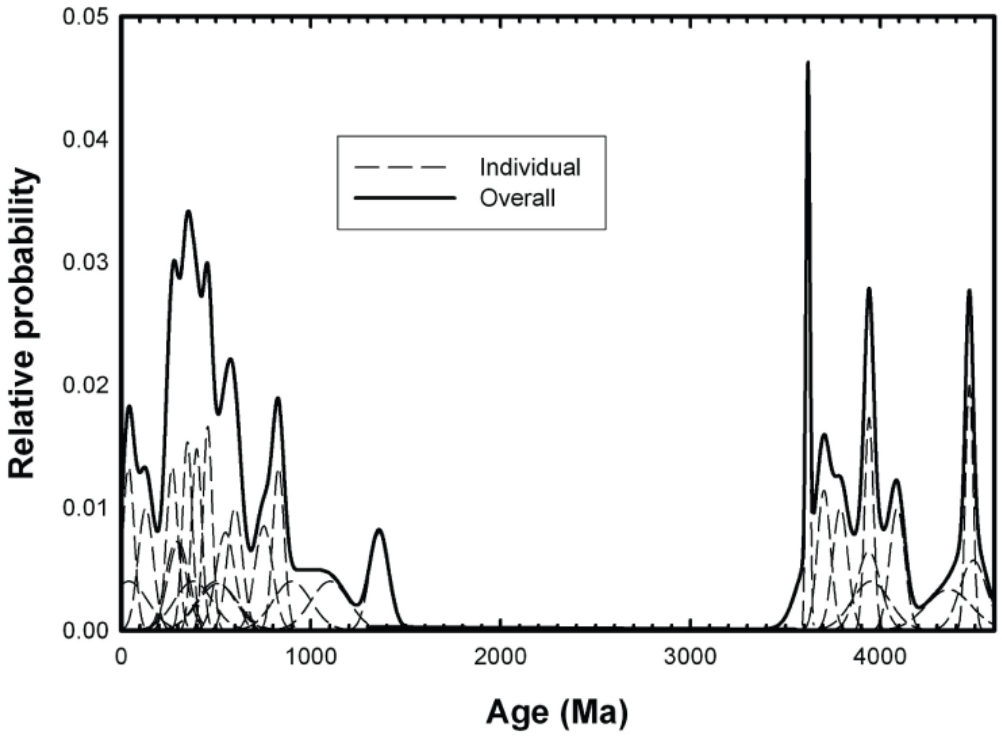

Figure 79. Bombardment history as shown by H-chondrites; data compiled from various sources by Swindle et al. (2009)

Diagram from Swindle et al. (2009)

5.6 Summary

Thirty impact spherules were selected for dating. Twenty-six yielded formation ages and fifteen yielded exposure ages. These data are used to establish the first impact spherule age distribution for the Apollo 16 site and consists mostly of locally-derived K-poor spherules. Impact spherule records from Apollo 12, 14, 16 (including this project), and 17 were combined to produce a more diverse impact spherule record. However, the combined record does not provide further constraints on the controversial idea of a late heavy bombardment. On the other hand, the more recent spherule record (i.e. <1Ga) appears similar to the impact-reset ages of meteorites, indicating that events that triggered the disruption of meteorites may have lead to an enhanced bombardment on the Moon. However, these interpretations do not take into account the nature of the spherule record including potential selection bias, which will be discussed in the following chapter.

5.7 Chapter References

BARRA F., SWINDLE T. D., KOROTEV R. L., JOLLIFF B. L., ZEIGLER R. A. and OLSON E. (2006) 40Ar/39Ar dating of Apollo 12 regolith: Implications for the age of Copernicus and the source of nonmare materials. *Geochimica et Cosmochimica Acta* **70**(24), 6016-6031.

BOGARD D. D., GARRISON D. H., SHIH C. Y. and NYQUIST L. E. (1994) ^{39}Ar-^{40}Ar dating of two lunar granites: The age of Copernicus. *Geochimica et Cosmochimica Acta* **58**(14), 3093-3100.

BOGARD D. (1995) Impact ages of meteorites: A synthesis. *Meteoritics* **30**, 244-268.

BOTTKE W. F., WALKER R. J., DAY J. M. D., NESVORNY D. and ELKINS-TANTON L. (2010) Stochastic Late Accretion to Earth, the Moon, and Mars. *Science* **330**(6010), 1527-1530.

BRERETON N. R. (1970) Corrections for interfering isotopes in the40Ar/39Ar dating method. *Earth and Planetary Science Letters* **8**(6), 427-433.

CARRIER D., III, OLHOEFT G. and MENDELL W. (1991) Physical Properties of the Lunar Surface. In *Lunar Sourcebook: A User's Guide to the Moon* (eds. G. Heiken, D. T. Vaniman and B. M. French), pp. 475-594. Cambridge University Press.

COHEN B. A., SWINDLE T. D. and KRING D. A. (2000) Support for the Lunar Cataclysm Hypothesis from Lunar Meteorite Impact Melt Ages. *Science* **290**(5497), 1754-1756.

CULLER T. S., BECKER T. A., MULLER R. A. and RENNE P. R. (2000) Lunar Impact History from 40Ar/39Ar Dating of Glass Spherules. *Science* **287**(5459), 1785-1788.

DELANO J. W., ZELLNER N. E. B., BARRA F., OLSON E., SWINDLE T. D., TIBBETTS N. J. and WHITTET D. C. B. (2007) An integrated approach to understanding Apollo 16 impact glasses: Chemistry, isotopes, and shape. *Meteoritics & Planetary Science* **42**, 993-1004.

DICKIN A. P. (2005) Chapter 10: K-Ar and Ar-Ar Dating. In *Radiogenic Isotope Geology*, pp. 254-290. Cambridge University Press, New York.

GOMES R., LEVISON H. F., TSIGANIS K. and MORBIDELLI A. (2005) Origin of the cataclysmic Late Heavy Bombardment period of the terrestrial planets. *Nature* **435**(7041), 466-469.

HARTMANN W. K. (1975) Lunar "cataclysm": A misconception? *Icarus* **24**(2), 181-187.

- (2003) Megaregolith evolution and cratering cataclysm models: Lunar cataclysm as a misconception (28 years later). *Meteoritics & Planetary Science* **38**(4), 579-593.

HARTMANN W. K., QUANTIN C. and MANGOLD N. (2007) Possible long-term decline in impact rates: 2. Lunar impact-melt data regarding impact history. *Icarus* **186**(1), 11-23.

HASKIN L. and WARREN P. H. (1991) Lunar Chemistry. In *Lunar Sourcebook: A User's Guide to the Moon* (eds. G. Heiken, D. T. Vaniman and B. M. French), pp. 357-476. Cambridge University Press.

HENNESSY J. and TURNER G. (1980) 40Ar-39Ar Ages and Irradiation History of Luna 24 Basalts. *Philosophical Transactions of the Royal Society of London. Series A, Mathematical and Physical Sciences* **297**(1428), 27-39.

HODGES R. R. (1977) Release of radiogenic gases from the moon. *Physics of The Earth and Planetary Interiors* **14**(3), 282-288.

HOFFMAN J. H., HODGES R. R., JR., JOHNSON F. S. and EVANS D. E. (1973) Lunar atmospheric composition results from Apollo 17. In *4th Lunar Science Conference*, pp. 2865-2875.

HOHENBERG C. M., PODOSEK F. A., SHIRCK J. R., MARTI K. and REEDY R. C. (1978) Comparisons between observed and predicted cosmogenic noble gases in lunar samples. In *9th Lunar and Planetary Science Conference*, pp. 2311–2344. Pergamon Press, Inc., Houston, Texas.

HUNEKE J. C., PODOSEK F. A., BURNETT D. S. and WASSERBURG G. J. (1972) Rare gas studies of the galactic cosmic ray irradiation history of lunar rocks. *Geochimica et Cosmochimica Acta* **36**(3), 269-301.

JOURDAN F., ANDREOLI M. A. G., MCDONALD I. and MAIER W. D. (2010) 40Ar/39Ar thermochronology of the fossil LL6-chondrite from the Morokweng crater, South Africa. *Geochimica et Cosmochimica Acta* **74**(5), 1734-1747.

JOURDAN F., MARZOLI A., BERTRAND H., CIRILLI S., TANNER L. H., KONTAK D. J., MCHONE G., RENNE P. R. and BELLIENI G. (2009) 40Ar/39Ar ages of CAMP in North America: Implications for the Triassic-Jurassic boundary and the 40K decay constant bias. *Lithos* **110**(1-4), 167-180.

JOURDAN F. and RENNE P. R. (2007) Age calibration of the Fish Canyon sanidine 40Ar/39Ar dating standard using primary K-Ar standards. *Geochimica et Cosmochimica Acta* **71**(2), 387-402.

JOURDAN F., VERATI C. and FÉRAUD G. (2006) Intercalibration of the Hb3gr 40Ar/39Ar dating standard. *Chemical Geology* **231**(3), 177-189.

KELLEY S. (1995) Ar-Ar Dating by Laser Microprobe. In *Microprobe Techniques in the Earth Sciences* (eds. P. Potts, J. Bowles, S. Reed and M. Cave), pp. 327-358. Chapman & Hall.

KELLEY S., TURNER G., BUTTERFIELD A. W. and SHEPHERD T. J. (1986) The source and significance of argon isotopes in fluid inclusions from areas of mineralization. *Earth and Planetary Science Letters* **79**(3-4), 303-318.

KOPPERS A. A. P. (2002) ArArCALC v2.4--software for 40Ar/39Ar age calculations. *Computers & Geosciences* **28**(5), 605-619.

KOROCHANTSEVA E. V., TRIELOFF M., LORENZ C. A., BUYKIN A. I., IVANOVA M. A., SCHWARZ W. H., HOPP J. and JESSBERGER E. K. (2007) L-chondrite asteroid breakup tied to Ordovician meteorite shower by multiple isochron 40Ar-39Ar dating. *Meteoritics & Planetary Science* **42**, 113-130.

LEVINE J. (2004) Lunar glass spherules as probes of the meteoroid impact history of the Moon. Ph.D. thesis. University of California, Berkeley.

LEVINE J., BECKER T. A., MULLER R. A. and RENNE P. R. (2005) $^{40}Ar/^{39}Ar$ dating of Apollo 12 impact spherules *Geophysical Research Letters* **32**(15), L15201.

LEVINE J., RENNE P. R. and MULLER R. A. (2007) Solar and cosmogenic argon in dated lunar impact spherules. *Geochimica et Cosmochimica Acta* **71**(6), 1624.

LUDWIG K. R. (2006) Isoplot/Ex v3.50--Excel Addin for manipulation and plotting of radiogenic isotope data.

MANKA R. H. and MICHEL F. C. (1970) Lunar Atmosphere as a Source of Argon-40 and Other Lunar Surface Elements. *Science* **169**(3942), 278-280.

MCDOUGALL I. and HARRISON T. M. (1999) *Geochronology and Thermochronology by the $^{40}Ar/^{39}Ar$ Method*. Oxford University Press. pp. 212.

MIN K., MUNDIL R., RENNE P. R. and LUDWIG K. R. (2000) A test for systematic errors in 40Ar/39Ar geochronology through comparison with U/Pb analysis of a 1.1-Ga rhyolite - Age, isotopic disturbances, and the tectonic evolution of western Gondwanaland. *Geochimica et Cosmochimica Acta* **64**, 73-98.

NEUKUM G., IVANOV B. A. and HARTMANN W. K. (2001) Cratering Records in the Inner Solar System in Relation to the Lunar Reference System. *Space Science Reviews* **96**(1), 55-86.

NYQUIST L. E. and SHIH C. Y. (1992) The isotopic record of lunar volcanism. *Geochimica et Cosmochimica Acta* **56**(6), 2213-2234.

PIDGEON R. T., NEMCHIN A. A., VAN BRONSWIJK W., GEISLER T., MEYER C., COMPSTON W. and WILLIAMS I. S. (2007) Complex history of a zircon aggregate from lunar breccia 73235. *Geochimica et Cosmochimica Acta* **71**(5), 1370-1381.

REEDY R. C., ARNOLD J. R. and LAL D. (1983) Cosmic-Ray Record in Solar System Matter. *Science* **219**(4581), 127-135.

RODDICK J. C. (1983) High precision intercalibration of 40Ar-39Ar standards. *Geochimica et Cosmochimica Acta* **47**(5), 887-898.

STEIGER R. H. and JÄGER E. (1977) Subcommission on geochronology: Convention on the use of decay constants in geo- and cosmochronology. *Earth and Planetary Science Letters* **36**(3), 359-362.

STROM R. G., MALHOTRA R., ITO T., YOSHIDA F. and KRING D. A. (2005) The Origin of Planetary Impactors in the Inner Solar System. *Science* **309**(5742), 1847-1850.

SWINDLE T. D., ISACHSEN C. E., WEIRICH J. R. and KRING D. A. (2009) 40Ar-39Ar ages of H-chondrite impact melt breccias. *Meteoritics & Planetary Science* **44**(5), 747-762.

TURNER G. (1971) $^{40}Ar/^{39}Ar$ ages from the lunar maria. *Earth and Planetary Science Letters* **11**(1-5), 169-191.

TURNER G., HUNEKE J. C., PODOSEK F. A. and WASSERBURG G. J. (1971) 40Ar-39Ar ages and cosmic ray exposure ages of Apollo 14 samples. *Earth and Planetary Science Letters* **12**(1), 19-35.

ULRICH G. E., HODGES C. A. and MUEHLBERGER W. R. (1981) Geology of the Apollo 16 Area, Central Lunar Highlands. In *Geological Survey Professional Paper 1048*, pp. 539. National Aeronautics and Space Administration.

WILHELMS D. (1987) The Geologic History of the Moon. In *US Geological Survey Professional Paper 1348*, pp. 302.

ZELLNER N. E. B., DELANO J. W., SWINDLE T. D., BARRA F., OLSEN E. and WHITTET D. C. B. (2009a) Apollo 17 regolith, 71501,262: A record of impact events and mare volcanism in lunar glasses. *Meteoritics & Planetary Science* **44**(6), 839-851.

- (2009b) Evidence from 40Ar/39Ar ages of lunar impact glasses for an increase in the impact rate ~800 Ma ago. *Geochimica et Cosmochimica Acta* **73**(15), 4590-4597.

CHAPTER 6:

UNDERSTANDING THE IMPACT SPHERULE RECORD

6.1 Introduction

One of the biggest advances of this project over previous impact spherule studies is the combination of major and trace element data with ages. This is the first study to integrate these data for individual impact spherules and can be used to understand the impact spherule record and constrain selection biases. This chapter begins with a description of individual impact spherule records and characteristics of the formation and exposure ages. Each individual impact spherule record from Apollo 12, 14, 16, and 17 are compared and contrasted. A model for the burial and exposure regimes is also established. These descriptions draw attention to the some of the potential problems with using impact spherules as proxies for impact history. Potential selection effects that could act on the impact spherule record are then described. Some of these selection effects can be constrained using the integrated data of this project, such as the contribution of exotic impact spherules and duplication of impact spherules. In light of these potential selection effects, the impact spherule record will be revisited with a focus on how these selection effects may influence the spherule record. However, despite the availability of integrated geochemistry and ages for impact spherules presented in this thesis, there are still shortcomings in the spherule record. The lack of integrated data in previous Apollo 12 and 14 age distributions and the lack of a sufficiently large population in the current study limit further constraint of the impact spherule record. A model to address some of the shortcomings identified in this study is proposed as future work. This simulation involves Monte Carlo modeling of impacts, spherule production, and the selection effects.

6.2 Characteristics of Individual Impact Spherule Records

Figure 80 presents the impact spherule age distributions for the Apollo 12, 14, 17, and Apollo 16 record established in the current study. These were combined to produce Figure 78, but are shown as separate records in Figure 80 to compare and contrast impact history from the perspective of spherules from each site. The differences between these records provide clues as to which selection effects may have affected the interpretation of results.

There are few impact spherules in the early Apollo 12 record (>3.6Ga: Figure 80a). The Apollo 12 site was resurfaced by basaltic volcanism around 3.3-3.1Ga (Nyquist et al., 1977; Nyquist et al., 1979), which may have buried or destroyed the older spherule record. Impact spherules with older ages were potentially transported into the Apollo 12 site at a later stage, or were excavated by impacts that exposed older material. An increase in spherule numbers is then observed between 3.6-2.0Ga followed by a minimum between 2.0Ga and 1.6Ga. From 1.6Ga to the present, an exponential increase in the number of impact spherules is observed with 42% of the spherules studied falling within the <800Ma age bins (Levine et al., 2005). Although the Apollo 12 record is skewed toward young ages, Levine et al. (2005) suggest that this may not relate to an increase in impact activity, but rather a selection bias related to the proximity to Sharp Crater.

The Apollo 14 record, on the other hand, is more strongly skewed towards older ages and shows a marked absence of impact spherules with ages >4.0Ga (Figure 80b). Between 4.0Ga and 2.8Ga, there is a peak containing 50% of the spherules dated by Culler et al. (2000); however it is unclear whether volcanic glasses contaminated this record. In a study of glasses in regolith and regolith breccias from Apollo 14, Delano (1988) indicated that volcanic glasses make up on average 30% (ranging between 8-47%) of the glass population. Delano et al. (2007) speculated that these volcanic glasses may be responsible for six peaks in the impact glass distribution of Culler et al. (2000) during the 3.2-3.8Ga eruption ages of volcanic glasses documented by Delano (1988). If

it is assumed that the sampling in Culler et al. (2000) is random, and 30% of the glass population in the 3.2-3.8Ga period is volcanic, impact glasses are still abundant enough to produce the early peak in Figure 80b. However, without actual data on spherule chemistry, the magnitude of volcanic glass contamination cannot be quantified. This early peak is followed by a minimum in spherule numbers from 2.4 to 0.4Ga. From 0.4Ga to present there is a small peak in spherule numbers which contains ~18% of the spherules dated by Culler et al. (2000). Despite being vastly different in age distribution, there are some common features between the Apollo 12 and 14 records. Both show a rapid decline of old impact spherules with ages >4.0Ga and have a common "U"-shaped distribution that result from a stronger representation of young and old spherules.

The Apollo 16 record established in this project appears to have features common to both the previous Apollo 12 and 14 records (Figure 80c). Like the Apollo 12 and 14 records, the Apollo 16 record consists of few impact spherules with ages >4.0Ga, although impact spherules between 4.4-4.0Ga appear to be better represented as a fraction of the total population (7.7%) compared to Apollo 12 and 14 records (1.2% and 4.6%), respectively. Between 4.4-3.2Ga there is a peak in impact activity that is not as significant as the Apollo 14 record, but more prominent than in the Apollo 12 record. From 3.2Ga to 2.0Ga there is a minimum in impact spherule numbers followed by an increase in impact spherule numbers that is steady from 2.0Ga to 0.4Ga. The <400Ma period is the most prominent feature of the Apollo 16 record with 38% ("useable" and statistically acceptable ages) of the impact spherules dated falling within this bin. Once again, spherules with >4.0Ga formation ages appears to be fairly under-represented compared to other parts of the records. The age distribution also appears to form the characteristic "U" shape.

As a whole selection effects are not apparent. However, individually it would seem that selection biases differ for each site. Unfortunately, the Apollo 17 record in its current state is too under-populated to offer any additional constraints (Figure 80d). Yet given that the other three sites are spatially and geologically unique, there are a number of

common features that may either represent common selection effects that act on all records or features that are unaffected by selection biases.

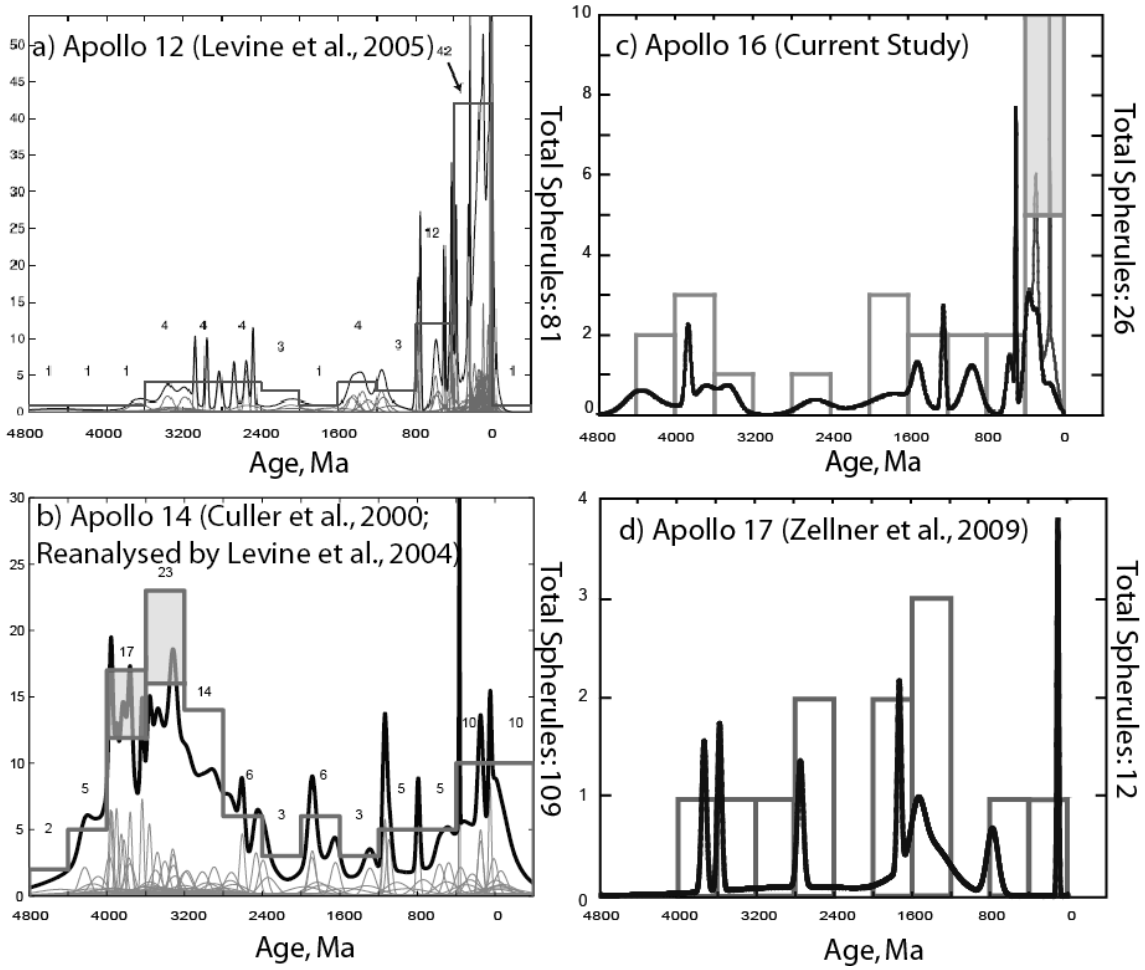

Figure 80. Histograms and ideograms of the production rate of lunar impact spherules from the **a)** Apollo 12 (Levine et al., 2005), **b)** Apollo 14 (Culler et al., 2000; Levine, 2004), **c)** Apollo 16 (current study), and **d)** Apollo 17 sites (Zellner et al., 2009a). Shaded region on **b)** shows an estimate of the number of volcanic spherules (average 30% of population) whereas the shaded region in **c)** shows the number of spherules without statistically acceptable ages (i.e. "useable" ages).

6.2.1 Characteristics of the Exposure History

Exposure ages add yet another layer of information that can be used to understand the impact spherule record. Figure 81 shows the exposure ages as a function of the formation ages for impact spherules collected from the Apollo 12, 14, and 16 sites. Note that exposure ages are integrated over the lifetime of impact spherules, which may have experienced multiple exposure/burial cycles. Impact spherules with formation ages <500Ma typically have similar exposure ages. Older impact spherules exhibit more complex histories as indicated by the scatter in exposure ages in Figure 81, but generally have a smaller exposure/formation age ratio (<1:2). Given that each spherule was formed at the surface and collected from the surface, some qualitative constraints may be placed on the exposure history. It is possible that impact spherules studied so far are not really random samples, but instead consist of distinct populations that were selectively sampled. Levine (2004) and Levine et al. (2005) have suggested that the spike in <400Ma impact spherules ages may have resulted from selective sampling of a stratified regolith and thus does not require an increase in impact activity. A method for evaluating these data is outlined in the following paragraphs.

In order to understand if the impact spherules studied so far originate from distinct reservoirs in the regolith, mixing models of the regolith need to be consulted. Gault et al. (1974) developed an early probabilistic study of overturn rates of the lunar regolith by using Monte Carlo modelling to simulate impact events using the meteorite flux of Shoemaker et al. (1970). Figure 82 is the result of this modelling and shows the probability of regolith overturn as a function of depth. It shows that the top ~1mm of regolith is overturned regularly, but deeper overturn is rarer as it requires larger impactors (which are also rarer relative to smaller impactors). For example, a particle at 1mm depth has a 99% probability of being overturned by large enough impactors only once every 10^4 years. However, without the formation age, the number of overturns this particle has experienced is not known. Now consider a dated impact spherule where both formation and exposure age is known. The formation age can be used to constrain the number of times which this spherule may have been overturned at any given depth. However, impact spherules may migrate to, and reside at, different depths during their

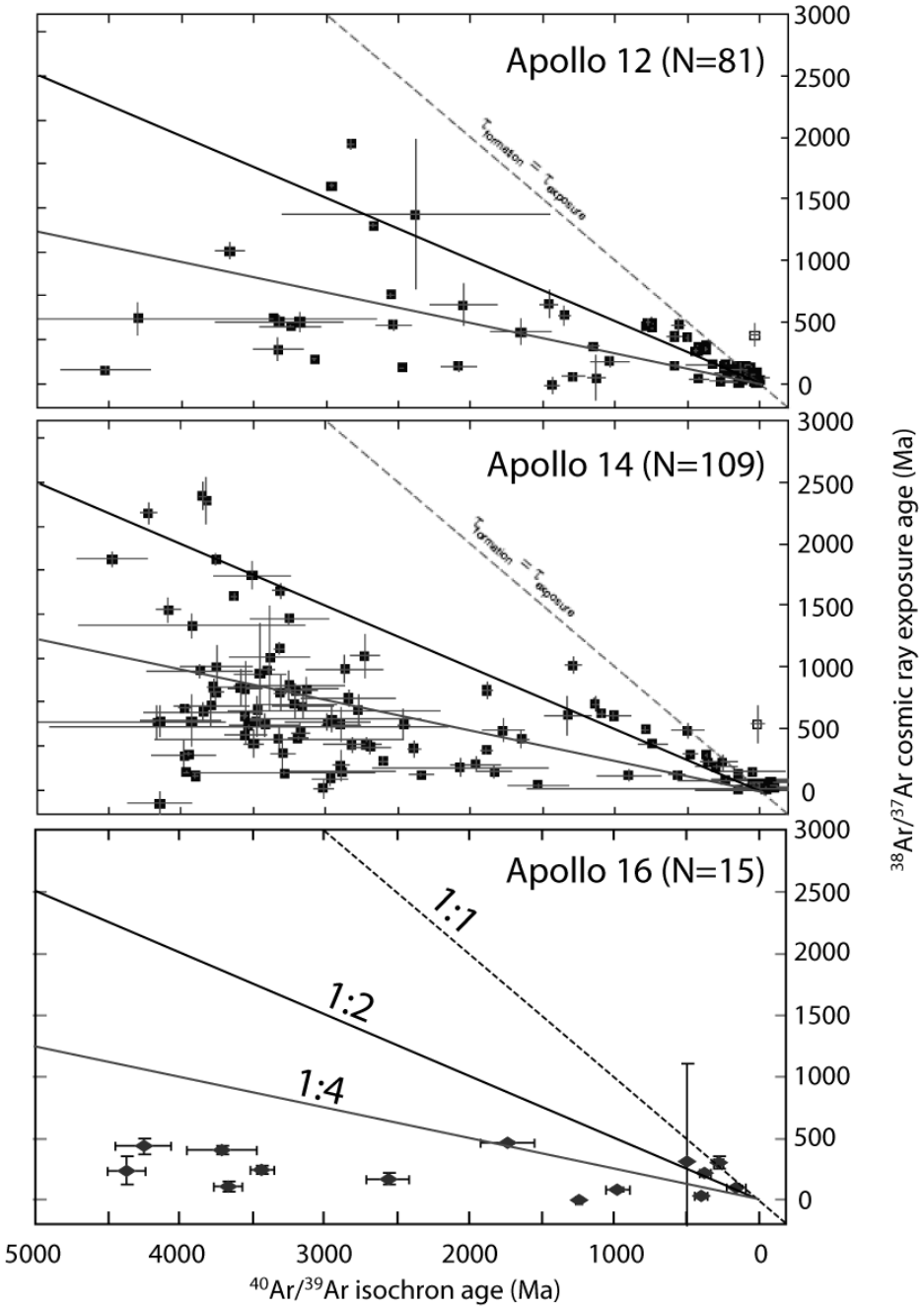

Figure 81. A modified plot of exposure age versus formation age in impact spherules from Apollo 12 and 14 (Levine et al., 2007) plus the Apollo 16 record developed in this study. The yield of impact spherules with exposure ages is 100% in these studies whereas it is only 58% in the current study. There are, however, certain similarities in these records. For example, the exposure ages of the impact spherules are generally younger than the formation ages. Error bars are at 1σ. The *e/f* ratios are also plotted as lines.

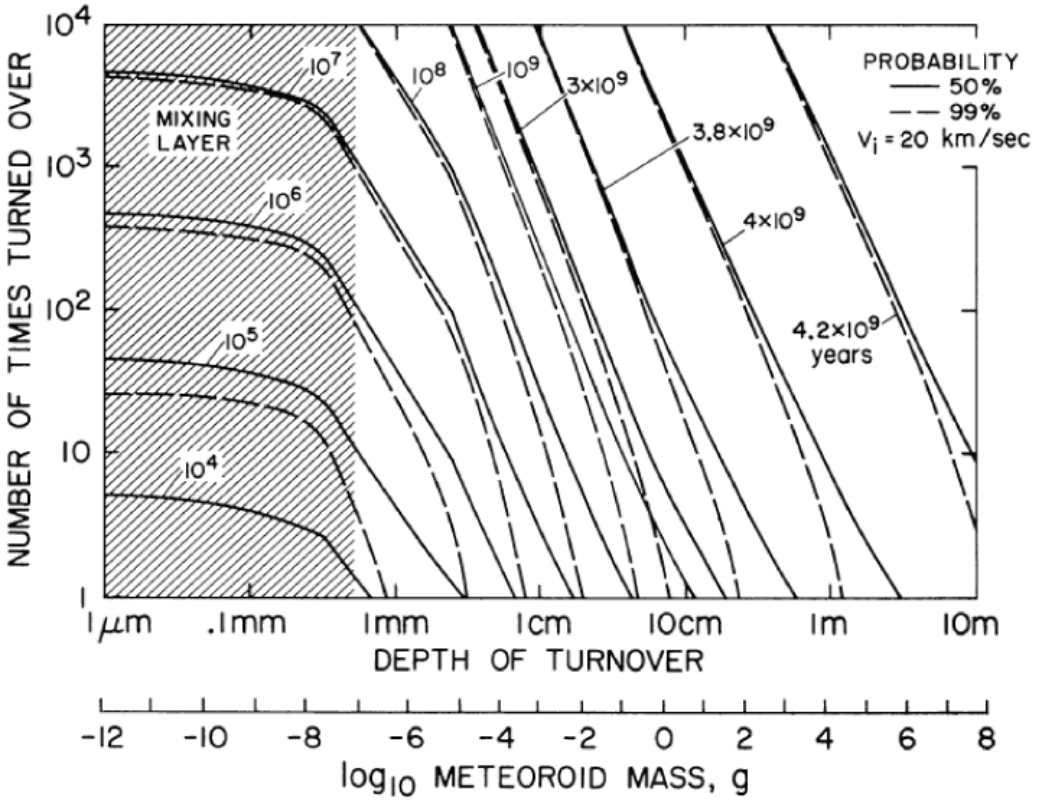

Figure 82. Number of times the regolith is turned as a function of turnover depth. The depth and probability of overturn is based on meteorite mass and the meteorite flux of Shoemaker et al. (1970), respectively. Using this diagram, it is possible to determine how often a particle at a certain depth is overturned.

Diagram from Gault et al. (1974)

lifetimes due to impact mixing; therefore the formation age alone cannot constrain the integrated burial history. The exposure age, in conjunction with the formation age, the fact that the impact spherules were collected on the surface, and a model of overturn, can be used to develop a probabilistic function that describes the integrated time-depth history, as will be discussed below.

Conceptually, the exposure/formation (*e/f*) ratio can be considered to represent a complex expression of a number of factors. The main constraint is the fact that the impact spherule must be on the surface to be sampled. Therefore, impact spherules with an *e/f* ratio of zero will never be sampled as they have never been exposed to depth less

than 1m. Conversely, an impact spherule with an *e/f* ratio of 1 indicates that it was never buried (i.e. formation age < time required for one burial/exposure cycle). As the *e/f* ratio approaches either extreme, some constraints can be made on the exposure history (concept illustrated in Figure 83a). The integrated time-depth history of an impact spherule can be described by a probability of residence at various depths (Figure 83b and c). There are three key factors that affect this depth-probability distribution: formation age, *e/f* ratio, and the number of overturns. The formation age determines how deep a spherule can reside in the regolith. Young spherules cannot be too deep or may not experience an impact that can excavate them prior to sampling; older spherules can be deeper as they have a better chance of being excavated. The *e/f* ratio describes the skew of the depth-probability distribution. As the *e/f* ratio approaches 1, the impact spherules are increasingly likely to have remained at shallower depths. The opposite is true for *e/f* ratio approaching $1/\infty$ as impact spherules are increasingly likely to be deeper in the regolith. The number of migrations describes the tightness of the distribution. If the impact spherules experienced multiple migrations, the depths where they might have resided broadens whereas a spherule that only experiences a single overturn must be excavated from a narrower range of depths. Naturally, the depth from which an impact spherule population was sampled will strongly affect the characteristics of that population. An impact spherule population sampled from the near surface, such as the populations in Figure 81, will be biased towards young spherules with high *e/f* ratios. As the sampling depth increases, the spherule population will consist of older spherules with high *e/f* ratios mixed with younger spherules with low *e/f* ratios.

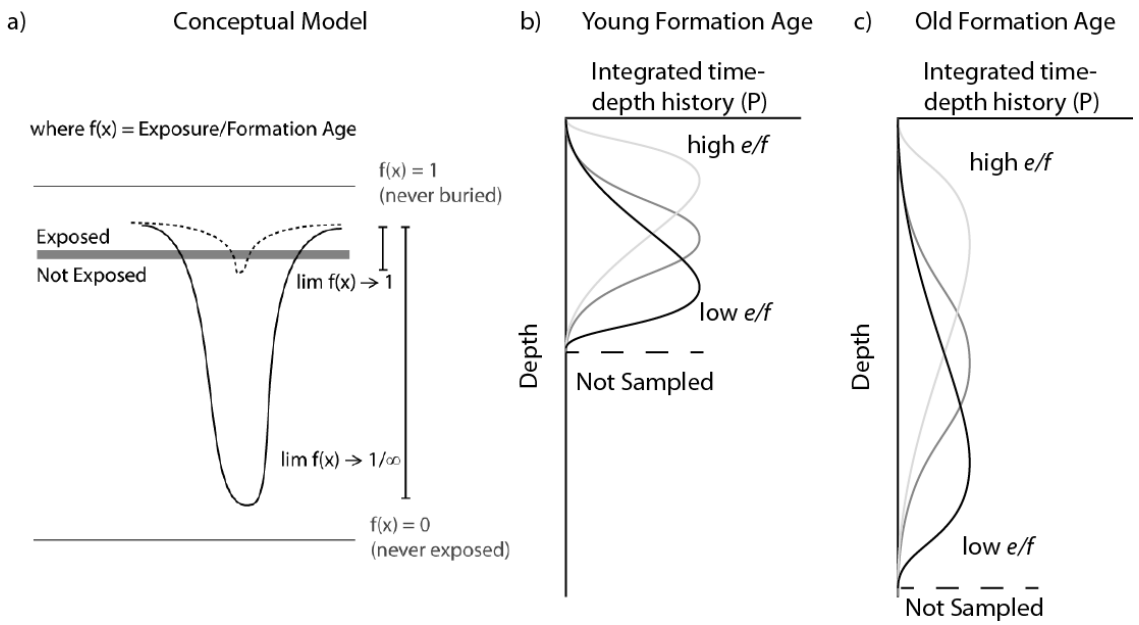

Figure 83. a) Conceptual model of the significance of the *e/f* ratio. **b** and **c)** conceptual model on how the formation age and *e/f* ratio can be used to determine the probability-depth function of young and old impact spherules. The formation age constrains the maximum depth at which the spherule can reside and the *e/f* ratio constrains the skew towards shallower or deeper depths. The number of impacts can further constrain these functions by making the curve narrower or broader. See text for a detailed description.

In light of the conceptual model regarding *e/f* ratios, the regolith gardening rates by Gault et al. (1974) can be revisited (see Figure 82). Note, however, this model indicates that all impact spherules with formation ages <4Ga would be considered exposed (top 1m) and actually underestimates the depths of overturn based on data from the Apollo drill cores (McKay et al., 1991). However, it is the only model with data that is presented in a format suitable for this discussion (also see Arnold, 1975; Mendell and McKay, 1975). According to the overturn rates of Gault et al. (1974), an impact spherule with a formation age of 1 Ma and an *e/f* ratio approaching 1/∞ has a maximum depth of ~5mm with a 99% probability of being overturned twice (i.e. one burial/exposure cycle). Although the maximum depth could be deeper, there is an increasing likelihood that this impact spherule will never experience a burial/exposure cycle (*e/f=0)*. An *e/f* ratio of 0.9 would indicate that the impact spherule was only buried for 0.1Ma. The maximum depth with a 99% probability of being overturned

twice would then be ~1mm if the impact spherule was recently exposed and only experienced a single burial/exposure cycle. Shallower depths are permitted if the impact spherule has experienced multiple burial/exposure cycles. However, the absolute number of times an impact spherule has been exposed is not known as exposure ages are integrated over the lifetime of the impact spherule. Therefore, the exact shape of the depth-probability distribution is indeterminate, but this concept can be used to understand the dated impact spherule populations.

Figure 84 shows the *e/f* ratio as a function of formation age for impact spherules in the current study. This figure shows that there are more impact spherules with *e/f* ratios >0.5 when formation ages are <500Ma (see also Figure 81). Given the shallow sampling depth this is not surprising that the Apollo 12, 14, and 16 spherule records share this feature. Based on the concepts introduced in the previous paragraph, Gault et al. (1974) overturn rates indicate that the maximum burial depth of these impacts was ~5cm, although the spherules are more likely to have been located shallower in the regolith as their *e/f* ratios are high. All impact spherules in the current study have been buried at some stage in their lifetime (i.e. formation age > time for one burial/exposure cycle), of which the three youngest have formation ages ~150Ma. Based on these data alone, one burial/exposure cycle could take less than 150Ma. Most impact spherules from Apollo 12, 14, and 16 with formation ages >2Ga typically have *e/f* ratios <0.2. The Gault et al. (1974) overturn rates place them between tens of centimetres to tens of metres depth. The typically low *e/f* ratios coupled with the old age of these spherules indicate that they were probably deeply buried, but have since migrated to the surface. The shear abundance of old spherules with relatively low *e/f* ratios at the Apollo 14 site is peculiar. However, these spherules were collected from a 10-50cm thick ejecta layer produced by the Cone Crater impact. Therefore, the old spherules were probably from a deep reservoir, brought to the surface by the Cone Crater impact, and subsequently mixed with younger material. This hypothesis suggests that there are two distinct impact spherule populations that contribute to all impact spherule records: one consisting of young impact spherules that have spent the majority of their lifetimes on the surface, and the other consisting of old impact spherules that have spent at least half of their

lifetime buried, but recently brought to the surface for sampling. This hypothesis also indicates that sampling depth, mixing, and routine destruction of older impact spherules are likely selection effects.

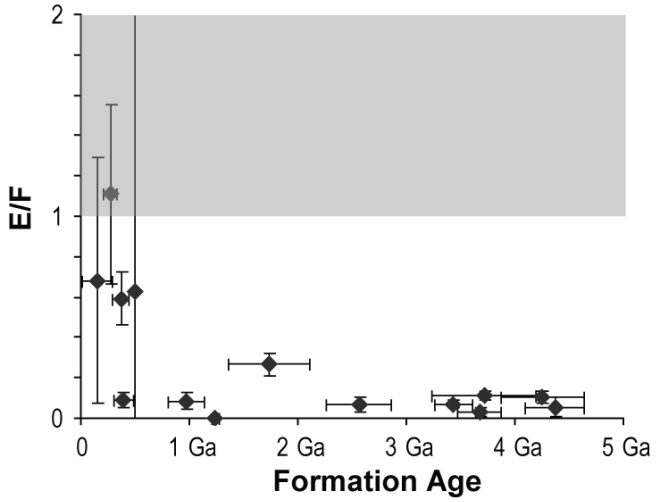

Figure 84. Plot of *e/f* as a function of formation age for impact spherules in this project. The shaded area is the forbidden zone where exposure age is greater than formation age.

Despite the potential use of this concept, there could be underlying problems with exposure age dating of impact spherules that limit its usefulness. In a study of the exposure ages of the Apollo 12 and 14 impact spherules, Levine et al. (2007) suggested that solar wind argon may saturate in an impact spherule over a period of 10^4 years. Further exposure to the solar wind results in either sputter of previously implanted solar wind argon or heating which may also liberate argon by diffusion. Levine et al. (2007) note that impact spherules with 3-4Ga formation ages contain little more $^{36}Ar_{solar}$ than younger spherules. These results, however, could also indicate fast and prolonged burial followed by exposure prior to collection, such as suggested in the previous discussion. If saturation is an issue, it implies that there will be physical limits to the exposure age as some function of the size of the impact spherule, orientation and duration of exposure. In the case of the Apollo 16 spherules, this could be a valid argument as all impact spherules do not appear to have exposure ages >500Ma. However, this does not appear to be the case in the Apollo 12 and 14 impact spherules as 3-4Ga impact spherules have *e/f* ratios >0.5.

6.3 Identification of Potential Selection Effects

A selection effect (or bias) is a process, or series of processes, that selects in favour of certain sample populations over others. Therefore, the sampling is no longer random or representative. However, the process(es) that introduce selection biases must first be identified before remedial action can be taken. Earlier studies utilised the formation age distributions of impact spherules as a direct proxy for impact flux (Culler et al., 2000; Levine et al., 2005). In Levine et al. (2005), and possibly Culler et al. (2000), the major element composition of each impact spherule was measured to distinguish volcanic spherules from impact spherules. Later, Delano et al. (2007) suggested integrating the major element composition as a way of characterising impact spherules in addition to linking them to formation ages. It was in this study where four glass shards were found to have a similar KREEPy composition and formation age. Delano et al. (2007) concluded that these shards were probably delivered from a single large distant event and did not represent four individual impact events. One glass shard could be used to represent this impact event and therefore avoid over-representing. However, such data were not available in previous studies and as such remidal action could not be taken. Over-correction should also be avoided as there is also the possibility that these shards were produced by a series of large impacts over a short period of time into the same terrain. In this case, treating all four glass shards as a single impact event will under-represent impacts during this period.

Methods developed during this project allowed the measurement and integration of major and trace element chemistry and ages on individual impact spherules. This development provides more geochemical constraints in addition to ages which can be used to identify and address some selection biases that may be intrinsic to the impact spherule record and therefore the interpretation of it. The age distributions for impact spherules collected at each of the Apollo landing sites are sufficiently different in many respects that it could be argued that the distributions not only record the impact history (see Figure 80), but a combination of impact history and various selection biases. Some of these biases cannot be tightly constrained, but should at least be considered as will be discussed in the following paragraphs.

6.3.1 Considerations – Geological, Impact, and Selection Effects

Intrinsic Bias of $^{40}Ar/^{39}Ar$ dating

The need for potassium-rich and large sized spherules for $^{40}Ar/^{39}Ar$ dating is a selection bias that affects every study of impact spherules. The need for such compositions would tend to favour impact spherules that have a KREEPy component or origin. Additionally, there may be a selection bias towards events that produce larger impact spherules (i.e. larger impact events?). As such, impact spherules will be selected based on a compromise between K content and volume. This may inadvertently exclude impact spherules produced from low-K terrains or small impact events. The actual effect on the impact records, however, cannot really be determined until the dating techniques or technologies improve to the point where K content and size are less important. The methods employed in this study are a step towards this goal as impact spherules from relatively low-K terrains, compared to previous studies, have been dated.

Sampling Location and Depth

A number of studies attempt to model mixing and regolith evolution that results from impacts as a function of time (see summary by Langevin and Arnold, 1977 and references therein). Many of these studies suggest that the regolith can be stratified, complex and exhibit great variety, which implies that any point sampling would be subject to spatial and depth-dependant selection effects. A number of impact and geological processes can also lead to redistribution of material and mixing between different impact spherule populations. Therefore, any sample of impact spherules will not be random and representative of the "true" impact history and why geological context is important.

In the previous studies, the impact spherules collected in both Culler et al. (2000) and Levine et al. (2005) were sourced from ejecta layers of relatively young craters at the Apollo 12 and 14 sites, respectively. The impact spherules collected from the Apollo 12 site are located in the ejecta of Sharp Crater, which is inferred to be ≤10Ma by Levine

(2004) based on a description by Jones and Glover (1995), although the age has not been measured. At the Apollo 14 site the 25Ma age of Cone Crater is based on exposure ages of coarse fragments (see Arvidson et al., 1975a; Drozd et al., 1977). Both Culler et al. (2000) and Levine et al. (2005) suggested that many young impact spherules could be created in the events that produced such craters and thus could account for the young spike without the need to invoke an actual change in impact rate. In addition, these craters would have brought impact spherules from deeper in the regolith onto the surface. Cone Crater (Apollo 14) is 370m in diameter, and assuming evacuation depth of 1/10 the transient crater diameter (Melosh, 1989), at least 37m of material were excavated. Excavation depths of up to 80m from the Cone Crater event have been suggested (Sutton et al., 1972), which would potentially bring a source of deeply buried impact spherules to the surface. Excavations from Sharp Crater (Apollo 12: Levine et al., 2005) and the unnamed crater (current study) can only bring material buried on the order of metres depth to the surface. Therein may be the explanation for why the Apollo 14 record has a 2.0-4.0Ga peak in spherule production that is absent in the Apollo 12 and 16 records (see Figure 80). Impact spherules from Apollo 14 are heavily biased towards spherules, possibly with the inclusion volcanic glasses, evacuated from depth mixed with younger impact spherules from the surface. The Apollo 12 and 16 records, however, are still relatively surficial by comparison and thus younger impact spherules are more abundant. This explanation agrees with the earlier concept that impact spherule populations collected from the surface are expected to be biased towards young formation ages with high *e/f* ratios (i.e. those in the <400Ma bin).

Geological processes can also be responsible for redistribution of material. Impact spherules in this project were collected from a site (Station 6 – Base of Stone Mountain) where there may have been mass wasting from the Descartes materials accumulating into a thick deposit at this site (Sanchez, 1981). Mass wasting (also known as regolith slumping) occurs when the slope of the regolith reaches an angle that is unstable, causing movement of regolith down-slope. This process often occurs on the rims of crater walls where the slope is unstable and is analogous to terrestrial landslides. However, impact spherules from mass-wasted regions are displaced and transported

relatively short distances compared to the ballistic transport of material during larger impacts. Therefore, recognising impact spherules from such a deposit using compositions is difficult. The mixing of soil components and possible strata may affect the impact spherule population from point to point. Such selection effects, however, can be statistically overcome by larger populations of studied impact spherules, provided that the population derives from diverse environments.

Impact History and the Stonewall Effect

The stonewall effect was conceived as an alternative to the LHB in explaining why there is a lack of lunar impact breccias with ages >4Ga (Hartmann, 2003), a feature also seen in the impact spherule record. This concept is more widely applicable to impact spherules as they also can be destroyed by a subsequent event. Modelling by Gault et al. (1974) in particular suggests that the near-surface layers are most likely to be highly remelted and vaporised. However, the efficiency of destruction will undoubtedly change through time as large impactors become rarer, thus restricting the affected regions to progressively shallower depths and smaller spatial scales. Constraining this effect, however, is difficult using just information obtained from the impact spherules. This is because parts of the record were eradicated by subsequent activity and thus no amount of representative sampling will produce an impact spherule age distribution that reflects the actual impact rate. The actual impact history, including any spikes in activity (e.g. LHB, chondrite break-up) if they occurred, will feed into how often a part of the record is eradicated. This may be the most significant of these potentially unconstrained selection effects since it overprints the impact history rather than redistributes the records. Thus, this problem cannot be overcome with sampling and must be modelled in an iterative process to determine how changes in the actual impact history can affect the impact spherule record. A schematic for a mathematical model to constrain the influence of this selection effect is presented in the section 6.6 Future Work – Modelling of Sampling Bias and the Stonewall Effect.

6.3.2 Constraints - Transport and Provenance

Impact processes are not only responsible for forming impact melts and spherules, but are also responsible for vertical and horizontal mixing of the regolith. Monte Carlo techniques for estimating the rates of vertical mixing provide some idea of the potential for burial and excavation of impact spherules within the regolith. Horizontal mixing, however, is responsible for the transport of the regolith across the surface of the Moon as ejecta. Ejecta models developed by Arvidson (1975b) indicate that impact ejecta are an important and significant process for inter-regional mixing. The fact that impact spherules have compositions that reflect the terrain of origin can thus be used as a discriminant for local or exotic origins. This is useful for a number of reasons:

1. Identification and removal of volcanic spherule contaminants which do not record impact history. Major element abundances were obtained solely for this purpose in the earlier impact spherule studies by Levine et al. (2005) and possibly by Culler et al. (2000).
2. Constraint of the impact history to smaller regions of the Moon by selecting locally-derived impact spherules. In addition, identification of the target, timing, and possible magnitude of large impact events resulting in horizontal transport of exotic impact spherules may be possible (e.g. see Delano et al., 2007; Zellner et al., 2009b).
3. Determination of the rate of horizontal transport whether or not there has been any change in target compositions (i.e. the composition of lunar surface) or availability (i.e. compositional terrains that are more spatially abundant are more likely to be impacted) as a function of time. This is only possible in large sample populations.

The integration of such data, however, has been limited to major element compositions and radioisotopic dates at present. The lack of trace element abundances limits the interpretations that can be made regarding the targets that produce the impact spherules. This issue is overcome by the methods employed in this study. Note that references will be made to trace element matches employed in the previous chapter. Refer to Chapter 3:

Background and Chapter 4: Petrography and Geochemistry for the definitions of the litho-chemical terms and chi-squared modelling results.

Impact Spherule Transport

Figure 85-Figure **87** illustrate methods for determining impact spherule provenance using major elements, trace element REE patterns, and diagnostic Sc/Sm ratios, respectively. These methods were employed in Chapter 5: Petrography and Geochemistry to identify impact spherules that may be exotic to the site. Here, the thirty impact spherules selected for radioisotopic dating will be described in more detail and combined with formation age data if applicable. Two of the most KREEPy impact spherules (LS2-62 and LS3-24) have relatively mafic major element compositions (mixed highlands-mare) and trace element compositions similar to the soil from Cone Crater at Apollo 14. Although KREEPy materials can be found in the form of MIMBs at Apollo 16, these impact spherules have more KREEPy compositions than that of materials available at the Apollo 16 site. Based on the spatial location of such compositions, as determined from remote sensing (Prettyman et al., 2006), these spherules are probably delivered from the Procellarum KREEP Terrain. Both spherules are also relatively young (<500Ma), but do not have the same age within uncertainties so represent two distinct impact events. Neither impact spherule shows signs of damage or shattering that may have occurred as a result of such distant transport, which Delano et al. (2007) suggest may be possible.

The next most KREEPy spherule (LS4-12) is older (3.86Ga) and has a composition that is similar to the High-Sc Very High Alumina (HScVHA) end-member of VHA "basalts" (see Morris et al., 1986). According to the mixing models of Morris et al. (1986), the HScVHA compositions are abundant in the surface regolith at Apollo 16. The VHA "basalts" are not igneous rocks, but a compositional grouping found in impact-melt breccias and clast-poor impact melts and are thus of an uncertain origin (Taylor et al., 1991). According to the Sc/Sm ratio, this impact spherule falls into the MIMB field in the Korotev (1997) model components of the Apollo 16 regolith, and thus may be of local origin. This impact spherule appears to be unrelated to the exotic

Apollo 16 glasses of Delano et al. (2007) as it is more feldspathic in composition (23.5wt% Al_2O_3 compared to ~11-13wt%) and formed ~100Ma earlier outside of 2σ errors.

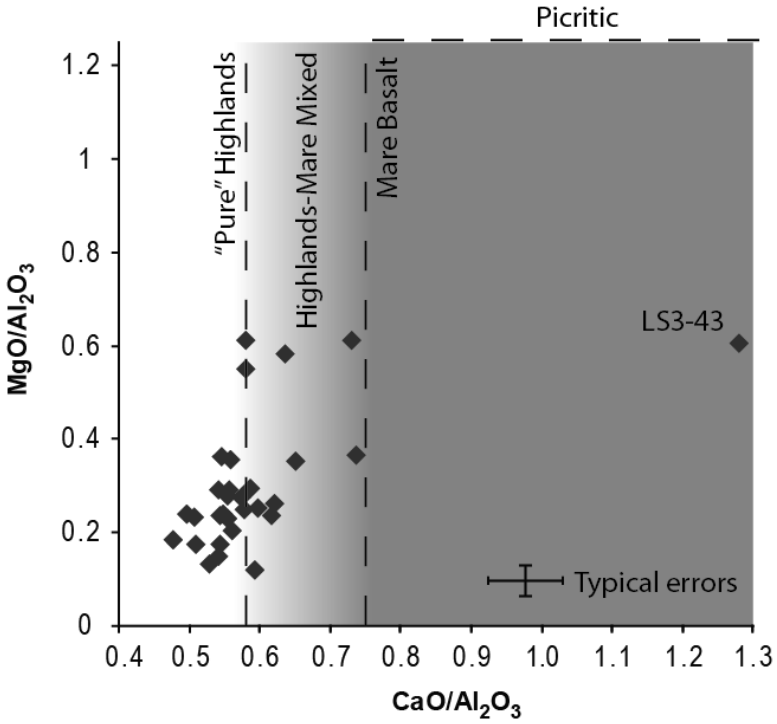

Figure 85. A plot of major element ratios of MgO/Al_2O_3 and CaO/Al_2O_3 of the thirty dated impact spherules. This plot was used in Zeigler et al. (2006) to distinguish impact glasses of highlands (CaO/Al_2O_3 ~ 0.58), mixed mare-highlands ($0.6 < CaO/Al_2O_3 < 0.75$), and mare basalts ($CaO/Al_2O_3 > 0.75$) from picritic glasses ($MgO/Al_2O_3 > 1.25$). Most of the dated impact spherules in this study are of highlands origin with the exception of LS3-43 which has a strong association with mare basalts. Note that this diagram is not able to identify KREEPy impact spherules. Typical errors at 1σ.

The next twenty-two impact spherules may be derived from local materials. The first of these is an impact spherule (LS2-43) with a REE composition slightly more enriched than that of the soils at Apollo 16. According to Figure 87, its composition places it just within the MIMB field. Twenty of the impact spherules have REE concentrations that fall within the variability of Apollo 16 soils in Figure 86. Interestingly, many of these impact spherules appear to have lower average Eu abundances than the Apollo 16 soils,

resulting in larger negative Eu/Eu* anomalies. Although within 2σ error of the typical Eu abundances in Apollo 16 soils, this may suggest that these impact spherules were formed from soils with a stronger mafic component (e.g. akin to Luna 20 soils).

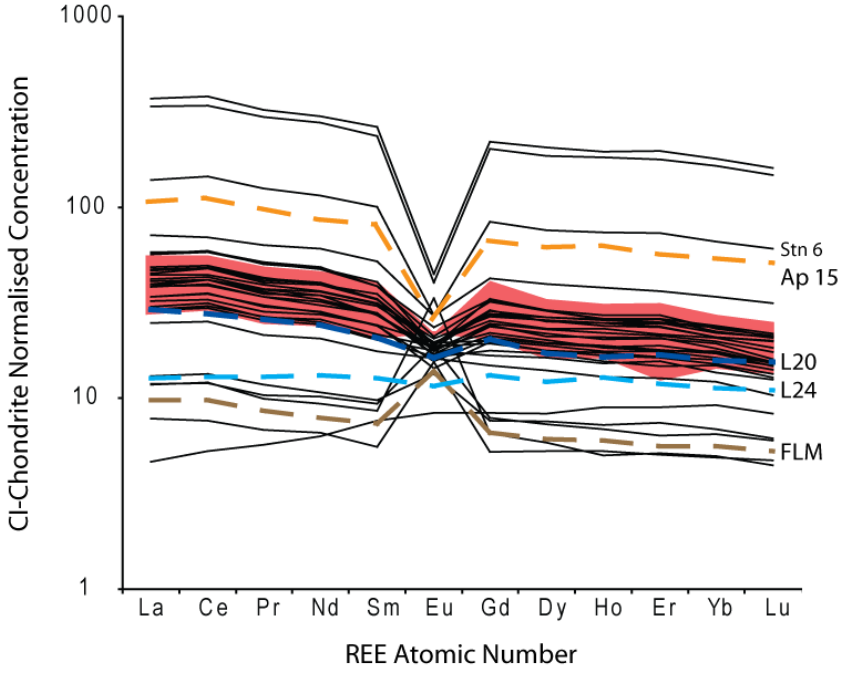

Figure 86. Chondrite-normalised concentration of rare earth elements in all thirty lunar impact spherules selected for dating. Not all samples, however, yielded acceptable formation ages. The shaded red region shows the variability of the rare earth elements in Apollo 16 soils. The dashed lines shows the rare earth patterns of soils from other selected regions (Apollo 15 station 6, Luna 20, and Luna 24) and the model feldspathic lunar meteorite (FLM: see Korotev et al., 2003). Chondrite compositions are from Wasson and Kallemeyn (1988) and soil compositions are from Lucey et al. (2006).

This may have manifested during selection of samples for radioisotopic dating as more mafic impact spherules are likely to contain higher abundances of potassium. According to the Sc/Sm plot of Figure 86, only two impact spherules (LS1-41 and LS3-21) are consistent with derivation from mature Cayley soils. Eighteen impact spherules trend toward more feldspathic compositions representing rocks and regolith fragments. The sample with REE abundances just lower than the typical Apollo soil band lacks a Eu anomaly. This impact spherule (LS2-45) plots close to the model feldspathic impact-melt breccia composition of Korotev (1997), which belongs to groups of impact-melts

that are typically found around North Ray Crater. Interestingly, the range of formation ages for these local impact spherules ranges from 0 (i.e. newly formed) through to 4.4Ga, suggesting that targets with Apollo 16-like compositions have been available through most of the Moon's history.

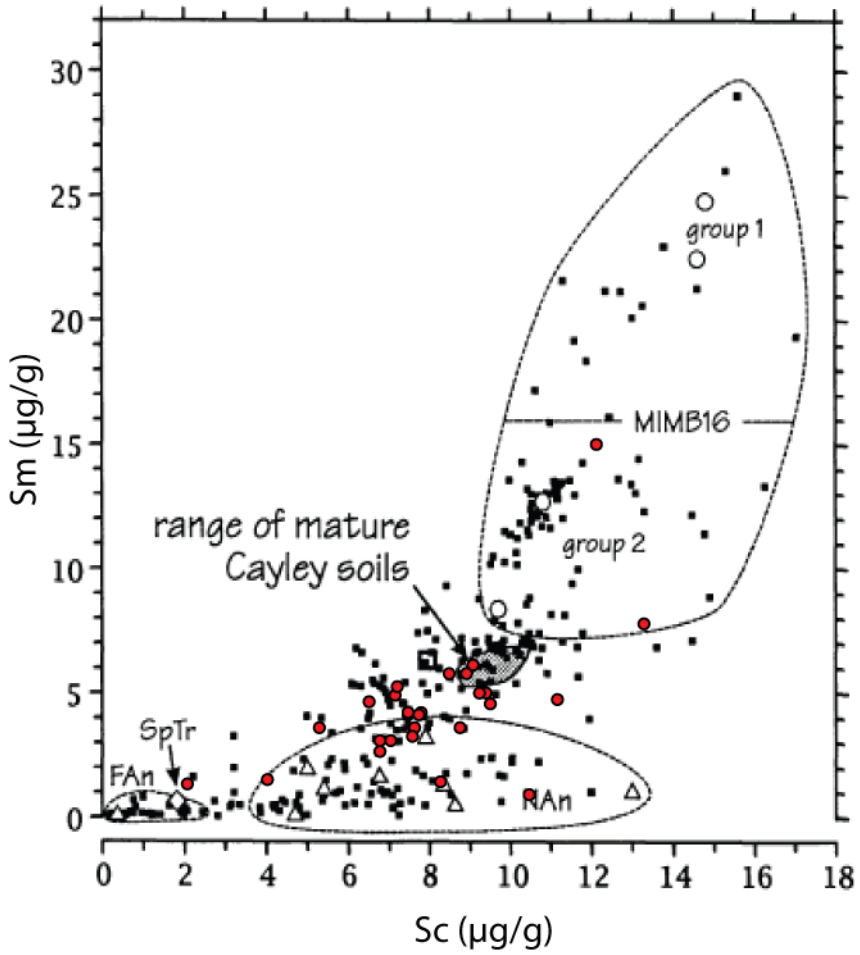

Figure 87. Concentration of Sc and Sm in model Apollo 16 rocks (open symbols and fields) and 1-2mm regolith particles from Korotev (1997) overlain with the dated lunar impact spherules of this project. Note that three impact spherules (LS2-62, LS3-24, and LS3-43) fall outside the bounds of this plot (KREEPy and mare provenance).

The four feldspathic impact spherules are of greatest interest because they exhibit lower REE abundances than typical Apollo 16 soil and positive Eu anomalies. Three of these impact spherules (LS1-22, LS1-73, and LS3-32) have major element compositions

similar to the Apollo 16 soils (highlands basalt) while the other (LS2-63) is slightly more felsic (31 wt.% Al_2O_3, 18.3 wt.% CaO). It is apparent in Figure 86 that these impact spherules were not formed from the bulk Apollo 16 soils and they do not fall into composition groups described in Korotev (1994) for impact breccias. Sample LS2-63 has the lowest incompatible trace element (ITE) compositions of the four impact spherules, suggesting that it is experienced the least amount of mixing with mafic ITE-rich impact materials, such as the breccias of Group 1 and 2 typically found at the Apollo 16 site (Korotev, 1994). The other three impact spherules have a more mafic major and trace element composition. As discussed in the previous chapter, potential targets with highly feldspathic compositions in the local vicinity are rocks and soils from North Ray Crater, or possibly immature soils at depth. However, the Descartes Mountains are also a potential source of feldspathic targets that are exotic to the Apollo 16 site (Lindstrom and Salpas, 1981; Norman, 1981; Norman et al., 2010; Ulrich, 1973).

The remaining and most unique impact spherule (LS3-43) dated has a slightly positive Eu anomaly and a trace element pattern showing a continuous rise in abundance of REEs from La to Lu (i.e. light REE depleted). If classified using the method of Neal and Taylor (1992), this impact spherule would be a Very Low Titanium (VLT: Ti = 0.82 wt.%), high-Al (~14wt.%), and high-K (~0.2 wt.%) mare basalt. The major element composition confirms that this impact spherule is derived from a target with a mare basalt composition (see Figure 85). At the Apollo 16 site, mafic glasses of VLT basalt composition are most likely to have been sourced from Mare Nectaris about 220km to the east (Zeigler et al., 2006). However, this spherule differs in a number of ways to typical VLT mare basalts (see Taylor et al., 1991) as it is relatively FeO-poor (~10wt.%), CaO-rich (~18wt.%), and Al_2O_3-rich (~14wt.%), and exhibits a positive Eu anomaly. However, it is unlike Luna 24 VLT basalts (see Ma et al., 1977). This impact spherule has a composition that is unlike other lunar materials and may have resulted from the mixing of a feldspathic component with VLT mare basalt. If this impact spherule is a mixture of VLT mare basalt and more local feldspathic materials, it could have been produced at the Apollo 16 site or within feldspathic terrains, but its provenance is unclear. Such glasses were also identified in a study of mafic glasses at

Apollo 16 by Zeigler et al. (2006). Interestingly, this impact spherule did not yield a measurable age, but is inferred to be very young due to its lack of measurable $^{40}Ar^*$. If this spherule is indeed an exotic spherule it would again highlight the possibility of large events transporting impact spherules great distances.

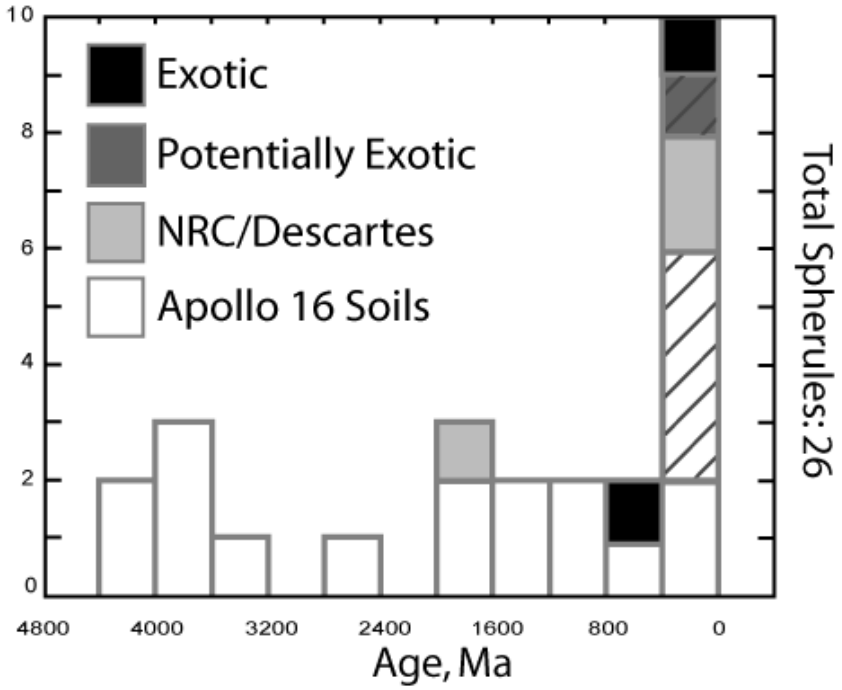

Figure 88. Histogram of impact spherule formation ages for samples in this project. Added are shadings that show the contribution of impact spherules formed from local materials and those that may be exotic to the site. The hashed areas highlight impact spherules without statistically acceptable ages.

Having determined the provenance of the dated impact spherules using major and trace element compositions, it is now possible to integrate the formation age data. Although there is only a small population of dated impact spherules available for use in this study, it is possible to begin to assess the contribution of impact spherules as a function of age and provenance (Figure 88). If impact spherules without statistically acceptable ages are removed from this figure, the <400Ma spike in activity is no longer so pronounced. However, as discussed in the previous chapter, the inference that these spherules may be young is still valid. The two KREEPy exotic spherules have ages <500Ma and indicate

that relatively large impacts are not restricted to the early eras of bombardment (>3.8Ga). It also indicates that impact activity in the past 400Ma may be responsible for an increase in horizontal exchange of material. This idea may be supported if the young spike in the Apollo 12 (Levine et al., 2005) and Apollo 14 (Culler et al., 2000) impact spherules was also made up of a significant amount of spherules exotic to their collection sites. However, this hypothesis cannot be tested since the previous studies lack the integration of comprehensive chemistry as published. Note, however, that exotic spherules in Figure 88 are over-represented proportionally to local impacts as these spherules were specifically selected for radioisotopic dating. Recall that only 3% of the impact spherules in the current study could not be produced from local materials, therefore large impacts that bring exotic spherules to the Apollo 16 site are comparatively rare. The Apollo 12 (Levine et al., 2005) and Apollo 14 (Culler et al., 2000) are less prone to this selection bias because they have studied larger and more randomly selected populations. On the other hand, impact spherules from low-K feldspathic terrains would probably not have been selected as they are less suitable for dating and therefore introduced another type of bias. This is apparent as impact spherules with feldspathic compositions are lacking in Levine et al. (2005).

The ability to determine impact spherule provenance is also useful for constraining the impact flux to a smaller region of the Moon. The shape of the Apollo 16 distribution is dominantly controlled by local spherules, reflecting the decision to focus on these spherules despite the fact that they are less suitable for $^{40}Ar/^{39}Ar$ dating. Without the contribution of the exotic spherule to the 400-800Ma bin, the local impact flux appears to reach an apparent minimum prior to the young spike. This is likely the result of small number statistics, the most significant (but unavoidable) flaw of the impact spherule distribution developed in the current study.

In summary, using the major and trace element compositions of individual impact spherules it is possible to constrain the target from which the impact spherule was formed. This allows for the impact fluxes as determined by impact spherules to be separated into impact flux from the local region and that resulting from ballistic

transport of impact spherules from other regions of the Moon. Combining these data with formation ages shows exotic or potentially exotic impact spherules contribute up to 40% of the population making up the young spike (0-400Ma) as seen on the Apollo 16 data. It could suggest that horizontal exchange may have been more common over the past 400Ma, but these exotic spherules are over-represented compared to local spherule production. The integration of comprehensive chemistry and formation ages allows for the distinction between local spherule production and total spherule production (i.e. local + transported to the collection site) to be made, thus impact rate can be constrained to a smaller region of the Moon. However, this study is limited by the small sample population and as such the interpretations and statistical significance of the data. Regardless, it has been demonstrated that methods which allow simultaneous collection of comprehensive chemistry and ages, such as the one employed here, support the findings of previous studies (Culler et al., 2000; Delano et al., 2007; Levine, 2004; Levine et al., 2005; Zellner et al., 2009b) and yield important information not just on the impact rate and selection effects that change it, but also horizontal transport processes and evolution of the lunar terrain.

Multi-Spherule Generation Constraints

In addition to being able to determine the provenance of individual impact spherules, the combined major and trace element data also allow for the identification of impact spherules that may have been produced from the same event. Currently, it is unclear what kinds of impact conditions produce impact spherules and how the number of impact spherules produced per event scales to the amount of melt generated. Do large events produce more spherules? Are impact spherules produced only in certain impact conditions (e.g. velocity, target composition and porosity)? While these questions cannot be addressed in this study, it is important to consider the possibility that an impact can produce more than one impact spherule which will have an identical composition and age. Previously, Delano et al. (2007) identified four glass fragments that shared formation ages of ~3.73-3.78Ga and exotic HKFM major element composition and concluded that all the fragments are likely to have been produced by one large and distant impact event. If this fact were not known, and all glasses were

treated as different events (as they would have without the integrated data), there is potential to bias the impact spherule record towards periods where multi-spherule producing events were prevalent if duplicate impact spherules saturate the surface. The addition of trace elements acquired in this study allow for duplicate spherules to be discriminated more comprehensively than previous studies (i.e. Culler et al., 2000; Delano et al., 2007; Levine et al., 2005).

The major and trace element composition of each impact spherule with a statistically acceptable age is compared with the other dated impact spherules instead of candidate soils to determine the probability of them being duplicates (see Chapter 5: Comparison of Impact Spherule and Soil Compositions). Recall that the effective degrees of freedom determined using this method were 18 (see Figure 65). Using this as the effective degree of freedom for the subset of 21 dated impact spherules that have statistically acceptable ages, a matrix showing the probabilistic match of the compositions and ages of the impact spherules can be produced (see Table 14). It is now possible to explore how potentially duplicate impact spherules can affect the impact spherule age distribution. The data in Table 14 is illustrated in Figure 89 which shows how duplicate impact spherules are determined using impact spherule pairs and the effect of removing the potential duplicates from the age distribution.

The results indicate that there are up to five duplicate impact spherules of statistical significance (i.e. P>5%). Interestingly, none of these are impact spherules from the 400Ma spike, but distributed towards the older impact spherules in the 3.2-4.4Ga peak. This might suggest that multi-spherule producing impacts have become rarer over time at the Apollo 16 site, which may relate to a change in the impactor population. Since it is unclear what types of impacts favour impact spherule formation, the change in impactor population could be related to the average size of the impactors, velocity, or perhaps composition (i.e. asteroid versus comet). If all five potential duplicates are removed from the impact record developed in this project, the age distribution indicates an exponential increase in activity from 4.4Ga to the present, much like that observed in the Apollo 12 impact spherule record. A more conservative approach would have only

three impact spherule pairs with P>50% removed, but the later 3.2-4.4Ga peak again is most affected. Only one pair (LS1-41/LS1-33) has P>85% agreement between compositions and ages making it the most likely duplicate pair. The formation age of the impact spherule pair is ~3.7Ga and overlaps with the peak in impact-reset ages of the lunar impact-melt breccias. While the age of this pair overlaps with the shards from Delano et al. (2007), they are produced from distinct impacts since the compositions are different (feldspathic versus KREEPy).

Overall, these results argue against multi-spherule inputs from young impacts contributing to the 400Ma spike in the Apollo 16 record. Therefore, if these results are applicable to the other spherule records, duplicate spherules do not appear to affect the earlier interpretations. Conversely, it suggests that older impact spherules may be preserved more readily in the record, relative to the younger spherules, because they were formed in multi-spherule impacts that may have produced larger quantities of duplicates. This leads to a scenario where there may be a balance between the preservation of the older record through duplication and burial of impact spherules versus destruction from subsequent impacts. However, note that although it is possible to identify potentially duplicate impact spherules, they may actually represent closely spaced impacts into regions where soils have similar compositions. Caution should be exercised when excluding impact spherules from the spherule record for this reason.

Table 14. Table consisting of probabilistic match of compositions (shaded grey regions) and formation ages (white regions). Highlighted in the lighter colours are two examples: The probabilistic match of composition and age for LS1-41 and LS1-33 is 87% and 100% respectively (highlighted yellow). Therefore they are flagged as potentially duplicate impact spherules. LS5-67 is similar in composition and age to two other impact spherules, LS2-31 and LS3-52. Although LS5-67 has a good compositional match to LS3-52, the age match is not of a significant percentage, therefore the LS5-67/LS3-52 pair is produced in unrelated events.

Probability of matching composition

Probability of matching age	LS1-22	LS1-31	LS1-33	LS1-41	LS1-42	LS1-43	LS1-73	LS2-31	LS2-45	LS2-62	LS2-63	LS3-15	LS3-21	LS3-24	LS3-52	LS3-71	LS4-12	LS4-21	LS5-67	LS5-72	LS6-31
LS1-22		0%	0%	0%	0%	0%	0%	0%	0%	0%	0%	0%	0%	0%	0%	0%	0%	0%	0%	0%	0%
LS1-31	0%		67%	13%	47%	0%	0%	0%	0%	0%	0%	0%	0%	0%	0%	85%	0%	0%	0%	0%	0%
LS1-33	0%	0%		100%	98%	55%	0%	0%	0%	0%	0%	93%	89%	0%	42%	98%	0%	4%	1%	47%	11%
LS1-41	0%	0%	87%		0%	0%	0%	0%	0%	0%	0%	0%	7%	0%	2%	14%	0%	0%	0%	0%	0%
LS1-42	0%	0%	0%	0%		0%	0%	0%	0%	0%	0%	0%	0%	0%	0%	22%	0%	0%	0%	0%	0%
LS1-43	86%	0%	0%	0%	0%		0%	0%	0%	0%	0%	20%	0%	0%	65%	17%	0%	0%	0%	0%	14%
LS1-73	0%	0%	0%	0%	1%	0%		0%	0%	0%	0%	0%	0%	0%	0%	0%	0%	0%	0%	0%	0%
LS2-31	0%	8%	0%	0%	29%	0%	79%		50%	0%	0%	0%	0%	0%	2%	0%	0%	0%	79%	0%	0%
LS2-45	0%	0%	0%	0%	0%	0%	24%	74%		0%	0%	0%	0%	0%	6%	0%	0%	0%	5%	0%	0%
LS2-62	0%	0%	0%	0%	0%	0%	0%	0%	0%		0%	0%	0%	91%	0%	0%	0%	0%	0%	0%	0%
LS2-63	1%	0%	0%	0%	0%	1%	0%	0%	0%	0%		0%	0%	0%	0%	0%	0%	0%	0%	0%	0%
LS3-15	0%	0%	2%	0%	0%	0%	0%	0%	0%	0%	0%		33%	0%	61%	55%	0%	0%	0%	0%	0%
LS3-21	0%	0%	27%	7%	0%	0%	0%	0%	0%	0%	0%	0%		0%	45%	22%	0%	0%	0%	0%	6%
LS3-24	14%	0%	0%	0%	0%	6%	0%	0%	0%	0%	10%	0%	0%		0%	0%	0%	0%	0%	0%	0%
LS3-52	0%	0%	8%	1%	0%	0%	0%	0%	0%	0%	0%	62%	0%	0%		9%	0%	44%	78%	0%	18%
LS3-71	0%	0%	0%	0%	0%	0%	0%	2%	0%	0%	0%	0%	0%	0%	0%		0%	0%	0%	0%	0%
LS4-12	0%	0%	55%	7%	0%	0%	0%	0%	0%	0%	0%	0%	0%	0%	4%	0%		0%	0%	0%	0%
LS4-21	81%	0%	0%	0%	0%	70%	0%	0%	0%	3%	6%	0%	0%	43%	0%	0%	0%		4%	0%	0%
LS5-67	0%	1%	0%	0%	7%	0%	67%	58%	27%	0%	0%	0%	0%	0%	0%	10%	0%	0%		0%	40%
LS5-72	0%	79%	0%	0%	0%	0%	0%	6%	0%	0%	0%	0%	0%	0%	0%	0%	0%	0%	1%		0%
LS6-31	0%	0%	0%	0%	0%	0%	0%	0%	0%	8%	0%	0%	0%	0%	0%	0%	0%	1%	0%	0%	

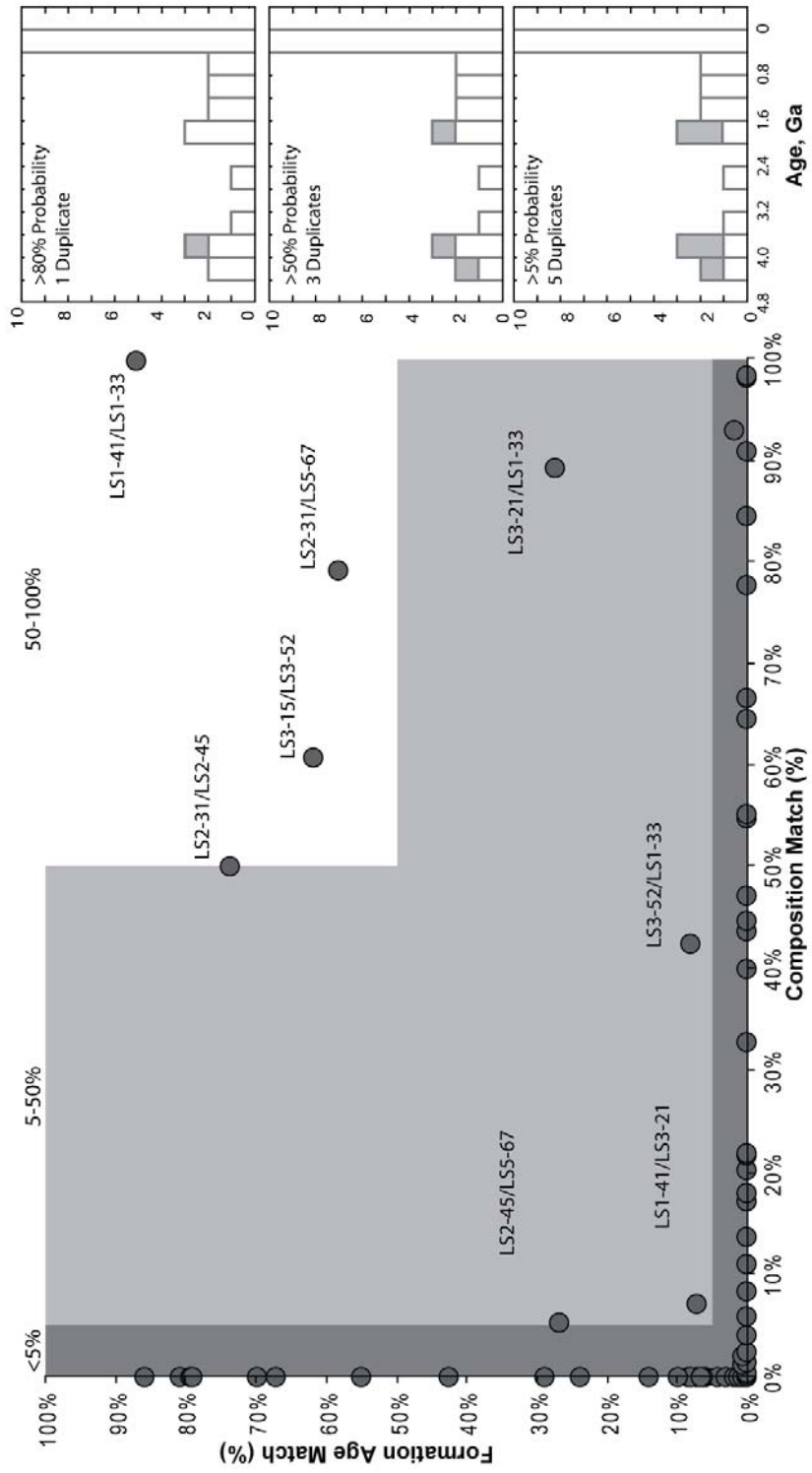

Figure 89. Plot of probability of composition versus formation age matches of impact spherule pairs generated using the twenty-one impact spherules with statistically acceptable formation ages. Impact spherule pairs not of statistical significance (P<5%) are plotted in the dark grey region, while impact spherule pairs likely to be the formed in the same event (P>50%) fall within the white region. The impact spherule age distributions to the right show the effect of removing the potentially duplicate impact spherules (grey boxes) as a function of probability.

6.3.3 Summary of Selection Effects: Considerations and Constraints

Given the previous discussion, it is clear that lunar impact spherules are a lunar bombardment record that is fraught with selection effects. The combination of major and trace element compositions and ages employed in this study have allowed constraints of two selection effects, the input of exotic impact spherules and multi-spherule events. The provenance of impact spherules is useful in both limiting impact spherule production to smaller regions, evaluating horizontal transport, and determining the contribution of exotic spherules to impact spherule age distributions at the local site. The latter is particularly important in studies, such as this, where the dated sample population is small and selection of more enticing exotic potassium-rich compositions is more likely. Although impact spherules derived from local rocks and soils were preferentially selected for dating in this project, there appears to be a selection effect towards impact spherules with compositions slightly more mafic than the local soils due to the need for K-rich glasses. Up to four of the twenty-six impact spherules with statistically acceptable or inferred young ages are potentially exotic to the collection site. Three of these have ages <800Ma suggesting that large events capable of transporting spherules hundreds of kilometres from their place of formation are still common at this late stage of lunar evolution. However, this does not appear to contribute significantly to the <400Ma spike. It has also been possible to remove duplicate impact spherules using methods employed in this study. However, the duplicate impact spherules produced in recent impacts do not contribute at all to the <400Ma spike. Conversely, duplicate impact spherules more commonly have ages >1Ga suggesting that more recent impacts may produce fewer duplicate spherules and therefore, the probability of recovering a duplicate pair is low.

Overall, the selection effects were described in this study can have a relatively large influence over the impact spherule age distribution. However, given the small population of spherules studied in this project, it is uncertain whether such interpretations will hold up in statistically larger populations. Additionally, it limits the applicability of these constraints to other impact records. It is clear that there are key

gaps in the understanding of how impact spherules are formed and subsequently affected by impact and geological processes. The question then is "are impact spherules still reliable records of impact history?".

6.4 Revisiting the Impact Spherule Record

Recall that Figure 78 showed a combined age distribution for impact spherules collected from Apollo 12, 14, 16, and 17 sites. Highlighted were a number of features that existed in each individual landing site record and the impact spherule record as a whole. The following paragraphs explore potential causes of each feature in light of the potential selection effects identified and discussed in the previous section.

Greater than 2.4Ga

The most significant feature of this period is the lack of impact spherules with ages >3.9Ga compared to the later peak between 3.9Ga-2.4Ga, as recorded by the Apollo 12, 14, and 16 impact spherule records. The lack of >3.9Ga spherules is even more prominent when the individual impact spherule records are combined (see Figure 78). Greater cratering rates prior to 4.1Ga are expected from crater production functions (Hartmann, 1975, 2003; Neukum et al., 2001), but the impact spherule record shows no increase in spherule production. Hartmann (2003) argues that this is due to the Stonewall Effect resulting from subsequent destruction. However, it is unclear whether this is applicable to the impact spherule population as there are processes that buffer impact spherules from destruction (e.g. burial, duplicate spherules). Additionally, if the 3.9Ga-2.4Ga peak were mostly produced from spherules resulting from a selection or sampling bias, the >3.9Ga period would lose its significance as there would not be a sudden decrease of spherules at ~3.9Ga. The lack of impact spherules in the >3.9Ga period can be interpreted in a number of ways:

1. The Stonewall Effect is real and the >3.9Ga record is erased. However, some impact spherules and other lunar materials with older ages have survived and made it to the surface for collection.
2. The Late Heavy Bombardment is real and the 3.9Ga-2.4Ga peak in spherule production results from impacts marking the tail-end of this episode.
3. The apparent increase in activity in the 3.9-2.4Ga period results from selection effects. The identification of duplicate impact spherules in this project and

Delano et al. (2007) for example, suggests that the characteristics of the impactor population may have changed between 3.9-2.4Ga to favour duplicate spherule production producing an apparent increase in impact activity. Without integrated data, duplicate spherules will have been treated as separate events in the Apollo 12 and 14 spherule records. Other effects may be possible since little is known about what impact conditions (velocity, size, composition of impactor) favour spherule production.

4. The apparent increase in activity in the 3.9-2.4Ga period results from sampling bias (selection effect from sampling a population that is not representative). For example, the 3.9-2.4Ga peak is best represented by impact and possible volcanic spherules collected from the Apollo 14 site. The *e/f* model suggests that the current spherule populations from Apollo 12, 14, and 16 can be divided into two populations, a reservoir of old deep spherules and young surficial spherules. Since impact spherules from Apollo 14 were collected from Cone Crater ejecta, which sampled the deepest regolith in all impact spherules records, mixing between the dominantly old population and surficial young population may bias the record. Conversely, the older Apollo 12 record may have been diluted by recent impact spherules excavated by Sharp Crater. Resurfacing and recent impact history at each landing site where impact spherules have been collected will strongly govern the effect of this sampling bias. The Imbrium event at ~3.8Ga (see Stöffler et al., 2006), for example, may have buried older impact spherules at the Apollo sites, thus requiring them to be excavated again by sufficiently large impacts if they are to be sampled. Note, however, that this whole argument will be invalidated if impact spherules saturate in solar wind argon, as suggested possible by Levine et al. (2007).

2.4Ga to 1.0Ga

The impact spherule records, both individually and as a whole, suggest that this is a period of minimal impact activity. This period of relative tranquillity is also present in the lunar meteorite records which show a declining flux from ~2.4 to present (Cohen, 2008b). Hartmann et al. (2007) advocates that the impact spherules and lunar meteorite

records are empirical evidence of a period of long term decline in impacts that was modelled in crater counting studies. However, the Nice model suggests that this decline should not relate to a late heavy bombardment as this would last a maximum of ~150Myr (Gomes et al., 2005). It is possible that rather than being a minimum, this period is under-represented compared to the periods before and after it.

Present – 1Ga

One of the main features of all impact spherule distributions was the observation an increasing abundance of impact spherules from ~500Ma to present. Based on the results of this project, it would appear that exotic and duplicate impact spherules contribute minimally, if at all, to the apparent increase in activity at the Apollo 16 site. Although this may be true for the impact spherule population of this project, it may not be applicable for the other spherule records. Figure 81 suggests that impact spherules with formation ages <500Ma typically had high *e/f* ratios and are likely to have been formed and remained on the near surface. Thus, any random collection of impact spherules from the surface is expected to be biased in favour of young spherules. This implies that the young spike is a sampling bias and that impact spherules collected from deeper sources are will produce different age distributions. For example, the Apollo 14 record spikes between 3.9-2.4Ga because it may consist mostly of deeply buried spherules excavated by Cone Crater. Therefore the ejecta were mixed with surface soils producing a second younger, but smaller spike in spherule ages. For the Apollo 12 and 16 records, however, either older material is scarcer or significantly diluted by younger spherules. Consequently, the magnitude of the young peak is proportional to the rate of regolith mixing in a representative population of impact spherules, but will be subject to a strong selection bias in smaller populations if samples were collected near young craters. The implication of this interpretation is that the <500Ma spherules are unfairly represented in impact spherules collected from the surface compared to the rest of the record due to sampling bias and therefore, are not concrete evidence for an increase in impact activity during this time.

Although there may not have been an increase in impact activity, there is evidence to suggest that large impacts may have become increasingly common. There are two, possibly three, impact spherules with ages <500Ma and exotic (2 KREEPy and 1 mare) compositions that have been identified in this study. These impact spherules were probably transported large distances by equally large impact events, suggesting such impacts may still have been common at this late stage of lunar evolution. The size of the event can be crudely estimated using Equation 18:

$$R_r = 10.5 R_c^{1.25} \quad \textbf{[18]}$$

Where R_r = Maximum radius of rays from a crater (km)

R_c = Radius of the crater (km)

Source: Baldwin (1963)

The nearest source of mare and KREEP are ~220km and ~350km respectively (Zeigler et al., 2006). Equation 18 indicates that mare and KREEP materials could have been brought to Apollo 16 site by crater rays from craters 23km and 33km in diameter, respectively. Zellner et al. (2009b) have also described multiple impact spherules from various Apollo landing sites with formation ages ~800Ma suggesting an increase in activity may be real and may have been triggered by the H-L chondrite events. Some of these impact spherules may have been formed by the Copernicus event, but it may only be one of many impact events (Zellner et al., 2009b). Interestingly, duplicate impact spherules are not more common in this late period of lunar evolution as would be expected if large events produced multi-spherules. In fact, duplicate spherules appear more common in the earlier impact record according to results of this study, suggesting that large impacts may not be a requisite for duplicate spherules.

6.5 Chapter Conclusions

This chapter presents the first Apollo 16 impact spherule age distribution for spherules that were probably produced from local soils and rocks. The field location for this study complements previous impact spherule studies at the Apollo 12, Apollo 14 and the emerging record at Apollo 17 sites. The focus on locally derived impact spherules from the Apollo 16 site also permits the comparison of three very different impact spherule records. Improvements were made to the previous methods that allowed acquisition of both major and trace element chemistry and formation and exposure ages on individual impact spherules. In addition to producing an impact spherule age distribution, the methods employed in this study also allowed for the constraints to be placed on some selection effects that affect the impact record.

Two selection effects could be constrained in this study, provenance and multi-spherule impacts. Knowledge of the provenance of impact spherules making up an age distribution can be used in many ways. The main use is to determine the contribution of impact spherules formed within the collection site and those that are transported to the site which allows the impact rate to be constrained to smaller regions. Previously, the major element compositions were only used to distinguish volcanic spherules from impact spherules and only later were used to classify them based on broad lunar terrains (highlands, KREEP, mare). The addition of trace element compositions in this study has allowed for impact spherule provenance to be narrowed more precisely, in this case, even down to regional differences around a landing site (Descartes versus Cayley). Another advantage of the multi-analysis approach used in this study is the identification of multi-spherule impacts. Such impacts may play a significant role in over-inflating the impact record if spherules from the same event are counted multiple times. Results of this study indicate that of the 26 spherules dated, there are up to five (P>5%) that could be potentially duplicates. Duplicates are identified using a combination of both major and trace element chemistry and formation ages so that only the most similar impact spherules are considered.

Using this information it has been possible to determine that the apparent <500Ma increase in impact activity may have resulted from selection effects probably due to relatively surficial sampling. The older impact spherules in surficial deposits are excavated from depth and mixed with the younger spherules. There appears to be evidence for an increasing occurrence of large impacts from ~800Ma in the literature which may be responsible for the mixing. This is supported by 3 out of 10 young impact spherules in this study which were transported from mare and KREEP terrains at least 220km and 350km from Apollo 16 respectively.

The *e/f* model used to characterise the exposure and formation ages of the impact spherules suggests that two populations can be established: a young population that has spent most of its lifetime within the top metre the surface and an older population that has been more recently excavated. This highlights the possibility that there were selection and sampling biases that may be acting on the impact spherule record. There appears to be a global selection effect that favours impact spherules between 2.4-3.9Ga, which can be explained by a change in impactor population to favour duplicate spherule impacts, sampling bias, or an actual increase in impact activity (i.e. the late heavy bombardment). A change in impactor population and increase in impact activity suggests that the 2.4-3.9Ga spherules may represent impacts resulting from a late heavy bombardment, which tailed off into a steady-state. However, a sampling bias resulting from surface samples intermixed with recent impact ejecta is also a distinct possibility. Combined with the selection effect towards <500Ma spherules due to surficial sampling, the characteristic "U"-shaped age distribution is produced in all impact records. However, these interpretations may not be valid in a larger study population. It is recommended that a larger study population be developed using multi-analytical approaches, such as that used in this study. Such methods are necessary to constrain the selection effects that influence the impact spherule record. Only then can a more representative lunar impact record can be developed.

6.6 Future Work – Modelling of Sampling Bias and the Stonewall Effect

Ideas and interpretations presented in this project currently lack the number of glasses to be statistically applicable to the larger impact spherule databases. Obviously, a larger number of impact spherules should be studied using methods that allow collection of both comprehensive chemistry and ages so that the ideas and interpretations can be tested and back-applied to previous impact spherule records. This project has also clarified that each lunar impact spherule record is influenced by a series of selection effects, some of which have been constrained using methods employed in this project. The effect of impact spherule provenance and multi-spherule impacts has been constrained in this study. In addition, the currently unconstrained selection effects associated with depth and spatial location can be reduced by study of the impact spherules from more diverse locations and depths though this may not be physically or financially feasible. However, there are some selection effects that remain unconstrained and will remain so without the use of mathematical models. The Stonewall Effect suggested by Hartmann (2003) is the most important since this process has the potential to essentially eliminate part of the record. However, this may be offset by multi-spherule impacts that are more resilient to destruction as multiple copies of the same impact are produced. There are also buffering processes to consider such as burial of impact spherules during subsequent impacts and other geological processes. Thus as future work, a model aimed at determining the relationship between impact history recorded from impact spherules and the interplay of selection effects should be of highest priority. A schematic of what the model might look like is illustrated in Figure 90 and described in the following text.

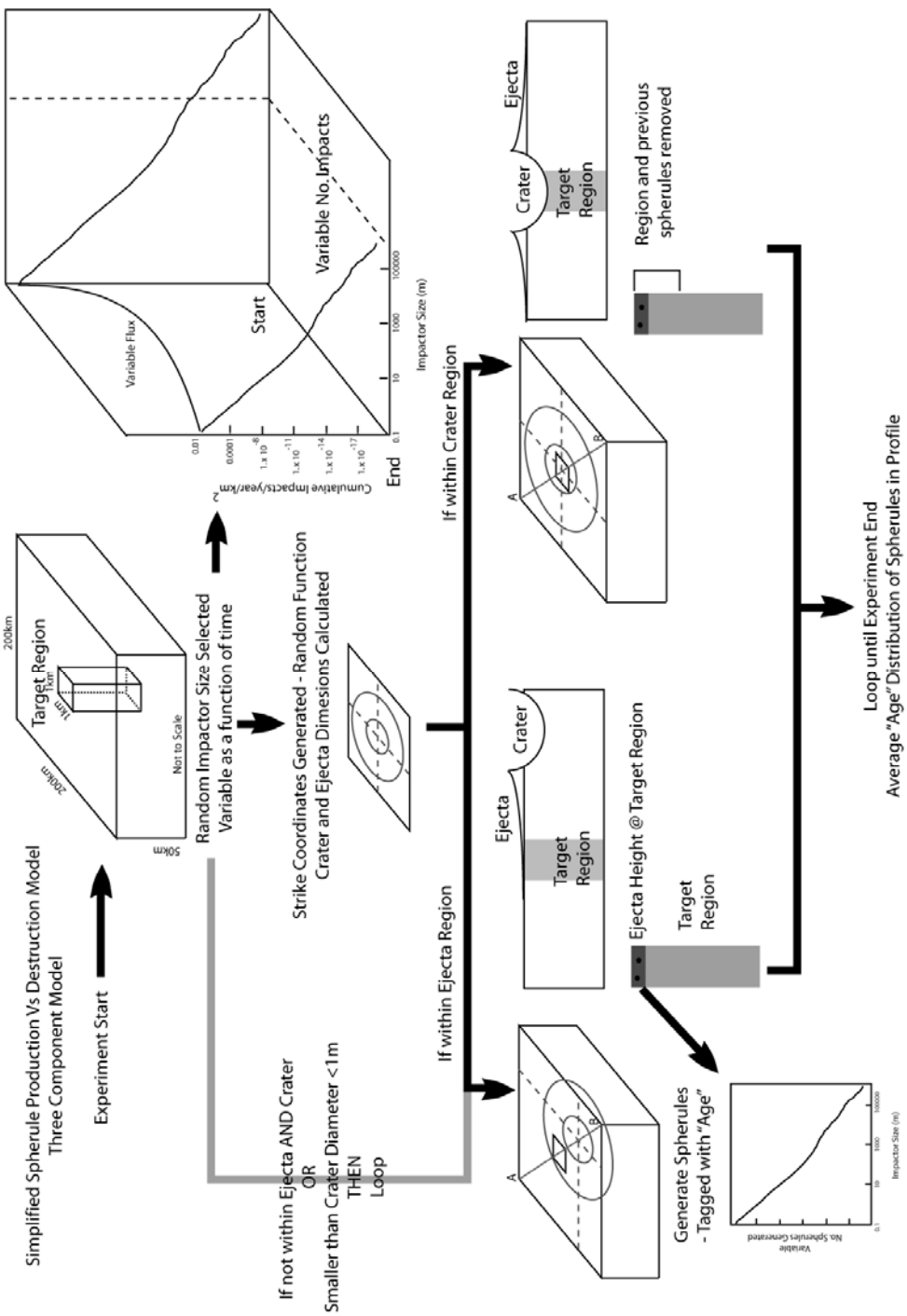

Figure 90. Schematic illustration of model aimed at quantifying the relationships between lunar impact history and that which is recorded by the impact spherules subject to selection effects.

The idea of this model comes from a paper by Richardson (2009) which models the effect of overprinting of impact craters by subsequent impacts. Using steady-state impact flux (probability as a function of time versus size of impactor) such as crater production functions (e.g. Hartmann et al., 2007; Neukum et al., 2001) as an input, this model generates random impacts on the model surface using the impact flux to determine the size of the impactor. After a set amount of time, an algorithm determines the impact flux using crater counting techniques and compares it to the impact flux that was input. Richardson (2009) determined that, prior to saturation of the regolith, the observed crater production functions closely resemble the actual input in shape. However, an equilibrium state will be reached at about 5-10% saturation if the impact population consists typically of small craters causing 'sandblasting' of the surface (i.e. crater density appears to level off). An impact population consisting of larger impactors will continue to reflect the actual input as large craters reset regions that are later repopulated with craters. A similar simulation could be used to model the effects of various geological and impact process and their effect on the impact spherule record. However, there are some over-simplifications that will need to be addressed.

A simple model would record impact spherule production/destruction in a small target region which is a subset of a much larger model region subject to impacts. The input to this model would not be a steady-state impact flux, but would need to be variable. Variations to the impact flux as function of time and specifically triggered events such as the possibility of a LHB would need to be explored in order to determine the effect of overprinting on the spherule record. For each impact event a random coordinate on the model surface is chosen and using the size of the impactor, a crater and ejecta curtain are produced. Should the target region fall within the impact ejecta, the "height" of the target region is increased and impact spherules are randomly dispersed in this added region. Note that this also provides an opportunity to model the effect of impact spherule production with impactor size. Each impact spherule is tagged with a formation age and impactor ID. Eventually the surface will saturate with impact spherules requiring that some be destroyed. If the target region falls within the crater, the depth of the crater at that point is removed from the "height" of the target region

along with any impact spherules within it. This represents destruction or removal of the impact spherules from the target region. Thus over time, changes to the profile of the target region and impact spherules within it can be determined. Multiple runs of this simulation would build up a statistical model for the importance of sampling depth and location, the effect of multi-spherule production and, with variations in the impact flux input including a LHB event, the influence of the Stonewall effect. More complex models could be designed to accommodate other factors not considered, but may be of significant importance such as tracking multiple target regions to evaluate the importance of horizontal transport.

6.7 Chapter References

ARNOLD J. R. (1975) A Monte Carlo model for the gardening of the lunar regolith. *Earth, Moon, and Planets* **13**(1), 159-172.

ARVIDSON R., CROZAZ G., DROZD R. J., HOHENBERG C. M. and MORGAN C. J. (1975a) Cosmic ray exposure ages of features and events at the apollo landing sites. *Earth, Moon, and Planets* **13**(1), 259-276.

ARVIDSON R., DROZD R. J., HOHENBERG C. M., MORGAN C. J. and POUPEAU G. (1975b) Horizontal transport of the regolith, modification of features, and erosion rates on the lunar surface. *Earth, Moon, and Planets* **13**(1), 67-79.

BALDWIN R. B. (1963) *The Measure of the Moon*. University of Chicago Press. pp. 374.

COHEN B. A. (2008) A Review of Lunar Meteorite Impact-Melt Clast Compositions and Ages (abstract No. 1439). In *Workshop on the Early Solar System Impact Bombardment*, pp. 27-28, Houston, Texas.

CULLER T. S., BECKER T. A., MULLER R. A. and RENNE P. R. (2000) Lunar Impact History from $^{40}Ar/^{39}Ar$ Dating of Glass Spherules. *Science* **287**(5459), 1785-1788.

DELANO J. W., ZELLNER N. E. B., BARRA F., OLSON E., SWINDLE T. D., TIBBETTS N. J. and WHITTET D. C. B. (2007) An integrated approach to understanding Apollo 16 impact glasses: Chemistry, isotopes, and shape. *Meteoritics & Planetary Science* **42**, 993-1004.

DROZD R. J., HOHENBERG C. M., MORGAN C. J., PODOSEK F. A. and WROGE M. L. (1977) Cosmic-ray exposure history at Taurus-Littrow. In *Proceedings of the 8th Lunar Science Conference*, pp. 3027-3043. Pergamon Press, Inc., Houston, Texas.

GAULT D. E., HOERZ F., BROWNLEE D. E. and HARTUNG J. B. (1974) Mixing of the lunar regolith. In *5th Lunar Science Conference*, pp. 2365-2386. Pergamon Press, Inc., Houston, Texas.

HARTMANN W. K. (1975) Lunar "cataclysm": A misconception? *Icarus* **24**(2), 181-187.

- (2003) Megaregolith evolution and cratering cataclysm models: Lunar cataclysm as a misconception (28 years later). *Meteoritics & Planetary Science* **38**(4), 579-593.

HARTMANN W. K., QUANTIN C. and MANGOLD N. (2007) Possible long-term decline in impact rates: 2. Lunar impact-melt data regarding impact history. *Icarus* **186**(1), 11-23.

JONES E. M. and GLOVER K. (1995) Apollo Lunar Surface Journal: A Visit with the Snowman.

KOROTEV R. (1997) Some things we can infer about the Moon from the composition of the Apollo 16 regolith. *Meteorit. Planet. Sci.* **32**, 447-478.

KOROTEV R. L. (1994) Compositional variation in Apollo 16 impact-melt breccias and inferences for the geology and bombardment history of the Central Highlands of the Moon. *Geochimica et Cosmochimica Acta* **58**(18), 3931-3969.

KOROTEV R. L., JOLLIFF B. L., ZEIGLER R. A., GILLIS J. J. and HASKIN L. A. (2003) Feldspathic lunar meteorites and their implications for compositional remote sensing of the lunar surface and the composition of the lunar crust. *Geochimica et Cosmochimica Acta* **67**(24), 4895-4923.

LANGEVIN Y. and ARNOLD J. R. (1977) The Evolution of the Lunar Regolith. *Annual Review of Earth and Planetary Sciences* **5**(1), 449-489.

LEVINE J. (2004) Lunar glass spherules as probes of the meteoroid impact history of the Moon. Ph.D. thesis. University of California, Berkeley.

LEVINE J., BECKER T. A., MULLER R. A. and RENNE P. R. (2005) $^{40}Ar/^{39}Ar$ dating of Apollo 12 impact spherules *Geophysical Research Letters* **32**(15), L15201.

LEVINE J., RENNE P. R. and MULLER R. A. (2007) Solar and cosmogenic argon in dated lunar impact spherules. *Geochimica et Cosmochimica Acta* **71**(6), 1624.

LINDSTROM M. M. and SALPAS P. A. (1981) Geochemical studies of rocks from North Ray Crater, Apollo 16. In *12th Lunar and Planetary Science Conference*, pp. 305-322. Pergamon Press, Houston Texas.

LUCEY P., KOROTEV R. L., GILLIS J. J., TAYLOR L. A., LAWRENCE D., CAMPBELL B. A., ELPHIC R., FELDMAN B., HOOD L. L., HUNTEN D., MENDILLO M., NOBLE S., PAPIKE J. J., REEDY R. C., LAWSON S., PRETTYMAN T., GASNAULT O. and

MAURICE S. (2006) New Views of Lunar Geoscience: Understanding the Lunar Surface and Space-Moon Interactions. In *New Views of the Moon* (eds. B. L. Jolliff, M. Wieczorek, C. K. Shearer and C. Neal), pp. 83-219.

MA M.-S., SCHMITT R. A., TAYLOR G. J., WARNER R. D., LANGE D. E. and KEIL K. (1977) Chemistry and petrology of Luna 24 lithic fragments and less than 250-micron soils - Constraints on the origin of VLT mare basalts. In *Mare Crisium: The view from Luna 24* (eds. R. B. Merrill and J. J. Papike), pp. 569-592. Pergamon Press, Inc., Houston, Texas.

MCKAY D. S., HEIKEN G., BASU A., BLANFORD G., SIMON S., REEDY R., FRENCH B. M. and PAPIKE J. (1991) The Lunar Regolith. In *Lunar Sourcebook: A User's Guide to the Moon* (eds. G. Heiken, D. T. Vaniman and B. M. French), pp. 285-356. Cambridge University Press.

MELOSH H. J. (1989) *Impact Cratering - A Geologic Process*. Oxford University Press.

MENDELL W. W. and MCKAY D. S. (1975) A lunar soil evolution model. *Earth, Moon, and Planets* **13**(1), 285-292.

MORRIS R. V., SEE T. H. and HÖRZ F. (1986) Composition of the Cayley formation at Apollo 16 as inferred from Impact Melt Splashes. *Journal of Geophysical Research* **91**(B13), E21-E42.

NEAL C. R. and TAYLOR L. A. (1992) Petrogenesis of mare basalts: A record of lunar volcanism. *Geochimica et Cosmochimica Acta* **56**(6), 2177-2211.

NEUKUM G., IVANOV B. A. and HARTMANN W. K. (2001) Cratering Records in the Inner Solar System in Relation to the Lunar Reference System. *Space Science Reviews* **96**(1), 55-86.

NORMAN M. D. (1981) Petrology of suevitic lunar breccia 67016. In *Proceedings of the 12th Lunar and Planetary Science Conference*, pp. 235-252. Pergamon Press, Houston, Texas.

NORMAN M. D., DUNCAN R. A. and HUARD J. J. (2010) Imbrium provenance for the Apollo 16 Descartes terrain: Argon ages and geochemistry of lunar breccias 67016 and 67455. *Geochimica et Cosmochimica Acta* **74**(2), 763-783.

NYQUIST L. E., BANSAL B. M., WOODEN J. L. and WIESMANN H. (1977) Sr-isotopic constraints on the petrogenesis of Apollo 12 mare basalts. In *8th Lunar Science Conference*, pp. 1383-1415. Pergamon Press, Inc., Houston, Texas.

NYQUIST L. E., SHIH C. Y., BANSAL B. M., WOODEN J. L. and WIESMANN H. (1979) The SR and Nd isotopic record of Apollo 12 basalts - Implications for lunar geochemical evolution. In *10th Lunar Science Conference*, pp. 77-114. Pergamon Press, Inc., Houston, Texas.

PRETTYMAN T. H., HAGERTY J. J., ELPHIC R. C., FELDMAN W. C., LAWRENCE D. J., MCKINNEY G. W. and VANIMAN D. T. (2006) Elemental composition of the lunar surface: Analysis of gamma ray spectroscopy data from Lunar Prospector. *J. Geophys. Res.* **111**.

RICHARDSON J. E. (2009) Cratering saturation and equilibrium: A new model looks at an old problem. *Icarus* **204**(2), 697-715.

SANCHEZ A. (1981) Geology of Stone Mountain. In *Geology of the Apollo 16 Area, Central Lunar Highlands* (eds. G. E. Ulrich, C. A. Hodges and W. R. Muehlberger), pp. 539. National Aeronautics and Space Administration.

SHOEMAKER E. M., HAIT M. H., SWANN G. A., SCHLEICHER D. L., SCHABER G. G., SUTTON R. L., DAHLEM D. H., GODDARD E. N. and WATERS A. C. (1970) Origin of the lunar regolith at Tranquillity Base. In *Proceedings of the Apollo 11 Lunar Science Conference*, pp. 2399-2412.

STÖFFLER D., RYDER G., IVANOV B. A., ARTEMIEVA N., CINTALA M. and GRIEVE R. (2006) Cratering History and Lunar Chronology. In *New Views of the Moon* (eds. B. L. Jolliff, M. A. Wieczorek, C. K. Shearer and C. R. Neal), pp. 519-596.

SUTTON R. L., HAIT M. H. and SWANN G. A. (1972) Geology of the Apollo 14 landing site. In *Proceedings of the Lunar Science Conference*, pp. 27.

TAYLOR G. J., WARREN P., RYDER G., DELANO J., PIETERS C. and LOFGREN G. (1991) Lunar Rocks. In *Lunar Sourcebook: A User's Guide to the Moon* (eds. G. Heiken, D. T. Vaniman and B. M. French), pp. 183-284. Cambridge University Press.

ULRICH G. E. (1973) A geologic model for North Ray Crater and stratigraphic implications for the Descartes region. In *4th Lunar Science Conference*, pp. 27-39.

WASSON J. T. and KALLEMEYN G. W. (1988) Compositions of Chondrites. *Philosophical Transactions of the Royal Society of London. Series A, Mathematical and Physical Sciences* **325**(1587), 535-544.

ZEIGLER R. A., KOROTEV R. L., JOLLIFF B. L., HASKIN L. A. and FLOSS C. (2006) The geochemistry and provenance of Apollo 16 mafic glasses. *Geochimica et Cosmochimica Acta* **70**(24), 6050-6067.

ZELLNER N. E. B., DELANO J. W., SWINDLE T. D., BARRA F., OLSEN E. and WHITTET D. C. B. (2009a) Apollo 17 regolith, 71501,262: A record of impact events and mare volcanism in lunar glasses. *Meteoritics & Planetary Science* **44**(6), 839-851.

- (2009b) Evidence from $^{40}Ar/^{39}Ar$ ages of lunar impact glasses for an increase in the impact rate ~800 Ma ago. *Geochimica et Cosmochimica Acta* **73**(15), 4590-4597.

Appendix 1: Compositions of Dated Impact Spherules

Data are for unpolished analyses – Raw data and limits of detection in electronic annex

See Chapter 4: Methods for analytical methods and data treatment

	LS 1-21		**LS 1-22**		**LS 1-31**		**LS 1-33**	
	Mean	SD	Mean	SD	Mean	SD	Mean	SD
EMPA derived major-element compositions								
SiO_2	45.47	0.22	45.96	1.98	43.99	1.14	46.37	2.42
TiO_2	0.34	0.00	0.80	0.07	0.75	0.24	0.94	0.49
Al_2O_3	26.75	0.11	23.68	0.09	20.26	1.09	21.38	3.56
Cr_2O_3	0.11	0.00	0.22	0.04	0.21	0.04	0.33	0.17
FeO	5.37	0.29	7.26	0.55	11.38	2.31	11.45	5.00
MgO	6.32	0.08	8.44	0.20	11.13	0.44	5.64	0.90
CaO	14.52	0.21	13.23	1.55	11.77	0.72	13.28	0.49
Na_2O	0.87	0.03	0.22	0.02	0.36	0.02	0.37	0.10
K_2O	0.23	0.01	0.09	0.00	0.14	0.02	0.12	0.03
Ratios								
CaO/Al_2O_3	0.54		0.56		0.58		0.62	
MgO/Al_2O_3	0.24		0.36		0.55		0.26	
Laser Ablation ICPMS derived trace-element compositions								
Sc	6.56	0.44	4.11	0.35	8.81	0.80	9.44	1.47
Ti	2154	57	1209	45	2731	289	2971	343
V	17.2	0.7	7.9	0.5	25.1	2.1	19.5	3.0
Cr	789	33	333	18	1172	102	1037	170
Mn	483	21	296	18	715	92	595	103
Co	17.0	4.0	12.9	2.3	22.5	10.8	24.1	4.6
Ni	90	22	165	49	308	165	475	90
Rb	0.99	0.26	0.65	0.18	1.31	0.47	1.70	0.55
Sr	148	4	135	5	126	5	144	6
Y	31	1	10	1	26	2	36	7
Zr	144	4	41	2	125	11	128	22
Nb	9.7	0.4	3.6	0.2	9.4	0.9	9.2	1.4
Ba	104	3	41	2	108	10	118	22
La	9.9	0.6	3.1	0.3	8.0	0.7	11.0	2.5
Ce	26.6	1.1	8.3	0.6	21.8	1.9	29.6	6.7
Pr	3.5	0.3	1.1	0.2	2.8	0.3	3.9	1.0
Nd	16.5	1.6	4.9	0.8	12.9	1.5	18.5	4.4
Sm	4.6	0.9	1.5	0.4	3.6	0.8	5.0	1.3
Eu	1.0	0.2	0.8	0.2	0.9	0.2	1.0	0.3
Gd	4.9	0.7	1.5	0.4	4.0	0.7	5.7	1.3
Dy	5.6	0.9	1.8	0.4	4.7	0.8	6.5	1.5
Ho	1.2	0.2	0.4	0.1	1.0	0.2	1.4	0.3
Er	3.4	0.6	1.2	0.2	3.0	0.5	4.0	1.1
Yb	3.2	0.4	1.1	0.3	2.7	0.5	3.5	0.8
Lu	0.4	0.1	0.2	0.1	0.4	0.1	0.5	0.2
Hf	3.1	0.5	0.9	0.2	2.8	0.4	2.9	0.7
Ta	0.4	0.1	0.2	0.0	0.4	0.1	0.4	0.1
Th	1.7	0.3	0.5	0.1	1.3	0.2	1.7	0.4
U	0.4	0.1	0.2	0.1	0.3	0.1	0.4	0.1

	LS 1-41		LS 1-42		LS 1-43		LS 1-53	
	Mean	SD	Mean	SD	Mean	SD	Mean	SD
EMPA derived major-element compositions								
SiO_2	46.63	0.57	41.92	1.22	45.54	0.55	46.63	0.65
TiO_2	0.61	0.07	0.36	0.10	0.55	0.03	0.60	0.33
Al_2O_3	23.60	0.43	15.51	0.96	27.30	0.31	24.87	1.99
Cr_2O_3	0.42	0.24	0.17	0.11	0.13	0.04	0.11	0.04
FeO	7.83	0.43	17.53	1.44	5.47	0.39	7.03	0.71
MgO	6.89	0.78	5.67	0.34	6.40	0.11	5.96	2.27
CaO	13.16	0.85	11.42	0.43	13.84	0.46	13.64	0.74
Na_2O	0.54	0.05	5.55	0.34	0.54	0.08	0.78	0.08
K_2O	0.23	0.05	1.72	0.04	0.15	0.01	0.30	0.09
Ratios								
CaO/Al_2O_3	0.56		0.74		0.51		0.55	
MgO/Al_2O_3	0.29		0.37		0.23		0.24	
Laser Ablation ICPMS derived trace-element compositions								
Sc	9.12	0.77	5.36	0.45	9.31	0.60	7.72	1.38
Ti	4396	587	1602	115	3511	107	6742	5551
V	18.9	1.5	13.5	0.8	17.9	1.5	20.4	4.3
Cr	753	71	636	54	801	305	981	412
Mn	524	41	434	24	531	19	682	123
Co	21.1	2.9	25.9	6.3	17.6	9.9	35.3	16.2
Ni	299	46	282	219	151	237	518	567
Rb	2.28	0.41	1.65	1.11	0.99	0.81	2.06	0.55
Sr	145	6	119	4	152	6	162	6
Y	40	4	24	2	36	1	25	5
Zr	129	8	101	7	163	6	115	25
Nb	12.2	1.2	6.7	0.7	12.3	0.6	22.5	24.6
Ba	128	8	81	5	139	5	100	15
La	13.6	1.9	7.6	0.6	11.2	0.7	8.0	1.3
Ce	36.5	4.8	20.2	1.2	29.8	1.2	21.7	3.3
Pr	4.7	0.7	2.6	0.2	3.8	0.3	2.9	0.4
Nd	21.9	3.5	12.5	1.5	18.4	1.8	12.9	2.3
Sm	6.1	1.3	3.6	0.7	4.9	1.0	3.6	1.0
Eu	1.0	0.2	0.8	0.2	1.1	0.2	1.1	0.3
Gd	6.5	1.1	3.9	0.7	5.5	0.8	3.9	0.9
Dy	7.1	1.1	4.3	0.6	6.5	0.9	4.6	1.1
Ho	1.5	0.3	0.9	0.2	1.4	0.2	1.0	0.3
Er	4.3	0.7	2.6	0.5	4.0	0.6	2.8	0.8
Yb	3.7	0.6	2.4	0.4	3.8	0.5	2.6	0.8
Lu	0.5	0.1	0.3	0.1	0.5	0.1	0.4	0.1
Hf	3.1	0.5	2.2	0.4	3.6	0.5	3.4	2.3
Ta	0.5	0.1	0.3	0.1	0.5	0.1	1.4	1.4
Th	2.2	0.4	1.1	0.2	2.0	0.2	1.2	0.3
U	0.4	0.1	0.3	0.1	0.4	0.1	0.3	0.1

Compositions of Dated Impact Spherules

	LS 1-73		LS 2-31		LS 2-43		LS 2-45	
	Mean	SD	Mean	SD	Mean	SD	Mean	SD
EMPA derived major-element compositions								
SiO_2	44.27	1.11	46.46	1.57	38.17	0.22	46.33	0.54
TiO_2	0.37	0.02	0.28	0.01	0.74	0.08	0.20	0.03
Al_2O_3	25.42	0.26	28.71	1.70	29.67	0.95	27.31	0.29
Cr_2O_3	0.44	0.22	0.08	0.01	0.07	0.01	0.11	0.01
FeO	4.56	0.91	4.01	1.86	5.87	0.43	5.08	1.19
MgO	9.18	0.34	4.25	0.07	6.99	0.45	4.77	0.45
CaO	13.89	0.26	15.52	1.97	18.33	0.82	14.84	0.59
Na_2O	1.63	0.11	0.54	0.12	0.12	0.06	1.26	0.07
K_2O	0.16	0.02	0.14	0.10	0.04	0.02	0.11	0.01
Ratios								
CaO/Al_2O_3	0.55		0.54		0.62		0.54	
MgO/Al_2O_3	0.36		0.15		0.24		0.17	
Laser Ablation ICPMS derived trace-element compositions								
Sc	8.35	0.41	6.86	0.67	13.34	0.67	6.86	0.75
Ti	2316	71	2107	218	4722	115	1523	225
V	29.9	1.3	16.5	1.3	18.2	0.8	13.5	1.5
Cr	1608	120	709	54	595	58	612	78
Mn	628	46	372	32	648	25	479	28
Co	5.4	4.2	8.8	3.5	19.0	1.5	11.8	6.3
Ni	79	118	75	85	70	26	104	133
Rb	0.34	0.34	0.86	0.82	0.19	0.28	0.72	0.31
Sr	157	4	158	5	201	6	147	4
Y	10	1	22	1	53	2	19	3
Zr	43	2	98	11	241	6	82	16
Nb	3.7	0.2	6.6	0.6	16.7	0.8	5.7	1.0
Ba	52	2	81	10	186	6	67	8
La	2.8	0.3	6.8	0.6	16.8	0.9	5.8	1.0
Ce	7.4	0.6	18.3	1.1	42.9	1.7	15.6	2.5
Pr	1.0	0.1	2.4	0.3	5.9	0.5	2.0	0.4
Nd	4.7	0.8	11.1	1.4	27.7	2.4	9.4	1.7
Sm	1.4	0.6	3.0	0.8	7.8	1.6	2.6	0.7
Eu	1.0	0.2	1.0	0.2	1.5	0.2	0.9	0.2
Gd	1.6	0.4	3.3	0.6	8.4	1.2	2.9	0.7
Dy	1.8	0.4	4.0	0.8	9.7	1.3	3.4	0.9
Ho	0.4	0.1	0.8	0.2	2.1	0.3	0.7	0.2
Er	1.0	0.3	2.5	0.5	5.8	0.8	2.0	0.5
Yb	1.0	0.3	2.2	0.5	5.4	0.7	1.9	0.4
Lu	0.1	0.1	0.3	0.1	0.8	0.1	0.3	0.1
Hf	1.0	0.3	2.2	0.6	5.3	0.8	1.8	0.5
Ta	0.2	0.1	0.3	0.1	0.7	0.1	0.2	0.1
Th	0.4	0.1	1.1	0.2	2.7	0.4	0.9	0.3
U	0.1	0.1	0.4	0.1	0.3	0.1	0.2	0.1

	LS 2-53		LS 2-62		LS 2-63		LS 2-71	
	Mean	SD	Mean	SD	Mean	SD	Mean	SD
EMPA derived major-element compositions								
SiO_2	43.38	0.84	49.42	1.39	39.85	1.01	43.61	0.50
TiO_2	0.40	0.03	1.93	0.25	0.28	0.07	0.39	0.01
Al_2O_3	26.55	0.56	15.90	0.64	30.93	1.15	26.62	0.37
Cr_2O_3	0.13	0.01	0.19	0.02	0.06	0.00	0.13	0.01
FeO	6.13	2.28	11.87	0.97	2.98	0.11	5.46	1.06
MgO	7.75	0.21	9.26	0.62	3.73	1.26	7.38	0.26
CaO	14.39	0.80	10.11	1.48	18.34	0.95	14.75	0.38
Na_2O	1.07	0.11	0.81	0.08	3.33	0.35	1.44	0.19
K_2O	0.19	0.07	0.51	0.04	0.51	0.02	0.22	0.07
Ratios								
CaO/Al_2O_3	0.54		0.64		0.59		0.55	
MgO/Al_2O_3	0.29		0.58		0.12		0.28	
Laser Ablation ICPMS derived trace-element compositions								
Sc	7.24	0.48	23.97	1.02	10.53	1.72	7.30	0.48
Ti	2477	62	12371	315	1869	146	2440	70
V	20.6	0.8	34.2	1.2	14.9	2.0	19.3	1.0
Cr	1018	57	1496	52	504	110	928	44
Mn	627	19	1202	30	377	239	572	23
Co	27.9	4.9	24.7	6.3	4.1	3.6	25.3	4.8
Ni	132	76	169	155	45	77	92	82
Rb	0.94	0.25	18.16	7.17	2.78	2.85	1.26	0.60
Sr	146	5	167	5	170	6	152	4
Y	34	1	279	8	7	2	35	2
Zr	156	5	1393	40	21	5	161	5
Nb	10.9	0.5	96.2	2.9	1.6	0.5	10.9	0.5
Ba	116	4	1052	36	25	7	119	4
La	10.6	0.6	87.5	3.6	1.8	0.8	11.5	0.6
Ce	29.5	1.2	234.9	8.7	4.7	1.8	30.5	1.2
Pr	3.8	0.3	30.0	1.3	0.6	0.3	4.0	0.3
Nd	17.9	1.9	137.2	7.1	3.0	1.3	18.0	2.0
Sm	4.9	0.8	39.3	2.8	0.8	0.5	5.2	0.8
Eu	1.1	0.2	2.5	0.4	0.9	0.2	1.1	0.2
Gd	5.4	0.9	43.5	3.0	1.0	0.5	5.7	0.7
Dy	6.2	0.8	50.4	3.4	1.3	0.5	6.2	1.0
Ho	1.3	0.2	10.7	0.6	0.3	0.1	1.4	0.2
Er	3.8	0.7	31.6	2.2	0.8	0.4	3.8	0.6
Yb	3.3	0.6	28.6	2.2	0.8	0.4	3.3	0.5
Lu	0.5	0.1	3.9	0.4	0.1	0.1	0.5	0.1
Hf	3.4	0.5	29.7	1.9	0.5	0.2	3.5	0.6
Ta	0.5	0.1	4.0	0.3	0.1	0.0	0.5	0.1
Th	1.7	0.3	17.4	1.1	0.2	0.2	1.8	0.3
U	0.5	0.1	5.0	0.5	0.1	0.1	0.5	0.1

Compositions of Dated Impact Spherules

	LS 3-15		LS 3-21		LS 3-24		LS 3-25	
	Mean	SD	Mean	SD	Mean	SD	Mean	SD
EMPA derived major-element compositions								
SiO_2	44.55	1.16	43.64	1.68	48.65	1.51	45.36	1.85
TiO_2	0.63	0.03	0.53	0.03	1.80	0.08	1.08	0.91
Al_2O_3	26.09	0.46	26.04	0.42	14.82	0.51	26.75	2.08
Cr_2O_3	0.13	0.00	0.12	0.00	0.17	0.02	0.11	0.01
FeO	6.50	0.27	7.17	1.80	11.81	1.58	6.31	0.60
MgO	6.51	0.40	7.14	0.68	9.06	0.01	6.40	0.87
CaO	15.11	1.36	14.93	0.39	8.61	0.45	13.28	0.30
Na_2O	0.38	0.03	0.34	0.12	1.45	0.19	0.57	0.03
K_2O	0.11	0.01	0.08	0.01	3.63	0.40	0.15	0.04
Ratios								
CaO/Al_2O_3	0.58		0.57		0.58		0.50	
MgO/Al_2O_3	0.25		0.27		0.61		0.24	
Laser Ablation ICPMS derived trace-element compositions								
Sc	11.22	1.05	8.57	0.67	21.04	0.94	7.84	1.17
Ti	3220	187	2532	157	10509	307	2459	519
V	23.0	2.5	18.1	1.0	27.1	1.1	16.9	2.4
Cr	927	83	818	63	1219	40	698	94
Mn	614	68	562	49	973	30	491	69
Co	29.5	1.5	25.3	5.3	22.8	2.6	21.0	4.3
Ni	436	39	403	92	64	46	277	71
Rb	1.80	0.30	2.78	0.31	6.04	0.51	2.36	0.73
Sr	158	6	165	4	145	5	139	3
Y	36	2	38	3	254	10	27	7
Zr	135	10	122	6	1257	45	104	29
Nb	9.9	1.1	9.0	0.7	84.1	2.6	8.8	2.1
Ba	118	12	115	6	928	28	112	22
La	10.5	1.1	13.7	1.2	79.9	3.2	9.0	2.5
Ce	27.2	2.7	36.3	3.1	210.9	9.1	24.4	6.6
Pr	3.7	0.4	4.8	0.6	27.5	1.5	3.2	0.9
Nd	16.7	2.5	22.2	2.3	127.3	7.1	14.1	3.9
Sm	4.7	1.1	5.8	1.0	35.2	2.9	4.1	1.3
Eu	1.1	0.3	1.2	0.2	2.3	0.4	0.9	0.2
Gd	5.3	1.0	6.3	1.1	40.0	3.1	4.2	1.3
Dy	6.3	1.0	7.0	1.0	45.7	2.5	4.8	1.5
Ho	1.4	0.2	1.4	0.2	10.0	0.7	1.0	0.3
Er	3.9	0.7	4.1	0.6	28.6	1.9	2.9	0.7
Yb	3.7	0.7	3.5	0.6	26.2	1.9	2.7	0.9
Lu	0.5	0.1	0.5	0.1	3.6	0.4	0.4	0.1
Hf	3.0	0.6	2.6	0.7	27.2	2.1	2.3	0.8
Ta	0.4	0.1	0.3	0.1	3.6	0.3	0.4	0.1
Th	1.7	0.4	1.9	0.4	15.7	1.2	1.4	0.4
U	0.4	0.1	0.5	0.1	3.9	0.3	0.4	0.1

	LS 3-32		LS 3-43		LS 3-52		LS 3-53	
	Mean	SD	Mean	SD	Mean	SD	Mean	SD
EMPA derived major-element compositions								
SiO_2	43.75	0.65	47.70	0.30	46.09	1.24	44.54	1.10
TiO_2	0.38	0.01	0.54	0.02	0.79	0.23	0.36	0.08
Al_2O_3	25.39	1.23	14.12	0.91	25.75	2.03	29.37	1.71
Cr_2O_3	0.14	0.00	0.39	0.05	0.11	0.01	0.07	0.02
FeO	6.67	1.44	9.61	0.79	6.38	0.91	4.98	0.78
MgO	7.50	0.22	8.54	0.82	5.89	1.05	3.94	0.93
CaO	14.90	1.02	18.08	0.71	14.26	1.07	15.52	0.63
Na_2O	1.07	0.17	0.82	0.13	0.51	0.03	0.92	0.26
K_2O	0.20	0.08	0.20	0.02	0.23	0.03	0.30	0.25
Ratios								
CaO/Al_2O_3	0.59		1.28		0.55		0.53	
MgO/Al_2O_3	0.30		0.60		0.23		0.13	
Laser Ablation ICPMS derived trace-element compositions								
Sc	2.11	0.32	66.13	2.56	7.78	1.01	7.63	2.39
Ti	609	56	3091	127	2447	340	2814	898
V	4.9	0.5	84.8	3.2	15.7	1.6	16.9	5.3
Cr	219	30	3361	162	663	93	754	259
Mn	152	13	2131	210	455	41	433	137
Co	13.2	6.5	80.2	15.8	21.8	3.6	18.7	8.7
Ni	249	240	692	254	293	57	342	375
Rb	0.60	0.26	0.98	0.38	1.69	0.39	1.28	0.35
Sr	246	9	81	6	149	4	155	6
Y	8	1	12	1	28	8	23	8
Zr	30	4	17	1	107	20	108	37
Nb	2.1	0.3	0.7	0.1	8.8	1.1	9.9	3.4
Ba	95	4	18	1	114	28	77	15
La	2.8	0.5	1.1	0.2	9.1	2.3	7.1	2.1
Ce	7.4	0.8	3.3	0.2	24.1	6.1	19.4	5.4
Pr	0.9	0.2	0.5	0.1	3.2	0.9	2.5	0.8
Nd	4.3	0.9	2.9	0.5	14.6	4.5	11.8	3.6
Sm	1.3	0.5	1.1	0.4	4.1	1.5	3.2	1.2
Eu	1.9	0.3	0.5	0.1	1.0	0.3	1.0	0.3
Gd	1.3	0.4	1.6	0.4	4.3	1.4	3.8	1.3
Dy	1.4	0.5	2.0	0.4	5.0	1.6	4.4	1.6
Ho	0.3	0.1	0.5	0.1	1.0	0.3	0.9	0.4
Er	0.8	0.3	1.4	0.3	2.8	0.8	2.6	1.1
Yb	0.8	0.3	1.5	0.2	2.8	1.0	2.5	1.1
Lu	0.1	0.1	0.2	0.1	0.4	0.1	0.3	0.1
Hf	0.7	0.3	0.5	0.2	2.4	0.6	2.4	1.0
Ta	0.1	0.0	0.0	0.0	0.4	0.1	0.4	0.2
Th	0.3	0.2	0.1	0.0	1.4	0.4	1.3	0.6
U	0.1	0.1	0.0	0.0	0.3	0.1	0.3	0.2

Compositions of Dated Impact Spherules

	LS 3-71		LS 4-12		LS 4-21		LS 5-67	
	Mean	SD	Mean	SD	Mean	SD	Mean	SD
EMPA derived major-element compositions								
SiO_2	43.76	1.44	43.76	0.38	48.11	0.43	46.10	0.35
TiO_2	0.64	0.09	0.55	0.02	0.32	0.03	0.70	0.28
Al_2O_3	23.19	2.61	23.50	0.14	25.60	0.17	28.62	1.35
Cr_2O_3	0.17	0.03	0.17	0.01	0.09	0.01	0.07	0.01
FeO	8.53	2.09	9.23	0.21	5.27	0.23	4.32	0.71
MgO	8.19	1.89	5.97	0.09	5.19	0.05	5.00	0.85
CaO	15.08	2.39	14.04	0.36	14.38	0.22	14.61	0.11
Na_2O	0.35	0.04	1.85	0.09	0.90	0.02	0.40	0.04
K_2O	0.10	0.03	0.93	0.02	0.15	0.02	0.12	0.01
Ratios								
CaO/Al_2O_3	0.65		0.60		0.56		0.51	
MgO/Al_2O_3	0.35		0.25		0.20		0.17	
Laser Ablation ICPMS derived trace-element compositions								
Sc	9.58	0.96	12.18	0.64	7.14	0.45	7.52	1.23
Ti	3154	180	6290	266	2199	88	2247	315
V	20.5	2.6	41.1	1.2	13.6	0.7	16.9	2.6
Cr	926	147	1491	74	653	60	757	165
Mn	637	71	910	27	393	18	396	45
Co	48.4	7.0	5.3	1.9	8.9	2.9	16.6	3.8
Ni	838	131	62	63	113	273	289	141
Rb	2.02	0.36	12.11	1.06	0.32	0.35	2.89	0.44
Sr	161	6	114	4	145	4	152	5
Y	32	2	104	3	22	2	29	8
Zr	125	11	544	15	102	14	79	13
Nb	9.6	0.7	35.4	1.2	7.0	1.0	7.2	0.9
Ba	120	7	503	17	74	4	99	18
La	9.7	0.7	32.8	1.2	6.9	0.5	9.2	2.8
Ce	25.7	1.6	89.8	3.7	18.7	1.0	25.6	7.1
Pr	3.4	0.4	11.7	0.6	2.5	0.3	3.3	1.0
Nd	15.9	2.1	52.7	3.2	11.4	1.7	15.8	5.1
Sm	4.5	1.1	14.9	1.4	3.1	0.8	4.1	1.6
Eu	1.1	0.3	1.5	0.3	0.9	0.2	1.0	0.2
Gd	5.0	0.9	16.6	1.2	3.5	0.7	4.8	1.6
Dy	5.7	1.0	18.6	1.1	4.2	0.8	5.2	1.5
Ho	1.3	0.3	4.1	0.3	0.9	0.2	1.1	0.4
Er	3.5	0.8	11.7	1.0	2.4	0.4	3.3	1.1
Yb	3.3	0.7	10.5	0.7	2.4	0.5	2.9	1.1
Lu	0.4	0.2	1.5	0.2	0.3	0.1	0.4	0.1
Hf	2.8	0.7	12.0	1.0	2.2	0.5	2.0	0.5
Ta	0.4	0.1	1.6	0.1	0.3	0.1	0.3	0.1
Th	1.6	0.4	6.2	0.4	1.1	0.3	1.3	0.4
U	0.3	0.1	1.6	0.2	0.3	0.2	0.4	0.1

	LS 5-72		LS 6-31	
	Mean	SD	Mean	SD
EMPA derived major-element compositions				
SiO_2	44.82	1.27	47.25	0.09
TiO_2	1.89	0.46	0.59	0.16
Al_2O_3	16.08	0.49	26.67	3.59
Cr_2O_3	0.37	0.09	0.07	0.03
FeO	14.19	2.43	5.43	2.21
MgO	8.86	1.62	4.94	2.11
CaO	11.20	0.55	12.75	1.37
Na_2O	1.71	0.17	1.61	0.17
K_2O	0.78	0.07	0.59	0.31
Ratios				
CaO/Al_2O_3	0.70		0.48	
MgO/Al_2O_3	0.55		0.19	
Laser Ablation ICPMS derived trace-element compositions				
Sc	7.56	0.53	8.96	1.10
Ti	3001	112	2971	382
V	16.8	1.0	17.3	2.4
Cr	804	86	762	108
Mn	494	30	730	68
Co	23.7	1.8	9.3	2.5
Ni	135	100	49	34
Rb	0.66	0.45	2.99	0.64
Sr	126	5	166	6
Y	29	1	37	5
Zr	133	5	68	8
Nb	9.9	0.4	7.8	1.0
Ba	114	5	147	18
La	9.4	0.6	13.3	1.8
Ce	25.8	1.5	35.8	4.7
Pr	3.3	0.3	4.7	0.7
Nd	15.0	1.4	21.6	3.6
Sm	4.2	0.7	5.7	1.2
Eu	1.0	0.2	1.3	0.3
Gd	4.7	0.7	6.4	1.2
Dy	5.3	0.7	7.0	1.5
Ho	1.1	0.2	1.4	0.3
Er	3.3	0.5	4.2	0.9
Yb	3.1	0.5	3.8	0.7
Lu	0.4	0.1	0.5	0.1
Hf	2.8	0.4	1.7	0.4
Ta	0.4	0.1	0.4	0.1
Th	1.5	0.2	2.0	0.4
U	0.4	0.1	0.4	0.1

Appendix 2: Plateau, Isochron, and Exposure Age Calculations

This appendix contains data acquired during radioisotopic dating showing argon release spectra, K/Ca ratios and inverse isochron graphs generated using Ar-Ar Calc for evaluation of data quality and calculation of formation. The "cosmochron" for the calculation of exposure ages is also shown where applicable. The criteria for interpretations and methods for the calculation of formation and exposure ages are detail in chapter 6: Methods. Each impact spherules has been classified according to the quality of the data using the following definitions:

Statistically Acceptable – Concordant Ages

These impact spherules consist of at least a mini-plateau supported by concordant inverse isochron ages. These are the best constrained impact spherules and often yield exposure ages. Eighteen impact spherules fall under this category.

Statistically Acceptable

These impact spherules consist of at least a mini-plateau OR reverse isochron ages. The reasons for the lack of either plateau or isochron ages varies and is detailed in the text. There are four impact spherules that under this category.

Useable

These impact spherules may have formation (e.g. total fusion) and exposure ages, but do not conform to the statistically acceptable criteria listed in Chapter 6: Methods. Often these are impact spherules with little radiogenic argon and are inferred to be young (i.e. formed within the last 400Ma). Five impact spherules fall into this category.

Discarded

These impact spherules typically show a disturbed release pattern (e.g. recoil, partial resetting, and discordant steps) or contain large uncertainties. No useful information can be extracted from these impact spherules. Four impact spherules fall into this category.

Steps that have been excluded during the calculation of both formation and exposure age are also noted. Exclusion steps will be coded such that a letter designating the reason for removal will follow after the step number. A = parentless $^{40}Ar^*$; B = Blank - No $^{40}Ar^*$; C = Undigested clast; D = Other - see text

Sample LS1-21

Status: Useable

Formation Age (Ma): 152 ± 8

Exposure Age (Ma): 2 ± 0.2

Comments:

Very little $^{40}Ar^*$ indicating potentially young formation age. The majority (80%) of the ^{39}Ar was released in the final step typical of young impact spherules. The final step has an age of 152 ± 8 Ma which could be used as a minimum age. Age is not very sensitive to the poorly constrained $^{40}Ar/^{36}Ar_{trapped}$.

Formation Age

Non-Blank Steps:	3	**Isochron Steps:**	1	**Exclusions:**	
Plateau Age (Ma):	142 ± 26	**Plateau Coverage:**	100%	**MSWD (Probability):**	13 (0%)
Inverse Isochron Age (Ma):	147 ± 37	**MSWD (Probability):**	75 (0%)	**Intercept (%1σ):**	0.65 (100%)

Exposure Age:

No. Steps:	3	**Isochron Steps:**	3	**Exclusions:**	
$^{38}Ar/^{37}Ar$:	0.000702 ± 0.00078	**MSWD (Probability):**	0.029 (86%)	**Exposure Age (Ma):**	2 ± 0.2

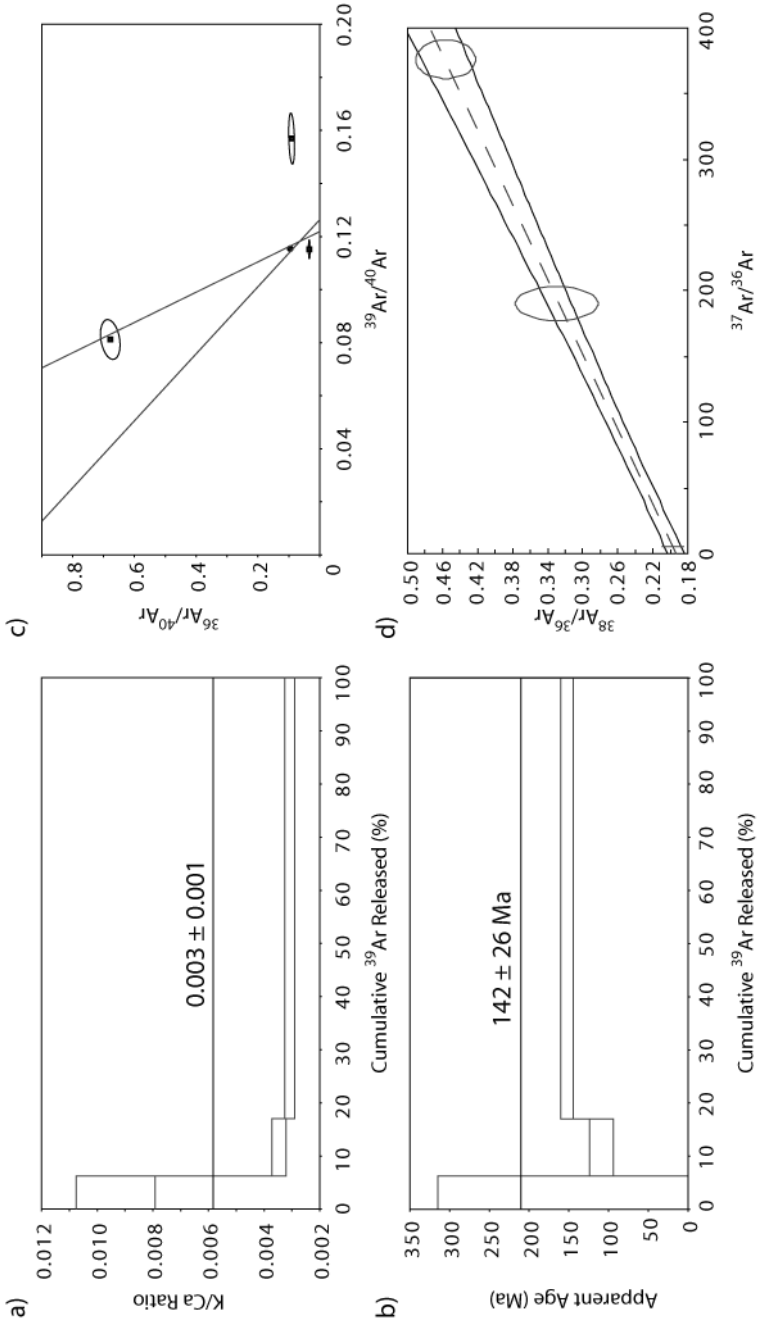

Figure A1. a) K/Ca Ratio **b)** Age spectra **c)** Reverse isochron **d)** Exposure age isochron

Sample LS1-22

Status: Statistically Acceptable – Concordant Ages

Formation Age (Ma): 360 ± 95 (plateau)

Exposure Age (Ma): 36 ± 12

Comments:

No ^{40}Ar* release until the final 5 steps though some parentless ^{40}Ar* was released in the first step. The five useable steps are well spread on the isochrons and give a consistent plateau age.

Formation Age

Non-Blank Steps:	13	**Isochron Steps:**	5	**Exclusions:**	1A 2-8B
Plateau Age (Ma):	360 ± 95	**Plateau Coverage:**	87%	**MSWD (Probability):**	0.41 (80%)
Inverse Isochron Age (Ma):	361 ± 157	**MSWD (Probability):**	2 (11%)	**Intercept (%1σ):**	1.5 (3.7%)

Exposure Age:

No. Steps:	5	**Isochron Steps:**	5	**Exclusions:**	
^{38}Ar/^{37}Ar:	0.0143 ± 0.0047	**MSWD (Probability):**	0.39 (76%)	**Exposure Age (Ma):**	36 ± 12

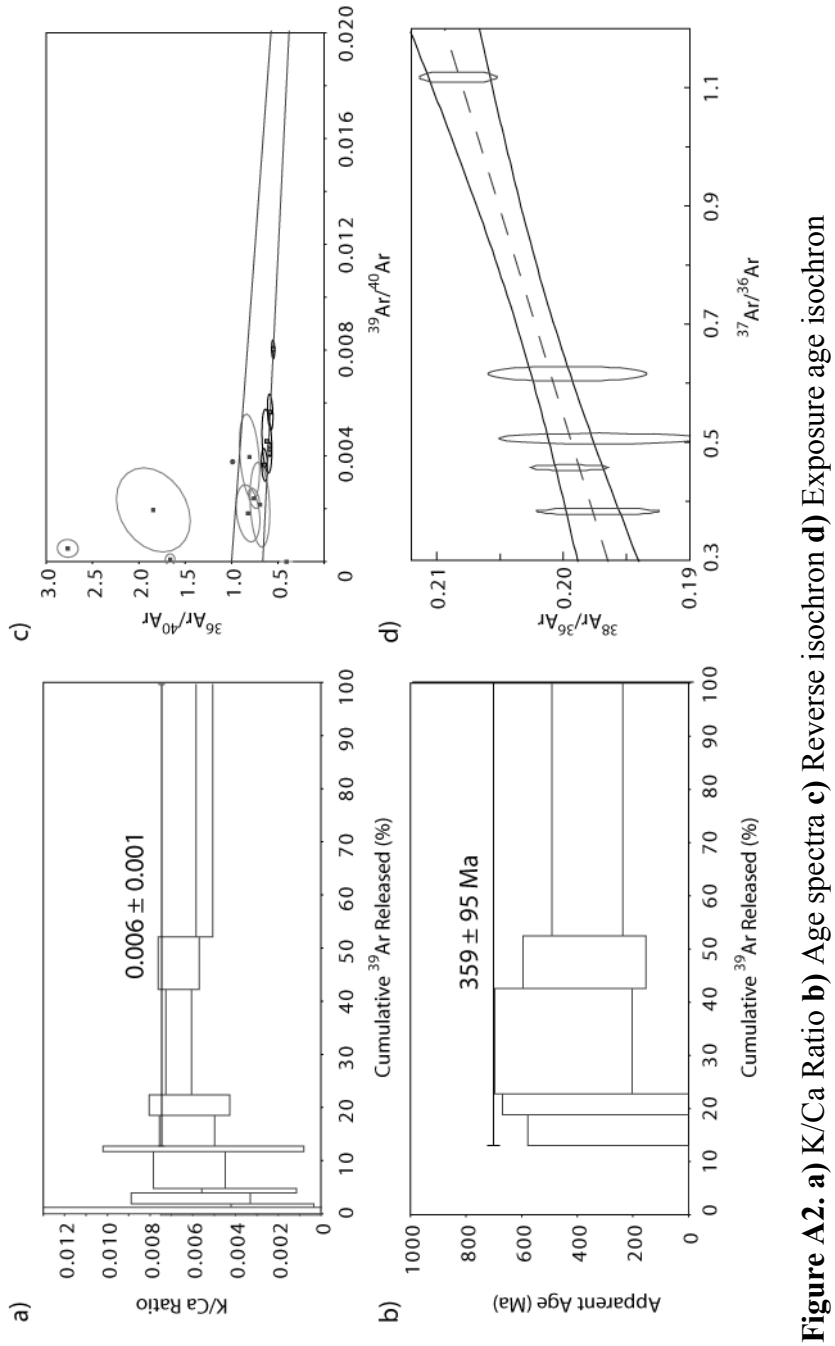

Figure A2. a) K/Ca Ratio **b)** Age spectra **c)** Reverse isochron **d)** Exposure age isochron

Sample LS1-31

Status: Statistically Acceptable – Concordant Ages

Formation Age (Ma): 970 ± 188 (mini-plateau)

Exposure Age (Ma): 83 ± 38

Comments:

Impact spherule appears to have experienced Ar loss in steps 7 and 8 possibly from a subsequent impact or heating event. An older Ca-rich clast (plagioclase?) also degasses at the higher temperature steps. A combination of isochron and age spectra was needed to determine the suitable points as there is some clustering in the isochrons. Exposure age is well constrained.

Formation Age

Non-Blank Steps:	22	**Isochron Steps:**	8	**Exclusions:**	1B, 2A, 3-6B, 7-8D, 17-22C
Plateau Age (Ma):	970 ± 188	**Plateau Coverage:**	58%	**MSWD (Probability):**	0.17 (99%)
Inverse Isochron Age (Ma):	986 ± 374	**MSWD (Probability):**	0.83 (55%)	**Intercept (%1σ):**	1.3 (4.1%)

Exposure Age:

No. Steps:	8	**Isochron Steps:**	8	**Exclusions:**	
$^{38}Ar/^{37}Ar$:	0.0327 ± 0.015	**MSWD (Probability):**	1.06 (38%)	**Exposure Age (Ma):**	83 ± 38

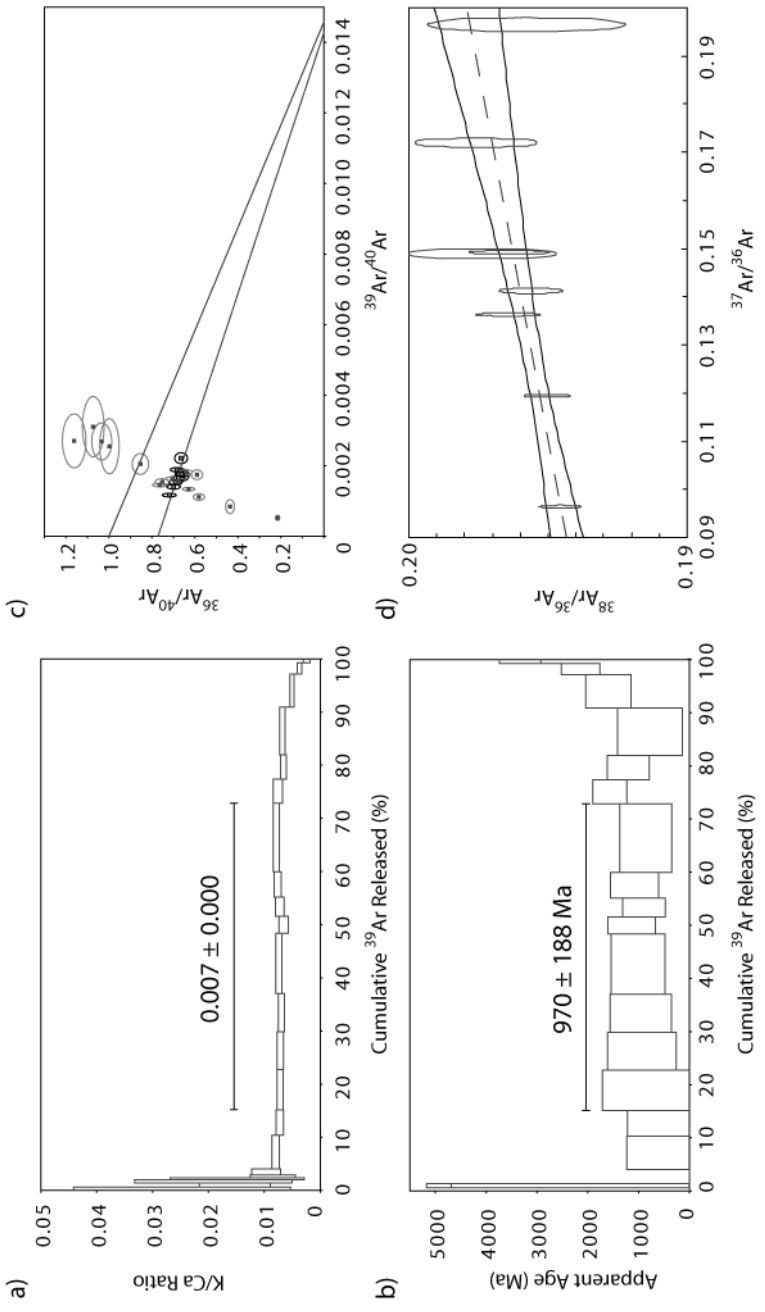

Figure A3. a) K/Ca Ratio **b)** Age spectra **c)** Reverse isochron **d)** Exposure age isochron

Sample LS1-33

Status: Statistically Acceptable – Concordant Ages

Formation Age (Ma): 3717 ± 482 (plateau)

Exposure Age (Ma): 407 ± 68

Comments:

K/Ca ratio appears to decrease from low temperature to higher temperature steps though the age obtained appears to be consistent in all steps except 2D. This step may be the result of release from undigested clasts or potentially Ar loss from a subsequent impact or heating event. Exposure age can only be calculated if step 5 is removed. Although there is no apparent reason to do so, it is the only outlier in the seven steps.

Formation Age

Non-Blank Steps:	9	**Isochron Steps:**	7	**Exclusions:**	1B, 2D
Plateau Age (Ma):	3717 ± 482	**Plateau Coverage:**	82%	**MSWD (Probability):**	0.16 (99%)
Inverse Isochron Age (Ma):	3693 ± 1565	**MSWD (Probability):**	0.85 (51%)	**Intercept (%1σ):**	1.2 (10%)

Exposure Age:

No. Steps:	7	**Isochron Steps:**	6	**Exclusions:**	5D
^{38}Ar/^{37}Ar:	0.161 ± 0.027	**MSWD (Probability):**	0.28 (89%)	**Exposure Age (Ma):**	407 ± 68

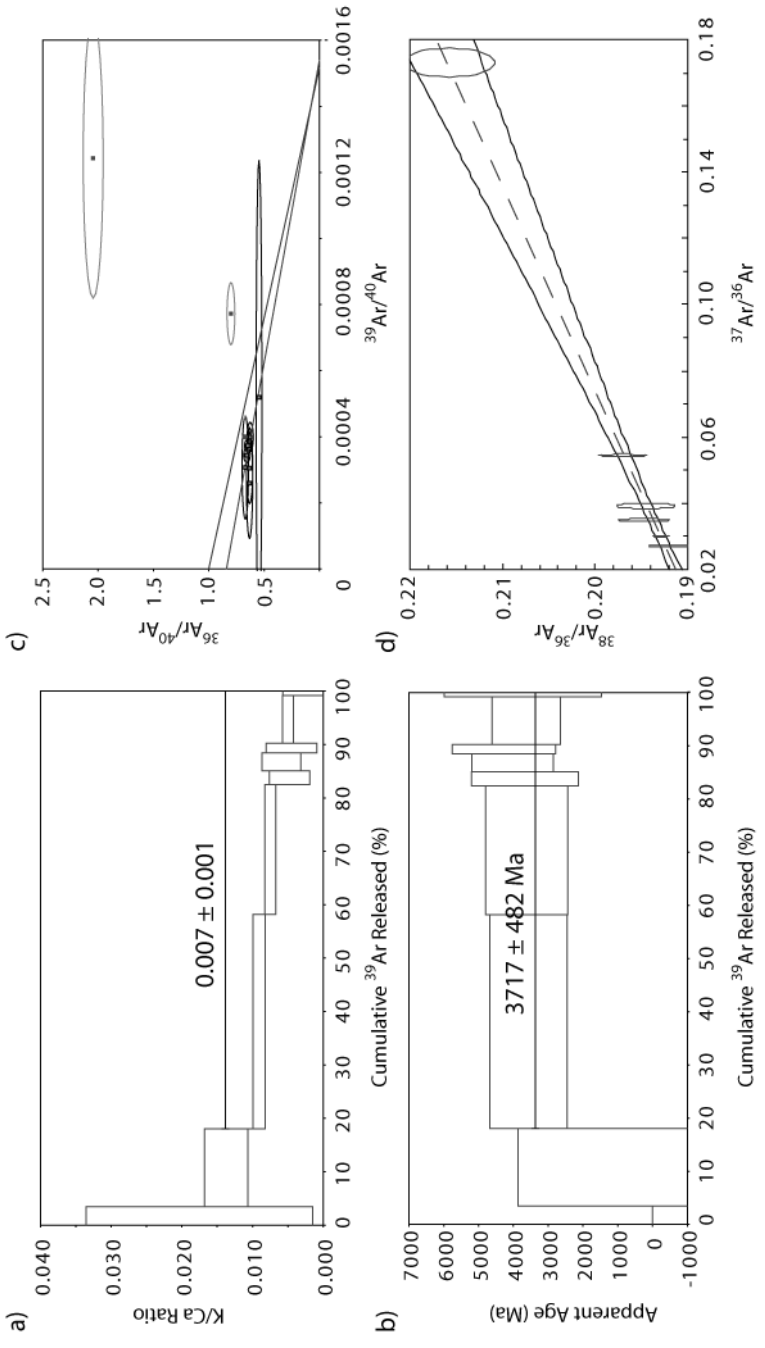

Figure A4. a) K/Ca Ratio **b)** Age spectra **c)** Reverse isochron **d)** Exposure age isochron

Sample LS1-41

Status: Statistically Acceptable

Formation Age (Ma): 3674 ± 201 (plateau age only)

Exposure Age (Ma): 111 ± 86

Comments:

This spherule contains a lot of argon gas, possibly from a number of different reservoirs. There is little spread in the points making up the inverse isochron as all the steps tend to cluster. This produces a positive isochron which cannot be used to determine the age as there is no $^{40}Ar/^{39}Ar$ intercept. Additionally, the trapped ratio is highly variable and based on observation, likely to fall between 1.0 ± 15% (1σ). The age is highly dependant on this ratio. K/Ca ratio decrease evident in the later steps, but the age is still consistent with previous steps. Exposure age isochron extremely complex leading to high MSWD values (9.4) if all steps are included. However, it is possible that there are undigested clasts that may be affecting the exposure ages. Based on the K/Ca ratios steps 14 and 21-26 may be clasts or be affected by degassing of clasts. If these steps are removed an exposure age can be obtained.

Formation Age

Non-Blank Steps:	26	**Isochron Steps:**	20	**Exclusions:**	1B, 2A, 3B, 4-6D
Plateau Age (Ma):	3674 ± 201	**Plateau Coverage:**	94%	**MSWD (Probability):**	0.41 (99%)
Inverse Isochron Age (Ma):	N/A	**MSWD (Probability):**	N/A	**Intercept (%1σ):**	N/A

Exposure Age:

No. Steps:	20	**Isochron Steps:**	13	**Exclusions:**	14C, 21-26C
$^{38}Ar/^{37}Ar$:	0.044 ± 0.034	**MSWD (Probability):**	1.6 (10%)	**Exposure Age (Ma):**	111 ± 86

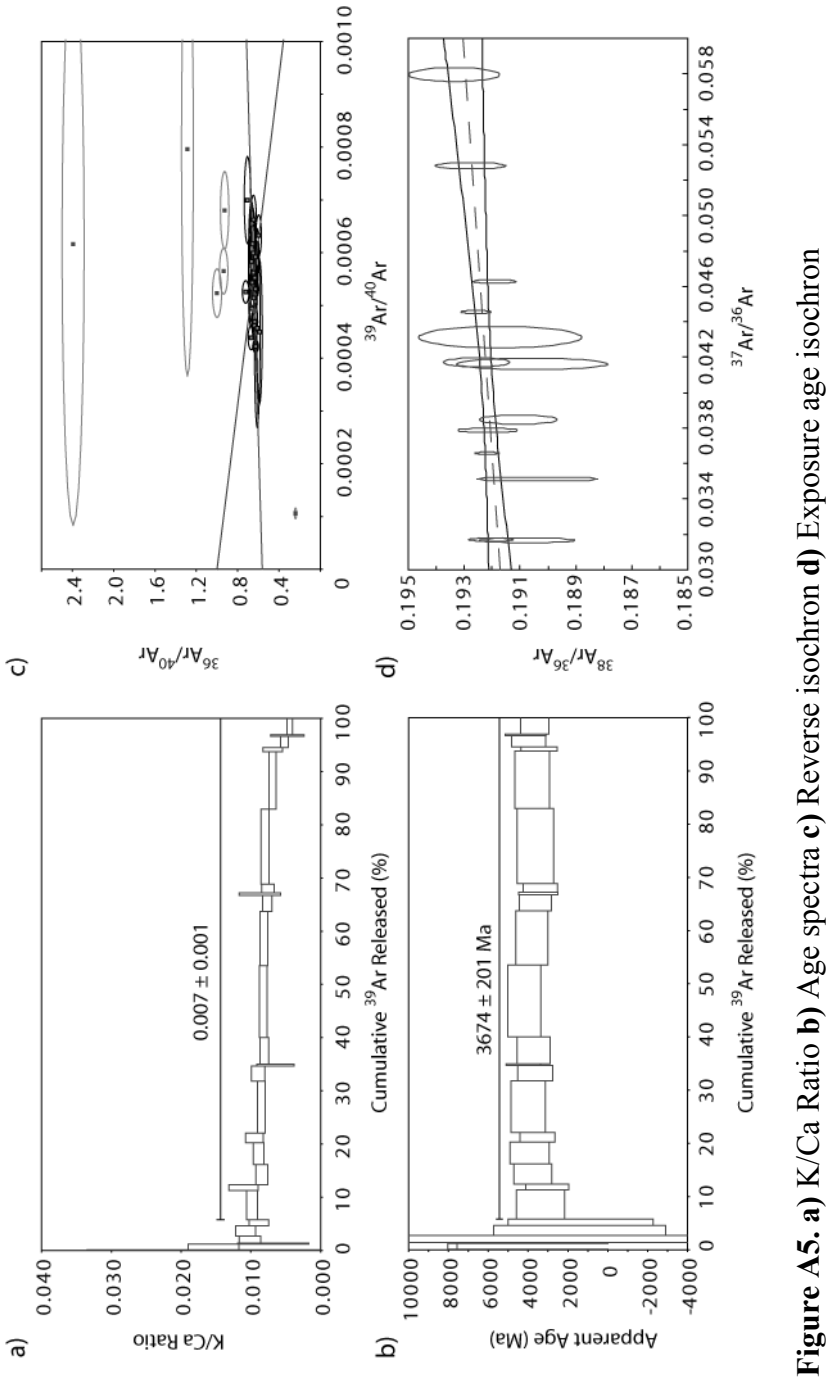

Figure A5. a) K/Ca Ratio **b)** Age spectra **c)** Reverse isochron **d)** Exposure age isochron

Sample LS1-42

Status: Statistically Acceptable – Concordant Ages

Formation Age (Ma): 1242 ± 39 (mini-plateau)

Exposure Age (Ma): 2 ± 1

Comments:

Low temperature steps have yielded an apparently older age than that of the mini-plateau possibly a result of a clast (high K/Ca) or Ar recoil (see McDougall and Harrison, 1988). The last three higher temperature steps may also be released from a low K/Ca ratio clast. A concordant mini-plateau can be found between these other features.

Formation Age

Non-Blank Steps:	16	**Isochron Steps:**	7	**Exclusions:**	1-2B, 3-6D, 14-16C?
Plateau Age (Ma):	1242 ± 39	**Plateau Coverage:**	64%	**MSWD (Probability):**	1.9 (8%)
Inverse Isochron Age (Ma):	1294 ± 64	**MSWD (Probability):**	2.2 (5%)	**Intercept (%1σ):**	8.16 (6.3%)

Exposure Age:

No. Steps:	7	**Isochron Steps:**	7	**Exclusions:**	
$^{38}Ar/^{37}Ar$:	0.00077 ± 0.00053	**MSWD (Probability):**	0.57 (72%)	**Exposure Age (Ma):**	2 ± 1

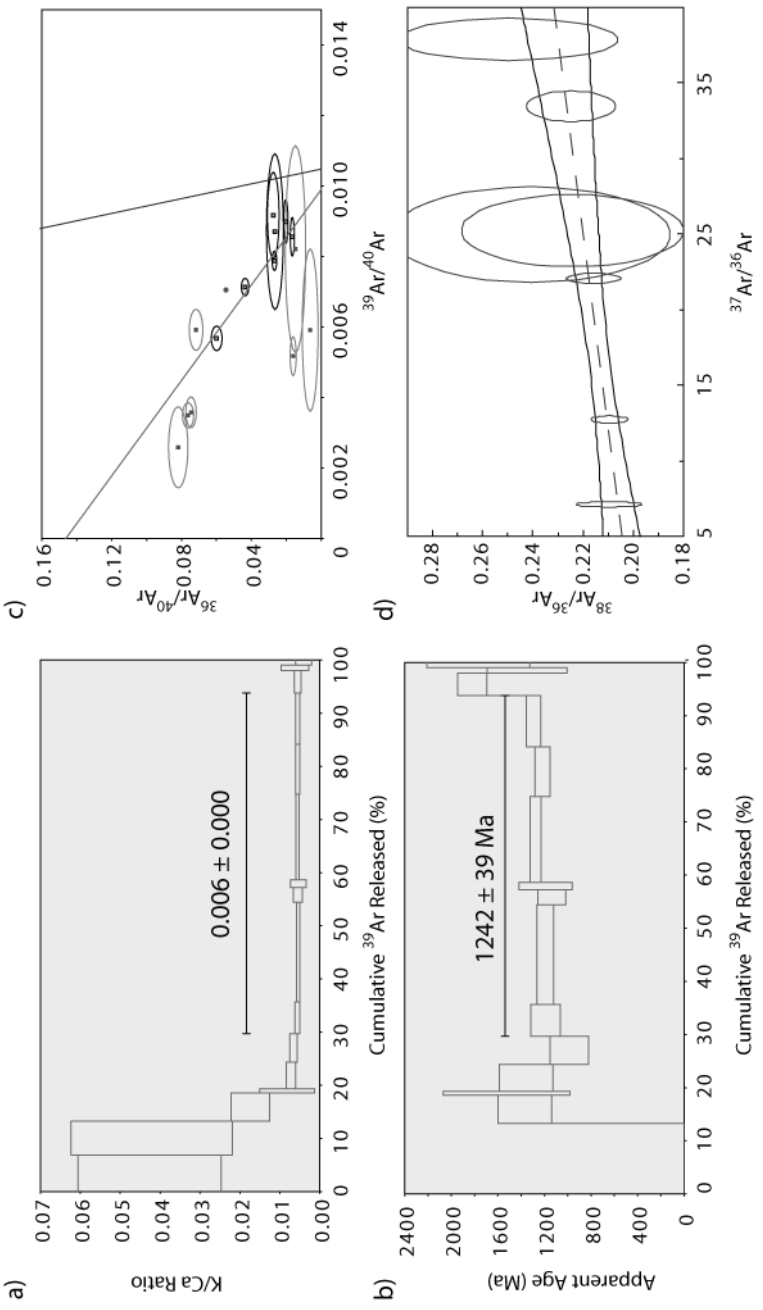

Figure A6. a) K/Ca Ratio **b)** Age spectra **c)** Reverse isochron **d)** Exposure age isochron

Sample LS1-43

Status: Statistically Acceptable – Concordant Ages

Formation Age (Ma): 371 ± 79 (plateau)

Exposure Age (Ma): 220 ± 6

Comments:

Very nice distribution of steps in the inverse diagram allowing for a well defined age and $^{40}Ar/^{36}Ar_{trapped}$. The K/Ca ratio decreases between the 4 and 5 though there does not appear to be any affect on the age.

Formation Age

Non-Blank Steps:	8	**Isochron Steps:**	7	**Exclusions:**	1B
Plateau Age (Ma):	371 ± 79	**Plateau Coverage:**	97%	**MSWD (Probability):**	0.16 (99%)
Inverse Isochron Age (Ma):	367 ± 83	**MSWD (Probability):**	0.26 (93%)	**Intercept (%1σ):**	0.8 (2.18%)

Exposure Age:

No. Steps:	7	**Isochron Steps:**	7	**Exclusions:**	
$^{38}Ar/^{37}Ar$:	0.0870 ± 0.0022	**MSWD (Probability):**	0.9 (48%)	**Exposure Age (Ma):**	220 ± 6

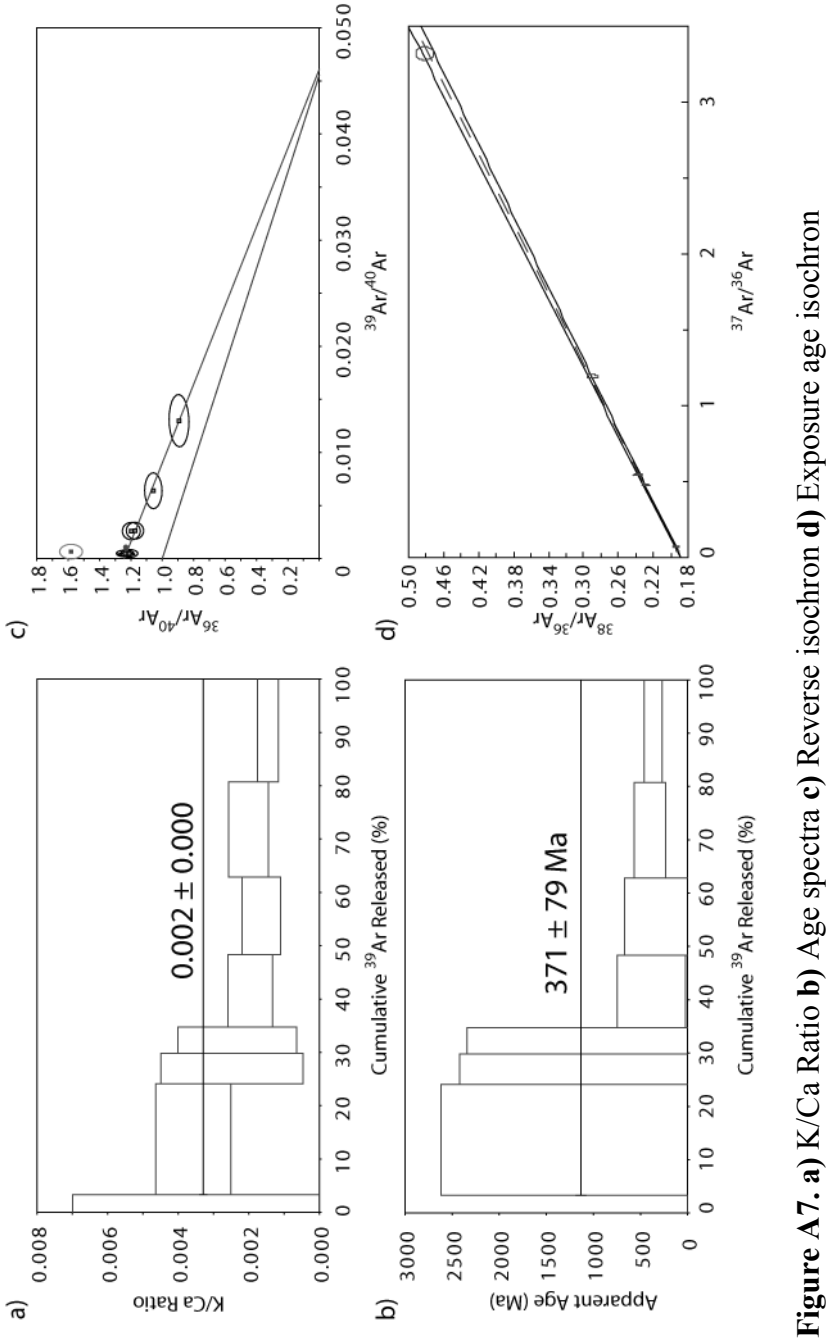

Figure A7. a) K/Ca Ratio **b)** Age spectra **c)** Reverse isochron **d)** Exposure age isochron

Sample LS1-53

Status: Discarded

Formation Age (Ma): N/A

Exposure Age (Ma): N/A

Comments:

This impact spherule has been discarded due to the inability to obtain an age plateau or isochron with probability >5%. There are many discordant steps that cannot be justifiably removed. Additionally, removal of any steps causes large changes in the age by 100Ma.

Formation Age

Non-Blank Steps:	10	**Isochron Steps:**	0	**Exclusions:**	1B, 5B
Plateau Age (Ma):		**Plateau Coverage:**		**MSWD (Probability):**	
Inverse Isochron Age (Ma):		**MSWD (Probability):**		**Intercept (%1σ):**	
Exposure Age:					
No. Steps:		**Isochron Steps:**		**Exclusions:**	
$^{38}Ar/^{37}Ar$:		**MSWD (Probability):**		**Exposure Age (Ma):**	

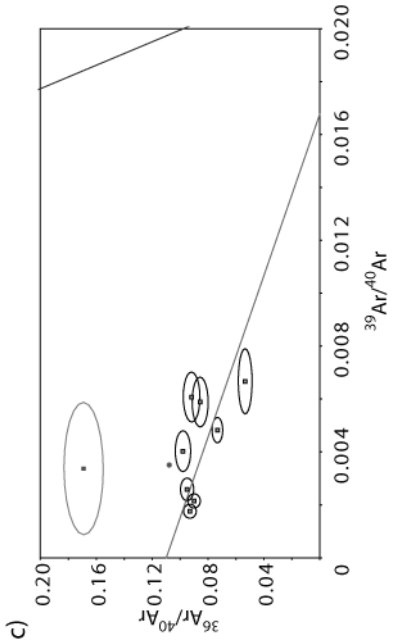

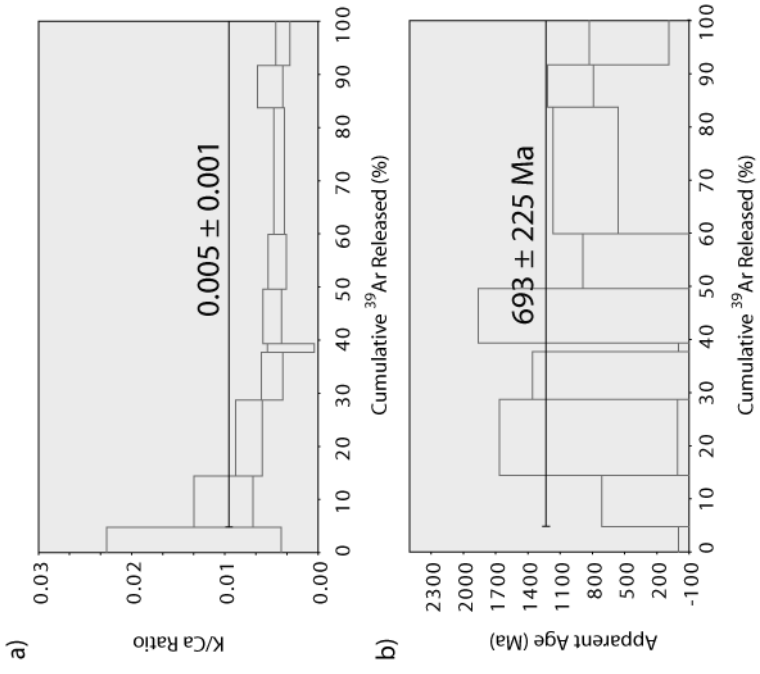

Figure A8. a) K/Ca Ratio **b)** Age spectra **c)** Reverse isochron

Sample LS1-73

Status: Statistically Acceptable – Concordant Ages

Formation Age (Ma): 1738 ± 380 (plateau)

Exposure Age (Ma): 461 ± 14

Comments:

K/Ca in this impact spherule decreases from the low to high temperature steps. Although this impact spherule was selected for high-K abundance, it appears to be only surficial as the K/Ca ratio drops to <0.001 by the 4th step. Age, however, remains consistent between each step allowing all steps to be included in the plateau. A well-constrained exposure age can be calculated only if one of the five steps is removed. This is the 3rd step and is an outlier though there is no other apparent reason for removing it. The formation age hinges heavily on this step as it contains a significant portion of the ^{39}Ar and the most precise point. It is, however, possible to justify removal of both steps 3 and 4 based on the K/Ca difference in these steps compared to later steps. The difference in K/Ca may indicate degassing of surficial deposits rather than from K-decay deeply bound in the impact spherule. Either way, both results are similar resulting in exposure age differences of a few million years.

Formation Age

Non-Blank Steps:	6	**Isochron Steps:**	5	**Exclusions:**	1B
Plateau Age (Ma):	1738 ± 380	**Plateau Coverage:**	86%	**MSWD (Probability):**	0.31 (87%)
Inverse Isochron Age (Ma):	1878 ± 626	**MSWD (Probability):**	0.43 (73%)	**Intercept (%1σ):**	0.76 (5.4%)

Exposure Age:

No. Steps:	5	**Isochron Steps:**	4	**Exclusions:**	2-3D
^{38}Ar/^{37}Ar:	0.1854 ± 0.0032	**MSWD (Probability):**	0.32 (57%)	**Exposure Age (Ma):**	461 ± 14

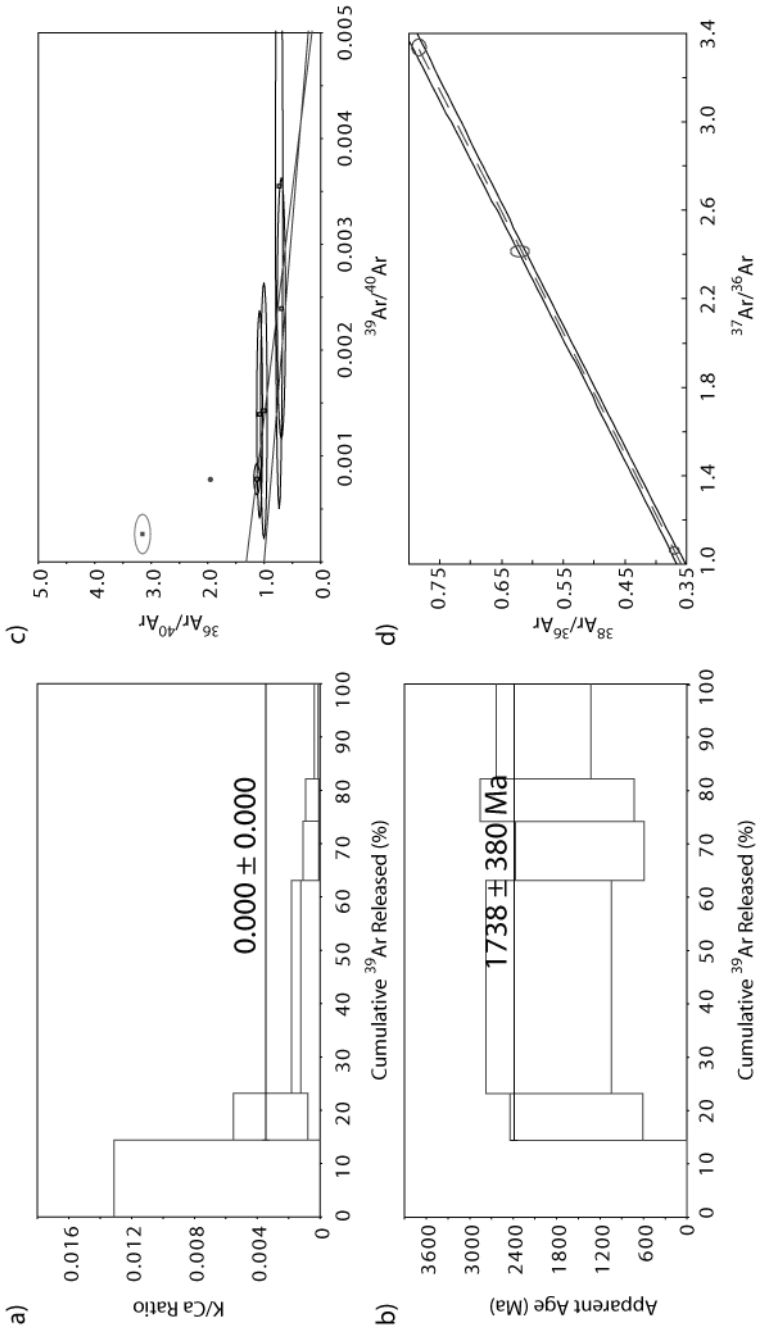

Figure A9. a) K/Ca Ratio **b)** Age spectra **c)** Reverse isochron

Sample LS2-31

Status: Statistically Acceptable

Formation Age (Ma): 1629 ± 729 (plateau age only)

Exposure Age (Ma):

Comments:

Barely usable sample, lots of scatter in the isochron with zero probability of fit and consequently poorly constrained intercept. First and second steps appear to largely consist of $^{40}Ar_{trapped}$ and their inclusion into the plateau increases the error substantially. Due to the already large uncertainties on the age, however, the $^{40}Ar/^{36}Ar_{trapped}$ is not sensitive to change. The last step contains the highest proportion of ^{39}Ar. No exposure age.

Formation Age

Non-Blank Steps:	3	**Isochron Steps:**	3	**Exclusions:**	
Plateau Age (Ma):	1629 ± 729	**Plateau Coverage:**	100%	**MSWD (Probability):**	0.86 (42%)
Inverse Isochron Age (Ma):	1926 ± 1338	**MSWD (Probability):**	35.83 (0%)	**Intercept (%1σ):**	0.22 (50%)

Exposure Age:

No. Steps:		**Isochron Steps:**		**Exclusions:**	
$^{38}Ar/^{37}Ar$:		**MSWD (Probability):**		**Exposure Age (Ma):**	

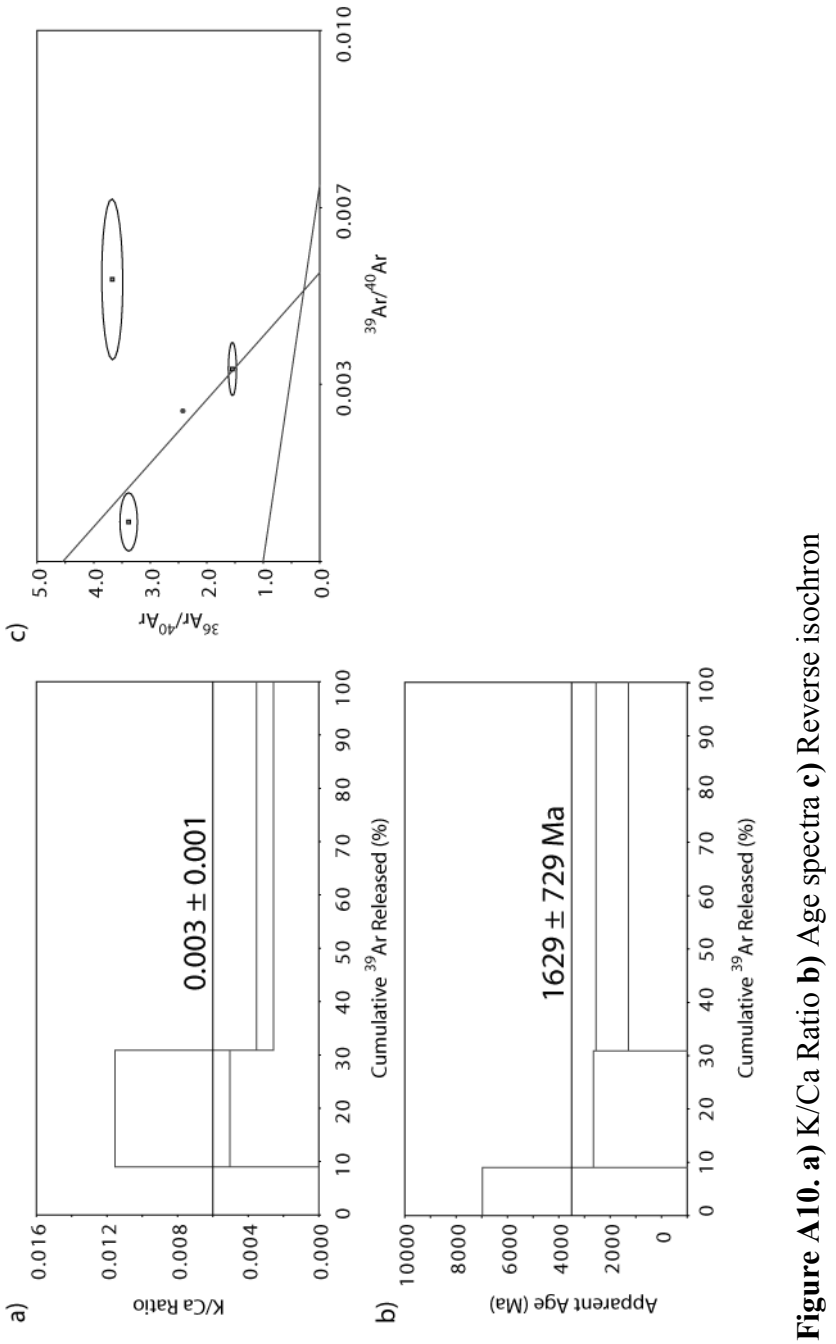

Figure A10. a) K/Ca Ratio **b)** Age spectra **c)** Reverse isochron

Sample LS2-43

Status: Useable

Formation Age (Ma): 200± 700

Exposure Age (Ma):

Comments:

Likely to be a very young impact spherule as there is little $^{40}Ar^*$ most of which was released in the final step. The first two steps largely consist of $^{40}Ar_{trapped}$, but allow for some constraint on the $^{40}Ar/^{36}Ar_{trapped}$. The age, however, hinges heavily on the final step though there is agreement between the age of the final step (120 ± 725) and that given by the isochron. No exposure age.

Formation Age

Non-Blank Steps:	3	**Isochron Steps:**	3	**Exclusions:**	
Plateau Age (Ma):	0.14 ± 26.47	**Plateau Coverage:**	100%	**MSWD (Probability):**	0 (100%)
Inverse Isochron Age (Ma):	200 ± 700	**MSWD (Probability):**	0 (100%)	**Intercept (%1σ):**	0.53 (2.25%)

Exposure Age:

No. Steps:		**Isochron Steps:**		**Exclusions:**	
$^{38}Ar/^{37}Ar$:		**MSWD (Probability):**		**Exposure Age (Ma):**	

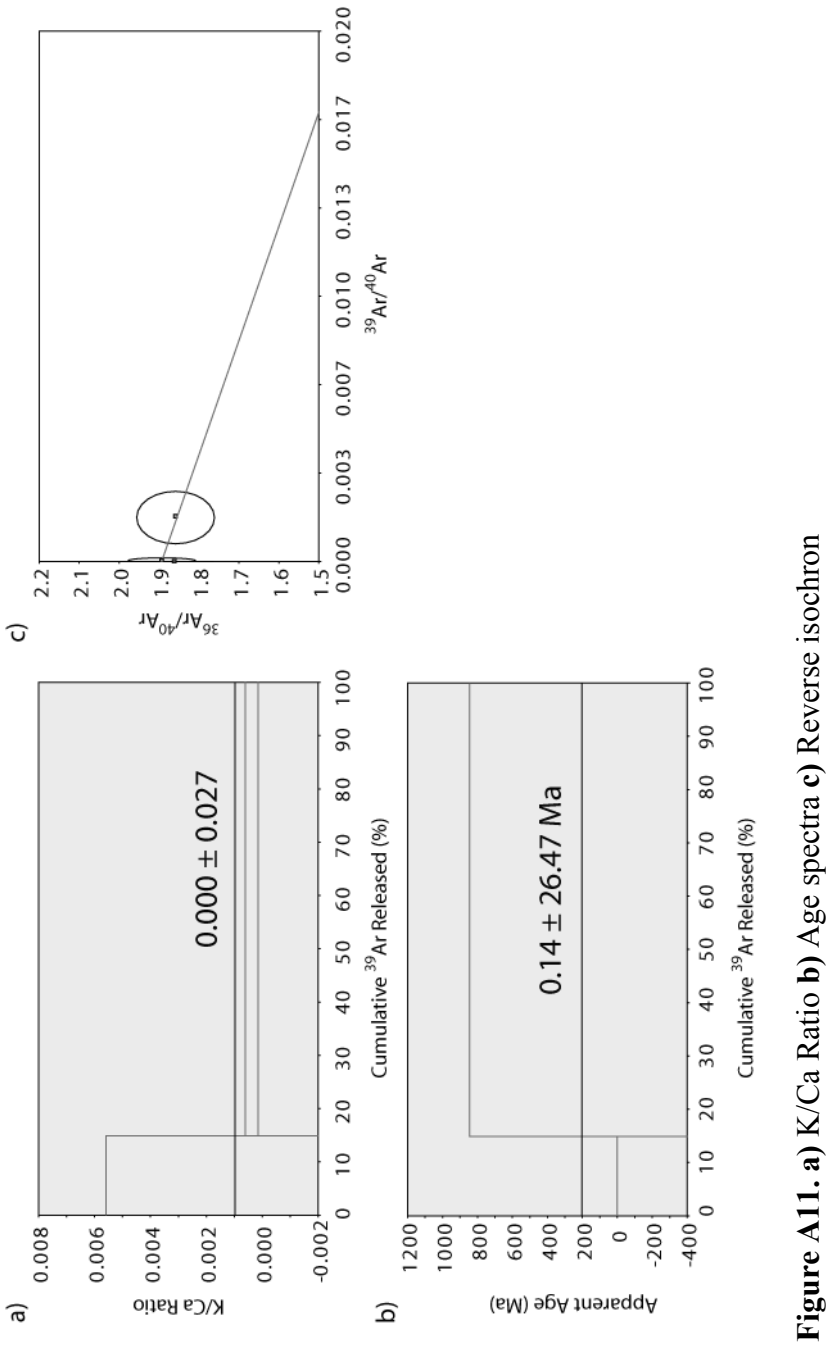

Figure A11. a) K/Ca Ratio **b)** Age spectra **c)** Reverse isochron

Sample LS2-45

Status: Statistically Acceptable – Concordant Ages

Formation Age (Ma): 1505 ± 104 (plateau)

Exposure Age (Ma):

Comments:

Nice spread on the isochron plots allowing for well constrained ages and $^{40}Ar/^{36}Ar_{trapped}$ ratio. The first step contains both radiogenic and a significant trapped component, but is removed based on the age which is much older (4.1 ± 1.2Ga) than that of the plateau. Exposure age, however, cannot be obtained without removing steps 2 and 5, but there is no valid reason to do so.

Formation Age

Non-Blank Steps:	6	**Isochron Steps:**	5	**Exclusions:**	1D
Plateau Age (Ma):	1505 ± 104	**Plateau Coverage:**	94%	**MSWD (Probability):**	0.63 (64%)
Inverse Isochron Age (Ma):	1530 ± 121	**MSWD (Probability):**	1.14 (33%)	**Intercept (%1σ):**	2.86 (5%)

Exposure Age:

No. Steps:		**Isochron Steps:**		**Exclusions:**	
$^{38}Ar/^{37}Ar$:		**MSWD (Probability):**		**Exposure Age (Ma):**	

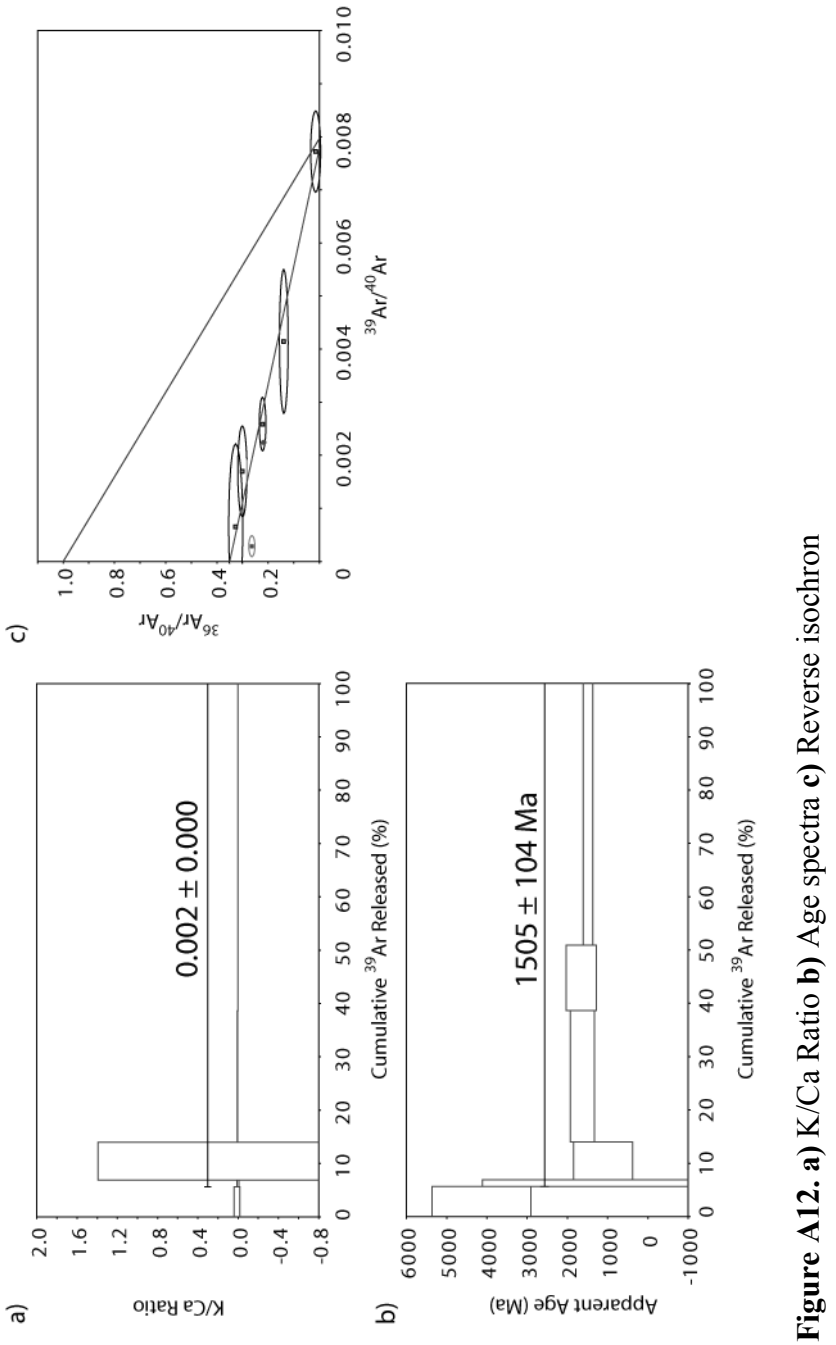

Figure A12. a) K/Ca Ratio **b)** Age spectra **c)** Reverse isochron

Sample LS2-53

Status: Useable

Formation Age (Ma): 147 ± 94 (plateau age only)

Exposure Age (Ma):

Comments:

Only two steps possible on this impact spherule as there is very little gas though the gas is very radiogenic. As a result the MSWD will be exceptionally good and there will be no isochron age. A nominal $^{40}Ar/^{36}Ar_{trapped}$ ratio was chosen by extrapolating from the two points and given a large error to account for the possible variability.

Formation Age

Non-Blank Steps:	2	**Isochron Steps:**	2	**Exclusions:**	
Plateau Age (Ma):	147 ± 94	**Plateau Coverage:**	100%	**MSWD (Probability):**	0.1 (100%)
Inverse Isochron Age (Ma):		**MSWD (Probability):**		**Intercept (%1σ):**	12.5 (50%)

Exposure Age:

No. Steps:		**Isochron Steps:**		**Exclusions:**	
$^{38}Ar/^{37}Ar$:		**MSWD (Probability):**		**Exposure Age (Ma):**	

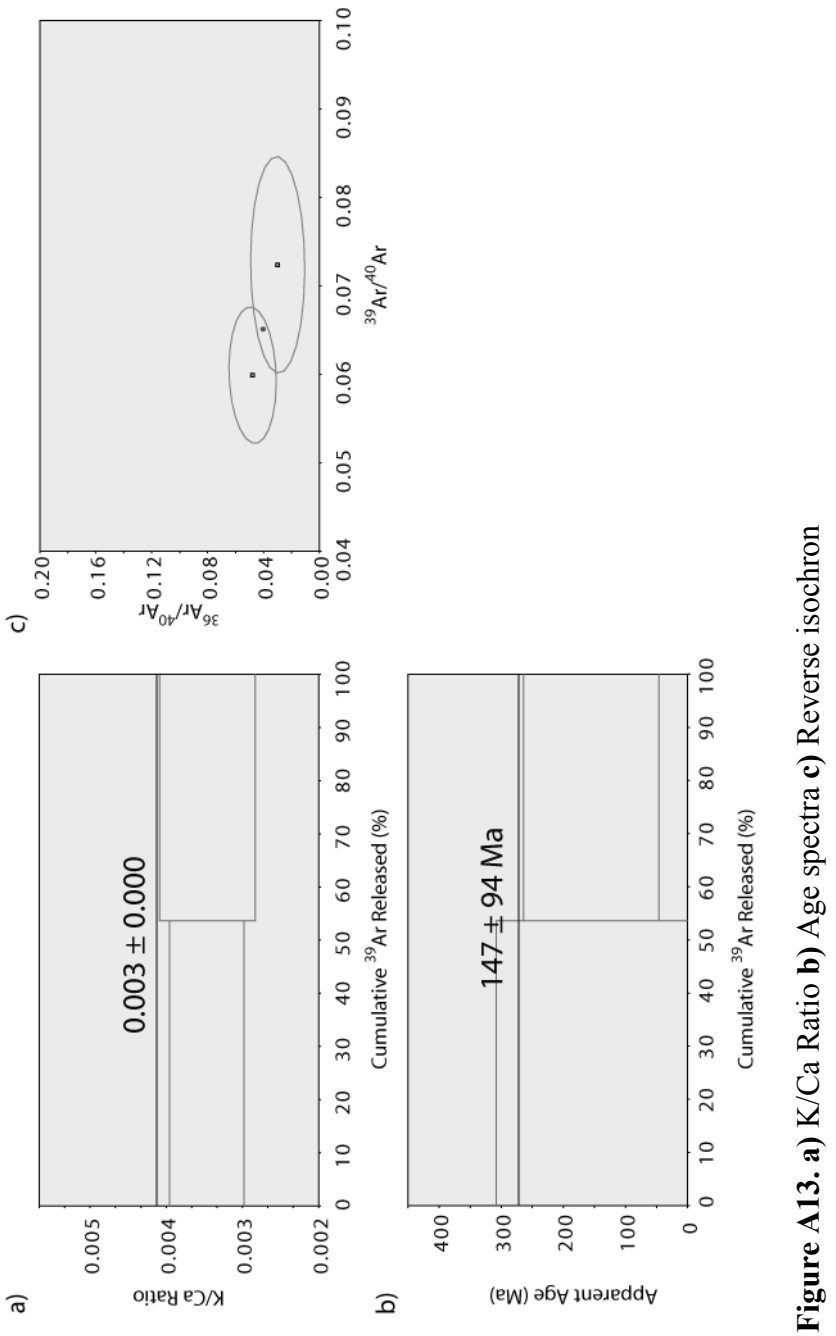

Figure A13. a) K/Ca Ratio **b)** Age spectra **c)** Reverse isochron

Sample LS2-62

Status: Statistically Acceptable – Concordant Ages

Formation Age (Ma): 498 ± 14 (mini-plateau)

Exposure Age (Ma): 311 ± 1591

Comments:

The first two steps in this impact spherule largely consist of $^{40}Ar_{trapped}$ with a smaller proportion of $^{40}Ar^*$. However, these steps and step 3 are not included in the calculations to determine formation age based on the misfits in the age spectra and isochrons. The remaining three later steps cluster in a group.

Formation Age

Non-Blank Steps:	6	**Isochron Steps:**	3	**Exclusions:**	1-2A, 3D
Plateau Age (Ma):	498 ± 14	**Plateau Coverage:**	63%	**MSWD (Probability):**	1.7 (19%)
Inverse Isochron Age (Ma):	497 ± 102	**MSWD (Probability):**	3.2 (7%)	**Intercept (%1σ):**	0.45 (2.9%)

Exposure Age:

No. Steps:	3	**Isochron Steps:**	3	**Exclusions:**	
$^{38}Ar/^{37}Ar$:	0.123 ± 0.63	**MSWD (Probability):**	2.7 (10%)	**Exposure Age (Ma):**	311 ± 1591

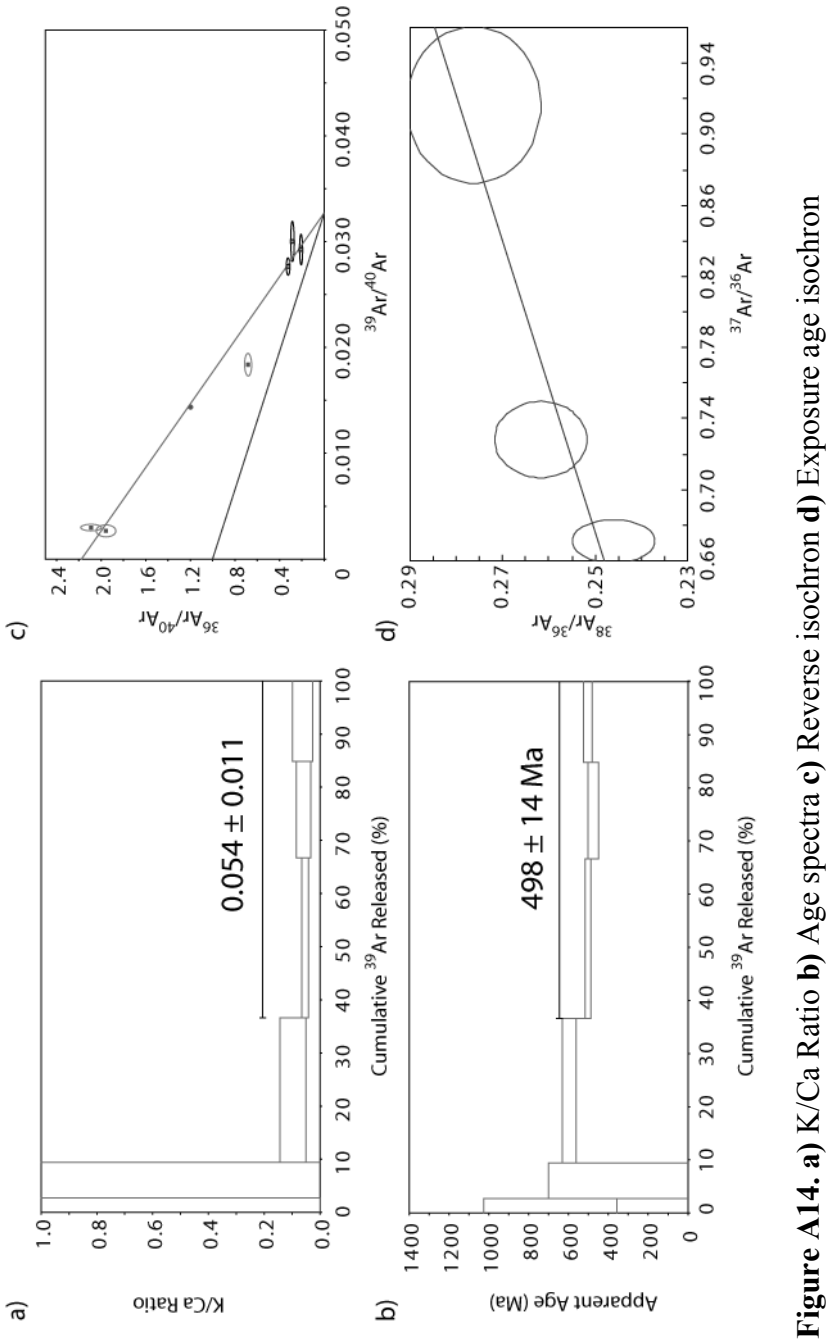

Figure A14. a) K/Ca Ratio **b)** Age spectra **c)** Reverse isochron **d)** Exposure age isochron

Sample LS2-63

Status: Statistically Acceptable

Formation Age (Ma): 154± 134 (isochron age only)

Exposure Age (Ma): 105 ± 21

Comments:

A plateau age on this impact spherule is not possible due to step 5 (2nd step of the plateau) being of zero age. The isochron age is still valid and fairly well constrained, however, the age hinges on the final step. The K/Ca ratio appears to decrease from low to high temperature steps.

Formation Age

Non-Blank Steps:	7	**Isochron Steps:**	4	**Exclusions:**	1-3A
Plateau Age (Ma):		**Plateau Coverage:**		**MSWD (Probability):**	
Inverse Isochron Age (Ma):	154 ± 134	**MSWD (Probability):**	0.89 (41%)	**Intercept (%1σ):**	1.56 (1.7%)

Exposure Age:

No. Steps:	4	**Isochron Steps:**	4	**Exclusions:**	
$^{38}Ar/^{37}Ar$:	0.0416 ± 0.0084	**MSWD (Probability):**	2.9 (5%)	**Exposure Age (Ma):**	105 ± 21

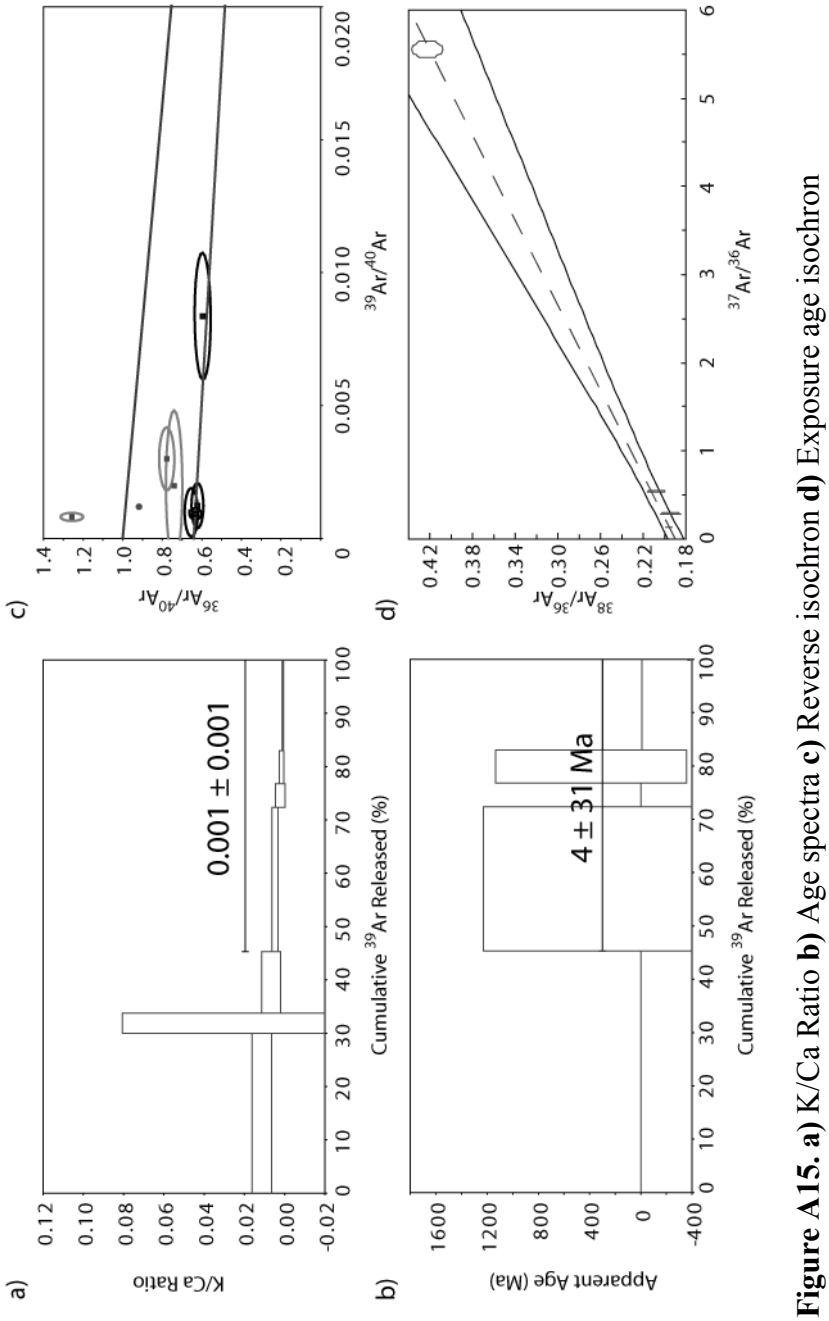

Figure A15. a) K/Ca Ratio **b)** Age spectra **c)** Reverse isochron **d)** Exposure age isochron

Sample LS2-71

Status: Useable

Formation Age (Ma): 294 ± 31 (Fusion age only)

Exposure Age (Ma):

Comments:

Eleven steps were attempted in total though none expect the final step yielded any $^{40}Ar^*$. The $^{40}Ar/^{36}Ar_{trapped}$ was assumed to be equal to 1 ± 50% (1σ).

Sample LS3-15

Status: Statistically Acceptable – Concordant Ages

Formation Age (Ma): 4372 ± 270 (plateau)

Exposure Age (Ma): 240 ± 222

Comments:

Well behaved impact spherule that has a well constrained formation age. The error on the age, however, is slightly large as the $^{40}Ar/^{36}Ar_{trapped}$ is not well constrained due to clustering of the steps in the isochron. The K/Ca ratio appears to decrease from low to high temperature steps.

Formation Age

Non-Blank Steps:	10	**Isochron Steps:**	6	**Exclusions:**	1A, 2-3B, 4A
Plateau Age (Ma):	4372 ± 270	**Plateau Coverage:**	88%	**MSWD (Probability):**	0.21 (96%)
Inverse Isochron Age (Ma):	4277 ± 1691	**MSWD (Probability):**	0.51 (73%)	**Intercept (%1σ):**	0.49 (18%)

Exposure Age:

No. Steps:	6	**Isochron Steps:**	6	**Exclusions:**	
$^{38}Ar/^{37}Ar$:	0.095 ± 0.088	**MSWD (Probability):**	0.55 (70%)	**Exposure Age (Ma):**	240 ± 222

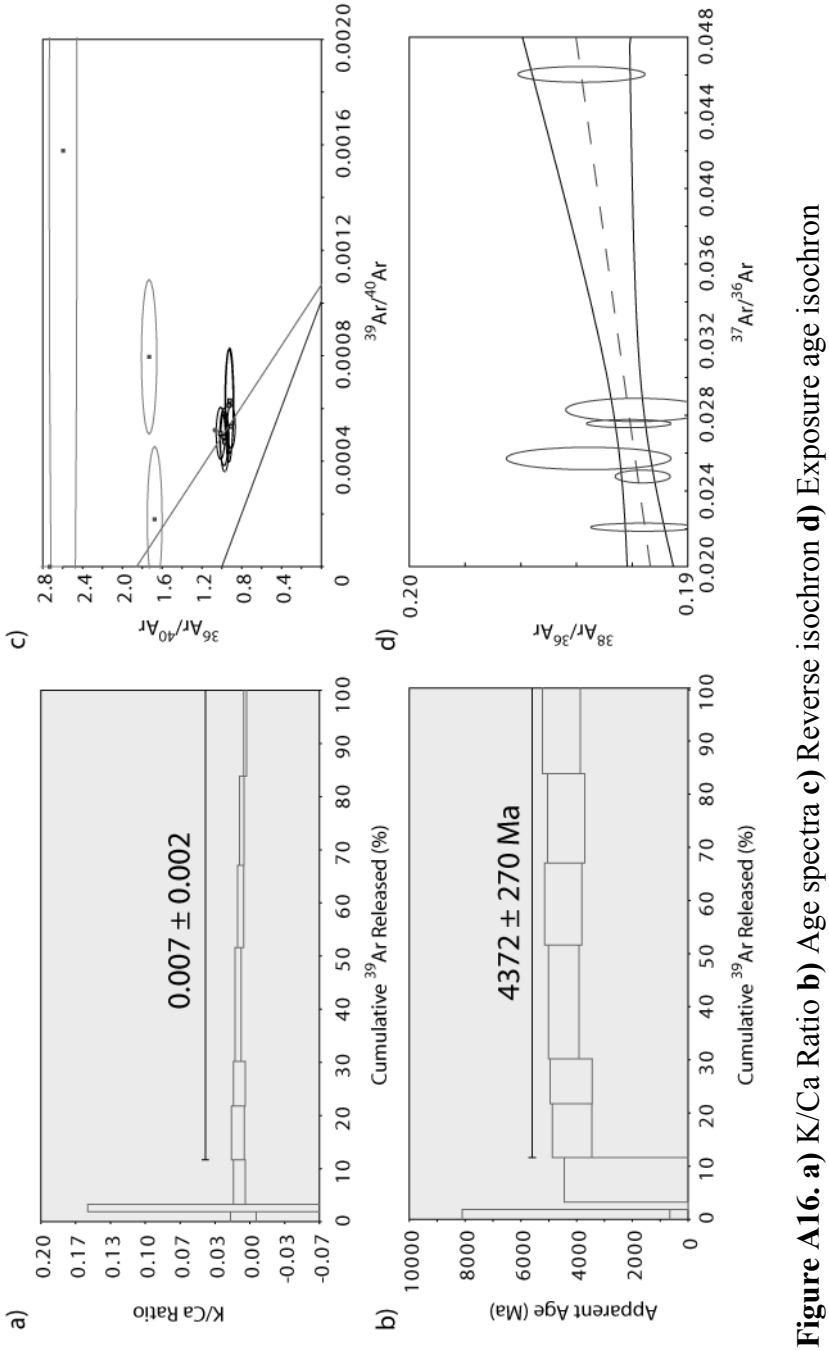

Figure A16. a) K/Ca Ratio **b)** Age spectra **c)** Reverse isochron **d)** Exposure age isochron

Sample LS3-21

Status: Statistically Acceptable – Concordant Ages

Formation Age (Ma): 3436 ± 171 (plateau)

Exposure Age (Ma): 243 ± 73

Comments:

Well behaved impact spherule that has a well constrained formation age. The error on the age, however, is slightly large as the $^{40}Ar/^{36}Ar_{trapped}$ is not well constrained due to clustering of points in the isochron. The exposure age requires removal of steps 4 and 7 as both are lacking in Ca-derived ^{37}Ar and have large uncertainties on the $^{40}Ar^*/^{39}Ar_K$ (i.e. formation age), possibly due to contribution of a trapped component. Additionally, it is necessary to remove step 11 to achieve a fit with a probability >5% as the $^{38}Ar/^{36}Ar$ ratio is higher than the other steps. However, there is no reason to do so other than this step being the only outlier in seven steps.

Formation Age

Non-Blank Steps:	11	**Isochron Steps:**	9	**Exclusions:**	1B, 2D
Plateau Age (Ma):	3436 ± 171	**Plateau Coverage:**	99%	**MSWD (Probability):**	0.67 (72%)
Inverse Isochron Age (Ma):	3521 ± 196	**MSWD (Probability):**	0.90 (51%)	**Intercept (%1σ):**	0.29 (5.6%)

Exposure Age:

No. Steps:	9	**Isochron Steps:**	7	**Exclusions:**	4D, 7D
$^{38}Ar/^{37}Ar$:	0.096 ± 0.029	**MSWD:**	0.16 (96%)	**Exposure Age (Ma):**	243 ± 73

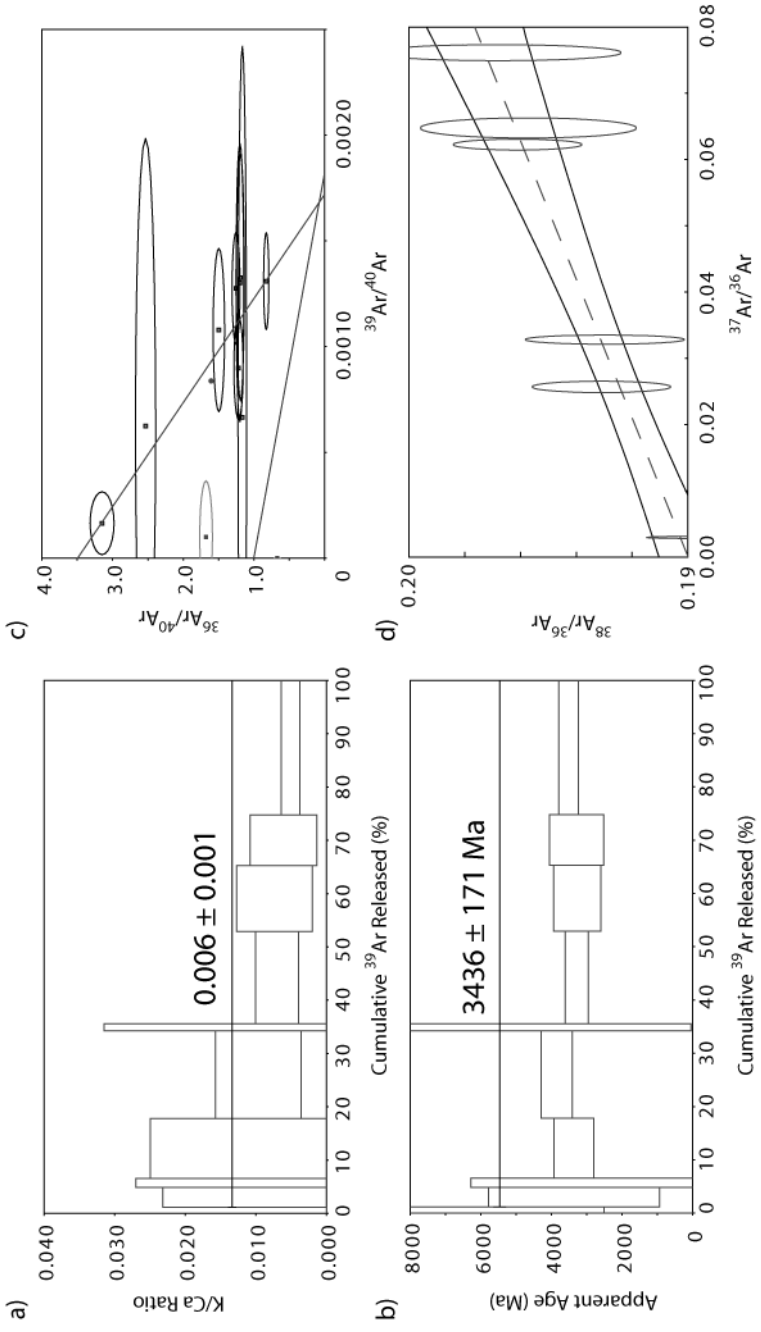

Figure A17. a) K/Ca Ratio **b)** Age spectra **c)** Reverse isochron **d)** Exposure age isochron

Sample LS3-24

Status: Statistically Acceptable – Concordant Ages

Formation Age (Ma): 276 ± 63 (plateau age only)

Exposure Age (Ma): 306 ± 101

Comments:

Each step has been determined very precisely, however, there is a lot of scatter in the isochrons leading to high MSWD and large uncertainties on the $^{40}Ar/^{36}Ar_{trapped}$. A diffusion profile is evident in the age spectra of this impact spherule though the uncertainties on the formation age are sufficiently large to allow inclusion of all the steps as a plateau. Exposure age (P >5%) can only be calculated with the removal of either steps 6 or 7. Removal of step 6 would result in a negative regression which is not valid there is no obvious reason for removing step 7 either. According to the release patterns, step 7 does contain a higher trapped component that may be throwing the result.

Formation Age

Non-Blank Steps:	7	**Isochron Steps:**	4	**Exclusions:**	1-3B
Plateau Age (Ma):	276 ± 63	**Plateau Coverage:**	89%	**MSWD (Probability):**	0.49 (69%)
Inverse Isochron Age (Ma):	286 ± 8	**MSWD (Probability):**	24 (0%)	**Intercept (%1σ):**	1.2 (22%)

Exposure Age:

No. Steps:	4	**Isochron Steps:**	3	**Exclusions:**	7D
$^{38}Ar/^{37}Ar$:	0.121 ± 0.040	**MSWD (Probability):**	0.25 (62%)	**Exposure Age (Ma):**	306 ± 101

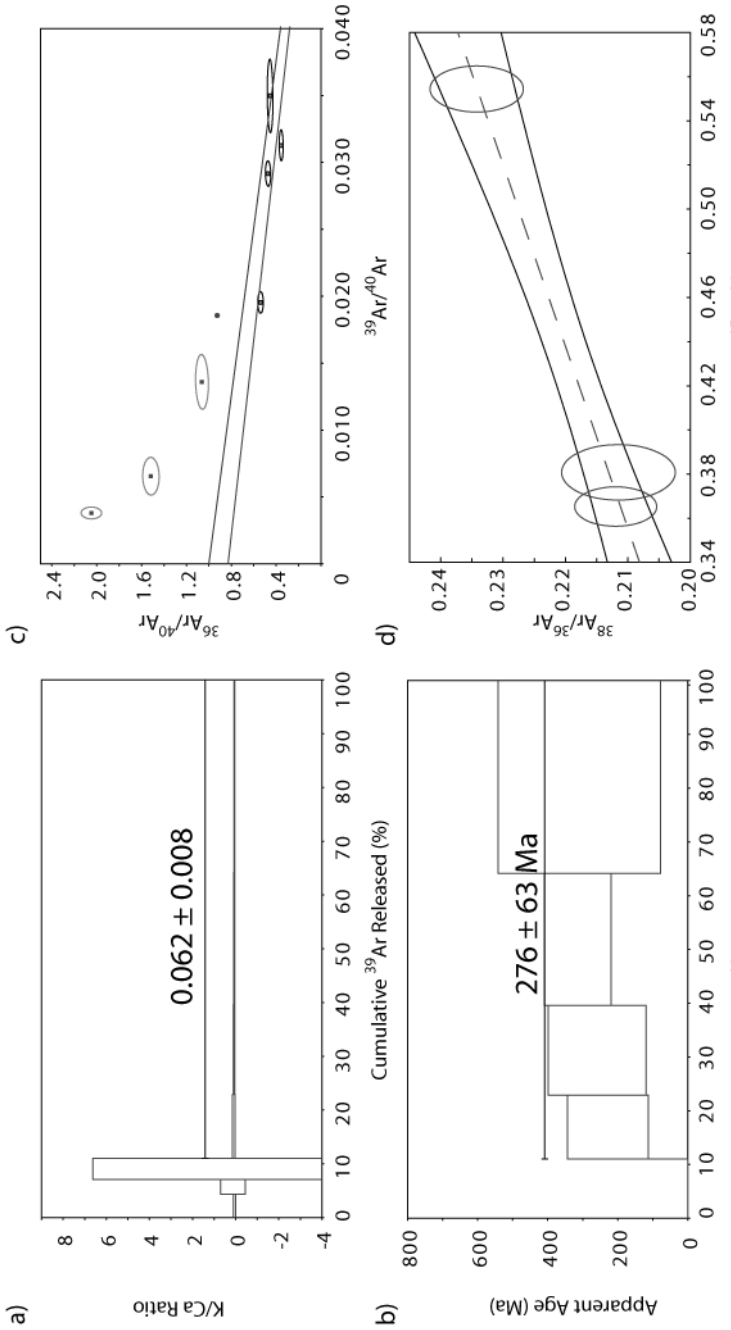

Figure A18. a) K/Ca Ratio **b)** Age spectra **c)** Reverse isochron **d)** Exposure age isochron

Sample LS3-25

Status: Discarded

Formation Age (Ma):

Exposure Age (Ma):

Comments:

Multiple sources present resulting in highly variable gas releases and large formation age uncertainties of 100%. A plateau can be established if step 3 not included in the plateau due to highly variable K/Ca ratio. However, the age is so highly variable that the result is of no use. Inverse isochron slope is positive so again, there is no result.

Formation Age

Non-Blank Steps:	7	**Isochron Steps:**	4	**Exclusions:**	1A, 2B, 3D
Plateau Age (Ma):	2813 ± 2699	**Plateau Coverage:**	74%	**MSWD (Probability):**	0.017 (100%)
Inverse Isochron Age (Ma):		**MSWD (Probability):**		**Intercept (%1σ):**	1 (50%)

Exposure Age:

No. Steps:		**Isochron Steps:**		**Exclusions:**	
$^{38}Ar/^{37}Ar$:		**MSWD (Probability):**		**Exposure Age (Ma):**	

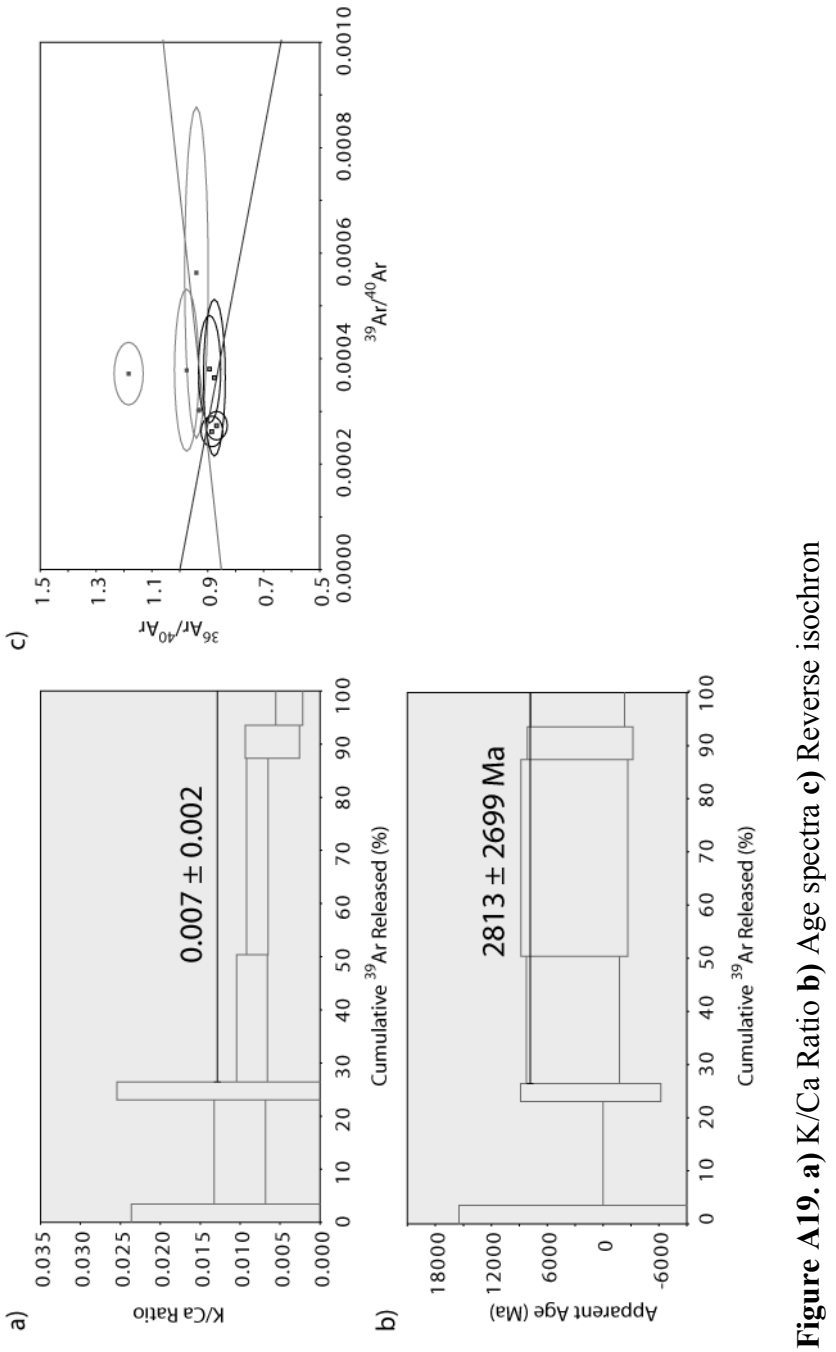

Figure A19. a) K/Ca Ratio **b)** Age spectra **c)** Reverse isochron

Sample LS3-32

Status: Discarded

Formation Age (Ma):

Exposure Age (Ma):

Comments:

The age spectra suggest that this impact spherule has experienced significant loss of argon. It is not possible establish the $^{40}Ar/^{36}Ar_{trapped}$ ratio using the isochrons which is needed to at least determine a minimum age.

Formation Age

Non-Blank Steps:	9	**Isochron Steps:**	N/A	**Exclusions:**	
Plateau Age (Ma):		**Plateau Coverage:**		**MSWD (Probability):**	
Inverse Isochron Age (Ma):		**MSWD (Probability):**		**Intercept (%1σ):**	

Exposure Age:

No. Steps:		**Isochron Steps:**		**Exclusions:**	
$^{38}Ar/^{37}Ar$:		**MSWD (Probability):**		**Exposure Age (Ma):**	

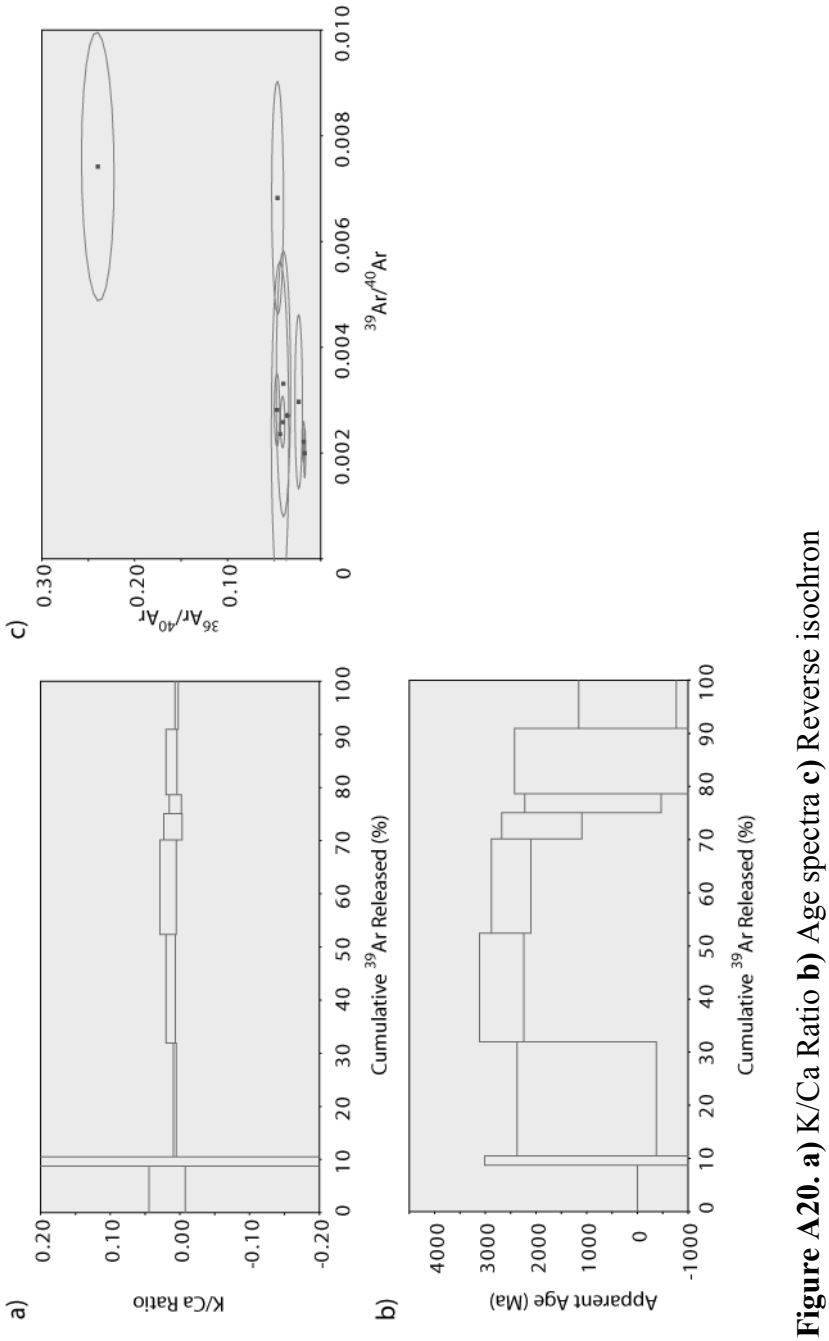

Figure A20. a) K/Ca Ratio **b)** Age spectra **c)** Reverse isochron

Sample LS3-43

Status: Useable

Comments:

A total of 10 heating steps were conducted on this impact spherule with only the first step yielding any gas. However, this impact spherule is devoid of any $^{40}Ar^*$, but these steps contain other argon isotope gasses. No age can be determined, but it is likely that it is very young.

Sample LS3-52

Status: Statistically Acceptable – Concordant Ages

Formation Age (Ma): 4255 ± 384 (mini-plateau)

Exposure Age (Ma): 437 ± 124

Comments:

This impact spherule contains a large amount of trapped component gasses that dominates the release in the earlier steps. Two steps, 5 and 7, have highly variable ages and K/Ca ratios due to the release of the trapped component in these steps. Overall, however, all steps are consistent allowing for a mini-plateau to be established. The final step (10) appears to have a lower K/Ca ratio than the rest of the plateau and is likely to be a clast. Large uncertainties and some clustering result in a more poorly defined $^{40}Ar/^{36}Ar_{trapped}$ ratio.

Formation Age

Non-Blank Steps:	10	**Isochron Steps:**	7	**Exclusions:**	1-3B
Plateau Age (Ma):	4255 ± 384	**Plateau Coverage:**	67%	**MSWD (Probability):**	0.57 (75%)
Inverse Isochron Age (Ma):	4507 ± 1046	**MSWD (Probability):**	2 (8%)	**Intercept (%1σ):**	1.53 (11%)

Exposure Age:

No. Steps:	7	**Isochron Steps:**	4	**Exclusions:**	5D, 7D, 10C
$^{38}Ar/^{37}Ar$:	0.173 ± 0.049	**MSWD (Probability):**	0.94 (39%)	**Exposure Age (Ma):**	437 ± 124

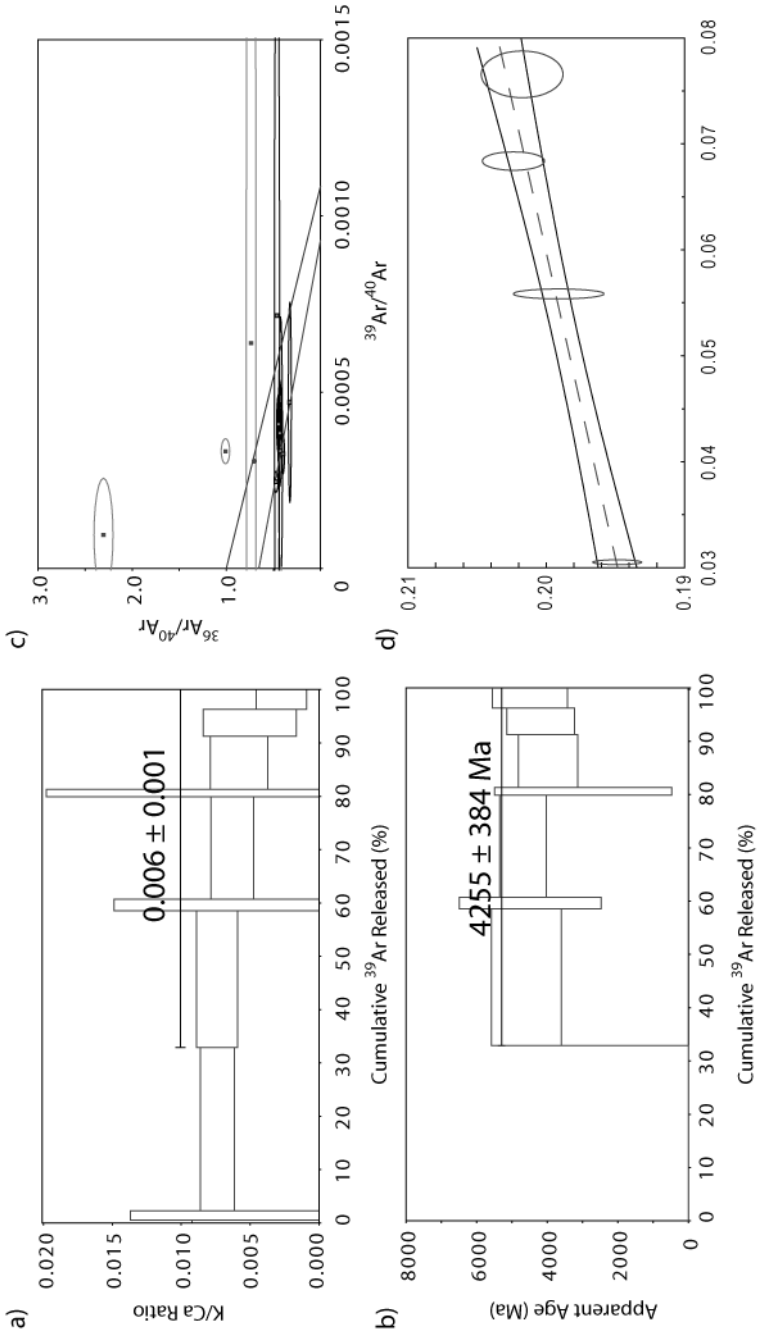

Figure A21. a) K/Ca Ratio **b)** Age spectra **c)** Reverse isochron **d)** Exposure age isochron

Sample LS3-53

Status: Discarded

Formation Age (Ma):

Exposure Age (Ma):

Comments:

The age spectra and isochrons indicate that this impact spherule has been highly disturbed due to the significant amount of scatter. This analysis cannot be used.

Formation Age					
Non-Blank Steps:	8	**Isochron Steps:**	N/A	**Exclusions:**	
Plateau Age (Ma):		**Plateau Coverage:**		**MSWD (Probability):**	
Inverse Isochron Age (Ma):		**MSWD (Probability):**		**Intercept (%1σ):**	
Exposure Age:					
No. Steps:		**Isochron Steps:**		**Exclusions:**	
$^{38}Ar/^{37}Ar$:		**MSWD (Probability):**		**Exposure Age (Ma):**	

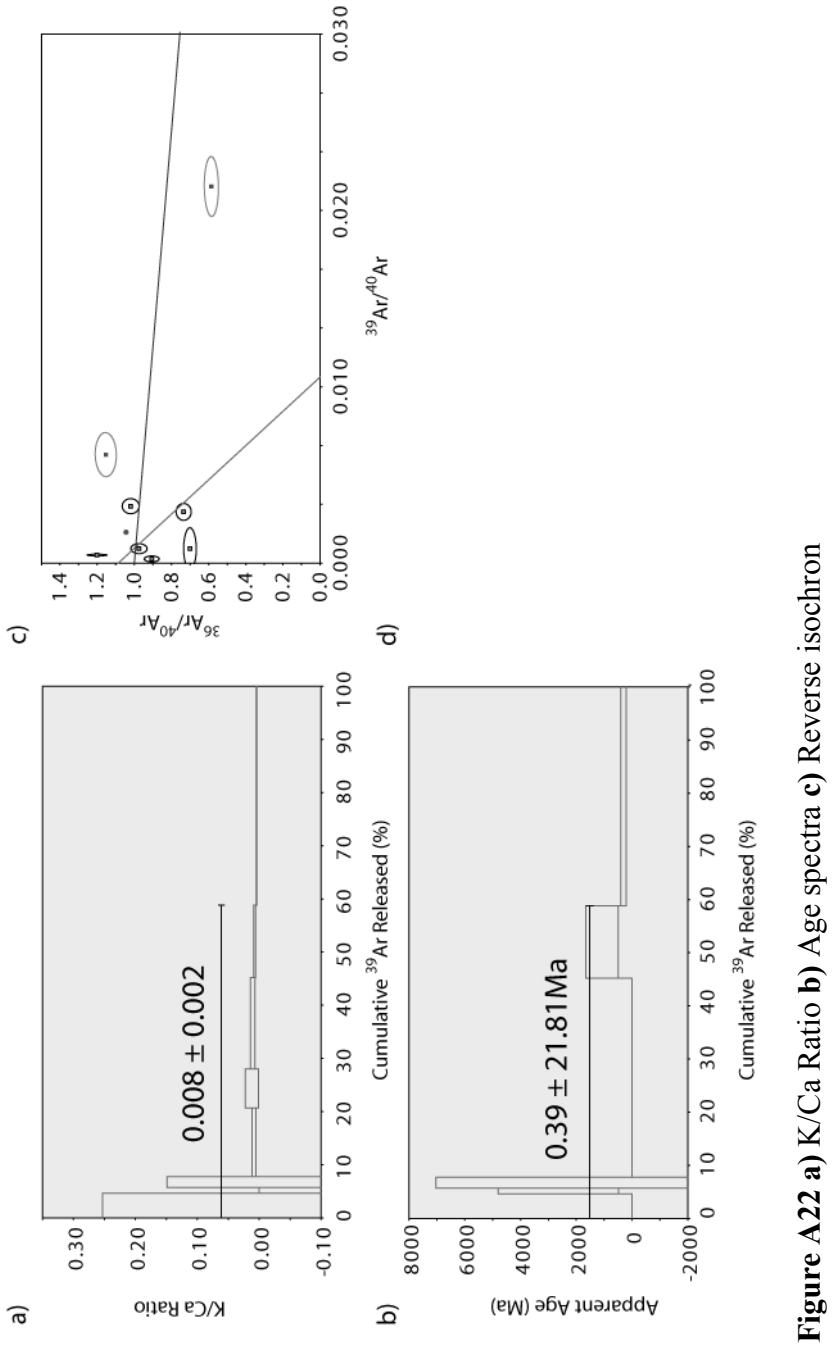

Figure A22 a) K/Ca Ratio **b)** Age spectra **c)** Reverse isochron

Sample LS3-71

Status: Statistically Acceptable – Concordant Ages

Formation Age (Ma): 2565 ± 299 (plateau)

Exposure Age (Ma): 172 ± 86

Comments:

A significant amount of the trapped component is present in this impact spherule. Reasonable spread of points in the isochrons and well constrained $^{40}Ar/^{36}Ar_{trapped}$ ratio. The K/Ca ratio decreases from low to high temperature steps. Steps 5 and 6 releases are dominantly from the trapped component and require removal prior to calculation of exposure age.

Formation Age

Non-Blank Steps:	11	**Isochron Steps:**	9	**Exclusions:**	1-2B
Plateau Age (Ma):	2565 ± 299	**Plateau Coverage:**	91%	**MSWD (Probability):**	0.31 (96%)
Inverse Isochron Age (Ma):	2620 ± 576	**MSWD (Probability):**	0.77 (59%)	**Intercept (%1σ):**	0.9 (3.6%)

Exposure Age:

No. Steps:	9	**Isochron Steps:**	7	**Exclusions:**	5-6D
$^{38}Ar/^{37}Ar$:	0.068 ± 0.034	**MSWD (Probability):**	0.72 (61%)	**Exposure Age (Ma):**	172 ± 86

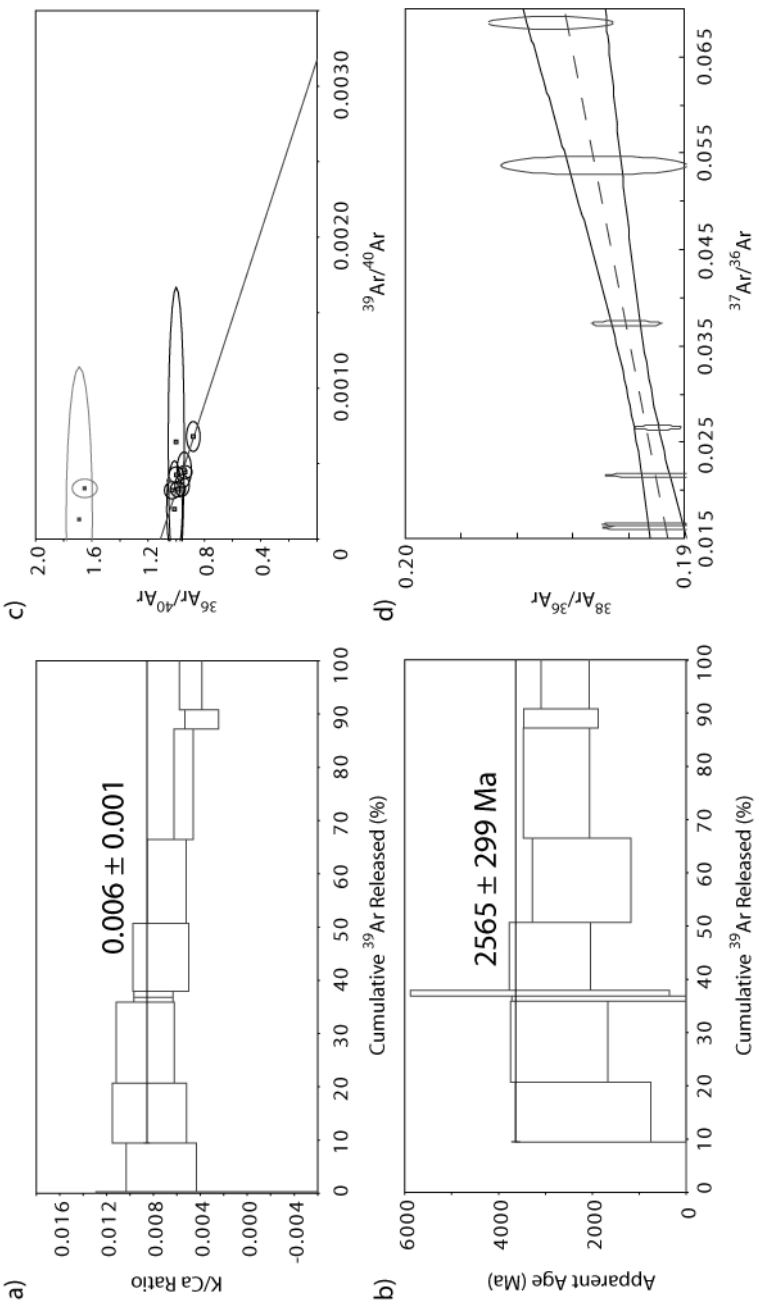

Figure A23 a) K/Ca Ratio **b)** Age spectra **c)** Reverse isochron **d)** Exposure age isochron

Sample LS4-12

Status: Statistically Acceptable – Concordant Ages

Formation Age (Ma): 3862 ± 52 (plateau)

Exposure Age (Ma):

Comments:

Unlike all other K/Ca profiles in this study, this impact spherule has an increasing K/Ca ratio from low to high temperature steps. There is also a significant contribution from the trapped component in the first and last heating steps. No exposure age can be obtained from this impact spherule as a regression with probability >5% is not possible.

Formation Age

Non-Blank Steps:	7	**Isochron Steps:**	7	**Exclusions:**	
Plateau Age (Ma):	3862 ± 52	**Plateau Coverage:**	100%	**MSWD (Probability):**	0.68 (67%)
Inverse Isochron Age (Ma):	3867 ± 53	**MSWD (Probability):**	0.93 (46%)	**Intercept (%1σ):**	5.1 (38%)

Exposure Age:

No. Steps:		**Isochron Steps:**		**Exclusions:**	
$^{38}Ar/^{37}Ar$:		**MSWD (Probability):**		**Exposure Age (Ma):**	

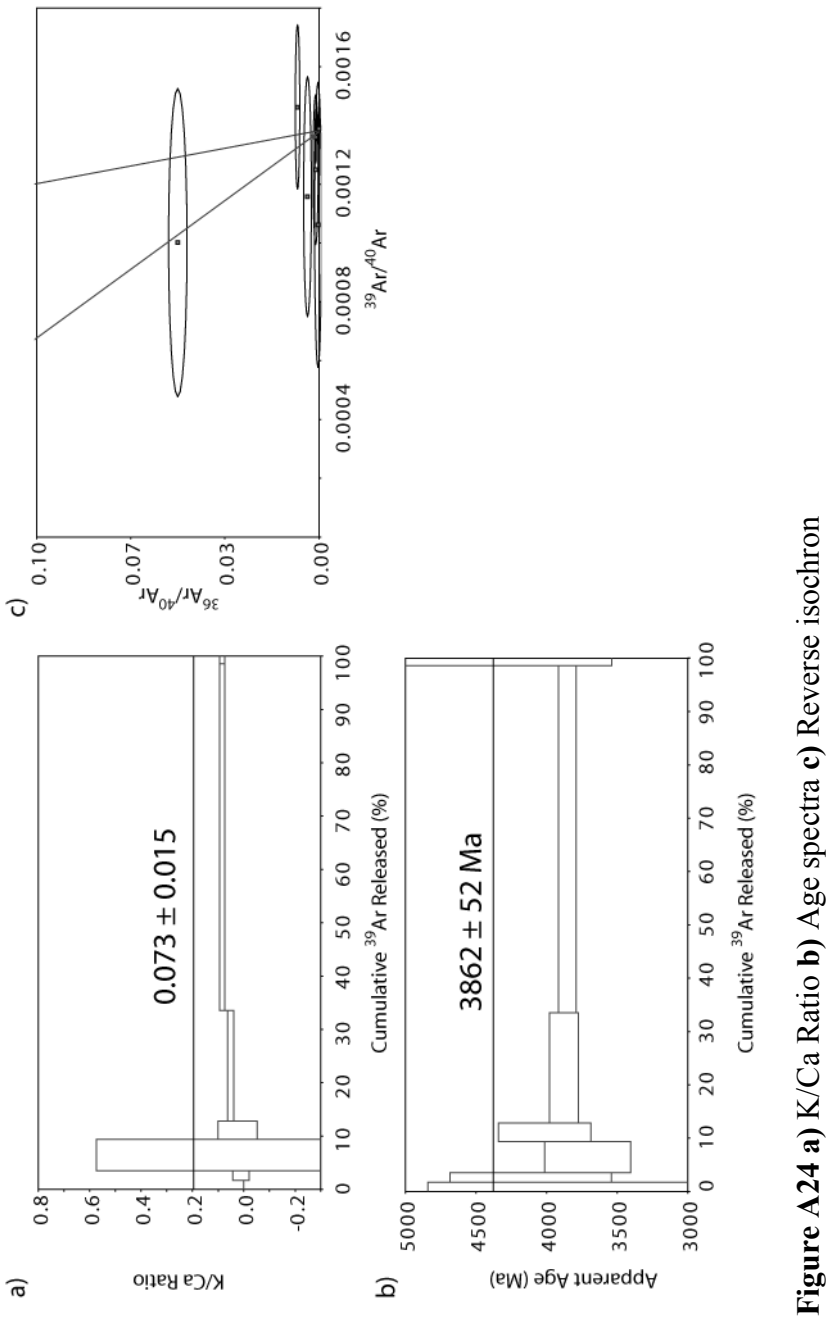

Figure A24 a) K/Ca Ratio **b)** Age spectra **c)** Reverse isochron

Sample LS4-21

Status: Statistically Acceptable

Formation Age (Ma): 339 ± 145 (plateau age only)

Exposure Age (Ma):

Comments:

A total of fours steps were possible on this impact spherule, the first of which contains a significant amount of trapped gasses. The last step yields an age much older than the previous steps possibly from the degassing of a clast with low K/Ca ratios (0.008 ± 0.011). An isochron age cannot be established from this impact spherule as there is too much scatter.

Formation Age

Non-Blank Steps:	4	**Isochron Steps:**	3	**Exclusions:**	4C?
Plateau Age (Ma):	339 ± 145	**Plateau Coverage:**	80%	**MSWD (Probability):**	1.07 (34%)
Inverse Isochron Age (Ma):	337 ± 305	**MSWD (Probability):**	13.15 (0%)	**Intercept (%1σ):**	0.3 (10%)

Exposure Age:

No. Steps:		**Isochron Steps:**		**Exclusions:**	
$^{38}Ar/^{37}Ar$:		**MSWD (Probability):**		**Exposure Age (Ma):**	

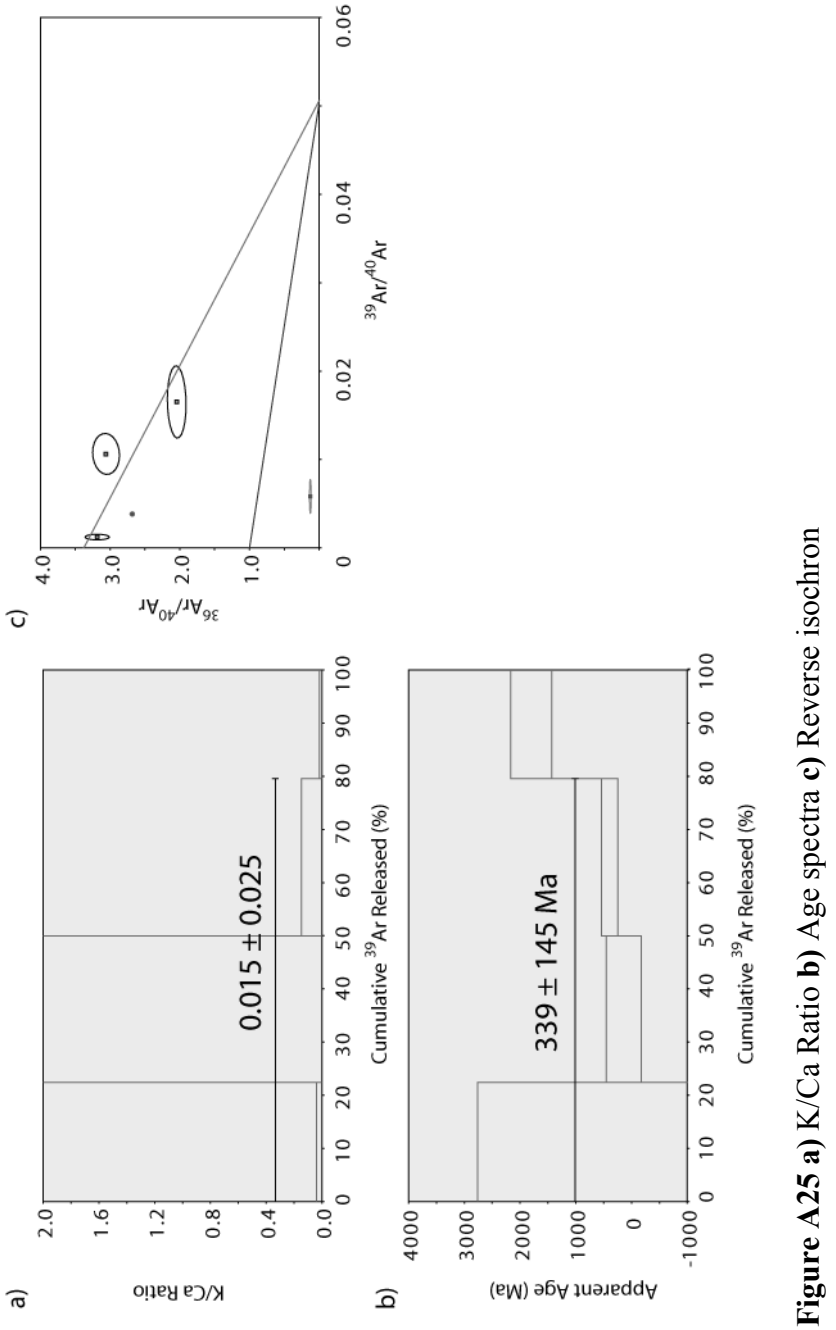

Figure A25 a) K/Ca Ratio **b)** Age spectra **c)** Reverse isochron

Sample LS5-67

Status: Statistically Acceptable – Concordant Ages

Formation Age (Ma): 1913 ± 728 (mini-plateau)

Exposure Age (Ma):

Comments:

The trapped component contributes significantly to all heating steps in this impact spherule. As a result, the uncertainties on the formation age are quite large. The isochron hinges on the 4th step as steps 5 and 6 are very similar. Exposure age cannot be calculated as inclusion of all the steps produces a negative exposure age.

Formation Age

Non-Blank Steps:	6	**Isochron Steps:**	3	**Exclusions:**	1A, 2-3B
Plateau Age (Ma):	1913 ± 728	**Plateau Coverage:**	69%	**MSWD (Probability):**	0.015 (99%)
Inverse Isochron Age (Ma):	1962 ± 1059	**MSWD (Probability):**	0.06 (81%)	**Intercept (%1σ):**	1.36 (3.3%)

Exposure Age:

No. Steps:		**Isochron Steps:**		**Exclusions:**	
$^{38}Ar/^{37}Ar$:		**MSWD (Probability):**		**Exposure Age (Ma):**	

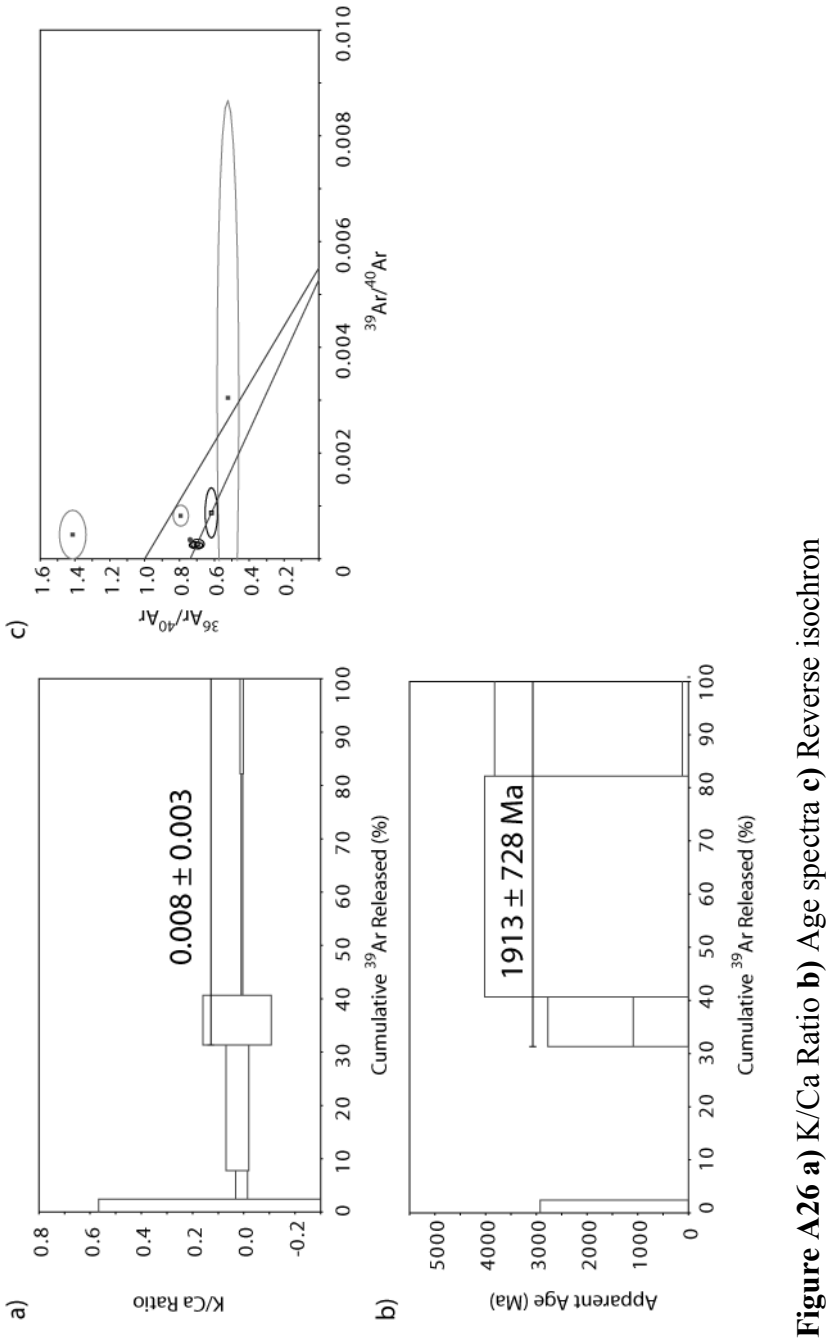

Figure A26 a) K/Ca Ratio **b)** Age spectra **c)** Reverse isochron

Sample LS5-72

Status: Statistically Acceptable – Concordant Ages

Formation Age (Ma): 938 ± 151 (plateau)

Exposure Age (Ma):

Comments:

The first heating step in this impact spherule contains a very large amount of trapped gasses. The isochron has good spread and concordant with the plateau age, but is quite scattered with probability just above the 5% threshold. The regression needed to calculate exposure age is below the 5% threshold and cannot be used.

Formation Age

Non-Blank Steps:	4	**Isochron Steps:**	3	**Exclusions:**	1A
Plateau Age (Ma):	938 ± 151	**Plateau Coverage:**	100%	**MSWD (Probability):**	1.14 (32%)
Inverse Isochron Age (Ma):	996 ± 324	**MSWD (Probability):**	3.7 (6%)	**Intercept (%1σ):**	0.53 (4%)

Exposure Age:

No. Steps:		**Isochron Steps:**		**Exclusions:**	
$^{38}Ar/^{37}Ar$:		**MSWD (Probability):**		**Exposure Age (Ma):**	

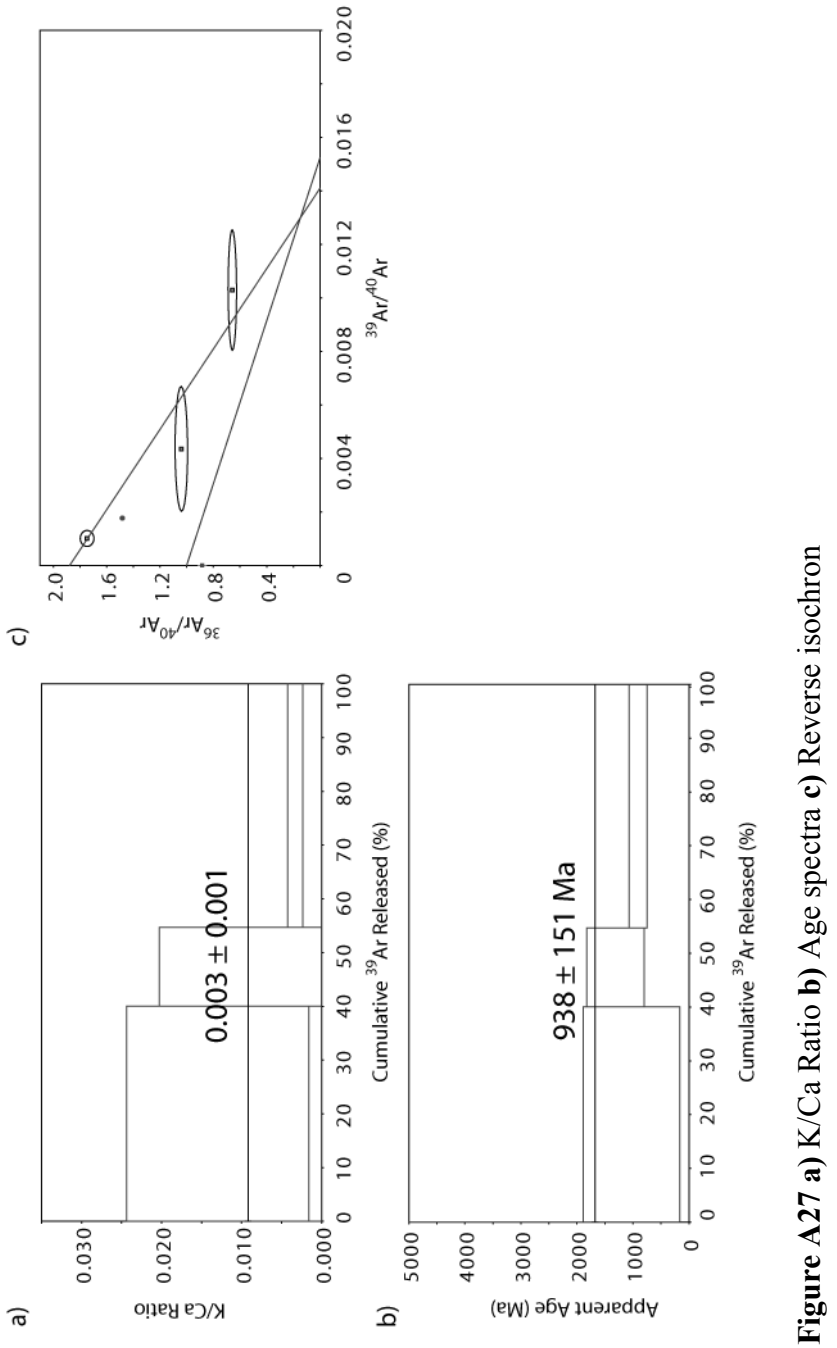

Figure A27 a) K/Ca Ratio **b)** Age spectra **c)** Reverse isochron

Sample LS6-31

Status: Statistically Acceptable – Concordant Ages

Formation Age (Ma): 560 ± 70 (plateau)

Exposure Age (Ma):

Comments:

The isochron has good spread and concordant with the plateau age, but is quite scattered with probability right on the 5% threshold. The regression needed to calculate exposure age is below the 5% threshold and cannot be used.

Formation Age

Non-Blank Steps:	3	**Isochron Steps:**	3	**Exclusions:**	
Plateau Age (Ma):	560 ± 70	**Plateau Coverage:**	100%	**MSWD (Probability):**	0.70 (50%)
Inverse Isochron Age (Ma):	565 ± 124	**MSWD (Probability):**	3.9 (5%)	**Intercept (%1σ):**	0.78 (6%)

Exposure Age:

No. Steps:		**Isochron Steps:**		**Exclusions:**	
$^{38}Ar/^{37}Ar$:		**MSWD (Probability):**		**Exposure Age (Ma):**	

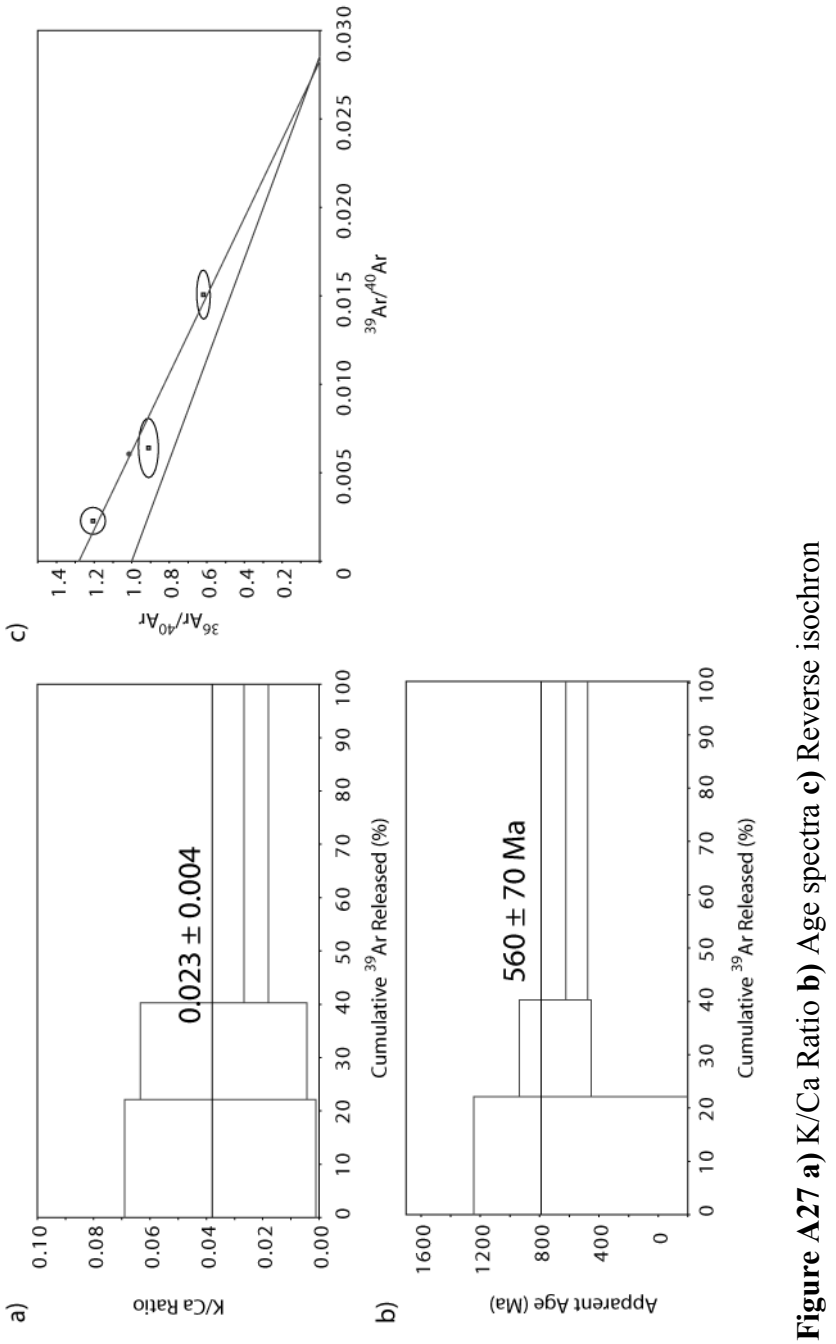

Figure A27 a) K/Ca Ratio **b)** Age spectra **c)** Reverse isochron

ADENA K., CHRISTY A. and NORMAN M. (2009) Geochemistry of volcanic and impact glasses from the Taurus-Littrow Region on the Moon. In *9th Australian Space Science Conference* (eds. W. Short and I. Cairns). National Space Society of Australia Ltd, Sydney, Australia.

AHRENS T. J. and OKEEFE J. D. (1977) Equations of state and impact-induced shock-wave attenuation on the moon. In *Impact and explosion cratering: Planetary and terrestrial implications - Proceedings of the Symposium on Planetary Cratering Mechanics* (eds. D. J. Roddy, R. O. Pepin and R. B. Merrill), pp. 639-656. Pergamon Press, Inc.

ALLEN C. C., MCKAY D. S. and MORRIS R. V. (1992) Lunar oxygen - The reduction of glass by hydrogen. In *Engineering, construction, and operations in space III* (eds. W. Z. Sadeh, S. Sture and R. J. Miller), pp. 629-640 Denver, Colorado.

ANDERS E. and GREVESSE N. (1989) Abundances of the elements: Meteoritic and solar. *Geochimica et Cosmochimica Acta* **53**(1), 197-214.

ANDRE C. G. and EL-BAZ F. (1981) Regional Chemical Setting of the Apollo 16 Landing Site and the Importance of the Kant Plateau (abstract). In *12th Lunar and Planetary Science Conference*, pp. 22-24.

APOLLO FIELD GEOLOGY INVESTIGATION T. (1973) Apollo 16 Exploration of Descartes: A Geologic Summary. *Science* **179**(4068), 62-69.

APOLLO SOIL S. (1971) Apollo 14: Nature and origin of rock types in soil from the Fra Mauro formation. *Earth and Planetary Science Letters* **12**(1), 49-54.

ARNDT J., FLAD K. and FETH M. (1979) Radiative cooling experiments on lunar glass analogues. In *10th Lunar and Planetary Science Conference*, pp. 355-373. Pergamon Press, Houston, Texas.

ARNDT J. and VON ENGELHARDT W. (1987) Formation of Apollo 17 Orange and Black Glass Beads. *J. Geophys. Res.* **92**(B4), E372-E376.

ARNOLD J. R. (1975) A Monte Carlo model for the gardening of the lunar regolith. *Earth, Moon, and Planets* **13**(1), 159-172.

ARVIDSON R., CROZAZ G., DROZD R. J., HOHENBERG C. M. and MORGAN C. J. (1975a) Cosmic ray exposure ages of features and events at the apollo landing sites. *Earth, Moon, and Planets* **13**(1), 259-276.

ARVIDSON R., DROZD R. J., HOHENBERG C. M., MORGAN C. J. and POUPEAU G. (1975b) Horizontal transport of the regolith, modification of features, and erosion rates on the lunar surface. *Earth, Moon, and Planets* **13**(1), 67-79.

BALDWIN R. B. (1963) *The Measure of the Moon*. University of Chicago Press. pp. 374.

BARRA F., SWINDLE T. D., KOROTEV R. L., JOLLIFF B. L., ZEIGLER R. A. and OLSON E. (2006) 40Ar/39Ar dating of Apollo 12 regolith: Implications for the age of Copernicus and the source of nonmare materials. *Geochimica et Cosmochimica Acta* **70**(24), 6016-6031.

BASTIN J. A. (1979) The origin of the shapes of lunar globules. *Moon and the Planets* **21**, 283-288.

- (1980) Rotating lunar globules. *Nature* **283**(5742), 108-108.

BASTIN J. A. and FRENCH W. J. (1970) The formation of lunar globules. *Proceedings of the Geological Society, London* **1664**, 238-246.

BASTIN J. A. and VOLBORTH A. (1974) The ellipsoidal and dumbbell-shaped inclusions within particulate lunar globules. *Icarus* **21**(1), 112-120.

BEST J. B. and MINKIN J. A. (1972) Apollo 15 glasses of impact origin. *The Apollo 15 lunar samples*, 34 - 39.

BLANCHARD M. B., BROWNLEE D. E., BUNCH T. E., HODGE P. W. and KYTE F. T. (1980) Meteoroid ablation spheres from deep-sea sediments. *Earth and Planetary Science Letters* **46**(2), 178-190.

BOGARD D. (1995) Impact ages of meteorites: A synthesis. *Meteoritics* **30**, 244-268.

BOGARD D. D., GARRISON D. H., SHIH C. Y. and NYQUIST L. E. (1994) 39Ar-40Ar dating of two lunar granites: The age of Copernicus. *Geochimica et Cosmochimica Acta* **58**(14), 3093-3100.

BOTTKE W. F., WALKER R. J., DAY J. M. D., NESVORNY D. and ELKINS-TANTON L. (2010) Stochastic Late Accretion to Earth, the Moon, and Mars. *Science* **330**(6010), 1527-1530.

BRERETON N. R. (1970) Corrections for interfering isotopes in the40Ar/39Ar dating method. *Earth and Planetary Science Letters* **8**(6), 427-433.

BROWNLEE D. E. (1985) Cosmic Dust: Collection and Research. *Annual Review of Earth and Planetary Sciences* **13**(1), 147-173.

BROWNLEE D. E., BATES B. and SCHRAMM L. (1997) The elemental composition of stony cosmic spherules. *Meteoritics and Planetary Science* **32**, 157-175.

BROWNLEE D. E., BATES B. A., PILACHOWSKI L. B., OLSZEWSKI E. and SIEGMUND W. A. (1980) Unmelted Cosmic Material in Deep Sea Sediments (Abstract). *Lunar and Planetary Science XI*, 109-111.

BROWNLEE D. E., BATES B. A. and WHEELOCK M. M. (1984) Extraterrestrial platinum group nuggets in deep-sea sediments. *Nature* **309**(5970), 693-695.

BROWNLEE D. E., PILACHOWSKI L. B. and HODGE P. W. (1979) Meteorite Mining on the Ocean Floor (abstract). In *10th Lunar and Planetary Science Conference*, pp. 157-158, Houston, Texas.

CARRIER D., III, OLHOEFT G. and MENDELL W. (1991) Physical Properties of the Lunar Surface. In *Lunar Sourcebook: A User's Guide to the Moon* (eds. G. Heiken, D. T. Vaniman and B. M. French), pp. 475-594. Cambridge University Press.

CASSIDY W., HARVEY R., SCHUTT J., DELISLE G. and YANAI K. (1992) The meteorite collection sites of Antarctica. *Meteoritics and Planetary Science* **27**(5), 490-525.

CHAO E. C. T., BEST J. B. and MINKIN J. A. (1972) Apollo 14 glasses of impact origin and their parent rock types. In *The 3rd Lunar Science Conference*, pp. 907-925.

CHAO E. C. T., BOREMAN J. A., MINKIN J. A., JAMES O. B. and DESBOROUGH G. A. (1970) Lunar Glasses of Impact Origin: Physical and Chemical Characteristics and Geologic Implications. *Journal of Geophysical Research* **75**(35), 7445-7479.

CHAPMAN C. R., COHEN B. A. and GRINSPOON D. H. (2007) What are the real constraints on the existence and magnitude of the late heavy bombardment? *Icarus* **189**(1), 233-245.

CHERNYAK Y. and NUSSINOV M. (1975) Some problems of dynamics of lunar regolith glass particle formation. *Earth, Moon, and Planets* **13**(4), 363-376.

CHERNYAK Y. B. and NUSSINOV M. D. (1976) On the mechanisms of lunar regolith glass particle formation. *Nature* **261**(5562), 664-666.

CLAYTON R. N., MAYEDA T. K. and BROWNLEE D. E. (1986) Oxygen isotopes in deep-sea spherules. *Earth and Planetary Science Letters* **79**(3-4), 235-240.

COHEN B. A. (2002) Geochemical and Geochronological Constraints on Early Lunar Bombardment History (Abstract No. 1984). In *33rd Annual Lunar and Planetary Science Conference*, Houston, Texas.
- (2008a) Lunar Meteorite Impact Melt Clasts and Lessons Learned for Lunar Surface Sampling (Abstract No. 2532). In *39th Lunar and Planetary Science Conference*, Houston, Texas.
- (2008b) A Review of Lunar Meteorite Impact-Melt Clast Compositions and Ages (abstract No. 1439). In *Workshop on the Early Solar System Impact Bombardment*, pp. 27-28, Houston, Texas.
COHEN B. A., SWINDLE T. D. and KRING D. A. (2000) Support for the Lunar Cataclysm Hypothesis from Lunar Meteorite Impact Melt Ages. *Science* **290**(5497), 1754-1756.
- (2005) Geochemistry and 40Ar-39Ar geochronology of impact-melt clasts in feldspathic lunar meteorites: Implications for lunar bombardment history. *Meteoritics & Planetary Science* **40**, 775.
COHEN B. A., SWINDLE T. D., TAYLOR L. A. and NAZAROV M. A. (2002) 40Ar-39Ar Ages from Impact Melt Clasts in Lunar Meteorites Dhofar 025 and Dhofar 026 (abstract. 1252). In *33rd Annual Lunar and Planetary Science Conference*, Houston, Texas.
CORDIER C., FOLCO L. and TAYLOR S. (2011) Vestoid cosmic spherules from the South Pole Water Well and Transantarctic Mountains (Antarctica): A major and trace element study. *Geochimica et Cosmochimica Acta* **75**(5), 1199-1215.
CORTI G., ZEOLI A. and BONINI M. (2003) Ice-flow dynamics and meteorite collection in Antarctica. *Earth and Planetary Science Letters* **215**(3-4), 371-378.
CULLER T. S., BECKER T. A., MULLER R. A. and RENNE P. R. (2000) Lunar Impact History from 40Ar/39Ar Dating of Glass Spherules. *Science* **287**(5459), 1785-1788.
CZAJKOWSKI J., ENGLERT P., BOSELLINI A. and OGG J. G. (1983) Cobalt enriched hardgrounds-New sources of ancient extraterrestrial materials. *Meteoritics and Planetary Science* **18**, 286-287.
DALRYMPLE G. B. and RYDER G. (1993) 40Ar/39Ar Age Spectra of Apollo 15 Impact Melt Rocks by Laser Step-Heating and Their Bearing on the History of Lunar Basin Formation. *J. Geophys. Res.* **98**(E7), 13085-13095.
- (1996) Argon-40/argon-39 age spectra of Apollo 17 highlands breccia samples by laser step heating and the age of the Serenitatis basin. *J. Geophys. Res.* **101**(E11), 26069-26084.
DELANO J. (1986) Pristine Lunar Glasses: Criteria, Data and Implications. *Proceedings of the 16th Lunar and Planetary Science Conference, Part 2* **91**(B4), D201-D213.
DELANO J. W. (1975) Petrology of the Apollo 16 mare component - Mare Nectaris. In *6th Lunar Science Conference*, pp. 15-47. Pergamon Press, Inc, Houston, Texas.
- (1988) Apollo 14 regolith breccias - Different glass populations and their potential for charting space time variations. In *Lunar and Planetary Science Conference XVIII*, pp. 59-65. Cambridge University Press/Lunar and Planetary Institute, Huston.

- (1991) Geochemical comparison of impact glasses from lunar meteorites ALHA81005 and MAC88105 and Apollo 16 regolith 64001. *Geochimica et Cosmochimica Acta* **55**(11), 3019-3029.
- (1992) Major-Element Compositions of Glasses in Apollo 16 Cores 60014 (Station 10) and 64001 (Station 4) (abstract). In *23rd Lunar and Planetary Science Conference*, pp. 303.
- (1993) Compositional heterogeneity within a dumbbell-shaped Apollo 15 green glass: Evidence for simultaneous eruption of different magmas. In *24th Lunar and Planetary Science Conference*, pp. 393-394, Houston, Texas.

DELANO J. W., LINDSLEY D. H. and RUDOWSKI R. (1982) Glasses of impact origin from Apollo 11, 12, 15, and 16 - Evidence for fractional vaporization and mare/highland mixing. In *Lunar and Planetary Science Conference XII*, pp. 339-370. Pergamon Press, Huston.

DELANO J. W., LIU Y.-G. and SCHMITT R. A. (1991) Geochemistry of Apollo 17 Impact Glasses: Regolith Compositions (abstract). *22nd Lunar and Planetary Science Conference*, 309-310.

DELANO J. W. and RUDOWSKI R. (1980) Apollo 16 green glass (abstract). In *11th Lunar and Planetary Science Conference*, pp. 222–224.

DELANO J. W., ZELLNER N. E. B., BARRA F., OLSON E., SWINDLE T. D., TIBBETTS N. J. and WHITTET D. C. B. (2007) An integrated approach to understanding Apollo 16 impact glasses: Chemistry, isotopes, and shape. *Meteoritics & Planetary Science* **42**, 993-1004.

DEUTSCH A., GRESHAKE A., PESONEN L. J. and PIHLAJA P. (1998) Unaltered cosmic spherules in a 1.4-Gyr-old sandstone from Finland. *Nature* **395**(6698), 146-148.

DICKIN A. P. (2005) Chapter 10: K-Ar and Ar-Ar Dating. In *Radiogenic Isotope Geology*, pp. 254-290. Cambridge University Press, New York.

DROUIN D., COUTURE A. R., JOLY D., TASTET X., AIMEZ V. and GAUVIN R. (2007) CASINO Monte Carlo Simulation Program v2.42. http://www.gel.usherbrooke.ca/casino/.

DROZD R. J., HOHENBERG C. M., MORGAN C. J., PODOSEK F. A. and WROGE M. L. (1977) Cosmic-ray exposure history at Taurus-Littrow. In *Proceedings of the 8th Lunar Science Conference*, pp. 3027-3043. Pergamon Press, Inc., Houston, Texas.

DROZD R. J., HOHENBERG C. M., MORGAN C. J. and RALSTON C. E. (1974) Cosmic-ray exposure history at the Apollo 16 and other lunar sites: lunar surface dynamics. *Geochimica et Cosmochimica Acta* **38**(10), 1625-1642.

DUPRAT J., ENGRAND C., MAURETTE M., KURAT G., GOUNELLE M. and HAMMER C. (2007) Micrometeorites from Central Antarctic snow: The CONCORDIA collection. *Advances in Space Research* **39**(4), 605-611.

EGGINS S. M., KINSLEY L. P. J. and SHELLEY J. M. G. (1998) Deposition and element fractionation processes during atmospheric pressure laser sampling for analysis by ICP-MS. *Applied Surface Science* **127-129**, 278-286.

ENGRAND C. and MAURETTE M. (1998) Carbonaceous micrometeorites from Antarctica. *Meteoritics & Planetary Science* **33**(4), 565-580.

ENGRAND C., MCKEEGAN K. D. and LESHIN L. A. (1999) Oxygen isotopic compositions of individual minerals in Antarctic micrometeorites: further links to

carbonaceous chondrites. *Geochimica et Cosmochimica Acta* **63**(17), 2623-2636.

ENGRAND C., MCKEEGAN K. D., LESHIN L. A., HERZOG G. F., SCHNABEL C., NYQUIST L. E. and BROWNLEE D. E. (2005) Isotopic compositions of oxygen, iron, chromium, and nickel in cosmic spherules: Toward a better comprehension of atmospheric entry heating effects. *Geochimica et Cosmochimica Acta* **69**(22), 5365-5385.

EUGSTER O. (1999) Chronology of dimict breccias and the age of South Ray crater at the Apollo 16 site. *Meteoritics & Planetary Science* **34**(3), 385-391.

FERNANDES V. A., ANAND M., BURGESS R. and TAYLOR L. A. (2004) Ar-Ar Studies of Dhofar Clast-rich Feldspathic Highland Meteorites: 025, 026, 280, 303 (Abstract). In *35th Lunar and Planetary Science*, pp. 1514, Houston, Texas.

FERNANDES V. A., BURGESS R. and TURNER G. (2000) Laser argon-40-argon-39 age studies of Dar al Gani 262 lunar meteorite. *Meteoritics & Planetary Science* **35**(6), 1355-1364.

FREDRIKSSON K. and GOWDY R. (1963) Meteoritic debris from the Southern California desert. *Geochimica et Cosmochimica Acta* **27**(3), 241-242.

FULCHIGNONI M., FUNICIELLO R., TADDEUCCI A. and TRIGILA R. (1971) Glassy spheroids in lunar fines from Apollo 12 samples 12070,37; 12001,73; and 12057,60. In *Lunar Science Conference*, pp. 937-948. The MIT Press.

GAULT D. E., HOERZ F., BROWNLEE D. E. and HARTUNG J. B. (1974) Mixing of the lunar regolith. In *5th Lunar Science Conference*, pp. 2365-2386. Pergamon Press, Inc., Houston, Texas.

GENGE M. J., ENGRAND C., GOUNELLE M. and TAYLOR S. (2008) The Classification of Micrometeorites. *Meteoritics and Planetary Science* **43**(3), 497-515.

GENGE M. J. and GRADY M. M. (1998) Melted micrometeorites from Antarctic ice with evidence for the separation of immiscible Fe-Ni-S liquids during entry heating. *Meteoritics and Planetary Science* **33**(3), 425-434.

GENGE M. J., GRADY M. M. and HUTCHISON R. (1997) The textures and compositions of fine-grained Antarctic micrometeorites: Implications for comparisons with meteorites. *Geochimica et Cosmochimica Acta* **61**(23), 5149-5162.

GIBSON E. K., JR. and MOORE G. W. (1972) Inorganic gas release and thermal analysis study of Apollo 14 and 15 soils. In *Proceedings of the 3rd Lunar Science Conference*, pp. 2092-2040. MIT Press.

GIBSON E. K., JR. and JOHNSON S. M. (1971) Thermal analysis-inorganic gas release studies of lunar samples. In *Proceedings of the 2nd Lunar Science Conference*, pp. 1351-1366. MIT Press.

GLASS B. P. (1971) Investigation of Glass Recovered from Apollo 12 Sample 12057. *Journal of Geophysical Research* **76**(23), 5649-5657.

- (1976) Major element composition of glasses from Apollo 11, 16, and 17 soil samples. In *7th Lunar Science Conference*, pp. 679-693. Pergamon Press, Inc., Houston, Texas.

GOLDSTEIN J., LYMAN C., NEWBURY D., LIFSHIN E., ECHLIN P., SAWYER L., JOY D. and MICHAEL J. (2003) *Scanning Electron Microscopy and X-Ray Microanalysis*. Springer.

GOMES R., LEVISON H. F., TSIGANIS K. and MORBIDELLI A. (2005) Origin of the cataclysmic Late Heavy Bombardment period of the terrestrial planets. *Nature* **435**(7041), 466-469.

GOUNELLE M., SPURNÝ P. and BLAND P. A. (2006) The orbit and atmospheric trajectory of the Orgueil meteorite from historical records. *Meteoritics & Planetary Science* **41**(1), 135-150.

GRESHAKE A., KLOCK W., ARND P., MAETZ M., FLYNN G. J., BAJT S. and BSICHOFF A. (1998) Heating experiments simulating atmospheric entry heating of micrometeorites: Clues to their parent body sources. *Meteoritics and Planetary Science* **33**, 267-290.

GRESHAKE A., KLOECK W., ARNDT P., MAETZ M. and BISCHOFF A. (1995) Volatile Element Abundances in Micrometeorites: Evidence for the Loss of Copper, Germanium, and Zinc During Atmospheric Entry Heating (abstract). *Lunar and Planetary Science Conference* **26**, 509.

GÜNTHER D., JACKSON S. E. and LONGERICH H. P. (1999) Laser ablation and arc/spark solid sample introduction into inductively coupled plasma mass spectrometers. *Spectrochimica Acta Part B: Atomic Spectroscopy* **54**(3-4), 381-409.

HANDWERKER C. A., ONORATO P. I. K. and UHLMANN D. R. (1977) Viscous flow, crystal growth, and glass formation of highland and mare basalts from Luna 24 pp. 483-493. Pergamon Press, Inc., Houston, Texas.

HAPKE B., CASSIDY W. and WELLS E. (1975) Effects of vapor-phase deposition processes on the optical, chemical, and magnetic properties OE the lunar regolith. *Earth, Moon, and Planets* **13**(1), 339-353.

HARTMANN W. K. (1965) Secular changes in meteoritic flux through the history of the solar system. *Icarus* **4**(2), 207-213.

- (1966) Early lunar cratering. *Icarus* **5**(1-6), 406-418.

- (1975) Lunar "cataclysm": A misconception? *Icarus* **24**(2), 181-187.

- (2003) Megaregolith evolution and cratering cataclysm models: Lunar cataclysm as a misconception (28 years later). *Meteoritics & Planetary Science* **38**(4), 579-593.

HARTMANN W. K., QUANTIN C. and MANGOLD N. (2007) Possible long-term decline in impact rates: 2. Lunar impact-melt data regarding impact history. *Icarus* **186**(1), 11-23.

HARTMANN W. K., RYDER G., DONES L. and GRINSPOON D. (2000) The Time-Dependent Intense Bombardment of the Primordial Earth/Moon System. In *Origin of the Earth and Moon* (eds. R. M. Canup and K. Righter), pp. 493-512. The University of Arizona Press.

HARVEY R. (2003) The Origin and Significance of Antarctic Meteorites. *Chemie der Erde - Geochemistry* **63**(2), 93-147.

HARVEY R. P. and MAURETTE M. (1991) The Origin and Significance of Cosmic Dust from the Walcott Névé, Antarctica. In *Proceedings of Lunar and Planetary Science*, pp. 569-578. Luna and Planetary Institute, Houston.

HASHIMOTO A. (1983) Evaporation metamorphism in the early solar nebula-evaporation experiments on the melt FeO-MgO-SiO2-CaO-Al2O3 and chemical fractionations of primitive material. *Journal of Geochimica* **17**, 111-145.

HASHIMOTO A. and KUMAZAWA M. (1979) Evaporation Metamorphism of Primitive Material in the Early Solar Nebula. *Earth and Planetary Science Letters* **43**, 13-21.

HASKIN L. and WARREN P. H. (1991) Lunar Chemistry. In *Lunar Sourcebook: A User's Guide to the Moon* (eds. G. Heiken, D. T. Vaniman and B. M. French), pp. 357-476. Cambridge University Press.

HASKIN L. A., KOROTEV R. L., GILLIS J. J. and JOLLIFF B. L. (2002) Stratigraphies of Apollo and Luna Highland Landing Sites and Provenances of Materials from the Perspective of Basin Impact Ejecta Modeling (abstract). In *33rd Annual Lunar and Planetary Science Conference*, Houston, Texas.

HASKIN L. A., KOROTEV R. L., ROCKOW K. M. and JOLLIFF B. L. (1998) The case for an Imbrium origin of the Apollo thorium-rich impact-melt breccias. *Meteoritics & Planetary Science* **33**(5), 959-975.

HEAD J. W. (1974) Stratigraphy of the descartes region (Apollo 16): implications for the origin of samples. *Earth, Moon, and Planets* **11**(1), 77-99.

HEIKEN G. H., MCKAY D. S. and BROWN R. W. (1974) Lunar deposits of possible pyroclastic origin. *Geochimica et Cosmochimica Acta* **38**(11), 1703-1704.

HENNESSY J. and TURNER G. (1980) 40Ar-39Ar Ages and Irradiation History of Luna 24 Basalts. *Philosophical Transactions of the Royal Society of London. Series A, Mathematical and Physical Sciences* **297**(1428), 27-39.

HERZOG G. F., XUE S., HALL G. S., NYQUIST L. E., SHIH C. Y., WIESMANN H. and BROWNLEE D. E. (1999) Isotopic and elemental composition of iron, nickel, and chromium in type I deep-sea spherules: implications for origin and composition of the parent micrometeoroids. *Geochimica et Cosmochimica Acta* **63**(9), 1443-1457.

HEWINS R. H. and FOX G. E. (2004) Chondrule textures and precursor grain size: an experimental study. *Geochimica et Cosmochimica Acta* **68**(4), 917-926.

HODGES C. A., MUEHLBERGER W. R. and ULRICH G. E. (1973) Geologic setting of Apollo 16. In *4th Lunar Science Conference*, pp. 1-25.

HODGES R. R. (1977) Release of radiogenic gases from the moon. *Physics of The Earth and Planetary Interiors* **14**(3), 282-288.

HOFFMAN J. H., HODGES R. R., JR., JOHNSON F. S. and EVANS D. E. (1973) Lunar atmospheric composition results from Apollo 17. In *4th Lunar Science Conference*, pp. 2865-2875.

HOHENBERG C. M., PODOSEK F. A., SHIRCK J. R., MARTI K. and REEDY R. C. (1978) Comparisons between observed and predicted cosmogenic noble gases in lunar samples. In *9th Lunar and Planetary Science Conference*, pp. 2311–2344. Pergamon Press, Inc., Houston, Texas.

HÖRZ F. and CINTALA M. (1997) The Barringer Award Address Presented 1996 July 25, Berlin, Germany: Impact experiments related to the evolution of planetary regoliths. *Meteoritics & Planetary Science* **32**(2), 179-209.

HÖRZ F., GRIEVE R., HEIKEN G., SPUDIS P. and BINDER A. (1991) Lunar Surface Processes. In *Lunar Sourcebook: A User's Guide to the Moon* (eds. G. Heiken, D. T. Vaniman and B. M. French), pp. 61-120. Cambridge University Press.

HORZ F., MULLER R. A., BECKER T. A., CULLER T. S., KARNER D. B. and RENNE P. R. (2000) Time-Variable Cratering Rates? *Science* **288**(5474), 2095a-.

HOUSLEY R. M., CIRLIN E. H. and GRANT R. W. (1973a) Characterization of Fines from the Apollo 16 Site. In *4th Lunar Science Conference*, pp. 2729-2735.

HOUSLEY R. M., GRANT R. W. and PATON N. E. Origin and characteristics of excess Fe metal in lunar glass welded aggregates. In *4th Lunar Science Conference*, pp. 2737-2749.

- (1973b) Origin and characteristics of excess Fe metal in lunar glass welded aggregates. In *Proceedings of the 4th Lunar Science Conference*, pp. 2737-2749.

HUI S. S. M., NORMAN M. D. and HARVEY R. P. (2007) The petrography and chemistry of cosmic spherules from Lewis Cliff, Antarctica. In *Australian Space Science Conference* (ed. W. Short), pp. 84-97. National Space Society of Australia Ltd, Sydney, Australia.

HUNEKE J. C., PODOSEK F. A., BURNETT D. S. and WASSERBURG G. J. (1972) Rare gas studies of the galactic cosmic ray irradiation history of lunar rocks. *Geochimica et Cosmochimica Acta* **36**(3), 269-301.

HUTCHISON R. (2004) *Meteorites: a petrologic, chemical and isotopic synthesis*. Cambridge University Press.

ICKERT R. B., HIESS J., WILLIAMS I. S., HOLDEN P., IRELAND T. R., LANC P., SCHRAM N., FOSTER J. J. and CLEMENT S. W. (2008) Determining high precision, in situ, oxygen isotope ratios with a SHRIMP II: Analyses of MPI-DING silicate-glass reference materials and zircon from contrasting granites. *Chemical Geology* **257**(1-2), 114-128.

IRELAND T. R. (1995) Ion Microprobe Mass Spectrometry. *Advances in Analytical Geochemistry* **2**, 1-118.

IWATA N. and IMAE N. (2002) Antarctic micrometeorite collection at a bare ice region near Syowa Station by JARE-41 in 2000. *Antarctic meteorite research* **15**, 25-37.

JAMES O. B. (1981) Petrologic and age relations of the Apollo 16 rocks - Implications for subsurface geology and the age of the Nectaris basin. In *12th Lunar and Planetary Science Conference*, pp. 209-233. Pergamon Press, Houston, Texas.

JANCHES D., DYRUD L. P., BROADLEY S. L. and PLANE J. M. C. (2009) First observation of micrometeoroid differential ablation in the atmosphere. *Geophys. Res. Lett.* **36**.

JOCHUM K. P., STOLL B., HERWIG K., WILLBOLD M., HOFMANN A. W., AMINI M., AARBURG S., ABOUCHAMI W., HELLEBRAND E., MOCEK B., RACZEK I., STRACKE A., ALARD O., BOUMAN C., BECKER S., DÜCKING M., BRÄTZ H., KLEMD R., DE BRUIN D., CANIL D., CORNELL D., DE HOOG C.-J., DALPÉ C., DANYUSHEVSKY L., EISENHAUER A., GAO Y., SNOW J. E., GROSCHOPF N., GÜNTHER D., LATKOCZY C., GUILLONG M., HAURI E. H., HÖFER H. E., LAHAYE Y., HORZ K., JACOB D. E., KASEMANN S. A., KENT A. J. R., LUDWIG T., ZACK T., MASON P. R. D., MEIXNER A., ROSNER M., MISAWA K., NASH B. P., PFÄNDER J., PREMO W. R., SUN W. D., TIEPOLO M., VANNUCCI R., VENNEMANN T., WAYNE D. and WOODHEAD J. D. (2006) MPI-DING reference glasses for in situ microanalysis: New reference values for element concentrations and isotope ratios. *Geochemistry Geophysics Geosystems* **7**.

JOLLIFF B. L., GILLIS J. J., HASKIN L. A., KOROTEV R. L. and WIECZOREK M. A. (2000) Major lunar crustal terranes: Surface expressions and crust-mantle origins. *J. Geophys. Res.* **105**.

JOLLIFF B. L. and HASKIN L. A. (1995) Cogenetic rock fragments from a lunar soil: Evidence of a ferroan noritic-anorthosite pluton on the Moon. *Geochimica et Cosmochimica Acta* **59**(11), 2345-2374.

JONES E. M. and GLOVER K. (1995) Apollo Lunar Surface Journal: A Visit with the Snowman.

JOURDAN F., ANDREOLI M. A. G., MCDONALD I. and MAIER W. D. (2010) 40Ar/39Ar thermochronology of the fossil LL6-chondrite from the Morokweng crater, South Africa. *Geochimica et Cosmochimica Acta* **74**(5), 1734-1747.

JOURDAN F., MARZOLI A., BERTRAND H., CIRILLI S., TANNER L. H., KONTAK D. J., MCHONE G., RENNE P. R. and BELLIENI G. (2009) 40Ar/39Ar ages of CAMP in North America: Implications for the Triassic-Jurassic boundary and the 40K decay constant bias. *Lithos* **110**(1-4), 167-180.

JOURDAN F. and RENNE P. R. (2007) Age calibration of the Fish Canyon sanidine 40Ar/39Ar dating standard using primary K-Ar standards. *Geochimica et Cosmochimica Acta* **71**(2), 387-402.

JOURDAN F., VERATI C. and FÉRAUD G. (2006) Intercalibration of the Hb3gr 40Ar/39Ar dating standard. *Chemical Geology* **231**(3), 177-189.

KALLEMEYN G. W., RUBIN A. E. and WASSON J. T. (1991) The compositional classification of chondrites: V. The Karoonda (CK) group of carbonaceous chondrites. *Geochimica et Cosmochimica Acta* **55**(3), 881-892.

- (1994) The compositional classification of chondrites: VI. The CR carbonaceous chondrite group. *Geochimica et Cosmochimica Acta* **58**(13), 2873-2888.

KALLIO A. (2007) LAB-RAT. In *On the Geochemistry and Cosmochemistry of Rubidium and Cesium*. Ph.D Thesis. Research School of Earth Sciences, Australian National University.

KELLER L. P. and MCKAY D. S. (1991) Analytical Electron Microscopy of Fine-Grained Glass Spheres in Apollo 16 Soil 61181 (abstact). *Abstracts of the Lunar and Planetary Science Conference* **22**, 703.

- (1992) Micrometer-sized glass spheres in Apollo 16 soil 61181 - Implications for impact volatilization and condensation. In *Lunar and Planetary Science Conference*, pp. 137-141. Lunar and Planetary Institute, Houston, Texas.

- (1993) Discovery of Vapor Deposits in the Lunar Regolith. *Science* **261**(5126), 1305-1307.

- (1997) The nature and origin of rims on lunar soil grains. *Geochimica et Cosmochimica Acta* **61**(11), 2331-2341.

KELLEY S. (1995) Ar-Ar Dating by Laser Microprobe. In *Microprobe Techniques in the Earth Sciences* (eds. P. Potts, J. Bowles, S. Reed and M. Cave), pp. 327-358. Chapman & Hall.

KELLEY S., TURNER G., BUTTERFIELD A. W. and SHEPHERD T. J. (1986) The source and significance of argon isotopes in fluid inclusions from areas of mineralization. *Earth and Planetary Science Letters* **79**(3-4), 303-318.

KEMPA M. J., PAPIKE J. J. and WHITE C. (1980) The Apollo 16 regolith - A petrographically-constrained chemical mixing model. In *11th Lunar and Planetary Science Conference*, pp. 1341-1355. Pergamon Press, Houston, Texas.

KITA N. T., USHIKUBO T., FU B. and VALLEY J. W. (2009) High precision SIMS oxygen isotope analysis and the effect of sample topography. *Chemical Geology* **264**(1-4), 43-57.

KLÖCK W., FLYNN G. J., SUTTON S. R., BAJT S. and NEUKING K. (1994) Heating Experiments Simulating Atmospheric Entry of Micrometeorites (abstract). In *25th Lunar and Planetary Science Conference*, pp. 713, Houston, Texas.

KOEBERL C. and HAGEN E. H. (1989) Extraterrestrial spherules in glacial sediment from the Transantarctic Mountains, Antarctica: Structure, mineralogy, and chemical composition. *Geochimica et Cosmochimica Acta* **53**(4), 937-944.

KOPPERS A. A. P. (2002) ArArCALC v2.4--software for 40Ar/39Ar age calculations. *Computers & Geosciences* **28**(5), 605-619.

KOROCHANTSEVA E. V., TRIELOFF M., LORENZ C. A., BUYKIN A. I., IVANOVA M. A., SCHWARZ W. H., HOPP J. and JESSBERGER E. K. (2007) L-chondrite asteroid breakup tied to Ordovician meteorite shower by multiple isochron 40Ar-39Ar dating. *Meteoritics & Planetary Science* **42**, 113-130.

KOROTEV R. (1997) Some things we can infer about the Moon from the composition of the Apollo 16 regolith. *Meteorit. Planet. Sci.* **32**, 447-478.

KOROTEV R. L. (1981) Compositional trends in Apollo 16 soils. In *12th Lunar and Planetary Science Conference*, pp. 577-605. Pergamon Press, Houston, Texas.

- (1982) Comparative geochemistry of Apollo 16 surface soils and samples from cores 64002 and 60002 through 60007. In *13th Lunar and Planetary Science Conference*, pp. A269-A278, Houston, Texas.

- (1994) Compositional variation in Apollo 16 impact-melt breccias and inferences for the geology and bombardment history of the Central Highlands of the Moon. *Geochimica et Cosmochimica Acta* **58**(18), 3931-3969.

- (1996) On the Relationship between the Apollo 16 Ancient Regolith Breccias and Feldspathic Fragmental Breccias, and the Composition of the Prebasin Crust in the Central Highlands of the Moon. *Meteoritics and Planetary Science Supplement* **31**, 403-412.

- (2001) On the Systematics of Lunar Regolith Compositions (abstract). In *32nd Annual Lunar and Planetary Science* Houston, Texas.

KOROTEV R. L., JOLLIFF B. L., ZEIGLER R. A., GILLIS J. J. and HASKIN L. A. (2003) Feldspathic lunar meteorites and their implications for compositional remote sensing of the lunar surface and the composition of the lunar crust. *Geochimica et Cosmochimica Acta* **67**(24), 4895-4923.

KOROTEV R. L. and KREMSER D. T. (1992) Compositional variations in Apollo 17 soils and their relationship to the geology of the Taurus-Littrow site. In *Proceedings of Lunar and Planetary Science*, pp. 275-301. Lunar and Planetary Institute, Houston, Texas.

KOROTEV R. L. and MORRIS R. V. (1993) Composition and maturity of Apollo 16 regolith core 60013/14. *Geochimica et Cosmochimica Acta* **57**(19), 4813-4826.

KOROTEV R. L., MORRIS R. V., JOLLIFF B. L. and SCHWARZ C. (1997) Lithological variation with depth and decoupling of maturity parameters in Apollo 16 regolith core 68001/2. *Geochimica et Cosmochimica Acta* **61**(14), 2989-3002.

KOROTEV R. L., MORRIS R. V. and LAUER H. V., JR. (1984) Stratigraphy and Geochemistry of the Stone Mountain Core (64001/2). *J. Geophys. Res.* **89**(S1), C143-C160.

KOROTEV R. L., ZEIGLER R. A. and FLOSS C. (2010) On the origin of impact glass in the Apollo 16 regolith. *Geochimica et Cosmochimica Acta* **74**(24), 7362-7388

KRINOV E. L. (1959) Über die Natur der Mikrometeoriten. *Chemie der Erde - Geochemistry* **20**, 28-35.

KURAT G. and KEIL K. (1972) Effects of vaporization and condensation on Apollo 11 glass spherules: implications for cooling rates. *Earth and Planetary Science Letters* **14**(1), 7-13.

KURAT G., KOEBERL C., PRESPER T., BRANDSTATTER F. and MAURETTE M. (1994) Petrology and geochemistry of Antarctic micrometeorites. *Geochimica et Cosmochimica Acta* **58**(18), 3879-3904.

LANGEVIN Y. and ARNOLD J. R. (1977) The Evolution of the Lunar Regolith. *Annual Review of Earth and Planetary Sciences* **5**(1), 449-489.

LAWRENCE D. J., ELPHIC R. C., FELDMAN W. C., PRETTYMAN T. H., GASNAULT O. and MAURICE S. (2003) Small-area thorium features on the lunar surface. *J. Geophys. Res.* **108**(E9), 5102.

LAWRENCE D. J., FELDMAN W. C., ELPHIC R. C., LITTLE R. C., PRETTYMAN T. H., MAURICE S., LUCEY P. G. and BINDER A. B. (2002) Iron abundances on the lunar surface as measured by the Lunar Prospector gamma-ray and neutron spectrometers. *J. Geophys. Res.* **107**(E12), 5130.

LEVINE J. (2004) Lunar glass spherules as probes of the meteoroid impact history of the Moon. Ph.D. thesis. University of California, Berkeley.

LEVINE J., BECKER T. A., MULLER R. A. and RENNE P. R. (2005) $^{40}Ar/^{39}Ar$ dating of Apollo 12 impact spherules *Geophysical Research Letters* **32**(15), L15201.

LEVINE J., MULLER R. A., RENNE P. R. and ROHDE R. A. (2006) Potassium and Calcium in Lunar Impact Spherules (abstract). In *37th Annual Lunar and Planetary Science Conference*. Lunar and Planetary Institute, Houston, Texas.

LEVINE J., RENNE P. R. and MULLER R. A. (2007) Solar and cosmogenic argon in dated lunar impact spherules. *Geochimica et Cosmochimica Acta* **71**(6), 1624.

LINDSTROM M. M. and LINDSTROM D. J. (1986) Lunar Granulites and Their Precursor Anorthositic Norites of the Early Lunar Crust. *J. Geophys. Res.* **91**(B4), D263-D276.

LINDSTROM M. M. and SALPAS P. A. (1981) Geochemical studies of rocks from North Ray Crater, Apollo 16. In *12th Lunar and Planetary Science Conference*, pp. 305-322. Pergamon Press, Houston Texas.

- (1983) Geochemical studies of feldspathic fragmental breccias and the nature of North Ray Crater ejecta. *J. Geophys. Res.* **88**(S2), A671-A683.

LINEWEAVER C. H. and NORMAN M. D. (2009) The Bombardment History of the Moon and the Origin of Life on Earth. In *8th Australian Space Science Conference* (eds. W. Short and I. Cairns). National Space Society of Australia Ltd, Canberra.

LIU Y., TAYLOR L. A., THOMPSON J. R., SCHNARE D. W. and PARK J.-S. (2007) Unique properties of lunar impact glass: Nanophase metallic Fe synthesis. *American Mineralogist* **92**(8-9), 1420-1427.

LOEFFLER M. J., BARAGIOLA R. A. and MURAYAMA M. (2008) Laboratory simulations of redeposition of impact ejecta on mineral surfaces. *Icarus* **196**(1), 285-292.

LOFGREN G. (1989) Dynamic cyrstallization of chondrule melts of porphyritic olivine composition: Textures experimental and natural. *Geochimica et Cosmochimica Acta* **53**(2), 461-470.

LOFGREN G. and RUSSELL W. J. (1986) Dynamic crystallization of chondrule melts of porphyritic and radial pyroxene composition. *Geochimica et Cosmochimica Acta* **50**(8), 1715-1726.

LOVE S. G. and BROWNLEE D. E. (1991) Heating and thermal transformation of micrometeoroids entering the Earth's atmosphere. *Icarus* **89**(1), 26-43.

- (1993) A Direct Measurement of the Terrestrial Mass Accretion Rate of Cosmic Dust. *Science* **262**(5133), 550-553.

LUCEY P., KOROTEV R. L., GILLIS J. J., TAYLOR L. A., LAWRENCE D., CAMPBELL B. A., ELPHIC R., FELDMAN B., HOOD L. L., HUNTEN D., MENDILLO M., NOBLE S., PAPIKE J. J., REEDY R. C., LAWSON S., PRETTYMAN T., GASNAULT O. and MAURICE S. (2006) New Views of Lunar Geoscience: Understanding the Lunar Surface and Space-Moon Interactions. In *New Views of the Moon* (eds. B. L. Jolliff, M. Wieczorek, C. K. Shearer and C. Neal), pp. 83-219.

LUCEY P. G., BLEWETT D. T. and JOLLIFF B. L. (2000) Lunar iron and titanium abundance algorithms based on final processing of Clementine ultraviolet-visible images. *J. Geophys. Res.* **105**(E8), 20297-20305.

LUDWIG K. R. (2006) Isoplot/Ex v3.50--Excel Addin for manipulation and plotting of radiogenic isotope data.

MA M.-S., SCHMITT R. A., TAYLOR G. J., WARNER R. D., LANGE D. E. and KEIL K. (1977) Chemistry and petrology of Luna 24 lithic fragments and less than 250-micron soils - Constraints on the origin of VLT mare basalts. In *Mare Crisium: The view from Luna 24* (eds. R. B. Merrill and J. J. Papike), pp. 569-592. Pergamon Press, Inc., Houston, Texas.

MADEY T. E., YAKSHINSKIY B. V., AGEEV V. N. and JOHNSON R. E. (1998) Desorption of alkali atoms and ions from oxide surfaces: Relevance to origins of Na and K in atmospheres of Mercury and the Moon. *J. Geophys. Res.* **103**.

MANKA R. H. and MICHEL F. C. (1970) Lunar Atmosphere as a Source of Argon-40 and Other Lunar Surface Elements. *Science* **169**(3942), 278-280.

MAURETTE M. (2006) *Micrometeorites and the Mysteries of Our Origins*. Springer. pp. 330.

MAURETTE M., DUPRAT J., ENGRAND C., GOUNELLE M., KURAT G., MATRAJT G. and TOPPANI A. (2000) Accretion of neon, organics, CO2, nitrogen and water from large interplanetary dust particles on the early Earth. *Planetary and Space Science* **48**(11), 1117-1137.

MAURETTE M., HAMMER C., REEH N., BROWNLEE D. E. and THOMSEN H. H. (1986) Placers of Cosmic Dust in the Blue Ice Lakes of Greenland. *Science* **233**(4766), 869-872.

MAURETTE M., JEHANNO C., ROBIN E. and HAMMER C. (1987) Characteristics and mass distribution of extraterrestrial dust from the Greenland ice cap. *Nature* **328**(6132), 699-702.

MAURETTE M., OLINGER C., MICHEL-LEVY M. C., KURAT G., POURCHET M., BRANDSTATTER F. and BOUROT-DENISE M. (1991) A collection of diverse micrometeorites recovered from 100 tonnes of Antarctic blue ice. *Nature* **351**(6321), 44-47.

MCDOUGALL I. and HARRISON T. M. (1988) *Geochronology and Thermochronology by the $^{40}Ar/^{39}Ar$ Method*. Oxford University Press. pp. 212.

- (1999) *Geochronology and Thermochronology by the $^{40}Ar/^{39}Ar$ Method*. Oxford University Press. pp. 212.
MCKAY D. S., HEIKEN G., BASU A., BLANFORD G., SIMON S., REEDY R., FRENCH B. M. and PAPIKE J. (1991) The Lunar Regolith. In *Lunar Sourcebook: A User's Guide to the Moon* (eds. G. Heiken, D. T. Vaniman and B. M. French), pp. 285-356. Cambridge University Press.
MCKAY G. A., KRIDELBAUGH S. J. and WEILL D. F. (1973) The occurrence and origin of schreibersite-kamacite intergrowths in microbreccia 66055. *Proceedings of the Lunar Science Conference* **4**, 811.
MCSWEEN H. Y. and RICHARDSON S. M. (1977) The composition of carbonaceous chondrite matrix. *Geochimica et Cosmochimica Acta* **41**(8), 1145-1161.
MELOSH H. J. (1982) A schematic model of crater modification by gravity. *Journal of Geophysical Research (Solid Earth)* **87**(B1), 371–380.
- (1989) *Impact Cratering - A Geologic Process*. Oxford University Press.
MENDELL W. W. and MCKAY D. S. (1975) A lunar soil evolution model. *Earth, Moon, and Planets* **13**(1), 285-292.
MEYER C., JR. (1978) Ion microprobe analyses of aluminous lunar glasses: A test of the "rock type" hypothesis. *Proceedings of the 9th Lunar and Planetary Science Conference*, 1551-1570.
MEYER H. O. A. and TSAI H.-M. (1975) Lunar glass compositions: Apollo 16 core sections 60002 and 60004. *Earth and Planetary Science Letters* **28**(2), 234.
MIN K., MUNDIL R., RENNE P. R. and LUDWIG K. R. (2000) A test for systematic errors in 40Ar/39Ar geochronology through comparison with U/Pb analysis of a 1.1-Ga rhyolite - Age, isotopic disturbances, and the tectonic evolution of western Gondwanaland. *Geochimica et Cosmochimica Acta* **64**, 73-98.
MORRIS R. V., SEE T. H. and HÖRZ F. (1986) Composition of the Cayley formation at Apollo 16 as inferred from Impact Melt Splashes. *Journal of Geophysical Research* **91**(B13), E21-E42.
MUEHLBERGER W. R., HÖRZ F., SEVIER J. R. and ULRICH G. E. (1980) Mission objectives for geological exploration of the Apollo 16 landing site. In *Conference on the Lunar Highlands Crust* (eds. R. B. Merrill and J. J. Papike), pp. 1-49. Pergamon Press, Houston, Texas.
MUELLER G. and HINSCH G. W. (1970) Glassy Particles in Lunar Fines. *Nature* **228**(5268), 254-258.
MURRAY J. and RENARD A. F. (1891) Report on the Deep-Sea deposits Based on the Specimens Collected During the Voyage. In *Report on the scientific results of the H.M.S. "Challenger" during the years 1873-76, Deep-Sea Deposits*.
NANEY M. T., CROWL D. M. and PAPIKE J. J. (1976) The Apollo 16 drill core - Statistical analysis of glass chemistry and the characterization of a high alumina-silica poor (HASP) glass. In *7th Lunar Science Conference*, pp. 155-184. Pergamon Press, Inc., Houston, Texas.
NASA, JSC and ARIZONA STATE UNIVERSITY (2008) Image of the Week - 12/30/2008: Exploring the Lunar Highlands pp. http://apollo.sese.asu.edu/LIW/20081230.html.
NEAL C. R. and TAYLOR L. A. (1992) Petrogenesis of mare basalts: A record of lunar volcanism. *Geochimica et Cosmochimica Acta* **56**(6), 2177-2211.

NEUKUM G. (1977) Different ages of lunar light plains. *Earth, Moon, and Planets* **17**(4), 383-393.
- (1983) Meteoritenbombardement and Datierung Planetarer Oberflächen. University of Munich.
NEUKUM G., IVANOV B. A. and HARTMANN W. K. (2001) Cratering Records in the Inner Solar System in Relation to the Lunar Reference System. *Space Science Reviews* **96**(1), 55-86.
NEUKUM G., KÖNIG B. and ARKANI-HAMED J. (1975) A study of lunar impact crater size-distributions. *Earth, Moon, and Planets* **12**(2), 201-229.
NITKIEWICZ A. and STERNER S. M. (1988) An improved Bond air mill for the preparation of spherical single crystals. *American Mineralogist* **73**(5-6), 662-666.
NORMAN M., ROBINSON P. and CLARK D. (2003a) Major and Trace Element Analysis of Sulfide Ores by Laser-Ablation ICP–MS, Solution ICP–MS, and XRF: New Data on International Reference Materials. *The Canadian Mineralogist* **41**, 293-305.
NORMAN M. D. (1981) Petrology of suevitic lunar breccia 67016. In *Proceedings of the 12th Lunar and Planetary Science Conference*, pp. 235-252. Pergamon Press, Houston, Texas.
- (2009) The Lunar Cataclysm: Reality or "Mythconception"? *ELEMENTS* **5**(1), 23-28.
NORMAN M. D., BORG L. E., NYQUIST L. E. and BOGARD D. D. (2003b) Chronology, geochemistry, and petrology of a ferroan noritic anorthosite clast from Descartes breccia 67215: Clues to the age, origin, structure, and impact history of the lunar crust. *Meteoritics & Planetary Science* **38**, 645-661.
NORMAN M. D., DUNCAN R. A. and HUARD J. J. (2006) Identifying impact events within the lunar cataclysm from 40Ar-39Ar ages and compositions of Apollo 16 impact melt rocks. *Geochimica et Cosmochimica Acta* **70**(24), 6032-6049.
- (2010) Imbrium provenance for the Apollo 16 Descartes terrain: Argon ages and geochemistry of lunar breccias 67016 and 67455. *Geochimica et Cosmochimica Acta* **74**(2), 763-783.
NORMAN M. D., GARCIA M. O. and BENNETT V. C. (2004) Rhenium and chalcophile elements in basaltic glasses from Ko'olau and Moloka'i volcanoes: Magmatic outgassing and composition of the Hawaiian plume. *Geochimica et Cosmochimica Acta* **68**(18), 3761-3777.
NORMAN M. D., PEARSON N. J., SHARMA A. and GRIFFIN W. L. (1996) Quantitative Analysis of Trace Elements in Geological Materials by Laser Ablation ICPMS: Instrumental Operating Conditions and Calibration Values of NIST Glasses. *Geostandards and Geoanalytical Research* **20**(2), 247-261.
NORMAN M. D. and RYDER G. (1980) Geochemical constraints on the igneous evolution of the lunar crust. In *11th Lunar and Planetary Science Conference*, pp. 317-331. Pergamon Press, Houston, Texas.
NORRIS J. A., KELLER L. P. and MCKAY D. S. (1992) Impact glasses from the less than 20-micrometer fraction of Apollo 17 soils 72501 and 78221 In *LPI Technical Report*, pp. 44-45 Lunar and Planetary Institute
- (1993) Impact glasses from the ultrafine fraction of lunar soils. *Twenty-Fourth Lunar and Planetary Science Conference. Part 3: N-Z*, 1093-1094.

NOZAKI W., NAKAMURA T., IIDA A., MATSUOKA K. and TAKAOKA N. (1998) Trace element concentrations in iron type cosmic spherules determined by the SR-XRF method. In *Twenty-third Symposium on Antarctic Meteorites, NIPR Symposium* (ed. T. Hirasawa), pp. 199. National Institute of Polar Research, National Institute of Polar Research, Tokyo.

NYQUIST L. E., BANSAL B. M., WOODEN J. L. and WIESMANN H. (1977) Sr-isotopic constraints on the petrogenesis of Apollo 12 mare basalts. In *8th Lunar Science Conference*, pp. 1383-1415. Pergamon Press, Inc., Houston, Texas.

NYQUIST L. E. and SHIH C. Y. (1992) The isotopic record of lunar volcanism. *Geochimica et Cosmochimica Acta* **56**(6), 2213-2234.

NYQUIST L. E., SHIH C. Y., BANSAL B. M., WOODEN J. L. and WIESMANN H. (1979) The SR and Nd isotopic record of Apollo 12 basalts - Implications for lunar geochemical evolution. In *10th Lunar Science Conference*, pp. 77-114. Pergamon Press, Inc., Houston, Texas.

OBERBECK V. R. (1975) The Role of Ballistic Erosion and Sedimentation in Lunar Stratigraphy. *Rev. Geophys.* **13**(2), 337-362.

PAPIKE J. J., RYDER G. and SHEARER C. K. (1998) Lunar samples. *Reviews in Mineralogy and Geochemistry* **36**(1), 5.1-5234.

PAPIKE J. J., SIMON S. B. and LAUL J. C. (1982) The lunar regolith: Chemistry, mineralogy, and petrology. *Rev. Geophys.* **20**(4), 761-826.

PERKINS W. and PEARCE N. (1995) Chapter 7: Mineral Microanalysis by laserprobe inductively coupled plasma mass spectrometry. In *Microprobe Techniques in the Earth Sciences* (eds. P. Potts, J. Bowles, S. Reed and M. Cave), pp. 291-325. Chapman & Hall.

PETRO N. E. and PIETERS C. M. (2006) Modeling the provenance of the Apollo 16 regolith. *Journal of Geophysical Research* **111**, E09005.

PIDGEON R. T., NEMCHIN A. A., VAN BRONSWIJK W., GEISLER T., MEYER C., COMPSTON W. and WILLIAMS I. S. (2007) Complex history of a zircon aggregate from lunar breccia 73235. *Geochimica et Cosmochimica Acta* **71**(5), 1370-1381.

PIETERS C. M., FISCHER E. M., RODE O. and BASU A. (1993) Optical Effects of Space Weathering: The Role of the Finest Fraction. *J. Geophys. Res.* **98**(E11), 20817-20824.

PRETTYMAN T. H., HAGERTY J. J., ELPHIC R. C., FELDMAN W. C., LAWRENCE D. J., MCKINNEY G. W. and VANIMAN D. T. (2006) Elemental composition of the lunar surface: Analysis of gamma ray spectroscopy data from Lunar Prospector. *J. Geophys. Res.* **111**.

PUGH M. J. (1972) Rotation of Lunar Dumbbell-shaped Globules during Formation. *Nature* **237**(5351), 158-159.

RAISBECK G. M. and YIOU F. (1989) Cosmic ray exposure ages of cosmic spherules. *Meteoritics and Planetary Science* **24**, 318.

RASBAND W. S. (1997-2008) ImageJ, http://rsb.info.nih.gov/ij/. National Institutes of Health, Bethesda, Maryland, USA.

REED S. (1995) Electron Probe Microanalysis. In *Microprobe Techniques in the Earth Sciences* (eds. P. Potts, J. Bowles, S. Reed and M. Cave), pp. 49-139. Chapman & Hall.

REED S. J. B. (1993) *Electron microprobe analysis*. Cambridge University Press.

REEDY R. C., ARNOLD J. R. and LAL D. (1983) Cosmic-Ray Record in Solar System Matter. *Science* **219**(4581), 127-135.

REID A. M., RIDLEY W. I., HARMON R. S., WARNER J., BRETT R., JAKES P. and BROWN R. W. (1972a) Highly aluminous glasses in lunar soils and the nature of the lunar highlands. *Geochimica et Cosmochimica Acta* **36**(8), 903-912.

REID A. M., WARNER J., RIDLEY W. I. and BROWN R. W. (1972b) Major Element Composition of Glasses in Three Apollo 15 Soils. *Meteoritics and Planetary Science* **7**(3), 395-415.

REID A. M., WARNER J., RIDLEY W. I., JOHNSTON D. A., HARMON R. S., JAKEŠ P. and BROWN R. W. (1972c) The major element compositions of lunar rocks as inferred from glass compositions in the lunar soils. In *Proceedings of the Lunar Science Conference*, pp. 363-378.

RHODES J. M., BRANNON J. C., RODGERS K. V., BLANCHARD D. P. and DUNGAN M. A. (1977) Chemistry of Apollo 12 mare basalts - Magma types and fractionation processes. In *8th Lunar Science Conference*, pp. 1305-1338. Pergamon Press, Inc., Houston, Texas.

RICHARDSON J. E. (2009) Cratering saturation and equilibrium: A new model looks at an old problem. *Icarus* **204**(2), 697-715.

RIDLEY W. I., REID A. M., WARNER J. L., BROWN R. W., GOOLEY R. and DONALDSON C. (1973) Glass compositions in Apollo 16 soils 60501 and 61221. In *4th Lunar Science Conference*, pp. 309-321.

ROBERTS A. and WITHERS P. (2007) StatistiXL. http://www.statistixl.com/default.aspx.

ROBIN E. (1988) Des poussieres cosmique dans les cryoconites du Groenland: Nature, origine et applications. Ph.D. thesis. Universite de Paris-Sud.

ROBIN E., CHRISTOPHE MICHEL-LEVY N., BOUROT-DENISE M. and JEHANNO C. (1990) Crystalline micrometeorites from Greenland blue lakes: their chemical composition, mineralogy and possible origin. *Earth and Planetary Science Letters* **97**(1-2), 162-176.

ROBIN E., JEHANNO C. and MAURETTE M. (1987) Characteristics and origin of Greenland Fe/Ni cosmic grains. In *18th Lunar and Planetary Science Conference*, pp. 593-598, Houston, Texas.

ROBINSON M. S. and JOLLIFF B. L. (2002) Apollo 17 landing site: Topography, photometric corrections, and heterogeneity of the surrounding highland massifs. *J. Geophys. Res.* **107**(E11), 5110.

ROCHETTE P., FOLCO L., SUAVET C., VAN GINNEKEN M., GATTACCECA J., PERCHIAZZI N., BRAUCHER R. and HARVEY R. P. (2008) Micrometeorites from the Transantarctic Mountains. *Proceedings of the National Academy of Sciences* **105**(47), 18206-18211.

RODDICK J. C. (1983) High precision intercalibration of 40Ar-39Ar standards. *Geochimica et Cosmochimica Acta* **47**(5), 887-898.

RYDER G. (1990) Lunar samples, lunar accretion and the early bombardment of the moon. *EOS Transactions* **71**, 313.

- (2002) Mass flux in the ancient Earth-Moon system and benign implications for the origin of life on Earth. *Journal of Geophysical Research (Planets)* **107**(E4), 13.

SANCHEZ A. (1981) Geology of Stone Mountain. In *Geology of the Apollo 16 Area, Central Lunar Highlands* (eds. G. E. Ulrich, C. A. Hodges and W. R. Muehlberger), pp. 539. National Aeronautics and Space Administration.

SASAKI S., KURAHASHI E., YAMANAKA C. and NAKAMURA K. (2003) Laboratory simulation of space weathering: Changes of optical properties and TEM/ESR confirmation of nanophase metallic iron. *Advances in Space Research* **31**(12), 2537-2542.

SASAKI S., NAKAMURA K., HAMABE Y., KURAHASHI E. and HIROI T. (2001) Production of iron nanoparticles by laser irradiation in a simulation of lunar-like space weathering. *Nature* **410**(6828), 555-557.

SCARLETT B., BUXTON R. E. and FAULKNER R. G. (1977) Formation of Glass Spheres on the Lunar Surface. *Philosophical Transactions of the Royal Society of London. Series A, Mathematical and Physical Sciences* **285**(1327), 279-284.

SEE T. H., HÖRZ F. and MORRIS R. V. (1986) Apollo 16 Impact-Melt Splashes: Petrography and Major-Element Composition. *J. Geophys. Res.* **91**.

SHEARER C. K. and PAPIKE J. J. (1993) Basaltic magmatism on the Moon: A perspective from volcanic picritic glass beads. *Geochimica et Cosmochimica Acta* **57**(19), 4785.

SHIMIZU N. and HART S. R. (1982) Applications of the Ion Microprobe to Geochemistry and Cosmochemistry. *Annual Review of Earth and Planetary Sciences* **10**(1), 483.

SHOEMAKER E. M., HAIT M. H., SWANN G. A., SCHLEICHER D. L., SCHABER G. G., SUTTON R. L., DAHLEM D. H., GODDARD E. N. and WATERS A. C. (1970) Origin of the lunar regolith at Tranquillity Base. In *Proceedings of the Apollo 11 Lunar Science Conference*, pp. 2399-2412.

SPANGLER R. R. and DELANO J. W. (1984) History of the Apollo 15 yellow impact glass and sample 15426 and 15427 *Journal of Geophysical Research, Supplement* **89**, B478-B486.

SPRAGUE A. L., KOZLOWSKI R. W. H., HUNTEN D. M., WELLS W. K. and GROSSE F. A. (1992) The sodium and potassium atmosphere of the moon and its interaction with the surface. *Icarus* **96**(1), 27-42.

SPUDIS P. D. (1984) Apollo 16 site geology and impact melts - Implications for the geologic history of the lunar highlands. In *15th Lunar and Planetary Science Conference*, pp. C95-C107, Houston, Texas.

STEIGER R. H. and JÄGER E. (1977) Subcommission on geochronology: Convention on the use of decay constants in geo- and cosmochronology. *Earth and Planetary Science Letters* **36**(3), 359-362.

STÖFFLER D., BISCHOFF A., BORCHARDT R., BURGHELE A., DEUTSCH A., JESSBERGER E. K., OSTERTAG R., PALME H., SPETTEL B., REIMOLD W. U., WACKER K. and WANKE H. (1985) Composition and evolution of the lunar crust in the Descartes highlands, Apollo 16. In *15th Lunar and Planetary Science Conference*, pp. C449-C506, Houston, Texas.

STÖFFLER D. and RYDER G. (2001) Stratigraphy and Isotope Ages of Lunar Geologic Units: Chronological Standard for the Inner Solar System. *Space Science Reviews* **96**(1), 9-54.

STÖFFLER D., RYDER G., IVANOV B. A., ARTEMIEVA N., CINTALA M. and GRIEVE R. (2006) Cratering History and Lunar Chronology. In *New Views of the Moon* (eds. B. L. Jolliff, M. A. Wieczorek, C. K. Shearer and C. R. Neal), pp. 519-596.

STROM R. G., CROFT S. K. and BARLOW N. G. (1992) The Martian impact cratering record. In *Mars*, pp. 383-423.

STROM R. G., MALHOTRA R., ITO T., YOSHIDA F. and KRING D. A. (2005) The Origin of Planetary Impactors in the Inner Solar System. *Science* **309**(5742), 1847-1850.

STROM R. G. and NEUKUM G. (1988) The cratering record on Mercury and the origin of impacting objects. In *Mercury*, pp. 336-373.

STRUCTURE PROBE INC. (2009) Crystalbond™ and Wafer-mount™ Mounting Adhesives, pp. http://www.2spi.com/catalog/mounts/crystalbond-wafer-mount.shtml.

SUAVET C., ALEXANDRE A., FRANCHI I. A., GATTACCECA J., SONZOGNI C., GREENWOOD R. C., FOLCO L. and ROCHETTE P. (2010) Identification of the parent bodies of micrometeorites with high-precision oxygen isotope ratios. *Earth and Planetary Science Letters* **293**(3-4), 313-320.

SUTTON R. L., HAIT M. H. and SWANN G. A. (1972) Geology of the Apollo 14 landing site. In *Proceedings of the Lunar Science Conference*, pp. 27.

SWINDLE T. D., ISACHSEN C. E., WEIRICH J. R. and KRING D. A. (2009) 40Ar-39Ar ages of H-chondrite impact melt breccias. *Meteoritics & Planetary Science* **44**(5), 747-762.

SYMES S. J. K., SEARS D. W. G., TAUNTON A., AKRIDGE D. G., HUANG S. and BENOIT P. H. (1998) The crystalline lunar spherules: Their formation and implications for the origin of meteoritic chondrules. *Meteoritics and Planetary Science* **33**(1), 13-29.

TAYLOR G. J., WARREN P., RYDER G., DELANO J., PIETERS C. and LOFGREN G. (1991) Lunar Rocks. In *Lunar Sourcebook: A User's Guide to the Moon* (eds. G. Heiken, D. T. Vaniman and B. M. French), pp. 183-284. Cambridge University Press.

TAYLOR S., ALEXANDER C. M. O. D., DELANEY J., MA P., HERZOG G. F. and ENGRAND C. (2005a) Isotopic fractionation of iron, potassium, and oxygen in stony cosmic spherules: Implications for heating histories and sources. *Geochimica et Cosmochimica Acta* **69**(10), 2647-2662.

TAYLOR S., HERZOG G. F. and DELANEY J. S. (2007) Crumbs from the crust of Vesta: Achondritic cosmic spherules from the South Pole water well. *Meteoritics & Planetary Science* **42**(2), 223-233.

TAYLOR S., LEVER J. H. and HARVEY R. P. (1998) Accretion rate of cosmic spherules measured at the South Pole. *Nature* **392**(6679), 899.

- (2000) Numbers, types, and compositions of an unbiased collection of cosmic spherules. *Meteoritics & Planetary Science* **35**(4), 651-666.

TAYLOR S., MATRAJT G., LEVER J. H., JOSWIAK D. J. and BROWNLEE D. E. (2005b) Size Distribution of Antarctic Micrometeorites. In *Dust in Planetary Systems*, pp. 145-148. European Space Agency Publications, Kauai, Hawaii.

TERA F., PAPANASTASSIOU D. A. and WASSERBURG G. J. (1974) Isotopic evidence for a terminal lunar cataclysm. *Earth and Planetary Science Letters* **22**(1), 1-21.

TURNER G. (1971) $^{40}Ar/^{39}Ar$ ages from the lunar maria. *Earth and Planetary Science Letters* **11**(1-5), 169-191.

TURNER G. and CADOGAN P. H. (1975) The history of lunar bombardment inferred from Ar-40-Ar-39 dating of highland rocks. In *6th Lunar Science Conference*, pp. 1509-1538. Pergamon Press, Inc., Houston, Texas.

TURNER G., CADOGAN P. H. and YONGE C. J. (1973) Argon selenochronology. In *Proceedings of the Lunar Science Conference*, pp. 1889-1914.

TURNER G., HUNEKE J. C., PODOSEK F. A. and WASSERBURG G. J. (1971) 40Ar-39Ar ages and cosmic ray exposure ages of Apollo 14 samples. *Earth and Planetary Science Letters* **12**(1), 19-35.

UHLMANN D. R. (1972) A kinetic treatment of glass formation. *Journal of Non-Crystalline Solids* **7**(4), 337-348.

ULRICH G. E. (1973) A geologic model for North Ray Crater and stratigraphic implications for the Descartes region. In *4th Lunar Science Conference*, pp. 27-39.

ULRICH G. E., HODGES C. A. and MUEHLBERGER W. R. (1981) Geology of the Apollo 16 Area, Central Lunar Highlands. In *Geological Survey Professional Paper 1048*, pp. 539. National Aeronautics and Space Administration.

VANIMAN D., DIETRICH J., TAYLOR G. J. and HEIKEN G. (1991) Exploration, Samples, and Recent Concepts of the Moon. In *Lunar Sourcebook: A User's Guide to the Moon* (eds. G. Heiken, D. T. Vaniman and B. M. French), pp. 4-26. Cambridge University Press.

VANIMAN D. T. (1990) Glass variants and multiple HASP trends in Apollo 14 regolith breccias. In *20th Lunar and Planetary Science Conference*, pp. 209-217, Houston, Texas.

VICKERY A. M. (1993) The Theory of Jetting: Application to the Origin of Tektites. *Icarus* **105**(2), 441-453.

WALTER J., KURAT G., BRANDSTATTER F., KOEBERL C. and MAURETTE M. (1995) The Abundance of Ordinary Chondrite Debris Among Antarctic Micrometeorites (abstract). *Meteoritics* **30**(5), 592-593.

WANG J., DAVIS A. M., CLAYTON R. N., MAYEDA T. K. and HASHIMOTO A. (2001) Chemical and isotopic fractionation during the evaporation of the FeO-MgO-SiO2-CaO-Al2O3-TiO2 rare earth element melt system. *Geochimica et Cosmochimica Acta* **65**(3), 479-494.

WARNER R. D., TAYLOR G. J. and KEIL K. (1979) Composition of glasses in Apollo 17 samples and their relation to known lunar rock types. *Proceedings of the 10th Lunar and Planetary Science Conference* **2**, 1437-1456.

WARREN P. H. (2008) Lunar rock-rain: Diverse silicate impact-vapor condensates in an Apollo-14 regolith breccia. *Geochimica et Cosmochimica Acta* **72**(14), 3562-3585.

WASSON J. T. and KALLEMEYN G. W. (1988) Compositions of Chondrites. *Philosophical Transactions of the Royal Society of London. Series A, Mathematical and Physical Sciences* **325**(1587), 535-544.

WEBER A. K., HEAD J. W., SAAL A. E., WEINREICH T. and WILSON L. (2010) Volatiles in Lunar Fire Fountaining Eruptions and the Effect of Rotation on Droplets in Free Flight. In *41st Lunar and Planetary Science Conference (abstract No. 1533)*, pp. 1208, Houston, Texas.

WENTWORTH S. J. and MCKAY D. S. (1991) Apollo 14 glasses and the origin of lunar soils. In *21st Lunar and Planetary Science Conference*, pp. 185-192, Houston, Texas.

WILHELMS D. (1987) The Geologic History of the Moon. In *US Geological Survey Professional Paper 1348*, pp. 302.

WILLIAMS D. R. (2003) Lunar Landing Site Map National Aeronautics and Space Administration, http://nssdc.gsfc.nasa.gov/planetary/lunar/moon_landing_map.jpg.

WILSHIRE H. G., STUART-ALEXANDER D. E. and JACKSON E. D. (1973) Apollo 16 Rocks: Petrology and Classification. *J. Geophys. Res.* **78**(14), 2379-2392.

WILSON S. A. (1997) The collection, preparation, and testing of USGS reference material BCR-2, Columbia River, Basalt. U.S. Geological Survey Open-File Report 98-xxx.

WINCHELL H. and SKINNER B. J. (1970) Glassy spherules from the lunar regolith returned by Apollo 11 expedition. In *Proceedings of the Apollo 11 Lunar Science Conference* (ed. A. A. Levinson), pp. 957-964. Pergammon Press, Houston, Texas.

WOOD J. A. (1970) Petrology of the Lunar Soil and Geophysical Implications. *J. Geophys. Res.* **75**(32), 6497-6513.

XUE S., HERZOG G. F., SOUZIS A., ERVIN M. H., LAREAU R. T., MIDDLETON R. and KLEIN J. (1995) Stable magnesium isotopes, ^{26}Al, ^{10}Be, and ^{26}Mg/^{26}Al exposure ages of iron meteorites. *Earth and Planetary Science Letters* **136**(3-4), 397-406.

YADA, TORU, NAKAMURA, TOMOKI, TAKAOKA, NOBUO, NOGUCHI, TAKAAKI, TERADA, KENTARO, YANO, HAJIME, NAKAZAWA, TAKAKIYO, KOJIMA and HIDEYASU (2004) *The global accretion rate of extraterrestrial materials in the last glacial period estimated from the abundance of micrometeorites in Antarctic glacier ice*. Terra, Tokyo, JAPAN. pp. 13.

YADA T. and KOJIMA H. (2000) The collection of micrometeorites in the Yamato Meteorite Ice Field of Antarctica in 1998. *Antarctic meteorite research* **13**, 9-18.

YADA T., NAKAMURA T., NOGUCHI T., MATSUMOTO N., KUSAKABE M., HIYAGON H., USHIKUBO T., SUGIURA N., KOJIMA H. and TAKAOKA N. (2005) Oxygen isotopic and chemical compositions of cosmic spherules collected from the Antarctic ice sheet: Implications for their precursor materials. *Geochimica et Cosmochimica Acta* **69**(24), 5789-5804.

YIOU F. and RAISBECK G. M. (1987) Cosmic Spherules from an Antarctic Ice Core. *Meteoritics* **22**, 539.

YIOU F., RAISBECK G. M. and BROWNLEE D. (1985) ^{10}Be in Iron Type Cosmic Spherules: Evidence for a Differentiated Parent Body. *Meteoritics* **20**, 791-792.

ZEIGLER R. A., KOROTEV R. L., JOLLIFF B. L., HASKIN L. A. and FLOSS C. (2004) Apollo 16 Mafic Glass: Geochemistry, Provenance, and Implications. In *Lunar and Planetary Science Conference XXXV*, Houston, Texas.

- (2006) The geochemistry and provenance of Apollo 16 mafic glasses. *Geochimica et Cosmochimica Acta* **70**(24), 6050-6067.

ZELLNER N. E. B., DELANO J. W., SWINDLE T. D., BARRA F., OLSEN E. and WHITTET D. C. B. (2009a) Apollo 17 regolith, 71501,262: A record of impact events and mare volcanism in lunar glasses. *Meteoritics & Planetary Science* **44**(6), 839-851.

- (2009b) Evidence from 40Ar/39Ar ages of lunar impact glasses for an increase in the impact rate ~800 Ma ago. *Geochimica et Cosmochimica Acta* **73**(15), 4590-4597.

ZELLNER N. E. B., SPUDIS P. D., DELANO J. W. and WHITTET D. C. B. (2002) Impact glasses from the Apollo 14 landing site and implications for regional geology. *Journal of Geophysical Research* **107**(E11), **12**-1 - **12**-13.

ZOLENSKY M. E., PIETERS C., CLARK B. and PAPIKE J. J. (2000) Small is Beautiful: The analysis of nanogram-sized astromaterials. *Meteoritics and Planetary Science* **35**, 9-29.